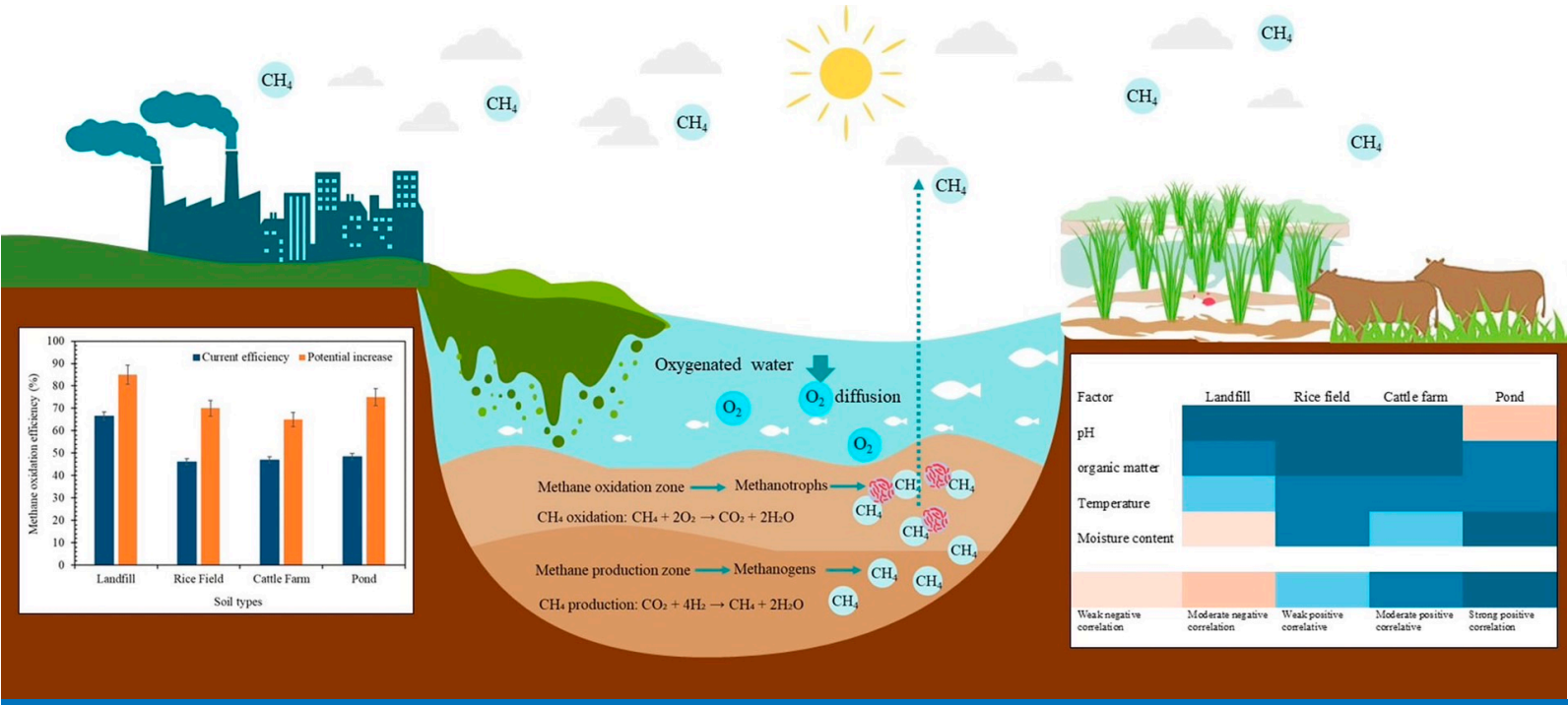
ASEAN Journal of Scientific and Technological Reports (AJSTR)

Vol. 28 No. 1, January-February 2025

Methane Oxidation Rates and Efficiencies Across Four Distinct Soil Environments: Implications for Greenhouse Gas Mitigation

Chonticha Leamdum et al.



ISSN 2773-8752 (online)

https://ph02.tci-thaijo.org/index.php/tsujournal/issue/view/17252



ASEAN
Journal of Scientific and Technological Reports
Online ISSN:2773-8752

ASEAN Journal of Scientific and Technological Reports (AJSTR)

Name ASEAN Journal of Scientific and Technological Reports (AJSTR)

Owner Thaksin University

Advisory Board Assoc. Prof. Dr. Nathapong Chitniratna
(President of Thaksin University, Thailand)
Assoc. Prof. Dr. Samak Kaewsuksaeng
(Vice President for Reserach and Innovation, Thaksin University, Thailand)
Assoc. Prof. Dr. Suttiporn Bunmak
(Vice President for Academic Affairs and Learning, Thaksin University, Thailand)
Assoc. Prof. Dr. Samak Kaewsuksaeng
(Acting Director of Reserach and Innovation, Thaksin University, Thailand)
Asst. Prof. Dr. Prasong Kessaratikoon
(Dean of the Graduate School, Thaksin University, Thailand)

Editor-in-Chief Assoc. Prof. Dr. Sompong O-Thong, Mahidol University, Thailand

Session Editors

1. Assoc. Prof. Dr. Jatuporn Kaew-On, Thaksin University, Thailand
2. Assoc. Prof. Dr. Samak Kaewsuksaeng, Thaksin University, Thailand
3. Assoc. Prof. Dr. Rattana Jariyaboon, Prince of Songkla University, Thailand
4. Asst. Prof. Dr. Noppamas Pukkhem, Thaksin University, Thailand
5. Asst. Prof. Dr. Komkrich Chokprasombat, Thaksin University, Thailand

Editorial Board Members

1. Prof. Dr. Hidenari Yasui, University of Kitakyushu, Japan
2. Prof. Dr. Jose Antonio Alvarez Bermejo, University of Almeria, Spain
3. Prof. Dr. Tjokorda Gde Tirta Nindhia, Udayana University in Bali, Indonesia
4. Prof. Dr. Tsuyoshi Imai, Yamaguchi University, Japan
5. Prof. Dr. Ullah Mazhar, The University of Agriculture, Peshawar, Pakistan
6. Prof. Dr. Win Win Myo, University of Information Technology, Myanmar
7. Prof. Dr. Yves Gagnon, University of Moncton, Canada
8. Assoc. Prof. Dr. Chen-Yeon Chu, Feng Chia University, Taiwan
9. Assoc. Prof. Dr. Gulam Murtaza, Government College University Lahore, Lahore, Pakistan
10. Assoc. Prof. Dr. Jompob Waewsak, Thaksin University, Thailand
11. Assoc. Prof. Dr. Khan Amir Sada, American University of Sharjah, Sarjah, United Arab Emirates.
12. Assoc. Prof. Dr. Sappasith Klomklao, Thaksin Univerrsity, Thailand
13. Asst. Prof. Dr. Dariusz Jakobczak, National University, Pakistan
14. Asst. Prof. Dr. Prawit Kongjan, Prince of Songkla University, Thailand
15. Asst. Prof. Dr. Shahrul Isamail, Universiti Malaysia Terengganu, Malaysia
16. Asst. Prof. Dr. Sureewan Sittijunda, Mahidol University, Thailand
17. Dr. Nasser Ahmed, Kyushu University, Fukuoka, Japan
18. Dr. Peer Mohamed Abdul, Universiti Kebangsaan Malaysia, Malaysia
19. Dr. Sriv Tharith, Royal University of Phnom Penh, Cambodia
20. Dr. Zairi Ismael Rizman, Universiti Teknologi MARA, Malaysia
21. Dr. Khwanchit Suwannoppharat, Thaksin University, Thailand

Staff: Journal Management Division

1. Miss Kanyanat Liadrak, Thaksin University, Thailand
2. Miss Ornkamon Kraiwong, Thaksin University, Thailand

Contact Us Institute of Research and Innovation, Thaksin University
222 M. 2 Ban-Prao sub-district, Pa-Pra-Yom district, Phatthalung province, Thailand
Tel. 0 7460 9600 # 7242 , E-mail: aseanjstr@tsu.ac.th

List of Contents

Efficient and Rapid Classification of Various Maize Seeds Using Transfer Learning and Advanced AI Techniques **e255200**
Hasan İbrahim Kozan, Hasan Ali AKYÜREK

Effect of Dietary Supplementation with *Durio zibethinus* Murr. cv. Monthong Rind on the Hematology and Innate Immune Response Against *Aeromonas hydrophila* in Red Tilapia (*Oreochromis niloticus x Oreochromis mossambicus*) **e255332**
Duangjai Pisuttharachai, Nataporn Sangkhonkhet, Warrapong Nalinanon, and Saichon Lerdsuwan

Enhancing Autonomous Driving: A Novel Approach of Mixed Attack and Physical Defense Strategies **e254093**
Chuanxiang Bi, Shang Shi, and Jian Qu

An AIoT-based Air Quality Monitoring System for Real-time PM2.5 Prediction in Urban Environments **e255168**
Nuth Otanasap, Siriwich Tadsuan, and Chanintorn Chalermsuk

Technology Transfer Needs Assessment for Turmeric Farmers in Paphayom District, Phatthalung Province **e254806**
Saowanee Lekbangpong, and Apinya Ratanachai

Mutation Induction in Toothbrush Orchids Using Ethylmethane Sulphonate (EMS) and Detection of Genetic Variation by SSR (Simple Sequence Repeat) Marker **e255125**
Yaowamarn Keawsaard, Parita Pentem, Phakarat Rotduang, Muntaka Weeraphong, and Supawadee Ramasoot

Effects of Different Manures on the Growth Performance of Pechay (*Brassica rapa* L.) Under Visayas State University Condition **e255634**
Roger Y. Ibañez, Jr., Goram C. Balansag, and Nova Grace D. Puod

Methane Oxidation Rates and Efficiencies Across Four Distinct Soil Environments: Implications for Greenhouse Gas Mitigation **e255939**
Chonticha Leamdum, Nantharat Phruksaphithak, Sukonlarat Chanthong, and Chaisit Niyasom

Preparation and Characterization of Sulfonated CaO Catalyst for Biodiesel Production from Waste Cooking Oil **e255558**
Chatchawin Dulymahakamtorn, Rattana Jariyaboon, Prawit Kongjan, Tanakorn Chantasuban, and Saowapa Chotisuwan

Biological Oxidation of Dissolved Methane in Palm Oil Mill Biogas Effluents Using an Anoxic Methane-Oxidizing Consortium **e255940**
Chonticha Leamdum, Chaisit Niyasom, Sukonlarat Chanthong, and Nantharat Phruksaphithak

Identifying Niche Factors for Planting Vetiver Grass in Thailand **e254975**
Yaowaret Jantakat, Pongpun Juntakut and Chomphak Jantakat

Risk Assessment and Geospatial Mapping of Ammonia Transportation Hazards: A Case Study of Thungsong, Thailand **e254894**
Pisit Kolsaman, Supabhorn Yimthiang, Preeda Sansakorn, Junjira Mahaboon

Ultrasonic-Assisted Production and Shelf-Life Assessment of Functional Beverage from Purple Rice (*Oryza sativa L.*) **e255396**
Pornsawan Sombatnan1, Yardfon Tanongkankit, Nukrob Narkprasom, Chanawat Nitatwichit, and Sureewan Rajchasom

The Effect of KOH and Fe_2O_3 on Natural Rubber Latex Film for Excretion Bag **e255538**
Sonchai Intachai, Kantrakorn Suwanraksa, Tantika Charoenlap, Nureeya Bintuan, Weerawut Naebpetch, and Panita Sumanatrakul

Influence of Molding Condition and Moisture Content of Arecanut Leaf Sheath on Quality of Food Plates **e254700**
Ladda Prasan, Chaiwat Jumpholkul, Ruamporn Nikhom, and Weerawut Naebpetch

Image Based Papaya (*Carica Papaya* Linn.) seed germination evaluation by ResNet50 **e254804**
Chomtip Pornpanomchai

List of Contents

Clove Position on the Induction of Single-Clove Garlic, Yield, and Bioactive Compounds **e256297**
Tanapon Tumsuk, Kamon Thippachote, Suriya Tateing, Siwaporn Thumdee, and Jutamas Kumchai

Estimating the Ratios of Masonry Wall and Wall Finishing Work to the Building Area, Considering Only the Area within the Building's Boundaries: A Case Study of a Two-story Reinforced Concrete House **e255748**
Watcharapong Deewong

Enhancing Voltage Stability of a Microgrid in the Presence of PV Plants Using Storage System **e254201**
Nirdesh Singh, and D. K. Jain

Detection of COVID-19, Pneumonia, and Tuberculosis Using Convolutional Neural Networks and Ensemble of Deep Learning Architectures **e253662**
Rituraj Jain, Simon Kasahun Bekele, Damodharan Palaniappan, Kumar Parmar, Ramesh Babu P, and Anandkumar M. Trivedi



ASEAN
Journal of Scientific and Technological Reports
Online ISSN:2773-8752

ASEAN
Journal of Scientific and Technological Reports
Online ISSN:2773-8752

Research article

Efficient and Rapid Classification of Various Maize Seeds Using Transfer Learning and Advanced AI Techniques

Hasan İbrahim Kozan[1], Hasan Ali AKYÜREK[2*]

[1] Necmettin Erbakan University, Meram Vocational School, Konya, Türkiye
[2] Necmettin Erbakan University, Faculty of Aviation and Space Sciences, Konya, Türkiye
* Correspondence: hakyurek@erbakan.edu.tr

Citation:
Kozan, H.İ.; Akyürek, H.A. Efficient and rapid classification of various maize seeds using transfer learning and advanced AI techniques. *ASEAN J. Sci. Tech. Report.* **2025**, *28*(1), e255200. https://doi.org/10.55164/ajstr.v28i1.255200

Article history:
Received: July 27, 2024
Revised: October 10, 2024
Accepted: October 17, 2024
Available online: December 14, 2024

Publisher's Note:
This article has been published and distributed under the terms of Thaksin University.

Abstract: The classification of maize (Zea mays) is crucial for agricultural efficiency, breeding programs, and market specifications. The EfficientMaize dataset was utilized alongside Google's Teachable Machine to develop a model separating maize varieties into classes: Bhihilifa, SanzalSima, and WangDataa. As a result, the study demonstrated that user-friendly machine learning tools are helpful in agriculture since they delivered high accuracy rates, such as 99% in Bhihilifa, 95% in SanzalSima, and 85% in WangDataa. This paper also emphasizes how modern machine-learning technologies can be accessible to farmers and researchers through tools such as Google's Teachable Machine, which does not require coding knowledge or online expertise. To validate the results obtained with Google Teachable Machine, further analyses were conducted using RESNET-50. These findings add to previous studies on deep learning and hyperspectral imaging, leading to seed classification by increasing the potential of using machine learning to improve agricultural practices and food security.

Keywords: Maize classification; Machine learning; Agricultural technology; EfficientMaize dataset; Sustainable farming.

1. Introduction

Corn is an important nutritional resource for both humans and animals. This product is also quite suitable for agricultural purposes in Türkiye and eligible for commercial animal feeding. Corn has high nutritional value and also has a high portion of yield and a well-adaptation potential [1]. Thus, the production of corn in Türkiye is popular. Although there are many corn varieties, 7 popular corn varieties are produced worldwide [2]. As in other agricultural production, yield and product quality in corn production are indispensable elements for agricultural processes [3]. To ensure seed quality and purity, the categorization of maize varieties is crucial for farming operations and agricultural research [4]. Classification of seed varieties, including maize seeds, is important for producers and farmers to maintain variety purity and product yield [5]. However, classifying corn seeds is not very easy. Maize seeds of different varieties are very similar, with significant overlap in morphology and color characteristics. Thus, it is very important to classify them using machine learning since mechanical classification does not make it possible to distinguish between species. Machine learning has become increasingly important in various technical breakthroughs [6]. Machine learning, a sub-field of artificial intelligence, improves computational algorithms with practice and makes precise analyses and predictions using training data [7].

The subject of machine learning is a very broad field. It involves supervised machine learning to develop predictive models based on the training data. In unsupervised machine learning, it aims to group observations or create simplified representations of the main structures within the data [8]. Each example in machine learning consists of a set of features or expressions that describe the situation in question. The training set is the set of examples the proposed algorithm uses to learn, and the test set is the set of new and never-before-seen cases it uses to see how good it is at classification [9]. Machine learning has become increasingly available in every field. For example, in food classification [10], improving the net yield rate of crops in a particular season [11] or product selection based on geographic information systems (GIS) and multi-criteria decision analysis (MCDA) was achieved [12].

There have been many new approaches to machine learning, and recently, a lot of research, such as herbal plant classification [13], leaf classification [14], plant disease detection [15] or fruit classification [16] has been done with the Google Teachable Machine tool because it enables fast and mobile use. Google Teachable Machine is a machine learning tool. It has a graphical user interface (GUI), and its usage depends on its platform. Teachable Machine is based on TensorFlow[17]. Previous studies have shown that cutting-edge technologies such as deep learning algorithms, machine vision, and hyperspectral imaging can improve the accuracy and speed of maize seed classification [18]. New studies have focused on developing low-cost tools and processes to increase the accessibility of these technologies [19]. Some recent studies have focused on low-cost and fast processing for certain corn varieties, and researchers have developed applied machine learning algorithms [20, 21].

Efficiency is very important in agricultural areas, and one of the important factors affecting productivity is the selection and classification of seeds. In this context, varieties of corn seeds have different growth needs. At the same time, these seeds do not have the same tolerance to pests and diseases. Also, precise classification helps agricultural workers choose the right variety for their specific conditions. This helps improve the management of products and increase technical efficiency [22]. However, classification is also advantageous for breeding programs. Growers must use the right grade of seeds for the R&D and P&D activities they want. Correct classification ensures the use of appropriate genetic materials on the subject. This subsequently aids the reproductive process [23]. Another important classification aspect is delivering the right product to the right buyer. Products with high commercial value suffer financial losses if the correct classification is not made. In other words, farmers working on this issue will not have problems meeting market demand and can increase their profits if their products are classified correctly [24].

As artificial intelligence has become increasingly widespread in recent years, significant progress has been made in agriculture. Classification studies using AI, along with forecasting [25], IoT[26], and prediction studies [27], have gained momentum. Recent works include studies such as "Maize Seed Variety Identification Using Hyperspectral Imaging and Self-Supervised Learning: A Two-Stage Training Approach Without Spectral Preprocessing" [28] and "Maize Seeds Forecasting With Hybrid Directional and Bi-Directional Long Short-Term Memory Models." [24] Additionally, studies like "Maize Seed Variety Classification Using Image Processing" [29] have been conducted in image processing. The growing use of YOLO has also been seen in studies such as "Soft X-ray Image Recognition and Classification of Maize Seed Cracks Based on Image Enhancement and Optimized YOLOv8 Model." [30]

There are different datasets containing corn types. In this study, the dataset named EfficientMaize was used. The main goal in creating the dataset is to classify corn on low-performing devices [31]. This study aimed to separate the seeds into three types: Bhihilifa, SanzalSima, and WangDataa, using artificial intelligence and transfer learning. Transfer learning and artificial intelligence were used to differentiate the seeds by taking advantage of current technological developments, and the study was carried out with the Google Teachable Machine tool, a machine learning tool.

2. Materials and Methods

2.1 Dataset used for the study

In this study, the EfficientMaize dataset was used. This dataset contains 4,846 images as raw and 17,724 images as augmented. The images were randomly rotated by 20 degrees, shifted horizontally and vertically by 20% of the image width and height, respectively. A maximum angle shift transformation of 0.2 radians was applied, and brightness adjustments were made in the range of 0.5 to 1.5. After these

transformations, the newly created pixels were filled using the nearest pixel values. The augmented dataset provided by these processes was applied equally to the dataset to ensure the model was trained on a more diverse dataset. As a result, the aim was to increase the model's performance. The dataset creators applied data augmentation techniques. All images had a blue background. Researchers compressed the augmented images to a size of 128 x 128. Total image size 57.82 MB. The images were captured with a 12 MP iPhone 11 Pro Max device. Display features include a Super Retina XDR display, HDR display, 2,688-by-1,242-pixel resolution at 458 ppi, True Tone display, and Triple 12MP Ultra-Wide, Wide, and Telephoto cameras [31]. Details of each class of seeds in the dataset are shown in Table 1.

Table 1. EfficientMaize dataset

Crop	Categories	No. of Classes	Background	No. of Images
Maize	Bhihilifa	1	Blue	6,480
Maize	SanzalSima	1	Blue	5,100
Maize	WangDataa	1	Blue	6,144

2.2 Google Teachable Machine Model

The Google Teachable Machine model used in this study is based on the MobileNet architecture, a lightweight convolutional neural network (CNN) specifically designed for mobile and resource-constrained environments. MobileNet employs depthwise separable convolutions, significantly reducing the computational complexity compared to traditional CNNs. This makes it an ideal choice for real-time applications, such as those in agricultural technology [32]. The architecture consists of the following layers: Input Layer: This accepts image inputs and is resized to 224x224 pixels, as the MobileNet architecture requires. Depthwise Separable Convolutions: These layers break down standard convolutions into two parts: a depthwise convolution (which filters each input channel separately) followed by a pointwise convolution (which combines these filtered outputs). This reduces the number of parameters and computations. Batch Normalization and ReLU Activation Functions: After each convolution operation, batch normalization is applied to stabilize and speed up training, followed by a Rectified Linear Unit (ReLU) activation function to introduce non-linearity into the model. Global Average Pooling: Reduces the spatial dimensions of the feature maps to a single value for each feature, thus minimizing overfitting and reducing the overall model complexity. Fully Connected Layer: The final layer of MobileNet is a fully connected layer that outputs predictions based on the learned features [33]. Additionally, transfer learning was employed using the pre-trained weights from ImageNet, a large dataset used to initialize the model with general image features. This allows the model to adapt quickly to our specific maize classification task by fine-tuning the final few layers while keeping the pre-trained layers fixed, thus leveraging existing learned features from similar image classification tasks [33].

The computational efficiency of the Google Teachable Machine, based on the MobileNet architecture, is one of its primary strengths, especially for practical agricultural applications where real-time or near-real-time inference may be required. Our study found that the inference time for Google Teachable Machine (GTM) was 6 ms, making it exceptionally fast for real-time applications, while ResNet50 had an inference time of 18 ms. Although ResNet50 is still reasonably fast, GTM's lower latency makes it more suitable for mobile and resource-constrained environments where real-time decisions are crucial, such as agricultural fieldwork. The differences in training time are equally significant. ResNet50 required 34 minutes and 19 seconds for training, while Google Teachable Machine only took 4 minutes and 53 seconds, demonstrating the efficiency of GTM in inference and the training phase. The short training time makes GTM more practical and valuable for scenarios where frequent retraining or model parameter updates may be required, such as adapting to changing agricultural conditions or adding new crop species to the dataset, making GTM more practical. Therefore, GTM is suitable for practical agricultural applications where both speed and computational efficiency are critical. The substantial reduction in training and inference times allows the model to be deployed on lower-end devices without compromising performance, enabling widespread use by farmers or agricultural technicians in real-world settings.

2.3 Training the Model

For the training phase of the model, the entire dataset was randomly divided into two main parts: training (85%) and test sets (15%) by default in Google Teachable Machine. There are some optimization possibilities for the training process with the Google Teachable Machine tool. The number of epochs, batch size, and learning rate adjustments for these optimization processes were determined before training, and the relevant settings are shown in Table 2.

Table 2. Model parameters

Model	Epochs	Batch Size	Learning Rate
Teachable Machine	50	16	0.001

There is some preliminary parametric process in determining these parameters, and the relevant parameters are determined as a result of routine experiments in standard machine learning processes [34]. After this optimization process, the images in the dataset were transmitted to the Google Teachable Machine tool with the help of a web tool, as illustrated in Figure 1. Subsequently, the training process was completed for corn seeds belonging to 3 different classes, specific to each class. The interface can update instantly, and the performance of the developed model can also be viewed instantly.

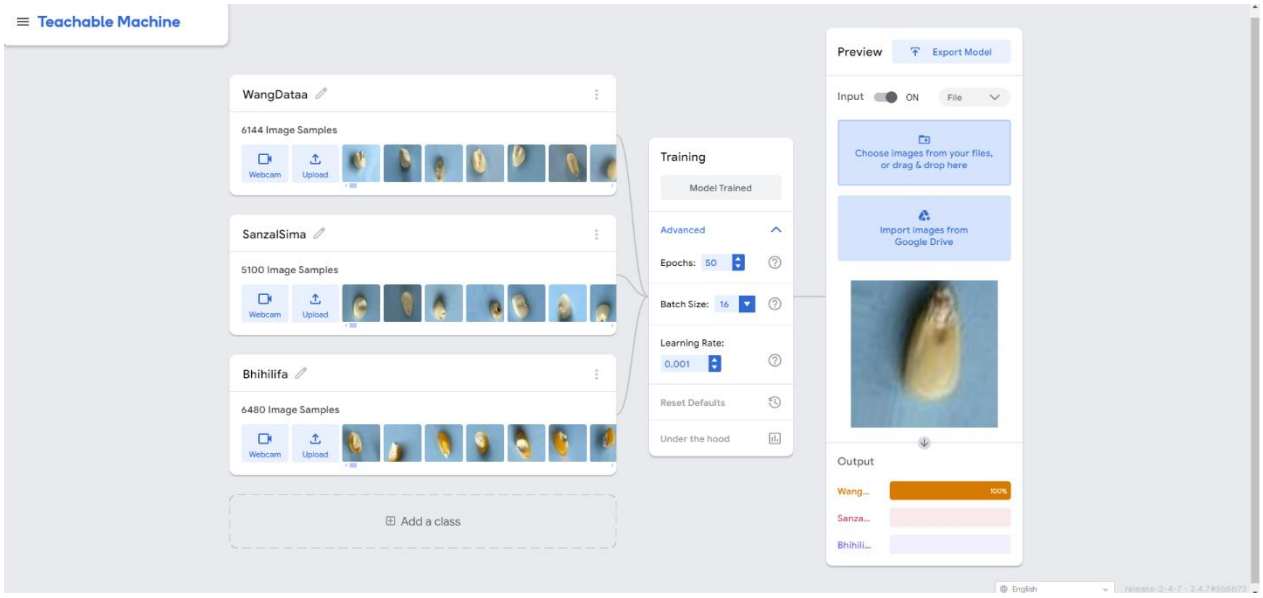


Figure 1. This is a figure. Schemes follow the same formatting.

As a basic machine learning process, the testing process was started in the second stage after completing the training. The model was re-evaluated with the test set. Unlike other machine learning tools, previews were provided at every stage during this process. The most important criterion of the developed model is performance evaluation. The main parameters in this evaluation can be listed as the confusion matrix, per-class accuracy, and overall performance metrics. Data augmentation techniques ensured that the developed model produced more accurate and sensitive results. More specifically, the dataset is digitally and artificially augmented. For the resulting model to produce more universal results, rotations, shifts, translations, and zooms were applied to the raw images [35]. The performance of the results of this model is determined by critical measurements based on accuracy, precision, recall, and F1 score. Accuracy shows the pattern of the prediction made with the actual result. Precision is another metric that measures the model's ability to remove false positives and represents the proportion of positive cases that are correctly and successfully predicted among all expected positives. Recall evaluates the model's ability to identify positive cases accurately. How effectively does it capture actual positive cases? The F-1 score takes the harmonic mean of precision and recall to provide a balanced assessment of the model's predictive performance.

Calculation formulas of the metrics are given in Table 3.

Table 3. Calculation formulas of metrics

Metric	Formula[1]
Accuracy	$\frac{TP+TN}{TP+TN+FP+FN}$
Precision	$\frac{TP}{TP+FP}$
Recall	$\frac{TP}{TP+FN}$
F1-Score	$2\frac{Precision*Recall}{Precision+Recall}$

[1] TP: True Positives TN: True Negatives FP: False Positives FN: False Negatives.

2.4 Software and Hardware Specifications

To ensure the reproducibility of the study, the hardware and software features must be known. In this context, this study was carried out on a workstation with the software and hardware information shown in Table 4.

Table 4. Software and hardware information

Name	Value
OS Name-Version:	Microsoft Windows 11 Pro - 10.0.26120
OS Configuration:	Standalone Workstation
Original Install Date:	12.04.2024, 14:09:46
System Boot Time:	18.07.2024, 04:18:02
System Model:	MS-7C71
System Type:	x64-based PC
Total Physical Memory:	32,686 MB
Network Card(s):	[01]: Intel(R) Wi-Fi 6 AX201
	[02]: Realtek PCIe 2.5GbE Family Controller
	[03]: Bluetooth Device (Personal Area Network)
Browser	Google Chrome (Chromium), Version: 126.0.6478.128 (64-bit)

3. Results and Discussion

After training the model with the EfficientMaize dataset and Google's Teachable Machine, the findings showed a high level of accuracy in categorizing maize varieties. The accuracy rates for each class were as follows: Bhihilifa achieved 99%, SanzalSima 95%, and WangDataa 85%, as shown in Table 5.

Table 5. Accuracy for GTM

Model	Class	Accuracy	Samples
Teachable Machine	Bhihilifa	0.99	972
Teachable Machine	SanzalSima	0.95	765
Teachable Machine	WangDataa	0.85	922

The confusion matrix in Figure 2 shows a detailed breakdown of the model's performance, including the number of instances correctly and wrongly classified for each class. For example, WangDataa has 787 correctly classified instances, 132 misclassified as SanzalSima, and 3 misclassified as Bhihilifa. The lower accuracy of WangDataa (85%) compared to Bhihilifa (99%) and SanzalSima (95%) could be due to several factors. One possible reason is the inherent variability in the visual characteristics of the WangDataa class, such as differences in color, texture, or shape, making it more challenging for the model to generalize across all samples.

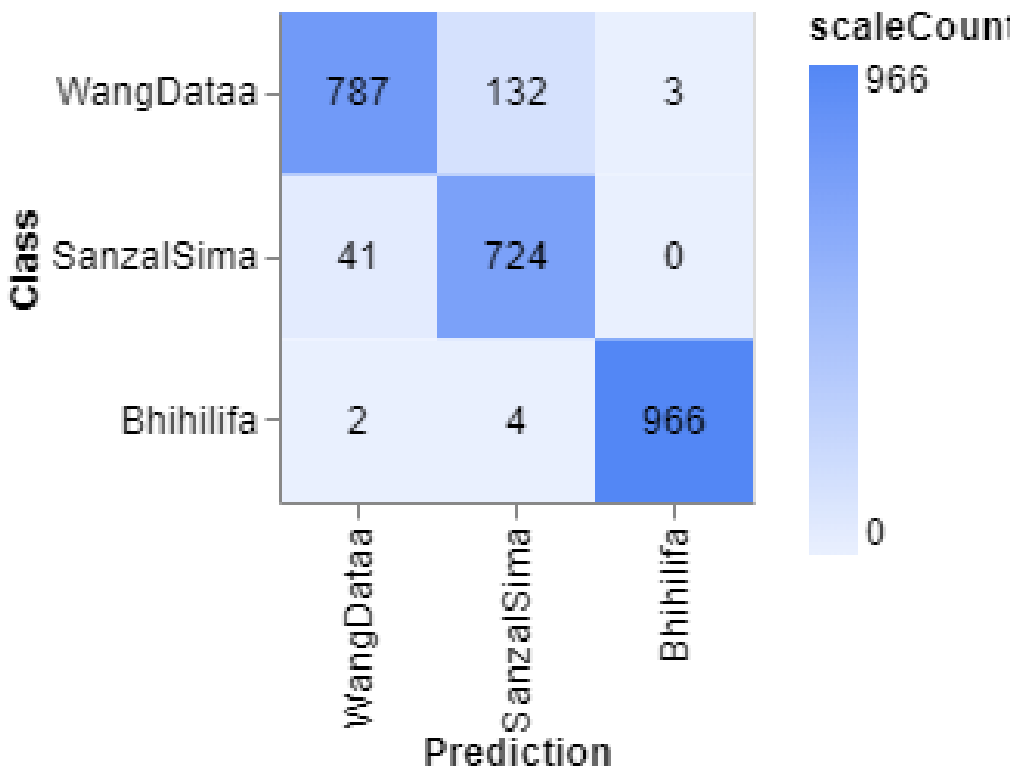


Figure 2. Confusion matrix.

Figure 3 shows the accuracy of training and validation throughout 50 epochs. The orange line depicts validation accuracy, whereas the blue line reflects training accuracy. The model's training accuracy improved steadily, reaching near-perfect levels, while validation accuracy fluctuated but remained excellent overall.

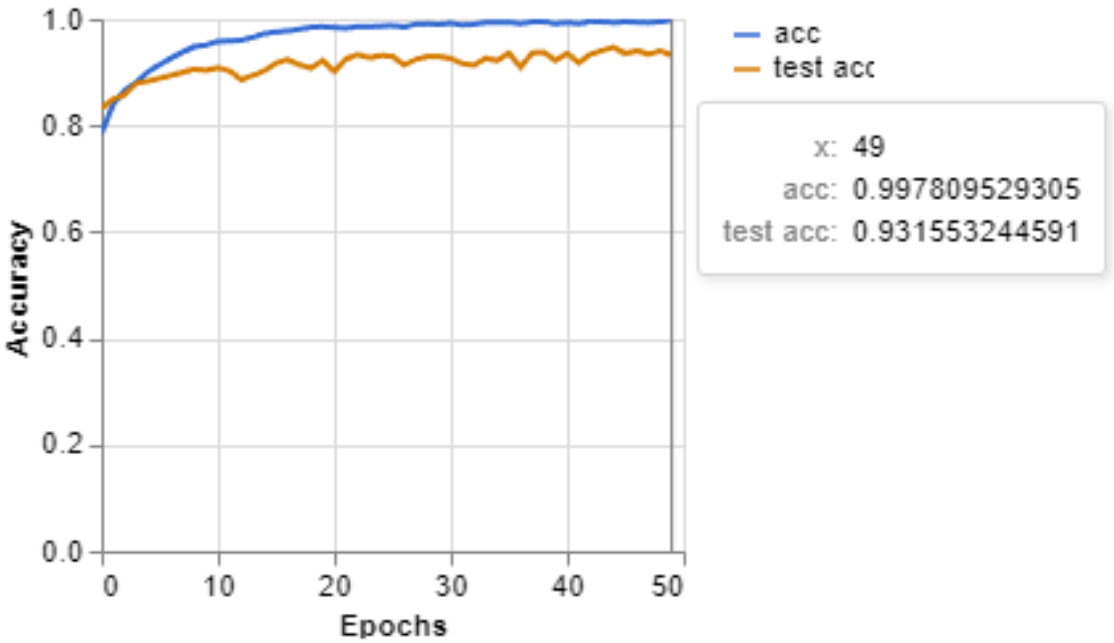


Figure 3. Accuracy per epoch.

Figure 4 shows the training and validation losses over 50 epochs. The blue line represents training loss, which fell in the first epochs before leveling out, showing effective learning from the training data. The orange line depicts validation loss, which fluctuated but decreased, showing that the model was successfully generalizing to new data.

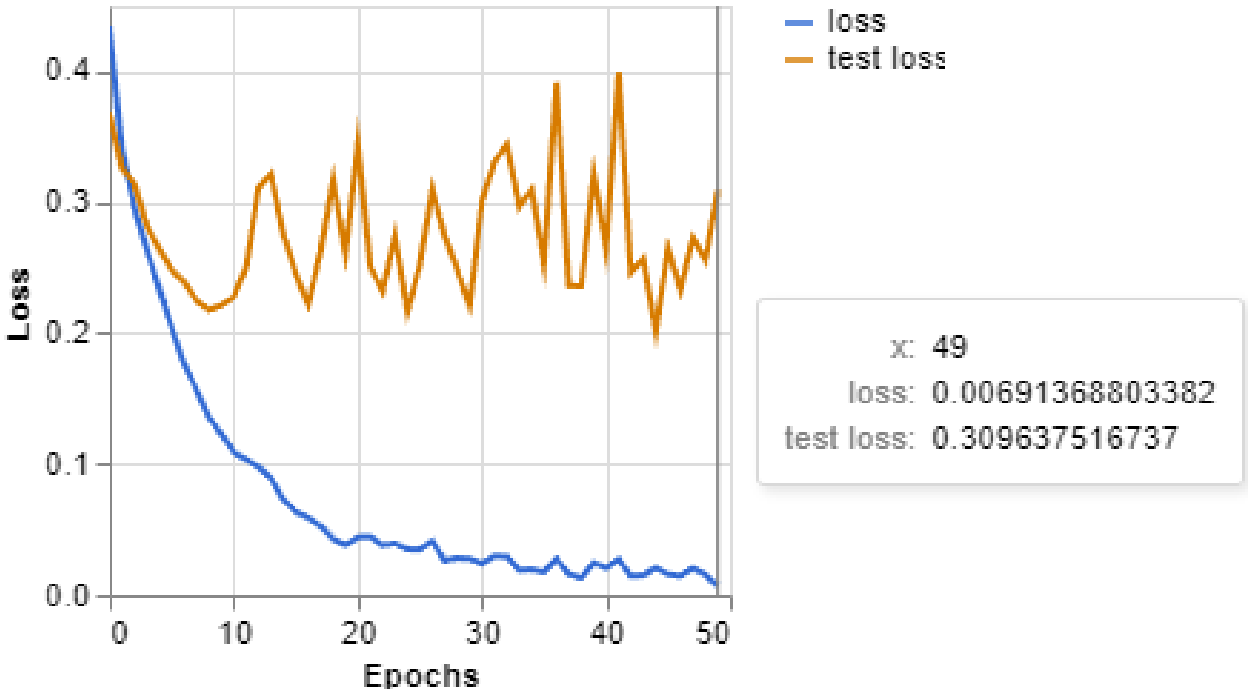


Figure 4. Loss per epoch.

Such evaluations and visual presentations throughout the testing process are critical for verifying the machine learning model's reliability and usability for the entire system. They help ensure the program runs successfully in real-world circumstances, which are critical to user pleasure and safety.

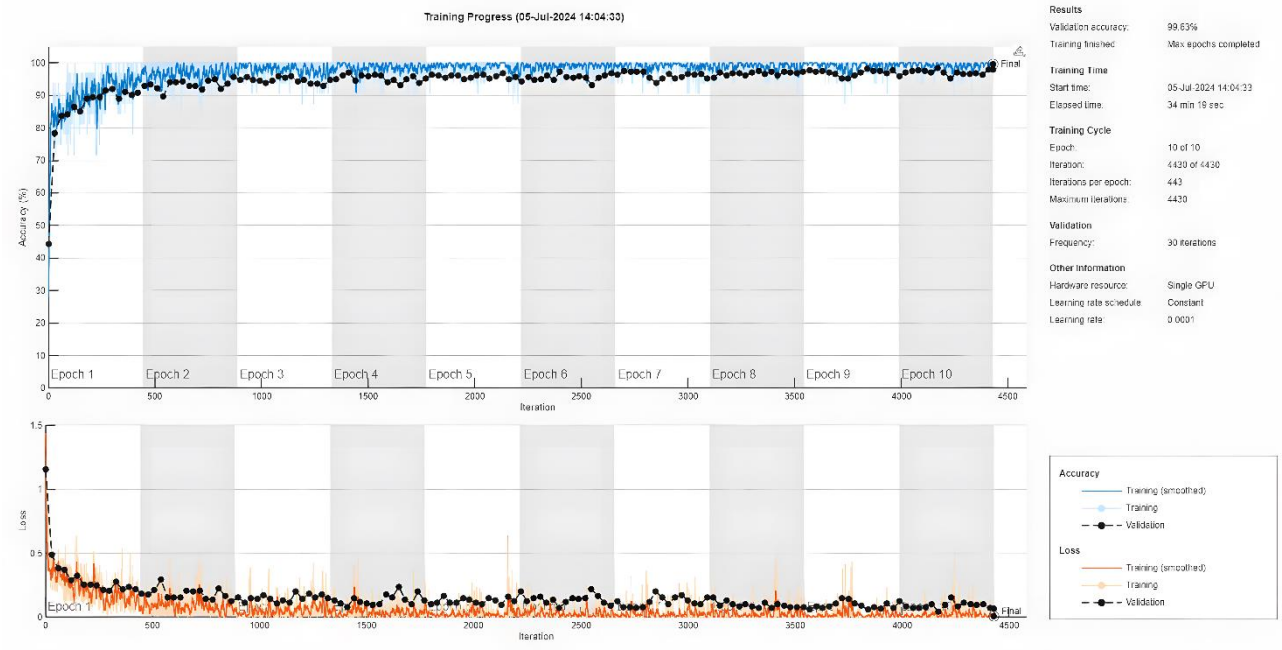


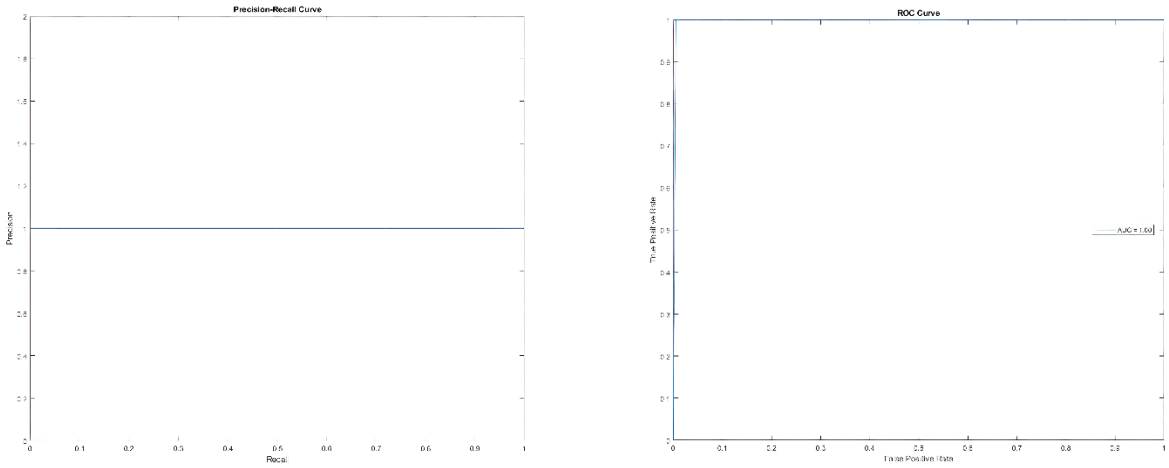
Figure 5. The training progress of ResNet-50.

ResNet-50's distinct architecture, which combines residual connections and a bottleneck structure, allows it to efficiently address the issues of training deep neural networks. Resnet-50 was used to verify the Google Teachable Machine results. For the Resnet-50, the entire dataset was randomly divided into two main parts: training (80%) and test sets (20%). For ResNet-50, the entire dataset was randomly divided into 80% and 20% training and test datasets for each class. For the training of the ResNet-50 model, standard training configurations of MATLAB were used to ensure stable performance. The 'adam' optimizer, known for its efficiency and adaptability in training deep learning models, was used. The mini-batch size was set to 32, a commonly used value, to balance memory efficiency and training speed. The learning rate was initialized at a typical setting of 0.0001 to achieve a stable and effective learning process without straining the convergence ability of the model. The model was trained for 10 epochs, and validation data was provided every 30 iterations to prevent overfitting of the model, thus running an effective learning process to increase the model's generalization ability. The data was shuffled in each epoch to ensure that the training data was exposed to the model in various ways. These choices were guided by standard practices in the machine learning literature and preliminary experiments, ensuring optimal model performance across various applications. MATLAB's default settings were used as they are well-regarded for producing consistent and successful results in deep learning tasks. Figure 5 depicts the training progress of Resnet-50, and Table 6 contains the Resnet-50 results.

Table 6. Software and hardware information

Parameter	Result
Validation accuracy	99.39%
Training finished	Max epochs completed
Training elapsed time	236 min 34 sec
Training epoch cycle	10 of 10
Iteration	9,480 of 9,480
Iteration per epoch	948
Max Iteration	9,480
Validation Frequency	30 iterations
Hardware resource	Single GPU
Learning rate schedule	Constant
Learning rate	0.0001

Figure 6 shows the precision-recall and ROC curves for ResNet-50.



(a) (b)

Figure 6. (a) Precision-Recall Curve, (b) ROC Curve.

Figure 7 shows the confusion matrix of the test dataset for ResNet-50.

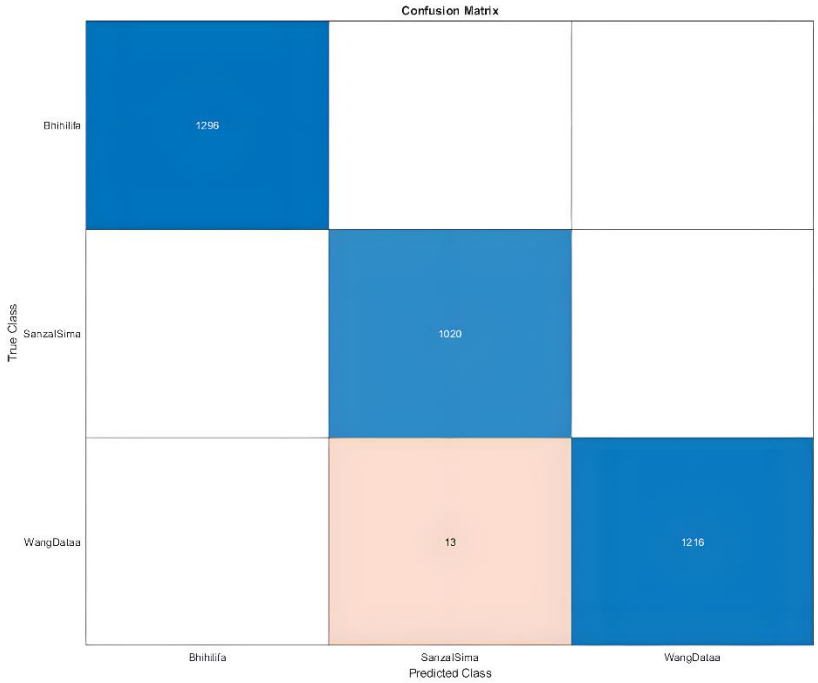


Figure 7. Confusion matrix of ResNet-50.

Table 7 shows the findings from Google Teachable Machine and ResNet-50, highlighting the precision, recall, and F1-score for the classes "Bhihilifa," "SanzalSima," and "WangDataa."

Table 7. Accuracy of ResNet-50

Class	Samples	Precision	Recall	F1-Score	Accuracy
Bhihilifa	1296	1.00	1.00	1.00	1.00
SanzalSima	1020	0.99	1.00	0.99	1.00
WangDataa	1229	1.00	0.99	0.99	0.99

The research shows that both classes' models have exceptionally high-performance metrics. The precision and recall values of classes “Bhihilifa,” “SanzalSima,” and “WangDataa” are consistently higher than 0.99, indicating a high level of classification accuracy. The accuracy, recall, and F1-Score value of the Bhihilifa class was 1.00, the precision and F-1 Score of the SanzalSima class was 0.99, while the recall value was 1.00. The recall and F1 score of WangDataa was 0.99, and the precision value was 1.00. Our results are consistent with recent studies on maize seed classification; [36, 37] however, GTM outperforms all these studies in terms of faster training, testing, and validation times, although its accuracy is slightly lower. However, it is anticipated that as the dataset grows, the learning curve will improve, increasing accuracy. Currently, one of the limitations of this platform is the maximum limit of 10,000 images per class.

When all the results were evaluated, the accuracy rate of the Bhihilifa class was found to be 99%, and this value was also quite high in classification success. Considering agricultural practices, it has been reported that this high-value classification success will also be advantageous to ensure seed quality and purity, which are very important for basic parameters such as yield and sustainability [4]. The accuracy values of the other two classes, SanzalSima and WangDataa, were 95% and 85%, respectively. Although these values were lower than the Bhihilifa class, it was thought that the model could be further improved by using different data augmentation techniques or optimization of preliminary parameter values, as mentioned before.

After a classifier is trained, the confusion matrix is generated by that classifier on a validation set. It can be used to find out which classes present some confusion in the classification, and then a more customized classification structure can be created [38]. When the confusion matrix of this study is examined, it is seen that the matrix values of two classes (WangDataa and SanzalSima) are higher than the other class (Bhihilifa). In other words, there is a possibility of confusion in classifying these two species. To prevent this, further optimization processes can be applied, or the training phase can be strengthened by increasing the source images to improve the model. When the model's training process was examined, it was observed that the training loss was reduced, and the training accuracy was high. These results show that the model is quite successful on the training set side. However, approaches to reduce overfitting should be used when evaluating model performance, validation accuracy, and loss oscillations. These approaches may be validation accuracy, loss oscillations, dropout regularization, or cross-validation [39]. Different machine-learning techniques have been applied to classify corn [40-42], and researchers have emphasized that low-cost devices and procedures should be prioritized when classifying [43, 44].

The implementation of this technology in real-world agricultural settings has the potential to enhance productivity and decision-making efficiency significantly. Farmers can reduce the time and labor required for manual seed sorting by AI-based maize seed classification, leading to more accurate and rapid processing. Using machine learning models like Google Teachable Machine in the field can also enable mobile-based solutions, allowing for on-the-spot classification with minimal infrastructure requirements. Economically, such technology could save costs by reducing the need for specialized labor and minimizing errors in seed selection, ultimately leading to higher crop yields [45]. However, challenges remain in the widespread adoption of this technology, including initial setup costs, the need for reliable internet connectivity in rural areas, and the integration of AI systems with existing farming equipment [46]. Further, it is necessary to ensure that these systems are adaptable to various crops and growing conditions to make them broadly applicable in diverse agricultural environments[47]. Future research could expand the model to classify additional maize varieties or adapt it for other crops like wheat or rice. Incorporating larger, more diverse datasets would enhance the model's generalization. Improvements could also include using more advanced neural networks, such as transformers, and domain-specific augmentations to increase robustness [48]. Additionally, integrating the system with IoT sensors or automated machinery could create comprehensive smart farming solutions, enabling real-time monitoring and decision-making [49]

This study investigated the classification success of different corn varieties with machine learning and transfer learning approaches using the Google Teachable Machine tool, which is low-cost, fast, and highly accurate, as the researchers suggested. There is no statistically significant difference ($p<0.01$) between the two models' weighted accuracies. The analysis and test results showed that these three types of corn seeds could be classified successfully and accurately. At the same time, this has shown that it is applicable in many agricultural applications due to its low costs and flexible structure. The accuracy of the results was evaluated by comparing them with ResNet-50, a well-known and successful method. As a result, this method is thought to be widely used in the classification of corn seeds and will be the basis for future studies that may include more varieties.

4. Conclusions

Maize (Zea mays), known as corn, is one of the world's most important grain crops. Correct classification of corn varieties is important in many areas as it is one of the basic foodstuffs for humanity and an important component of animal feed and various industrial products. This study proposes using Google's Teachable Machine to successfully differentiate maize seeds belonging to Bhihilifa, SanzalSima, and WangDataa species. In this study using the EfficientMaize dataset, it was observed that Bhihilifa was successfully classified with 99% accuracy, SanzalSima with 95% accuracy, and WangDataa with 85% accuracy. These findings suggest that using Google's Teachable Machine will increase the accessibility and usefulness of modern machine learning technology in agricultural applications. It can be run on low-cost devices, thus demonstrating the potential of machine learning techniques to increase precision and efficiency in agricultural applications. The most important findings of the research are high classification accuracy, improvement potential, and usability of machine learning. The model has been highly successful in classifying maize species, especially Bhihilifa. SanzalSima and WangDataa's classification performance has been achieved with relatively

lower accuracy than Bhihilifa. Still, it is thought that the performance will be increased by improving the model with new data and various optimizations. It has been evaluated that when the advantages obtained from the model and the new technologies to be developed are paired with user-friendly tools, they can be widely used in agricultural practices by improving seed quality evaluation, breeding program assistance, and marketability of agricultural products.

Author Contributions: Conceptualization, H.İ.K. and H.A.A.; methodology, H.İ.K. and H.A.A.; software, H.İ.K. and H.A.A.; validation, H.İ.K. and H.A.A.; formal analysis, H.İ.K. and H.A.A.; investigation, H.İ.K. and H.A.A.; resources, H.İ.K. and H.A.A.; data curation, H.İ.K. and H.A.A.; writing—original draft preparation, H.İ.K. and H.A.A.; writing—review and editing, H.İ.K. and H.A.A.; visualization, H.İ.K. and H.A.A.; supervision, H.İ.K. and H.A.A.; project administration, H.İ.K. and H.A.A.. All authors have read and agreed to the published version of the manuscript.

Funding: This research received no external funding

Conflicts of Interest: The authors declare no conflict of interest.

References

[1] Erdurmuş, D.; Soylu, S. Afyonkarahisar koşullarında silajlık mısır çeşitlerinin yeşil ot ve kuru madde verimlerinin belirlenmesi. *Eregli Journal of Agricultural Science* **2023**, *3*(2), 43-50. DOI: 10.54498/ETBD.2023.21.

[2] Yerlikaya Sümbül, D.; Soylu, S. Karapınar Koşullarında Şeker Mısır (Zea mays L. saccharata) Çeşitlerinin Taze Koçan ve Hasıl Verimlerinin Belirlenmesi. *Eregli Journal of Agricultural Science* **2022**, 81-89. DOI: 10.54498/etbd.2022.15.

[3] Özyiğit, İ. İ. Tarım topraklarında ağır metaller; kökenleri, yayılışları ve etkileri. *Eregli Journal of Agricultural Science* 2021, *1*(1), 46-72. DOI: 10.54498/etbd.2021.5.

[4] Gebeyehu, S.; Sintayehu Shibeshi, Z. Maize seed variety identification model using image processing and deep learning. *Indonesian Journal of Electrical Engineering and Computer Science* **2024**, *33*(2), 990. DOI: 10.11591/ijeecs.v33.i2.pp990-998.

[5] Taner, A.; Öztekin, Y. B.; Tekgüler, A.; Sauk, H.; Duran, H. Classification of varieties of grain species by artificial neural networks. *Agronomy* 2018, *8* (7), 123. DOI: 10.3390/agronomy8070123.

[6] Chen, J.; Luo, T.; Wu, J.; Wang, Z.; Zhang, H. A Vision Transformer network SeedViT for classification of maize seeds. *Journal of Food Process Engineering* **2022**, *45*(5). DOI: 10.1111/jfpe.13998.

[7] Zhang, X.; Cheng, J.; Shi, Z.; Zhang, Y.; Wang, M. Design and Experiment of a Clamp-Holding Precision Maize-Seed-Metering Device. *Engenharia Agrícola* **2022**, *42*(6). DOI: 10.1590/1809-4430-eng.agric. v42n6e20220049/2022.

[8] Asnicar, F.; Thomas, A. M.; Passerini, A.; Waldron, L.; Segata, N. Machine learning for microbiologists. *Nature Reviews Microbiology* **2024**, *22*(4), 191-205. DOI: 10.1038/s41579-023-00984-1 From NLM Medline.

[9] Attri, I.; Awasthi, L. K.; Sharma, T. P. Machine learning in agriculture: a review of crop management applications. *Multimedia Tools and Applications* **2024**, *83*(5), 12875-12915. DOI: 10.1007/s11042-023-16105-2.

[10] Özel, M. A.; Gül, M. Y.; Güneş, E. YOLO Algoritması ile Gastronomide Yemek İçeriklerini Tespit Etmede Bir Makine Öğrenimi Yaklaşımı. *Necmettin Erbakan Üniversitesi GastroMedia Dergisi (NEU GastroMedia)* **2023**, *2*(1), 31-38. DOI: 10.54497/Gastromedia.2023.7.

[11] Kumar, R.; Singh, M.; Kumar, P.; Singh, J. Crop Selection Method to maximize crop yield rate using machine learning technique. In *2015 international conference on smart technologies and management for computing, communication, controls, energy and materials (ICSTM)*, **2015**, IEEE: pp 138-145. DOI: 10.1109/ICSTM.2015.7225403.

[12] Wotlolan, D. L.; Lowry, J. H.; Wales, N. A.; Glencross, K. Land suitability evaluation for multiple crop agroforestry planning using GIS and multi-criteria decision analysis: A case study in Fiji. *Agroforestry systems* **2021**, *95*(8), 1519-1532. DOI: 10.1007/s10457-021-00661-3.

[13] Malahina, E. A. U.; Saitakela, M.; Bulan, S. J.; Lamabelawa, M. I. J.; Belutowe, Y. S. Teachable Machine: Optimization of Herbal Plant Image Classification Based on Epoch Value, Batch Size and Learning Rate. *Journal of Applied Data Sciences* **2024**, *5*(2), 532-545. DOI: 10.47738/jads.v5i2.206.

[14] Chalmers, J.; Thangavel, S. K.; Johnson, I. LeafYogi: Deep Learning based Mobile Application Framework for Ayurvedic Leaf Classification. In *2024 International Conference on Inventive Computation Technologies (ICICT)*, **2024**, IEEE: pp 950-954.

[15] Tejaswi, D.; Vaishnavi, T. S.; Nandini, B.; Raju, P. N.; Deepika, B. Plant disease detection using deep learning. *International Journal of Science and Research Archive* **2024**, *12*(1), 2476-2488. DOI: 10.30574/ijsra.2024.12.1.1043.

[16] Vikraman, B. P.; Mahadevan, V.; Gadi, R. B.; Al Shekili, A. K.; Al Yahmadi, M. K. Iot-Based Multiclass Fruit Classification System using Transfer Learning. *Journal of Electrical Systems* **2024**, *20*(7s), 1308-1314. DOI: 10.52783/jes.3703.

[17] Setiawan, F. B.; Adipradana, C. B.; Pratomo, L. H. Fruit Ripeness Classification System Using Convolutional Neural Network (CNN) Method. *PROtek: Jurnal Ilmiah Teknik Elektro* **2023**, *10*(1), 46. DOI: 10.33387/protk.v10i1.5549.

[18] Hu, Y.; Wang, Z.; Li, X.; Li, L.; Wang, X.; Wei, Y. Nondestructive classification of maize moldy seeds by hyperspectral imaging and optimal machine learning algorithms. *Sensors* **2022**, *22*(16), 6064. DOI: 10.3390/s22166064 From NLM Medline.

[19] ElMasry, G.; Mandour, N.; Wagner, M. H.; Demilly, D.; Verdier, J.; Belin, E.; Rousseau, D. Utilization of computer vision and multispectral imaging techniques for classification of cowpea (Vigna unguiculata) seeds. *Plant Methods* **2019**, *15*(1), 24. DOI: 10.1186/s13007-019-0411-2 From NLM PubMed-not-MEDLINE.

[20] Bi, C.; Zhang, S.; Chen, H.; Bi, X.; Liu, J.; Xie, H.; Yu, H.; Song, S.; Shi, L. Non-Destructive Classification of Maize Seeds Based on RGB and Hyperspectral Data with Improved Grey Wolf Optimization Algorithms. *Agronomy* **2024**, *14*(4), 645. DOI: 10.3390/agronomy14040645.

[21] Ma, R.; Wang, J.; Zhao, W.; Guo, H.; Dai, D.; Yun, Y.; Li, L.; Hao, F.; Bai, J.; Ma, D. Identification of Maize Seed Varieties Using MobileNetV2 with Improved Attention Mechanism CBAM. *Agriculture* **2022**, *13*(1), 11. DOI: 10.3390/agriculture13010011.

[22] Miao, A.; Zhuang, J.; Tang, Y.; He, Y.; Chu, X.; Luo, S. Hyperspectral Image-Based Variety Classification of Waxy Maize Seeds by the t-SNE Model and Procrustes Analysis. *Sensors (Basel)* **2018**, *18*(12), 4391. DOI: 10.3390/s18124391 From NLM PubMed-not-MEDLINE.

[23] Xu, P.; Sun, W.; Xu, K.; Zhang, Y.; Tan, Q.; Qing, Y.; Yang, R. Identification of Defective Maize Seeds Using Hyperspectral Imaging Combined with Deep Learning. *Foods* **2022**, *12*(1), 144. DOI: 10.3390/foods12010144 From NLM PubMed-not-MEDLINE.

[24] Isik, H.; Tasdemir, S.; Taspinar, Y. S.; Kursun, R.; Cinar, I.; Yasar, A.; Yasin, E. T.; Koklu, M. Maize seeds forecasting with hybrid directional and bi-directional long short-term memory models. *Food Sci Nutr* **2024**, *12*(2), 786-803. DOI: 10.1002/fsn3.3783 From NLM PubMed-not-MEDLINE.

[25] Tamasiga, P.; Onyeaka, H.; Bakwena, M.; Happonen, A.; Molala, M. Forecasting disruptions in global food value chains to tackle food insecurity: The role of AI and big data analytics–A bibliometric and scientometric analysis. *Journal of Agriculture and Food Research* **2023**, *14*, 100819.

[26] Khang, A. *Handbook of Research on AI-Equipped IoT Applications in High-Tech Agriculture*; IGI Global, 2023.

[27] Akintuyi, O. B. Adaptive AI in precision agriculture: a review: investigating the use of self-learning algorithms in optimizing farm operations based on real-time data. *Research Journal of Multidisciplinary Studies* **2024**, *7*(02), 016-030.

[28] Zhang, L.; Zhang, S.; Liu, J.; Wei, Y.; An, D.; Wu, J. Maize seed variety identification using hyperspectral imaging and self-supervised learning: A two-stage training approach without spectral preprocessing. *Expert Systems with Applications* **2024**, *238*, 122113.

[29] Pareek, C.; Singh, N.; Tewari, V.; Dhruw, L.; Singh, H. D. Classification of broken maize kernels using artificial neural network-assisted image-processing approach. *Journal of Biosystems Engineering* **2023**, *48*(1), 55-68.

[30] Chen, S.; Li, Y.; Zhang, Y.; Yang, Y.; Zhang, X. Soft X-ray image recognition and classification of maize seed cracks based on image enhancement and optimized YOLOv8 model. *Computers and Electronics in Agriculture* **2024**, *216*, 108475.
[31] Asante, E.; Appiah, O.; Appiahene, P.; Adu, K. EfficientMaize: A Lightweight Dataset for Maize Classification on Resource-Constrained Devices. *Data in Brief* **2024**, *54*, 110261. DOI: 10.1016/j.dib.2024.110261 From NLM PubMed-not-MEDLINE.
[32] Lab, G. C. *Teachable Machine Community*. **2024**. https://github.com/googlecreativelab/teachablemachine-community/ (accessed 2024 30/09/2024).
[33] Howard, A. G. Mobilenets: Efficient convolutional neural networks for mobile vision applications. *arXiv preprint arXiv:1704.04861.* **2017**.
[34] Goodfellow, I.; Bengio, Y.; Courville, A. *Deep learning*; MIT press, **2016**.
[35] Shorten, C.; Khoshgoftaar, T. M. A survey on image data augmentation for deep learning. *Journal of big data* **2019**, *6*(1), 1-48. DOI: 10.1186/s40537-019-0197-0.
[36] Xu, P.; Tan, Q.; Zhang, Y.; Zha, X.; Yang, S.; Yang, R. Research on maize seed classification and recognition based on machine vision and deep learning. *Agriculture* **2022**, *12*(2), 232.
[37] Huang, S.; Fan, X.; Sun, L.; Shen, Y.; Suo, X. Research on classification method of maize seed defect based on machine vision. *Journal of Sensors* **2019**, *2019* (1), 2716975.
[38] Cavalin, P.; Oliveira, L. Confusion matrix-based building of hierarchical classification. In *Progress in Pattern Recognition, Image Analysis, Computer Vision, and Applications: 23rd Iberoamerican Congress, CIARP 2018, Madrid, Spain, November 19-22, 2018, Proceedings 23*, **2019**, Springer, pp 271-278.
[39] Bacanin, N.; Zivkovic, M.; Al-Turjman, F.; Venkatachalam, K.; Trojovský, P.; Strumberger, I.; Bezdan, T. Hybridized sine cosine algorithm with convolutional neural networks dropout regularization application. *Scientific Reports* **2022**, *12*(1), 6302.
[40] Velesaca, H. O.; Mira, R.; Suárez, P. L.; Larrea, C. X.; Sappa, A. D. Deep learning based corn kernel classification. In *Proceedings of the IEEE/CVF conference on computer vision and pattern recognition workshops*, **2020**; pp 66-67.
[41] Kishore, B.; Yasar, A.; Taspinar, Y. S.; Kursun, R.; Cinar, I.; Shankar, V. G.; Koklu, M.; Ofori, I. Computer-aided multiclass classification of corn from corn images integrating deep feature extraction. *Computational Intelligence and Neuroscience* **2022**, *2022*(1), 2062944.
[42] Javanmardi, S.; Ashtiani, S.-H. M.; Verbeek, F. J.; Martynenko, A. Computer-vision classification of corn seed varieties using deep convolutional neural network. *Journal of Stored Products Research* **2021**, *92*, 101800.
[43] Labati, R. D.; Gamassi, M.; Piuri, V.; Scotti, F. A low-cost neural-based approach for wood types classification. In *2009 IEEE International Conference on Computational Intelligence for Measurement Systems and Applications*, **2009**, IEEE: pp 199-203.
[44] Teisseyre, P.; Zufferey, D.; Słomka, M. Cost-sensitive classifier chains: Selecting low-cost features in multi-label classification. *Pattern Recognition* **2019**, *86*, 290-319.
[45] Hamed, M. A.; El-Habib, M. F.; Sababa, R. Z.; Al-Hanjor, M. M.; Abunasser, B. S.; Abu-Naser, S. S. Artificial Intelligence in Agriculture: Enhancing Productivity and Sustainability. **2024**.
[46] Senoo, E. E. K.; Anggraini, L.; Kumi, J. A.; Luna, B. K.; Akansah, E.; Sulyman, H. A.; Mendonça, I.; Aritsugi, M. IoT Solutions with Artificial Intelligence Technologies for Precision Agriculture: Definitions, Applications, Challenges, and Opportunities. *Electronics* **2024**, *13*(10), 1894.
[47] Chaterji, S.; DeLay, N.; Evans, J.; Mosier, N.; Engel, B.; Buckmaster, D.; Ladisch, M. R.; Chandra, R. Lattice: A vision for machine learning, data engineering, and policy considerations for digital agriculture at scale. *IEEE Open Journal of the Computer Society* **2021**, *2*, 227-240.
[48] Rogers, H.; De La Iglesia, B.; Zebin, T.; Cielniak, G.; Magri, B. Advancing precision agriculture: domain-specific augmentations and robustness testing for convolutional neural networks in precision spraying evaluation. *Neural Computing and Applications* **2024**, 1-19.
[49] Mandapuram, M.; Mahadasa, R.; Surarapu, P. Evolution of smart farming: Integrating IoT and AI in agricultural engineering. *Global Disclosure of Economics and Business* **2019**, *8*(2), 165-178.

ASEAN
Journal of Scientific and Technological Reports
Online ISSN:2773-8752

Research article

Effect of Dietary Supplementation with *Durio zibethinus* Murr. cv. Monthong Rind on the Hematology and Innate Immune Response Against *Aeromonas hydrophila* in Red Tilapia (*Oreochromis niloticus x Oreochromis mossambicus*)

Duangjai Pisuttharachai[1*], Nataporn Sangkhonkhet[2], Warrapong Nalinanon[3], and Saichon Lerdsuwan[4]

[1] Fishery Science and Aquatic Resources, Disciplines of Technology Agriculture, King Mongkut's Institute of Technology Ladkrabang, Prince of Chumphon Campus, Chumphon, 86160, Thailand
[2] Scientist, King Mongkut's Institute of Technology Ladkrabang, Prince of Chumphon Campus, Chumphon, 86160, Thailand
[3] Fishery Science and Aquatic Resources, Disciplines of Technology Agriculture, King Mongkut's Institute of Technology Ladkrabang, Prince of Chumphon Campus, Chumphon, 86160, Thailand
[4] Animal Science, Disciplines of Technology Agriculture, King Mongkut's Institute of Technology Ladkrabang, Prince of Chumphon Campus, Chumphon, 86160, Thailand
* Correspondence: duangjai.pi@kmitl.ac.th

Citation:
Pisuttharachai, D.; Sangkhonkhet, N.; Nalinanon, W.; Lerdsuwan, S. Effect of dietary supplementation with *Durio zibethinus* murr. cv. monthong rind on the hematology and innate immune response against *Aeromonas hydrophila* in red tilapia (*Oreochromis niloticus x Oreochromis mossambicus*). *ASEAN J. Sci. Tech. Report*. **2025**, *28*(1), e255332. https://doi.org/10.55164/ajstr.v28i1.255332.

Article history:
Received: August 6, 2024
Revised: October 11, 2024
Accepted: October 17, 2024
Available online: December 14, 2024

Publisher's Note:
This article has been published and distributed under the terms of Thaksin University.

Abstract: *In vivo* activity study of durian rind (*Durio zibethinus* Murr. cv. Monthong) as a supplement in the tilapia diet was performed to evaluate its effect on the hematology and innate immune response against *Aeromonas hydrophila*. Red Tilapia (*Oreochromis niloticus* x *Oreochromis mossambicus*), with an initial average weight range of 40-45 g, were fed diets supplemented with durian rind at 0, 10, 15, and 20% for 140 days and were injected intraperitoneally with *A. hydrophila.* Blood was collected at 1 and 3 hours post-injection to determine the phagocytic activity and the durian rind efficiency in protecting fish red blood cells from hemolysin produced by *A. hydrophila*. Ensuing results showed that red blood cell counts in fish-fed durian rind supplemented diets, regardless of inclusion levels, did not decrease at 3 hours post bacterial infection and were significantly higher than control ($P<0.05$). Furthermore, we observed that the total white blood cells and phagocytic activity of all fish fed with diets supplemented with durian rind increased from 1-hour post-infection, indicating a heightened innate immune response. Taken together, durian rind supplementation of at least 10% in the tilapia diet can act as an immunostimulant and improve innate immune response and anti-hemolytic activity against *A. hydrophila* infection.

Keywords: *Durio zibethinus* Murr. cv. Monthong; *Oreochromis niloticus x Oreochromis mossambicus*; *Aeromonas hydrophila*; Hematological; Phagocytic activity

1. Introduction

Aeromonas hydrophila is one of the most concerning etiological agents in cultured finfish and is reportedly responsible for outbreaks in freshwater fish, including tilapia [1-4]. This bacterium produces several virulence factors, such as hemolysin, aerolysin, and cytotonic enterotoxins, which are harmful to its hosts [5, 6]. In fish, major symptoms include ulcerative lesions, hemorrhages, and necrosis of the visceral organs leading to death [1, 7]. Antibiotics often treat *A. hydrophila* infections [8-10]. Recently, consumers have become more concerned about residues in food, making it necessary to develop aquaculture

practices that deter disease outbreaks in cultured finfish and ensure that the products are safe for consumption. Among these, using herbal medicines and other natural products to replace antibiotics in treating fish diseases has been getting significant consideration.

Durian (*Durio zibethinus* Murr.), also referred to as the "king of fruits," is a tropical fruit grown in Southeast Asian countries, including Malaysia, Indonesia, the Philippines, and Thailand [11, 12]. Durian rind, which makes up about 75-80% of the whole fruit, is often discarded after durian fruit consumption or processing [13]. It was previously reported that durian rind is a good source of polysaccharides (PG) [14]. PG has been shown to exhibit anti-hemolytic [15, 16] and immunomodulating properties [17, 18]. As *A. hydrophila* can produce hemolysin that causes lysis of red blood cells, we investigated the effect of durian rind supplementation in fish diets on the innate immunological responses and its efficiency in preventing fish red blood cell hemolysis against this bacterium. Moreover, the valorization of durian waste as a potential dietary supplement relieves disposal problems and adheres to the country's drive for a circular economy.

2. Materials and Methods

2.1 Experimental design and feeding management

This study was approved by the Ethics Committee of King Mongkut's Institute of Technology Ladkrabang (Approval no. ACUC-KMITL-RES/2021/034). The experiment was carried out in a completely randomized design with 4 treatments and 4 replications. Four hundred red tilapia, acclimated before the feeding trials, with an average weight range of 40-45 g, were randomly distributed in 500-L plastic tanks with aeration at 25 fish/tank. The fish were fed diets supplemented with durian rind at 0 (control), 10, 15, and 20 % twice daily, at 8:30 a.m. and 4:00 p.m., at 3 % of their body weight for 140 days. The tanks were scrubbed daily, and water changes were done every two days at 50% water volume. Water quality parameters were monitored throughout the feeding trial to ensure optimal culture conditions.

2.2 Preparation of durian rind and experimental diets

The preparation of durian rind and the composition of the experimental diets were performed following the protocols described earlier [19]. The white inner rind from ripe durian was cleaned, cut into small pieces, dried at 60 ^{o}C for 48 hours, and then ground. The powdered rind was mixed with other feedstuff to make four experimental diets: Diet 1, control without powder rind; Diets 2-4, with powder rind at 10, 15, and 20 %, respectively. The pelleted experimental diets were stored in polyethylene bags at 4 °C until used.

2.3 Preparation of bacterial solution

The *Aeromonas hydrophila* strains were kindly provided by the Aquatic Animal Health Research and Development Division, Department of Fisheries, Bangkok Province, Thailand. The procedure was adapted from Julie et al. [20]. It was cultured in tryptic soy broth (DifcoTM, France) at 37 ^{o}C for 24 h. The pellet from the bacterial cultured broth was extracted by centrifuging at 5000 rpm for 10 min (Eppendorf 5920 R, Germany). The pellets were then suspended in sterile 0.85 % NaCl and adjusted to the optical density of 1.0 at 540 nm (Thermo Scientific-Evolution 201, United States of America), equivalent to a bacterial concentration of 4.1 x 10^7 CFU/ml.

2.4 Blood sampling for hematology and phagocytic activity

After the 140-day feeding trial, 4 fish were randomly collected from each tank. The fish were injected intraperitoneally with 0.1 ml bacterial solution containing 4.1 x 10^7 CFU/ml of *A. hydrophila*. This bacterial concentration was used based on an earlier LC50 analysis [19]. Blood was collected from two fish 1 hour after injection and the other 3 hours after injection. A total of 8 fish per treatment per period were evaluated. One milliliter of blood was taken from each fish using 3-mL syringes and 21-gauge needles [21] pre-rinsed with 0.5 M EDTA (Ajax-Finechem (Univar), Australia) as an anticoagulant. The total red blood cell count, white blood cell count, and phagocytic activity were determined.

2.5 Red blood cell and white blood cell counts

Following the protocol of Fazio et al. [22], blood samples were first attenuated at 1:250 using Dacie's fluid as a diluent to count the total red blood cells. To get the total white blood cell count, blood was initially

attenuated at 1:100 with Turk's fluid as diluent. After dilution, the cells were counted immediately in a Neubauer chamber.

2.6 Phagocytic activity

Leukocytes were separated from the blood by density gradient separation. Briefly, 1 ml of the lymphoprep (density 1.077) (Corning, United States of America) was distributed into corning centrifuge tubes. One milliliter of blood solution, composed of 0.5 ml of blood and 0.5 ml of RPMI medium (Sigma, United Kingdom), was meticulously layered on the top of the lymphoprep. The ready samples were centrifuged at 400 g for 30 min at 4 ^{o}C. After that, leukocytes between the lymphoprep and plasma layers were painstakingly removed and transferred into new corning tubes containing 1 ml RPMI medium and then centrifuged at 400 g for 10 min at 4 ^{o}C. Leukocytes were washed twice in RPMI medium and diluted to 1×10^6 cells/ml. Phagocytic activity was then evaluated. Two hundred microliters of leukocyte suspension were pipetted on top of a cover slide and incubated at 4 ^{o}C for 1 h. Subsequently, the cover slides were rinsed softly 3 times with RPMI medium. Then, 200 µL of latex beads (1×10^7 cells/ml) were dispensed onto the cover slide. The slides with latex beads were incubated at 4 ^{o}C for 1 h. After that, the cover slides were gently washed with RPMI medium and fixed with methanol 96 % (v/v). The dried cover slides were stained using Dip Quick staining. Randomly, two hundred leukocytes on each slide were observed for the number of ingested latex beads and phagocytizing cells under a microscope. The leukocyte phagocytic activity, phagocytic index, and average number of latex beads ingested per cell were calculated according to formulas described in Itami et al. [23] and Rengpipat et al. [24].

2.7 Data analysis

Statistical analyses were performed using ANOVA, and the mean difference in each experiment was compared using Duncan's new multiple range test with a statistical program at a 95 percent assurance level.

3. Results and Discussion

Earlier research on the effect of durian rind on the growth performance of red tilapia suggests that there was no significant difference in growth performance among fish fed different levels of durian rind in the diets, and the survival rate of these treatments was more than 90% [19[. Here, we wanted to know how tilapia, fed diets with durian rind, respond to bacterial infection. Our findings showed that the total red blood cell (RBC) counts of red tilapia fed a control diet decreased after 3 h post-infection with *A. hydrophila* (Fig. 1). Previous reports suggest that *A. hydrophila* infection could reduce the number of blood cells by advocating erythrocyte hemolysis [25, 26]. *A. hydrophila* has been shown to produce a variety of extracellular products which act as essential virulent factors, such as hemolysin which is associated with hemolysis [27-31]. On the other hand, fish fed with diets supplemented with durian rind at all inclusion levels showed no decrease in total RBCs at 3 h post-infection and were significantly higher than the control ($P<0.05$) (Fig. 1). This could be because of the polysaccharide (PG) contained in durian rind. Previous studies have demonstrated that polysaccharides from plant sources, for instance *Diaphragma juglandis fructus* (the dry wooden diaphragm inside walnuts), *Schinus terebinthifolius* (Brazilian pepper-tree) and *Schinus* mole (Peruvian pepper-tree, California pepper-tree) exhibit anti-hemolytic properties [32, 33]. Snega Priya et al. [17] demonstrated that zebrafish, given encapsulated *Artemia* with PG as food for 20 days and then challenged with *Vibrio anguillarum* by immersion, showed significantly higher total RBCs than control fish.

Moreover, previous reports showed that PG extracted from durians exhibited antibacterial activity against Gram-positive and Gram-negative bacteria, including *Streptococcus agalactiae*, *Vibrio harveyi*, *Staphylococcus aureus*, *Escherichia coli* [34-36]. Thunyakipisal et al. [37] showed scanning electron micrographs of bacteria incubated in PG. Irregular-shaped cells and various-sized blebs were found on the bacterial membrane incubated in PG. In contrast, bacteria incubated in the culture broth medium without PG appeared round-shaped (cocci) with a smooth surface, suggesting that the antibacterial activity of PG may affect bacterial membrane integrity. In addition to PG substances, flavonoid extract of durian rind also has antibacterial activity [38, 39].

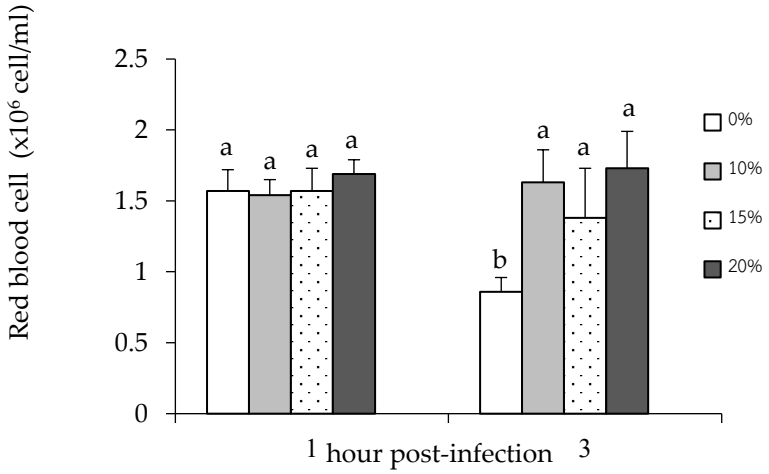


Figure 1. Red blood cell counts of red tilapia-fed diets supplemented with durian rind at varying inclusion levels and challenged with *A. hydrophila* at 1 and 3 hours post-infection. The data are represented as mean ± standard deviation (n = 8)

The innate immune system mediates the immune response to a bacterial infection almost instantaneously [40]. White blood cells (WBC), or leukocytes, are the key cells of vertebrate innate immunity in fish. Their major function is to combat infection by phagocytosing foreign organisms [41]. Therefore, the effect of durian rind on the innate immune response was examined through WBC counts and phagocytic activity. Our results indicate that a fish-fed diet supplemented with durian rind, regardless of inclusion levels, showed significantly increased WBC counts at 1 h post-infection with *A. hydrophila* compared to control ($P<0.05$). The increase in WBCs was directly proportional to the inclusion levels of durian rind in the diet (Fig. 2). Similarly, the increase in WBC count also increased phagocytic activity at 1 h post *A. hydrophila* infection. Fish fed a diet supplemented with 20% durian rind exhibited the highest phagocytic activity (Fig. 3A) and phagocytic index (Fig. 3B), both significantly different compared to control but not from 10% and 15% ($P<0.05$). The average number of the bead ingested per cell (ABPC) was not significant among treatment ($P>0.05$) (Fig. 3C). Our result is in line with Wang et al. [42] reported that crucian carp fed with plant PG exhibited enhanced innate immune response including serum bactericidal activity, lysozyme activity, total protein level, complement C3, superoxide dismutase activity as well as leukocyte phagocytosis activity. Hokputsa et al. [43] have isolated water-soluble polysaccharides from durian rinds (*Durio zibethinus*) and revealed that the principal components were pectic polysaccharides. Pectins are complex mixtures of polysaccharides and varieties of neutral sugars such as galactose, arabinose, glucose, mannose, and xylose [44]. Whole durian rind pectin yield is 73.67 % [45], of which white rind has 14.97% [46]. Pectin displays diverse biological activities, including immunomodulation [47]. The activity of pectin has been reported to increase the phagocytic activity of neutrophils, promote the formation of reactive oxygen species in these cells, and enhance NADPH oxidase activity, which plays a key role in the oxygen-dependent bactericidal activity of neutrophils [48]. Doan et al. [49] studied the effects of orange peel-derived pectin on the innate immune response of Nile tilapia (*Oreochromis niloticus*). Fish-fed orange peel-derived pectin showed significantly higher serum lysozyme and phagocytosis activity than the control.

The innate immunity of fish is propelled by pattern recognition receptors (PRRs), similar to immunological sensors, and protects the host from incursion of pathogens [50-52]. Several PRRs have been found and described in fish, including the Toll-like receptors (TLRs), retinoic acid-inducible gene-I (RIG-I)-like receptors (RLRs), and nucleotide-binding oligomerization domain (NOD)-like receptors (NLRs) [52]. PRRs function by recognizing pathogen-associated molecular patterns (PAMPs) derived from various microbial pathogens such as lipopolysaccharide [53], Flagellin [54], peptidoglycans, and lipoteichoic acids [55]. The recognition of PAMPs by PRRs leads to the production of inflammatory responses [53] and antiviral or antibacterial responses [56, 57]. Other than PAMPs derived from microbial organisms, complex pectin from

plant cell walls has been gaining research interest as a source of novel innate immune modulators. Hyun et al. [58] investigated the interactions in pattern recognition for common glycostructures of pectic heteropolysaccharides (HPSs) by Toll-like receptors (TLRs). They showed that pectic HPSs were selectively clustered with TLR4 during endocytosis. In fish, TLR4s are presumed sensors of bacterial ligands [56, 57]. In the current study, the increase in total white blood cells, phagocytosis activity, and phagocytic index may be because of pectin in durian rind that can stimulate the fish's immune response and primes it to fight pathogens. Thus, when fish fed with durian rind supplemented feeds are infected with the bacteria, they can quickly respond and eliminate the pathogen better than the control group. Over time, the immune system of the control fish began to develop, which is why there was no difference in the total white blood cells, phagocytosis activity, and phagocytic index at 3 hours post-infection. These earlier reports and our current results, substantiate the potential of durian rind supplementation in fish diets.

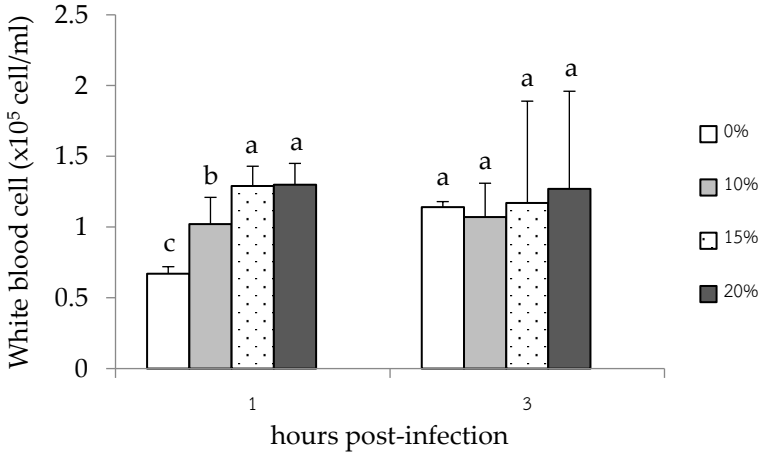


Figure 2. White blood cell counts of red tilapia-fed diets supplemented with durian rind at varying inclusion levels and challenged with *A. hydrophila* at 1 and 3 hours post-infection. The data are represented as mean ± standard deviation (n = 8)

4. Conclusions

Our results suggested that feed supplementation with durian rind can increase the level of white blood cells and phagocytic activity and prevent red blood cell lysis in red tilapia. Supplementing at least 10% durian rind can improve innate immune response and exhibit anti-hemolytic activity against *A. hydrophilla.* Furthermore, our results showed that discarded fruit wastes, such as durian peels, can be potentially used as feed additives/supplements in fish diets. We stress, however, that the current results are only limited to tilapia and that future studies can be conducted on its potential use as a feed additive for other cultured fish species. Further studies on other forms of durian rind supplemented in fish diet and combined with other feed additives to improve fish health are currently being undertaken.

5. Acknowledgements

The authors would like to thank Dr. Fernand F. Fagutao for his help in proofreading the manuscript.

Author Contributions: Conceptualization, D. P.; performed the experiments, D. P., N. S., W. N., and S. L.; writing-original draft preparation, D. P.; writing-review and editing, D. P.; supervision, D. P. All authors have read and agreed to the published version of the manuscript.

Funding: This research received no external funding.

Conflicts of Interest: The authors declare no conflict of interest.

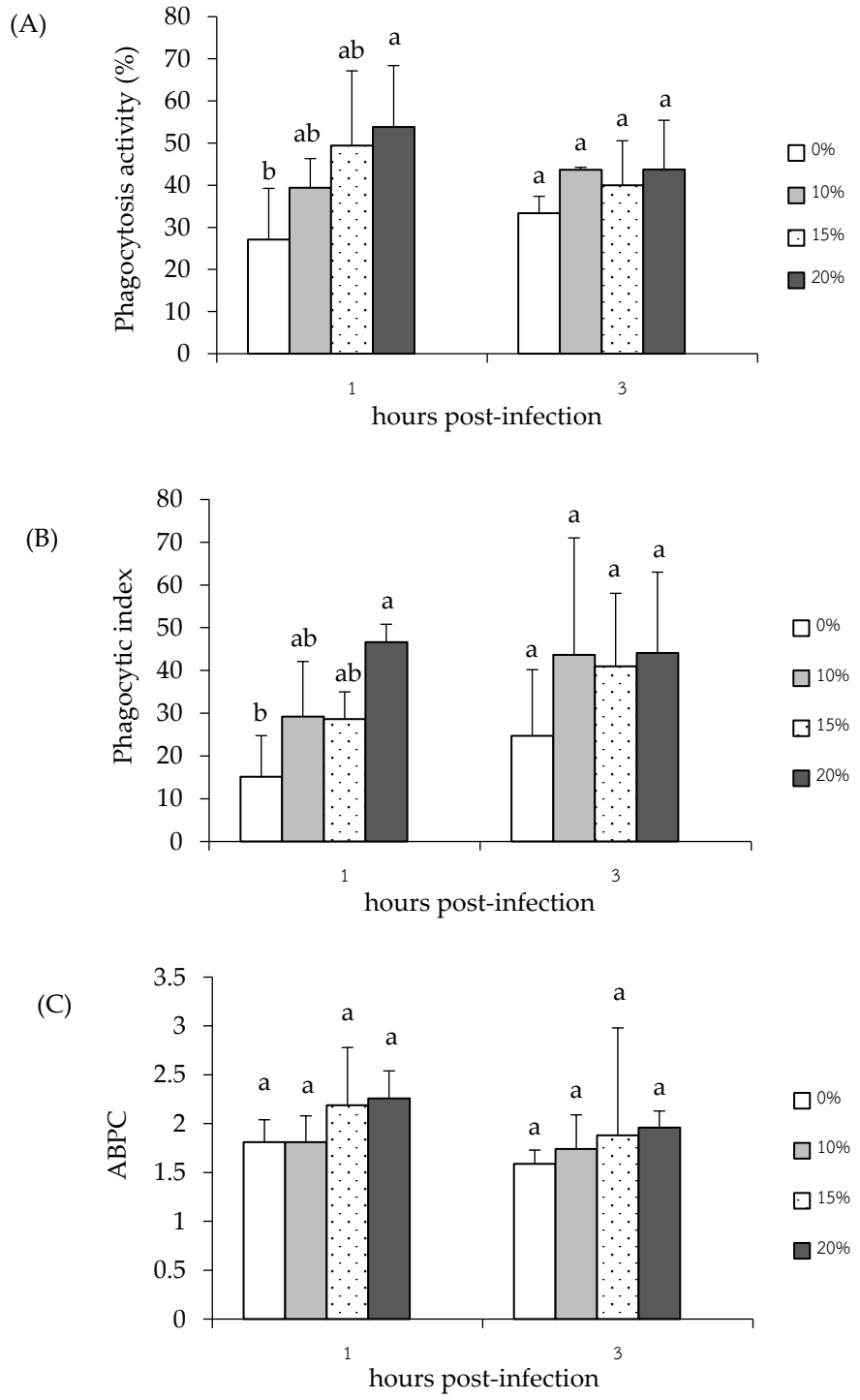


Figure 3. Phagocytosis activity (A), phagocytic index (B), and average number of beads ingested per cell : ABPC (C) of red tilapia-fed diets supplemented with durian rind at varying inclusion levels and challenged with *A. hydrophila* at 1 and 3 hours post-infection. The data are represented as mean ± standard deviation (n = 8)

References

[1] Yardimci, B.; Aydin, Y. Pathological findings of experimental *Aeromonas hydrophila* infection in Nile tilapia (*Oreochromis niloticus*). *Ankara Universitesi Veteriner Fakultesi Dergisi*. **2011**, *58*, 47-54.

[2] Pauzi, N. A.; Mohamad, N.; Azzam-Sayuti, M.; Yasin, I. S. M.; Saad, M. Z.; Nasruddin, N. S.; Azmai, M. N. A. Antibiotic susceptibility and pathogenicity of *Aeromonas hydrophila* isolated from red hybrid tilapia (*Oreochromis niloticus* × *Oreochromis mossambicus*) in Malaysia. *Veterinary World*. **2020**, *13*, 2166-2171.

[3] Saleh, A.; Elkenany, R.; Younis, G. Virulent and multiple antimicrobial resistance *Aeromonas hydrophila* isolated from diseased Nile tilapia fish (*Oreochromis niloticus*) in egypt with sequencing of some virulence-associated genes. *Biocontrol science*. **2021**, *26*, 167-176.

[4] Sukhavachana, S.; Ampolsak, K.; Poompuang, S. Positive genetic correlation between resistance to Aeromonasis and Streptococcosis in Nile tilapia *Oreochromis niloticus* (Linnaeus, 1758). *Journal of Fisheries and Environment*. **2020**, *44*, 45–54.

[5] Sen, K.; Rodgers, M. Distribution of six virulence factors in Aeromonas species isolated from US drinking water utilities: a PCR identification. *Journal of applied microbiology*. **2004**, *97*, 1077-1086.

[6] Sherif, A. H.; AbuLeila, R. H. Prevalence of some pathogenic bacteria in caged-Nile Tilapia (*Oreochromis niloticus*) and their possible treatment. *Jordan Journal of Biological Sciences*. **2022**, *15*, 239-247.

[7] Swann, L.; White, M. R. Diagnosis and treatment of "*Aeromonas hydrophila*" infection of fish. *Aquaculture Extension Illinois- Indiana Sea Gran Program.* **1991**.

[8] Tipmongkolsilp, N.; del Castillo, C. S; Hikima, J. I; Jung, T. S; Kondo, H; Hirono, I; Aoki, T. Multiple drug-resistant strains of *Aeromonas hydrophila* isolated from tilapia farms in Thailand. *Fish Pathology*. **2012**, *47*(2), 56-63.

[9] Samal, S. K; Das, B. K; Pal, B. B. Isolation, biochemical characterization, antibiotic susceptibility study of *Aeromonas hydrophila* isolated from freshwater fish. *International Journal of Current Microbiology and Applied Sciences*. **2014**, *3*(12), 259-267.

[10] Ali, S.; Akhter, S.; Muhammad, A.; Khan, I.; Khan, W. A.; Iqbal, M. N.; Umar, S.; Ahmed, H.; Ali, Q. Identification, characterization and antibiotic sensitivity of *Aeromonas hydrophila* a causative agent of epizootic ulcerative syndrome in wild and farmed fish from Potohar, Pakistan. *Pakistan Journal of Zoology*. **2016**, *48*(3), 899-901.

[11] Rachtanapun, P.; Luangkamin, S.; Tanprasert, K.; Suriyatem, R. Carboxymethyl cellulose film from durian rind. *LWT - Food Science and Technology*. **2012**, *48*, 52-58.

[12] Foo, K. Y.; Hameed, B. H. Textural porosity, surface chemistry and adsorptive properties of durian shell derived activated carbon prepared by microwave assisted NaOH activation. *Chemical Engineering Journal*. **2012**, *187*, 53-62.

[13] Lubis, R.; Saragih, S. W.; Wirjosentono, B.; Eddyanto, E. (2018, July 18-19). *Characterization of durian rinds fiber (Durio zubinthinus, murr) from North Sumatera*. The 3rd international seminar on chemistry: green chemistry and its role for sustainability. Surabaya, Indonesia. https://doi.org/10.1063/1.5082474

[14] Pongsamart, S.; Panmuang, T. Isolation of polysaccharide from fruit-hulls of durian (*Durio zibethinus* L.). *Songklanakarin Journal of Science and Technology*. **1998**, *20*, 323-332.

[15] González-Vega, R.; Del-Toro-Sánchez, C. L.; Moreno-Corral, R.; López-Elías, J. A.; Reyes-Díaz, A.; García-Lagunas, N.; Carvajal-Millán, E.; Fimbres-Olivarría, D. Sulfated polysaccharide-rich extract from *Navicula incerta*: physicochemical characteristics, antioxidant activity, and anti-hemolytic property. *AIMS Bioengineering*. **2022**, *9*, 364-382.

[16] Yang, H.; Bai, J.; Ma, C.; Wang, L.; Li, X.; Zhang, Y.; Xu, Y.; Yang, Y. Degradation models, structure, rheological properties and protective effects on erythrocyte hemolysis of the polysaccharides from *Ribes nigrum* L. *International Journal of Biological Macromolecules*. **2020**, *165*, 738-746.

[17] Snega Priya, P.; Ashwitha, A.; Thamizharasan, K.; Harishkumar, M.; Dinesh, S.; Nithya, T. G.; Kamaraj, M. Synergistic effect of durian fruit rind polysaccharide gel encapsulated prebiotic and probiotic dietary supplements on growth performance, immune-related gene expression, and disease resistance in Zebrafish (*Danio rerio*). *Heliyon*. **2021**, 7, https://doi.org/10.1016/j.heliyon.2021.e06669

[18] Pholdaeng, K.; Pongsamart, S. Studies on the immunomodulatory effect of polysaccharide gel extracted from *Durio zibethinus* in *Penaeus monodon* shrimp against *Vibrio harveyi* and WSSV. *Fish and Shellfish Immunology*. **2010**, *28*, 555-561.

[19] Sangkhonkhet, N.; Phanchindawan, N.; Lerdsuwan, S.; Nalinanon, W.; Pisuttharachai, D. Effect of *Durio zibethinus* Murr. cv. Monthong rind as a dietary ingredient in feed on the growth performance and disease resistance against *Aeromonas hydrophila* in Red Tilapia (*Oreochromis niloticus x Oreochromis mossambicus*). *ASEAN Journal of Scientific and Technological Reports*. **2023**, *26*, 39-48.

[20] Julie, B.; Julio, C.G.; Ahmed, D. Effect of copper sulfate on *Aeromonas hydrophila* infection in channel catfish fingerlings. *North American Journal of Aquaculture*. **2012**, *74*, 494-498.

[21] Duran, U.; Çenesiz, S.; Şahin, B. Blood sampling techniques and preparing for analysis in rainbow trout (*Oncorhynchus mykiss*). *Black Sea Journal of Agriculture*. **2023**, *6*(1), 68-73.

[22] Fazio, F.; Marafioti, S.; Filiciotto, F.; Buscaino, G.; Panzera, M.; Faggio, C. Blood hemogram profiles of farmed onshore and offshore gilthead sea bream (*Sparus aurata*) from Sicily, Italy. *Turkish Journal of Fisheries and Aquatic Sciences*. **2013**, *13*, 415-422.

[23] Itami, T.; Takahashi, Y.; Tsuchihira, E.; Igusa, H.; Kondo, M. Enhancement of disease resistance of kuruma prawn *Penaeus japonicus* and increase in phagocytic activity of prawn hemocytes after oral administration of ß-1, 3-glucan (Schizophyllan). In L.M. Chou, A.D. Munro, T.J. Lam, T.W. Chen, L.K.K. Cheong, J.K. Ding, K.K. Hooi, H.W. Khoo, V.P.E. Phang, K.F. Shim & C.H. Tan (Eds.), *The 3rd Asian Fisheries Forum* (pp. 375–378). Asian Fisheries Society, Manila, Philippines. **1994**.

[24] Rengpipat, S.; Rukpratanporn, S.; Piyatiratitivorakul, S.; Menasaveta, P. Immunity enhancement in black tiger shrimp (*Penaeus monodon*) by a probiont bacterium (*Bacillus* S11). *Aquaculture*. **2000**, *191*, 271-288.

[25] Xiong, N.X.; Luo, S.W.; Fan, L.F.; Mao, Z.W.; Luo, K.K.; Liu, S.J.; Wu, C.; Hu, F.Z.; Wang, S.; Wen, M.; Liu, Q.F. Comparative analysis of erythrocyte hemolysis, plasma parameters and metabolic features in red crucian carp (*Carassius auratus* red var) and triploid hybrid fish following *Aeromonas hydrophila* challenge. *Fish and Shellfish Immunology*. **2021**, *118*, 369-384.

[26] Xiong, N. X.; Ou, J.; Fan, L. F.; Kuang, X. Y.; Fang, Z. X.; Luo, S. W.; Mao, Z. W.; Liu, S. J.; Wang, S.; Wen, M.; Luo, K. K.; Hu, F. Z.; Wu, C.; Liu, Q. F. Blood cell characterization and transcriptome analysis reveal distinct immune response and host resistance of different ploidy cyprinid fish following *Aeromonas hydrophila* infection. *Fish and Shellfish Immunology*. **2022**, *120*, 547-559.

[27] Allan, B. J.; Stevenson, R. M. Extracellular virulence factors of *Aeromonas hydrophila* in fish infection. *Canadian journal of microbiology*. **1981**, *27*, 1114-1122.

[28] Pansare, A. C.; Lewis, N. F.; Venugopal, V. Characterization of extracellular proteases of *Aeromonas hydrophila*. *Agricultural and Biological Chemistry*. **1986**, *50*, 1743-1749.

[29] Santos, Y.; Toranzo, A. E.; Barja, J. L.; Nieto, T. P.; Villa, T. G. Virulence properties and enterotoxin production of Aeromonas strains isolated from fish. *Infection and immunity*. **1988**, *56*, 3285-3293.

[30] Esteve, C.; Birbeck, T. H. Secretion of haemolysins and proteases by *Aeromonas hydrophila* EO63: separation and characterization of the serine protease (caseinase) and the metalloprotease (elastase). *Journal of applied microbiology*. **2004**, *96*. 994-1001.

[31] Subashkumar, R.; Thayumanavan, T.; Vivekanandhan, G.; Lakshmanaperumalsamy, P. Occurrence of *Aeromonas hydrophila* in acute gasteroenteritis among children. *The Indian journal of medical research*. **2006**, *123*, 61-66.

[32] Meng, Q.; Chen, F.; Xiao, T.; Zhang, L. Inhibitory effects of polysaccharide from *Diaphragma juglandis* fructus on α-amylase and α-d-glucosidase activity, streptozotocin-induced hyperglycemia model, advanced glycation end-products formation, and H_2O_2-induced oxidative damage. *International Journal of Biological Macromolecules*. **2019**, *124*, 1080-1089.

[33] Feriani, A.; Tir, M.; Hamed, M.; Sila, A.; Nahdi, S.; Alwasel, S.; Harrath, A. H.; Tlili, N. Multidirectional insights on polysaccharides from *Schinus terebinthifolius* and *Schinus molle* fruits: Physicochemical and functional profiles, *in vitro* antioxidant, anti-genotoxicity, antidiabetic, and antihemolytic capacities, and *in vivo* anti-inflammatory and anti-nociceptive properties. *International journal of biological macromolecules*. **2020**, *165*, 2576-2587.

[34] Maktrirat, R.; Pongsamart, S.; Ajariyakhajorn, K.; Chansiripornchai, P. Bactericidal effect of post-milking teat dip prepared from polysaccharide gel from durian rinds on streptococci causing clinical bovine mastitis. *Acta Horticulturae*. **2008**, *786*, 33-40.

[35] Pholdaeng, K.; Pongsamart, S. Studies on the immunomodulatory effect of polysaccharide gel extracted from *Durio zibethinus* in *Penaeus monodon* shrimp against *Vibrio harveyi* and WSSV. Fish and Shellfish Immunology. **2010**, *28*, 555-561.

[36] Lipipun, V.; Nantawanit, N.; Pongsamart, S. Antimicrobial activity (*in vitro*) of polysaccharide gel from durian fruit-hulls. *Songklanakarin Journal of Science and Technology*. **2002**, *24*, 31-38.

[37] Thunyakipisal, P.; Saladyanant, T.; Hongprasong, N.; Pongsamart, S.; Apinhasmit, W. Antibacterial activity of polysaccharide gel extract from fruit rinds of *Durio zibethinus* Murr. against oral pathogenic bacteria. *Journal of investigative and clinical dentistry*. **2010**, *1*, 120-125.

[38] Hong, J.; Du, H. X.; Hu, J. Y. Ultrasonic-assisted extraction of flavonoids from durian peel and their antioxidant and antimicrobial activities. *Journal of Henan Agricultural University*. **2014**, *48*, 653-657.

[39] Hong, J.; Hu, J. Y.; Zhang, X.; Ma, X. M.; Han, S. Antioxidant and antibacterial activities of flavonoids extracted from durian peel. *Guizhou Agricultural Sciences*. **2014**, *42*, 41-43.

[40] Janeway, C. A.; Travers, P.; Walport, M.; Shlomchik, M. J. *Immunobiology: The Immune System in Health and Disease.* New York: Garland Science. **2001**. https://www.ncbi.nlm.nih.gov/books/NBK27090/

[41] Peter, S. G.; Gakuya, D. W.; Maingi, N.; Mulei, C. M. Prevalence and risk factors associated with *Ehrlichia* infections in smallholder dairy cattle in Nairobi City County, Kenya. *Veterinary World*. **2019**, *12*, 1599–1607.

[42] Wang, E.; Chen, X.; Wang, K.; Wang, J.; Chen, D.; Geng, Y.; Lai, W.; Wei, X. Plant polysaccharides used as immunostimulants enhance innate immune response and disease resistance against *Aeromonas hydrophila* infection in fish. *Fish and Shellfish Immunology*. **2016**, *59*, 196-202.

[43] Hokputsa, S.; Gerddit, W.; Pongsamart, S.; Inngjerdingen, K.; Heinze, T.; Koschella, A.; Harding, S.; Paulsen, B. (2004). Water-soluble polysaccharides with pharmaceutical importance from Durian rinds (*Durio zibethinus* Murr.): Isolation, fractionation, characterisation and bioactivity. *Carbohydrate Polymers*. **2004**, *56*, 471-481.

[44] Garna, H.; Mabon, N.; Wathelet, B.; Paquot, M. New method for a two-step hydrolysis and chromatographic analysis of pectin neutral sugar chains. *Journal of Agricultural and Food Chemistry*. **2004**, *52*, 4652-4659.

[45] Hasem, N. H.; Fuzi, S. F.; Kormin, F.; Bakar, M. F.; Sabran, S. F. (2018, November 11-13). *Extraction and Partial Characterization of durian Rind Pectin* [Earth and Environmental Science 269]. International conference on biodiversity. Johor Darul Takzim, Malaysia. doi:10.1088/1755-1315/269/1/012019

[46] Wang, H. Y.; Liao, M. S.; Zhang, M.; Wen, B.; Li, P. S.; Huang, C. X.; Wang, X. B. Study on the extraction of pectin technology from durian shell. *Science and Technology of Food Industry*. **2012**, *33*, 246-250.

[47] Popov, S. V.; Ovodov, Y.S. Polypotency of the immunomodulatory effect of pectins. *Biochemistry (Mosc)*. **2013**, *78*, 823-835.

[48] Zaitseva, O. O.; Polezhaeva, T. V.; Khudyakov, A. N.; Solomina, O. N.; Laptev, D. S.; Svedentsov, E. P.; Utemov, S. V.; Kostyaev, A. A. Influence of pectins on NADPH oxidase and phagocytic activity of neutrophils during cryopreservation. *Cryo Letters*. **2013**, *34*, 544-548.

[49] Doan, H. V.; Hoseinifar, S. H.; Elumalai, P.; Tongsiri, S.; Chitmanat, C.; Jaturasitha, S.; Doolgindachbaporn, S. Effects of orange peels derived pectin on innate immune response, disease resistance and growth performance of Nile tilapia (*Oreochromis niloticus*) cultured under indoor biofloc system. *Fish and Shellfish Immunology*. **2018**, *80*, 56-62.

[50] Liao, Z.; Su, J. Progresses on three pattern recognition receptor families (TLRs, RLRs and NLRs) in teleost. *Developmental and comparative immunology*. **2021**, *122*, 104131, https://doi.org/10.1016/j.dci.2021.104131.

[51] Sahoo, B. R. Structure of fish Toll-like receptors (TLR) and NOD-like receptors (NLR). *International Journal of Biological Macromolecules*. **2020**, *161*, 1602-1617.

[52] Li, Y.; Li, Y.; Cao, X.; Jin, X.; Jin, T. Pattern recognition receptors in zebrafish provide functional and evolutionary insight into innate immune signaling pathways. *Cellular and molecular immunology*. **2017**, *14*, 80-89.

[53] Li, Y.; Xia, P.; Wu, J.; Huang, A.; Bu, G.; Meng, F.; Kong, F.; Cao, X.; Han, X.; Yu, G.; Pan, X.; Yang, S.; Zeng, X.; Du, X. The potential sensing molecules and signal cascades for protecting teleost fishes against lipopolysaccharide. *Fish and Shellfish Immunology*. **2020**, *97*, 235-247.

[54] Wangkahart, E.; Secombes, C. J.; Wang, T. Studies on the use of flagellin as an immunostimulant and vaccine adjuvant in fish aquaculture. *Frontiers in immunology*. **2019**, *9*, 3054. https://doi.org/10.3389/fimmu.2018.03054

[55] Ribeiro, C. M.; Hermsen, T.; Taverne-Thiele, A. J.; Savelkoul, H. F.; Wiegertjes, G. F. Evolution of recognition of ligands from gram-positive bacteria: similarities and differences in the TLR2-mediated response between mammalian vertebrates and teleost fish. *Journal of immunology*. **2010**, *184*, 2355-2368.

[56] Pietretti, D.; Wiegertjes, G. F. Ligand specificities of Toll-like receptors in fish: indications from infection studies. *Developmental and comparative immunology*. **2014**, *43*, 205-222.

[57] Zhang, J.; Kong, X.; Zhou, C.; Li, L.; Nie, G.; Li, X. Toll-like receptor recognition of bacteria in fish: ligand specificity and signal pathways. *Fish and Shellfish Immunology*. **2014**, *41*, 380-388.

[58] Hyun, G. H.; Cho, I. H.; Yang, Y. Y.; Jeong, D. H.; Kang, Y. P.; Kim, Y. S.; Lee, S. J., Kwon, S. W. Mechanisms of interactions in pattern-recognition of common glycostructures across pectin-derived heteropolysaccharides by Toll-like receptor 4. *Carbohydrate Polymers*. **2023**, *314*, 120921, https://doi.org/10.1016/j.carbpol.2023.120921

ASEAN
Journal of Scientific and Technological Reports
Online ISSN:2773-8752

Research article

Enhancing Autonomous Driving: A Novel Approach of Mixed Attack and Physical Defense Strategies

Chuanxiang Bi[1], Shang Shi[2], and Jian Qu[3]*

[1] School of Engineering and Technology, Panyapiwat Institute of Management, Nonthaburi, 11120, Thailand
[2] School of Engineering and Technology, Panyapiwat Institute of Management, Nonthaburi, 11120, Thailand
[3] School of Engineering and Technology, Panyapiwat Institute of Management, Nonthaburi, 11120, Thailand
* Corresponding E-mail: jianqu@pim.ac.th

Citation:
Bi, C.; Shi, S.; Qu, J. Enhancing autonomous driving: A novel approach of mixed attack and physical defense strategies. *ASEAN J. Sci. Tech. Report.* **2025**, *28*(1), e254093. https://doi.org/10.55164/ajstr.v28i1.254093.

Article history:
Received: May 13, 2024
Revised: October 8, 2024
Accepted: October 17, 2024
Available online: December 14, 2024

Publisher's Note:
This article has been published and distributed under the terms of Thaksin University.

Abstract: Adversarial attacks are a significant threat to autonomous driving safety, especially in the physical world where there is a prevalence of "sticker-paste" attacks on traffic signs. However, most of these attacks are single-category attacks with little interference effect. This paper builds an autonomous driving platform and conducts extensive experiments on five single-category attacks. Moreover, we proposed a new physical attack - a mixed attack consisting of different single-category physical attacks. The proposed method outperforms existing methods and can reduce the accuracy of traffic sign recognition of an autonomous driving platform by 38%. Furthermore, we proposed a new anti-jamming model for physical adversarial defense, CBAM-ResNet26 & CBAM-Alexnet, which improves an autonomous driving platform's traffic sign recognition accuracy to 63% under mixed attack. Finally, experiments were also conducted with datasets with different ratios of adversarial attack examples, and the experimental results showed that in adversarial training, the higher the ratio of adversarial examples, the higher the recognition accuracy. However, a too high ratio would reduce the accuracy of normal traffic signs. Finally, the optimal ratio for physical adversarial defense training is 1:2.

Keywords: Autonomous Driving, Physical Attack, Mixed Attack, Physical Defenses, Adversarial Training.

1. Introduction

Adversarial attacks [1] have gradually become a research topic that attracts attention today. They can be used to deceive machine learning models and then produce wrong predictions. Even deep neural networks (DNN) [2] that have succeeded in recent years are also subject to such threats. Therefore, many aspects are susceptible to adversarial attacks, such as autonomous driving [3-5], image classification [6, 7], natural language processing [8-10], etc., thus creating huge security risks. There are two different attack forms: In digital form, the attacker can directly input the input digital image into the DNN classifier, and adversarial examples can also be generated by generative adversarial networks (GAN) [11-13]. However, since the generation process is challenging to control, using GANs to perform an aqueous attack on a given test image is difficult. (2)

Physical form, where the DNN classifier only accepts input from the camera, and the attacker can only present adversarial images to the camera. Kurakin et al. [14] printed adversarial pictures on paper and took pictures with a camera to successfully deceive the Inception v3 model. Evtimov et al. [15] placed black and white stickers on traffic signs to fool the classifier. Athalye et al. [16] created a 3D-printed turtle mistaken for a rifle or game by a DNN classifier. These illustrate that physical attacks require large or unlimited perturbations [17]. In contrast, digital attacks, it is usually small perturbations, but small perturbations are too subtle to be captured by cameras in complex physical world environments, which shows that although the generation of adversarial samples in the digital world is similar to that in the physical world, the generation methods in the digital world are difficult to transfer and apply to the physical world directly. On the one hand, there is a lot of noise in the actual physical environment, which may cause perturbation produced by perturbing unobservable limits. On the other hand, in the physical world, an attacker cannot directly modify the input data of the model. Moreover, most digital attacks are white-box attacks [18, 19], while most adversarial physical attacks are black-box attacks[20-22], so it is more practical to study adversarial physical attacks. Take the recognition of traffic signs by self-driving cars as an example. Under normal circumstances, self-driving cars correctly recognize real stop signs. However, if an attacker can physically and robustly manipulate the traffic sign, the deep neural network may misjudge it as other actions. Well, this could have serious consequences. Therefore, this paper focuses on traffic sign classification, establishes an autonomous driving platform, and deeply studies the nuances of the physical world. Through comparative experiments on the effectiveness of several single categories of physical attacks, such as QR code sticker attacks, Colored bar, and graffiti attacks, this paper proposes a real and effective adversarial physical attack, a mixed attack, can pose a huge threat to self-driving cars in recognizing traffic signs, and proves that physical adversarial perturbations can exist robustly under realistic assumptions.

Current research on adversarial attacks in the physical world reveals potential threats and encourages researchers to explore effective methods to defend against adversarial attacks. Several approaches have been proposed, such as adversarial training [23], an adversarial sample-based generation and training strategy designed to improve the ability of machine learning models against attacks. During training, the model is exposed to adversarial examples with minor perturbations to force it to learn representations that are robust to these perturbations. These techniques do not rely on detecting adversarial examples but formulate models that perform equally well under adversarial and normal inputs. In terms of physical defense, this paper proposes a model CBAM-ResNet26 & CBAM-Alexnet with better anti-interference performance based on the improvement of ResNet18 for the currently popular sticker attacks and the mixed attack proposed in this paper. It also proposes a model based on the currently popular adversarial training method. The optimal proportion of the dataset for adversarial training of physical attacks. This paper aims to reduce the threat of physical attacks on autonomous cars in identifying traffic signs by proposing a new model with better anti-interference and improving physical defense methods. Our main contributions to this paper are:

1: An extensive comparison of single-category physical attacks.

2: This paper proposed a novel mixed attack. When compared to single-category physical attacks, our mixed attack is more effective.

3: This paper proposes a new anti-interference model, CBAM-ResNet26 & CBAM-Alexnet. It has been proven through experiments that it exhibits higher accuracy in the face of interference, which is better than the current ResNet18 and Alex Net.

4: In terms of physical defense training methods, this paper established different proportions of datasets containing adversarial examples, trained different models, and compared them. As the proportion of adversarial examples increases, the recognition accuracy of smart cars gradually increases. However, an excessively high ratio of adversarial examples will reduce the model's recognition accuracy of normal traffic signs. Finally, this paper determined that the optimal ratio of the physical adversarial training dataset is 1:2.

2. Literature Review

2.1 Digital Attacks

Existing research on adversarial examples mainly focuses on two domains: the digital world and the

physical world. Adversarial examples from the digital world are embedded directly into the input of the model, and their amplitude is usually limited by the lp norm, such as l∞-norm [6, 24, 25], l2-norm, and l0-norm, to ensure that they are overlooked. In a white-box attack, after the attacker knows all the model details, he can use the gradient to generate perturbations [26, 27]. For example, the L-BFGS attack [28] was an early method to deceive models in image recognition tasks such as deep neural networks. This attack could already successfully deceive state-of-the-art classification models at the time, such as Alex Net [6] and QuocNet [29], resulting in the Misclassification of many image instances. In addition, digital attacks may also be black-box attacks, where the attacker can only query the target model and obtain the corresponding output without understanding its internal structure. In a black-box scenario, an attacker can exploit the cross-model generalization capabilities of adversarial examples or reconstruct the internal information of the model through multiple queries. Papernot et al. [30] proposed the Substitute Black Box Attack (SBA), an early practical black box method. The key idea is to train a substitute model to imitate the target black box model and use the white box attack method on the substitute model.

2.2 Physical Attacks

Academic research in recent years has examined whether adversarial attacks are effective in the physical world. Some research has been applied to the physical world by generating attacks in the digital world. ShapeShifter [31] generates adversarial stop signs with complex patterns by executing formulas, but applying them to real traffic signs is difficult. AdvCam [32] uses neural style transfer to create naturally corroded stop signs similar to the surrounding environment, making it difficult for humans to notice and maintain significant disturbances. However, those perturbations that modify the image's pixels must survive printing to be effective, and there is a high likelihood that the pixels will be lost in the printer's copy. Also, noise-based perturbations are impractical in the physical world because they are difficult to capture with distant cameras. Lu et al. [33] conducted experiments using traffic signs printed on poster paper and added fixed perturbations to the background of the traffic signs. However, this method is less feasible in practical applications because, in real life, the background is often not fixed. Evtimov et al. [15] proposed a Robust Physical Perturbation (RP2) attack, successfully showing how the generated landmarks can be physically implemented and fool the victim model in a controlled environment. The sticker attack proposed in it is a scenario where the attacker prints some stickers containing adversarial perturbations and pastes them on real traffic signs. Still, the mask used in the sticker attack only allows the perturbation to be generated on certain parts of the traffic signs, and the attack target is more limited to stop signs. The mixed attack proposed in this paper fully considers the suspiciousness of the attack, and its suspiciousness is low; this is achieved by adding a small part of the modified object, and the modification is similar to the common "noise" in the physical world; for example, people who are outside all year round There will be some stains, black spots on the traffic signs, advertisements posted on the traffic signs, etc. Therefore, to most observers, a mixed attack on the traffic signs may only be seen as vandalism or lack of quality and will not Arouse too much suspicion. Moreover, the mixed attack in this paper can attack a wide range of traffic sign types in terms of attack targets and can have different combinations of attack methods.

2.3 Physical Defenses

Adversarial training [23] is an effective defense method that retrains the model by injecting adversarial examples into the training set at each training iteration. Although adversarial training is relatively simple to implement and performs reasonably well, an adversarial trained model may still be susceptible to other types of adversarial examples that the model was not trained on. For example, adversarial training using examples generated by single-step gradient-based attacks (e.g., FGSM) shows robustness against the same type of attacks even when evaluated at scale, but not against single-step methods. The training results in less robust models for iterative gradient-based attacks such as BIM. Many methods have been proposed to make models more robust to adversarial attacks. Ensemble adversarial training [34] is a variant of adversarial training in which the model is retrained on generated adversarial examples to attack other pre-trained models. This decoupling of the target model and adversarial training examples overcomes the overfitting problem observed in ordinary versions of adversarial training. Trammell et al. [35] argue that ensemble adversarial

training is a good approximation of internal maximization due to the transferability of adversarial examples between different models. Furthermore, since the adversarial example generation process is independent of the trained model, they hypothesize that overall adversarial training will be more robust to future black-box attacks than standard adversarial training. Chen et al. [36] proposed the Drift Diffusion Model (DDDM) based on Dropout. They applied dropout technology to generate a cropped model of the target model and then used the output of each cropped model to perform threshold accumulation. When the decision evidence accumulates to a certain threshold, the result is a robust output, formulating a model that performs equally well under adversarial and normal inputs. Essentially, many of these methods attempt to reduce the model's sensitivity to irrelevant changes in the input, effectively regularizing the model to reduce the attack surface and limit the response to manifold perturbations. However, this paper starts from the model itself, proposes a new anti-interference model, and applies it to physical adversarial training based on the principles of adversarial training methods. By studying the different proportions of adversarial examples in the dataset, the results of physical adversarial training are obtained the optimal proportion of the dataset.

3. Materials and Methods

3.1 Mixed Attacks

This paper proposes an innovative adversarial physical attack strategy—mixed attack. A mixed attack is a multi-category combination attack, as shown in Figure 1. It mainly consists of QR code sticker attacks, Colord bars, graffiti attacks, and several single-category physical jamming combinations, and these attack elements can be combined in different ways or pasted in different locations to carry out mixed attacks on traffic signs, so according to the combination of the way and the location of the paste, the mixed attacks are very varied styles. Therefore, many types of mixed attacks depend on the combination and location. These single-category interferences are relatively common in the physical world. In subsequent experiments, we will compare the effectiveness of physical attacks such as QR code sticker attacks, Colored bars, and graffiti attacks. Compared with traditional single-category physical attacks, mixed attacks combine multiple elements and are more likely to mislead the judgment of deep learning models. The attack method mainly uses physical stickers. As shown in Figure 2, the mixed attack is carried out by sticking it on the traffic sign to be interfered with. It is designed to confuse the traffic sign recognition system of the autonomous car, causing it to generate wrong predictions.

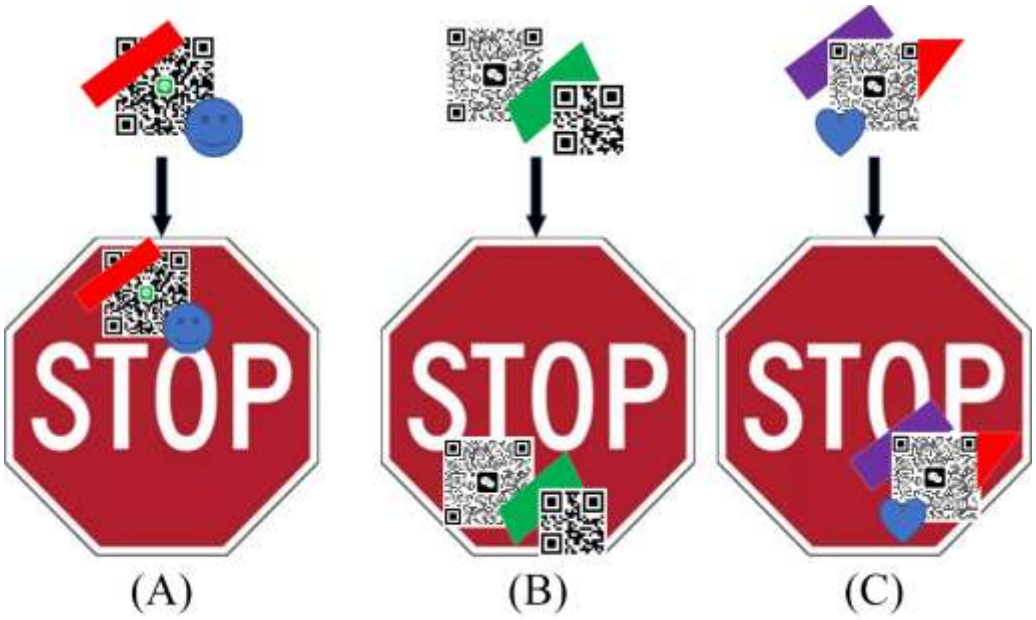


Figure 1. Example of mixed attack applied to a traffic traffic sign. (A) is a mixture of three attacks: QR code sticker attack, Colord bar, graffiti attack pasted on a traffic sign, (B) is a mixture of QR code sticker attack and Colord bar pasted on a traffic sign, (C) is a mixture of Colord bar, graffiti attack three

attacks mixed pasted on the traffic sign but at different locations on the traffic sign.

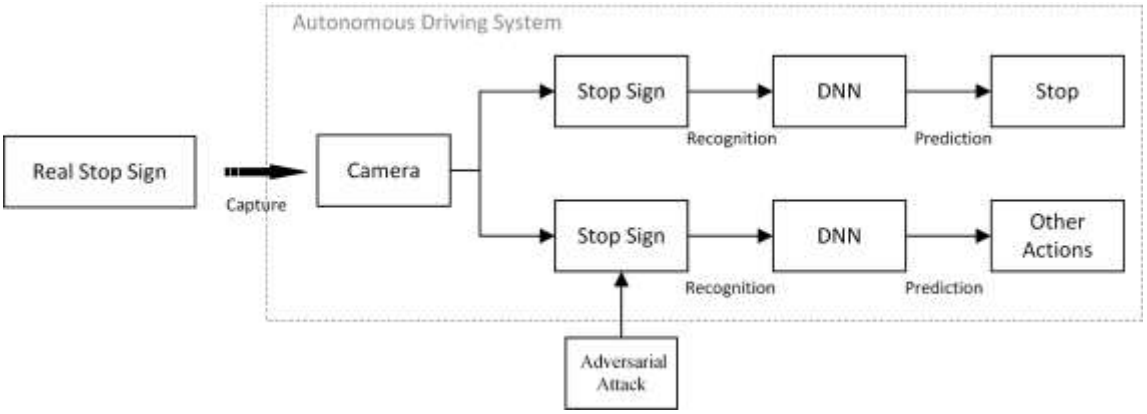


Figure 2. In the face of a real stop sign, the self-driving car normally acquires an image through the camera and then makes a stop action. Still, in the case of an adversarial attack, the camera acquires an image of the attack and is interfered with to make other actions.

3.2 CBAM-ResNet26&CBAM-AlexNet

We introduce the CBAM (Convolutional Block Attention Module) module, as shown in Figure 3, which combines channel and spatial attention mechanisms to enhance the model's feature extraction and learning capabilities. Channel attention obtains global information through global average pooling and maximum pooling, learns correlations between channels using convolutional layers and activation functions, and highlights essential channels by applying weights to the feature map through a sigmoid function. The spatial attention module, on the other hand, captures the spatial information between channels by performing average and maximum pooling along the channel dimensions and applies the attention weights to optimize the feature map. This channel and spatial attention combination enables the model to adaptively adjust the importance of different channels and locations in the feature map, thus improving the model's ability to recognize different targets and further enhancing the overall performance.

Based on this, we propose CBAM-Resnet26 & Alexnet. ResNet, as a deep convolutional neural network, solves the problem of gradient vanishing and explosion during deep network training by the design of residual blocks. Each residual block contains two consecutive convolutional layers, and the output of the second convolutional layer is added to the first output to form a residual connection. Based on the original ResNet-18 model, we propose a deeper Resnet26 model by adding convolutional layers and batch normalization layers to enhance its representation and feature learning capabilities. Subsequently, the CBAM module is introduced to construct CBAM-Resnet26. For better performance comparison, we added the CBAM module to the classical model AlexNet to form the CBAM-AlexNet model.

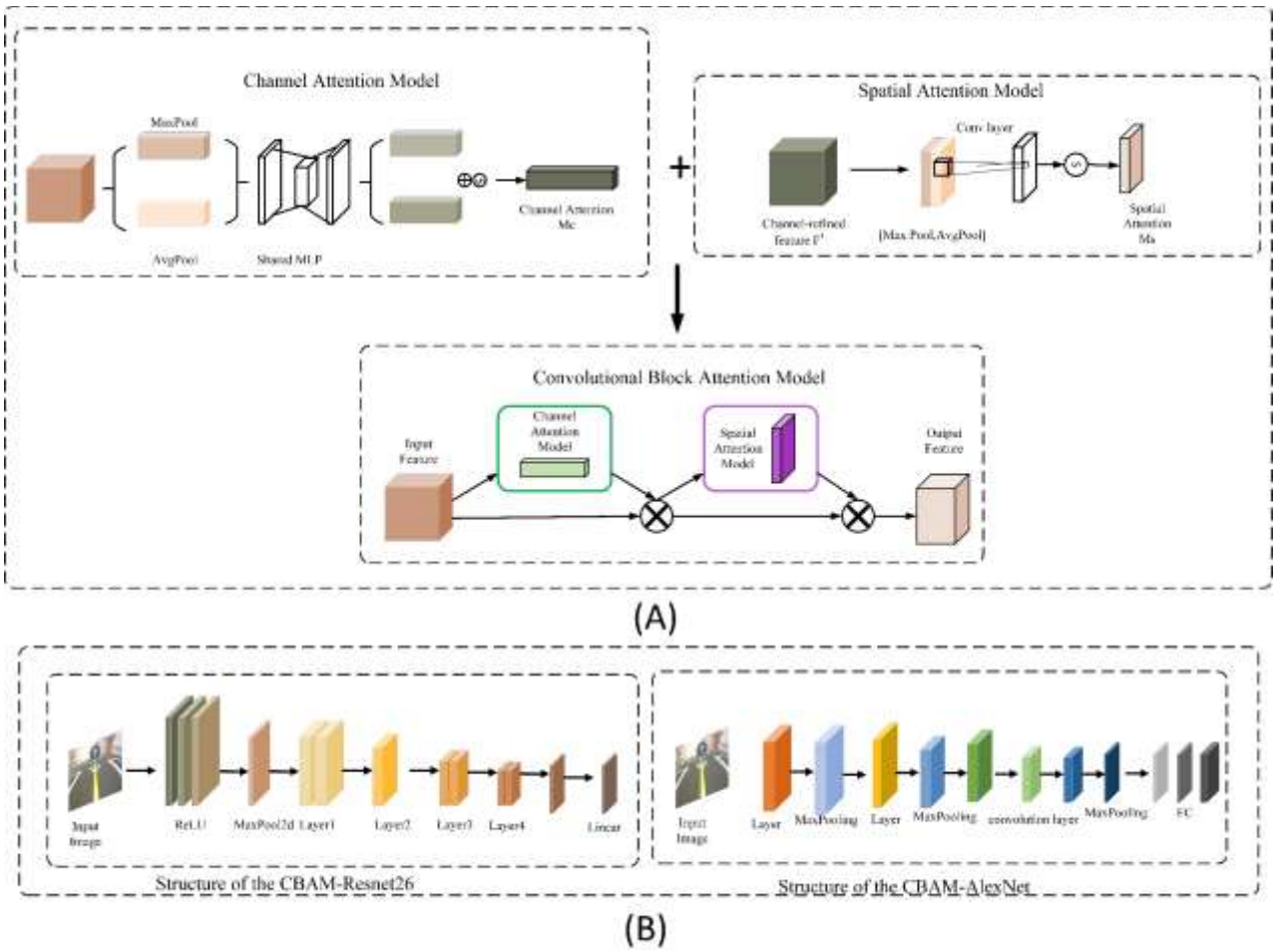


Figure 3. (A) CBAM consists of a combination of channel attention and spatial attention. (B) CBAM-ResNet26 and CBAM-AlexNet framework diagram proposes a deeper ResNet26 model based on the ResNet18 model.

3.3 Adversarial Physics Training

In addition to proposing a new model with better anti-interference performance to improve the robustness of the autonomous driving system to physical attacks, this paper also introduces an adversarial training method. It explores the optimal proportion of adding adversarial physical examples to the dataset. Adversarial physics training improves the robustness of the model by adding adversarial examples to the training data. We collected the adversarial examples in this paper, and then we constructed a training dataset that contains images of normal traffic signs and images of traffic signs using mixed attacks. However, the ratio of normal and adversarial example images in the dataset here is not optimal. For specific research, we tried datasets with different proportions of adversarial examples to train new model test effects and obtain the optimal proportion of adversarial examples in adversarial physics training. Specifically, we set different proportions of attack samples, such as 20%, 30%, 40%, 50%, etc., and trained corresponding deep-learning models. We use advanced deep learning models to train the model during the training process. During the experiment, we conducted a mixed attack on traffic signs. We evaluated the training effect of the model at different scales and recorded its performance.

4. Experimental Setup

4.1 Experimental environment

This research is not limited to only using deep neural network (DNN) classifiers for testing. This

research built an autonomous driving platform to study autonomous cars traffic sign recognition problems. It used a smart car equipped with a Jetson Nano motherboard as the research object to simulate real scenarios. Jetson Nano is a high-performance computing platform specially designed for embedded systems. It has the characteristics of small size and low power consumption. It is very suitable for use in scenarios such as smart cars so that they can complete tasks related to autonomous driving. The smart car is shown in Figure 4. To be close to the most primitive self-driving car, the smart car does not add any sensors except a camera. It is also combined with a deep neural network classifier to observe the traffic sign recognition process in a more realistic situation; thus, experiments were conducted to evaluate model performance more accurately.

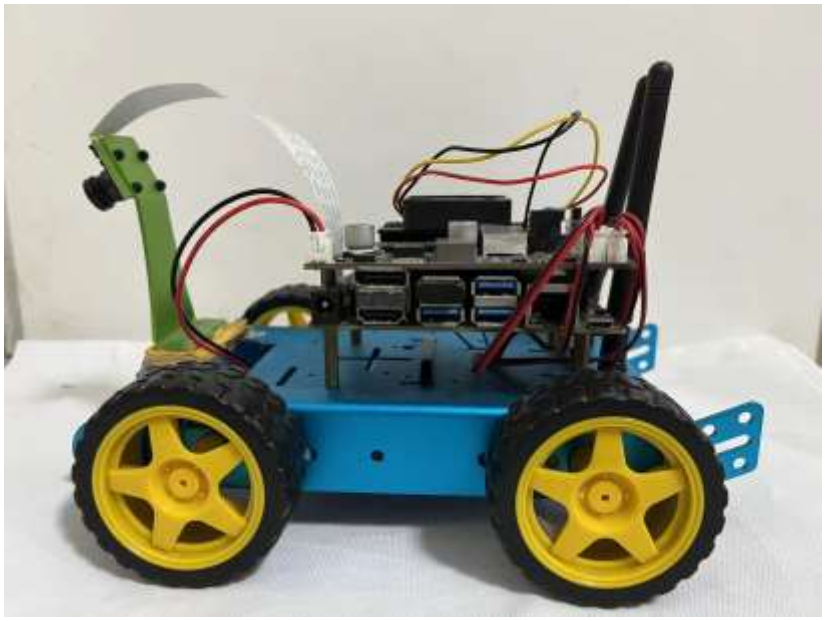


Figure 4. Smart car structure.

In the experimental environment, since the smart car continues to move forward while driving, the distance and angle of its camera relative to the traffic sign will change, so we need to fully consider the influence of these factors when designing the experiment. To simulate the real road environment, we chose a map to imitate the black road as the road where the smart car travels, as shown in Figure 5. At the same time, we took a series of measures to ensure the stability of the experimental environment. To create consistent light conditions, we blocked out external light, minimized other potentially intrusive noises, and kept the interior lighting steady, with a light intensity of 170lux. This paper chooses the four most basic functional indicators of traffic signs in the physical world: “forward,” “left,” “right,” and “stop.” To prevent the experiment from being accidental, two common traffic signs were chosen for each type of functional signage; these eight traffic signs had a radius of 12 cm, and we made sure that they had bases made of the same material with a base height of 6 cm, as shown in Figure 6. Such a design can reduce the possibility of the model identifying traffic signs by observing differences in other aspects of the traffic signs and improve the reliability and reproducibility of experimental results. At the same time, we also considered the importance of increasing the number and diversity of traffic signs. By introducing more types of traffic signs, we can more comprehensively evaluate the model's ability to recognize different traffic signs, thereby improving the rigor and practicality of the research. This study can conduct effective autonomous driving research in a more realistic road environment through the above comprehensive design..

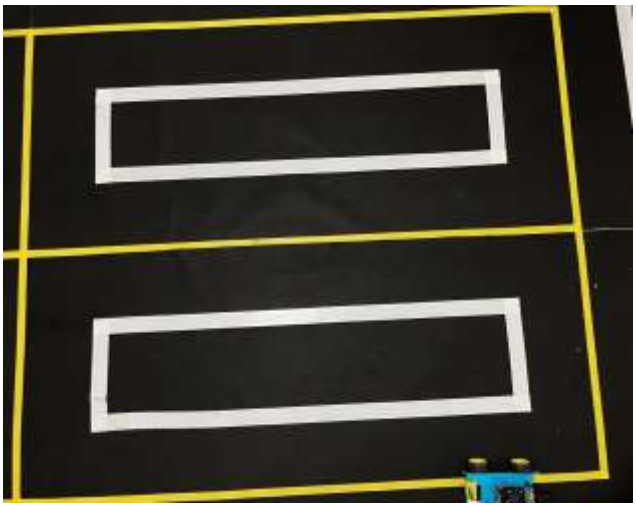


Figure 5. Smart car driving map.

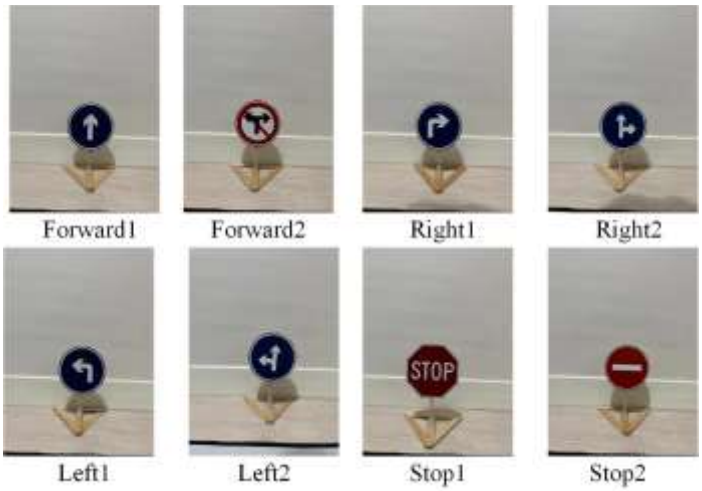


Figure 6. There are two types of "forward," "left," "right," and "stop" traffic signs, and there are a total of eight traffic signs.

4.2 Experimental design

In this paper's experimental design, mixed attacks apply multiple single-category interferences to traffic signs in a combined manner compared with the traditional single-category attack method. Therefore, mixed attacks have multiple combinations. We randomly add mixed attacks on the traffic signs, which can be grouped into 5 ways, as shown in Figure 7. A higher combination method (Figure 6) pastes these 5 ways of attack on 8 traffic signs in sequence. It conducts 10 tests at five different angles and distance settings (tests at each different angle and distance Twice). As shown in Figure 8, this multi-faceted testing method gives us a more comprehensive understanding of the model's ability to cope with complex environments. We recorded the smart car's response to the traffic signs during the test. We displayed the action probability distribution in real-time through the car's visual interface, as shown in Figure 9. When the probability value is higher than 0.5, the smart car will judge it as belonging to a category with a high probability value and successfully make the corresponding action. When the probabilities of the four categories do not exceed 0.5, the smart car will keep swinging left and right and pass the action. By analyzing probability distribution, we can more accurately assess the impact of attacks on the model. This study can conduct effective autonomous driving research in a more realistic road environment through the above comprehensive design.

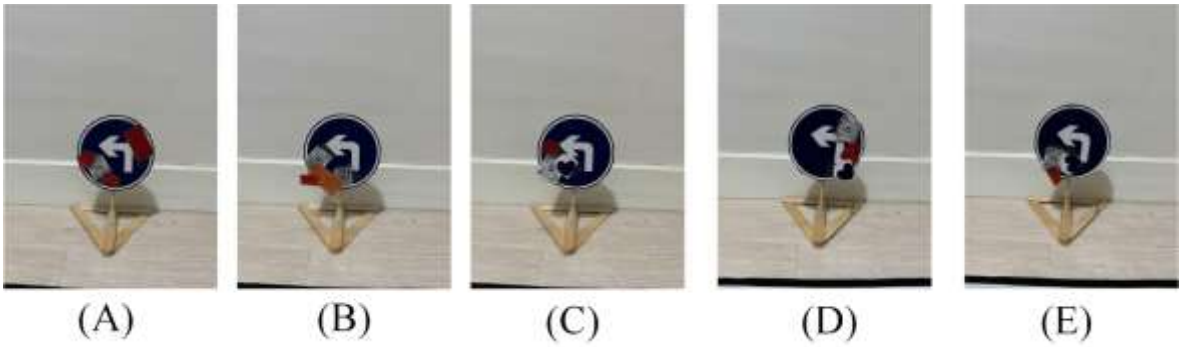


Figure 7. (A) QR code sticker attack, graffiti attack on the left side of the traffic sign, and Colord bar on the right side. (B) There were two QR code sticker attacks and a Colord bar on the left side of the traffic sign. (C) Only QR code sticker attacks and graffiti attacks are posted on the left side of the traffic sign. (D) Only QR code sticker attacks and graffiti attacks are posted on the right side of the traffic sign. (E) Only QR code sticker attacks, graffiti attacks, and Colord bars are posted below the traffic sign.

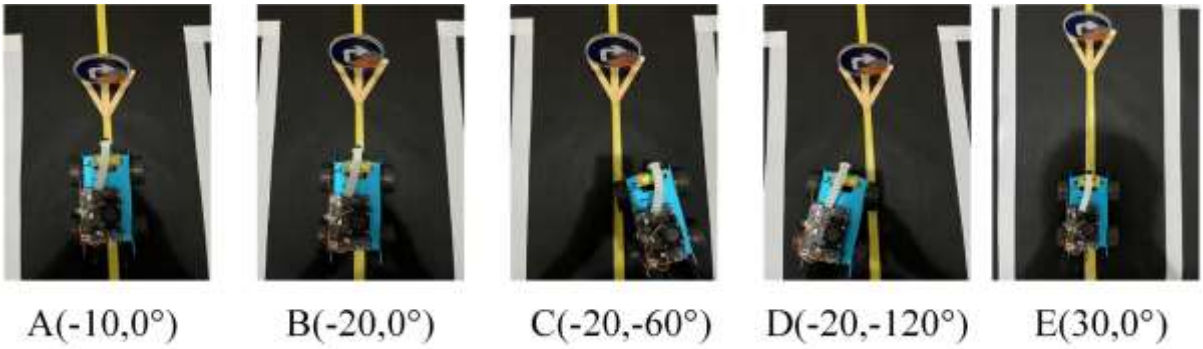


Figure 8. The location of the signpost is the origin (0, 0), the x-axis is the angle, and the y-axis is the distance. a is 10cm from the signpost, 0°, b is 20cm from the signpost, 0°, c is 20cm from the signpost, -60°, d is 20cm from the signpost, -120°, and e is 30cm from the signpost, 0°.

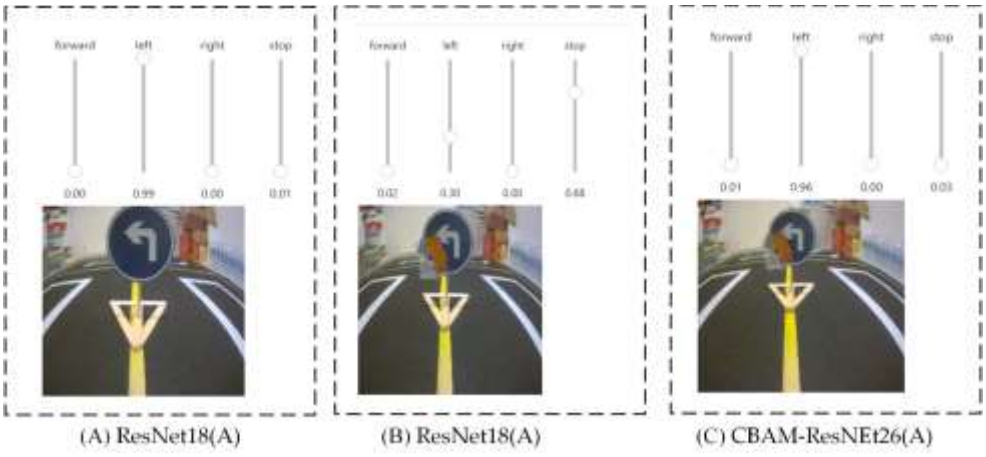


Figure 9. Probability distributions of actions shown in the visualization interface of the smart car, (A) ResNet18(A) test without physical attack, the probability of left is 0.99, (B) ResNet18(A) test with physical attack, the probability of left is 0.30, (C) CBAM-ResNet26(A) test with physical attack, the probability of left is 0.96.

4.3 Dataset

Aiming at the traffic sign recognition problem proposed above to study the traffic sign recognition

problem of the autonomous driving system, this study used self-collected data. Each dataset contains four categories: forward, left, right, and stop. As shown in Table 1, first, we established a basic dataset A, which collects normal pictures, which can ensure that smart cars can recognize traffic signs normally. Secondly, to deeply explore the effect of mixed attacks and the impact of the ratio of normal pictures to models in the dataset on model performance, we designed a series of adversarial physics training datasets, namely datasets B, C, D, and E, where each the datasets all include varying proportions of adversarial examples to evaluate the model's robustness and adversarial capabilities more fully. Next, we will detail the construction and design of these adversarial physics training datasets.

Table 1. The construction of five datasets.

Dataset	A	B	C	D	E
Number of attack images	0	800	1200	1600	2400
Normal images	4800	4000	3600	3200	2400
Total	4800	4800	4800	4800	4800
Proportions		1:5	1:3	1:2	1:1

4.3.1 Basic Dataset A

Firstly, we create a base dataset called Dataset A, designed to provide the basic data for the smart car to recognize traffic signs properly and make corresponding actions. The dataset contains four main categories: forward, left, right, and stop. We collected about 600 images covering eight types of traffic signposts and categorized them according to their function. There are about 1,200 images for each classification, totaling 4,800 images.

This basic dataset provides an important foundation for subsequent experiments, allowing smart cars to complete the basic functions of normal recognition of traffic signs. The model's recognition performance of traffic signs with different physical attacks can be compared on this basis. You can also compare the anti-interference effects of different models. Moreover, during the construction of Dataset A, we paid attention to the diversity and sufficiency of the data to ensure that the model can accurately identify and make decisions in various scenarios.

4.3.2 Dataset B

In Dataset B, we maintained a ratio of 1:5 between normal images and adversarial example images. Specifically, we collected 500 normal images for each traffic sign and 100 images with adversarial examples simultaneously. This ratio was chosen to enable the impact of the adversarial examples to be significantly represented in the dataset so that the robustness of the model can be better assessed.

4.3.3 Dataset C

In dataset C, we slightly reduced the proportion of adversarial examples, keeping the ratio of normal images to adversarial examples at 1:3. 450 normal images and 150 images with adversarial examples were collected for each traffic sign. By adjusting the ratio of adversarial examples, we can observe the model's performance under different interference levels in more detail, providing more references for the model's performance evaluation.

4.3.4 Dataset D

In Dataset D, we adjusted the ratio of adversarial examples to normal images to 1:2. 400 normal images and 200 images with adversarial examples were collected for each traffic sign. With this setup, we can further enhance the impact of adversarial examples in the dataset to assess the robustness and adversarial capability of the model more comprehensively.

4.3.5 Dataset E

Finally, in dataset E, we keep the ratio of normal images to adversarial examples at 1:1. 300 normal images and 300 images with adversarial examples are collected for each traffic signpost. This balanced ratio setting is intended to allow the model to have an equal number of training samples in the normal and adversarial cases, thus better evaluating the overall performance and adversarial capabilities of the model.

4.4 Model training

In our research, we conducted model training through the Google Colab platform. We uploaded the organized datasets to Google Drive, which makes data access and management more convenient. We chose PyTorch version 1.11.0 and the corresponding torch vision version 0.12.0 to ensure we could use the functions and optimizations. At the same time, we adopted Python 3.11. In addition, we also use CUDA 12.1 to utilize GPU for accelerated calculations to improve the efficiency of model training.

During the model training process, we divided the Dataset into a training set and a test set to ensure the independence and fairness of training and testing. This method can effectively evaluate the model's generalization ability and reduce the bias introduced by uneven partitioning of the Dataset. We set the number of training epochs to 60, a reasonable value verified through experiments, which can avoid overfitting problems while ensuring model performance. The learning rate is set to 0.001, a commonly used initial learning rate that can maintain a faster convergence speed in the early stages of training and avoid oscillation during the training process. We chose the Adam optimizer, an adaptive learning rate optimization method that can automatically adjust the learning rate to adapt to the characteristics of different parameters, thereby improving the model's convergence speed and generalization ability.

4.5 Evaluation methodology

In terms of evaluation methods, since our dataset is a four-category, the traditional average calculation or simple accuracy evaluation method is not accurate for our statistical experimental results. We chose the four-category confusion matrix method [5, 37]. This evaluation method is very suitable for our experiments. We introduce the four evaluation indicators of precision, recall, F1 Score, and accuracy. The formula is as follows:

$$\text{precision} = \frac{\text{TP}}{\text{TP} \pm \text{FP}} \tag{1}$$

$$\text{recall} = \frac{\text{TP}}{\text{TP} \pm \text{FN}} \tag{2}$$

$$\text{F1} = 2 \times \frac{\text{precision} \times \text{recall}}{\text{precision} + \text{recall}} \tag{3}$$

$$\text{accuracy} = \frac{\text{TP}}{\text{Total}} \tag{4}$$

Table 1. The distribution of TP, FN, FP, and TN is forward as the positive classification.

		Predicted			
		Forward	**Left**	**Right**	**Stop**
Actual	Forward	TP		FN	
	Left Right Stop	FP		TN	

In the calculation of evaluation indicators, we introduced four indicators: P (Positive), N (Negative), T (True), and F (False) to evaluate the environmental perception ability of smart cars. Among them, P means that the smart car predicts a positive classification, and N means that the smart car predicts an adverse classification. T means that the smart car's prediction is correct, and F means that the smart car's prediction is wrong. We took the related indicators of the forward class as an example to illustrate. By using forward as a positive classification and other categories as a negative classification, we obtained a 4×4 confusion matrix. In this matrix, TP means that the smart car correctly recognizes the positively classified traffic signs, FP means that the smart car incorrectly recognizes the negatively classified traffic signs as positive classification, TN means that the smart car correctly identifies the negatively classified traffic signs as negative. FN means the smart car mistakenly identifies positively classified traffic signs as negatively classified.

4.6 Experiment

4.6.1 Experiment 1: Evaluation of the effectiveness of different physical attacks in traffic sign attack recognition

This experiment evaluates the effectiveness of using the ResNet18 deep neural network model to test different physical attacks. As a commonly used model for image recognition, ResNet18 has the advantages of depth and residual connection. The model can learn identity mapping and avoid information loss when processing complex image scenes. We fully trained and tuned Dataset A on colab, obtained the deep learning model ResNet18(A), and deployed it to the smart car. Then, we conducted experiments on a series of single-type adversarial attacks, including colored bars, background noise, QR codes, graffiti attacks, PR2, and the mixed attacks we proposed (Figure 10), to compare the performance of ResNet18(A) in different physical the accuracy, recall rate, precision and F1 Score of identifying traffic signs under attacks are used to comprehensively evaluate the performance of the model in the face of various attacks.



Figure 10. Six different physical attacks.

4.6.2 Experiment 2: Comparative analysis of different deep learning models in traffic sign attack recognition

This experiment explores the differences in the performance of different deep learning models for traffic road marking under the same physical attack. In addition to ResNet18, which is mentioned in Experiment 1, AlexNet is a classical model, and CBAM-ResNet26&CBAM-AlexNet is also used. Firstly, we trained and deployed these four models, and then, based on the results of Experiment 1, we applied the most interfering physical attack on traffic road signs to compare the performance of these four models in recognizing the attacked road signs. Performance. By analyzing the performance of the models in depth, we can compare the models that are more resistant to interference.

4.6.3 Experiment 3: Exploring the effectiveness of Channel Attention and Spatial Attention

This experiment explores the effectiveness of Channel Attention and Spatial Attention in CBAM (Convolutional Block Attention Module). To verify whether both need to be applied simultaneously, we designed ablation experiments to remove the Channel Attention or Spatial Attention Module, respectively, and evaluate their effects on the model performance. We chose dataset A, used ResNet26 as the base model, added the following three modules: channel attention, spatial attention, and applied channel and spatial attention at the same time, conducted training and testing, and generated a total of three deep learning models deployed sequentially on a smart vehicle platform for testing and recorded the performance of the models in the mixed attack. The main metrics we focus on include model accuracy and robustness to environmental changes.

4.6.4 Experiment 4: Exploring the optimal ratio of physical adversarial training datasets

This experiment explores the defensive effect of models trained on Datasets with different proportions of adversarial examples against physical attacks. We selected Dataset B, Dataset C, Dataset D, and Dataset E as experimental objects. We used ResNet18, Alex Net, and CBAM-ResNet26 & CBAM-Alexnet to train and test each dataset and generated 12 deep-learning models. They are deployed on smart cars, and then mixed attacks are applied to traffic signs to record the performance of these models for evaluation. During the experiment, we focused on the accuracy of the model on the attacked traffic signs and tested the accuracy of the better-performing model on the original traffic signs. Finally, through the experimental results, we can confirm the good effect of the adversarial training method in physical defense and derive the optimal proportion of adversarial examples in the physical adversarial training set.

5. Result and Discussion

According to Experiment 1, this paper loaded ResNet18(A) trained with Dataset A into the smart car to test the accuracy of applying different physical attacks to traffic signs. The results can be seen in Table 3. The smart car can identify the original traffic signs. The accuracy is 100%, indicating that the model fits well. However, after applying physical attacks, the recognition accuracy decreases significantly. Among them, the mixed attack designed in this paper has the greatest interference, with a recognition accuracy of 38%, which shows that the mixed attack is very effective in attacking smart cars to recognize traffic signs. The background noise has the smallest impact, with an accuracy rate of 98%, indicating that background interference has very little interference with the smart car's recognition of traffic signs, indicating that the smart car's attention is on the pattern of traffic signs. Among single-category physical attacks, the application of QR code attacks also greatly interferes with recognizing traffic signs, with a recognition accuracy of 50%. Followed by color stickers, the recognition accuracy is 75%. Graffiti attack interference is average, and the recognition accuracy is 89%. Then, this paper imitated the robust physical perturbation (RP2) sticker attack proposed by Evtimov et al. and applied it to traffic signs. It was found that the recognition accuracy was not very low, at 67%. This shows that the sticker attack of PR2 is very important to this paper. The experimental interference of multiple traffic signs is not great, and PR2 has certain limitations. The multi-category mixed attacks proposed in this paper will more significantly interfere with smart cars' recognition of traffic signs.

Table 3.b Test results of smart cars against different physical attacks.

Evaluation indicators	Class	Original	Mixed Attack	QR-code	Background noise	Colored bar	Graffiti attack	PR2
Precision	Forward	1	0.44	0.48	0.96	0.72	0.93	0.77
	Left	1	0.42	0.53	1	0.81	0.86	0.68
	Right	1	0.61	0.87	0.96	1	1	0.76
	Stop	1	0.3	0.36	1	0.61	0.79	0.61
Recall	Forward	1	0.33	0.56	1	0.96	0.93	0.8
	Left	1	0.4	0.5	0.96	0.73	0.86	0.66
	Right	1	0.43	0.46	1	0.63	0.86	0.66
	Stop	1	0.46	0.5	96	0.7	0.9	0.7
F1	Forward	1	0.36	0.51	0.97	0.85	0.93	0.78
	Left	1	0.4	0.51	0.97	0.76	0.86	0.66
	Right	1	0.5	0.6	0.97	0.77	0.92	0.7
	Stop	1	0.36	0.41	0.97	0.65	0.84	0.65
Accuracy		**100%**	**38%**	**50%**	**98%**	**75%**	**89%**	**67%**

According to Experiment 2, this paper compares the robustness of three models to physical attacks. We use dataset A to train four models, which are ResNet18 (A), AlexNet (A), CBAM-ResNet26 (A), and CBAM-AlexNet (A), and then from the results of Experiment 1, it can be seen that there is a greater interference with the mixed attack, so this experiment applies the mixed attack is applied to traffic signposts. The experimental results are shown in Table 4. Among the four models, CBAM-ResNet26 (A) shows better anti-interference performance, with a recognition accuracy of 63%, followed by CBAM-AlexNet (A) model, with a recognition accuracy of 51%, which indicates that the introduction of the CBAM module is beneficial to improve the robustness of the model to physical attacks. In contrast, the recognition accuracy of the AlexNet(A) model is 51%. AlexNet(A) model has the lowest recognition accuracy of 30%.

Table 4. Test results of ResNet18(A), Alex Net(A), and CBAM-ResNet26(A)&CBAM-AlexNet(A) on traffic signs applying mixed attacks.

Evaluation indicators	Class	ResNet18(A)	Alex Net(A)	CBAM-ResNet26(A)	CBAM-AlexNet(A)
Precision	Forward	0.44	0.4	0.51	0.52
	Left	0.42	0.3	0.58	0.47
	Right	0.61	0.5	1	0.56
	Stop	0.3	0.18	0.45	0.46
Recall	Forward	0.33	0.4	0.7	0.6
	Left	0.4	0.3	0.56	0.45
	Right	0.43	0.26	0.56	0.47
	Stop	0.46	0.26	0.5	0.5
F1	Forward	0.36	0.4	0.59	0.55
	Left	0.4	0.3	0.56	0.46
	Right	0.5	0.34	0.71	0.51
	Stop	0.36	0.21	0.47	0.48
Accuracy		**38%**	**30%**	**63%**	**51%**

Table 5. Performance comparison of CA-ResNet26(A), SA-ResNet26(A) and CBAM-ResNet26(A).

Evaluation indicators	Class	CA-ResNet26(A)	SA-ResNet26(A)	CBAM-ResNet26(A)
Precision	Forward	0.62	0.6	0.51
	Left	0.58	0.55	0.58
	Right	0.62	0.61	1
	Stop	0.56	0.53	0.45
Recall	Forward	0.65	0.65	0.7
	Left	0.55	0.5	0.56
	Right	0.57	0.55	0.56
	Stop	0.6	0.6	0.5
F1	Forward	0.63	0.62	0.59
	Left	0.56	0.52	0.56
	Right	0.6	0.58	0.71
	Stop	0.58	0.56	0.47
Accuracy		**59%**	**57%**	**63%**

According to Experiment 3, by analyzing the experimental results of the three models, we can confirm that channel attention and spatial attention contribute to the model's performance improvement. According to Table 5, the experiments show that the CBAM model with complete model addition performs best under environmental changes, verifying the necessity of applying channel and spatial attention.

According to experiment 4, we collected dataset B, C, D, and E based on the ratios of 1:5, 1:3, 1:2, and 1:1. Each dataset was trained using ResNet18, Alex Net, and CBAM-ResNet26. A total of 12 deep learning models were generated for testing traffic signs applying mixed attacks. As can be seen from Tables 6, 7, and 8, we found that increasing the proportion of adversarial physical attack samples within a certain range can improve the robustness of the model. The most significant increase in accuracy was observed in the 1:5 and 1:3 ratios. In contrast, the increase in accuracy gradually slowed down in the 1:3 and 1:2 ratios, which demonstrated that physical adversarial training provides a good defense against physical attacks. However, the accuracy of some models decreases compared with the accuracy of the 1:2 ratio and the 1:1 ratio, which makes it difficult to determine the optimal ratio. Therefore, we further analyzed the training effect of the model

at different scales to determine the optimal adversarial physics training scale. We used ResNet18(D) and ResNet18(E) to test the recognition accuracy of original traffic signs. As shown in Table 9, although ResNet18(E) has a slightly higher accuracy than ResNet18(D) for traffic signs with mixed attacks, it does not. According to the original roadmap, ResNet18(D) accuracy is close to 100%. In comparison, the accuracy of ResNet18(E) is 78%, which has declined. When the proportion of attacking samples is too high, it may negatively affect the model's performance, decreasing the model's generalization ability. This suggests that if the proportion of adversarial examples in the total dataset is too high, the model's task of recognizing normal traffic signs will be affected, which confirms that the optimal ratio for physical adversarial training is 1:2 and demonstrates that the adversarial physical training methodology can effectively improve the resilience of the autopilot system against physical attacks.

Table 6. Test results of ResNet18 trained on different proportions of datasets for mixed attacks.

Evaluation indicators	Class	ResNet18(B)	ResNet18(C)	ResNet18(D)	ResNet18(E)
Precision	Forward	0.72	0.74	0.77	0.79
	Left	0.36	0.59	0.78	0.77
	Right	0.68	0.86	0.84	0.83
	Stop	0.3	0.62	0.64	0.69
Recall	Forward	0.52	0.72	0.77	0.75
	Left	0.4	0.65	0.72	0.7
	Right	0.37	0.62	0.7	0.77
	Stop	0.5	0.75	0.8	0.85
F1	Forward	0.6	0.72	0.77	0.76
	Left	0.37	0.61	0.74	0.73
	Right	0.48	0.72	0.76	0.79
	Stop	0.37	0.67	0.71	0.76
Accuracy		**45%**	**68%**	**75%**	**77%**

6. Conclusions

Due to the threat of adversarial attacks on automated driving, this paper is dedicated to studying adversarial physical attacks, physical defense models on automated driving and physical defense training methods. This paper conducts experiments by building an autonomous driving platform. The experimental results show that in terms of adversarial attacks, the mixed attack proposed in this paper performs better than the QR code sticker attack, Colored bar attack, graffiti attack, background attack, and PR2 attack. A mixed attack can reduce the accuracy of traffic sign recognition of an autonomous driving platform by 38%. The CBAM-ResNet26 proposed in this paper has better anti-interference performance regarding physical defense models. Using the same dataset to train and compare the recognition accuracy, the recognition accuracy of CBAM-ResNet26(A) reaches 63%, but the recognition accuracy of Alex Net is only 30%. Furthermore, this paper collects datasets of adversarial physical training with different proportions. Through comparison, it is found that as the proportion of adversarial examples increases, the recognition accuracy of smart cars is higher. However, an excessively high ratio of adversarial examples will reduce the model's recognition accuracy of normal traffic signs. Therefore, this paper finally concluded that the optimal ratio of physical adversarial training is 1:2. The source code and, dataset video for this study can be found at https://github.com/BiChuanxiang/Mixed-Attack-and-Physical-Defense-Strategies.

Table 7. Test results of Alex Net trained on different proportions of datasets for mixed attacks.

Evaluation indicators	Class	Alex Net(B)	Alex Net(C)	Alex Net(D)	Alex Net(E)
Precision	Forward	0.53	0.62	0.66	0.63
	Left	0.34	0.46	0.7	0.64
	Right	0.6	0.84	0.82	0.71
	Stop	0.23	0.5	0.46	0.59
Recall	Forward	0.45	0.57	0.65	0.7
	Left	0.3	0.5	0.6	0.6
	Right	0.35	0.52	0.6	0.62
	Stop	0.4	0.62	0.67	0.65
F1	Forward	0.48	0.59	0.65	0.66
	Left	0.31	0.47	0.64	0.62
	Right	0.44	0.64	0.69	0.66
	Stop	0.29	0.55	0.54	0.61
Accuracy		**37%**	**55%**	**63%**	**64%**
Precision	Forward	0.7	0.81	0.93	0.88
	Left	0.68	0.83	0.86	0.85
	Right	0.87	0.94	1	0.94
	Stop	0.62	0.77	0.79	0.85
Recall	Forward	0.72	0.9	0.93	0.95
	Left	0.65	0.77	0.86	0.87
	Right	0.67	0.8	0.86	0.8
	Stop	0.77	0.87	0.9	0.9
F1	Forward	0.7	0.85	0.93	0.91
	Left	0..66	0.79	0.86	0.85
	Right	0.75	0.86	0.92	0.86
	Stop	0.68	0.81	0.84	0.87
Accuracy		**71%**	**84%**	**89%**	**88%**

Table 9. Test results of CBAM-ResNet26-D and CBAM-ResNet26-E on the original traffic signs.

Evaluation indicators	Class	CBAM-ResNet26(D)	CBAM-ResNet26(E)
Precision	Forward	0.95	0.78
	Left	0.97	0.78
	Right	0.97	0.82
	Stop	0.9	0.73
Recall	Forward	0.95	0.9
	Left	0.92	0.65
	Right	0.95	0.72
	Stop	0.97	0.85
F1	Forward	0.95	0.83
	Left	0.94	0.71
	Right	0.95	0.76
	Stop	0.93	0.78
Accuracy		**95%**	**78%**

7. Acknowledgments

Author Contributions: "Conceptualization, C.X.B., S.S., and J.Q.; methodology, C.X.B., S.S., and J.Q.; software, C.X.B., S.S., and J.Q.; validation, C.X.B., S.S., and J.Q.; formal analysis, C.X.B., S.S., and J.Q.; investigation, C.X.B., S.S., and J.Q.; resources, C.X.B., S.S., and J.Q.; data curation, C.X.B., S.S., and J.Q.; writing—original draft preparation, C.X.B., S.S., and J.Q.; writing—review and editing, C.X.B., S.S., and J.Q.; visualization, C.X.B., S.S., and J.Q.; supervision, J.Q.; project administration, J.Q.; C.X.B contributed 45%, S.S. contributed 5% and J.Q contributed 50%. J.Q is the corresponding author. All authors have read and agreed to the published version of the manuscript."

Funding: C.X.B. and S.S. received full scholarships from CPALL while conducting this research in PIM.

Conflicts of Interest: The authors declare no conflict of interest.

References

[1] Akhtar N.; Mian A. Threat of adversarial attacks on deep learning in computer vision: A survey[J]. *Ieee Access*, **2018**, 6, 14410-14430. https://doi.org/10.1109/ACCESS.2018.2807385

[2] Ni, J.; Chen, Y.; Chen, Y.; Zhu, J.; Ali, D.; Cao, W. A survey on theories and applications for self-driving cars based on deep learning methods.*AS*. **2020**, *10*(8), 2749. https://doi.org/10.3390/app10082749.

[3] Li, Y.; Qu, J. Intelligent road tracking and real-time acceleration-deceleration for autonomous driving using modified convolutional neural networks. *CAST*. **2022**, *22*(6), 10.55003-10.55003 (26 pages). https://doi.org/10.55003/cast.2022.06.22.013.

[4] Bai, T.; Luo, J.; Zhao, J. Inconspicuous adversarial patches for fooling image-recognition systems on mobile devices. *IEEE Internet of Things Journal*. **2021**, *9*(12), 9515-9524. .https://doi.org/10.1109/JIOT.2021.3124815.

[5] Ding, S.; Qu, J. Research on Multi-tasking Smart Cars Based on Autonomous Driving Systems.*SN.* **2023**, *4*(3), 292. https://doi.org/10.1007/s42979-023-01740-1.

[6] Krizhevsky, A.; Sutskever, I.; Hinton, G. E. ImageNet classification with deep convolutional neural networks.*Communications of the ACM*. **2017**, *60*(6), 84-90. https://dl.acm.org/doi/abs/10.1145/3065386

[7] He, K.; Zhang, X.; Ren, S.; Sun, J. Deep residual learning for image recognition. *In Proceedings of the IEEE conference on computer vision and pattern recognition*, **2016**, 770-778.

[8] Li, J.; Chen, X.; Hovy, E.; Jurafsky, D. Visualizing and understanding neural models in NLP. **2015**. arXiv preprint arXiv:1506.01066.https://doi.org/10.48550/arXiv.1506.01066

[9] Cambria, E.; White, B. Jumping NLP curves: A review of natural language processing research.*IEEE Computational intelligence magazine*. **2014**, *9*(2), 48-57.https://ieeexplore.ieee.org/abstract/document/6786458

[10] Strubell, E.; Ganesh, A.; McCallum, A. Energy and policy considerations for modern deep learning research. *Proceedings of the AAAI conference on artificial intelligence*. **2020**, *34*(09), 13693-13696. https://doi.org/10.1609/aaai.v34i09.7123.

[11] Hu, Y. C. T.; Kung, B. H.; Tan, D. S., et al. Naturalistic physical adversarial patch for object detectors. *Proceedings of the IEEE/CVF International Conference on Computer Vision*. **2021**, 7848-7857.

[12] Sharif, M.; Bhagavatula, S.; Bauer, L.; Reiter, M. K. A general framework for adversarial examples with objectives.*ACM Transactions on Privacy and Security (TOPS)*. **2019**, *22*(3), 1-30. https://doi.org/10.1145/3317611.

[13] Xiao, Z.; Gao, X.; Fu, C.; et al. Improving transferability of adversarial patches on face recognition with generative models. *Proceedings of the IEEE/CVF conference on computer vision and pattern recognition*. **2021**, 11845-11854.

[14] Kurakin, A.; Goodfellow, I. J.; Bengio, S. Adversarial examples in the physical world. *In Artificial intelligence safety and security*, **2018**.

[15] Evtimov, I.; Eykholt, K.; Fernandes, E.; Kohno, T.; Li, B.; Prakash, A.; Rahmati, A.; Song, D. Robust physical-world attacks on machine learning models. *arXiv preprint arXiv:1707.08945*. **2017**, *2*(3), 4.

[16] Athalye, A.; Engstrom, L.; Ilyas, A., et al. Synthesizing robust adversarial examples[C]. *International conference on machine learning. PMLR*, **2018**, 284-293.

[17] Zheng, S.; Song, Y.; Leung, T.; et al. Improving the robustness of deep neural networks via stability training[C]. *Proceedings of the ieee conference on computer vision and pattern recognition*. **2016**, 4480-4488. https://www.cv-foundation.org/openaccess.
[18] Kurakin, A.; Goodfellow, I. J.; Bengio, S. Adversarial examples in the physical world[M]//Artificial intelligence safety and security. *Chapman and Hall/CRC*, **2018**, 99-112.
[19] Madry A. Towards deep learning models resistant to adversarial attacks[J]. *arXiv preprint arXiv:1706.06083*, **2017**.
[20] Wei, X.; Guo, Y.; Yu, J. Adversarial sticker: A stealthy attack method in the physical world. *IEEE Transactions on Pattern Analysis and Machine Intelligence*. **2022**, *45*(3), 2711-2725. https://doi.org/10.1109/TPAMI.2022.3176760.
[21] Wei, X.; Guo, Y.; Yu, J., et al. Simultaneously optimizing perturbations and positions for black-box adversarial patch attacks[J]. *IEEE transactions on pattern analysis and machine intelligence*, **2022**, *45*(7), 9041-9054. https://doi.org/10.1109/TPAMI.2022.3231886.
[22] Wei, X.; Yan, H.; Li, B. Sparse black-box video attack with reinforcement learning. International Journal of Computer Vision. **2022**, *130*(6), 1459-1473. https://link.springer.com/article/10.1007/s11263-022-01604-w.
[23] Goodfellow, I. J.; Shlens, J.; Szegedy, C. Explaining and harnessing adversarial examples[J]. *arXiv preprint arXiv:1412.6572*, **2014.** https://doi.org/10.48550/arXiv.1412.6572.
[24] Girshick, R.; Donahue, J.; Darrell, T., et al. Rich feature hierarchies for accurate object detection and semantic segmentation[C]. *Proceedings of the IEEE conference on computer vision and pattern recognition*. **2014**, 580-587.
[25] Gehring, J.; Auli, M.; Grangier, D.; Yarats, D.; Dauphin, Y. N. Convolutional sequence to sequence learning. *In International conference on machine learning, PMLR*; **2017**.
[26] Graves, A.; Mohamed, A.; Hinton, G. Speech recognition with deep recurrent neural networks. *IEEE international conference on acoustics,* **2013**, 6645-6649. https://doi.org/10.1109/ICASSP.2013.6638947.
[27] McCauley, R. N.; Henrich, J. Susceptibility to the Müller-Lyer illusion, theory-neutral observation, and the diachronic penetrability of the visual input system. *Philosophical Psychology*. **2006**, *19*(1), 79-101. https://doi.org/10.1186/s13229-017-0127-y.
[28] Szegedy C. Intriguing properties of neural networks[J]. *arXiv preprint arXiv:1312.6199*, **2013**.
[29] Le, Q. V. Building high-level features using large scale unsupervised learning. *international conference on acoustics, speech and signal processing. IEEE*, **2013**, 8595-8598. https://doi.org/10.1109/ICASSP.2013.6639343.
[30] Papernot, N.; McDaniel, P.; Goodfellow, I. Jha, S.; Celik, Z. B.; Swami, A. Practical black-box attacks against deep learning systems using adversarial examples. *arXiv preprint arXiv:1602.02697*. **2016**, *1*(2), 3.
[31] Lu. J.; Sibai, H.; Fabry, E. Adversarial examples that fool detectors[J]. *arXiv preprint arXiv:1712.02494*, **2017**. https://doi.org/10.48550/arXiv.1712.02494.
[32] Duan, R.; Ma, X.; Wang, Y.; Bailey, J.; Qin, A. K.; Yang, Y. Adversarial camouflage: Hiding physical-world attacks with natural styles. *In Proceedings of the IEEE/CVF conference on computer vision and pattern recognition*, **2020**.
[33] Lu, J.; Sibai, H.; Fabry, E., et al. No need to worry about adversarial examples in object detection in autonomous vehicles[J]. *arXiv preprint arXiv:1707.03501*, **2017**.
[34] Kurakin, A. Goodfellow I, Bengio S. Adversarial machine learning at scale[J]. *arXiv preprint arXiv:1611.01236*, **2016**.
[35] Tramèr F, Kurakin A, Papernot N, et al. Ensemble adversarial training: Attacks and defenses[J]. *arXiv preprint arXiv:1705.07204*, **2017**.
[36] Chen, X.; Li, X.; Zhou, Y., et al. DDDM: a Brain-Inspired Framework for Robust Classification[J]. *arXiv preprint arXiv:2205.10117*, **2022.**
[37] Qu.; J. Multi-Task in Autonomous Driving through RDNet18-CA with LiSHTL-S Loss Function.*ECTI Transactions on Computer and Information Technology (ECTI-CIT)*. **2024**, *18*(2), 158-173. https://doi.org/10.37936/ecti-cit.2024182.254780.

ASEAN
Journal of Scientific and Technological Reports
Online ISSN:2773-8752

Research article

An AIoT-based Air Quality Monitoring System for Real-time $PM_{2.5}$ Prediction in Urban Environments

Nuth Otanasap[1*], Siriwich Tadsuan[2], and Chanintorn Chalermsuk[3]

[1] Department of Computer Engineering, Faculty of Engineering, Southeast Asia University, Bangkok, 10160, Thailand
[2] Department of Electrical Engineering, Faculty of Engineering, Southeast Asia University, Bangkok, 10160, Thailand
[3] Department of Digital Technology and Innovation, Faculty of Arts and Sciences, Southeast Asia University, Bangkok, 10160, Thailand
* Correspondence: E-mail: nuto@sau.ac.th

Citation:
Otanasap, N. ; Tadsuan, S.; Chalermsuk, C. An AIoT based air quality monitoring and forecasting system for real-time $PM_{2.5}$ prediction in urban environments. *ASEAN J. Sci. Tech. Report.* **2025**, *28*(1), e255168. https://doi.org/10.55164/ajstr.v28i1.255168

Article history:
Received: July 24, 2024
Revised: October 20, 2024
Accepted: October 25, 2024
Available online: December 14, 2024

Publisher's Note:
This article has been published and distributed under the terms of Thaksin University.

Abstract: This study aimed to develop an air quality monitoring and forecasting system focusing on $PM_{2.5}$ using a combination of AI of Things (AIoT) technology. The system was designed to provide warnings of $PM_{2.5}$ levels through a mobile application. Air pollution, particularly $PM_{2.5}$, is a significant health concern globally, with Southeast Asia being heavily affected. Bangkok, Thailand, experiences high $PM_{2.5}$ concentrations during cool weather. Existing research explores short-term $PM_{2.5}$ prediction using AIoT. Still, there is a need for improved software, hardware, and ML algorithms for user-friendly mobile applications with real-time data access and health advisories. The system was installed on a building next to a main road in Bangkok. It collected data on $PM_{2.5}$. The Air Quality Index (AQI) was used to categorize $PM_{2.5}$ levels and their health impacts. Time series analysis with moving averages and the Random Forest algorithm were employed in advance for $PM_{2.5}$ forecasting. A mobile application was developed to provide a user interface and data visualization. The MARF (Moving Average and Random Forest) model emerged as a success, achieving higher accuracy (average of 92.59%) for 1-hour advance forecasts compared to the Moving Average (MA) model (average of 84.16%). The developed system demonstrates the potential of AIoT for accurate $PM_{2.5}$ monitoring and forecasting. Future research could explore more advanced ML algorithms and integrate additional environmental factors for enhanced forecasting accuracy.

Keywords: AIoT; $PM_{2.5}$; Random Forest; Moving Average; Forecasting; AQI

1. Introduction

Research worldwide shows that air pollution, known as $PM_{2.5}$, refers to fine particles with an aerodynamic diameter smaller than 2.5 microns. Populations around the world, especially in Southeast Asia, are greatly affected. According to research reports [1-2], deaths occurred in the highest proportion due to $PM_{2.5}$ worldwide in 2015. Thailand is one of the regions heavily affected by $PM_{2.5}$, especially Bangkok, the capital [3]. During the cold weather of the year, various districts in Bangkok will have $PM_{2.5}$ concentrations exceeding the standard level compared to the 24-hour air quality average of more than 50 $\mu g/m^3$ [4]. The Nong Khaem district has the highest average $PM_{2.5}$ concentration out of the 50 districts [5], especially along Phet Kasem Road. $PM_{2.5}$ data from the $PM_{2.5}$ monitoring system from satellite and geoinformatics technology [6] of Geo-Informatics and Space Technology Development Agency (Public Organization) or GISTDA found that the density value of $PM_{2.5}$ in the Nong Khaem district of

Bangkok in the first quarter of 2024, when Bangkok was still influenced by cool air from the north, was 38.48 μg/m^3. When compared to the Krung Thonburi area, which is on the west side of Bangkok and has similar characteristics, it was found that the average $PM_{2.5}$ density was 35.61 μg/m^3 or an average rate of 8.06 percent. On the day that Nong Khaem District had the highest $PM_{2.5}$ density at 104.59 μg/m^3, it was 193.74 percent higher than the average in the entire Krung Thonburi area. Therefore, monitoring $PM_{2.5}$ density and air quality is essential and helps affected people understand the situation [7-9]. In addition, developing a system that can predict air quality and $PM_{2.5}$ in advance is an important issue that will help them deal with problems better, such as managing time for outdoor activities and protecting themselves with dust masks. Several researchers [10-12] are interested in developing short-term $PM_{2.5}$ predictions using IoT technology combined with AI, which has shown that this technology can predict $PM_{2.5}$ levels in advance. However, this research area still needs to be improved in terms of software, hardware, and even better AI algorithms, such as notification of $PM_{2.5}$ forecast results in advance through a mobile app system. Make it easy for users to understand the meaning of AQI, accurate forecasts with less complex algorithms, etc. For example, researchers [13] have developed a machine learning algorithm to predict $PM_{2.5}$, which tends to increase in the short term, 60 minutes in advance. $PM_{2.5}$ forecasting has also been studied using current ground-level meteorological data to estimate $PM_{2.5}$ concentrations 1-5 hours in advance [14, 15]. Even though Nong Khaem District is a suburb of Bangkok, there are few high-rise buildings, and most of the area is still green. The design and development of this air quality measurement and forecasting system aims to apply IoT technology and artificial intelligence to measure and forecast air quality [16], especially $PM_{2.5}$, to provide warnings in advance via mobile application.

This research developed an air quality monitoring station. It was installed on the 6th floor of the Polakrit Building, Southeast Asia University, next to Phet Kasem Road in the Nong Khaem District, Bangkok. This measurement station is approximately 40 meters above ground level, providing comprehensive air quality measurements. This research aims to develop a $PM_{2.5}$ monitoring and forecasting system with the AQI index using IoT technology and artificial intelligence to notify users of forecast results in advance through mobile applications. The station includes sensors measuring $PM_{2.5}$, temperature, humidity, air pressure, wind speed, and wind direction.

2. Related Works

This section represents several research papers relevant to developing a $PM_{2.5}$ monitoring and forecasting system using a mixed model of IoT and Machine Learning (ML) accessible through a mobile application. Data Collection and Sensor Technology: Balogun, Alaka, & Egwim (2021) [17] demonstrate the use of IoT sensors to collect air quality data, including NO_2, alongside weather and traffic data. This highlights the potential of IoT for $PM_{2.5}$ data collection in the proposed method.

Machine Learning for $PM_{2.5}$ Prediction: Many researchers are interested in presenting their research papers [18-23], which examine various machine learning algorithms for air quality prediction, including NO_2 (similar to $PM_{2.5}$) prediction [17]. These reports showcase the effectiveness of Artificial Neural Networks (ANN) [22], Long Short-Term Memory (LSTM) [20, 21], Fuzzy Time Series (FTS) [18], Multilinear Regression (MLR) [19], ARIMA models [B6], and CEEMDAN-ARMA-LSTM model [23]. These findings suggest we explore a combination of these algorithms to find the optimal model for $PM_{2.5}$ prediction in the proposed research.

Factors Affecting $PM_{2.5}$ Concentration: Baharfar et al. [24] examine factors influencing indoor $PM_{2.5}$ concentration, including outdoor $PM_{2.5}$ levels, number of occupants, ambient temperature, wind speed, and wind direction. While this paper focuses on indoor settings, open doors, and windows highlight the importance of considering various environmental factors alongside $PM_{2.5}$ sensor data for improved prediction accuracy.

Mobile Application Integration: The papers above focus on data collection and prediction models. However, recent advancements in mobile cloud computing and secure data transmission protocols must be considered for mobile application integration to ensure user privacy and real-time data access.

Novelty and Contribution: While existing research provides a strong foundation, this project offers a novel contribution focusing on $PM_{2.5}$ prediction using a combination of the most effective ML algorithms and integrating a user-friendly mobile application for real-time data access, visualization, and potential health advisories based on $PM_{2.5}$ levels. Furthermore, to enhance prediction accuracy, especially for outdoor environments, consider a more comprehensive range of environmental factors beyond those explored in [24].

3. Materials and Methods

3.1 Air Quality Index

The Air Quality Index is an easy-to-understand air quality report for the public. To make the public aware of the level of air pollution in each area, how much does it affect health? One air quality index represents the concentration of 6 air pollutants: Particulate matter no larger than 2.5 microns in size ($PM_{2.5}$) that arises from combustion from vehicles, agricultural materials, forest fires, and industrial processes. It causes respiratory disease.

In addition, if accumulated for a long time or received in large amounts, it will accumulate in the lung membranes, reducing the efficiency of the lungs and causing bronchitis and asthma symptoms. Particulate matter no larger than 10 microns (PM_{10}) is dust with a diameter of no more than 10 microns. Burning fuel, open burning, industrial processes, grinding, milling, or pulverization from construction produce it. It affects health because when inhaled, it can accumulate in the respiratory system. Ozone gas (O_3) is a colorless or light blue gas with a pungent odor, is slightly soluble in water, and occurs both in the atmosphere high above the Earth's surface and near the ground. Ozone gas, an air pollutant, is ozone gas in the Earth's surface atmosphere. It is caused by a reaction between nitrogen oxides and volatile organic compounds, with sunlight acting as a catalyst. It affects health by causing eye irritation and irritation of the respiratory system and various mucous membranes, decreased lung capacity, and early fatigue, especially in children, the elderly, and people with diabetes cystic fibrosis. Nitrogen dioxide (NO_2) is a colorless and odorless gas slightly soluble in water. It is commonly found in nature or caused by human actions, such as burning various fuels, some industries, etc. This gas affects the visual system and people with asthma or other respiratory diseases. Sulfur dioxide (SO_2) is a colorless to pale yellow gas with a taste and odor at high concentrations. It is caused by nature and the combustion of fuels that contain sulfur. It is highly soluble in water and can combine with other pollutants to form small dust particles. This gas directly impacts health, irritating the mucous membranes of the eyes, skin, and respiratory system. If you take it for a long time, it can cause chronic bronchitis.

Thailand's Air Quality Index (AQI) [5] is divided into five levels, from 0 to 201 and above. Each level uses a color to symbolize the level of impact on health. An air quality index of 100 is equivalent to air quality standards in the general atmosphere. If the air quality index exceeds 100, the air pollution concentration exceeds the standard, and that day's air quality will begin to affect public health. The air quality index is between 0 and 25, represented by blue, which means the air quality level is excellent, and all citizens can lead everyday lives. The air quality index value is between 26 and 50, represented by green, meaning the air quality level is good, and the public can do outdoor activities as usual. People in at-risk groups should monitor themselves for unusual symptoms such as coughing, chest tightness, fatigue, or dizziness. Air quality index values between 51 and 100, represented by yellow, indicate moderate air quality. The public should reduce activity time or exercise outdoors. People in high-risk groups should wear protective equipment, such as masks, to prevent $PM_{2.5}$ exposure every time they go outside the building. In addition, they need to reduce the time they spend doing activities or exercising outdoors and consult a doctor if they encounter any irregular symptoms. An AQI value between 101 and 200, represented by orange, means the air quality level is starting to impact health. The public should use personal protective equipment such as a $PM_{2.5}$ mask outside the building. Limit your time in outdoor activities or exercise and watch for unusual symptoms such as coughing, sneezing, or eye irritation. People in at-risk groups should wear personal protective equipment, such as masks, to prevent $PM_{2.5}$ exposure every time they go outside the building. Avoid doing activities or exercising outdoors, and follow your doctor's advice. If you have any unusual symptoms, consult your doctor immediately. Air quality index values greater than 201, represented by red, mean air quality levels affect health. To prevent $PM_{2.5}$, all citizens must avoid outdoor activities and always wear personal protective equipment, such as masks. If you have any abnormal symptoms, please consult a doctor immediately. For patients with chronic diseases, stay in areas safe from air pollution. Prepare necessary medicines and equipment and strictly follow the doctor's instructions.

Calculation of the daily air quality index of each type of air pollutant. It is calculated from air pollutant concentration values and air quality measurement results. The air pollutant concentration values are equivalent to the air quality index values at various levels. Calculating the air quality index within a level range is a linear equation.

$$1 = \frac{I_j - I_i}{X_j - X_i}(X - X_i) + I_i \quad (1)$$

I = Air quality sub-index value,
X = concentration of air pollutants from measurement,
X_i, X_j = minimum, maximum values of the pollutant concentration range with values of X,
I_i, I_j = minimum, maximum values of the air quality index range corresponding to the concentration range X from the calculated sub-index values.

Which air pollutant has the highest index value was used as the Air Quality Index (AQI) at that time.

3.2 Time Series Analysis and Moving Average

According to the emergence of $PM_{2.5}$, the values measured by sensors are time series data. Time series analysis [25] is the prediction of future values of a dependent variable by using data on that variable to study various patterns of relationships. Time series analysis involves separating the various components in the data and analyzing their interrelationship patterns to predict their future value. Time series data can be separated into four movement patterns: Secular Trend, Seasonal Movement, Cyclical Movement, and Irregular Movement [26]. The Moving Average (MA) model is one of four used for time series forecasting. It is a mathematical technique for finding the average value changing over time. It replaces the oldest data set with the most recent dataset, then re-averages it over periods such as 3, 6, 12, and 24 hours in advance, as used in this study. There are two methods of calculating the moving average: Simple Moving Average and Weighted Moving Average.

This research uses the Simple Moving Average model to forecast $PM_{2.5}$ air quality because the system collects data hourly, with 24 items per day and 168 items per week. To forecast from historical data throughout the week, which has different data characteristics each day, this research uses 168 historical data items for calculation, as shown in the following equation.

$$F_t = \frac{A_{t-1} + A_{t-2} + \cdots + A_{t-168}}{n} \quad (2)$$

$$F_3 = \frac{A_{t-1} + A_{t-1} + \cdots + A_{t-166} + F_{t-1} + F_{t-2}}{n} \quad (3)$$

$$F_6 = \frac{A_{t-1} + A_{t-1} + \cdots + A_{t-163} + F_{t-1} + \cdots + F_{t-5}}{n} \quad (4)$$

$$F_{12} = \frac{A_{t-1} + A_{t-1} + \cdots + A_{t-157} + F_{t-1} + \cdots + F_{t-11}}{n} \quad (5)$$

$$F_{24} = \frac{A_{t-1} + A_{t-1} + \cdots + A_{t-143} + F_{t-1} + \cdots + F_{t-23}}{n} \quad (6)$$

Where

F_t = the forecast value for the period t.
$A_{t,n}$ = actual value in period t-n
n = number of data sets to find the moving average.

Forecasting 1 hour ahead, using 168 past actual $PM_{2.5}$ values (2), 3-hour advance forecast (3), 166 past actual $PM_{2.5}$ values, and 1-and 2-hour advance forecasts (4). Forecasting 6 hours, using 163 past actual $PM_{2.5}$ values along with forecast values 1-5 hours ahead (5); forecast 12 hours in advance, using 157 past actual $PM_{2.5}$ values together with forecast values from 1-11 hours in advance and 24-hour advance forecast (6), using 143 past actual $PM_{2.5}$ values along with 1 – 23-hour advance forecast values.

3.3 Random Forest

The research team proposed a method for integrating forecasting techniques with machine learning to improve the accuracy of $PM_{2.5}$ air quality forecasts. Due to the conditions of the developed system are designed to be adaptable, ensuring that the forecast results can be displayed 1, 3, 6, 12, and 24 hours in advance

at any given time. Using historical data, including $PM_{2.5}$, temperature, humidity, air pressure, wind speed, and wind direction, to train the system according to the principles of supervised machine learning, we have chosen a method that balances processing time with accuracy and reliability, ensuring dependable performance. Therefore, the research team proposes using the random forest technique, a widespread algorithm used in regression and classification forecasting without needing hyperparameter tuning to get better results.

Random Forest is a popular model developed from a decision tree. The principle of random forest is to create a model from many decision trees. Each model receives a different subset of the data set. Then, forecasting is assigned to each decision tree model to calculate its forecast results. In the case of classification, the vote output is obtained from each forecast that the decision tree selects the most. This improves the prediction results from the decision tree, which are more accurate and control over-fitting.

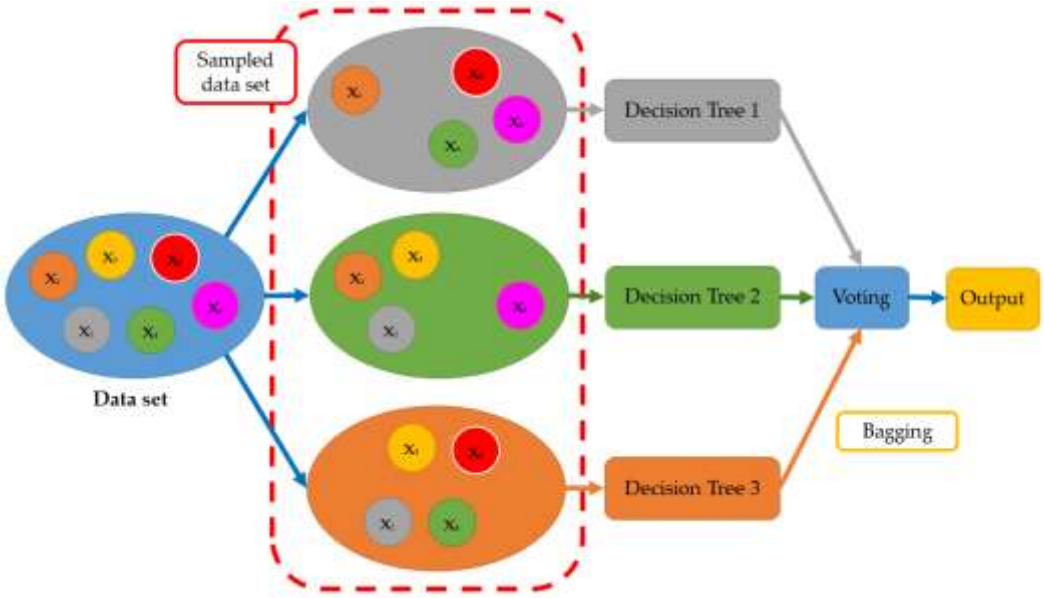


Figure 1. Random forest process

In this research, Bootstrapping from all data sets is used to get *n* data sets that differ according to the number of decision trees in random forests from a total of 6 features, including wind speed, wind direction, humidity, air pressure, temperature, and $PM_{2.5}$ (X_1, X_2, ..., and X_6), to create a model decision tree for each dataset. Then, the results are aggregated from each model or bagged with voting. The *RandomForestClassifier* of Scikit-learn ensemble methods for classification is used in forecasting processing, with the *n_estimators* parameter set to 100 trees. The supported criteria are the *Gini impurity*, *log_loss*, and *entropy* for the Shannon information gain [27]. The developed system will take the forecast values obtained from the moving average process, separate them, and specify $PM_{2.5}$ levels from 1, the lowest, to 5, which is a very high $PM_{2.5}$ value, as input and use them. All data from the database is used to train the system every hour. Then, the obtained model with moving average (MA) and random forest (RF) forecasting (MARF) will be used to forecast $PM_{2.5}$ air quality 1, 3, 6, 12, and 24 hours in advance.

3.4 System Framework

Figure 2 shows an overview of the system's operation. The sensors measure temperature, humidity, air pressure, wind speed, wind direction, and the amount of $PM_{2.5}$ dust in the air. All collected information is stored in a database, which can display $PM_{2.5}$ air quality values at the current time and label each frame according to the five class $PM_{2.5}$ values with rule-based classification. The system then processes air quality forecasts 1, 3, 6, 12, and 24 hours in advance. The research team has chosen two comparative methods to compare the forecasts: A moving average (MA) and a mixed method with a moving average and a Random Forest (MARF). Moving Average processing uses 168 historical data frames (24 hours, seven days) to forecast the future. In addition, the system will take the forecast values obtained from the six moving averages in

advance as input data to create a forecast model with MARF. Forecasts are processed with an impurified random forest of 100 trees every 1-hour using Scikit-learn's Python library, and the forecast results are divided into five classes stored in the database. While mobile applications are developed in Dart, a programming language developed by Google, it is designed to create mobile and web applications. It is developed on the Flutter framework to work cross-platform, and it can be used on Windows, Mac OS, Linux, iOS, or Android.

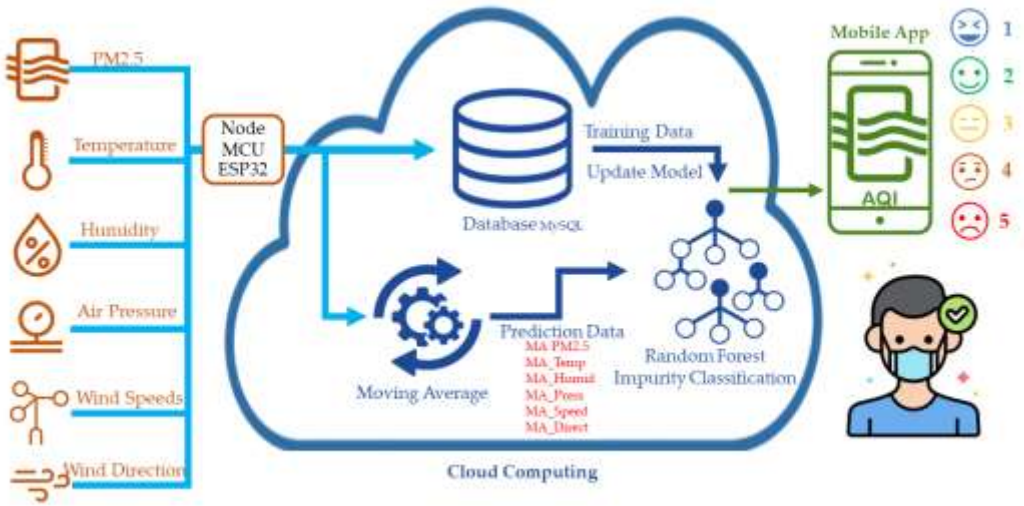


Figure 2. Framework of the AQI $PM_{2.5}$ monitoring and forecasting system

Forecast data is divided into five classes: Class 1 means very good air quality with an average $PM_{2.5}$ not exceeding 15 ug/m^3; Class 2 means good air quality with an average $PM_{2.5}$ between 15.1-25.0 μg/m^3; Class 3 means that the air quality is moderate with an average $PM_{2.5}$ between 25.1 - 37.5 μg/m^3; Class 4 means that the air quality is starting to have an impact on health, with an average $PM_{2.5}$ between 37.6 – 75.0, and Class 5 means Air quality affects health, the average $PM_{2.5}$ is more than 75.1 μg/m^3.

3.5 Hardware Design and Development

The hardware development of this air quality monitoring and forecasting system consists of the following hardware: BME280 Temperature Humidity Barometric Pressure Sensor [28] is a sensor device for measuring temperature, air humidity, and barometric pressure. It is connected via Inter-Integrated Circuit (I2C) and uses a current of 1.7 - 3.6V. It can measure temperature from -40 to 85 degrees Celsius, humidity from 0 to 100%, and barometric pressure from 300 to 1,100 hPA. Temperature accuracy class ± 0.5 degrees Celsius (at 25 degrees Celsius). The Laser Dust Sensor PM 2.5 PMS7003 [29] measures the amount of dust in the air by detecting dust particles with laser light. It can detect small particles ranging from 0 to 500 micrograms per cubic meter. The particles it can detect are $PM_{1.0}$, $PM_{2.5}$, and PM_{10}.

The smallest particle that can be detected is 0.3 micrometers. This sensor's output is qualitative and quantitative information on individual particles of different sizes per unit volume. The particle count volume unit is 0.1 liter, and the mass concentration unit is μg/m^3. Wind Direction Sensor Signal 0-5V [30] measures wind direction. Its output voltage is 0-5 volts, input power is 10-30 volts, it can rotate 360 degrees, measure in eight directions, and works at temperatures from 20 to 60 degrees Celsius. In addition, Wind Speed Sensor Signal 0-5V [31] is used to measure wind speed. It is a 3-cup wind-measuring device with an output voltage of 0-5 volts and an input voltage of 7-24 volts. It measures wind speed in the 0-30 m/s range, with a value accuracy of 0.1 m/s. It works at a temperature of -20 to 60 degrees Celsius.

According to Figure 3 (a) and (b), an ESP32 board [32] is used as an embedded processing unit to receive sensor values, process them, and forward the data to cloud computing. The ESP32 Board uses an Xtensa single-core 32-bit, LX6 microprocessor, running at 160 or 240 MHz. It has 520 KB SRAM, Wi-Fi: 802.11 b/g/n, and Bluetooth: v4.2 BR/EDR and BLE. It operates at temperatures of -40ºC to 125ºC. The private server

used for processing is a Dell PowerEdge T150 Server with an Intel Xeon E-2314 2.8 GHz, 8M Cache, 4C/4T 16GB UDIMM, 3200M/Ts, and ECC 3*2TB HDD SATA 6Gbps, installed at the IT Center, Polakrit Building, Southeast Asia University, Bangkok.

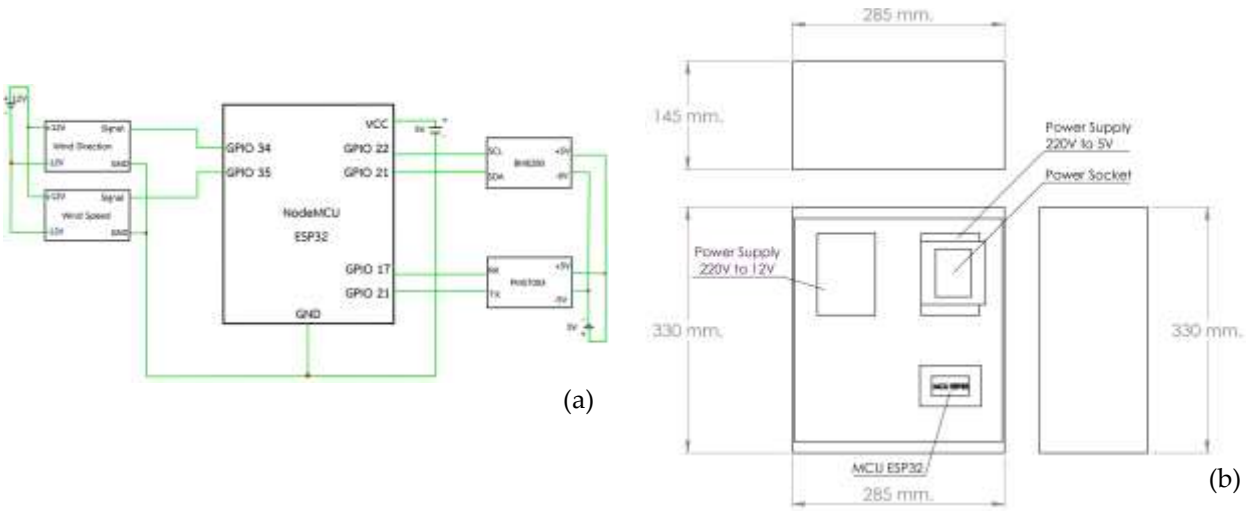


Figure 3. Electronic circuit diagram of the AQI $PM_{2.5}$ monitoring and forecasting system.

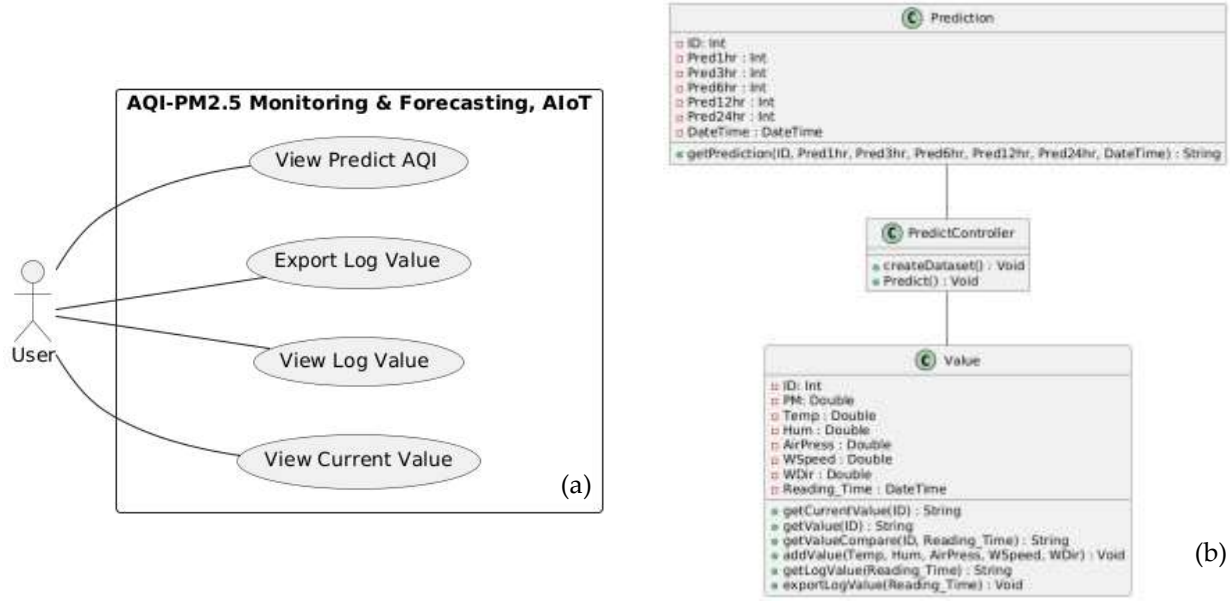


Figure 4. Use case and class diagram of AQI $PM_{2.5}$ monitoring and forecasting system

3.6 Software Design and Development

System Analysis and Design (SAD) for this research include: 1. Functional Requirements consist of (1) being able to track wind speed, wind direction, humidity, air pressure, temperature, and $PM_{2.5}$ at the current time and historical data and (2) being able to follow the future air quality index forecast AQI $PM_{2.5}$. 2. Non-functional requirements consist of (1) $PM_{2.5}$ data and other values that can be tracked 24 hours a day and (2) can be used by both web and mobile applications. The basic working principles of the $PM_{2.5}$ air quality monitoring and forecasting system using artificial intelligence are as follows. PMS7003 measures the amount of $PM_{2.5}$ in the air. The BME280 measures temperature, air pressure, and humidity in the air. Meanwhile, turbines measure the speed and direction of the wind, as shown in Figure 4.

All sensors are connected to a Node MCU ESP32 to collect data and then forward it to the MySQL Database at 1 hour per frame. The code program was developed with PHP to communicate with the Node MCU ESP32, and the MySQL database system, which manages both current and historical data, was installed on the private server. Examining past dust values, processing current data to forecast future air quality indexes, and storing the processed forecast data in a database system. Users can choose to use it through web applications or mobile applications. The display of $PM_{2.5}$ values is divided into five levels according to Thailand's air quality index classification, as shown in Figures 5 and 6. By using only the density of $PM_{2.5}$ in the air, each level uses color to symbolize the level of impact on health. When measured, the $PM_{2.5}$ value is between 0 – 15.00 μg/m^3, meaning that the $PM_{2.5}$ density is very low, represented by a blue color. If the value is measured between 15.10 – 25.00 μg/m^3, the $PM_{2.5}$ density is low and represented by a green color. If the value is measured between 25.1 and 37.5 μg/m^3, the $PM_{2.5}$ density is moderate and starting to impact health, represented by a yellow value. If the value is measured between 37.6 – 75.0 μg/m^3, the $PM_{2.5}$ density is high and dramatically impacts health, represented by orange. If the value is more than 75.1 μg/m^3 or more, the $PM_{2.5}$ density is very high and has a very high impact on health, represented in red.

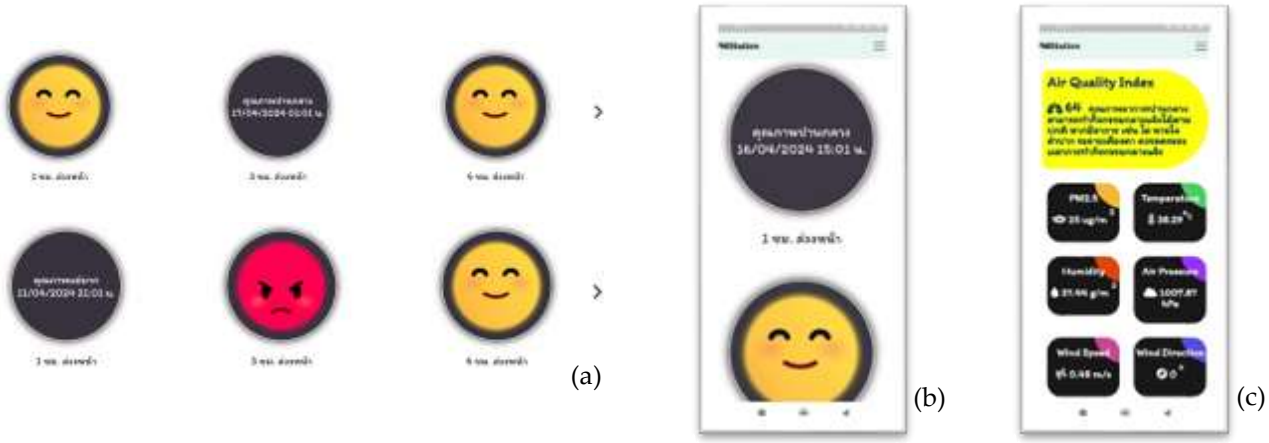


Figure 5. Example of User Interface of AQI $PM_{2.5}$ monitoring and forecasting system

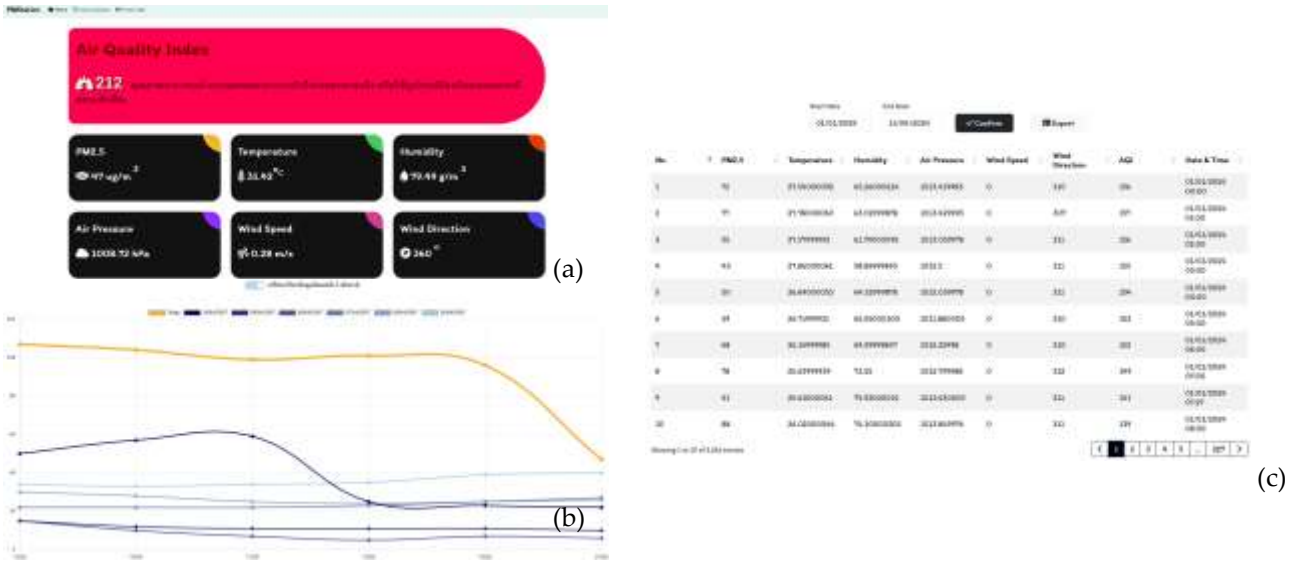


Figure 6. Example of user interface showing notifications and historical data

4. Results and Discussion



Figure 7. The acquisition station is installed on the Polakrit Building, Southeast Asia University, and the location of the installation point

This research installed equipment to measure $PM_{2.5}$ dust, temperature, humidity, air pressure, wind speed, and wind direction on the 5th floor of the Polakrit Building, approximately 40 meters above ground level. The Polakrit Building, situated on Petchkasem Road, Figure 7, a major thoroughfare with heavy daily traffic, especially during the morning and evening rush hour, provides a significant context for this research Figure 7. Data collection lasted 175 days, from Saturday, November 25, 2023, to Thursday, May 30, 2024. From December to February, Bangkok is significantly affected by high pressure from China, which causes cool weather and a substantial increase in $PM_{2.5}$ dust yearly. Therefore, Thailand enters summer from March to May every year. Low air pressure influences Bangkok, which is less affected by $PM_{2.5}$ dust [6]. This allows the experiment of this air quality monitoring and forecasting system to compare different weather conditions. The system collects data from various sensors once an hour and records it in the MySQL database, with 24 daily records and 4,209 records. Random forest prediction requires a dataset to train the system. Therefore, the forecast runs from March 4, 2024, to May 31, 2024, a total of 88 days and 2,112 records for forecasting and analysis.

Confusion matrix, also known as error matrix, and cross-entropy loss, also known as log loss, are used in machine learning to evaluate the performance of classification models. In this specific study, these two techniques were used to evaluate the performance of MA and MARF for classification purposes. A confusion matrix is a summary table showing how well a model predicts different class samples. When optimizing the classification model, calculate the difference between the predicted and actual responses. Cross-entropy can be used as a loss function [33].

$$Recall = \frac{TP}{TP + FN} \tag{7}$$

$$Specificity = \frac{TN}{FP\ +\ TN} \tag{8}$$

$$Precision = \frac{TP}{TP + FP} \tag{9}$$

$$Accuracy = \frac{TP + TN}{TP + TN + FP + FN} \tag{10}$$

$$F1\ Score = 2 * \frac{Recall * Precision}{Recall + Precision} \tag{11}$$

TP, TN, FP, and FN are True Positive, True Negative, False Positive, and False Negative, respectively [34].

After analyzing the confusion matrix, various performance parameters, including Sensitivity or Recall, Specificity, F1 score, Accuracy, and Precision, are calculated to evaluate the model's performance. Accuracy is defined as the proportion of correct predictions out of all predictions. Recall, also known as true positive rate, is calculated as the proportion of correctly predicted positive instances to the total number of positive instances. Specificity, also known as true negative rate, refers to the proportion of predicted negative instances that are accurate relative to the total number of negative instances. Accuracy, also known as positive prediction value, refers to the proportion of positive instances correctly predicted compared to the total number of cases predicted to be positive. The F1 score can be defined as the harmonic average of Recall and Accuracy, two crucial data analysis parameters [34]. Equations (1-5) can be used to calculate these parameters.

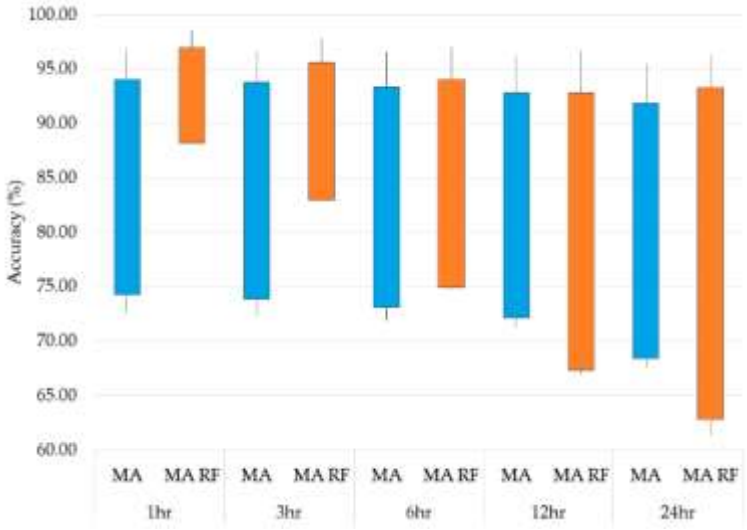


Figure 8. Comparison of the accuracy of forecasts 1, 3, 6, 12, and 24 hours in advance using the MA and MARF methods.

Figure 8 shows the results of comparing the average percentage accuracy of the 1-hour advance forecast results, including all classes; it was found that the MA model had a total average of 84.16 percent (±9.87), which was less than the MARF model, which had an average total of 92.59 percent (±4.39). When comparing the average percentage accuracy of the 3-hour advance forecast results for all classes, it was found that the MA model had an overall average of 83.80 percent (±9.96), which was less than the MARF model, which had an overall average of 89.29 percent (±6.33). When comparing the average percentage accuracy of the 6-hour forecast results for all classes, it was found that the MA model had an overall average of 83.23 percent (±10.14), which was less than the MARF model, which had an overall average of 84.50 percent (±9.54). When comparing the average percentage accuracy of the 12-hour forecast results for all classes, it was found that the MA model had an overall average of 82.49 percent (±10.34), which was higher than the MARF model, which had an overall average of 80.12 percent (±12.74). When comparing the average percentage accuracy of the 24-hour forecast results for all classes, it was found that the MA model had an overall average of 80.18 percent (±11.71), which was higher than the MARF model, which had an overall average of 78.06 percent (±15.26). The above comparison results show that in the 1, 3, and 6-hour forecasts, the MARF model is more accurate than the MA model. Still, when the estimates are extended 12 and 24 hours in advance, the MA model is more accurate than the MARF model. Moreover, the candlestick chart also shows that the MA forecast has an average standard deviation between 9.87 and 11.71, which mostly stays the same compared to the MARF model; the average standard deviation has increased accordingly. More extended forecast periods are 4.39, 6.33, 9.54, 12.74, and 15.26.

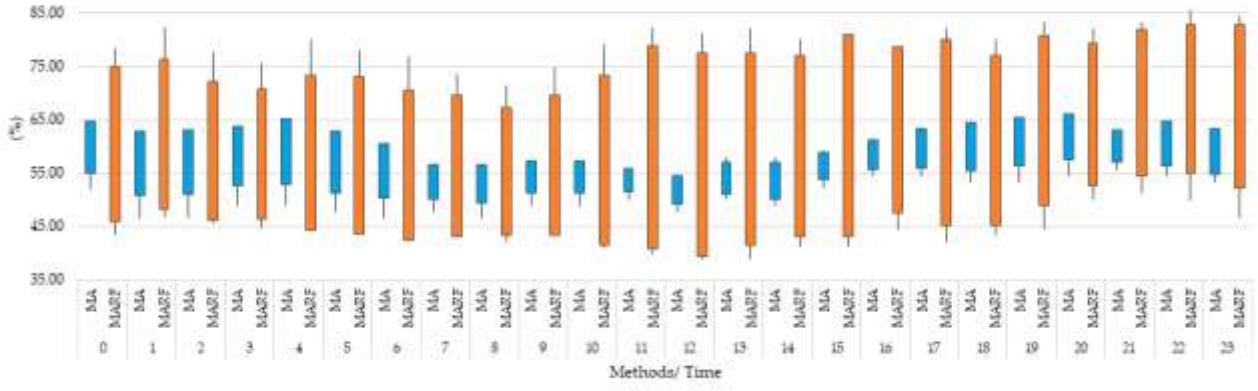


Figure 9. Average accuracy (%) of MA and MARF methods, distributed hourly.

Figure 9 reveals a significant finding in our comparative analysis. The MARF forecast, when compared to the MA forecast, demonstrated a higher average percentage accuracy from 11:00 AM to 11:00 PM. This was particularly articulated during the period 00:00 AM to 10:00 AM of the day. Meanwhile, the average percentage accuracy of MA forecasts remained constant throughout the day. One notable difference we observed was in the variability of the forecasts. The candlestick chart shows that the MARF forecasts have a more spread-out mean standard deviation than the MA forecasts.

Table 1. A comparison of the data analysis results of the MA and MARF methods on an hourly basis.

Methods		Acc.	Precis.	Recall	F1	Spec.
1hr	**MA**	84.16	50.57	59.78	52.81	89.26
	MARF	92.59	76.10	8.27	79.18	95.19
3hr	**MA**	83.80	49.67	18.93	51.79	89.03
	MARF	89.29	65.20	11.05	68.81	93.01
6hr	**MA**	83.23	48.09	55.29	49.98	88.66
	MARF	84.50	51.45	64.42	54.44	89.73
12hr	**MA**	82.49	46.14	21.28	47.61	88.17
	MARF	80.12	37.68	54.08	38.60	86.70
24hr	**MA**	80.18	41.47	43.78	42.34	86.53
	MARF	78.06	30.60	43.47	28.90	85.07

Refer to Table 1 and Figure 10, showing the results of the comparative analysis of Accuracy, Precision, Recall, F1 Score, and Specificity of forecasts using MA and MARF methods 1, 3, 6, 12, and 24 hours in advance. Accuracy's comparative analysis found that the MARF one-hour forecast is accurate at 92.59 percent, more than the MA model, which has an average accuracy of 84.16 percent. It is in the same direction as the 3-hour and 6-hour forecasts, which found that the MARF model had an average percent accuracy of 89.29 and 84.50, more than the MA model, which had an average percent accuracy of 83.80 and 83.23, respectively. However, when considering the 12-hour and 24-hour forward forecasts, the MA model had an average accuracy percentage of 82.49 and 80.18, respectively, compared to the MARF model, which had an average accuracy percentage of 80.12 and 78.06, respectively. This is consistent with the hourly average accuracy percentage analysis. One key takeaway from our results is the noticeable impact of more extended advance forecasts on accuracy. As the forecast duration increases, the accuracy of the forecasts is affected.

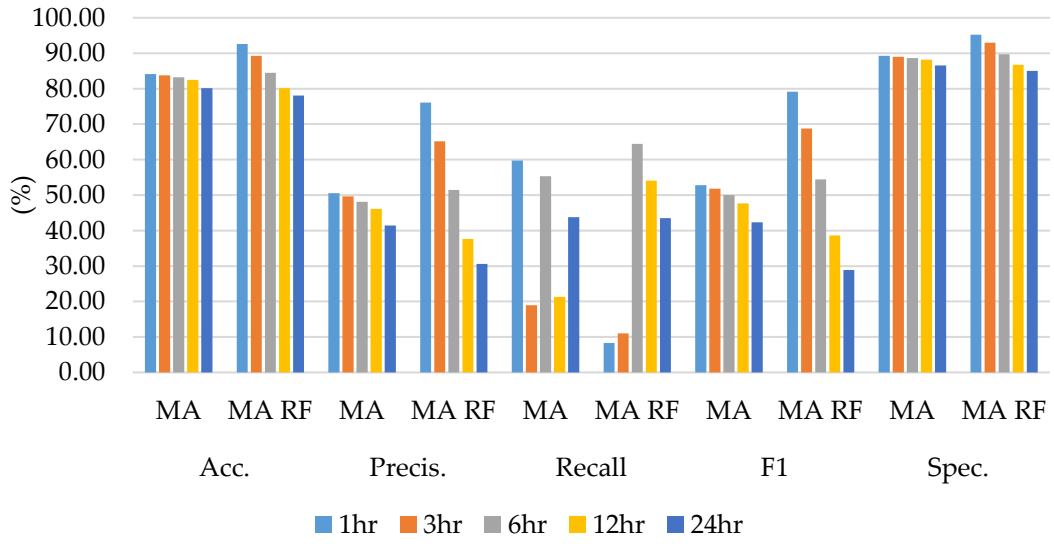


Figure 10. A comparison of the data analysis results of the MA and MARF methods on a 1, 3, 6, 12, and 24 hours in advance.

When considering the Precision, it is also found to correspond to the Accuracy value. The 1, 3, and 6-hour forecasts using the MARF method have averages of 76.10, 65.20, and 51.45 percent, respectively, higher than those of the MA method, with averages of 50.57, 49.67, and 48.09 percent. On the other hand, when forecasting 12 and 24 hours in advance, MARF had an average precision percentage of 37.68 and 30.60, less than MA, which had an average of 46.14 and 41.47 percent, respectively. When considering recall, it was found that the 1-and 3-hour forecasts using the MARF method had an average of 8.27 percent and 11.05 percent, less than the MA method, which had an average of 59.78 percent and 18.93 percent, respectively. On the other hand, when forecasting 6, 12, and 24 hours in advance, it was found that MARF had average recall percentages of 64.42, 54.08, and 43.47, higher than MA, which had average percentages of 55.29, 21.28, and 43.78, respectively. This shows that MARF forecasting can recall long-term forecasts better than MA forecasting. On the other hand, MA forecasts have better short-term recall ability.

In addition, when considering the F1-Score, which shows the model's performance by taking Precision and Recall values to calculate the Harmonic Mean, it was found that MA forecasts have average percentages of 1, 3, 6, 12, and 24 percent, with forecasts of 52.81, 51.79, 49.98, 47.61, and 42.34 percent. The trend decreases with longer forecast periods. While the MARF forecasts had average percentages of 1, 3, 6, 12, and 24 percent of forecasts at 79.18, 68.81, 54.44, 38.60, and 28.90, the trend decreased with more extended forecasts. When comparing the F1-Score, it was found that the MA forecast was 48.91 percent, lower than the MARF's 53.98, indicating that the MARF was more effective.

Finally, considering the Specificity, it was found that the MA forecasts are 1, 3, 6, 12, and 24 hours ahead. The results were 89.26, 89.03, 88.66, 88.17, and 86.53 percent, with a slightly decreasing trend. The MARF forecast is 1, 3, 6, 12, and 24 hours ahead. The results were 95.19, 93.01, 89.73, 86.70, and 85.07 percent, with a slight decrease in trend.

Table 2 compares the average Accuracy, Precision, Recall, F1, and Specificity percentage, separated by class. It was found that class 5, the MARF model, has the highest Accuracy at 97.28, and the MA model is next at 96.34 in the same class, respectively, as shown in Figure 11 (a). Meanwhile, MARF and MA in class 3 have the highest precision values, 82.07 and 69.48, respectively, as shown in Figure 11 (b). For Recall, the MARF and MA models in Class 1 had the highest values of 94.16 and 83.47, respectively, as shown in Figure 11 (c). The MA model of class 1 and the MARF model of class 3 have the highest F1 values of 71.44 and 70.13, respectively, as shown in Figure 11 (d). For Specificity, it was found that MARF and MA models in class 5 had the highest values of 97.78 and 97.21, respectively, as shown in Figure 11 (e).

Table 2. A comparison of the data analysis results of the MA and MARF methods on a Class basis.

	Class									
	1		2		3		4		5	
	MA	MARF	MA	MARF	MA	MARF	MA	MARF	MA	MARF
Accuracy	90.54	89.87	79.54	86.92	71.13	75.11	76.31	75.39	96.34	97.28
Precision	62.56	49.15	36.91	30.85	69.48	82.07	53.86	67.93	13.13	31.04
Recall	83.47	94.16	35.05	58.18	56.47	61.66	58.32	55.90	34.69	52.37
F1	71.44	61.95	35.94	38.28	62.29	70.13	56.00	61.24	18.86	38.32
Specificity	91.77	89.55	88.22	88.50	81.87	87.80	82.60	86.06	97.21	97.78

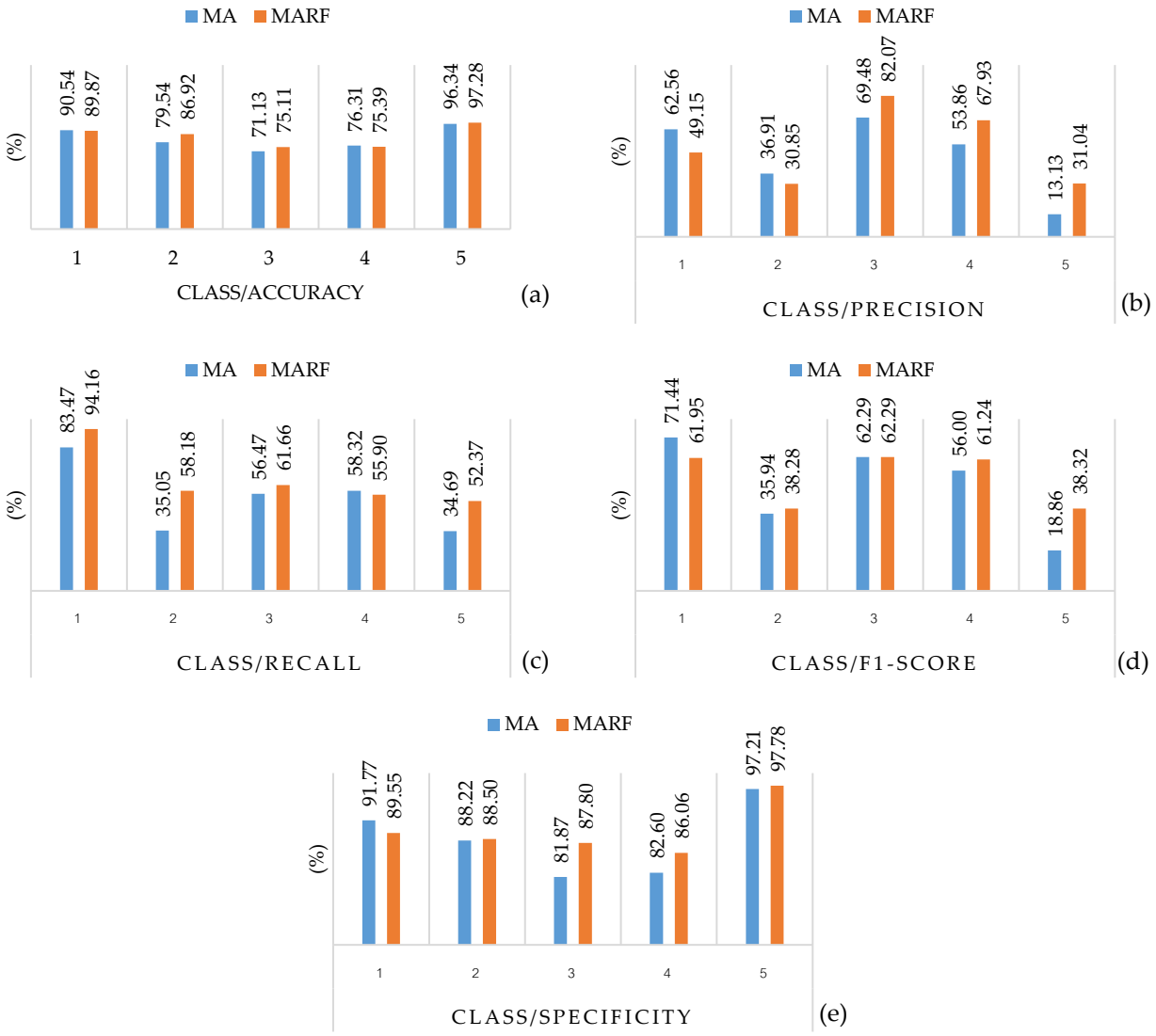


Figure 11. A comparison of the data analysis results of the MA and MARF methods on a Class basis.

4. Conclusions

The AQI $PM_{2.5}$ monitoring and forecasting system was developed, and the experimental results show that it can monitor and forecast $PM_{2.5}$ according to the objective. Moreover, the system has a user-friendly interface. It displays $PM_{2.5}$ concentration status notifications in a 5-color level visual symbol that is easily recognizable according to Thailand's AQI-$PM_{2.5}$ measurement standard. This feature ensures that users can navigate the system with ease and comfort. Unlike most similar studies, which focus solely on machine learning forecasting algorithms, our system stands out as a more comprehensive framework. It begins with sensors for data collection, aggregates the data, and sends it to a MySQL database and cloud computing using an ESP32 board. This comprehensive approach instills confidence in the system's capabilities. It then demonstrates the processing of time-series forecasts with moving averages compared to a combination of moving averages and random forest, a popular machine learning model. It also showcases current and historical data, especially the five-level notification symbols, making it easy for users to understand through mobile and web applications. While the current system is effective, there is always room for improvement.

The system's future looks promising, with the potential to conduct more extended experiments covering all seasons and expand the station installations for more data collection. This information will make the audience feel optimistic about the system's development. Considering the cloud's processing load, it may also integrate other machine learning models, such as ANN, XGBoost, Gradient Descent, and LSTM. The cloud must train the model every hour using all the available data in the database, which can be a heavy workload. The researcher may adjust the time to teach the system to be less suitable for the model.

When comparing the effectiveness and accuracy of the prediction results with similar research that forecasts only time-series $PM_{2.5}$ and is a forward prediction class, it is found that the prediction results of this research using MARF have a Total average accuracy of 84.91%. That is slightly better than Masinde, Gitahi, & Hahn (2020) [35, 36], which achieved an average of 82.00% using a Stochastic gradient descent model with a Gated Recurrent Unit (GRU), which has a more complex computation.

5. Acknowledgements

The authors thank the Thai Pipe Industry Co., Ltd. for the financial support. Thank you, Mr. Natthaphon Yuyuenyong, Mr. Thanakrit Phrompong, and Mr. Ekkanut Prasitthiyannawong, who assisted in installing and maintaining both hardware and software. We also want to thank Dr. Panuwat Taerakul, Dean of Engineering Faculty at Southeast Asia University, for his significant support and guidance throughout the project.

Author Contributions: Conceptualization, N.O. and S.T.; methodology, N.O. S.T.; software, N.O. and C.C.; validation, N.O. and S.T.; formal analysis, N.O.; investigation, N.O.; resources, N.O., S.T., and C.C.; data curation, N.O. and S.T.; writing-original draft preparation, N.O.; writing-review and editing, N.O.; visualization, N.O.; supervision, N.O. and S.T.; project administration, N.O.; funding acquisition, N.O.

Funding: This research was funded by Thai Pipe Industry Co., Ltd.

Conflicts of Interest: The authors declare no conflict of interest.

References

[1] Nazarenko, Y.; Pal, D.; Ariya, P. A. Air Quality Standards for the Concentration of Particulate Matter 2.5, Global Descriptive Analysis. *Bulletin of the World Health Organization* **2020**, *99*(2), 125–137D. https://doi.org/10.2471/blt.19.245704.

[2] Cohen, A. J.; Brauer, M.; Burnett, R.; Anderson, H. R.; Frostad, J.; Estep, K.; Balakrishnan, K.; Brunekreef, B.; Dandona, L.; Dandona, R.; Feigin, V.; Freedman, G.; Hubbell, B.; Jobling, A.; Kan, H.; Knibbs, L.; Liu, Y.; Martin, R.; Morawska, L.; Pope, C. A. Estimates and 25-Year Trends of the Global Burden of Disease Attributable to Ambient Air Pollution: An Analysis of Data from the Global Burden of Diseases Study 2015. *The Lancet* **2017**, *389*(10082), 1907–1918. https://doi.org/10.1016/s0140-6736(17)30505-6.

[3] The Lancet Respiratory Medicine. Air Pollution—Time to Address the Silent Killer. *The Lancet Respiratory Medicine* **2021**, *9*(11), 1203. https://doi.org/10.1016/s2213-2600(21)00448-3.

[4] Narita, D.; Oanh, N.; Sato, K.; Huo, M.; Permadi, D.; Chi, N.; Ratanajaratroj, T.; Pawarmart, I. Pollution Characteristics and Policy Actions on Fine Particulate Matter in a Growing Asian Economy: The Case of Bangkok Metropolitan Region. *Atmosphere* **2019**, *10*(5), 227. https://doi.org/10.3390/atmos10050227.

[5] Air Quality Monitoring Station. Air Quality in Bangkok. *Air Quality Division, Bangkok Metropolitan Administration.* https://airquality.airbkk.com/ (accessed 2024-06-01).

[6] Air Quality Division, Geo-Informatics and Space Technology Development Agency (GISTDA). PM2.5 Thailand. [https://pm25.gistda.or.th/](https://accessed 2024-06-01).

[7] Chirasophon, S.; Pochanart, P. The Long-Term Characteristics of PM10 and PM2.5 in Bangkok, Thailand. *Asian Journal of Atmospheric Environment* **2020**, *14*(1), 73–83. https://doi.org/10.5572/ajae.2020.14.1.073.

[8] Alas, H. D.; Stöcker, A.; Umlauf, N.; Senaweera, O.; Pfeifer, S.; Greven, S.; Wiedensohler, A. Pedestrian Exposure to Black Carbon and PM2.5 Emissions in Urban Hot Spots: New Findings Using Mobile Measurement Techniques and Flexible Bayesian Regression Models. *Journal of Exposure Science & Environmental Epidemiology* **2021**, *32*(4), 604–614. https://doi.org/10.1038/s41370-021-00379-5.

[9] Pozzer, A.; Anenberg, S. C.; Dey, S.; Haines, A.; Lelieveld, J.; Chowdhury, S. Mortality Attributable to Ambient Air Pollution: A Review of Global Estimates. *GeoHealth* **2022**. https://doi.org/10.1029/2022gh000711.

[10] Mclean Cabaneros, S.; Calautit, J.; Hughes, B.; Author, C. A review of artificial neural network models for ambient air pollution prediction. *Environmental Modelling & Software* **2019**, *119*, 285-304. https://strathprints.strath.ac.uk/69357/1/Cabaneros_etal_EMS_2019_A_review_of_artificial_neural_network_models_for_ambient.pdf (accessed 2023-06-01).

[11] Chen, J.; de Hoogh, K.; Gulliver, J.; Hoffmann, B.; Hertel, O.; Ketzel, M.; Bauwelinck, M.; van Donkelaar, A.; Hvidtfeldt, U. A.; Katsouyanni, K.; Janssen, N. A. H.; Martin, R. V.; Samoli, E.; Schwartz, P. E.; Stafoggia, M.; Bellander, T.; Strak, M.; Wolf, K.; Vienneau, D.; Vermeulen, R. A Comparison of Linear Regression, Regularization, and Machine Learning Algorithms to Develop Europe-Wide Spatial Models of Fine Particles and Nitrogen Dioxide. *Environment International* **2019**, *130*, 104934. https://doi.org/10.1016/j.envint.2019.104934.

[12] Chu, Y.; Liu, Y.; Li, X.; Liu, Z.; Lu, H.; Lu, Y.; Mao, Z.; Chen, X.; Li, N.; Ren, M.; Liu, F.; Tian, L.; Zhu, Z.; Xiang, H. A Review on Predicting Ground PM2.5 Concentration Using Satellite Aerosol Optical Depth. *Atmosphere* **2016**, *7*(10), 129. https://doi.org/10.3390/atmos7100129.

[13] Kumar, U.; Jain, V. K. ARIMA Forecasting of Ambient Air Pollutants (O3, NO, NO_2 and CO). *Stochastic Environmental Research and Risk Assessment* **2009**, *24*(5), 751–760. https://doi.org/10.1007/s00477-009-0361-8.

[14] Shah, J.; Mishra, B. Analytical Equations Based Prediction Approach for PM2.5 Using Artificial Neural Network. *SN Applied Sciences* **2020**, *2*(9). https://doi.org/10.1007/s42452-020-03294-w.

[15] Zheng, Y.; Zhang, Q.; Wang, Z.; Zhu, Y. Application Research on PM2.5 Concentration Prediction of Multivariate Chaotic Time Series. *IOP conference series. Earth and environmental science (Online)* **2019**, *237*, 022010–022010. https://doi.org/10.1088/1755-1315/237/2/022010.

[16] Otanasap, N.; Chalermsuk, C.; Bungkomkhun, P. A Survey of IoT: Advances in Smart and Dynamic Environmental Monitoring. *In Proceeding of 8th International Conference on Environmental Engineering, Science and Management; The Environmental Engineering Association of Thailand (EEAT): BKK, THA,* **2019**; pp. 1–10.

[17] Balogun, H.; Alaka, H.; Egwim, C. N. Boruta-Grid-Search Least Square Support Vector Machine for NO2 Pollution Prediction Using Big Data Analytics and IoT Emission Sensors. *Applied computing and informatics* **2021**. https://doi.org/10.1108/aci-04-2021-0092.

[18] Bhagat, L.; Goyal, G.; Bisht, D. C. S.; Ram, M.; Kazancoglu, Y. Air Quality Management Using Genetic Algorithm Based Heuristic Fuzzy Time Series Model. *The TQM Journal* **2021**. https://doi.org/10.1108/tqm-10-2020-0243.

[19] Mani, G.; Viswanadhapalli, J. K.; Stonie, A. A. Prediction and Forecasting of Air Quality Index in Chennai Using Regression and ARIMA Time Series Models. *Journal of Engineering Research* **2021**, *9*. https://doi.org/10.36909/jer.10253.

[20] Kim, D.; Han, H.; Wang, W.; Kang, Y.; Lee, H.; Kim, H. S. Application of Deep Learning Models and Network Method for Comprehensive Air-Quality Index Prediction. *Applied Sciences* **2022**, *12*(13), 6699. https://doi.org/10.3390/app12136699.

[21] Kök, İ.; Şimşek, M. U.; Özdemir, S. A deep learning model for air quality prediction in smart cities. *International Conference on Big Data (Big Data)* **2017**. IEEE Xplore. https://doi.org/10.1109/BigData.2017.8258144.
[22] Maleki, H.; Sorooshian, A.; Goudarzi, G.; Baboli, Z.; Tahmasebi Birgani, Y.; Rahmati, M. Air Pollution Prediction by Using an Artificial Neural Network Model. *Clean Technologies and Environmental Policy* **2019**, *21*(6), 1341–1352. https://doi.org/10.1007/s10098-019-01709-w.
[23] Sun, Y.; Liu, J. AQI Prediction Based on CEEMDAN-ARMA-LSTM. *Sustainability* **2022**, *14*(19), 12182. https://doi.org/10.3390/su141912182.
[24] Baharfar, Y.; Mohammadyan, M.; Moattar, F.; Nassiri, P.; Behzadi, M. H. Indoor PM2.5 Concentrations of Pre-Schools; Determining the Effective Factors and Model for Prediction. *Smart and Sustainable Built Environment* **2021**. https://doi.org/10.1108/sasbe-12-2020-0183.
[25] Ansari, M.; Alam, M. An Intelligent IoT-Cloud-Based Air Pollution Forecasting Model Using Univariate Time-Series Analysis. *Arabian journal for science and engineering* **2023**. https://doi.org/10.1007/s13369-023-07876-9.
[26] Sooktawee, S.; Kanchanasuta, S.; Bunplod, N. Assessment of 24-h Moving Average PM2.5 Concentrations in Bangkok, Thailand against WHO Guidelines. *Sustain Environ Res* **2023**, *33*(1). https://doi.org/10.1186/s42834-023-00165-y.
[27] Pedersen, T. scikit-learn: Machine Learning in Python [Software]. **2020**. https://scikit-learn.org/stable/modules/generated/sklearn.ensemble.RandomForestClassifier.html (accessed 2024-06-01).
[28] alldatasheet.com. BME280 Datasheet, PDF. www.alldatasheet.com. https://www.alldatasheet.com/view.jsp?Searchword=BME280&sField=4 (accessed 2024-06-01).
[29] Digital Universal Particle Concentration Sensor PMS7003 Series Data Manual; **2016**. https://download.kamami.pl/p564008-PMS7003%20series%20data%20manua_English_V2.5.pdf.
[30] Renke, S. Wind Direction Transmitter Instruction Manual (Type 485) RS-FXJT-N01 Wind Direction Transmitter User's Manual (Type 485). https://instrucenter.com/wp-content/uploads/2022/03/RS-FXJT-N01.pdf (accessed 2024-06-01).
[31] Renke, S. Instruction Manual of Wind Speed Transmitter (Type 485) RS-FSJT-N01 Wind Speed Transmitter User's Guide (Type 485). https://instrucenter.com/wp-content/uploads/2022/03/RS-FSJT-No1.pdf (accessed 2024-07-24).
[32] Espressif. ESP32 Series Datasheet Including; **2024**. https://www.espressif.com/sites/default/files/documentation/esp32_datasheet_en.pdf.
[33] Mohammadi, F.; Teiri, H.; Hajizadeh, Y.; Abdolahnejad, A.; Ebrahimi, A. Prediction of Atmospheric PM2.5 Level by Machine Learning Techniques in Isfahan, Iran. *Scientific Reports* **2024**, *14*(1), 2109. https://doi.org/10.1038/s41598-024-52617-z.
[34] Attaallah, A.; Ahmad Khan, R. SMOTEDNN: A Novel Model for Air Pollution Forecasting and AQI Classification. *Computers, Materials & Continua* **2022**, 71(1), 1403–1425. https://doi.org/10.32604/cmc.2022.021968.
[35] Masinde, C. J.; Gitahi, J.; Hahn, M. TRAINING RECURRENT NEURAL NETWORKS for PARTICULATE MATTER CONCENTRATION PREDICTION. *The International Archives of the Photogrammetry, Remote Sensing and Spatial Information Sciences* **2020**, XLIII-B2-2020, 1575–1582. https://doi.org/10.5194/isprs-archives-xliii-b2-2020-1575-2020.
[36] Tripathi, K.; Pathak, P. Deep Learning Techniques for Air Pollution. *3rd International Conference on Intelligent Technologies (CONIT)* **2023**. IEEE Xplore. https://doi.org/10.1109/ICCCIS51004.2021.9397130.

MA

1hr

Predict \ Actual	1	2	3	4	5	Sum
1	250	30	0	0	0	280
2	108	149	66	32	0	355
3	40	120	529	210	12	911
4	0	31	131	337	45	544
5	0	0	0	11	10	21
Sum	398	330	726	590	67	2111

3hr

Predict \ Actual	1	2	3	4	5	Sum
1	249	36	0	0	0	285
2	106	139	67	41	0	353
3	43	123	525	205	13	909
4	0	32	132	333	44	541
5	0	0	2	11	10	23
Sum	398	330	726	590	67	2111

6hr

Predict \ Actual	1	2	3	4	5	Sum
1	246	42	0	0	0	288
2	107	128	67	52	3	357
3	45	126	519	203	12	905
4	0	34	136	324	43	537
5	0	0	4	11	9	24
Sum	398	330	726	590	67	2111

12hr

Predict \ Actual	1	2	3	4	5	Sum
1	249	49	3	8	0	309
2	96	110	63	64	8	341
3	53	130	508	195	10	896
4	0	41	143	312	41	537
5	0	0	9	11	8	28
Sum	398	330	726	590	67	2111

24hr

Predict \ Actual	1	2	3	4	5	Sum
1	251	54	2	22	7	336
2	81	83	67	82	9	322
3	65	140	441	192	2	840
4	1	53	191	283	42	570
5	0	0	25	11	7	43
Sum	398	330	726	590	67	2111

MARF

1hr

Predict \ Actual	1	2	3	4	5	Sum
1	311	8	0	0	0	319
2	31	206	17	0	0	254
3	8	75	657	80	12	832
4	48	41	52	503	12	656
5	0	0	0	7	43	50
Sum	398	330	726	590	67	2111

3hr

Predict \ Actual	1	2	3	4	5	Sum
1	267	11	1	1	0	280
2	40	158	21	1	0	220
3	19	104	630	118	20	891
4	72	57	74	460	16	679
5	0	0	0	10	31	41
Sum	398	330	726	590	67	2111

6hr

Predict \ Actual	1	2	3	4	5	Sum
1	194	14	3	3	0	214
2	34	97	22	4	0	157
3	39	142	582	167	32	962
4	131	77	119	399	14	740
5	0	0	0	17	21	38
Sum	398	330	726	590	67	2111

12hr

Predict \ Actual	1	2	3	4	5	Sum
1	110	11	0	5	0	126
2	28	39	20	4	0	91
3	60	176	557	227	53	1073
4	200	100	149	347	5	801
5	0	4	0	7	9	20
Sum	398	330	726	590	67	2111

24hr

Predict \ Actual	1	2	3	4	5	Sum
1	96	0	0	0	0	96
2	8	9	0	9	1	27
3	88	207	553	283	66	1197
4	206	110	169	295	0	780
5	0	4	4	3	0	11
Sum	398	330	726	590	67	2111

MA			Class						
1hr (%)	1	2	3	4	5	X	SD	Min	Max
Accuracy	91.57	81.67	72.57	78.21	96.78	84.16	9.87	72.57	96.78
Precision	62.81	45.15	72.87	57.12	14.93	50.57	22.30	14.93	72.87
Recall	89.29	41.97	58.07	61.95	47.62	59.78	18.33	41.97	89.29
F1	73.75	43.50	64.63	59.44	22.73	52.81	20.08	22.73	73.75
Specificity	91.92	89.69	83.58	83.85	97.27	89.26	5.76	83.58	97.27

MA RF			Class						
1hr (%)	1	2	3	4	5	X	SD	Min	Max
Accuracy	95.50	91.85	88.44	88.63	98.53	92.59	4.39	88.44	98.53
Precision	78.14	62.42	90.50	85.25	64.18	76.10	12.49	62.42	90.50
Recall	97.49	81.10	78.97	76.68	86.00	84.05	8.27	76.68	97.49
F1	86.75	70.55	84.34	80.74	73.50	79.18	6.95	70.55	86.75
Specificity	95.15	93.32	94.61	94.02	98.84	95.19	2.15	93.32	98.84

MA			Class						
3hr (%)	1	2	3	4	5	X	SD	Min	Max
Accuracy	91.24	80.81	72.29	77.97	96.68	83.80	9.96	72.29	96.68
Precision	62.56	42.12	72.31	56.44	14.93	49.67	22.30	14.93	72.31
Recall	87.37	39.38	57.76	61.55	43.48	57.91	18.93	39.38	87.37
F1	72.91	40.70	64.22	58.89	22.22	51.79	20.30	22.22	72.91
Specificity	91.84	89.14	83.28	83.63	97.27	89.03	5.87	83.28	97.27

MA RF			Class						
3hr (%)	1	2	3	4	5	X	SD	Min	Max
Accuracy	93.18	88.92	83.09	83.47	97.82	89.29	6.33	83.09	97.82
Precision	67.09	47.88	86.78	77.97	46.27	65.20	17.96	46.27	86.78
Recall	95.36	71.82	70.71	67.75	75.61	76.25	11.05	67.75	95.36
F1	78.76	57.45	77.92	72.50	57.41	68.81	10.66	57.41	78.76
Specificity	92.85	90.90	92.13	90.92	98.26	93.01	3.05	90.90	98.26

MA			Class						
6hr (%)	1	2	3	4	5	X	SD	Min	Max
Accuracy	90.81	79.58	71.91	77.31	96.54	83.23	10.14	71.91	96.54
Precision	61.81	38.79	71.49	54.92	13.43	48.09	22.75	13.43	71.49
Recall	85.42	35.85	57.35	60.34	37.50	55.29	20.20	35.85	85.42
F1	71.72	37.26	63.64	57.50	19.78	49.98	21.15	19.78	71.72
Specificity	91.66	88.48	82.84	83.10	97.22	88.66	6.07	82.84	97.22

MA RF			Class						
6hr (%)	1	2	3	4	5	X	SD	Min	Max
Accuracy	89.39	86.12	75.18	74.80	97.02	84.50	9.54	74.80	97.02
Precision	48.74	29.39	80.17	67.63	31.34	51.45	22.27	29.39	80.17
Recall	90.65	61.78	60.50	53.92	55.26	64.42	15.04	53.92	90.65
F1	63.40	39.84	68.96	60.00	40.00	54.44	13.64	39.84	68.96
Specificity	89.25	88.08	87.47	86.07	97.78	89.73	4.65	86.07	97.78

MA			Class						
12hr (%)	1	2	3	4	5	X	SD	Min	Max
Accuracy	90.10	78.64	71.29	76.17	96.26	82.49	10.34	71.29	96.26
Precision	62.56	33.33	69.97	52.88	11.94	46.14	23.54	11.94	69.97
Recall	80.58	32.26	56.70	58.10	28.57	51.24	21.28	28.57	80.58
F1	70.44	32.79	62.64	55.37	16.84	47.61	22.21	16.84	70.44
Specificity	91.73	87.57	82.06	82.34	97.17	88.17	6.43	82.06	97.17

MA RF			Class						
12hr (%)	1	2	3	4	5	X	SD	Min	Max
Accuracy	85.60	83.75	67.55	66.98	96.73	80.12	12.74	66.98	96.73
Precision	27.64	11.82	76.72	58.81	13.43	37.68	28.85	11.82	76.72
Recall	87.30	42.86	51.91	43.32	45.00	54.08	18.92	42.86	87.30
F1	41.98	18.53	61.92	49.89	20.69	38.60	18.75	18.53	61.92
Specificity	85.49	85.59	83.72	81.45	97.23	86.70	6.12	81.45	97.23

MA			Class						
24hr (%)	1	2	3	4	5	X	SD	Min	Max
Accuracy	89.01	76.98	67.60	71.86	95.45	80.18	11.71	67.60	95.45
Precision	63.07	25.15	60.74	47.97	10.45	41.47	22.96	10.45	63.07
Recall	74.70	25.78	52.50	49.65	16.28	43.78	23.17	16.28	74.70
F1	68.39	25.46	56.32	48.79	12.73	42.34	22.79	12.73	68.39
Specificity	91.72	86.19	77.58	80.08	97.10	86.53	8.07	77.58	97.10

MA RF			Class						
24hr (%)	1	2	3	4	5	X	SD	Min	Max
Accuracy	85.69	83.94	61.30	63.05	96.31	78.06	15.26	61.30	96.31
Precision	24.12	2.73	76.17	50.00	0.00	30.60	32.44	0.00	76.17
Recall	#####	33.33	46.20	37.82	0.00	43.47	36.15	0.00	#####
F1	38.87	5.04	57.51	43.07	0.00	28.90	25.12	0.00	57.51
Specificity	85.01	84.60	81.07	77.84	96.81	85.07	7.18	77.84	96.81

ASEAN
Journal of Scientific and Technological Reports
Online ISSN:2773-8752

Research article

Technology Transfer Needs Assessment for Turmeric Farmers in Paphayom District, Phatthalung Province

Saowanee Lekbangpong[1], and Apinya Ratanachai[2*]

[1] Agricultural Innovation and Management Division, Faculty of Natural Resources, Prince of Songkla University, Songkla, 90110, Thailand
[2] Agricultural Innovation and Management Division, Faculty of Natural Resources, Prince of Songkla University, Songkla, 90110, Thailand
* Correspondence: apinya.r@psu.ac.th

Citation:
Lekbangpong, S.; Ratanachai, A. Technology transfer needs assessment for turmeric farmers in paphayom district, Phatthalung province. *ASEAN J. Sci. Tech. Report.* **2025**, *28*(1), e254806.https://doi.org/10.55164/ajstr.v28i1.254806.

Article history:
Received: July 1, 2024
Revised: October 2, 2024
Accepted: October 25, 2024
Available online: December 14, 2024

Publisher's Note:
This article has been published and distributed under the terms of Thaksin University.

Abstract: These research findings indicated that most farmers in the study were female, with an average age of 55.88 years and an average of 10.80 years of experience in cultivating turmeric. Often, turmeric is grown in conjunction with rubber cultivation. Farmers typically cultivated turmeric on 1.38 rai, preferring sandy loam soil conditions. Their preferred turmeric variety was Trang 84-2. The planting method involves digging holes 10 centimeters deep, with a spacing of 25 cm x 25 cm. Turmeric cultivation usually commences in June and concludes with its harvest in April. During planting, farmers apply a combination of chemical and biological fertilizers, along with organic manures. Weed control is primarily achieved by manual removal, while chemical treatments are employed to manage diseases and insect pests. During the 2021/2022 production season, farmers achieved an average turmeric yield of 1,675.81 kg. Farmers encounter various problems in turmeric production, particularly in maintenance, disease, and insect management. These issues adversely affect the planting area, often reducing production yields. The most pressing need for farmers is to acquire turmeric production technology, particularly in pest mitigation and elimination. Farmers want to receive knowledge transfer, such as with individualized guidance through farm visits. The media that farmers require include brochures and the assistance of extension officers. Additionally, the level of experience in turmeric production significantly influenced the farmers' technology transfer needs at a 0.01 significance level.

Keywords: Production; Problems; Technology transfer; Turmeric

1. Introduction

According to Euromonitor, the herbal products market in Thailand in 2021 was valued at 45.64 billion baht, a slight decrease of approximately 1% from 2020. Notably, some products showed declining demand while there was increasing demand for dietary supplements. Therefore, it is anticipated that herbal products will continue to experience demand growth, with the market value projected to reach 59.5 billion baht by 2026 [1]. This presents a favorable outlook to encourage the cultivation of medicinal plants, providing trade opportunities and a potential way for farmers to generate income within local communities[2]. Turmeric (*Curcuma longa* L.) has a rich history of medicinal use dating back to ancient times. It possesses properties for treating digestive issues, including flatulence, and is considered one of the six essential Thai herbal medicines. Turmeric is widely utilized as an ingredient in both food and

cosmetic products. Extracts derived from turmeric primarily contain two substances: curcuminoids and essential oils.

In Phatthalung province, farmers have adopted the cultivation of turmeric as an intercrop within fruit tree orchards and rubber plantations. This method optimizes land use and allows farmers to generate income while waiting for their fruit trees and perennials to become established. Furthermore, according to a recent survey [3], the total land area in Phatthalung province is 127,962 rai, distributed across Paphayom, Khuan Khanun, Sri Banphot, Srinakarin, Kong Ra, and Khao Chaison districts. This region holds significant potential for turmeric cultivation and is classified as an "S1" area, indicating its suitability for crop cultivation. According to a research report [4], turmeric products cultivated in the Paphayom district of Phatthalung province exhibit higher levels of curcuminoid and volatile oil than standard values and with turmeric produced in other regions. The suitability of the planting area in the Paphayom district lies in its terrain, characterized by mountainside slopes that cannot be flooded.

Additionally, the soil does not retain water, contributing to the production of high-quality turmeric. Moreover, turmeric cultivation is characterized by its simplicity, minimal capital investment, and potential to generate substantial farmer income, leading to a growing interest among farmers in the Paphayom district. Turmeric is frequently intercropped with other plants, and the land is continuously utilized without fallow periods. However, this continuous cultivation can lead to challenges in turmeric farming, including rot or wilt diseases. These diseases are primarily attributed to a buildup of bacteria in the soil, particularly in regions with extensive and uninterrupted planting, ultimately leading to reduced turmeric yields. Reduced turmeric yields and income have compelled many farmers to discontinue turmeric cultivation. Those farmers who continue turmeric cultivation often do so with less intensive care since their primary focus is on selling the harvested produce, be it fresh turmeric or turmeric powder. They primarily use turmeric as a component in various curry pastes rather than directing it toward pharmaceutical applications. Attaining the desired curcuminoid levels is paramount, especially when striving to produce turmeric that meets the necessary quality and standards for pharmaceutical applications. This requires a meticulous commitment to production processes and ongoing vigilance by the farmers. In a study conducted [5], it was discovered that the majority of farmers cultivated turmeric without adhering to certification standards.

Consequently, the quality of their produce falls short of meeting market requirements. Therefore, their turmeric tends to fetch relatively lower prices in the market. However, suppose farmers adhere to proper cultivation practices that align with production principles and strive to meet GAP (Good Agricultural Practices) standards for certification. In that case, it can lead to increased market demand and the ability to sell their products at higher prices. Additionally, through interviews conducted with local farmers, it was found that issues in turmeric production stemmed from farmers' insufficient knowledge and understanding of correct turmeric cultivation practices. Their turmeric cannot be utilized in health products due to the use of chemicals in production. Additionally, the soil condition where turmeric is planted can be degraded, leading to potential issues for future plantings. This includes diseases during planting and improper harvesting of the produce while it is still in its early stages, resulting in a lower-quality product. Consequently, the selling price is significantly reduced.

From the observations above, it becomes evident that turmeric production by farmers in the Paphayom district lacks integration with academic knowledge and modern production practices. Consequently, the harvested products still do not meet the quality standards necessary for their utilization in the production of high-value products. Therefore, farmers receive meager returns from their efforts, leading to a lack of motivation to sustain their cultivation activities despite the region's high suitability for turmeric production. Furnishing farmers with customized turmeric production technology tailored to their specific needs is crucial to enabling them to cultivate turmeric correctly and achieve superior product quality. Transfer of appropriate turmeric production technology that meets farmers' needs. What should it be? Consequently, this will empower farmers to command higher prices for their produce. In light of these factors, it becomes apparent that addressing production challenges and the imperative requirement for technology transfer are essential for improving turmeric production by farmers in the Paphayom district. This research gives valuable insights for devising effective strategies in technology transfer to farmers. This effort aimed to equip them

with the knowledge and skills needed to enhance the quality of their production. By addressing the existing production and delivering technology transfer tailored to their requirements, farmers can resolve their current issues and pave the way for a more profitable future.

2. Materials and Methods

Study area

The turmeric cultivation area in the Paphayom district of Phatthalung province encompasses the Lan Khoi subdistrict, comprising four villages. These include Village No. 3, Ban Thung Chumphon; Village No. 5, Ban Tham La; Village No. 8, Ban Huai Ramphueng; and Village No. 9, Ban Khuan Yao. It extends into the Ko Tao subdistrict, encompassing four villages: Village No. 3, Ban Bang Lo; Village No. 5, Ban Sai; Village No. 9, Ban Khuan Tabaek; and Village No. 11, Baan Ko Yuan. The research population of turmeric farmers Purposive Sampling of 118 farmers within Paphayom district, Phatthalung province.

Data collection and statistical analyses

The research utilizes a questionnaire to gather data on the transfer of turmeric production technology divided into 5 parts. Part 1: Basic farmer information. Part 2: Turmeric production practices among farmers. Part 3: Problems of turmeric production. Part 4: Needs and methods for technology transfer to do turmeric production. Part 5: Media is needed for technology transfer to produce turmeric. The severity of problems in turmeric production will be measured using a rating scale: a mean of 0.00–0.67 indicates no problems, 0.68–1.33 indicates minor problems, and 1.34–2.00 indicates significant problems. The level of need for technology transfer in turmeric production will be measured using a rating scale: a mean of 0.00–0.74 indicates no need, 0.75–1.49 indicates low need, 1.50–2.24 indicates moderate need, and 2.25–3.00 indicates high need. The need for media in technology transfer for turmeric production will be measured using a rating scale: a mean of 1.00–1.67 indicates a low need, 1.68–2.33 indicates a moderate need and 2.34–3.00 indicates a high. To ensure the quality of the questionnaire, a review was conducted by three experts. They focused on assessing the congruence between the questions, their contents, and their alignments with the research objectives, as measured by the Item Objective Congruence (IOC). The revised structured interview was then administered as a trial to a group of 30 non-sample farmers. Its reliability was assessed using Cronbach's alpha coefficient, which yielded a high confidence value of 0.96 for the entire interview. The data analysis in this study was conducted using IBM SPSS, a software for social science statistics. Descriptive statistics were used, including frequency distribution, percentage, mean, and standard deviation. The results were presented as a frequency distribution table, showcasing maximum and minimum values for each variable. Stepwise multiple regression correlation analysis was employed to determine the factors influencing the need for technology transfer in turmeric production.

3. Results and Discussion

3.1 Personal characteristics, economic status, and social position of farmers in Paphayom district, Phatthalung province

The research findings indicate that turmeric producers in Paphayom District, Phatthalung Province, are predominantly female, with an average age of 55.88, and most completed their primary education. On average, there are 3.63 members per household, with 2.15 household members engaged in agricultural activities. The average total agricultural landholding per household was 13.94 rai. Mountainside slopes primarily characterize the agricultural area. Farmers have an average of 10.80 years of experience in turmeric cultivation. This is consistent with the study of [6], which suggests that farmers with experience or those who have participated in agriculture-related activities are more likely to prioritize and show greater interest in activities promoting organic vegetable cultivation than farmers without such experiences. A notable proportion of them, 46.61% of the total, are members of agricultural groups or organizations. These organizations encompass a range of entities such as the Bank for Agriculture and Agricultural Cooperatives (BAAC), farmer occupational groups, community enterprise groups, and agricultural cooperative groups.

3.2 Turmeric production practices among farmers in Paphayom district, Phatthalung province

Turmeric producers among farmers in the Paphayom district, Phatthalung province, typically cultivate an average total area of 1.38 rai of turmeric. Most of them (67.80%) engage in intercropping turmeric with rubber trees. The prevalent soil type for cultivation is sandy loam, constituting 72.03%. The overwhelmingly favored turmeric variety is Trang 84-2, chosen by 98.31% of farmers due to its well-rooted structure, vibrant color, appealing taste, and high market demand. The most grown type of turmeric tuber among farmers is the mother tuber with stems, accounting for 79.31% of the cases. This preference is attributed to the cost-effectiveness of mother tubers with stems compared to those without stems. Farmers predominantly cultivate turmeric from purchased plants, accounting for 72.03% of cases. The planting area preparation typically involves 13.52 days, including a single plowing session and seven days of soil drying. Lime is applied once to adjust the soil's pH. The planting process entails digging holes 10 centimeters deep and maintaining a maximum planting distance of 25 cm x 25 cm. The planting season commences in June, with harvesting in April of the subsequent year. Natural rainwater is primarily used for irrigation during the production process. In turmeric production, farmers apply fertilizer at different stages, including a single application of biological fertilizer at a rate of 50 kilograms per rai, administered before the planting phase, followed by two chemical fertilizer applications at a rate of 50 kilograms per rai. The first application of chemical fertilizer is done one month after planting. The second application utilizes a 0-0-60 chemical fertilizer formula administered during the tillering stage to nourish the bulbs. Manure is applied once, two months after the initial planting, at 80 kilograms per rai. Finally, a 13-13-21 chemical fertilizer formula is applied three months or more after planting turmeric to stimulate growth. Weed control is primarily achieved through manual removal, practiced by 98.31% of the farmers. Additionally, chemical treatments are used to manage diseases and insects. Chemical agents are employed alongside biological agents and biological fermentation techniques. The average time required for harvesting turmeric is 29.51 days. Farmers in this region prefer to use hoes to harvest their turmeric, consistent with a report [7] on turmeric harvesting in Bagalkot, Karnataka, India. In Bagalkot, turmeric is typically harvested when the leaves begin to yellow, and the stem eventually dries down. This harvesting season typically spans the period from February to April. The rhizomes become ready for harvest approximately 7-9 months after planting. The harvesting process involves digging underground clumps of rhizomes using a pickaxe or digging fork, followed by separation of the fingers from the mother rhizomes. During the 2021/2022 production season, farmers achieved an average turmeric yield of 1,675.81 kg. Farmers utilize their turmeric in three ways: outright sale, for use as seed heads, and for personal consumption. Turmeric sales are segmented into three primary categories. The first was turmeric powder, which accounted for 77.96% of the sales. This preference is driven by the convenience it offers, as it requires minimal grading and can be readily cleaned and sold. The average price for turmeric powder is 29.51 baht per kilogram. Next, turmeric produce is also sold as mother bulbs with stems, representing 51.69% of sales. These are sold at an average price of 43.19 baht per kilogram. Finally, a smaller proportion, 5.08%, is sold as tubers without stems, fetching an average price of 50 baht per kilogram. The price of tubers without stems is higher than those with stems attached due to the absence of attached stems. This results in a shorter growth period for stems and leaves than rooted varieties, contributing to the price difference.



Figure 1. Harvesting turmeric of farmers in Paphayom district, Phatthalung province.

3.3 Problems of turmeric production in Paphayom district, Phatthalung province

An overview of the challenges faced by farmers in Pa Phayom district, Phatthalung province, in turmeric production revealed that their primary issues were related to maintenance, diseases, and insects affecting their crops. While they encountered some challenges in receiving state support, these were relatively minor. (Table 1).

Table 1. Level of farmer's problems with turmeric production in Paphayom district, Phatthalung province

Problems of turmeric production	⚜	S.D.	Description
1. Preparation before planting	0.48	0.36	No problems
2. Planting	0.57	0.33	No problems
3. Preservation	1.00	0.64	Less problematic
4. Diseases and Insects	0.70	0.38	Less problematic
5. Harvest and Post-harvest	0.30	0.34	No problems
6. Marketing	0.67	0.58	No problems
7. Government Support	1.03	0.43	Less problematic
	0.67	**0.28**	**No problems**

Remark: Levels problems of turmeric production: mean 0.00-0.67 = No problems, mean 0.68-1.33 = Less problematic, mean 1.34-2.00 = Very troubling

3.4 Needs of farmers for technology transfer to do turmeric production in Paphayom district, Phatthalung province

3.4.1 Needs and methods for technology transfer to do turmeric production

There is a need to transfer technology and improved turmeric production techniques to farmers in the Paphayom district, Phatthalung province. An overall assessment reveals that farmers have a significant demand for technology transfer for turmeric production. When examining specific aspects of their requirements, it becomes evident that farmers have particularly pronounced needs related to pest mitigation and eradication. They express a need for individualized knowledge transmission methods, such as farm visits, and mass communication methods like campaigns. Campaigns are valuable for disseminating information persuasively, establishing trust, and facilitating the adoption of ideas and behaviors among farmers. This finding aligns with the research [8], which emphasized the effectiveness of electronic and mass media platforms in disseminating knowledge, skills, and improved technology to rice farmers. These media channels play pivotal roles in delivering extension services, particularly in light of the limited effectiveness of public extension agencies in providing essential agricultural extension services to farmers. Additionally, it is noteworthy that farmers have moderate needs for maintenance technology. For maintenance technology, the preferred method of knowledge transfer is mass communication, specifically through campaigns, rather than group-based approaches. This preference stems from the belief that group methods may not effectively address important issues and alternative methods are deemed more suitable for acquiring knowledge related to maintenance. For moderate priority needs, specifically those related to preparation before planting and the planting phase, farmers prefer technology transfer through both mass methods and individualized methods. Farmers exhibit reluctance to receive technology transfer in pre- and post-harvest phases. They perceive academic technology in these aspects as time-consuming and prefer to rely on knowledge obtained from diverse sources along with their accumulated experience to manage the pre- and post-harvest periods. (Table 2).

Table 2. Level of farmers' needs and methods for technology transfer for turmeric production in Paphayom district, Phatthalung province

Needs and method for technology transfer of turmeric production	⚜	S.D.	Description
1. Preparation before planting	1.29	0.56	Lowest
Individual method	1.52	0.12	Moderate
Group method	0.66	0.02	Needless
Mass method	1.99	0.06	Moderate
2. Planting	0.88	0.80	Lowest
Individual method	1.50	0.03	Moderate
Group method	0.67	0.40	Needless
Mass method	1.98	0.60	Moderate
3. Preservation	1.71	0.58	Moderate
Individual method	1.49	0.10	Lowest
Group method	0.67	0.04	Needless
Mass method	2.00	0.05	Moderate
4. Prevention and pest control	2.35	0.67	High
Individual method	1.50	0.07	Moderate
Group method	0.66	0.03	Needless
Mass method	1.99	0.05	Moderate
5. Before and after harvest	0.73	0.84	Needless
Individual method	1.50	0.08	Moderate
Group method	0.66	0.09	Needless
Mass method	2.00	0.05	Moderate

Remark: Levels needs for technology transfer of turmeric production:
mean 0.00 – 0.74 = needless, mean 0.75 – 1.49 = Lowest, mean 1.50 - 2.24 = Moderate, mean 2.25 – 3.00 = High

3.4.2. Needs media for technology transfer to do turmeric production

The overall level of demand for media-based technology transfer in turmeric production among farmers in the Paphayom district is assessed as moderate. The desired medium for technology transfer among farmers is brochures. Farmers find brochures easily accessible, enabling them to open and read them immediately, and they appreciate the comprehensive information provided. When examining the specific media needs for each aspect, it becomes evident that for preparation before the planting phase, farmers prefer brochures, followed by television and information from neighbors. Regarding the planting phase, farmers similarly prioritize brochures as their preferred media, followed by television and the Internet. For maintenance, pamphlets are in the highest demand, followed by consultations with government officials and community leaders. Regarding pest mitigation and elimination, most farmers prefer information broadcast by government officials, followed by online resources and instructional manuals. Pamphlets are the most preferred media for the pre-and post-harvest periods, followed by television and information from neighbors. This finding is consistent with the research conducted [9], on the effectiveness of print media in technology transfer among rural farm households in Imo State, Nigeria. The study revealed that farm households in Imo State most commonly used print media, specifically flyers, to access information and knowledge about the improved technologies being transferred to them. (Table 3).

Table 3. Level of farmers' needs for media technology of turmeric production in Paphayom district, Phatthalung province

The technology of turmeric production	Needs media	⚜	S.D.	Description
1. Preparation before planting	Neighbor	2.17	0.96	Moderate
	Community leader	2.13	0.46	Moderate
	Government official	1.71	0.85	Moderate
	Brochure	2.58	0.63	High
	Manual	2.13	0.56	Moderate
	Poster	1.26	0.61	Low
	Television	2.23	0.70	Moderate
	Video	1.62	0.76	Low
	Internet	2.11	0.85	Moderate
2. Planting	Neighbor	2.06	0.93	Moderate
	Community leader	2.10	0.59	Moderate
	Government official	1.87	0.86	Moderate
	Brochure	2.53	0.66	High
	Manual	2.10	0.67	Moderate
	Poster	1.41	0.70	Low
	Television	2.17	0.76	Moderate
	Video	1.60	0.68	Low
	Internet	2.16	0.84	Moderate
3. Preservation	Neighbor	1.50	0.83	Low
	Community leader	2.20	0.49	Moderate
	Government official	2.29	0.83	Moderate
	Brochure	2.34	0.75	High
	Manual	2.16	0.64	Moderate
	Poster	1.49	0.79	Low
	Television	2.25	0.70	Moderate
	Video	1.55	0.69	Low
	Internet	2.17	0.86	Moderate
4. Prevention and pest control	Neighbor	1.37	0.72	Low
	Community leader	2.11	0.44	Moderate
	Government official	2.57	0.73	High
	Brochure	2.25	0.68	Moderate
	Manual	2.29	0.68	Moderate
	Poster	1.44	0.78	Low
	Television	2.06	0.72	Moderate
	Video	1.57	0.69	Low
	Internet	2.30	0.86	Moderate
5. Before and after harvest	Neighbor	2.18	0.94	Moderate
	Community leader	2.14	0.51	Moderate
	Government official	1.72	0.86	Moderate
	Brochure	2.38	0.76	High
	Manual	2.10	0.61	Moderate
	Poster	1.50	0.81	Low
	Television	2.31	0.72	Moderate
	Video	1.60	0.68	Low
	Internet	2.07	0.87	Moderate

Remark: Levels needs media for technology transfer of turmeric production:
mean 1.00-1.67 = Low, mean 1.68-2.33 = Moderate, mean 2.34-3.00 = High

3.5 Factors affecting the need for technology transfer to do turmeric production for farmers in Paphayom district, Phatthalung province

The relationship between the independent and dependent variables was analyzed using stepwise multiple regression analysis. A total of 8 independent variables were considered, including gender, age, education level, the number of household members, the number of workers in the household, turmeric production experience, turmeric growing area, and turmeric production. The dependent variable in this analysis is the farmers' need for technology transfer in turmeric production. Analysis results are displayed in Table 4.

Table 4. Mean and standard deviation of the analyzed variables

Independent variables	⚜	S.D.
Sex (1= male / 2= female)	2.00	0.49
Age (years)	55.88	9.55
Education level (years)	2.38	0.82
Number of household members	3.63	1.14
Number of workers in the household	2.15	0.72
Turmeric production experience (years)	10.80	5.05
Landholding area (rai)	1.38	0.82
Turmeric yield (kg)	1,672.81	960.42

The multiple regression analysis obtained an F-value of 6.097 with a significance level of 0.01. When considering the multiple coefficients of determination (R^2), which is 0.73, it indicates that independent variables collectively explain 73 percent of the variation in the dependent variable. Specifically, one independent variable, experience in producing turmeric, significantly affects the dependent variable at the 0.01 level, with a coefficient value of Y = 1.186 + 0.239 x (turmeric production experience).

Farmers with extensive experience in turmeric production exhibit a greater need for technology transfer compared to farmers with limited experience. This finding aligns with the research conducted [10]. Their study investigated factors influencing farmers' need to promote organic vegetables in the Maefaekmai sub-district, Sansai district, Chiang Mai province. The study explained that farmers with experience or involvement in agricultural-related activities tend to place greater importance on and exhibit more interest in initiatives aimed at promoting organic vegetable cultivation compared to farmers without this background. This result aligns with the research conducted [11], which investigated the technical efficiency of turmeric (*Curcuma Longa* L.) production in Benue State, Nigeria. Their study found that producers' participation in and adoption of improved turmeric production techniques can effectively reduce the technical inefficiency of turmeric production in the study area. Additionally, this shows that as production experience increases, producers are likely to acquire more knowledge and technological insights on addressing issues related to turmeric production. This, in turn, can lead to increased output and income for the producers. (Table 5)

Table 5. Analysis of factors affecting farmers' needs for technology transfer in turmeric production in Paphayom district, Phatthalung province

Variables	Coefficient (b)	Beta	t	p-value
(Constant)	1.186		12.066	0.00
Sex	0.015	0.02	0.277	0.78
Age	-0.035	-0.02	-0.322	0.74
Education level	0.093	0.08	0.937	0.35
Number of household members	0.119	0.09	1.055	0.29
Number of workers in the household	0.183	0.12	1.341	0.18
Turmeric production experience	0.239	0.12	2.667	0.01*
Landholding area	0.067	0.11	1.001	0.32
Turmeric yield	0.050	0.02	0.251	0.80
SEest = 0.82, Durbin-Watson = 0.82, R = 0.30, R^2 = 0.73, F = 5.21, p-value = 0.01				

Significance level: * $p < 0.01$

4. Conclusions

The current study's findings indicate that turmeric production by farmers in the Paphayom district, Phatthalung province, typically involves intercropping alongside rubber cultivation. Sandy loam soil condition is ideal, with the preferred turmeric variety being Trang 84-2. The cultivation area is prepared through plowing and soil drying, followed by the application of fertilizers, including both biological and chemical fertilizers, along with manure. Weed control is achieved through manual removal, while chemicals are utilized for disease and insect management. Additionally, farmers incorporate biological substances and employ biological fermentation techniques. Notably, farmers prefer selling their produce in the form of turmeric powder. Farmers encounter various problems in turmeric production, with maintenance issues, diseases, insects, and inadequate state support being prominent concerns. These problems impact the planting area and yield, leading to a heightened need for turmeric production technology, particularly in pest mitigation and elimination. Farmers have the greatest need for prevention and pest control promotion methods and require moderate individual and mass promotion methods. Farmers need media for preparation before planting, planting, preservation, before and after harvest. There is the highest demand for brochures to convey turmeric production technology. As for prevention and pest control, farmers need government officials to transfer turmeric production technology. Based on the findings of this research, it is recommended that agricultural extension officers or relevant agencies establish a structured plan for visiting farms regularly and continuously to provide continuous guidance and support in turmeric production practices. Furthermore, it is suggested that user-friendly brochures on turmeric production technology be developed, with a focus on practical, hands-on methods that farmers can implement independently. These materials should cater to the specific needs of farmers, enabling them to acquire knowledge for producing higher-quality turmeric and addressing production challenges more effectively. This approach will empower farmers to produce consistently well-suited turmeric to their local conditions.

5. Acknowledgements

The authors thank the household respondents in Paphayom District, Phatthalung, Thailand. This study was conducted using the Human Ethics Study code PSU-HREC-2023-049-1-3, which participated in this study.

Author Contributions: Conceptualized, data collection and formal analysis writing- review and editing, S.L. and A.R. review, editing, and supervision. All authors have read and agreed to the published version of the manuscript.

Funding: This research was funded by a research grant for a thesis in the 2023 fiscal year, provided by the Prince of Songkla University, Songkla, Thailand.

Conflicts of Interest: The authors declare no conflict of interest

References

[1] Department of International Trade Promotion. Herbs and herbal products. **2022,** Available online: https://www.ditp.go.th/contents_attach/777079/777079.pdf. (accessed on 13/5/2024).

[2] Chanasuwan, P.; Keaowan, B.; Saranrom, P. Guidelines for Extension of Medicinal Plant Production of Farmer in Krabi Province. The 10th STOU National Research Conference. **2020**, 1456-1467.

[3] Land Development Department. Appropriate agricultural promotion guidelines according to the proactive agricultural map database agri-map Phatthalung province. 2021. Available online: https://e-library.ldd.go.th/library/flip/bib10631f/bib10631f.html. (accessed on 11/11/2023).

[4] Petppradit, R. Agricultural and Agro-industry technology transfer project in the central southern region. Thaksin University. **2017**. Available online: https://ppi.psu.ac.th/project/1411. (accessed on 14/11/2023).

[5] Sungkajorn, M.; Treewannakul, P.; Sukprasert, P. Possibility of Turmeric production with good agricutural practice of farmers in Papahayom district, Phatthalung province. *The Agricultural Science Journal.* **2021**, *52*(2), 107-117.

[6] Sompor, W.; Kruekum, P.; Parapanya, P.; Jeerat, P. Factors affecting farmers' needs for promoting vegetable growing under good agricultural practices in Mon ngo Royal project development center, mae Tang district, Chiang Mai province. *Journal of Agricultural Production (JAP).* **2021**, *3*(2), 23-32.
[7] Mirjanaik, H.; YC, R. V. Advances in production technology of turmeric. *Journal of Pharmacognosy and Phytochemistry*. **2020**, *9*(4), 1198-1203.
[8] Baanni A. S.; A. Donkoh, S.; Awuni, A. J. The perceived effectiveness of agricultural technology transfer methods: Evidence from rice farmers in Northern Ghana. *Cogent Food & Agriculture*. **2018**, *4*, 1-11.
[9] Njoku, J. I. K. Effectiveness of print media in technology transfer among rural farm households in Imo state, Nigeria. *Association of Deans of Agriculture in Nigerian Universities (ADAN) Journal of Agriculture.* **2022**, *3*, 8-19.
[10] Thitisutthi, S.; Kruekum, P. Factors affecting the farmers' need for organic vegetables promotion in the Maefaekmai sub-district, Sansai district, Chaing Mai province. *Journal of Agri Research and Extension*. **2019**, *36*(3), 86-95.
[11] Ayilla,V.N.; Mbanasor, J.A. Technical efficiency of Turmeric (*Curcuma Longa* L.) production in Benue State, Nigeria. *American Journal of Economics.* **2022**, *6*(1), 48-55.

ASEAN
Journal of Scientific and Technological Reports
Online ISSN:2773-8752

Research article

Mutation Induction in Toothbrush Orchids Using Ethylmethane Sulphonate (EMS) and Detection of Genetic Variation by SSR (Simple Sequence Repeat) Marker

Yaowamarn Keawsaard[1], Parita Pentem[2], Phakarat Rotduang[3], Muntaka Weeraphong[4], and Supawadee Ramasoot[5]*

[1] Department of Agricultural, Faculty of Science and Technology, Nakhon Si Thammarat Rajabhat University, Tumbon Thayew, Mueang district, Nakhon Si Thammarat Province, 80280, Thailand
[2] Department of Biology, Faculty of Science and Technology, Nakhon Si Thammarat Rajabhat University, Tumbon Thayew, Mueang district, Nakhon Si Thammarat Province, 80280, Thailand
[3] Department of General Science, Faculty of Education, Nakhon Si ThammaratRajabhat University, Tumbon Thayew, Mueang district, Nakhon Si Thammarat Province, 80280, 80280, Thailand
[4] Department of Education in Science (Biology), Faculty of Science and Technology, Nakhon Si Thammarat Rajabhat University, Tumbon Thayew, Mueang district, Nakhon Si Thammarat Province, 80280, 80280, Thailand
[5] Department of Education in Science (Biology), Faculty of Science and Technology, Nakhon Si Thammarat Rajabhat University, Tumbon Thayew, Mueang district, Nakhon Si Thammarat Province, 80280, 80280, Thailand
* Correspondence: supawadee_ram@nstru.ac.th

Citation:
Keawsaard, Y.; Pentem, P.; Rotduang, P.; Weerapong, M.; Ramasoot, S. Induction of mutation in yoothbrush orchids using ethylmethane sulphonate (EMS) and detection of genetic variation by SSR (Simple Sequence Repeat) marker. *ASEAN J. Sci. Tech. Report.* **2025**, *28*(1), e255125. https://doi.org/10.55164/ajstr.v28i1.255125.

Article history:
Received: July 22, 2024
Revised: October 24, 2024
Accepted: November 18, 2024
Available online: December 14, 2024

Publisher's Note:
This article has been published and distributed under the terms of Thaksin University.

Abstract: *Dendrobium secundum* is a monocotyledonous plant. It is classified in the *Dendrobium* genus, an important and outstanding economic flowering plant. It is an orchid sold domestically and internationally due to its overall toothbrush-like design, both in the flower arrangement and stem. In recent years, the number of toothbrush orchids has decreased. Therefore, this study aimed to study the effects of ethylmethane sulfonate (EMS) and the detection of genetic variation in toothbrush orchids using simple sequence repeat (SSR) markers. EMS solution was used to soak 0.5x0.5 cm in diameter of the protocorm-like bodies (PLBs) at concentrations of 0.5, 1.0, and 2.0%. After that, they were cultured on Vacin and Went (VW) medium supplemented with 1 mg/l BA and 20 g/l sucrose, adjusted to pH 5.7, and solidified with 0.2 % phytagel. The cultures were maintained at 26 ±2°C under light at 3,000 lux for 14 hours daily. After culturing for 30 days, the results showed that PLBs immersed in EMS solution at 1.7% for 90 minutes gave a survival rate of 50% (Lethal dose; LD_{50}). For the development of PBLs, PBLs immersed in 0.5 % EMS for 60 minutes gave the highest PLB induction (7.37%) and average number of PLBs (1.41 PLBs/explant) after culturing for 8 weeks. For the detection of genetic variation, a total of 9 SSR primers were used, including EgCIR0409, EgCIR0905, EgCIR0781, EgCIR0446, EgCIR1772, EgCIR0337, EgCIR0337, EgCIR0243, mEgCIR0465, and mEgCIR008. The results found that only one primer gave polymorphic banding. EgCIR0905 primer gave polymorphic banding at 50% and specific DNA banding size at 200 bp.

Keywords: Toothbrush orchid; Mutation; Ethylmethane sulphonate; Genetic variation; Simple sequence repeat marker

1. Introduction

Dendrobium secundum is a significant and exceptional economic plant, better known as the toothbrush orchid. It is an orchid sold domestically and

internationally due to its overall toothbrush-like design, both in the flower arrangement and stem. Consequently, there are now fewer toothbrush orchids. The orchids mentioned above also lack variety [1]. One method to alter the characteristics of orchids, from their appearance to their growth potential, is in vitro plant breeding and propagation. In vitro, mutation treatment can be used to create new, improved orchid varieties by using both chemical and physical mutagens, which can broaden the possibilities for orchid variants while accelerating the generation of mutants. [2]. The resulting mutations are expected to increase the diversity and value of orchids. There are numerous methods for breeding. Both chemical and physical methods can be used to accomplish this. The physical ones are ultraviolet, gram, X-rays, and so forth. Mutagenic compounds are used as part of the chemical side. Numerous chemical species can induce mutations, each with a unique set of consequences. Gene mutations will likely result from EMS, a chemical mutagen that can cause alkylation. [3]. According to Li et al. (2021) [4], there is no research on the mutations that lead to increased heterozygosity in orchids due to chemical mutagens that are part of alkylating agents. In orchids such as *Cymbidium*, *Dendrobium*, *Oncidium*, and *Phalaenopsis*, mutation induction—which has been successfully applied in multiple studies—uses the polyploidization breeding technique in combination with colchicine and nitric oxide (NO) mutagens. [4]. Using EMS concentrations, Romiyadi et al. (2018) [5] generated mutations and illustrated interactions with three hybrid Phalaenopsis species on root variables by employing EMS concentrations. Qosim et al. (2016) [6] showed that the development of shoots from hybrid Phalaenopsis spp. was impacted by immersing EMS in a 0.025% and 0.05% concentration for 12 hours. EMS enhances the genetics of other crops, such as sugarcane, to achieve high yields. [7]. EMS induces random point mutations in the plant genome [8,9]. Therefore, molecular analysis must be performed. A sequence repeat (SSR) molecular marker is ideal for genome-level research [10]. Co-dominant, repeatable, easily distinct alleles, high degree of polymorphism, and easily detectable by PCR technology are some characteristics of a simple sequence repeat [11,12]. Microsatellite-specific primer development is relatively expensive and time-consuming to acquire DNA sequence information. [13]. However, no study has been done on applying EMS materials to toothbrush orchids. Therefore, this research aims to study and determine the effect of various concentrations of EMS and durations of time on mutation and investigate genetic variation in toothbrush orchids with SSR markers for various morphology in this orchid and some commercial cultivars.

2. Materials and Methods

2.1 Plant materials

Protocorm-like bodies (PLBs) of toothbrush orchids at 0.5x0.5 cm in diameter were cultured on VW medium supplemented with 1 mg/l BA, 0.2% phytagel and 20 g/l sucrose [14]. The pH was adjusted to 5.7. The culture condition was maintained at 25±2 °C and 3000 lux light intensity for 14 hours of photoperiod.

.

2.2 Effect of various concentrations of EMS and duration time on the development of PLBs

PLBs at 0.5x0.5 cm in diameter were soaked with various concentrations of EMS at 0, 0.5, 1.0, and 2.0% for 60 and 90 min by incubating on a shaker at 100 rpm. After that, filter to separate PLBs from EMS solution, wash with sterile distilled water 2-3 times, and blot with sterile filter paper. PLBs were cultured on VW medium supplemented with 1 mg/l BA, 0.2% phytagel, and 20 g/l sucrose. The culture was subcultured on the same medium component every four weeks for three months. The percentage of survival rate (lethal dose: LD_{50}), the proliferation of PLBs induction (%), and the number of PLBs (PLBs/explant) were recorded.

2.3 Detection of genetic variation of PLBs by SSR markers

2.3.1 DNA Extraction

DNA from each PLBs was extracted using the cetyltrimethyl ammonium bromide (CTAB) method by Doyle and Doyle (1990) with some modification [15] with some modification. In brief, 100 mg of explants were ground to a fine powder in approximately 500 µl of CTAB buffer. The plant extract mixtures were put into microcentrifuge tubes and incubated for 45 minutes at 60°C in a water bath. Following incubation, the extract mixtures were centrifuged for 15 minutes at 12,000 rpm, and the supernatant was then moved to a fresh, clean microcentrifuge tube. 500 µl of chloroform was added to each tube, and the mixture was mixed by inverting

the tube. The tube was thoroughly mixed and then centrifuged for 10 minutes at 13,000 rpm to extract the upper aqueous phase containing the DNA and transfer it to a fresh microcentrifuge tube. To precipitate the DNA, 750 µl of isopropanol was added to the solution, and the tube was slowly inverted several times. Following precipitation, the DNA pellet was dried in a temperature-controlled environment and twice washed with 70% ethanol. In TE buffer, the DNA pellet was dissolved [20 mM Tris-HCl (pH 8.0) and 0.1 M EDTA (pH 8.0)], electrophoresed on 0.75% agarose gel, explored in UV light, and photographed. The amount of DNA was qualitatively measured by comparison with the known quality of λDNA.

2.3.2 SSR Analysis

The Thawaro method [16] was used to analyze DNA differences using the SSR technique. Nine primer pairs (EgCIR0008, EgCIR0243, EgCIR0337, EgCIR0409, EgCIR0446, EgCIR0465, EgCIR0781, EgCIR0905, and EgCIR1772) were used for PCR amplification of DNA. Twenty ng of template DNA, 1.5 units of Tag polymerase, 0.3 mM primer, 10X Tag buffer, 2.5 mM MgCl2, and 100 µl of each dNTP were included in each 10 µl amplification mixture. A thermocycler was used to perform PCR amplification. Using the following program: one minute of denature at 95°C; thirty seconds at 94°C, sixty seconds at 52°C, and one minute at 72°C; and eight minutes of final elongation at 72°C. Afterward, the amplified products were denatured at 94°C for 5 minutes before adding an equal volume of loading buffer (98% formamide, 0.025% bromophenol blue, 0.05% xylene cyanol). The PCR products were then electrophoresed at 150 V in 1%X TAE buffer on 2.0% (w/v) agarose gels. Gel documentation was used to view the gels under ultraviolet light after they had been stained with ethidium bromide for 15 minutes. The reproducibility of the amplification patterns was verified by using different DNA preparations from the mother plant.

2.4 Statistical analysis

A completely randomized design with three replicates, each containing ten explants, was used for the experimental design and statistical analysis. Duncan's Multiple Range Test (DMRT) was used to compare the mean differences. Data was analyzed using ANOVA.

3. Results and Discussion

3.1 Effect of various concentrations of EMS and duration time on the survival rate of PLBs

After immersing the PLBs in EMS solution at different concentrations and durations, they were grown on VW medium and added 1.0 mg/l BA and 0.2% phytagel. The results showed that PLBs immersed in EMS solution at 1.7% for 90 minutes gave the lethal dose at 50% (LD_{50}) after culturing for 1 month (Figure 1). In contrast, all EMS solutions (0, 0.5, 1, and 2 %) gave the highest average survival rates at 93.33, 70, 63.33 and 53.33%, respectively (Figure 2). According to Sirinya and Te-chato (2008) [17], it was found that the survival rate of *Dendrobium friedericksianum* tends to decrease with a longer immersion time in each concentration of EMS.

For the effect of EMS solution on proliferation of PLBs induction, the result found that PLBs were soaked in 0.5% EMS for 60 minutes gave the highest PLBs induction at 7.37% and average number of PLBs at 1.41 PLBs/explant, significant difference with other treatments ($p \leq 0.05$) (Table 1). Samala et al. (2014) [18] found that PLBs immersed in EMS at 0 and 0.75% concentrations for 60 and 90 minutes gave a more than 50% survival rate. In addition, PLBs immersed in EMS at a concentration of 0.75% for 90 minutes showed dark green and succulent PLBs, while control treatment (without EMS) gave light green and no succulent PLBs. Exposure to many substances can disrupt the germination process's enzymes and prevent auxin production [19]. It is a reaction to cell damage and will show PLB growth. For characteristics of PLBs, the result found that PLBs have a light green and pale yellow (Figure 3). Romeida et al. (2012) [20] described that in every area of the cell exposed to the mutagen, PLBs either lose their capacity to produce chlorophyll or cannot do so.

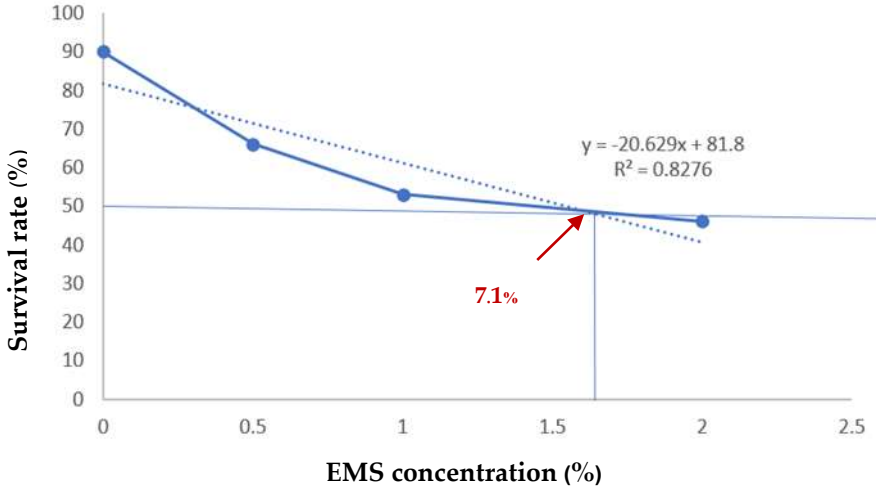


Figure 1 Survival rate of PLBs of toothbrush orchid after having been treated with 0, 0.5, 1, and 2 % for 90 minutes and cultured on VW medium with 1.0 mg/l BA and 0.2% phytagel for 1 month.

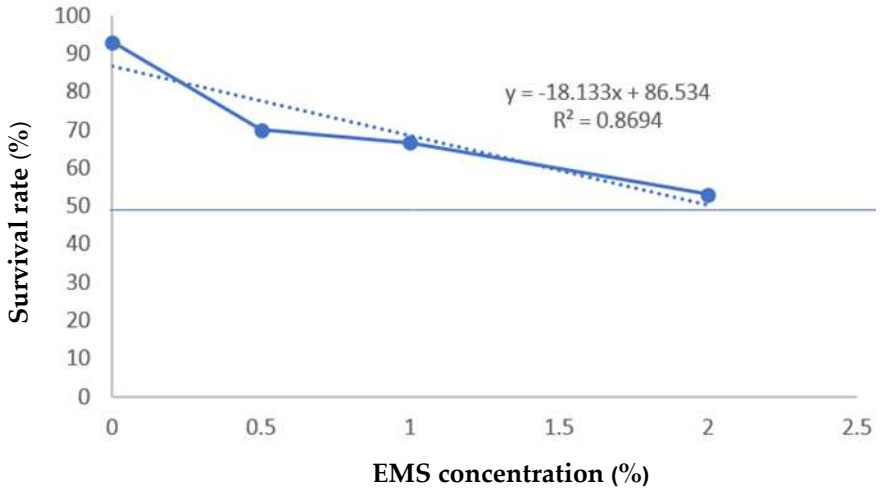


Figure 2 Survival rate of PLBs of toothbrush orchid after being treated with 0, 0.5, 1, and 2 % for 60 minutes and cultured on VW medium with 1.0 mg/l BA and 0.2% phytagel for 1 month.

Table 1 Effect of EMS solution concentration and immersion time on proliferation of PLBs after 2 months of culture

EMS concentrations (%)	Duration time (minute)	PLBs proliferation (%)	No. of PLBs (PLBs/explant)
0	60	3.73abc	0.75abc
0.5	60	7.37a	1.41a
1	60	3.63abc	0.73abc
2	60	0.93c	0.19c
0	90	2.57bc	0.51bc
0.5	90	5.53ab	1.11ab
1	90	3.67abc	0.73abc
2	90	1.80bc	0.37bc
F-test		*	*
C.V.(%)		19.68	19.22

* significant difference at $p \leq 0.05$ means that the different letters in the same column are significantly different by DMRT

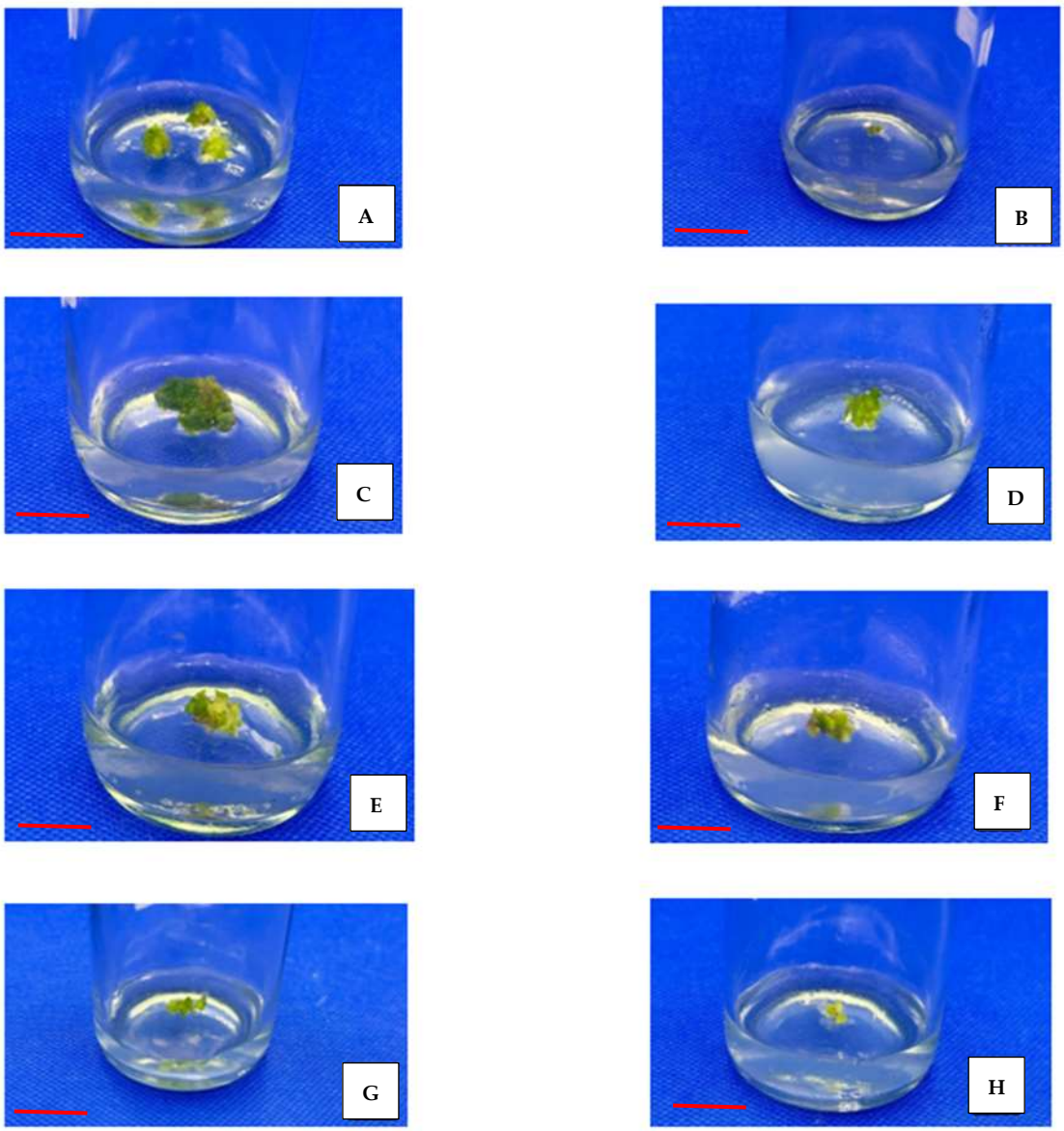


Figure 3 Characteristics of PLBs derived from soaking in various EMS and duration time concentrations and were cultured on VW medium with 1.0 mg/l BA and 0.2% phytagel after 8 weeks of culture. (Bar = 1 cm.)

A. 0% EMS + 60 minute duration time
B. 0.5% EMS + 60 minute duration time
C. 1% EMS + 60 minute duration time
D. 2% EMS + 60 minute duration time
E. 0% EMS + 90 minute duration time
F. 0.5% EMS + 90 minute duration time
G. 1% EMS + 90 minute duration time
H. 2% EMS + 90 minute duration time

3.2 Detection of genetic variation of PLBs by SSR markers

In this present study work, nine SSR-primers tested (EgCIR0008, EgCIR0243, EgCIR0337, EgCIR0409, EgCIR0446, EgCIR0465, EgCIR0781, EgCIR0905 and EgCIR1772) only one primer (EgCIR0905) could provide polymorphic patterns of DNA among treated PLBs with EMS solutions. The EgCIR0905 primer gave a DNA banding with polymorphism, and a specific DNA band at 200 bp of PLBs was treated with 2% EMS for 60 minutes (Figure 4). In this study, EMS-induced mutation induction resulted in genomic change, as evidenced by the appearance of new alleles or the loss of alleles in specific sizes compared to the control plant. Depending on the plant's genotype, EMS treatment can cause different amounts of genomic change. DNA damage,

nucleotide modification, DNA fragment breakage, and chromosome rearrangement brought on by EMS treatment can all result in the disappearance of an allele. Multiple nucleotide changes in the mutant plant's primer binding region can result in the emergence of new alleles [21]. A mutagenesis mechanism that changes the G/C to A/T nucleotides in the primer binding regions of the SSR marker can cause genomic alterations in plant-induced mutations with EMS [22, 23, 24]. Furthermore, nucleotide insertions or deletions in mutant plant DNA sequences cause the microsatellite marker's repeat region to lengthen or shorten [25, 26, 27]. Boonsrangsom et al. (2008) [28] found that Eight primer pairs could be used to amplify the products giving the expected sizes and detect genetic polymorphism in the population with the allele numbers ranging from 4 to 7 (averaged 5.25 alleles per locus).

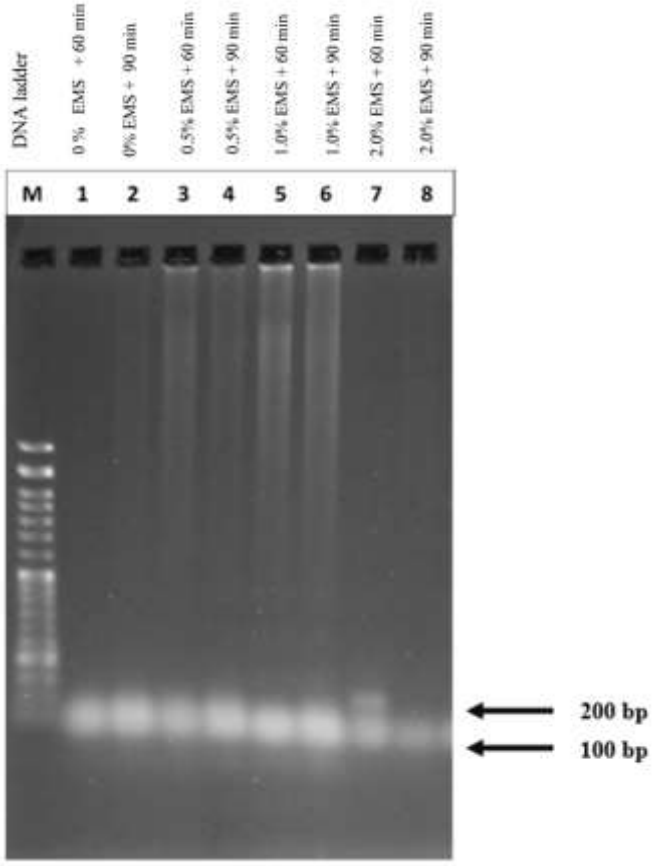


Figure 4 DNA band patterns of PLBs of toothbrush orchids immersed in EMS solution concentrations were examined with SSR markers using the primer EgCIR0905.

4. Conclusions

The effect of EMS on the characteristics of PLBs and their genetic variability after verification with SSR markers was investigated. EMS solution was used to soak a 0.5 cm piece of the protocorm-like bodies (PLBs) at concentrations of 0.5, 1.0, and 2.0%. After that, they were cultured on VW medium supplemented with 1 mg/l BA and 20 g/l sucrose, adjusted to pH 5.7, and solidified with 0.2 % phytagel. The cultures were maintained at 26 ±2°C under light at 3,000 lux for 14 hours daily. After culturing for 30 days, the results showed that PLBs immersed in EMS solution at 1.7% for 90 minutes gave the highest average survival rates at 50% (LD_{50}). For the development of PBLs, PBLs were derived and immersed in 0.5 % EMS for 60 minutes, giving the highest PLB induction (7.37%) and average number of PLBs (1.41 PLBs/explant) after culturing for 8 weeks. A total of 9 SSR primers were used to detect genetic variation. The results found that EgCIR0905 primer gave polymorphic banding at 50% and specific DNA banding size at 200 bp. The present study recorded 90 days of interval observation and suggests that further studies need to obtain more compressive mutation.

5. Acknowledgements

The authors thank the Science Center in Faculty of Science and Technology for the research laboratory. Agricultural Diversity and Biotechnology Research Unit, Research and development institute, Nakhon Si Thammarat Rajabhat University partially supports this research.

Author Contributions: Conceptualization, P.R. and S.R.; methodology, P.R.; software, S.R.; validation, P.R., S.R., and T.K.; formal analysis, P.R.; investigation, P.R.; resources, P.R. and T.K..; data curation, P.R..; writing—original draft preparation, P.R.; writing—review and editing, S.R.; visualization, T.K.; supervision, S.R..; project administration, P.R. and S.R All authors have read and agreed to the published version of the manuscript." Please turn to the CRediT taxonomy for the term explanation. Authorship must be limited to those who have contributed substantially to the work reported.

Funding: This research received no external funding

Conflicts of Interest: The authors declare no conflict of interest.

References

[1] Orchidtropical. Available online: https://www.orchidtropical.com/. (access on 7 October 2022).
[2] Agatha, S.; Fenny, I.; Sulistyo, E.; Popy, H. Induction of protocorm-like bodies (PLBs) Phalaenopsis spp. hybrids mutation through ultraviolet irradiation (UV254) and ethyl methane sulfonate (EMS). *Journal of Applied Agricultural Sciences*. **2023**, *7*(1), 1-15. DOI: 10.25047/agriprima.v7i1.512.
[3] Talebi, A.B.; Talebi, A.B.; Shahrokhifar, B. Ethyl methane sulphonate (EMS) induced mutagenesis in Malaysian rice (cv.MR219) for lethal dose determination. *American Journal of Plant Sciences*. **2012**, *3*. 1661-1665. http://dx.doi.org/10.4236/ajps.2012.312202.
[4] Li, C.; Dong, N.; Zhao, Y.; Wu, S.; Liu, Z.; Zhai, J. A review for the breeding of orchids: Current achievements and prospects. *Horticultural Plant Journal*. **2021**, *7*(5), 380-392. https://doi.org/10.1016/j.hpj.2021.02.006
[5] Romiyadi, R.; Komariah, A.; Amien, S. Keragaan tiga jenis planletanggrek Phalaenopsis asal Protocorm yang diinduksi Ethyl Methyl Sulfonate (EMS) secara *in vitro*. *Kultivasi*. **2018**, *17*(1), 596–607. https://doi.org/10.24198/kultivasi.v17i1.16077
[6] Qosim, W. A.; Istifadah, N.; Djatnika, I.; Y. Pengaruh. Mutagen Etil Metan Sulfonat terhadap Kapasitas Regenerasi Tunas Hibrida Phalaenopsis, *in vitro*. *Jurnal Hortikultura*. **2016**, *22*(4), 360-365. https://doi.org/10.21082/jhort.v22n4.2012.
[7] Avivi, S.; Hariyono, K.; Hartatik, S.; Pertanian, F.; Jember, U. Analisis Pendugaan Parameter Genetik pada Genotipe Tebu Mutan. Agriprima: *Journal of Applied Agricultural Sciences*, **2022**, *26(*2), 124-134. https://agriprima.polije.ac.id/index.php/journal/article/view/v6i2-c
[8] Arisha, M, H.; Shah, S.N.M.; Gong, Z. Ethyl methane sulfonate induced mutations in M2 gene ratio and physiological variations in M1 generation of peppers (*Capsicum annum* L.). *Fronteirs in Plant Science*, **2025**, 6(399), 1-7. doi:10.3389/fpls.2015.00399.
[9] Tadmor, Y.; Katzir, N.; Meir, A. Induced mutagenesis to augment the natural genetic variability of melon (Cucumismelo L.). *Israel Journal of Plant Sciences*, **2007**, *55*(2), 159-169. doi: 10.1560/IJPS.55.2.159
[10] Temnykh, S.; Park, W.D.; Ayers, N. Mapping and genome organization of microsatellite sequence in rice (*Oryza sativa* L.). *Theoretical and Applied Genetics*, **2000,** *100*(5), 697-712. doi: 0.1007/s001220051342.
[11] Prasanna, B.M; Pixley, K.; Warburton, M.L.; Xie, C.X. Molecular marker-assisted breeding options for maize improvement in Asia. *Molecular Breeding*, **2010**, *26*(2), 339–356. doi:10.1007/2Fs11032-009-9387-3.
[12] Ciampi, A.Y.; Azevedo, V.C.R.; Gaiotto, F.A. Isolation and characterization of microsatellite loci for Hymenaea courbaril and transferability to *Hymenaea stigonocarpa*, two tropical timber species. *Molecular Ecology Resources*, **2008**, *8*(5), 1074-1077. doi: 10.1111/j.1755-0998.2008.02159.x
[13] Lorieux, M.; Ndjiondjop, M.N.; Ghesquiere, A. A first interespecific *Oryza sativa* x *Oryza glaberrima* microsatellite based genetic linkage map. *Theoretical and Applied Genetics*, **2000**, *100*(3–4), 593-601. doi: 10.1007/2Fs001229900061.
[14] Ramasoot, S.; Weerapong, M.; Keawsaard, Y.; Ritchuay, S.; Rotduang, P. Enhance efficiency propagation and conservation of toothbrush orchid *in vitro*. *Songklanakarin Journal of Plant Science*, **2022**, *9*(1), 15-23.

[15] Doyle, J.J.; Doyle, J.L. *Isolation of plant DNA from fresh tissue*. Focus. **1990**, pp.12- 15.
[16] Thawaro, S.; Te-chato, S. Application of molecular markers in the hybrid verification and assessment of somaclonal variation from oil palm propagated *in vitro*. *Science Asia*, **2009**, *35*, 142-149. http://dx.doi.org/10.2306/scienceasia1513-1874.2009.35.142
[17] Sirinya, M.; Te-chato, S. Use of ems to induce mutation in *Dendrobium friedericksianum* Rchb.f., *Journal of Agriculture*, **2008**, *24*(2), 153-164.
[18] Samala, S.; Te-chato, S.; Yenchon, S. Effect of ethyl methanesulphonate (EMS) on *Dendrobium Sonia*. *Khon kaen agr. Journal*, **2014**, *42*(3), 506-511.
[19] Arisha, M. H.; Liang, B.K.; Muhammad, S. S. N.; Gong, Z.H.; Li, D.W. Kill curve analysis and response of first-generation *Capsicum annuum* L. B12 cultivar to ethyl methane sulfonate. *Genetics and Molecular Research*, **2014**, *13*(4), 10049-10061. https://doi.org/10.4238/2014.November.28.9
[20] Romeida, A.; Stujahjo, S. H.; Purwito, A.; Sukma, D.; Rurstikawati, S. Induksi Mutasi Protocorm Like Bodies (PLBs) Anggrek Spathoglottis plicataBlume. Aksesi Bengkulu pada Sebelas Taraf Dosis Iradiasi Sinar Gamma. *Prosiding Simposium Dan Seminar Bersama PERAGI-PERHORTI-PERIPIHIGI Mendukung Kedaulatan Pangan Dan Energi Yang Berkelanjutan*, **2012**, 381-387. https://repository.ipb.ac.id/handle/123456789/59898
[21] Sharmin, A.; Hoque, M.E.; Haque, M.M.; Khatun, F. Molecular diversity analysis of some chilli (*Capsicum* spp.) genotypes using SSR markers. *American Journal of Plant Science*, **2018**, *9*(3), 368-379. doi: 10.4236/ajps.2018.93029.
[22] Botstein, D.; White, R.L.; Skolnik, M.; Davis, R.W. Construc-tion of a genetic linkage map in man using restriction fragment lenght polymorphisms. *American Journal of Human Genetics*, **1980**, *32*(3), 314–331.
[23] Greene, E.A.; Codomo, C.A.; Taylor, N.E. Spectrum of chemically induced mutations from a large scale reverse genetic screen in Arabidopsis. *Genetics*, **2003**, *164*(2), 731-740.
[24] Powell, W.; Morgante, M.; Andre, C. The comparison of RFLP, RAPD, AFLP and SSR (microsatellite) markers for germplasm analysis. *Molecular Breeding*, **1996**, *2*(3), 225–238. doi: 10.1007/BF00564200.
[25] Zhang, G.; Wang, Y.; Guo, Y. Characterization and mapping of QTLs on chromosome 2D for grain size and yield traits using a mutant line induced by EMS in wheat. *The Crop Journa*l, **2015**, *3*(2), 135-144. doi: 10.1016/j.cj.2014.11.002
[26] Tautz, D.; Renz, M. Simple sequences are ubiquitous repetitive components of eukaryotic genomes. *Nucleic Acids Research*, **1987**, *12*(10), 4127-4138. doi: 10.1093/nar/12.10.4127.
[27] Kim, Y.S.; Schumaker, K.S.; Zhu, J.K. EMS Mutagenesis of Arabidopsis. In: Salinas J, Sanchez-Serrano JJ (eds) Arabidop-sis Protocols. *Methods in Molecular Biology; New Jersey, Hu-mana Press*. **2006**. pp 101-103. doi: 10.1385/1-59745-003-0:101.
[28] Boonsrangsom, T.; Pongtongkam, P.; Masuthon, S.; Peyachoknagu, S. Development of microsatellite markers for Dendrobium orchids. Thai Journal of Genetics, **2008**, *1*(1), 47-56.

ASEAN
Journal of Scientific and Technological Reports
Online ISSN:2773-8752

Research article

Effects of Different Manures on the Growth Performance of Pechay (*Brassica rapa* L.) Under Visayas State University Condition

Roger Y. Ibañez, Jr.[1*], Goram C. Balansag[2], and Nova Grace D. Puod[3]

[1] Faculty of Cawayan Campus, Dr. Emilio B. Espinosa Sr. Memorial State College of Agriculture and Technology, 5405, Philippines
[2] Faculty of Mara, Central Mindanao University, 8714, Philippines
[3] Faculty of Hamtic Campus, University of Antique, 5715, Philippines
* Correspondence: ryibanez@debesmscat.edu.ph

Citation:
Ibañez Jr., R.; Balansag, G.; Puod, N.G. Effects of different soil potting media on the growth performance of pechay (*Brassica rapa* L.) under visayas state university condition. *ASEAN J. Sci. Tech. Report.* **2025**, *28*(1), e255634. https://doi.org/10.55164/ajstr.v28i1.255634.

Article history:
Received: August 24, 2024
Revised: November 1, 2024
Accepted: November 20, 2024
Available online: December 14, 2024

Publisher's Note:
This article is published and distributed under the terms of Thaksin University.

Abstract: The sudden rise in the demand for food in global markets has led farmers to adopt sustainable agricultural practices to reduce the negative impacts of synthetic fertilizers on soil, water, and ecosystems. This study assessed the effectiveness of vermicast, cattle manure, and goat manure and their combinations on the growth performance, nutrient content, and heavy metal accumulation in peachy. The study used a Completely Randomized Design (CRD) with six treatments and three replicates each and collected the data on plant height, number of leaves, leaf area, chlorophyll content, root biomass, and fresh and dry weight. Proximate tissue analysis was done to determine the NPK content and accumulated heavy metals. Data were analyzed using ANOVA in CRD, and a post-hoc analysis using Tukey's HSD test was conducted after significance was found. The results indicated significant differences ($P<0.05$) in several growth parameters like plant height with cattle manure, number of leaves with vermicast, leaf area with vermicast, and chlorophyll content with mixed manures. Significant differences ($P<0.05$) were also found in fresh weight with vermicast and root biomass with mixed manures. These treatments improved soil nutrient profiles post-harvest, although there were reductions in available phosphorus and exchangeable potassium. The findings highlight the potential of organic fertilizers to enhance pechay growth performance, supporting sustainable agricultural practices that align with the Sustainable Development Goals (SDGs). Further research on organic fertilizer applications and their long-term effects on soil health and crop nutrition is recommended.

Keywords: Growth performance; organic fertilizers; potting media; sustainable agriculture; synthetic fertilizer

1. Introduction

The growing demand for food in world markets leads farmers to adopt various strategies in agriculture to enhance their production [1]. While chemical fertilizers have traditionally been seen as the most effective way to increase crop yields worldwide, their negative impact on soil, water, and ecosystems limits their long-term use in farming practices, and the types and levels of fertilizers utilized in crop production are crucial factors that significantly impact cropping systems [2]. Farmers employ alternative and

economical techniques to make food production more sustainable, including crop rotation, biological pest management, composts, and organic fertilizers, which help mitigate the adverse environmental effects [3]. Currently, there has been a noticeable shift towards reducing the reliance on synthetic fertilizers, particularly those applied to the soil, such as nitrogen (N), phosphorus (P), and potassium (K), resulting in a significant decrease in their usage. Additionally, health-conscious consumers' rising preference for organically grown agricultural products has increased interest in foliar fertilization and the adoption of organic fertilizers as viable alternatives to fulfill plant nutrient requirements throughout the growing season [4].

Pechay (*Brassica rapa* L.) is one of the most cultivated leafy vegetables across the globe due to its short time production (35 days after transplanting) and contributes substantially to vegetable production in Asia, Europe, and North America [5]. Pechay has consistently grown in the Philippines, becoming an essential component of the country's vegetable output at approximately 47,000 metric tons in 2022, based on the Philippine Statistics Authority data [6]. Although plants only require small amounts of nutrients, their growth can be improved by soluble mineral nutrients from soil amendments like manure. This has been supported by studies conducted by Waniyo et al. [7] and Han et al. [8] Additionally, using organic fertilizers has been found to enhance vegetable yield, per the study by Li et al. [9] As highlighted in the study, these amendments improve yield and nutritional quality and significantly affect the soil microbiome due to compost's beneficial impacts [10]. However, more scientific research needs to be discovered on the effects of locally available ameliorants on pechay production in Leyte. This is primarily because, based on the study of Gonzaga et al. [11] Pechay is traditionally cultivated in open fields using conventional farming methods that involve synthetic fertilizers and pesticides. Therefore, this study aimed to investigate the effects of four different animal manures on the growth performance of pechay under the conditions at Visayas State University. Specifically, it assessed the growth performance of Pechay treated with four different animal manures. It analyzed the levels of nitrogen (N), phosphorus (P), and potassium (K), as well as heavy metals like lead (Pb) and cadmium (Cd) in the Pechay tissues. This research has made significant contributions to sustainable agriculture that align with global and national initiatives toward a more responsible and ecologically sound future. The results of this study help achieve the Sustainable Development Goals [12], more importantly, Goal 2 (Zero Hunger), Goal 12 (Responsible Consumption and Production), and Goal 15 (Life on Land). By exploring the effect of soil potting media on the growth characteristics of Pechay, we are actively engaging in practices that promote food security, responsible resource consumption, and the preservation of land ecosystems. The study addresses the pressing need for sustainable agricultural practices to enhance crop nutrition, increase food production, improve soil health, and enhance microbial activity.

2. Methodology

2.1 Location

This study was conducted to determine and assess the effects of various animal manures on Pechay's growth characteristics. It was conducted at the Department of Agronomy laboratory of Visayas State University in Baybay City, Leyte, Philippines, located at coordinates 10°44'54.1 N 124°47'33.9 E. The study offers insights into growth performance and heavy metals associated with applying different organic fertilizers- vermicast, cattle manure, and goat manure- alongside inorganic fertilizers.

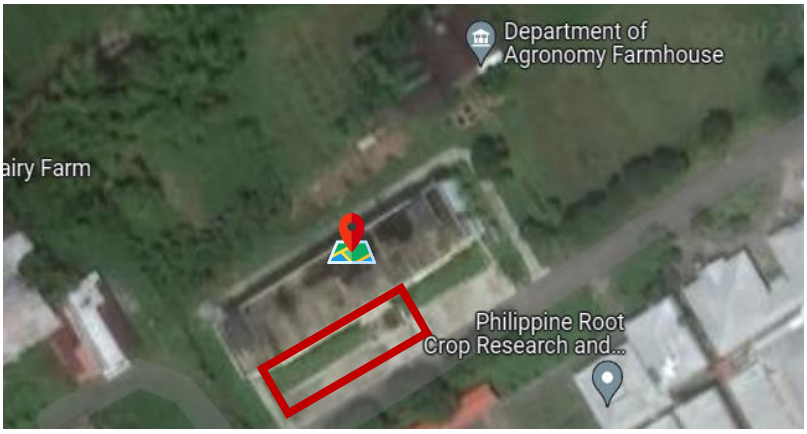


Figure 1. Location of the study within Visayas State University

2.2 Inputs, Treatment Preparations and Application

Farm supplies such as 5 inches by 5 inches polyethylene pots, pechay seeds, urea (46-0-0), and complete fertilizer (14-14-14) were acquired from Agrivet or other reputable agricultural input suppliers in Baybay City, Leyte. Pechay, which has an 85% germination rate and 99% purity, was used in the study. Vermicast was purchased from reliable vermi raisers within Baybay City, Leyte. Cattle and sheep manure was sourced from the Department of Animal Science of the Visayas State University. The nutrient content of each soil amendment, including nitrogen (N), which is determined by the Kjeldahl method; phosphorus (P), which is determined by the molybdenum antimony colorimetric method; and potassium (K), which is determined by flame photometry, was analyzed to determine the nutrient components of the soil. The gathered soil ameliorants were added and mixed with the soil collected from the field laboratory area of the Department of Agronomy, Visayas State University. A total of three (3) kilograms of soil and the computed amount of organic fertilizer (0.86 kg of vermicast, 0.71kg of cattle manure, 0.771 kg of sheep manure, and 0.78kg of mixed manures) were placed per 5 inches by 5 inches polyethylene pots. The application of synthetic fertilizers will be based on the soil analysis results, considering the fertilizer recommendation of 135kg N, 90kg P, and 90kg K per hectare [13]. The application rate was based on the recommended rate to meet the specific nutrient requirements of the soil, promoting a balanced and efficient use of synthetic fertilizers.

2.3 Planting of Pechay

Seeds were sown in a seedling tray and kept in a nursery for ten days. After the seedlings have two to three true leaves, they are transplanted into polyethylene pots containing the prepared soil media. Cultural management practices like weeding, controlling insect pests, and managing water were employed whenever necessary until harvest.

2.4 Research Design

The study was arranged in a one-way, Completely Randomized Design (CRD). The study had six treatments, namely the Control (A), Synthetic Fertilizer (B), Vermicast (C), Cattle Manure (D), Sheep Manure (E), and a Mix of Vermi, Cattle, and Sheep Manure (F) with a ratio of 1:1:1. Each treatment was randomly assigned with three replicates. This design ensures an equitable distribution of treatments across all experimental units, mitigating potential biases and allowing for a comprehensive and unbiased evaluation of the influence of different animal manures on the nutritional profile of Pechay.

2.5 Data Collection

Growth Performance. Plant height measurements and number of leaves were gathered weekly until harvest, 35 days after transplanting. The leaf area index was measured using a digital leaf area meter. The chlorophyll content of the leaves and leaf temperature were analyzed using SPAD 502 Plus Chlorophyll Meter. Root biomass, fresh weight, and leaf-to-root ratio were also computed after the study.

Nutritional Content Analysis: Pechay samples were harvested at maturity (35 days after transplanting), and their nutritional content, including nitrogen, nitrogen (N), which is determined by the Kjeldahl method,

phosphorus (P) is determined by the molybdenum antimony colorimetric method, and potassium (K) that is determined by flame photometry, and the heavy metal contents – lead and cadmium using the atomic absorption spectrometry was analyzed in Central Analytical Soil Laboratory of Visayas State University.

Soil Analysis Post-Crop Removal. After harvesting, composite pooled samples of soil, organic and complete fertilizers from bulk mixes of each treatment were then collected and brought to the Central Analytical Soil Laboratory of Visayas State University for chemical analyses for the nitrogen (N), phosphorus (P), and potassium (K).

2.6 Statistical Analysis

The data was analyzed using the analysis of variance (ANOVA) in CRD to evaluate significant differences among treatments. The data was processed using STAR software. A post hoc Test using Tukey's Honestly Significant Difference (Tukey's HSD) test was performed to determine significant differences among treatment means.

3. Results and Discussion

3.1 Organic amendment properties before the conduct of the study

Table 1 presents the nutrient content of the organic amendments used in the study before they were applied to the soil. The amendments analyzed include sheep manure, vermicast, cattle manure, and a mix of these materials. The nutrients measured were nitrogen (N), phosphorus (P), and potassium (K), expressed as a percentage of the total composition.

Table 1. Organic amendment properties before the conduct of the study
Source: Central Analytical Laboratory of Visayas State University

Organic Amendments	Measured Values		
	Total N (%)	Total P (%)	Total K (%)
Sheep Manure	1.514	368.36	113.65
Vermicast	1.723	366.59	117.36
Cattle Manure	1.695	335.43	118.38
Mix	1.630	367.54	115.28

3.2 Soil properties with organic amendments after harvesting

Table 2 shows the soil nutrient content after applying the different organic amendments. The same nutrients—nitrogen (N), phosphorus (P), and potassium (K)—were measured to assess how the amendments impacted the soil properties throughout the study.

Table 2. Soil properties with organic amendments after the conduct of the study
Source: Central Analytical Laboratory of Visayas State University

Treatments	Measured Values		
	Total N (%)	Total P (%)	Total K (%)
Soil with Sheep Manure	0.211	368.36	113.65
Soil with Vermicast	0.242	366.59	117.36
Soil with Cattle Manure	0.167	335.43	118.38
Soil with Mix	0.208	367.54	115.28

3.3 Average plant height

The average plant height showed a significant difference ($p=0.0101$) during the second to fourth week after transplanting, while no significant differences ($P>0.05$) were observed during the first week after

transplanting. As presented in Table 3, data showed that plant heights of Pechay were highest on pots fertilized with cattle manure and mixed manures at 17.80 cm and 17.5 cm, respectively. However, the plant height of both organic fertilizers was statistically comparable with vermicast, sheep manure, and synthetic fertilizer at 15.37 cm. 13.93 cm, and 13.5 cm, respectively.

Table 3. The weekly average plant height (cm) of Pechay is affected by the different potting mediums.

Treatment	Weeks				
	Initial	**1st**	**2nd**	**3rd**	**4th**
Control	9.17	9.80	11.23 b	12.23 a	12.73 b
Vermicast	8.87	8.97	12.77 b	14.03 a	15.47 ab
Cattle manure	9.97	9.80	16.10 a	16.80 a	17.80 a
Sheep manure	9.53	10.37	12.73 b	13.33 a	13.93 ab
Synthetic fertilizer	8.50	9.17	12.77 b	13.13 a	13.50 ab
Mix manures	7.80	8.83	16.30 a	16.90 a	17.50 a
Mean	8.64	9.49	13.65	14.41	15.16
CV (%)	10.64	11.70	14.17	12.39	10.83
p-value	0.2244	0.5335	0.0379	0.0298	0.0101

This means that columns with different letters are significantly different at a 5% significance level in Tukeys's Honest Significant Difference (HSD) Test.

In contrast, the lowest plant height was recorded on Pechay planted on soils without ameliorants at 12.73 cm. Furthermore, the height of peachy in vermicast, sheep manure, and synthetic fertilizer is also statistically comparable with that of the control treatment. A similar result was observed in Pechay, where plant height is highest on organic fertilizers such as vermicompost [14].

3.3 Average number of leaves

Table 4 presented the effect of treatments on the number of pechay leaves on weeks 1, 2, 3, and 4 after transplanting. Data showed that treatment means on the number of leaves at weeks 2, 3, and 4 are significantly different and are influenced by the different potting mediums at $\alpha 0.05$.

Table 4. The different potting mediums affect the weekly average number of Pechay leaves.

Treatment	Weeks				
	Initial	**1st**	**2nd**	**3rd**	**4th**
Control	2.00	3.00	4.00 b	5.33 bc	6.33 bc
Vermicast	2.00	3.67	4.33 b	8.67 a	10.33 a
Cattle manure	2.33	4.00	7.00 a	8.00 ab	9.33 ab
Sheep manure	2.00	3.00	4.67 ab	5.00 c	5.00 c
Synthetic fertilizer	2.00	2.67	4.00 b	5.33 bc	6.00 bc
Mix manures	2.33	4.00	7.00 a	8.00 ab	9.67 ab
Mean	2.11	3.39	5.17	6.72	7.78
CV (%)	15.79	19.67	17.07	16.07	18.43
p-value	0.5705	0.1190	0.0016	0.00026	0.0022

This means that the columns with the different letters are significantly different from each other at a 5% level of significance in Tukeys's Honest Significant Difference (HSD) Test.

The number of leaves was shown to increase significantly two weeks after transplanting, and this was observed in pots where cattle manure and mixed manure were applied; however, statistically, it is comparable with sheep manure. Three (3) weeks and the fourth week after transplanting, the most significant number of leaves was recorded in the Pechay on vermicast, statistically comparable with cattle manure and mixed manures. Throughout weeks 2, 3, and 4 after transplanting, the least number of leaves was observed on the control treatment where soil ameliorants were added with a mean value of 4, 5.33, and 6.33 leaves, respectively, but is statistically comparable with those Pechay applied with synthetic fertilizer and sheep manure.

The results are consistent with those of Kaur[15], who found that organic waste processed by naturally occurring earthworms produces vermicast. This vermicast supplies nutrients and other soil stimulants, enhancing soil quality and boosting vegetable and ornamental crops' growth, flowering, and yields.

3.4 Plant weight, root biomass, and leaf-to-shoot ratio

Dry biomass for both the shoot and the root significantly differed for pechay at α0.05 grown under different potting media. Table 5 shows that the vermicast had the highest fresh weight (29.50 grams) but is statistically comparable with mixed manure (27.50 grams) and cattle manure (27.17 grams). Though statistically different, sheep manure, synthetic fertilizer, and control had lower fresh weights of 16.67 grams, 16.08 grams, and 12.92 grams, respectively.

Table 5. Plant weight, Root biomass, and leaf-to-shoot ratio of Pechay as affected by different potting mediums.

Treatment	Whole Plant (g)	Shoot biomass (g)	Root Biomass (g)	Shoot to Root Ratio
Control	12.92 ^{b}	4.33	0.50 ^{b}	8.86 ^{a}
Vermicast	29.50 ^{a}	11.33	1.18 ^{ab}	8.70 ^{a}
Cattle manure	27.17 ^{a}	14.00	1.85 ^{ab}	7.46 ^{ab}
Sheep manure	16.67 ^{b}	3.67	0.81 ^{ab}	4.06 ^{c}
Synthetic fertilizer	16.08 ^{b}	4.33	1.26 ^{ab}	3.74 ^{c}
Mix manures	27.50 ^{a}	15.33	2.63 ^{a}	5.66 ^{bc}
Mean	2.11	8.83	5.17	6.72
CV (%)	15.79	47.28	17.07	16.07
p-value	0.0000	0.0000	0.0345	0.0001

This means columns with the same letters are not significantly different from each other at a 5% significance level in Tukeys's Honest Significant Difference (HSD) Test.

Differences in treatment means of root biomass showed significant differences as mixed manure has the highest root biomass with 2.63 grams/pot and is statistically comparable with organic and inorganic fertilizers. Cattle manure weighed 1.85 grams/pot, synthetic fertilizer weighed 1.26 grams/pot, and vermicast weighed 1.18 grams/pot. On the other hand, the control treatment has the significantly lowest root biomass, weighing 0.50 grams/pot.

In leaf to root ratio, differences in treatment means showed significant differences at α0.05. Control has the highest leaf-to-root ratio, with 8.86, statistically comparable to vermicast (8.70) and cattle manure (7.46). In contrast, the leaf-to-shoot ratio of cattle manure was comparable to that of mixed manures. [16] found that pechay applied with organic fertilizer had higher dry matter weights of its shoots and roots compared to no fertilizer and inorganic fertilizer. Similarly, [17] found that applying organic fertilizer to lettuce significantly increased the dry weight of leaves and roots compared to the control with 0% compost.

3.6 Leaf Area, Chlorophyll, and Leaf Temperature

Table 6 indicates that the leaf area (cm^2) of plants in vermicast has the highest leaf area of 90.12 cm^2, which is statistically comparable with mixed manure (80.34 cm^2) and cattle manure (78.02 cm^2). These treatments showed to be significantly different compared to treatments with sheep manure, synthetic fertilizer, and control. Mrabet et al. [17] observed similar results, noting that lettuce treated with vermicompost produced significantly broader leaves compared to the control group ($p < 0.05$). Since photosynthesis is a crucial physiological process responsible for most dry matter production in crop plants, the presence of different photosynthetic pigments, such as chlorophyll, can measure it. In the mean differences of the chlorophyll content, significant differences were observed among treatment means at α0.05. The highest chlorophyll content was recorded on Pechay on mixed manures with 55.79 SPAD, which is statistically comparable with vermicast, 47.63 SPAD, cattle manure, 44.18 SPAD, and sheep manure, 40.92 SPAD. It is, however, significantly different on Pechay planted on pots applied with synthetic fertilizer at 29.54 SPAD, control treatment with 33.15 SPAD, and also with that of the vermicast, cattle manure, and sheep manure.

The treatment means on temperature showed no significant difference based on statistical analysis at α0.05, where the temperature consistently ranges from 25.19 °C to 28.81°C.

Table 6. Average leaf area index, chlorophyll, and leaf temperature of Pechay as affected by different potting media

Treatment	Leaf Area (cm^2)	Chlorophyll (SPAD)	Temperature (°C)
Control	28.51 ^{b}	33.15 ^{b}	28.81
Vermicast	90.12 ^{a}	47.63 ^{ab}	27.78
Cattle manure	78.02 ^{a}	44.18 ^{ab}	25.19
Sheep manure	36.88 ^{b}	40.92 ^{ab}	28.79
Synthetic fertilizer	34.76 ^{b}	29.54 ^{b}	28.61
Mix manures	80.34 ^{a}	55.79 ^{a}	28.61
Mean	58.10	41.87	27.96
CV (%)	19.94	18.96	8.56
p-value	0.0000	0.0167	0.4362

This means columns with the same letters are not significantly different from each other at a 5% significance level in Tukey's Honest Significant Difference (HSD) Test.

3.7 Tissue Analysis of Pechay

The proximate analysis of Pechay tissues revealed significant variations in nutrient content and heavy metal accumulation across different potting media, as shown in Table 7. Based on statistical results, the gross energy content did not differ significantly among treatments (p=0.1272), with the mix manures treatment yielding the highest gross energy content (3312.33 cal/g) and vermicast the lowest (2863.33 cal/g). The lack of significant differences in gross energy content suggests that the choice of potting media is independent of the gross energy levels in Pechay. Regarding nitrogen content, although differences were observed (ranging from 2.38% in the control to 4.25% in the synthetic fertilizer treatment), these differences were not statistically significant (p=0.3971). The elevated nitrogen levels in the synthetic fertilizer treatment are expected, as synthetic fertilizers typically have higher nitrogen availability than organic amendments. However, the lack of significant differences across treatments could indicate that Pechay's nitrogen uptake efficiency is relatively stable across different potting media.

The phosphorus content, however, showed significant differences (p=0.0001) among treatments. The vermicast treatment exhibited the highest phosphorus content (0.2413%), significantly higher than the control and synthetic fertilizer treatments. This aligns with studies indicating that vermicast enhances phosphorus availability due to its high phosphatase enzyme activity, which increases phosphorus solubilization [18]. In

contrast, the synthetic fertilizer treatment had the lowest phosphorus content (0.2183%), possibly due to the fixation of phosphorus in less available forms. Potassium content also varied significantly across treatments ($p = 0.0161$). The cattle manure treatment resulted in the highest potassium content (3.06%), significantly higher than the synthetic fertilizer treatment, with the lowest potassium content (2.38%). Organic amendments like cattle manure enhance potassium availability through the slow release of nutrients, as Khaitov et al. [19] mentioned, which might explain the observed differences.

Table 7. Proximate analysis of Pechay tissues as affected by different potting media.

Treatment	Gross Energy (cal/g)	Total N (%)	Total P (%)	Total K (%)	Heavy Metals	
					Total Cd (ppm)	Total Pb (ppm)
Control	3297.67	2.38	0.2313^{b}	2.46^{ab}	<0.001	4.98^{b}
Vermicast	2863.33	2.86	0.2413^{a}	3.00^{ab}	<0.001	11.58^{a}
Cattle manure	2972.33	3.35	0.2307^{b}	3.06^{a}	<0.001	10.72^{a}
Sheep manure	3028.00	3.21	0.2357^{ab}	2.68^{ab}	<0.001	7.77^{ab}
Synthetic fertilizer	2974.33	4.25	0.2183^{c}	2.38^{c}	<0.001	5.05^{b}
Mix manures	3312.33	3.20	0.2350^{ab}	2.72^{ab}	<0.001	8.82 ^{ab}
Mean	**3074.67**	**3.21**	**0.2321**	**2.71**	**<0.001**	**8.15**
CV (%)	**7.14**	**31.63**	**1.50**	**8.34**		**24.02**
p-value	**0.1272**	**0.3971**	**0.0001**	**0.0161**		**0.0051**

This means columns with the same letters are not significantly different from each other at 5% significance level in Tukey's Honest Significant Difference (HSD) Test.

Heavy metal analysis revealed that cadmium (Cd) levels were below detection limits (<0.001 ppm) across all treatments, suggesting that none of the potting media contributed significantly to cadmium contamination. However, lead (Pb) content varied significantly ($p=0.0051$). It was higher than the set brassicas maximum limit (0.03 ppm) by the Codex Alimentarius [20], with the vermicast and cattle manure treatments showing the highest lead concentrations (11.58 ppm and 10.72 ppm, respectively), which were significantly higher than the control. These findings align with concerns raised in studies that organic amendments, particularly those of animal origin, can sometimes introduce heavy metals into the soil, as Rashid [21] noted, potentially leading to higher uptake by plants. However, the increased lead content of these vegetables can be reduced or removed by thoroughly washing the vegetables before removing the outer leaves before consumption or cooking.

3.8 Nutritional composition of soil before planting and soil nutritional properties of bulk mixes of each treatment after harvesting

Suleiman et al. [22] state that soil's physical and chemical properties determine the availability of nutrients to plants. For optimal crop production, it is essential to regularly monitor these properties to ensure long-term development and increased yields. Table 5 presents the soil properties before and after the study. Based on the results of the soil analysis, the total nitrogen after the study was increased to 0.101 % compared to 0.092 % before the study was conducted; however, in available phosphorus and exchangeable potassium, the results of the analysis were reduced to 85.83 mg/kg and 109.65 mg/kg compared to 250.10 mg/kg and 173.55 mg/kg respectively.

The analysis indicates that an increase in total nitrogen content could improve plant nutrient availability; a decrease in available phosphorus and exchangeable potassium could also affect plant growth and development and decrease soil fertility.

Table 8. Nutritional composition of soil before planting and soil nutritional properties of bulk mixes of each treatment after harvesting.

Properties	Measured values before the study	Measured values after the study
Total N (%)	0.092	0.101
Available P (mg/kg)	250.10	85.83
Exchangeable K (mg/kg)	173.55	109.65

Source: Central Analytical Soil Laboratory of Visayas State University

4. Conclusions

Based on the results, using vermicast, cattle manure, and mixed manures significantly improved the growth and yield performance of Pechay. This was evident in plant height, number of leaves, leaf area index, fresh weight, root biomass, shoot-to-root ratio, and chlorophyll content. Additionally, the study demonstrated that organic fertilizers greatly enhanced Pechay's growth and yield. Therefore, it is recommended to apply organic fertilizers, particularly vermicast, cattle manure, and mixed manure, as they positively influence growth and yield, especially regarding the number of leaves, leaf area, and fresh weight. Based on the results and conclusion of the study, the application of organic fertilizers such as vermicast, cattle manure, and mixed manure (vermicast, cattle, and Sheep) is recommended for Pechay cultivation due to their positive influence on growth and yield, particularly in terms of the number of leaves, leaf area, and fresh weight. However, thorough cleaning or removal of the outer leaves of the plants is recommended to decrease the lead content of the plants. For further improvement in this study, it is recommended that research be conducted on the use of other organic fertilizer sources and different amendment concentrations to achieve optimal harvest and post-harvest data. Additionally, further studies on Pechay production utilizing different methods of fertilizer applications, both organic and inorganic, should be pursued. Testing plant tissue for levels of antioxidants and other essential nutrients to assess and compare the nutritional value of plants treated with organic and inorganic fertilizers is also advised.

5. Acknowledgements

The authors sincerely thank Professor Dr. Berta C. Ratilla for her invaluable guidance and support throughout the study. Also, thanks are extended to the Central Analytical Soil Laboratory at Visayas State University for generously providing a discount for analyzing soils, manures, and tissues.

Author Contributions: R.Y.I.J: Conceptualization, methodology, validation, and editing; G.C.B: Literature review, data collection, and recording; N.G.D.P: Discussion and interpretation of results. All authors have read and agreed to the published version of the manuscript

Funding: This research received no external funding.

Conflicts of Interest: The authors declare no conflict of interest.

References

[1] Staugaitis, G.; Viškelis, P.; Rimantas Venskutonis, P. Optimization of application of nitrogen fertilizers to increase the yield and improve the quality of Chinese cabbage heads. *Acta Agriculturae Scandinavica. Section B, Soil and Plant Science* **2008**, *58*(2), 176-181. https://doi.org/10.1080/09064710701467118

[2] Adekiya, A.O.; Agbede, T.M. Effect of methods and time of poultry manure application on soil and leaf nutrient concentrations, growth and fruit yield of tomato (Lycopersicon esculentum Mill). *Journal of the Saudi Society of Agricultural Sciences* **2017**, *16*(4), 383-388. https://doi.org/10.1016/j.jssas.2016.01.006

[3] Siavoshi, M.; Nasiri, A.; Laware, S. Effect of organic fertilizer on growth and yield components in rice (Oryza sativa L.). *Journal of Agricultural Science* **2010**, *3*, 217-221. https://doi.org/10.5539/jas.v3n3p217

[4] Lian, H.; Ouyang, L.; Liu, J.; Yang, L.; Zou, P. Effects of different proportions of inorganic fertilizer and organic fertilizer on yield and quality of amaranth. Proceedings of the 2017 6th International Conference on Energy, Environment and Sustainable Development. *Advances in Engineering Research* **2017**, *129*, 911-915. https://doi.org/10.2991/iceesd-17.2017.166

[5] Shahbandeh, M. Vegetables production worldwide 2021, by type. Statista. **2023**. https://www.statista.com/statistics/264065/global-production-of-vegetables-by-type/

[6] Philippine Statistics Authority. Selected Statistics on Agriculture and Fisheries (SSAF). Gov.Ph. **2022**. Retrieved January 26, 2024, from https://psa.gov.ph/system/files/main-publication/%2528ons-cleared%2529_SSAF%25202022%2520as%2520of%252030082022_ONS-signed.pdf

[7] Waniyo, U.U.; Sauwa, M.M.; Ngala, A.L.; Abubakar, G.A.; Anelo, E.C. Influence of sources and rates of manure on yield and nutrient uptake of maize (Zea mays L.) in Maiduguri, Nigeria. *Nigerian Journal of Basic and Applied Science* **2013**, *21*(4), 259-265. http://dx.doi.org/10.4314/njbas.v21i4.3

[8] Han, S. H.; An, J.Y.; Hwang, J.; Kim, S.B.; Park, B.B. The effects of organic manure and chemical fertilizer on the growth and nutrient concentrations of yellow poplar (Liriodendron tulipifera L.) in a nursery system. *Forest Science and Technology* **2016**, *12*(3), 137-143. https://doi.org/10.1080/21580103.2015.1135827

[9] Li, S.;Li, J.; Zhang, B.; Li, D.; Li, G.; Li, Y. Effect of different organic fertilizers application on growth and environmental risk of nitrate under a vegetable field. *Scientific Reports* **2017**, *7*, 17020. https://doi.org/10.1038/s41598-017-17219-y

[10] Pant, A. P.; Radovich, T. J. K.; Hue, N. V.; Talcott, S. T.; Krenek, K. A. Vermicompost extracts influence growth, mineral nutrients, phytonutrients and antioxidant activity in pak choi (Brassica rapa cv. Bonsai, Chinensis group) grown under vermicompost and chemical fertiliser. Journal of the Science of Food and Agriculture **2009**, *89*(14), 2383–2392. https://doi.org/10.1002/jsfa.3732

[11] Gonzaga, Z.; Capuno, O.; Labonite, M.; Lonzaga, E.; Napuran, N.; Sarco, A.; Gorme, A.; Rom, J.; Dimabuyu, H.; Jomoc, D.; Estillore, J.; Sentorias, A.; Goldwater,A.; Rogers, G.; McDougall, S. Increasing pechay (Brassica rapa L. ssp. chinensis) production through suitable seedling establishment under two cultivation systems in the Southern Philippines. *Annals of Tropical Research* **2017**, *39* (Supplement B),129-136. https://doi.org/10.32945/atr39sb10.2017

[12] United Nations The 17 goals. Sdgs.un.org. **2015**. Retrieved January 26, 2024, from https://sdgs.un.org/goals

[13] Jimenez, E. F.; Mariano, J. S.; Ferrer, M. J.; De Leon, V. *Pechay Production Guide*. Gov.Ph. (n.d.). Retrieved January 26, 2024, from https://library.buplant.da.gov.ph/images/1641885337Pechay%20Production%20Guide.pdf

[14] Lagon, J.R.; Abad, R.; Bayogan, E.M.; Silvosa-Millado, C.S. Growth and Yield of Screenhouse-grown potted Pechay (Brassica rapa L. ssp. chinensis cv. Black Behi) in selected Davao-produced Composts. *Mindanao Journal of Science and Technology* **2022**, *20*(2), 206-227

[15] Kaur, P.; Bhardwaj, M.; Babbar, I. Effect of vermicompost and vermiwash on growth of vegetables. *Research Journal of Animal, Veterinary and Fishery Sciences* **2015**, *3*(4), 9-12.

[16] Pascual P. R. L.; Jarwar A. D.; Nitural P. S. Fertilizer, fermented activators, and EM utilization in pechay (Brassica pekinensis L.) production. *Pakistan Journal of Agriculture, Agricultural Engineering and Veterinary Sciences* **2013**, *29*(1), 56-69.

[17] Mrabet L.; Belghyti D.; Loukili A.; Attarassi B. Effect of household waste compost on the productivity of maize and lettuce. *Agricultural Science Research Journals* **2012**, *2*(8), 462-469.

[18] Oyege, I.; Balaji Bhaskar, M. S. Effects of vermicompost on soil and plant health and promoting sustainable agriculture. *Soil Systems* **2023**, *7*(4), 101. https://doi.org/10.3390/soilsystems7040101

[19] Khaitov, B.; Yun, H. J.; Lee, Y.; Ruziev, F.; Le, T. H.; Umurzokov, M.; Bo Bo, A.; Cho, K. M.; Park, K. W. Impact of organic manure on growth, nutrient content and yield of Chilli pepper under various temperature environments. *International Journal of Environmental Research and Public Health* **2019**, *16*(17), 3031. https://doi.org/10.3390/ijerph16173031

[20] Codex Alimentarius. Codex General Standard for Contaminants and Toxins in Food and Feed. Fao.org, **2009**. https://rb.gy/m9v04w.

[21] Rashid, A.; Schutte, B. J.; Ulery, A.; Deyholos, M. K.; Sanogo, S.; Lehnhoff, E. A.; Beck, L. Heavy metal contamination in agricultural soil: Environmental pollutants affecting crop health. *Agronomy (Basel, Switzerland)* **2023**, *13*(6), 1521. https://doi.org/10.3390/agronomy13061521

[22] Suleiman, R.; Ibrahim, J. Assessment of Soil Physical and Chemical Properties Under Vegetable Cultivation in Abuja Metropolitan Area, Nigeria. *Zaria Geographer* **2017**, *24*(1), 89-99

ASEAN
Journal of Scientific and Technological Reports
Online ISSN:2773-8752

Research article

Methane Oxidation Rates and Efficiencies Across Four Distinct Soil Environments: Implications for Greenhouse Gas Mitigation

Chonticha Leamdum[1, 4], Nantharat Phruksaphithak[2, 4], Sukonlarat Chanthong[3, 4], and Chaisit Niyasom[5*]

[1] International College, Thaksin University, Songkhla 90000, Thailand
[2] Department of Chemistry, Faculty of Science and Digital Innovation, Thaksin University, Phatthalung 93210, Thailand
[3] Bio4gas (Thailand) Company Limited, Phatthalung 93210, Thailand
[4] Center of Excellence for Agricultural Innovation and Bioproducts of Thaksin University, Phatthalung 93210, Thailand
[5] Department of Biology, Faculty of Science and Digital Innovation, Thaksin University, Phatthalung 93210, Thailand
* Correspondence: nchaisit@gmail.com; (C. Niyasom)

Citation:
Leamdum, C., Phruksaphithak, N., Chanthong, S., Niyasom, C. Methane Oxidation Rates and Efficiencies Across Four Distinct Soil Environments: Implications for Greenhouse Gas Mitigation. *ASEAN J. Sci. Tech. Report.* **2025**, *28*(1), e255939. https://doi.org/10.55164/ajstr.v28i1.255939.

Article history:
Received: September 17, 2024
Revised: October 28, 2024
Accepted: October 30, 2024
Available online: December 14, 2024

Publisher's Note:
This article has been published and distributed under the terms of Thaksin University.

Abstract: Methane oxidation by soil microorganisms is crucial in mitigating greenhouse gas emissions. This study investigated methane oxidation potential across four distinct soil environments through standardized laboratory enrichment cultures. Soil samples were collected from landfill-cover soils, rice fields, cattle farms, and pond sediments, with environmental parameters monitored to understand their influence on oxidation rates and efficiencies. Using gas chromatography analysis, we quantified methane oxidation under controlled conditions. Statistical analysis revealed significant differences in oxidation rates across soil types. Landfill cover soils exhibited the highest oxidation rate of 0.39 μmol-CH_4/g-soil dry weight/h and efficiency of 66.5 %. Pond sediments, cattle farm soils, and rice field soils followed with rates of 0.29, 0.28, and 0.27 μmol-CH_4/g-soil dry weight/h, respectively. Oxidation efficiencies for these environments ranged from 46.1% to 48.4%. pH and organic matter content showed strong positive correlations with oxidation rates across all soil types, while environmental moisture content effects varied. The superior performance of landfill soils was attributed to optimal environmental conditions and stable substrate availability. This analysis revealed significant potential for enhancing oxidation efficiencies: landfill soils from 66.5% to 75-85%, rice fields from 46.1% to 60-70%, cattle farms from 47.0% to 55-65%, and pond sediments from 48.4% to 60-75%. Implementing optimized management strategies could reduce methane emissions by 70-90% in landfills, 30-50% in agricultural systems, and 40-60% in aquatic environments compared to current practices. This study highlights the substantial potential for enhancing biological methane oxidation across diverse ecosystems and emphasizes the need for targeted management approaches to optimize methane mitigation strategies.

Keywords: Methane Oxidation; Enrichment Cultures; Diverse Soil Environments; Environmental Factors; Oxidation Efficiency; Methane Mitigation

1. Introduction

Methane (CH_4) is a potent greenhouse gas with a global warming potential 28-34 times that of carbon dioxide over 100 years [1]. Atmospheric methane concentrations have doubled since pre-industrial times, reaching 1,889

parts per billion (ppb) in 2021 [2]. This dramatic increase has significantly contributed to global climate change, with methane accounting for approximately 20% of the total radiative forcing from all greenhouse gases [3]. Understanding and enhancing natural methane oxidation processes in various environments has become crucial for developing effective climate change mitigation strategies. Soil microorganisms play a crucial role in the global methane cycle, with methanotrophic bacteria capable of oxidizing methane to carbon dioxide, effectively reducing its greenhouse potency. Depending on environmental conditions, these microorganisms can oxidize 30-90% of the methane produced in the soil before reaching the atmosphere [4-5]. Methanotrophs are diverse, with Type I (Gammaproteobacteria) and Type II (Alphaproteobacteria) being the most well-studied groups, each adapted to different methane concentrations and environmental niches [6-9].

Different soil environments exhibit varying capacities for methane oxidation due to differences in physical, chemical, and biological properties. Landfill soils can oxidize up to 60% of methane emissions in well-managed cover systems [10]. Rice paddy soils may oxidize 10-90% of produced methane, depending on water management and soil properties [11]. Upland soils, including those in cattle farms, can serve as methane sinks, with oxidation rates ranging from 0.1 to 9.1 kg-CH_4/ha/year [12-13]. Pond sediments can oxidize 30-99% of the methane produced in anaerobic layers, acting as essential regulators of methane emissions from aquatic systems [14-15]. Despite the recognized importance of methane oxidation in these environments, comprehensive comparative studies across different soil types under standardized conditions are limited. Understanding the variations in oxidation potential and the factors influencing these differences is crucial for developing targeted methane mitigation strategies. Environmental factors such as pH, organic matter content, moisture, and oxygen availability can significantly affect methanotrophic activity, but their relative importance may vary across different ecosystems [4, 7, 16].

The present study aims to quantify and compare methane oxidation rates in enrichment cultures from four distinct soil types (landfill cover, rice field, cattle farm, and pond sediment). Analyze the variability of methane oxidation potential within each soil type. Identify key factors that influence methane oxidation efficiency across different soil environments. Evaluate the implications of our findings for developing targeted methane mitigation strategies. Through standardized laboratory enrichment cultures and detailed analysis of environmental parameters, this research provides insights into the potential for enhancing methane oxidation across diverse ecosystems. These findings contribute to understanding how different environmental factors influence methanotrophic activity and offer practical implications for optimizing methane mitigation strategies in various soil environments.

2. Materials and Methods

2.1 Soil sample collection

Soil samples were collected from four distinct environments (landfill, rice field, cattle farm, and pond sediment). All samples were collected in July 2022 using sterile techniques to minimize contamination. At each site, multiple subsamples were taken and homogenized to ensure representativeness. Landfill soil samples (n=5) were collected from the Waste and Waste Disposal Center (Sanitary Landfill), Phatthalung Municipality (7.58'N, 100.14W), Phatthalung province, Thailand. Samples were taken from the top 20 cm of the landfill cover soil at five locations, each separated by at least 50 meters. The soil was primarily clay loam with an average pH of 7.2 and organic matter content of 3.5%. Rice soil samples (n=25) were obtained from a paddy field in the Pa Phayom district (7.84'N, 99.91'W), Phatthalung province, Thailand. The field has been under continuous rice cultivation for the past 10 years. Samples were collected from the rhizosphere (0-15 cm depth) at 25 randomly selected points across a 1-hectare area. The soil was classified as silty clay with an average pH of 6.8 and organic matter content of 2.8%. Cattle farm soil samples (n=4) were collected from a beef cattle farm in Thaksin University (7.81'N, 99.94'W), Phatthalung province, Thailand. The farm had been in operation for over 30 years with a stocking density of approximately 2 cattle per hectare. Four composite samples were taken from different pasture areas, each with 10 cores (0-10 cm depth) collected in a W-shaped pattern across a 0.5-hectare plot. The soil was characterized as sandy loam with an average pH of 6.5 and organic matter content of 4.2%. Pond sediment samples (n=2) were collected from the sediment of a freshwater pond in Thaksin University (7.81'N, 99.94'W), Phatthalung province, Thailand. The pond had an area of approximately 2 hectares and a maximum depth of 5 meters. Sediment cores were taken from two locations near the shore at a water depth of 1 meter using a gravity corer. The top 10 cm of each core was used for analysis. The sediment

was rich in organic matter (12.5%) with a pH of 6.9. All soil samples were immediately placed in sterile, airtight containers and transported to the laboratory on ice. Upon arrival, a portion of each sample was air-dried and sieved (2 mm mesh) for physicochemical analysis. At the same time, the remainder was stored at 4°C for no more than 48 hours before being used to establish enrichment cultures. The sampling strategy was designed based on preliminary site assessment and power analysis ($\alpha = 0.05$, $\beta = 0.20$), ensuring adequate representation of each environment while accounting for site-specific characteristics and practical constraints.

2.2 Enrichment culture setup

Enrichment cultures were established to promote the growth of methanotrophic bacteria from each soil sample. The setup was designed to provide optimal conditions for methane oxidation while allowing for comparative analysis across soil types. For each soil sample, 10 g (wet weight) was added to a 500 mL Erlenmeyer flask containing 100 mL of nitrate mineral salts (NMS) medium [16]. The NMS medium composition was as follows (in g/L): $MgSO_4 \cdot 7H_2O$, 1.0; KNO_3, 1.0; $Na_2HPO_4 \cdot 12H_2O$, 0.717; KH_2PO_4, 0.272; $CaCl_2 \cdot 2H_2O$, 0.02; and 0.5 mL trace element solution [17]. The flasks were sealed with rubber stoppers fitted with gas-tight sampling ports. The headspace of each flask (400 mL) was flushed with a mixture of methane and air to achieve an initial concentration of 20% (v/v) methane. This concentration was chosen to support low- and high-affinity methanotrophs [9]. The landfill soil had 10 replicates (2 per sample). Rice field soil had 25 replicates (1 per sample). Cattle farm soil had 8 replicates (2 per sample). Pond sediment had 4 replicates (2 per sample). Control flasks containing sterilized soil samples (autoclaved at 121°C for 30 minutes) were prepared in duplicate for each soil type to account for abiotic methane loss. All flasks were incubated at 28°C on a rotary shaker at 150 rpm to ensure adequate gas-liquid mass transfer. The incubation lasted 7 days, during which headspace gas samples were taken at 24-hour intervals for methane concentration analysis. To maintain methane concentrations and prevent oxygen limitation, the headspace of each flask was flushed with the 20% methane-air mixture every 48 hours after gas sampling. The pH of the enrichment cultures was monitored at the beginning and end of the incubation period using a calibrated pH meter (Mettler Toledo, FiveEasy Plus).

2.3 Analytical methods

Methane concentrations in the headspace of enrichment cultures were analyzed using gas chromatography (GC) to quantify methane oxidation rates. A Shimadzu GC-2014 gas chromatograph with a thermal conductivity detector (TCD) was used for methane analysis. The GC was fitted with a 2.0 m packed column (Shin carbon ST 100/120 Restek) to efficiently separate methane from other gases. Injector temperature: 50°C, Detector temperature: 120°C, Oven temperature: Isothermal at 100°C, Carrier gas: High-purity argon gas at a flow rate of 15 mL/min. Headspace gas samples (500 μL) were taken from each flask using a gas-tight syringe (Hamilton) at 24-hour intervals. Samples were immediately injected into the GC to minimize potential losses. A five-point calibration curve was prepared using certified methane standards (1%, 5%, 10%, 15%, and 20% v/v methane in nitrogen). The calibration was performed at the beginning of each analysis day, and every 20 samples were checked to ensure consistent instrument performance. A methane standard (10% v/v) was analyzed every 10 samples as a continuing calibration verification. Duplicate injections were performed for 10% of the samples to assess analytical precision. Method blanks (ambient air samples) were analyzed at the beginning and end of each analytical run to check for potential contamination. Peak areas were integrated using Shimadzu GC solution software. Methane concentrations were calculated based on the calibration curve, accounting for dilution factors. Environmental parameters (pH, temperature, organic matter, and moisture) were measured using standardized protocols with rigorous quality control measures to ensure data reliability and reproducibility.

2.4 Calculation

Methane oxidation rates were calculated using the data obtained from gas chromatography analysis. The calculations accounted for changes in headspace methane concentration over time, considering the amount of soil and the volume of the enrichment culture system. The methane oxidation rate for each enrichment culture was calculated using the following equation (1).

$$R = (C_0 - C_t) \times V / (m \times t) \quad (1)$$

Where R is methane oxidation rate (μmol-CH_4/g-soil dry weight/h), C_0 is initial methane concentration (μmol-mL), C_t is methane concentration at time t (μmol-mL), V is headspace volume (mL), m is dry weight of soil sample (g), and t is incubation time (h). Methane concentrations from GC analysis (% v/v) were converted to μmol-mL using the ideal gas law, accounting for temperature and pressure. Soil dry weight was determined by oven-drying subsamples at 105°C for 24 hours. Rates were calculated for each 24-hour interval over the 7-day incubation period. The average rate over the entire incubation period was also determined for each sample. The methane oxidation efficiency was calculated as a percentage of initial methane consumed using the following equation (2).

$$\text{Efficiency (\%)} = [(C_0 - C_f) / C_0] \times 100 \quad (2)$$

C_0 is initial methane concentration (μmol-mL), and C_f is the final after 7 days (μmol/mL). Mean oxidation rates and efficiencies were calculated for each soil type. Standard deviation and coefficient of variation were determined to assess variability within each soil type. One-way ANOVA followed by Tukey's HSD test was performed to compare oxidation rates among soil types, with significance set at $p < 0.05$. Rates were corrected for any methane loss observed in sterilized control samples. Any samples showing unusual patterns (e.g., sudden increases in methane concentration) were flagged for further investigation and potential exclusion from analysis. Oxidation rates were also calculated per gram organic matter basis to account for differences in organic matter content among soil types. Michaelis-Menten kinetics were applied for samples exhibiting non-linear methane consumption to determine V_{max} and Km values using the following equation (3).

$$V = (V_{max} \times S) / (K_m + S) \quad (3)$$

V is the oxidation rate, V_{max} is the maximum oxidation rate, S is substrate (methane) concentration, and K_m is the Half-saturation constant.

2.5 Statistical analysis

Statistical analysis was designed to ensure robust interpretation of experimental data while accounting for variations in sample numbers across different soil types. Initial power analysis was performed to validate sample sizes, using parameters of $\alpha = 0.05$ (significance level), $\beta = 0.20$ (power = 0.80), and a minimum detectable difference of 0.05 μmol-CH_4/g-soil dry weight/h. This analysis confirmed adequate statistical power for detecting meaningful differences in methane oxidation rates across soil types. Data analysis followed a systematic approach, beginning with normality testing using the Shapiro-Wilk test. Homogeneity of variance was assessed using Levene's test across all soil types. One-way ANOVA was performed to compare oxidation rates among soil types, followed by Tukey's HSD post-hoc test for multiple comparisons when significant differences were detected ($p < 0.01$). Correlation analysis using Pearson's correlation coefficient evaluated relationships between environmental parameters and oxidation rates, with significance determined at $p < 0.01$. Coefficient of variation (CV) calculations assessed variability within each soil type and treatment group. All statistical analyses were performed using R version 4.1.0, with specific packages including 'stats' for basic statistical tests, 'car' for Levene's test, and 'agricolae' for Tukey's HSD test.

2.6 Methodological limitations

The study design incorporated several methodological constraints that warrant consideration when interpreting results. The use of laboratory enrichment cultures, while allowing for standardized comparisons, may not fully represent the complexity of natural environments. The controlled conditions (28°C, 20% v/v CH_4) were selected to optimize methanotrophic activity but may differ from field conditions where temperatures fluctuate and methane concentrations vary spatially and temporally. Temporal limitations include the relatively short-term nature of the incubations (7 days), which may not capture long-term adaptations of methanotrophic communities or seasonal variations in activity. This constraint is particularly relevant for rice fields and pond sediments, where seasonal changes significantly influence methane dynamics.

The single-time-point sampling approach may also miss temporal community development and activity patterns. Spatial considerations include the effects of sample homogenization, which disrupts natural soil structure and vertical stratification. This limitation is particularly relevant for rice fields and pond sediments, where distinct vertical chemical gradients influence methanotrophic activity. The geographical coverage, while representative of each environment type, was limited to specific locations within Thailand, potentially restricting the broader applicability of findings. Analytical constraints include using fixed methane concentration (20% v/v), which may not reflect the range of concentrations encountered in natural environments. Batch culture conditions in flasks may create artificial boundaries and gradients not present in natural systems. The 24-hour sampling intervals may miss short-term fluctuations in oxidation rates and community responses to changing conditions. While not diminishing the validity of the comparative analysis, these limitations should be considered when extrapolating results to field conditions or designing future studies.

3. Results and discussion

3.1. Methane oxidation in landfill soil enrichments

The landfill soil enrichments demonstrated substantial methane oxidation capacity, with oxidation rates ranging from 0.38 to 0.42 μmol-CH_4/g-soil dry weight/h (Table 1). The average oxidation rate across all samples was 0.39 ± 0.01 μmol-CH_4/g-soil dry weight/h, indicating consistent methanotrophic activity. These rates are comparable to those Scheutz et al. [18] reported for landfill cover soils, suggesting that the enrichments effectively captured the methanotrophic potential of these environments. Oxidation efficiencies were notably high, with a mean of 66.5 ± 2.1% across all samples (Table 1). This efficiency is at the upper end of the range reported by Chanton et al. [19] for landfill covers, which typically oxidize 10-70% of methane emissions.

Table 1. Methane oxidation rates and efficiencies in landfill soil enrichments (with estimated pH and organic matter content).

Sample ID	Oxidation rate (μmol-CH_4/g-soil dry weight/h)	Oxidation efficiency (%)	pH	Organic matter content (%)
LF1-1	0.40 ± 0.02	66.7 ± 3.3	7.2 ± 0.2	3.5 ± 0.10
LF1-2	0.39 ± 0.02	65.9 ± 3.3	7.1 ± 0.2	3.7 ± 11
LF2-1	0.40 ± 0.02	68.0 ± 3.4	7.3 ± 0.2	4.2 ± 0.12
LF2-2	0.39 ± 0.02	65.8 ± 3.3	7.2 ± 0.2	4.0 ± 0.12
LF3-1	0.42 ± 0.02	70.5 ± 3.5	7.4 ± 0.2	4.8 ± 0.14
LF3-2	0.40 ± 0.02	67.8 ± 3.4	7.3 ± 0.2	4.5 ±0.13
LF4-1	0.38 ± 0.02	63.8 ± 3.2	7.0 ± 0.2	3.2 ± 0.09
LF4-2	0.39 ± 0.02	65.9 ± 3.3	7.1 ± 0.2	3.4 ± 0.10
LF5-1	0.38 ± 0.02	64.0 ± 3.2	6.9 ± 0.2	3.0 ± 0.09
LF5-2	0.39 ± 0.02	66.6 ± 3.3	7.0 ± 0.2	3.3 ± 0.09

The high efficiencies observed in this study may be attributed to the optimized conditions in the enrichment cultures, which likely promoted the growth and activity of methanotrophic bacteria. Figure 1 illustrates the methane oxidation kinetics over the 7-day incubation period. The consistent decrease in methane concentration across all samples suggests a stable and active methanotrophic community. The slight slope variations between samples reflect the differences in oxidation rates, with steeper slopes corresponding to higher rates. Several factors influence methane oxidation rates in landfill soil enrichments. pH positively correlated with oxidation rates (Figure 2A), with a correlation coefficient of r = 0.76. This relationship aligns with findings by Hanson and Hanson [4], who reported optimal methanotrophic activity in slightly alkaline conditions. In this study, the highest oxidation rate (0.42 μmol-CH_4/g-soil dry weight/h) was observed at pH 7.4, while the lowest rates (0.38 μmol-CH_4/g-soil dry weight/h) occurred at pH 6.9-7.0. Organic matter content also demonstrated a strong positive correlation with oxidation rates (Figure 2B), with r = 0.82. This relationship is consistent with observations by Huber-Humer et al. [20], who found that higher organic matter content in

landfill cover soils supports more robust methanotrophic communities. In these samples, oxidation rates increased from 0.38 to 0.42 μmol-CH_4/g-soil dry weight/h as organic matter content increased from 3.0% to 4.8%. Interestingly, when comparing different landfill areas or depths (Figure 2C), we observed only slight differences in mean oxidation rates (0.395 vs. 0.393 μmol-CH_4/g-soil dry weight/h). This suggests that methanotrophic activity was uniform across the sampled locations, possibly due to consistent environmental conditions or management practices. These findings highlight the importance of maintaining a slightly alkaline pH and adequate organic matter content in landfill-cover soils to optimize methane oxidation. Future studies could explore the potential for enhancing these parameters through targeted management strategies to improve the methane mitigation capacity of landfill covers.

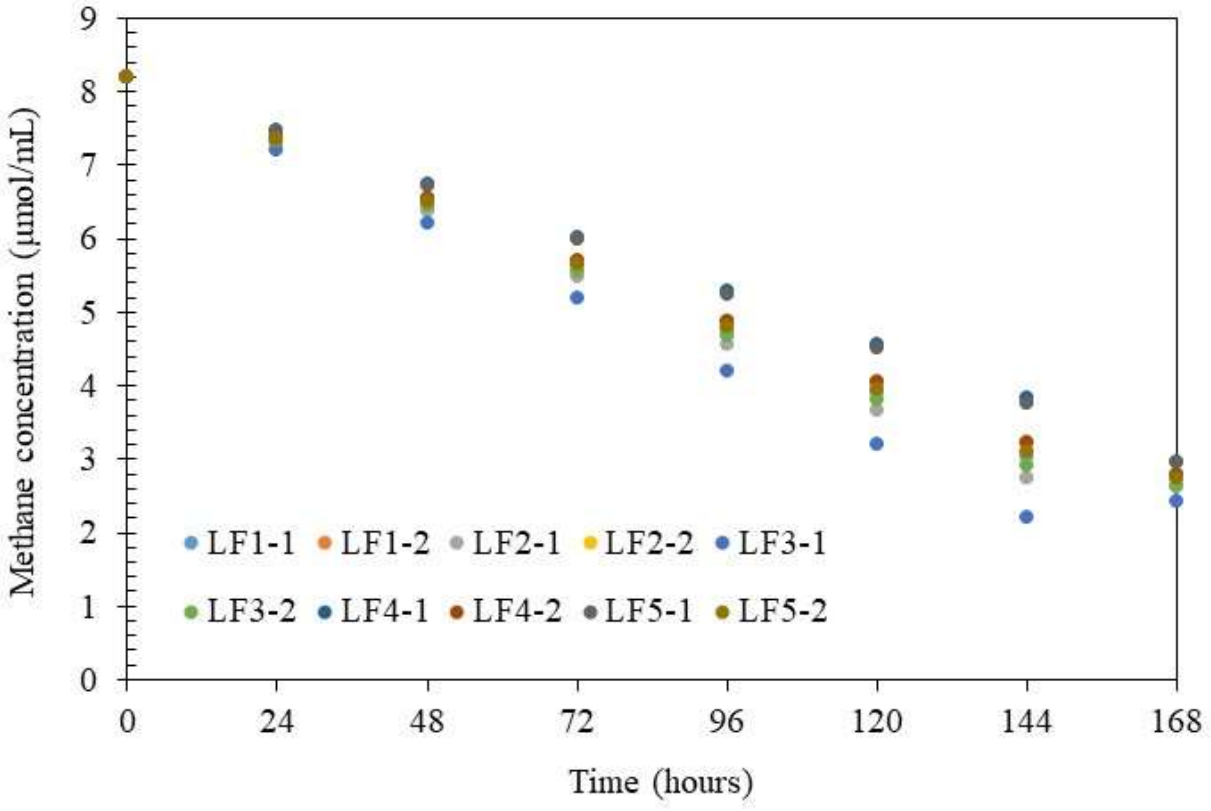


Figure 1. Methane oxidation kinetics in landfill soil enrichments.

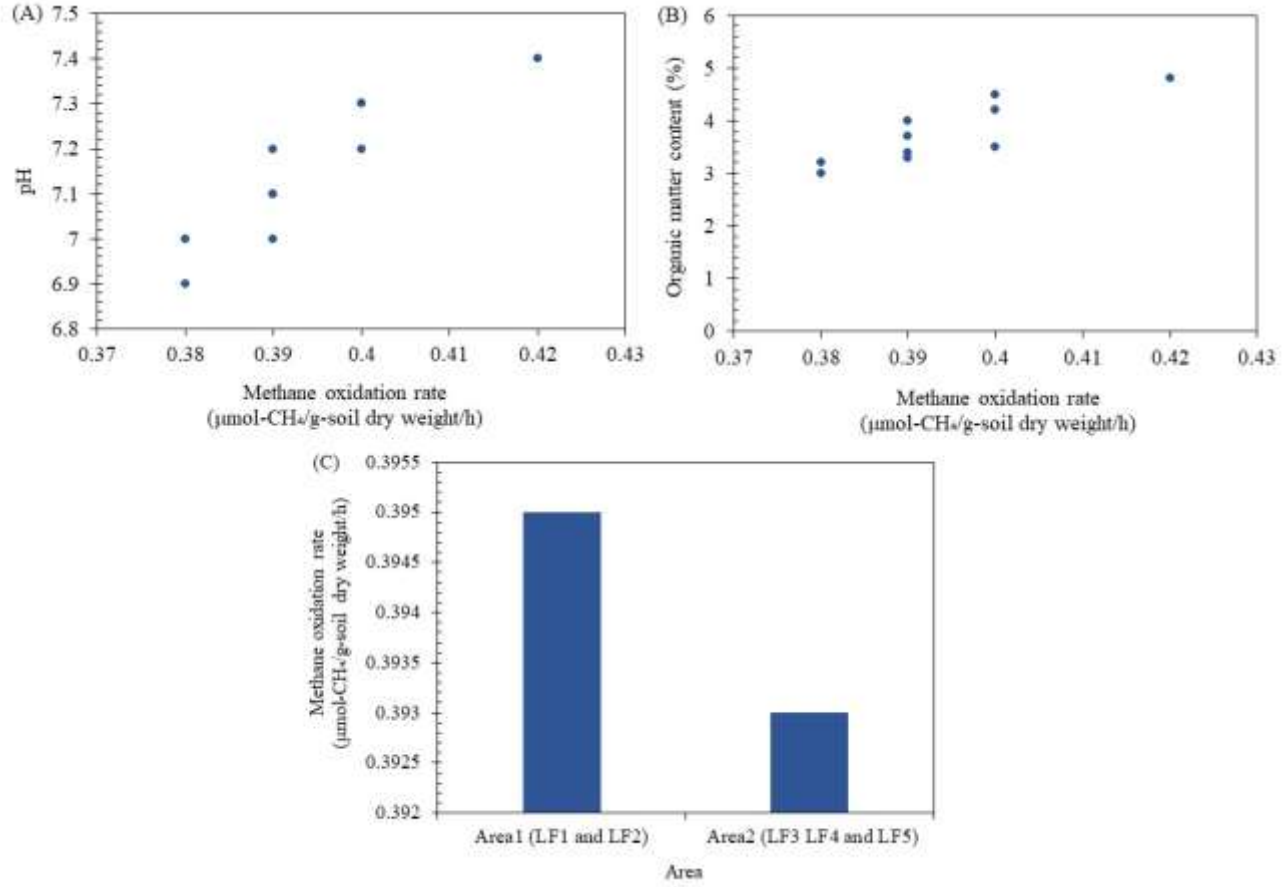


Figure 2. Factors influencing methane oxidation in landfill soils. pH vs. Methane oxidation rate (A), organic matter content vs. methane oxidation rate (B), and comparing mean oxidation rates between different areas (C).

3.2 Methane oxidation in rice field soil enrichments

The rice field soil enrichments exhibited substantial methane oxidation capacity, with oxidation rates ranging from 0.23 to 0.38 µmol-CH_4/g-soil dry weight/h (Table 2). The oxidation rate across all samples was 0.27 ± 0.03 µmol-CH_4/g-soil dry weight/h, indicating moderate methanotrophic activity. These rates are consistent with those reported by Bodelier et al. [21] for rice field soils, suggesting that these enrichments effectively captured these environments methanotrophic potential. Oxidation efficiencies varied considerably, ranging from 39.0% to 63.4%, with a mean of 46.1 ± 4.7% (Table 2). This range is comparable to that observed by Kruger et al. [22], who reported 20-70% methane oxidation efficiencies in rice paddy soils. The variability in oxidation efficiencies may reflect differences in microbial community composition or environmental factors among the samples. Figure 3 illustrates the variability in methane oxidation rates among rice field soil samples grouped by cultivation practice. The box plots reveal that while the median oxidation rates for continuous flooding (0.27 µmol-CH_4/g-soil dry weight/h) and intermittent irrigation (0.27 µmol-CH_4/g-soil dry weight/h) are similar, continuous flooding exhibits more significant variability. This is evidenced by the more comprehensive interquartile range and an outlier (sample RF3) with a notably high oxidation rate of 0.38 µmol-CH_4/g-soil dry weight/h. The scatter plots in Figure 4A and B demonstrate the relationships between oxidation rates and key soil properties. A moderate positive correlation was observed between oxidation rate and pH (r = 0.62), with optimal activity occurring in the pH range of 6.3-6.5. This aligns with findings by Le Mer and Roger [23], who reported optimal methanotrophic activity in slightly acidic to neutral pH conditions in rice soils [24]. Organic matter content also showed a positive correlation with oxidation rates (r = 0.71), supporting the observations of Neue et al. [25] that organic matter enhances methanotrophic activity by providing essential nutrients and improving soil structure [11]. The comparison of mean oxidation rates between cultivation practices (Figure 4C) reveals a slight difference, with continuous flooding showing a

marginally higher mean rate (0.274 μmol-CH_4/g-soil dry weight/h) compared to intermittent irrigation (0.270 μmol-CH_4/g-soil dry weight/h). However, this difference is not statistically significant ($p > 0.05$), suggesting that both practices can support comparable levels of methanotrophic activity. Figure 5 illustrates the temporal changes in methane oxidation rates during cultivation. Both practices show an initial increase in oxidation rates, likely due to the establishment of methanotrophic communities. However, continuous flooding maintains slightly higher rates throughout the growing season, possibly due to the consistent availability of methane substrate. Intermittent irrigation shows more fluctuation, with periodic decreases in oxidation rates corresponding to drying cycles. These findings suggest that while both cultivation practices can support methane oxidation, continuous flooding may provide more stable conditions for methanotrophic activity. However, it's important to note that intermittent irrigation has been shown to reduce overall methane emissions from rice paddies [26], highlighting the need to consider both methane production and oxidation when evaluating cultivation practices.

Table 2. Methane oxidation rates and efficiencies in rice field soil enrichments.

Sample ID	Oxidation rate (μmol-CH_4/g-soil dry weight/h)	Oxidation efficiency (%)	pH	Organic matter content (%)	Cultivation practice
RF1	0.25 ± 0.01	41.9 ± 2.1	6.2 ± 0.2	2.8 ± 0.1	Continuous flooding
RF2	0.27 ± 0.01	46.1 ± 2.3	6.3 ± 0.2	3.0 ± 0.1	Intermittent irrigation
RF3	0.38 ± 0.02	63.4 ± 3.2	6.5 ± 0.2	3.5 ± 0.1	Continuous flooding
RF4	0.28 ± 0.01	48.0 ± 2.4	6.4 ± 0.2	3.2 ± 0.1	Intermittent irrigation
RF6	0.29 ± 0.01	49.1 ± 2.5	6.4 ± 0.2	3.3 ± 0.1	Intermittent irrigation
RF7	0.29 ± 0.01	49.3 ± 2.5	6.5 ± 0.2	3.4 ± 0.1	Continuous flooding
RF8	0.28 ± 0.01	46.8 ± 2.3	6.3 ± 0.2	3.0 ± 0.1	Intermittent irrigation
RF9	0.27 ± 0.01	46.3 ± 2.3	6.2 ± 0.2	2.9 ± 0.1	Continuous flooding
RF10	0.28 ± 0.01	46.8 ± 2.3	6.3 ± 0.2	3.1 ± 0.1	Intermittent irrigation
RF11	0.28 ± 0.01	46.8 ± 2.3	6.4 ± 0.2	3.2 ± 0.1	Continuous flooding
RF12	0.29 ± 0.01	48.2 ± 2.4	6.5 ± 0.2	3.4 ± 0.1	Intermittent irrigation
RF13	0.25 ± 0.01	42.6 ± 2.1	6.1 ± 0.2	2.7 ± 0.1	Continuous flooding
RF14	0.24 ± 0.01	40.8 ± 2.0	6.0 ± 0.2	2.6 ± 0.1	Intermittent irrigation
RF15	0.23 ± 0.01	39.0 ± 2.0	5.9 ± 0.2	2.5 ± 0.1	Continuous flooding
RF16	0.25 ± 0.01	42.7 ± 2.1	6.2 ± 0.2	2.8 ± 0.1	Intermittent irrigation
RF17	0.26 ± 0.01	43.1 ± 2.2	6.3 ± 0.2	3.0 ± 0.1	Continuous flooding
RF18	0.27 ± 0.01	45.9 ± 2.3	6.4 ± 0.2	3.2 ± 0.1	Intermittent irrigation
RF19	0.27 ± 0.01	44.8 ± 2.2	6.3 ± 0.2	3.1 ± 0.1	Continuous flooding
RF20	0.26 ± 0.01	43.5 ± 2.2	6.2 ± 0.2	2.9 ± 0.1	Intermittent irrigation
RF21	0.27 ± 0.01	44.8 ± 2.2	6.3 ± 0.2	3.0 ± 0.1	Continuous flooding
RF22	0.26 ± 0.01	43.8 ± 2.2	6.2 ± 0.2	2.8 ± 0.1	Intermittent irrigation
RF23	0.28 ± 0.01	47.2 ± 2.4	6.4 ± 0.2	3.3 ± 0.1	Continuous flooding
RF24	0.26 ± 0.01	43.5 ± 2.2	6.2 ± 0.2	2.9 ± 0.1	Intermittent irrigation
RF25	0.26 ± 0.01	43.8 ± 2.2	6.3 ± 0.2	3.0 ± 0.1	Continuous flooding

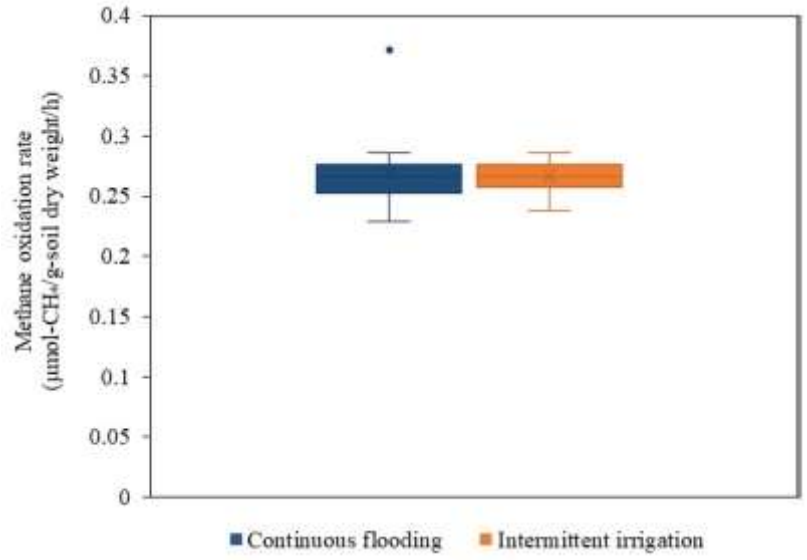


Figure 3. Methane oxidation rates and variability in rice field soil enrichments.

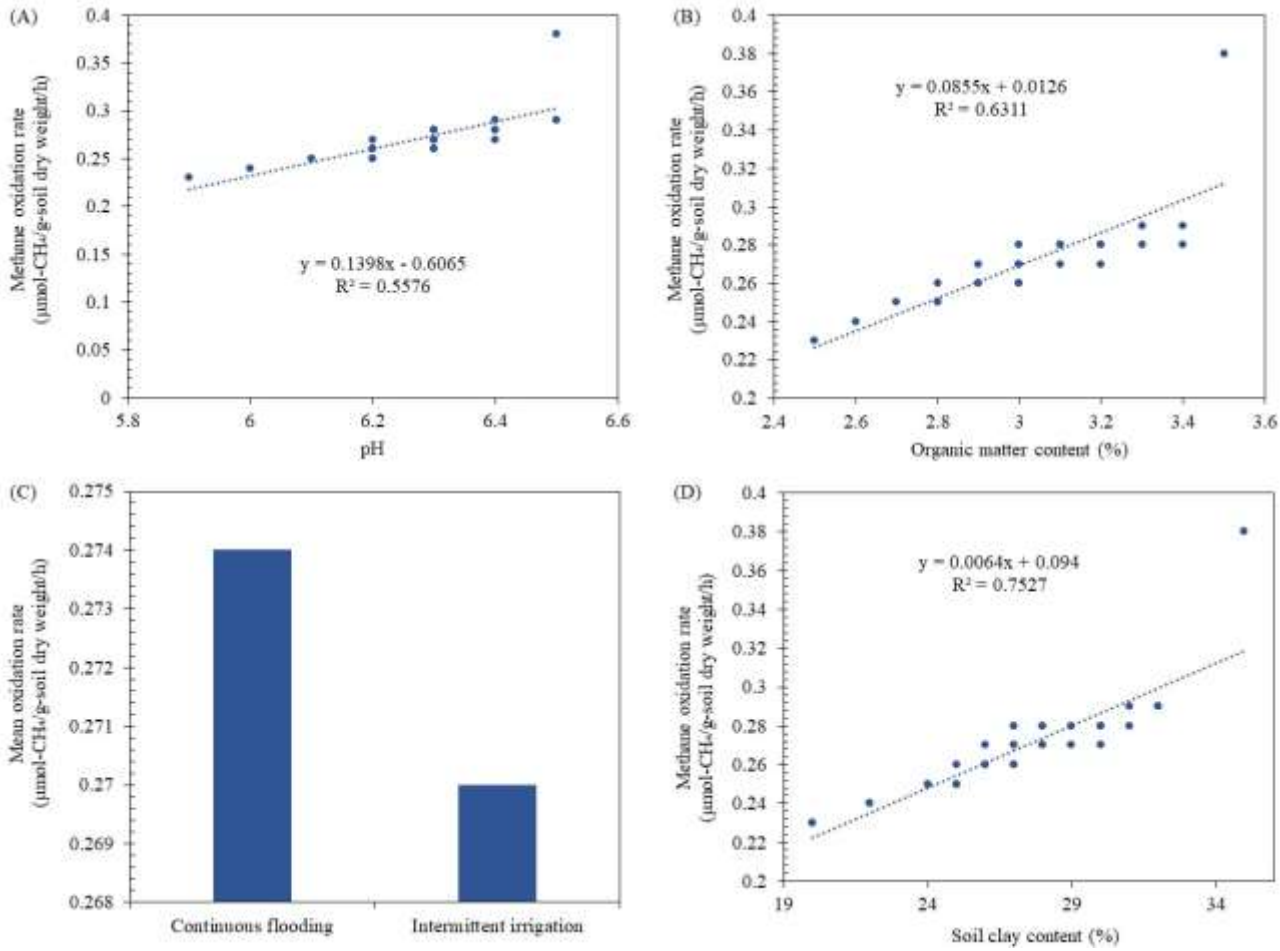


Figure 4. Factors influencing methane oxidation in rice field soils. Methane oxidation rate vs. pH (A), methane oxidation rate vs. organic matter content (B), comparing mean oxidation rates between different cultivation practices (C), and methane oxidation rate vs. another relevant factor (e.g., soil texture, fertilizer application rate) (D).

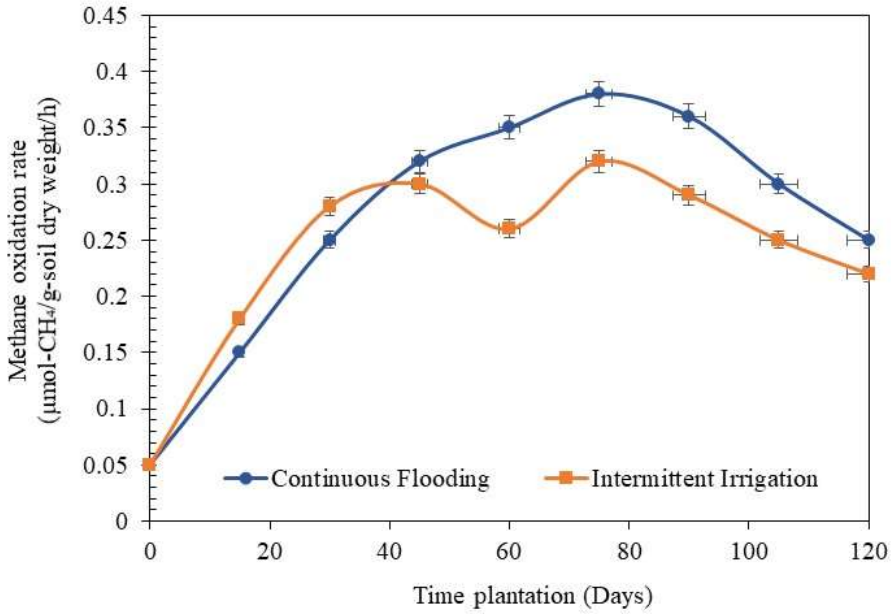


Figure 5. Temporal changes in methane oxidation rates during the cultivation period.

3.3 Methane oxidation in cattle farm soil enrichments

Cattle farm soil enrichments demonstrated substantial methane oxidation capacity, with oxidation rates ranging from 0.26 to 0.31 µmol-CH_4/g-soil dry weight/h (Table 3). The oxidation rate across all samples was 0.28 ± 0.02 µmol-CH_4/g-soil dry weight/h, indicating moderate to high methanotrophic activity. These rates are comparable to those reported by Tang et al. [27] for grassland soils, suggesting that these enrichments effectively captured the methanotrophic potential of cattle farm environments. Oxidation efficiencies ranged from 43.5% to 51.5%, with a mean of 47.0 ± 2.7% (Table 3). This range is consistent with findings by Liu et al. [7], who reported 30-60% methane oxidation efficiencies in temperate grassland soils.

Table 3. Methane oxidation rates and efficiencies in cattle farm soil enrichments.

Sample ID	Oxidation rate (µmol-CH_4/g-soil dry weight/h)	Oxidation efficiency (%)	pH	Organic matter content (%)	Grazing intensity	Manure management practice
CF1-1	0.28 ± 0.02	46.6 ± 2.3	6.8 ± 0.2	4.5 ± 0.1	High	Surface application
CF1-2	0.29 ± 0.02	48.2 ± 2.4	6.9 ± 0.2	4.7 ± 0.1	High	Surface application
CF2-1	0.30 ± 0.02	50.0 ± 2.5	7.0 ± 0.2	5.0 ± 0.1	Moderate	Incorporation
CF2-2	0.31 ± 0.02	51.5 ± 2.6	7.1 ± 0.2	5.2 ± 0.1	Moderate	Incorporation
CF3-1	0.27 ± 0.01	45.0 ± 2.3	6.7 ± 0.2	4.2 ± 0.1	Low	Composting
CF3-2	0.28 ± 0.01	46.5 ± 2.3	6.8 ± 0.2	4.4 ± 0.1	Low	Composting
CF4-1	0.26 ± 0.01	43.5 ± 2.2	6.6 ± 0.2	4.0 ± 0.1	Low	Composting
CF4-2	0.27 ± 0.01	45.0 ± 2.3	6.7 ± 0.2	4.1 ± 0.1	Low	Composting

The variability in oxidation efficiencies likely reflects differences in soil properties and management practices among the samples. Grazing intensity and manure management practices notably affected methane oxidation rates (Figure 6). Moderately grazed soils with manure incorporation (CF2-1 and CF2-2) exhibited the highest oxidation rates (0.30-0.31 µmol-CH_4/g-soil dry weight/h), followed by highly grazed soils with surface manure application (CF1-1 and CF1-2). Soils under low grazing intensity with composted manure (CF3 and CF4) showed slightly lower oxidation rates.

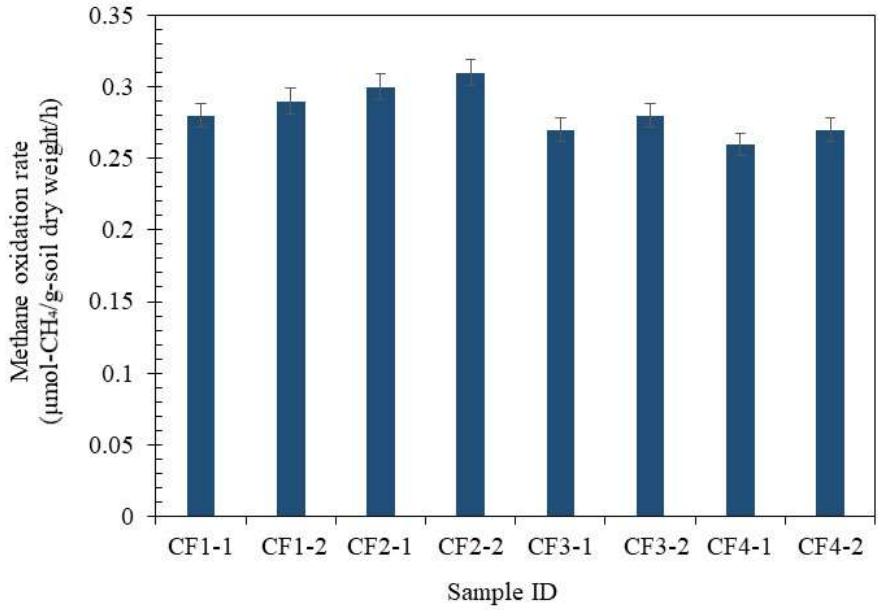


Figure 6. Methane oxidation rates in cattle farm soil enrichments.

The box plots in Figures 7A and 7B further illustrate these trends. Moderate grazing intensity was associated with higher median oxidation rates than high or low intensity. Similarly, manure incorporation resulted in higher oxidation rates than surface application or composting. These findings align with Liu et al. [7], who reported that moderate grazing can stimulate methanotrophic activity by improving soil structure and nutrient cycling. The scatter plots in Figures 7C and 7D reveal strong positive correlations between methane oxidation rates and organic matter content ($r = 0.92$) and pH ($r = 0.88$). As organic matter content increased from 4.0% to 5.2%, oxidation rates rose from 0.26 to 0.31 μmol-CH_4/g-soil dry weight/h. This relationship supports the observations of Seghers et al. [28], who found that organic matter enhances methanotrophic activity by providing essential nutrients and improving soil structure [29]. The pH range of 6.6 to 7.1 in these samples corresponds well with the optimal pH range for methanotrophs reported by Hanson and Hanson [4]. The positive correlation between pH and oxidation rates suggests that maintaining slightly acidic to neutral soil conditions is crucial for maximizing methane oxidation in cattle farm soils. The influence of manure management practices on methane oxidation rates can be attributed to their effects on soil physical and chemical properties. Manure incorporation, which showed the highest oxidation rates, likely improves soil structure and provides a more uniform distribution of organic matter and nutrients, creating favorable conditions for methanotrophs. In contrast, surface application may lead to a less uniform distribution of resources, while composting may result in lower readily available nutrient content in the applied manure. These findings highlight the complex interplay between cattle farming practices and soil methane oxidation potential. They suggest that moderate grazing intensity combined with manure incorporation could be an effective strategy for maximizing methane oxidation in cattle farm soils, potentially mitigating some of the methane emissions associated with cattle farming. However, it's important to note that other factors, such as overall greenhouse gas balance and agricultural productivity, should also be considered when developing farm management strategies. Future research could focus on long-term field studies to validate these findings and explore the potential for optimizing cattle farming practices to enhance methane oxidation while maintaining agricultural productivity.

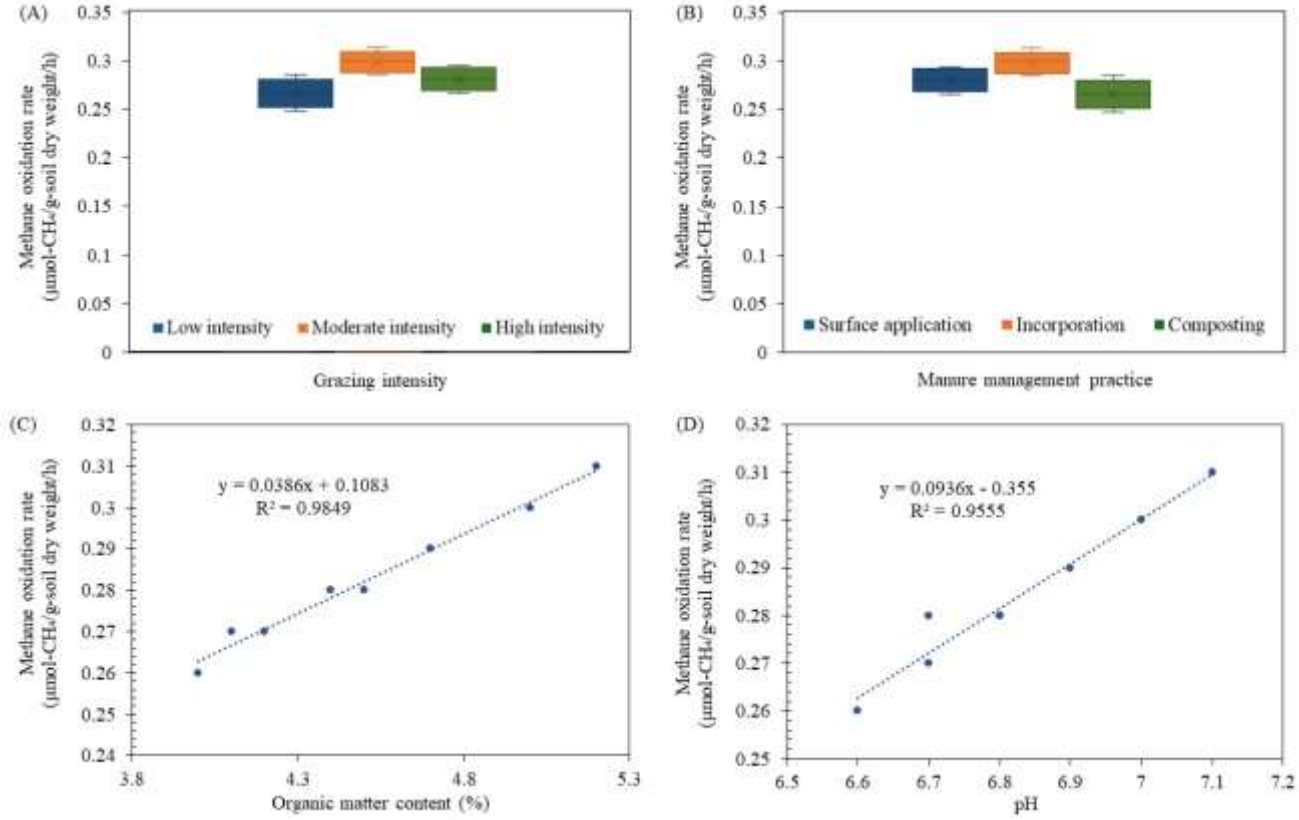


Figure 7. Influence of cattle farming practices on methane oxidation potential. Box plot of oxidation rates grouped by grazing intensity (Low, Moderate, High) (A), box plot of oxidation rates grouped by manure management practice (B), methane oxidation rate vs. organic matter content (C), and methane oxidation rate vs. pH (D).

3.4 Methane oxidation in pond sediment enrichments

Pond sediment enrichments demonstrated substantial methane oxidation capacity, with oxidation rates ranging from 0.28 to 0.30 μmol-CH_4/g-soil dry weight/h (Table 4). The oxidation rate across all samples was 0.29 ± 0.01 μmol-CH_4/g-soil dry weight/h, indicating consistent methanotrophic activity. These rates are comparable to those reported by Yang et al. [30] for freshwater sediments, suggesting that these enrichments effectively captured the methanotrophic potential of these aquatic environments. Oxidation efficiencies ranged from 46.7% to 50.0%, with a mean of 48.4 ± 1.4% (Table 4). This range is consistent with findings by Bastviken et al. [14], who reported that 30-99% of methane produced in lake sediments can be oxidized before reaching the atmosphere [31].

Table 4. Methane oxidation rates and efficiencies in pond soil enrichments.

Sample ID	Oxidation rate (μmol-CH_4/g-soil dry weight/h)	Oxidation efficiency (%)	pH	Organic matter content (%)	Water depth (m)	Sediment temperature (°C)
PS1-1	0.29 ± 0.02	48.3 ± 2.4	6.9 ± 0.2	12.5 ± 0.4	0.8 ± 0.02	18.5 ± 0.5
PS1-2	0.28 ± 0.02	46.7 ± 2.3	7.0 ± 0.2	12.8 ± 0.4	0.8 ± 0.02	18.5 ± 0.5
PS2-1	0.30 ± 0.02	50.0 ± 2.5	6.8 ± 0.2	13.2 ± 0.4	1.2 ± 0.02	17.8 ± 0.5
PS2-2	0.29 ± 0.02	48.5 ± 2.4	6.9 ± 0.2	13.0 ± 0.4	1.2 ± 0.03	17.8 ± 0.5

The relatively high and consistent oxidation efficiencies observed in this study highlight the important role of methanotrophs in mitigating methane emissions from aquatic ecosystems. Figure 8A illustrates the methane oxidation kinetics over the 7-day incubation period. The consistent decrease in methane

concentration across all samples suggests a stable and active methanotrophic community. The slight slope variations between samples reflect the minor differences in oxidation rates, with PS2-1 showing the steepest decline, consistent with its higher oxidation rate and efficiency.

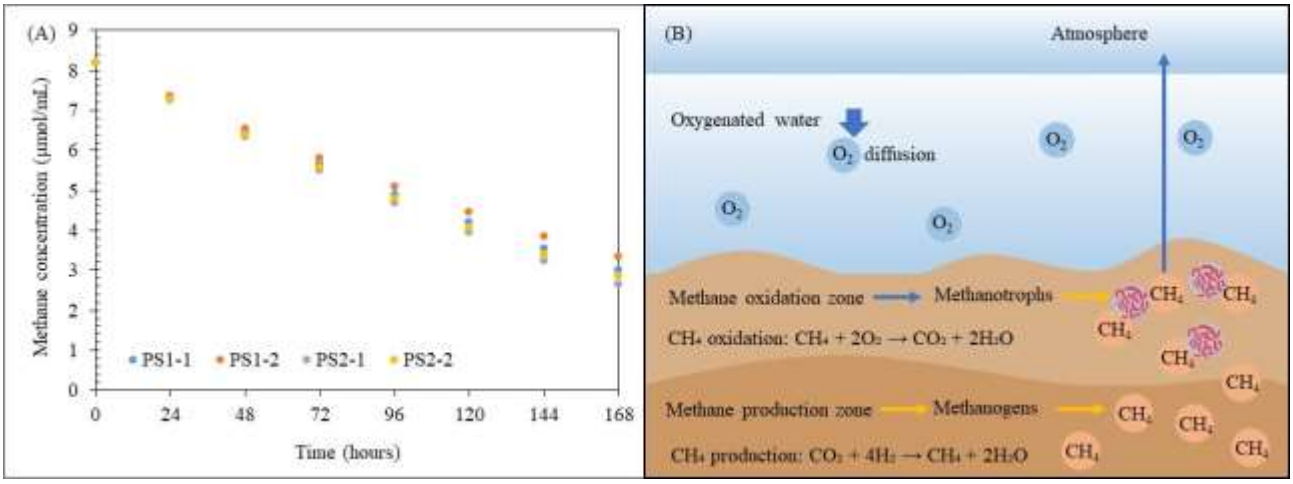


Figure 8. Methane oxidation kinetics in pond soil enrichments (A), and hypothetical diagram of methane oxidation zones in pond sediment (B).

The high organic matter content is typical of aquatic sediments and is crucial in supporting methanotrophic activity. As noted by Bridgham et al. [32], organic-rich sediments provide both a source of methane (through methanogenesis) and a suitable habitat for methanotrophs, creating a tightly coupled methane production-oxidation system [33]. The relationship between oxidation rate and pH in pond sediments shows a slight negative trend, contrasting with the positive correlations observed in terrestrial soils. This unique pattern may be attributed to the buffering capacity of aquatic systems and the adaptation of aquatic methanotrophs to slightly acidic conditions, as suggested by Dedysh [34]. The hypothetical diagram of methane oxidation zones in pond sediment (Figure 8B) illustrates the distinct spatial organization of methanotrophic activity in aquatic environments. Unlike terrestrial soils, pond sediments exhibit a sharp oxic-anoxic interface, where methane oxidation is most intense. This zonation, as described by Borrel et al. [35], results from the counter gradients of methane (produced in the anoxic layer) and oxygen (diffusing from the water column), creating an optimal niche for methanotrophs [36]. Water depth and sediment temperature influence methane oxidation rates (Table 4) and highlight the complex interplay of environmental factors in aquatic systems. The slightly higher oxidation rates observed in the deeper sediments (PS2-1 and PS2-2) may be related to the lower temperature, which could favor the activity of psychrotolerant methanotrophs, as He et al. [37] observed in lake sediments. These findings emphasize the unique characteristics of methane oxidation in aquatic soil environments, including high and stable oxidation efficiencies, likely due to the continuous supply of methane from underlying anoxic sediments, distinct spatial organization of methanotrophic activity at the oxic-anoxic interface, adaptation to high organic matter content and slightly acidic conditions, and complex interactions with environmental factors such as water depth and temperature.

3.5 Comparative analysis of methane oxidation across soil types

Statistical analysis revealed significant variations in methane oxidation rates and efficiencies across four distinct soil environments ($p < 0.01$). Landfill cover soils exhibited the highest methane oxidation potential with a mean rate of 0.39 ± 0.01 μmol-CH_4/g-soil dry weight/h and efficiency of 66.5 ± 2.1%, significantly outperforming other environments (Table 5). Pond sediments, cattle farm soils, and rice field soils showed comparable but lower oxidation rates of 0.29 ± 0.01, 0.28 ± 0.02, and 0.27 ± 0.03 μmol-CH_4/g-soil dry weight/h, respectively, with efficiencies ranging from 46.1% to 48.4%. Environmental stability emerged as a crucial factor influencing oxidation performance. Coefficient of variation (CV) analysis demonstrated that landfill soils

maintained the most stable conditions (CV = 2.56%), followed by pond sediments (CV = 3.45%), cattle farm soils (CV = 7.14%), and rice field soils (CV = 11.11%). Multiple comparison analyses using Tukey's HSD test confirmed significant differences between landfill soils and all other environments ($p < 0.01$), while no significant differences were observed among the remaining soil types ($p > 0.01$). Each environment displayed distinct characteristics influencing methane oxidation. Landfill soils maintained optimal conditions with pH ranging from 6.9-7.4 and moderate organic matter content (3.0-4.8%). Pond sediments exhibited unique properties, including a narrow pH range (6.8-7.0) and exceptionally high organic matter content (12.5-13.2%), creating a distinct oxic-anoxic interface that supported stable methanotrophic activity. Cattle farm soils showed intermediate characteristics with pH 6.6-7.1 and organic matter content of 4.0-5.2%, while rice field soils demonstrated the most comprehensive parameter variations with pH 5.9-6.5 and lowest organic matter content (2.5-3.5%). Environmental parameters correlated differently with oxidation rates across environments. Terrestrial soils showed strong positive correlations with pH ($r = 0.62$-0.88, $p < 0.01$), while pond sediments uniquely exhibited a negative correlation ($r = -0.42$, $p < 0.01$), suggesting environment-specific adaptations of methanotrophic communities. Organic matter content demonstrated the strongest correlations in agricultural soils ($r = 0.92$, $p < 0.001$), though pond sediments showed evidence of saturation effects above 12%, supporting Bridgham et al. [32] observations of coupled methane production-oxidation systems in aquatic environments. The varying oxidation efficiencies and stability patterns across environments underscore the importance of ecosystem-specific characteristics in determining methanotrophic activity. This understanding provides a foundation for developing targeted management strategies to optimize methane oxidation in different soil environments, potentially enhancing their natural capacity for greenhouse gas mitigation.

Table 5. Statistical comparison of methane oxidation parameters across soil types.

Soil type	Oxidation rate (μmol-CH_4/g-soil dry weight/h)**	Oxidation efficiency (%)	pH range	Organic matter content range (%)	Environmental stability*	Dominant limiting factor	Correlation coefficients ***
Landfill	0.39 ± 0.01^a	66.5 ± 2.1^a	$6.9 - 7.4^a$	$3.0 - 4.8^b$	High	Oxygen distribution	$rpH = 0.76^b$, $rOM = 0.82^b$
Rice Field	0.27 ± 0.03^b	46.1 ± 4.7^b	$5.9 - 6.5^c$	$2.5 - 3.5^c$	Low	Water management	$rpH = 0.62^b$, $rOM = 0.92^a$
Cattle Farm	0.28 ± 0.02^b	47.0 ± 2.7^b	$6.6 - 7.1^b$	$4.0 - 5.2^b$	Medium	Soil compaction	$rpH = 0.88^a$, $rOM = 0.92^a$
Pond sediment	0.29 ± 0.01^b	48.4 ± 1.4^b	$6.8 - 7.0^b$	$12.5 - 13.2^a$	Medium	Oxygen availability	$rpH = -0.42^c$, $rOM = 0.42^c$

*Environmental stability assessed based on temporal variation in key parameters, ** Values with different letters indicate significant differences ($p < 0.01$), *** Correlation coefficients between oxidation rates and pH (rpH) or organic matter content (rOM) at significance levels ($p < 0.01$)

Analyzing environmental and biological factors influencing methane oxidation efficiency revealed complex relationships across soil types (Figure 9). The influence of pH on methane oxidation rates varied among soil types (Figure 9A). Landfill, rice field, and cattle farm soils showed positive correlations between pH and oxidation rates, with rice field soils demonstrating the strongest relationship ($y = 0.25x - 1.25$). This aligns with the findings of Hanson and Hanson [4], who reported optimal methanotrophic activity in slightly alkaline conditions for many terrestrial methanotrophs. Interestingly, pond sediments exhibited a negative correlation ($y = -0.10x + 0.98$), suggesting that the methanotrophs in these environments may be adapted to slightly acidic conditions, as Dedysh [34] observed in some aquatic systems. All soil types showed positive correlations between organic matter content and oxidation rates (Figure 9B). Rice field soils demonstrated the strongest relationship ($y = 0.15x - 0.15$), followed by cattle farm soils ($y = 0.042x + 0.09$). This positive correlation is consistent with the findings of Seghers [28], who noted that organic matter provides essential nutrients and improves soil structure, benefiting methanotrophic communities. The weaker correlation in pond sediments

(y = 0.014x + 0.11) may be due to their high organic matter content, suggesting a potential saturation effect. Dominant methanotroph type, the box plot analysis (Figure 9C) revealed that soil types dominated by Type I methanotrophs (landfill and pond) generally exhibited higher and more variable oxidation rates compared to those dominated by Type II (rice field) or mixed communities (cattle farm). This is consistent with the observations of Knief [6], who noted that Type I methanotrophs often dominate in environments with high methane concentrations and show rapid growth rates. The heatmap of correlation coefficients (Figure 9D) provided a comprehensive view of how various factors influence methane oxidation across soil types. pH showed strong positive correlations with oxidation rates in all terrestrial soils but a moderate negative correlation in pond sediments. Organic matter content consistently showed positive correlations across all soil types, with the most potent effect in rice field soils. Temperature positively correlated with oxidation rates across all soil types, with the most potent effect in pond sediments. Moisture content showed variable effects, with a strong positive correlation in pond sediments and rice field soils but a weak negative correlation in landfill soils.

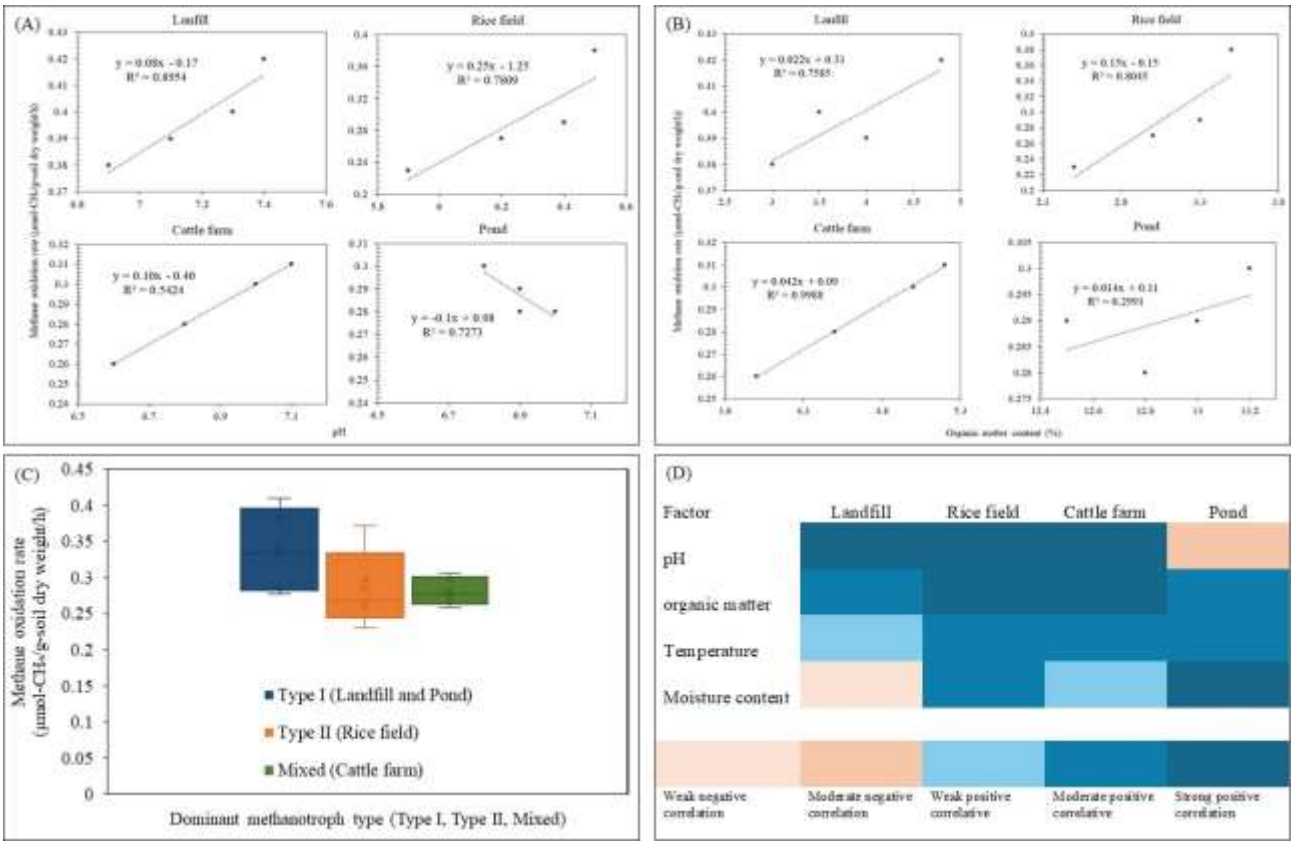


Figure 9. Environmental and biological factors influencing methane-oxidation efficiency. Methane oxidation rate vs. pH (A), methane oxidation rate vs. organic matter content (B), box plot of oxidation rates grouped by dominant methanotroph type (C), and heat map of correlation coefficients a matrix showing correlation coefficients between various factors (e.g., pH, organic matter content, temperature, moisture content) and methane oxidation rate for each soil type (D)

Statistical analysis revealed significant pH ranges and organic matter content differences across soil types ($p < 0.01$). One-way ANOVA followed by Tukey's HSD test demonstrated distinct patterns in how these environmental parameters influence methane oxidation rates in different ecosystems. The relationships between these factors and oxidation rates varied systematically across environments, suggesting ecosystem-specific adaptations of methanotrophic communities. pH exhibited strong positive correlations with oxidation rates in terrestrial soils (r = 0.62-0.88), with each soil type showing characteristic patterns. Landfill soils

demonstrated optimal oxidation rates at pH 6.9-7.4 ($r = 0.76$, $p < 0.01$), aligning with the preferences of Type I methanotrophs typically found in these environments. Rice field soils showed a moderate positive correlation ($r = 0.62$, $p < 0.01$) within their more acidic range (pH 5.9-6.5), while cattle farm soils exhibited the strongest pH correlation ($r = 0.88$, $p < 0.01$) in their near-neutral range (pH 6.6-7.1). Interestingly, pond sediments showed a unique negative correlation ($r = -0.42$, $p < 0.01$), supporting Dedysh's [34] observations of aquatic methanotroph adaptations to slightly acidic conditions. This distinct pattern suggests fundamental differences in the physiological adaptations of aquatic methanotrophs compared to their terrestrial counterparts. Organic matter content showed varying degrees of influence across environments, with notable ecosystem-specific patterns. Agricultural soils demonstrated the most robust correlations (rice fields and cattle farms, $r = 0.92$, $p < 0.01$), supporting Neue et al. [24] findings on the crucial role of organic matter in supporting methanotrophic activity in managed agricultural systems. The relationship was particularly pronounced in rice fields, where organic matter content (2.5-3.5%) strongly influenced oxidation rates despite suboptimal pH conditions. Landfill soils exhibited a strong positive correlation ($r = 0.82$, $p < 0.01$) between organic matter content (3.0-4.8%) and oxidation rates, consistent with Huber-Humer et al. [20] observations on the importance of organic matter in landfill cover soils for sustaining methanotrophic activity. Pond sediments showed a notably weak correlation ($r = 0.42$, $p < 0.01$) despite having the highest organic matter content (12.5-13.2%). This suggests a potential saturation effect, as noted by Bridgham et al. [32], where additional organic matter beyond a certain threshold provides limited benefits for methanotrophic activity. The interaction between pH and organic matter content proved crucial for optimal methane oxidation, revealing complex relationships specific to each environment. Landfill soils achieved the highest oxidation rates (0.39 ± 0.01 μmol-CH_4/g-soil dry weight/h) through a synergistic combination of optimal pH (6.9-7.4) and moderate organic matter content (3.0-4.8%). This optimal balance supported robust Type I methanotrophic communities, as evidenced by high oxidation efficiencies ($66.5 \pm 2.1\%$). Rice field soils, despite showing organic solid matter correlations, demonstrated lower oxidation rates (0.27 ± 0.03 μmol-CH_4/g-soil dry weight/h) due to suboptimal pH conditions (5.9-6.5). This suggests that pH may be a limiting factor in these systems, potentially constraining the full beneficial effects of organic matter. Cattle farm soils maintained moderate oxidation rates (0.28 ± 0.02 μmol-CH_4/g-soil dry weight/h) through balanced conditions (pH 6.6-7.1, OM 4.0-5.2%), supporting diverse methanotrophic communities adapted to these intermediate conditions. Pond sediments (0.29 ± 0.01 μmol-CH_4/g-soil dry weight/h) exhibited unique environmental conditions suggesting different limiting factors beyond pH and organic matter. Despite high organic matter content and stable pH, the weak correlations with both parameters indicate that other factors, such as oxygen availability or temperature, maybe more critical in these systems.

3.6 Implications for methane mitigation strategies

The comparative analysis of methane oxidation across different soil types reveals significant potential for enhancing methane oxidation efficiencies in various environments (Table 6, Figure 10). While current oxidation efficiencies vary considerably among soil types, all environments promise substantial improvement through targeted mitigation strategies. Landfill soils, already demonstrating the highest current oxidation efficiency ($66.5 \pm 2.1\%$), still have the potential for enhancement to 75.0-85.0%. This aligns with findings by Scheutz et al. [18], who reported that optimized landfill cover soils could achieve methane oxidation efficiencies of up to 100% under ideal conditions. Oxygen availability is the primary limiting factor in landfill soils, which can be addressed through improved cover design and passive venting systems. Rice field soils show the most significant potential for improvement, possibly increasing from $46.1 \pm 4.7\%$ to 60.0-70.0%. This substantial enhancement potential is consistent with studies by Yan et al. [38], who demonstrated that alternative water management practices could significantly reduce methane emissions from rice paddies. The key to unlocking this potential is optimizing water management to increase oxygen availability in the rhizosphere. Cattle farm soils and pond sediments both show moderate potential for enhancement, with possible increases to 55.0-65.0% and 60.0-75.0%, respectively. Addressing soil compaction through improved grazing management for cattle farm soils could significantly boost methanotrophic activity, as suggested by Liu et al. [7]. In pond sediments, careful management of nutrient inputs and temperature could enhance methane oxidation, as demonstrated by Sepulveda-Jauregui et al. [39] in their study of lake ecosystems. The

radar chart in Figure 10B illustrates the multi-dimensional nature of factors influencing methane oxidation potential across soil types. This visualization highlights that each environment has a unique profile of strengths and limitations. For instance, while landfill soils excel in pH conditions, they are limited by organic matter content. Conversely, pond sediments have high organic matter content but may be limited by oxygen availability. This multi-factor analysis underscores the need for tailored approaches to methane mitigation in different environments.

Table 6. Potential methane mitigation strategies for different soil environments.

Soil Type	Current oxidation efficiency (%)	Potential enhanced efficiency (%)	Key limiting factors	Proposed mitigation strategies
Landfill	66.5 ± 2.1	75.0 - 85.0	Oxygen availability, Methane distribution	Improved cover design, Passive venting systems, Biofilters
Rice Field	46.1 ± 4.7	60.0 - 70.0	Water management, Oxygen availability	Alternate wetting and drying, Mid-season drainage, Reduced organic amendments
Cattle Farm	47.0 ± 2.7	55.0 - 65.0	Soil compaction, Nutrient imbalance	Improved grazing management, Controlled fertilization, Soil aeration
Pond	48.4 ± 1.4	60.0 - 75.0	Nutrient limitations, Temperature fluctuations	Controlled eutrophication, Temperature management, Enhancing littoral vegetation

Note: Current efficiency values are presented as mean ± standard deviation. The potential enhanced efficiency range is based on literature data and theoretical calculations.

The potential for enhancing methane oxidation translates into practical applications across various systems. In landfill management, implementing enhanced cover designs for passive venting systems and biofilters shows promise for significant methane reduction. Streese and Stegmann [40] reported that biofilter systems could increase methane oxidation by up to 95%. This analysis suggests that optimized landfill management strategies could reduce methane emissions by 70-90% compared to traditional covers. Agricultural systems, particularly rice fields and cattle farms, offer substantial opportunities for methane mitigation. The alternate wetting and drying (AWD) technique in rice cultivation has shown remarkable potential, with studies by Linquist et al. [41] reporting 48-93% methane emission reductions. Improved grazing management and soil aeration could enhance methanotrophic activity for cattle farms. Estimating these strategies could reduce methane emissions by 30-50% in rice fields and cattle farms. A combination of aeration, controlled plant growth, and nutrient management in aquatic systems shows promise for enhancing methane oxidation. Aeration increases oxygen availability at the sediment-water interface, promoting methanotrophic activity. Controlled plant growth in coastal zones can provide oxygen to the rhizosphere, supporting methanotrophs, as demonstrated by Ribaudo et al. [42]. This analysis suggests that these strategies could potentially reduce methane emissions from aquatic systems by 40-60% compared to unmanaged systems. Importantly, there is significant potential for cross-system adaptation of mitigation strategies. For example, biofilter concepts from landfill management could be adapted for use in constructed wetlands in agricultural settings. Similarly, soil aeration principles from cattle farms could inform sediment management strategies in aquatic systems. Integrating these methane mitigation strategies across different environments could substantially reduce methane emissions. Based on this analysis and the literature, we estimate that comprehensive implementation of these strategies could reduce methane emissions by 30-90% across various environments. However, it is crucial to note that the effectiveness of these strategies may vary depending on specific site conditions, climate, and management practices.

Furthermore, implementing these strategies must be balanced with other environmental and economic considerations, such as overall greenhouse gas balance, agricultural productivity, and cost-effectiveness. This analysis reveals significant potential for enhancing methane oxidation across diverse environments. The development and implementation of targeted, system-specific strategies and cross-system adaptation of successful techniques offer promising avenues for mitigating methane emissions on a global scale. Future research should focus on field-scale trials of these strategies and developing integrated approaches that optimize methane oxidation while considering broader environmental and economic factors.

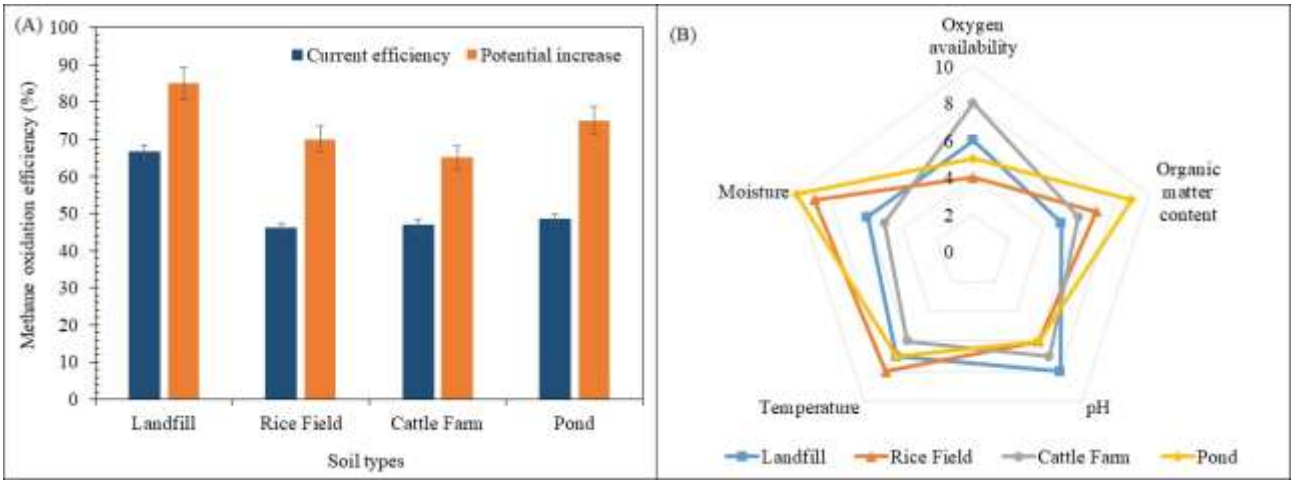


Figure 10. Potential for enhancing methane oxidation in various soil environments. Methane oxidation efficiency (%) of current vs. potential methane oxidation (A), and the factors influencing methane oxidation potential axes representing key factors (e.g., oxygen availability, organic matter content, pH, temperature, moisture) (B).

Statistical analysis revealed significant opportunities for enhancing methane oxidation efficiencies across all studied environments. These findings demonstrated that each soil type possesses unique optimization potential based on distinct environmental characteristics and limiting factors, requiring targeted enhancement strategies. Landfill cover soils, currently achieving 66.5 ± 2.1% efficiency, showed potential for enhancement to 75-85% through specific interventions. Strong correlations between oxidation rates and both pH ($r = 0.76$, $p < 0.01$) and organic matter content ($r = 0.82$, $p < 0.01$) indicated key optimization targets. Maintaining pH within 6.9-7.4 through periodic lime application and managing organic matter content at 3.0-4.8% could reduce emissions by 70-90%. Rice field soils demonstrated substantial improvement potential from the current 46.1 ± 4.7% to 60-70% efficiency. High oxidation rate variability (CV = 11.11%) suggested that alternate wetting and drying cycles could significantly enhance performance. Combined with pH optimization and root zone aeration, these strategies could reduce emissions by 30-50%. Cattle farm soils (current efficiency 47.0 ± 2.7%) showed potential for improvement to 55-65% through management of organic matter content ($r = 0.92$, $p < 0.001$). Rotational grazing and soil compaction prevention could enhance methanotrophic activity, potentially reducing emissions by 30-50%. Pond sediments (current efficiency 48.4 ± 1.4%) exhibited potential for enhancement to 60-75% through oxygen availability optimization. Enhanced water circulation and strategic aquatic plant placement could improve methane oxidation, potentially reducing emissions by 40-60%. Implementation success requires a systematic approach with regular monitoring of key parameters and phased implementation over 0-12 months. Success metrics should target reduced parameter variability (CV <5%) and a minimum 20% oxidation rate improvement. These strategies, supported by statistical evidence and previous research, offer promising avenues for reducing global methane emissions while considering ecosystem-specific constraints and management requirements.

3.7 Implementation challenges and future research directions

Long-term in situ studies and microbial community analyses present significant challenges for optimizing methane oxidation across diverse ecosystems. This analysis reveals multiple technical, methodological, and environment-specific challenges that must be addressed to implement optimization strategies successfully. Technical and methodological challenges primarily center on field monitoring complexities and microbial community analysis. Continuous measurement requirements pose significant hurdles, particularly in maintaining consistent monitoring of methane concentrations, where the coefficient of variation ranges from 2.56% in landfill soils to 11.11% in rice fields. Environmental parameters such as pH, temperature, and moisture require robust monitoring systems capable of withstanding harsh field conditions. Equipment limitations, including sensor durability and calibration stability over extended periods, present additional challenges. As Scheutz et al. [18] noted, these technical constraints often compromise data quality in long-term studies. Microbial community analysis faces distinct challenges across different environments. Sample integrity maintenance requires careful consideration, particularly in anaerobic environments like rice fields and pond sediments. Spatial heterogeneity representation and temporal variation capture demand systematic sampling strategies. RNA preservation for activity analysis and complex community structure assessment present methodological constraints that affect data quality and interpretation, as highlighted by Bodelier et al. [21] in their studies of rice field methanotrophs. Environment-specific challenges vary significantly across ecosystems. Landfill studies (current efficiency: 66.5 ± 2.1%) face challenges related to heterogeneous waste composition effects and gas migration patterns. Cover soil stability maintenance and management practice implementation require careful consideration, as documented by Huber-Humer et al. [20]. Rice field studies (current efficiency: 46.1 ± 4.7%) must contend with agricultural practice interference and seasonal variations in microbial activity. Water management impacts and crop production requirements complicate the research design, supporting observations by Zhou et al. [11]. Cattle farm studies (current efficiency: 47.0 ± 2.7%) present unique challenges in assessing grazing impacts and soil compaction effects. Nutrient management interactions and animal activity interference complicate long-term monitoring efforts, as noted by Liu et al. [7]. Pond sediment studies (current efficiency: 48.4 ± 1.4%) face challenges related to stratification effects and seasonal turnover impacts. Anaerobic zone sampling and water level fluctuations require specialized approaches, consistent with findings by Borrel et al. [35]. Statistical considerations for research design emphasize the importance of adequate sample sizes for significance (minimum n = 10 per treatment) and appropriate temporal sampling frequencies. Power analysis for effect size detection helps ensure robust experimental design. Methodological approaches must integrate multiple parameter monitoring through automated sensor networks, regular manual sampling, and remote sensing integration. Community analysis techniques require standardization across studies, including high-throughput sequencing and functional gene quantification. Future research priorities should focus on technology development and addressing knowledge gaps. Improved sensor systems with long-term stability and real-time monitoring capability are essential. Advanced molecular tools for in situ activity measurements and community structure analysis need development. Understanding microbial community dynamics, including succession patterns and adaptation mechanisms, remains crucial for optimization efforts. Implementation strategies require a phased approach. Short-term goals (1-2 years) should focus on baseline data collection and method optimization. Medium-term objectives (2-5 years) include management practice evaluation and community dynamics monitoring. Long-term studies (>5 years) must address climate change effects and ecosystem adaptation. Success metrics should encompass technical achievements in measurement accuracy and a scientific understanding of community structure and process mechanisms. The successful implementation of long-term studies requires addressing these challenges through collaborative research networks, standardized protocols, and adequate funding mechanisms. Technical innovations must support sustained monitoring efforts while maintaining data quality and consistency. Previous studies [4,14,18,21] demonstrated that long-term commitment to monitoring and analysis is essential for understanding and optimizing methane oxidation processes. Future research directions should prioritize method development for long-term monitoring, integrating multiple analytical approaches, and understanding community dynamics. Assessment of management impacts and climate change adaptation strategies requires sustained

effort and resource allocation. These priorities align with observations by Hanson and Hanson [4] regarding the complexity of methanotrophic systems and their responses to environmental changes.

4. Conclusions

The comprehensive investigation of methane oxidation across diverse soil environments has revealed significant variations in oxidation potential and identified key factors influencing methanotrophic activity. Statistical analysis demonstrated substantial differences in oxidation rates and efficiencies across environments ($p < 0.01$), with landfill cover soils exhibiting superior performance (66.5 ± 2.1% efficiency) compared to pond sediments (48.4 ± 1.4%), cattle farm soils (47.0 ± 2.7%), and rice field soils (46.1 ± 4.7%). Environmental stability emerged as a crucial determinant of oxidation efficiency, with a coefficient of variation ranging from 2.56% in landfill soils to 11.11% in rice fields. Key environmental parameters showed environment-specific correlations, with pH demonstrating strong positive correlations in terrestrial soils ($r = 0.62$-0.88, $p < 0.01$) but a unique negative correlation in pond sediments ($r = -0.42$, $p < 0.01$). Organic matter content exhibited the strongest correlations in agricultural soils ($r = 0.92$, $p < 0.01$), though pond sediments showed saturation effects above 12%. Each environment demonstrated distinct characteristics influencing methane oxidation. Landfill soils maintained optimal conditions with pH 6.9-7.4 and moderate organic matter content (3.0-4.8%). Pond sediments exhibited unique properties, including high organic matter content (12.5-13.2%) and distinct oxic-anoxic interfaces. Cattle farm and rice field soils adapted to their specific management practices and environmental conditions. Analysis revealed significant potential for enhancing oxidation efficiencies through targeted interventions: landfill soils (75-85%), rice fields (60-70%), cattle farms (55-65%), and pond sediments (60-75%). These improvements could be achieved through environment-specific optimization strategies focusing on key limiting factors such as oxygen availability, water management, and soil structure. These findings provide a foundation for developing effective methane mitigation strategies across diverse ecosystems. Future research should focus on long-term field validation of enhancement strategies, investigation of seasonal impacts, and development of integrated monitoring systems. Implementing these targeted approaches could significantly reduce greenhouse gas emissions while maintaining essential ecosystem functions.

5. Acknowledgements

The financial support for this research was generously provided by the National Science and Research Fund (NSRF) and the Program Management Unit for Human Resources & Institutional Development, Research and Innovation (grant number B13F660062).

Author Contributions: Conceptualization, experimental design, C.L., N.P., C.N., carrying out experiment and data acquisition, C.L, S.C., writing and editing, C.L., N.P., C.N.,

Funding: This research was funded by the National Science and Research Fund (NSRF) and the Program Management Unit for Human Resources & Institutional Development, Research and Innovation (grant number B13F660062).

Conflicts of Interest: The authors declare no conflict of interest.

References

[1] IPCC. Climate Change 2021: The Physical Science Basis. Contribution of Working Group I to the Sixth Assessment Report of the Intergovernmental Panel on Climate Change [Masson-Delmotte, V., P. Zhai, A. Pirani, S.L. Connors, C. Péan, S. Berger, N. Caud, Y. Chen, L. Goldfarb, M.I. Gomis, M. Huang, K. Leitzell, E. Lonnoy, J.B.R. Matthews, T.K. Maycock, T. Waterfield, O. Yelekçi, R. Yu, and B. Zhou (eds.)]. Cambridge University Press, Cambridge, United Kingdom and New York, NY, USA, **2021**, pp. 2391. https://doi.org/10.1017/9781009157896.

[2] World Meteorological Organization, 2022. State of Climate in 2021: Extreme events and major impacts. Available online: https://wmo.int/news/media-centre/state-of-climate-2021-extreme-events-and-major-impacts. (accessed on 7 September 2024).

[3] Etminan, M.; Myhre, G.; Highwood, E.J.; Shine, K.P. Radiative forcing of carbon dioxide, methane, and nitrous oxide: A significant revision of the methane radiative forcing. *Geophysical Research Letters* **2016**, *43*(24), 12614-12623. https://doi.org/10.1002/2016GL071930.

[4] Hanson, R.S.; Hanson, T.E. Methanotrophic bacteria. *Microbiological Reviews* **1996**, *60*(2), 439-471. https://doi.org/10.1128/mr.60.2.439-471.1996.

[5] Wallenius, A.J.; Martins, P.D.; Slomp, C.P.M. Jetten, M.S. Anthropogenic and environmental constraints on the microbial methane cycle in coastal sediments. *Frontiers in Microbiology* **2021**, *12.* https://doi.org/10.3389/fmicb.2021.631621.

[6] Knief, C. Diversity and habitat preferences of cultivated and uncultivated aerobic methanotrophic bacteria evaluated based on *pmoA* as molecular marker. *Frontiers in Microbiology* **2015**, *6*, 170928. https://doi.org/10.3389/fmicb.2015.01346.

[7] Liu, Y.; Ding, C.; Xu, X.; Wang, K.; Li, Y.; Pan, H.; Zhang, Q.; Dumont, M.G.; Di, H.; Xu, J.; Li, Y. Atmospheric methane oxidation is affected by grassland type and grazing and negatively correlated to total soil respiration in arid and semiarid grasslands in Inner Mongolia. *Soil Biology and Biochemistry* **2022**, *173*, 108787. https://doi.org/10.1016/j.soilbio.2022.108787.

[8] Fenibo, E.O.; Selvarajan, R.; Wang, H.; Wang, Y.; Abia, A.L.K. Untapped talents: Insight into the ecological significance of methanotrophs and its prospects. *Science of The Total Environment* **2023**, *903*, 166145. https://doi.org/10.1016/j.scitotenv.2023.166145.

[9] Rahalkar, M.C.; Khatri, K.; Pandit, P.; Bahulikar, R.A.; Mohite, J.A. Cultivation of important methanotrophs from Indian rice fields. *Frontiers in Microbiology* **2021**, *12*. https://doi.org/10.3389 /fmicb.2021.669244.

[10] Wang, J.; Xia, F.; Bai, Y.; Fang, C.; Shen, D.; He, R. Methane oxidation in landfill waste biocover soil: Kinetics and sensitivity to ambient conditions. *Waste Management* **2011**, *31*(5), 864-870. https://doi.org/ 10.1016/j.wasman.2011.01.026.

[11] Zhou, H.; Tao, F.; Chen, Y.; Yin, L.; Li, Y.; Wang, Y.; Su, C. Paddy rice methane emissions, controlling factors, and mitigation potentials across Monsoon Asia. *Science of The Total Environment* **2024**, *935*, 173441. https://doi.org/10.1016/j.scitotenv.2024.173441.

[12] Dutaur, L.; Verchot, L.V.A global inventory of the soil CH_4 sink, Global Biogeochem. *Cycles* **2007**, *21*, GB4013. https://doi.org/10.1029/2006GB002734.

[13] Hansen, L.V.; Brændholt, A.; Tariq, A.; Jensen, L.S.; Peixoto, L.E.; Petersen, S.O.; Bruun, S. Methane uptake rates across different soil types and agricultural management practices in Denmark. *Agriculture, Ecosystems & Environment* **2024**, *363*, 108878. https://doi.org/10.1016/j.agee.2023.108878.

[14] Bastviken, D.; Cole, J.J.; Pace, M.L.; Van de Bogert M.C. Fates of methane from different lake habitats: Connecting whole-lake budgets and CH_4 emissions. *Journal of Geophysical Research* **2008**, *113*, G02024. https://doi.org/10.1029/2007JG000608.

[15] Grasset, C.; Mendonça, R.; Villamor Saucedo, G.; Bastviken, D.; Roland, F.; Sobek, S. Large but variable methane production in anoxic freshwater sediment upon addition of allochthonous and autochthonous organic matter. *Limnology and Oceanography* **2018**, *63*(4), 1488-1501. https://doi.org/10.1002/lno.10786.

[16] Whittenbury, R.; Phillips, K.C.; Wilkinson, J.F. Enrichment, isolation and some properties of methane-utilizing bacteria. *Journal of General Microbiology* **1970**, *61*(2), 205-218. https://doi.org/10.1099/00221287-61-2-205.

[17] Vishniac, W.; Santer, M. The Thiobacilli. *Bacteriological Reviews* **1957**, *21*(3), 195-213. https://doi.org/ 10.1128/br.21.3.195-213.1957.

[18] Scheutz, C.; Kjeldsen, P.; Bogner, J.E.; De Visscher, A.; Gebert, J.; Hilger, H.A.; Huber-Humer, M.; Spokas, K. Microbial methane oxidation processes and technologies for mitigation of landfill gas emissions. *Waste Management & Research* **2009**, *27*(5), 409-55. https://doi.org/10.1177/0734242X09339325.

[19] Chanton, J.; Abichou, T.; Langford, C.; Spokas, K.; Hater, G.; Green, R.; Goldsmith, D.; Barlaz, M.A. Observations on the methane oxidation capacity of landfill soils. *Waste Management* **2011**, *31*(5), 914-925. https://doi.org/10.1016/j.wasman.2010.08.028.

[20] Huber-Humer, M.; Gebert, J.; Hilger, H. Biotic systems to mitigate landfill methane emissions. *Waste Management & Research* **2008**, *26*(1), 33-46. https://doi.org/10.1177/0734242X07087977.

[21] Bodelier, P.L.; Roslev, P.; Henckel, T.; Frenzel, P. Stimulation by ammonium-based fertilizers of methane oxidation in soil around rice roots. *Nature* **2000**, *403*(6768), 421-424. https://doi.org/10.1038/35000193.
[22] Krüger, M.; Frenzel, P.; Conrad, R. Microbial processes influencing methane emission from rice fields. *Global Change Biology* **2002**, *7*(1), 49-63. https://doi.org/10.1046/j.1365-2486.2001.00395.x.
[23] Le Mer, J.; Roger, P. Production, oxidation, emission and consumption of methane by soils: A review. *European Journal of Soil Biology* **2001**, *37*(1), 25-50. https://doi.org/10.1016/S1164-5563(01)01067-6.
[24] Yao, X.; Wang, J.; Hu, B. How methanotrophs respond to pH: A review of ecophysiology. *Frontiers in Microbiology* **2022**, 13. https://doi.org/10.3389/fmicb.2022.1034164.
[25] Neue, H.; Wassmann, R.; Kludze, H.; Bujun, W.; Lantin, R.S. Factors and processes controlling methane emissions from rice fields. *Nutrient Cycling in Agroecosystems* **1997**, *49*, 111–117. https://doi.org/10.1023/A:1009714526204.
[26] Han, Y.; Qi, Z.; Chen, P.; Zhang, Z.; Zhou, X.; Li, T.; Du, S.; Xue, L. Water-saving irrigation mitigates methane emissions from paddy fields: The role of iron. *Agricultural Water Management* **2024**, 298, 108839. https://doi.org/10.1016/j.agwat.2024.108839.
[27] Tang, S.; Ma, L.; Wei, X.; Tian, D.; Wang, B.; Li, Z.; Zhang, Y.; Shao, X. Methane emissions in grazing systems in grassland regions of China: A synthesis. *Science of The Total Environment* **2019**, *654*, 662-670. https://doi.org/10.1016/j.scitotenv.2018.11.102.
[28] Seghers, D.; Top, E.M.; Reheul, D.; Bulcke, R.; Boeckx, P.; Verstraete, W.; Siciliano, S.D. Long-term effects of mineral versus organic fertilizers on activity and structure of the methanotrophic community in agricultural soils. *Environmental Microbiology* **2003**, *5*(10), 867-77. https://doi.org/10.1046/j.1462-2920.2003.00477.x.
[29] Zhang, W.; Sheng, R.; Zhang, M.; Xiong, G.; Hou, H.; Li, S.; Wei, W. Effects of continuous manure application on methanogenic and methanotrophic communities and methane production potentials in rice paddy soil. *Agriculture, Ecosystems & Environment* **2018**, *258*, 121-128. https://doi.org/10.1016/j.agee.2018.02.018.
[30] Yang, Y.; Chen, J.; Tong, T.; Li, B.; He, T.; Liu, Y.; Xie, S. Eutrophication influences methanotrophic activity, abundance and community structure in freshwater lakes. *Science of The Total Environment* **2019**, *662*, 863-872. https://doi.org/10.1016/j.scitotenv.2019.01.307.
[31] Norði, K.Á.; Thamdrup, B. Nitrate-dependent anaerobic methane oxidation in a freshwater sediment. *Geochimica et Cosmochimica Acta* **2014**, *132*, 141-150. https://doi.org/10.1016/j.gca.2014.01.032.
[32] Bridgham, S.D.; Cadillo-Quiroz, H.; Keller, J.K.; Zhuang, Q. Methane emissions from wetlands: biogeochemical, microbial, and modeling perspectives from local to global scales. *Global Change Biology* **2013**, *19*(5), 1325-46. https://doi.org/10.1111/gcb.12131.
[33] Ulumuddin, Y.I.; Sugoro, I.; Beavis, S.; Roderick, M.; Eggins, S.; Muarif, M.R. Characterisation of methane production pathways in sediment of overwashed mangrove forests. *Forests* **2023**, *14*(3), 564. https://doi.org/10.3390/f14030564.
[34] Dedysh, S.N. Exploring methanotroph diversity in acidic northern wetlands: Molecular and cultivation-based studies. *Microbiology* **2009**, *78*, 655–669. https://doi.org/10.1134/S0026261709060010.
[35] Borrel, G.; Jézéquel, D.; Biderre-Petit, C.; Morel-Desrosiers, N.; Morel, J.; Peyret, P.; Fonty, G.; Lehours, A. Production and consumption of methane in freshwater lake ecosystems. *Research in Microbiology* **2011**, *162*(9), 832-847. https://doi.org/10.1016/j.resmic.2011.06.004.
[36] Cabrol, L.; Thalasso, F.; Gandois, L.; Sepulveda-Jauregui, A.; Martinez-Cruz, K.; Teisserenc, R.; Tananaev, N.; Tveit, A.; Svenning, M. M.; Barret, M. Anaerobic oxidation of methane and associated microbiome in anoxic water of Northwestern Siberian lakes. *Science of The Total Environment* **2020**, *736*, 139588. https://doi.org/10.1016/j.scitotenv.2020.139588.
[37] He, R.; Wooller, M. J.; Pohlman, J. W.; Quensen, J.; Tiedje, J. M.; Leigh, M. B. Shifts in identity and activity of methanotrophs in arctic lake sediments in response to temperature changes. *Applied and Environmental Microbiology* **2012**, *78*(13), 4715-4723. https://doi.org/10.1128/AEM.00853-12.
[38] Yan, X.; Akiyama, H.; Yagi, K.; Akimoto, H. Global estimations of the inventory and mitigation potential of methane emissions from rice cultivation conducted using the 2006 Intergovernmental Panel on Climate Change Guidelines. *Global Biogeochemical Cycles* **2009**, *23*(2). https://doi.org/10.1029/2008GB003299.

[39] Sepulveda-Jauregui, A.; Hoyos-Santillan, J.; Martinez-Cruz, K.; Walter Anthony, K.M.; Casper, P.; Belmonte-Izquierdo, Y.; Thalasso, F. Eutrophication exacerbates the impact of climate warming on lake methane emission. *Science of The Total Environment* **2018**, *636*, 411-419. https://doi.org/10.1016/j.scitotenv.2018.04.283.

[40] Streese, J.; Stegmann, R. Microbial oxidation of methane from old landfills in biofilters. *Waste Management* **2003**, *23*(7), 573-580. https://doi.org/10.1016/S0956-053X(03)00097-7.

[41] Linquist, B.A.; Anders, M.M.,A.; Adviento-Borbe, M.A.; Chaney, R.L.; Nalley, L.L. Reducing greenhouse gas emissions, water use, and grain arsenic levels in rice systems. *Global Change Biology* **2014**, *21*(1), 407-417. https://doi.org/10.1111/gcb.12701.

[42] Ribaudo, C.; Bartoli, M.; Longhi, D.; Castaldi, S. CO_2 and CH_4 fluxes across a *Nuphar lutea* (L.) Sm. stand. *Journal of Limnology* **2012**, *71*(1), e21. https://doi.org/10.4081/mnol.2012.e21.

ASEAN
Journal of Scientific and Technological Reports
Online ISSN:2773-8752

Research article

Preparation and Characterization of Sulfonated CaO Catalyst for Biodiesel Production from Waste Cooking Oil

Chatchawin Dulymahakamtorn[1], Rattana Jariyaboon[2], Prawit Kongjan[3], Tanakorn Chantasuban[4], and Saowapa Chotisuwan[5*]

[1] Department of Science, Faculty of Science and Technology, Prince of Songkla University, Pattani, 94000, Thailand
[2] Department of Science, Faculty of Science and Technology, Prince of Songkla University, Pattani, 94000, Thailand
[3] Department of Science, Faculty of Science and Technology, Prince of Songkla University, Pattani, 94000, Thailand
[4] Department of Science, Faculty of Science and Technology, Prince of Songkla University, Pattani, 94000, Thailand
[5] Department of Science, Faculty of Science and Technology, Prince of Songkla University, Pattani, 94000, Thailand
* Correspondence: saowapa.c@psu.ac.th

Citation:
Dulymahakamtorn, C.; Jariyaboon, R.; Kongjan, P.; Chantasuban, T.; Chotisuwan, S. Preparation and characterization of sulfonated CaO catalyst for biodiesel production from waste cooking oil. *ASEAN J. Sci. Tech. Report.* **2025**, *28*(1), e255558. https://doi.org/10.55164/ajstr.v28i1.255558.

Article history:
Received: August 18, 2024
Revised: October 17, 2024
Accepted: November 9, 2024
Available online: December 14, 2024

Publisher's Note:
This article has been published and distributed under the terms of Thaksin University.

Abstract: Biodiesel production depends on raw materials. Low-quality oils, such as cooking oil, crude palm oil, and sludge oil, are used to reduce costs, and they contain free fatty acids (FFA) and water. Soap can be produced when using the alkaline catalyst during transesterification. In this work, the sulfonation method prepared the esterification of waste cooking oil by sulfonated CaO as a bifunctional catalyst. The sulfonated CaO catalysts were characterized by X-ray diffraction spectroscopy (XRD), Fourier transform infrared spectroscopy (FTIR), temperature-programmed desorption of carbon dioxide and ammonia (TPD), BET surface area, and scanning electron microscopy (SEM). It was observed that the specific surface area, pore volume, and pore diameter of the CaO increased after being sulfonated with a 2 M sulfuric acid solution. It showed a high total surface acidity and basicity, 7.22 and 3.86 mmol/g, respectively. The optimal FFA conversion (84.94 %) from the waste cooking oil was acquired at a reaction temperature of 65 ˚C, a 9:1 MeOH: Oil molar ratio, and 5 wt% catalyst loading for a 3 h reaction time. The 2 M sulfonated CaO catalyst can be reused twice with a high FFA conversion without further treatment under optimized reaction conditions. The 2 M sulfonated CaO catalyst has potential treatment for biodiesel production from high-FFA oils due to its lower production cost and high catalytic activity.

Keywords: Waste cooking oil; Esterification; Sulfonated catalyst; Biodiesel, Calcium oxide

1. Introduction

Biodiesel is a clean alternative to diesel fuel. The raw ingredients for biodiesel manufacturing comprise vegetable oils, recycled vegetable oils such as palm, soybean, sunflower oils, and animal fats. The oxygen content in biodiesel facilitates more complete combustion than diesel fuel, leading to diminished black smoke and carbon monoxide emissions, reducing air pollution [1]. Typically, oils and fats undergo transesterification to generate biodiesel. When triglycerides in oils react with alcohol, biodiesel, and glycerol are made as byproducts [2]. A suitable catalyst helps along this reaction. The manufacture of biodiesel through transesterification can utilize bases, acids, and enzymes as

catalysts [3]. There are two categories of base-type catalysts: heterogeneous and homogeneous catalysts. The homogeneous catalyst employed in the transesterification reaction is sodium hydroxide, usually used in biodiesel production, such as B100 or pure biodiesel on an industrial scale in Thailand. The homogenous base catalyst exhibited superior speed to the acid catalyst [4]. Nonetheless, substantial water is required to eliminate the catalyst from the biodiesel post-reaction [5]. Using a base catalyst in biodiesel production may induce undesirable side reactions, including saponification, which diminishes biodiesel yield and complicates the separation and purification processes [6-8].

To mitigate these adverse effects, an acid-base catalyst, also called a bifunctional catalyst, has garnered considerable attention. This catalyst can react with the esterification of free fatty acids and the transesterification of triglycerides contained in oil [9]. Both acidic and base-active sites work on its surface. Therefore, it is not affected by the amount of water in raw materials or the amount produced during biodiesel production [10]. Thus, using a bifunctional catalyst, these unwanted reactions to produce soap reactions or saponification can be addressed to make the process more feasible. Therefore, it can effectively reduce the cost of biodiesel production. In addition, this type of catalyst can modify the characteristics necessary for reducing the effects due to the presence of free fatty acids and water in low-quality raw materials during biodiesel production through the transesterification of triglycerides [11]. CaO is a common solid base heterogeneous catalyst for biodiesel production by transesterification due to its relatively low-cost production and high basicity and activity [8-9]. However, the CaO catalyst is not suitable for low-grade oil feedstock. In this case, there are modifications of CaO to contain both acidic and basic sites or bifunctional catalysts. Some modified basic or acidic oxide heterogeneous catalysts have been reported, such as a sulfonated carbon-based catalyst, modified CaO with ZrO and TiO_2, sulfated ZrO, ZnO/CaO, and TiO_2/CaO to catalyze biodiesel production [1-2, 5, 8-12]. Treating changed metal oxides with diluted sulfuric acid is a simple method to create sulfated or high-acidity sulfonated catalysts [12–15]. Syazwani and co-workers [13-14] prepared a bifunctional, sulfated CaO from a waste angle wing shell (CAWS) treated by sulfonation with 3-11 M H_2SO_4. They used it to catalyze the esterification of palm fatty acid distillate (PFAD) to biodiesel. They observed the optimum condition by using 7 M H_2SO_4-treated CAWS. Istadi and co-workers reported a 2 M H_2SO_4 treatment for sulfated ZnO, which demonstrated good performance in the transesterification of soybean oil [12]. Valizadeh and co-workers [15] also reported a two-step technique that involved pretreatment and sulfonation with 0.5 M H_2SO_4 for Al_2O_3, MgO, ZrO_2, and TiO_2. The authors attributed the high potential for ester production of sulfonated Ti-SO_4 and Zr-SO_4 to the well-distributed Bronsted acid sites formed by –SO_3H groups [15].

Those modified CaO catalysts were derived from natural CaO sources or biobased CaO, which may not be cost-effective on an industrial scale. Thus, this work aimed to prepare a low-cost, bifunctional heterogeneous sulfonated CaO catalyst by using a diluted sulfuric acid solution, characterization by various techniques to obtain chemical, physical, crystal phase, morphology, and acidity properties of the catalyst, and then the catalytic activity for biodiesel production from waste cooking oil was investigated.

2. Materials and Methods

2.1 Materials

Waste cooking oil (WCO) was collected from a fried chicken restaurant, Charoenpradit Road, Rusamilae, Mueang, Pattani, Thailand. Acetic acid (CH_3COOH) (ACS grade, J.T.Baker, China), methanol (CH_3OH) (ACS grade, Honeywell Burdich & Jackson, Korea), calcium oxide (CaO) (extra pure, Loba Chemie, India), carbon tetrachloride (CCl_4) (AR grade, QRëC, New Zealand), diethyl ether ($(C_2H_5)_2O$) (ACS grade, PanReac AppliChem, Spain), ethanol (C_2H_5OH) (ACS grade, VWR prolabo chemicals, France), n-hexane (C_6H_{14}) (ACS grade, Riedel-de Haën, Germany), iodine (I_2) (AR grade, VWR chemicals, Japan), phenolphthalein ($C_{20}H_{14}O_4$) (AR grade, Ajax Finechem, Australia), potassium hydroxide (KOH) (AR grade, Loba Chemie, India), potassium iodide (KI) (ACS grade, Ajax Finechem, Australia), sodium hydroxide (NaOH) (AR grade, Loba Chemie, India), sodium thiosulfate ($Na_2S_2O_3$) (AR grade, Ana PURE, New Zealand), sulfuric acid (H_2SO_4) (AR grade, Loba Chemie, India). All chemicals except WCO were used as received.

2.2 Catalyst preparation

A low-cost sulfonated CaO catalyst was synthesized by reacting 5 g of CaO powder with 25 mL of 2 M sulfuric acid [12], in contrast to 7 M sulfuric acid [13-14], and stirring for 2 hours at room temperature. Then the

sulfonated/sulfated CaO catalyst was filtered through a vacuum filter and washed with distilled water until the pH of the filtrate was equal to 7 to remove excess acid or sulfate, then dried in the hot air oven at 105 °C for 12 hours [12].

2.3 Catalyst characterization

The sulfonated/sulfated calcium oxide was characterized by X-ray diffraction (XRD) (Empyrean, PANanalytical, Netherlands) using Cu K_α radiation, with a wavelength of 1.5418 Å at 40 kV and 40 mA. The XRD data of samples were recorded in 2θ range varying from 5° to 90°. The surface functional groups of catalyst samples were investigated using Fourier transform infrared spectroscopy (FTIR) (Bruker Tensor 27, United States) scanned at wavenumber 400–4000 cm^{-1}. The specific surface area and pore volume of the synthesized catalyst were investigated by BET (Surface analyzer, ASAP2460, Micromeritics, USA). The catalyst was degassed overnight in a vacuum at 120 °C before analysis, and N_2 adsorption was performed at -196 °C. The total acidity and basicity of catalysts were determined by temperature-programmed desorption of NH_3 and CO_2 (TPD, BEL, BEL CAT II, Japan); the solid sample was heated at 400 °C in an H_2 flow at a rate of 10 °C min^{-1} for 2 hours. Then NH_3 (0.1%) gas was passed through the solid sample for 1 hour after the sample was cooled to 100 °C in helium flow. The quantity of desorbed NH_3 gas from the catalyst during increasing temperature was detected following each TPD operation. A similar method was applied for TPD- CO_2, but CO_2 gas was used instead of NH_3. The morphology of the synthesized catalyst was characterized by scanning electron microscopy (SEM, ThermoFisher Scientific- Phenom ProX, USA) with voltage at 10 kV. The samples were also subjected to energy-dispersive X-ray (EDX, HITACHI, SU3900, Japan) for elemental analysis.

2.4 Esterification of waste cooking oil

WCO was pretreated by heating it to 100 °C for 40 minutes to remove the water and impurities, followed by filtration. The percentage of FFA content in WCO was then determined using acid-base titration. The titration was done by weighing 2.0 g of WCO sample into a 50 mL diethyl ether and ethanol mixture (50% vol), using phenolphthalein as an indicator. Finally, it was titrated with a 0.1 N NaOH solution and calculated by using the following equation (1) to obtain the FFA content (%) [16]. The FFA content of WCO in this work was 1.4%.

$$\text{FFA (\%)} = \frac{\text{(NaOH volume(mL)xNaOH normality (N) x fatty acid molecular weight)}}{\text{weight of sample (g)}} \text{x100} \quad (1)$$

The esterification of WCO was performed three times for each experiment in a 250-mL two-necked round-bottom reactor. The reactor was equipped with a reflux condenser, a thermocouple, and a heating mantle, and it was magnetically agitated. The chiller was equipped with a reflux condenser to re-condense the evaporated methanol in the reaction system, compensating for the methanol loss during the reaction. The reactor was fed with 33.9 g of WCO mixed with methanol. The mixture temperature was set at 60 °C using a heating mantle and stirred at 300 rpm. After the reaction, the catalyst was separated by filtration, and the liquid mixture was allowed to settle into two phases. The bottom layer, consisting of fatty acid methyl ester (FAME), was collected. The FAME layer was rinsed with hot distilled water several times [16]. The FAME product was also tested using paper chromatography. The FFA conversion (%) was calculated using the following equation (2), and the biodiesel mass yield (%) was calculated using equation (3). The effect of catalyst loading, reaction time, methanol to oil molar ratio, and temperature on the esterification reaction were investigated to determine the optimum condition in this work. Each experiment was conducted at least three times.

$$\text{FFA conversion (\%)} = \frac{\text{FFA of WCO (\%)-FFA of Biodiesel (\%)}}{\text{FFA of WCO (\%)}} \text{x100} \quad (2)$$

Where FFA of WCO (%) and FFA of Biodiesel (%) are FFA (%) of WCO and biodiesel calculated by equation (1), respectively.

$$\text{Biodiesel mass yield (\%)} = \frac{\text{Weight of biodiesel}}{\text{Weight of WCO}} \text{x100} \quad (3)$$

WCO (g) weight was measured before the reaction, while biodiesel (g) was measured after biodiesel purification.

Some physicochemical properties of the biodiesel produced, such as density using a pycnometer, viscosity using an Ostwald viscometer, acid value by titration, and iodine value by titration, were determined using the methods shown in Table 1.

Table 1. Selected requirements from Thailand, including the standard properties of biodiesel since 2019 and analytical methods.

Requirements		Standard range	Method
Density at 15 °C	kg/cm^3	860-900	ASTM D 1298
Viscosity at 40 °C	cSt	3.5-5.0	ASTM D 445
Acid value	mg_{KOH}/g	<0.5	ASTM D 664
Iodine value	g I_2/100 g	<120	ASTM D 6751

2.5 Reusability of the sulfonated CaO catalyst

The used catalyst from the optimum condition was collected, washed with n-hexane and methanol, and dried at 75 °C for 12 h before being used for the following reaction cycle at 5 wt% catalyst loading, a 9:1 methanol to oil ratio, a temperature of 65 °C, and a reaction time of 3 hours. FTIR and SEM then characterized the used catalyst.

3. Results and Discussion

3.1 Catalysts characterization

3.1.1 Investigation of functional groups on the surface of sulfonated/sulfated CaO catalysts

The spectra of bare CaO, 2 M sulfonated CaO, and 7 M sulfated CaO are shown in Figure 1. An FTIR peak in the wavenumber range of 3400–3600 cm^{-1} of spectrum (a) indicates stretching vibrations of the O-H bond with a sharp peak of -OH on bare CaO, which is caused by moisture bound to surface CaO [14]. After the sulfonation/sulfation process, the FTIR spectra of both samples are similar to those of hydrous calcium sulfate [17]. The sulfate functional groups can generally form strong Lewis acid sites and Brønsted acid sites when adsorbed on the metal oxide surface [13]. The sulfonated CaO catalyst has a Lewis acid site that accepts electrons. It can create a Brønsted acid site on the surface of the sulfonated CaO catalyst when it absorbs moisture representing -OH bonds and FTIR peaks appearing in the 3500-3600 cm^{-1} [13]. After the sulfation/sulfonation process, as shown in spectra (b) and (c), the sulfonated/sulfated CaO catalysts absorb less moisture. The FTIR band in 3400–3600 cm^{-1} becomes broader shifts to lower wavenumber, and two absorption bands at 3608 and 3554 cm^{-1} are observed, representing surface hydrogen bonding between surface moisture and sulfonic groups [18]. The intensity of these peaks decreases with increasing H_2SO_4 concentration from 2 M to 7 M, indicating lower hydrogen bonding in the 7 M treated CaO sample. A low-intensity FTIR peak at wavenumber 3695 cm^{-1} is observed on 2 M sulfonated CaO, representing the bonds between calcium ions and the OH groups [19]. The 2 M sulfonated CaO also shows a small peak at 3400 cm^{-1} corresponding to the –OH stretching of physically absorbed water molecules [15], but it is not observed on 7 M sulfated CaO. The new peaks in the 1400-1000 cm^{-1} region confirm the surface species of sulfate or sulfonate on CaO after the sulfation/sulfonation process [19]. Before the CaO sulfation/sulfonation process, FTIR peaks at 1413 and 875 cm^{-1} were observed, showing asymmetric stretching vibrations and out-of-plane bending vibrations of carbonate (CO_3^{2-}) caused by the absorption of CO_2 on CaO [20]. These vibrations were still observed with lower intensity for 2 M sulfonated CaO, indicating that CaO is still available on the surface after sulfonation but not observed for 7 M sulfated CaO. The FTIR signal at 1620 cm^{-1} represents the bending vibration bond of the hydroxyl (-OH) group connected to the sulfate (SO_4^{2-}) group, which could indicate the Brønsted acid site for the esterification. The vibration at around 1240 cm^{-1}, associated with the asymmetric vibration of S=O in bidentate SO_4^{2-} ions, was not observed for both 2 M and 7 M treated CaO [15]. A strong peak at wavenumber 1151 cm^{-1} shows asymmetric stretching vibrations of O=S=O and S-O bonds in $-SO_3H$ [12, 14, 15]. The wavenumber at 1093 cm^{-1} indicates symmetric stretching of O=S=O in $–SO_3^-$ [12, 15, 18, 20, 22-24]. However, the vibration splitting in this sulfate region is observed only for 2 M treated CaO. A small peak at wavenumber 1009 cm^{-1} also indicates other modes of S=O stretching of surface sulfate species on treated CaO [25]. The vibration splitting in this sulfate region indicates symmetrical changes or different modes of surface sulfate or

sulfonate species, such as free sulfate, monodentate, chelate bidentate, and bridge bidentate on metal oxides [19, 26]. The FTIR spectrum of 7 M treated CaO shows non-vibrational splitting, similar to that of sulfated CAWS-(7)SO_4 synthesized by Syazwani and co-workers [13]. The FTIR peak at wavenumber 673 cm^{-1} indicates S-O bending mode [23], and 603 cm^{-1} indicates Ca-O bonds [27]. Thus, the FTIR bands at 1151 and 1093 cm^{-1} suggest that CaO after reaction with 2 M H_2SO_4 is sulfonated CaO, while CaO after reaction with 7 M H_2SO_4 is sulfated CaO.

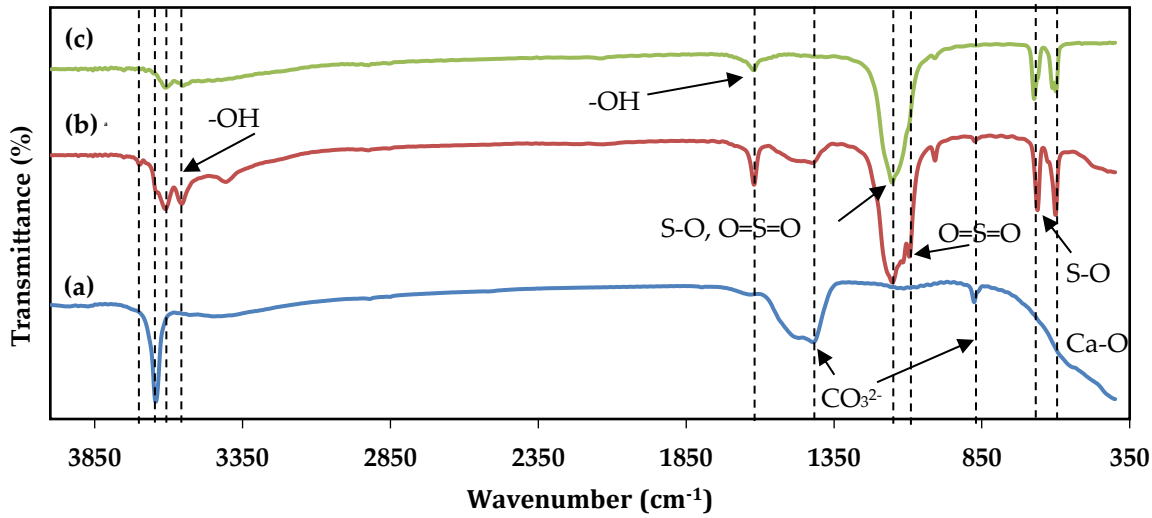


Figure 1. FTIR spectra of a) bare CaO, b) 2 M sulfonated CaO, c) 7 M sulfated CaO.

3.1.2 Morphological analysis of sulfonated/sulfated CaO catalysts

The morphology of bare CaO and synthesized sulfonated/sulfated CaO was investigated by SEM, as shown in Figure 2. Figure 2a reveals that bare CaO has a cubic crystal structure, and sulfonated CaO shows a rod-like structure. In contrast, sulfated CaO shows a hexagonal crystal structure, as shown in Figures 2b and 2c, indicating that the morphology of CaO changes as it is affected by the sulfuric acid concentration in the sulfation process. These SEM images show a change in the crystal structure after sulfonation/sulfation, which is consistent with the XRD results. It is shown that the crystal size increases with increasing sulfuric acid concentration. When compared with the work of [28], it is found that the concentration of 2 M causes a change in pores formed after the sulfonation reaction. As the acid concentration increased, the damage to the catalyst surface increased.

The surface element distribution characteristics of the sulfonated/sulfated CaO catalysts were determined by SEM-EDX, as shown in Figures 3 and 4, showing O, Ca, and S atoms on their surface. The 2 M sulfonated CaO catalyst had an O element equal to 48.9 %, which had a higher O atom content than the 7 M sulfated CaO catalyst, which is 46.4%, consistent with the results of FTIR and TPD, indicating that there was a functional group of M-OH and a stronger acidic strength on the catalyst than the 7 M sulfated CaO catalyst. When the concentration of sulfuric acid increases, the amount of S atom distribution increases accordingly, resulting in a reduction in the pore volume of the catalyst. This is consistent with the results of BET surface area in Table 4 [29].

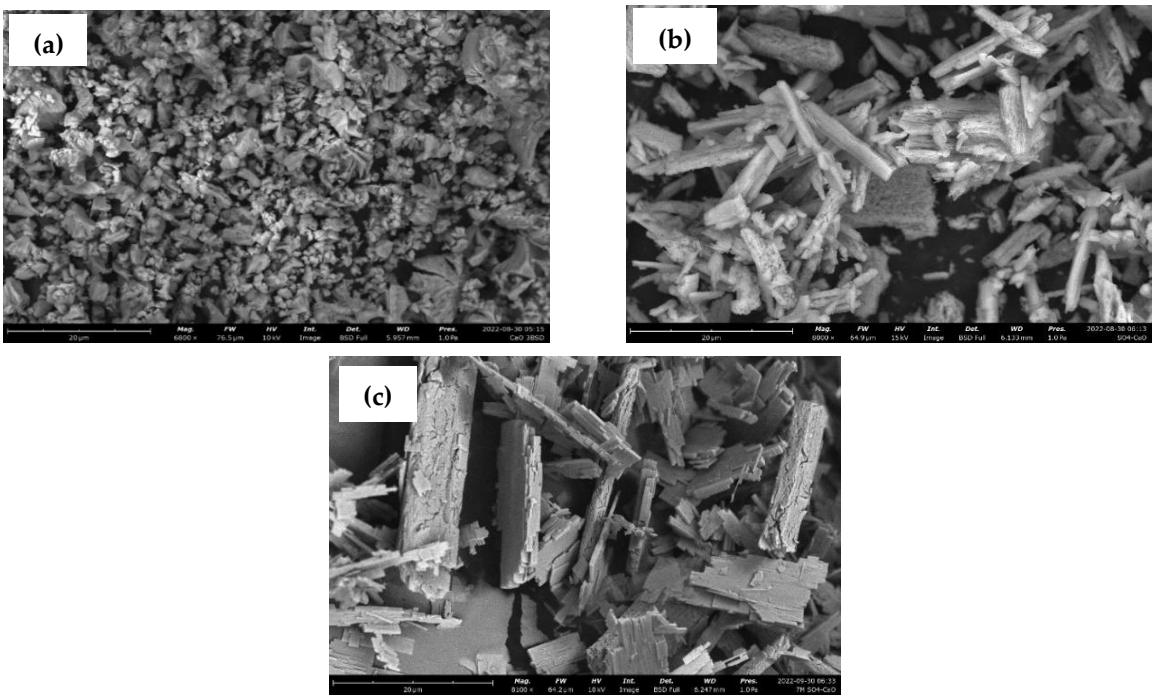


Figure 2. SEM images of a) bare CaO, b) 2 M sulfonated CaO, and c) 7 M sulfated CaO.

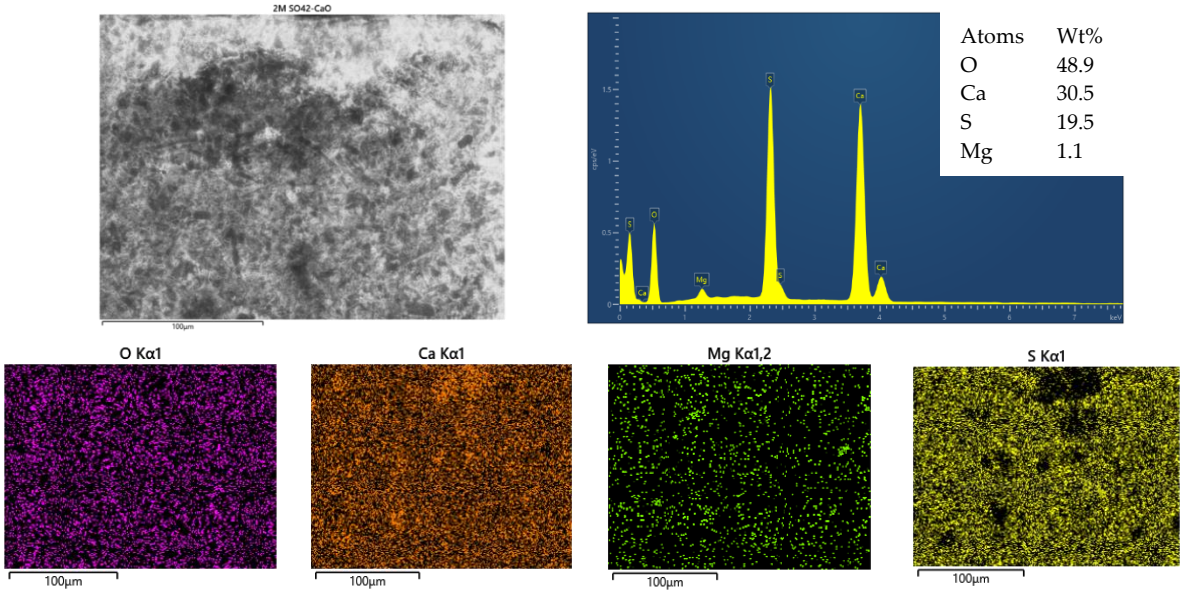


Figure 3. SEM-EDX image of 2 M sulfonated CaO catalyst.

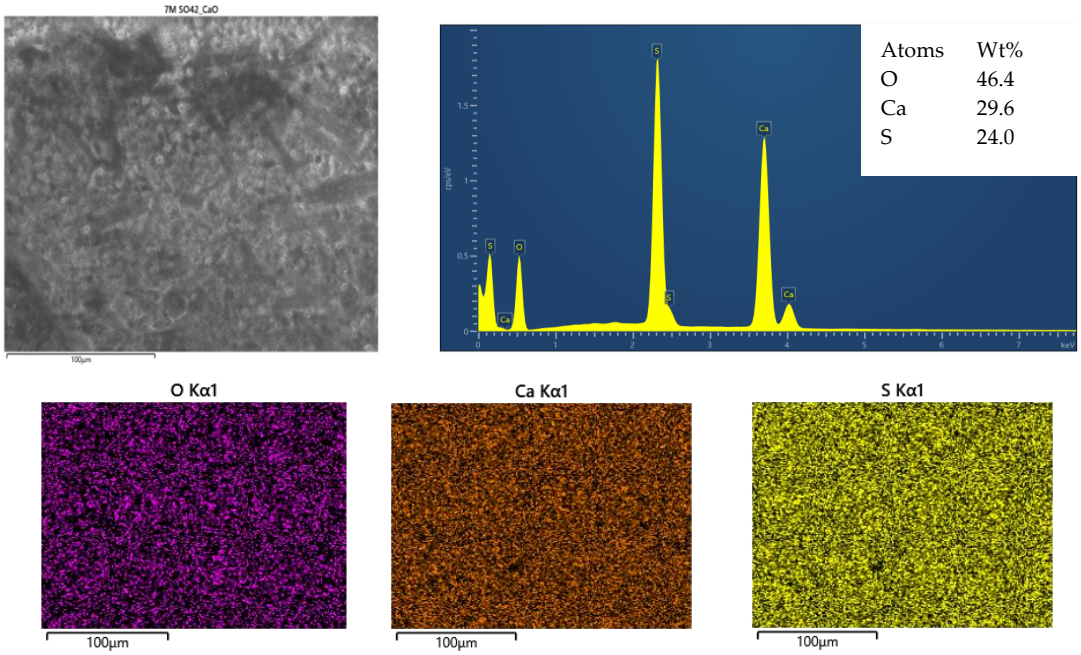


Figure 4. SEM-EDX image of 7 M sulfated CaO catalyst.

3.1.3 Crystal structure analysis of sulfonated/sulfated CaO catalysts

The phase and crystallinity of the 2 M sulfonated and 7 M sulfated CaO catalysts were determined, as shown in Figures 5a and 5b, respectively. The phase of $CaSO_4.2H_2O$ (JCPDS File: 21-0816) was observed. Figure 5a of the 2 M sulfonated CaO catalyst shows an XRD pattern at the 2θ position: 11.65, 20.76, 23.40, 31.12, 40.62, and 42.63, representing crystal planes at (020), (021), (040), (-221), (151), and (042) that have a monoclinic structure. The 7 M sulfated CaO catalyst showed XRD peaks at the 2θ position equal to 14.77, 25.72, 29.75, 31.84, and 49.32, which were similar to the hexagonal crystal form of $CaSO_4{\cdot}0.5H_2O$ (JCPDS File: 14-0224) [28], with follow crystal planes at (200), (020), (400), (204), and (424), respectively [30]. These XRD data demonstrated that the lattice anions of CaO had been replaced by sulfate ions, resulting in a new crystal structure of calcium sulfate.

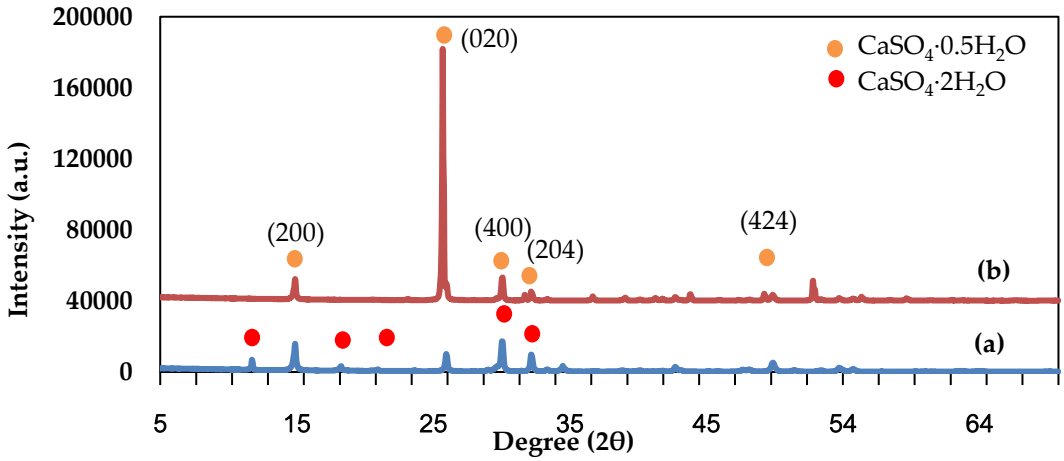


Figure 5. XRD patterns of (a) 2 M sulfonated CaO and (b) 7 M sulfated CaO catalysts.

3.1.3 Acidity-basicity analysis of sulfonated/sulfated CaO catalysts

The acidity-basicity of the sulfonated/sulfated CaO catalysts was investigated by TPD, as shown in Tables 2 and 3. By increasing the sulfuric acid concentration from 2 M to 7 M, the acid content of sulfonated CaO decreased from 7.22 to 0.05 mmol/g due to the structural change of CaO to $CaSO_4$. The NH_3-TPD profile (data not shown here) shows a desorption peak of NH_3 gas from the sulfonated CaO catalyst at a temperature of 200 °C, which indicates the presence of a weak acid site [14], while a peak position at 450–600 °C indicates the presence of a strong Lewis acid site. The data in Table 2 also shows that the 2 M sulfonated CaO catalyst had a higher acidity than the 7 M sulfated CaO catalyst. This acid content is also higher than that of the CAWS-$_{(7)}$ SO_4 catalyst (acid content of 4.73 mmol/g) prepared by Syazwani and co-workers [13] by burning angel wing shells and soaking them in 7 M sulfuric acid. It indicates that the 2 M sulfonated CaO catalyst may have more suitable catalytic properties than the 7 M sulfated CaO catalyst, which is consistent with the FTIR results indicating the -SO_3H group on the 2 M sulfonated CaO catalyst surface at 1151 cm^{-1}. This group acts as the activation and adsorption sites during the NH_3-TPD and catalytic processes. In addition, the basicity amounts of 2 M sulfonated CaO and 7 M sulfated CaO were 3.86 and 0.05 mmol/g, respectively, due to the adsorption of CO_2 on the residual Ca-O-Ca sites on the catalyst surface. [13, 31].

Table 2. NH_3-TPD and acidity data of sulfonated/sulfated CaO catalysts.

Catalysts	Temperature (°C)	Amount of NH_3 desorbed (mmol/g)	Total amount of acidity (mmol/g)
2 M sulfonated CaO	478.6	5.16	7.22
	741.2	2.06	
7 M sulfated CaO	93.2	0.02	0.05
	699.0	0.02	

Table 3. CO_2-TPD and basicity data of sulfonated/sulfated CaO catalysts.

Catalysts	Temperature (°C)	Amount of CO_2 desorbed (mmol/g)	Total amount of basicity (mmol/g)
2 M sulfonated CaO	97.1	0.05	3.86
	468.9	2.29	
	741.7	1.52	
7 M sulfated CaO	99.8	0.02	0.05
	680.6	0.03	

3.1.5 BET surface area investigation of sulfonated/sulfonated CaO catalysts.

The BET surface areas of the 2 M sulfonated and 7 M sulfated CaO catalysts were investigated, as shown in Table 4. Normally, the surface area of commercial CaO is equal to 3.98 m^2/g [28]. In this work, after chemical treatment with 2 and 7 M sulfuric acid, the surface area of the catalyst increased to 9.10 m^2/g and decreased to 3.51 m^2/g, respectively. This is because sulfonate ions from sulfuric acid are attached to the surface of CaO. When sulfuric acid concentration increases, the sulfate ions from the acid get stuck in CaO pores, decreasing the pore volume of the sulfated catalyst. This result is consistent with the SEM-EDX data in Figure 3, indicating an increase in the surface area of the 2 M sulfonated catalyst due to the sulfuric acid effect. Increasing surface area can increase reaction space and rate [20]. The nitrogen gas absorption and desorption profiles of the 2 M sulfonated and 7 M sulfated CaO catalysts are shown in Figure 5. The N_2-absorption and desorption of these catalysts represent a type IV adsorption isotherm, consisting of the multilayer adsorption of the gas sample with the mesopore size of the catalyst. The relative pressure region in the range of 0.0 to 0.1 shows monolayer adsorption; when the relative pressure increases, the adsorption still occurs, forming multilayers; then there is capillary condensation at a relative pressure range of 0.8 to 1, indicating a type 3 hysteresis loop [32]. In contrast to the CaO synthesized by [33] through calcination at 850 °C for 4 hours, the average pore diameter of the 2 M sulfonated CaO catalyst was 196.14 Å, which was greater than that of [33] (17.047 Å). Additionally, the pore volume was 0.045 cm^3/g, which was higher than the 0.036 cm^3/g synthesized

by [33] due to the reaction with sulfuric acid. The higher average pore diameter is possibly suitable for oil reactant mass transfer into the pore during catalysis.

Table 4. Surface properties of 2 M sulfonated and 7 M sulfated calcium oxide catalysts

Catalyst	BET surface area (m^2/g)	Average pore diameter (Å)	Pore volume (cm^3/g)
2 M sulfonated CaO	9.20	196.14	0.05
7 M sulfated CaO	3.51	190.32	0.02
CaO commercial [28]	3.98	3.82	0.02

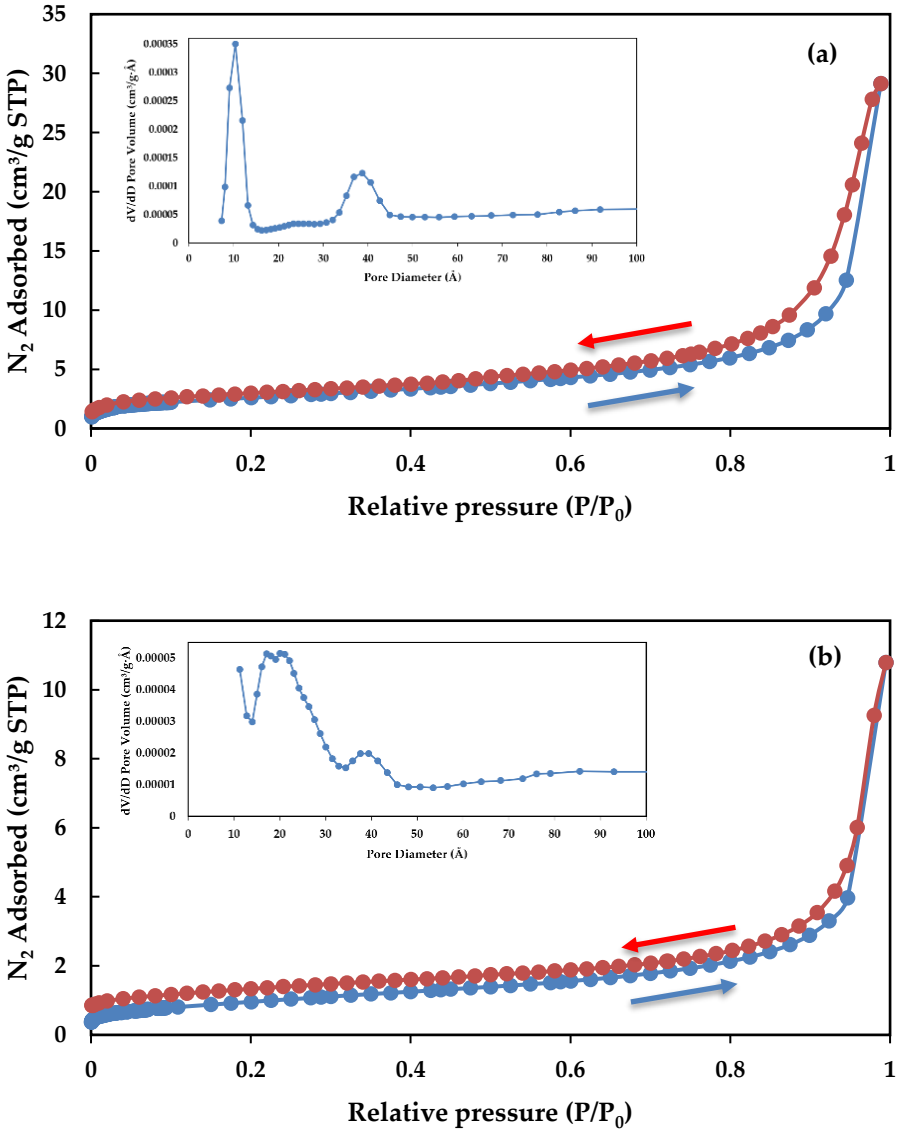


Figure 5. N_2-adsorption and desorption isotherms of (a) 2 M sulfonated calcium oxide and (b) 7 M sulfated calcium oxide catalysts with pore size distribution.

The inset in Figure 5 shows the pore size distribution of the sulfonated/sulfated CaO catalysts. It could be observed that upon chemical treatment of CaO with sulfuric acid, the CaO catalyst particles exhibited a pore size distribution that consisted of a primary pore at 10.41 Å and a secondary pore at 38.72 Å for 2 M sulfonated CaO, and a pore size distribution of 17.10, 21.06, and 39.46 Å for 7 M sulfated CaO. These pores can

be classified as mesopores [34]. Based on the characterization data, the 2 M sulfonated CaO catalyst was selected to catalyze esterification to produce biodiesel from WCO.

3.2 Optimization of biodiesel production

3.2.1 Effect of catalyst loading

The 2 M sulfonated CaO catalyst with various catalyst loadings of 3–9 wt%, a methanol to oil ratio of 9:1, and a reaction time of 3 h was selected to perform the esterification reaction at 65 °C. The biodiesel mass yield (%) and FFA conversion (%) are shown in Figure 6. It was found that the amount of catalysts in this work significantly affects the percentage of FFA conversion but is not significant for biodiesel mass yield (%). At the amount of catalyst equal to 5 wt%, the biodiesel mass yield is 61.19%, with the highest FFA conversion, 69.65%. The reaction may primarily be esterification; fatty acid interacts first at the Brønsted acid site of Ca-SO_3H, then methanol attacks to form an intermediate, thereby continuing the reaction [15]. However, when the amount of catalyst is greater than 5 wt%, FFA conversion slightly decreases due to a high amount of catalyst that affects the mixture's viscosity during mixing, resulting in poor interaction between oil and the catalyst. In addition, excess catalysts can adsorb the product on the catalyst's surface [35]. The 2 M sulfonated CaO catalyst in this work at 5 wt% catalyst gave a similar percentage when compared with the $SO_4^{2-}/Fe_3O_4–Al_2O_3$ catalyst at a catalyst dosage of 8 wt% for biodiesel production, showing FFA conversion was 66.8% [36]. Therefore, a catalyst amount of 5 wt% was selected to find the best condition.

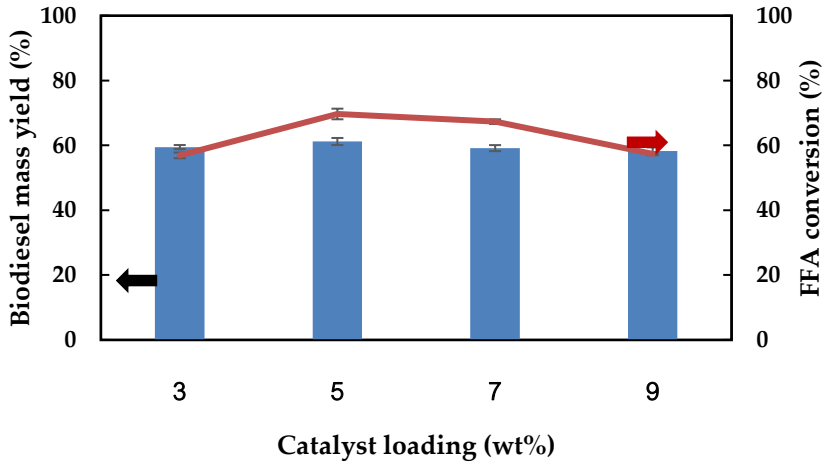


Figure 6. Effect of catalyst amount on biodiesel mass yield (%) and FFA conversion (%) using a methanol to oil ratio of 9:1, a temperature of 65 °C, and a reaction time of 3 h.

3.2.2 Effect of methanol to oil molar ratio

The effect of the methanol to oil ratio between 6:1, 9:1, and 15:1 using a 2 M sulfonated CaO catalyst at 5 wt%, a reaction time of 3 h, and a temperature of 65 °C were performed for the esterification reaction. The amount of methanol makes the reaction proceed forward to produce FAME. From Figure 7, the biodiesel mass yield is 66.77%, and the highest FFA conversion occurs at the methanol to oil ratio of 9:1. The FFA conversion obtained was 72.16%. When the methanol to oil ratio increased to 15:1, the mass yield and FFA conversion decreased to 65.65 and 67.64%, respectively. This data is consistent with data from the work of [31]; at the conditions of catalyst loading of 3.5 wt%, temperature of 150 °C, reaction time equal to 6 h, and methanol to oil molar ratio of 12:1, the amount of FFA conversion was equal to 83.26%. When the ratio of methanol to oil increases above 12:1, the FFA conversion (%) decreases as well due to two reasons: (1) the dissolution of glycerol in methanol inhibits the reaction with the reactant, and (2) excess methanol may reduce the active site of the catalyst and cause deactivation [36].

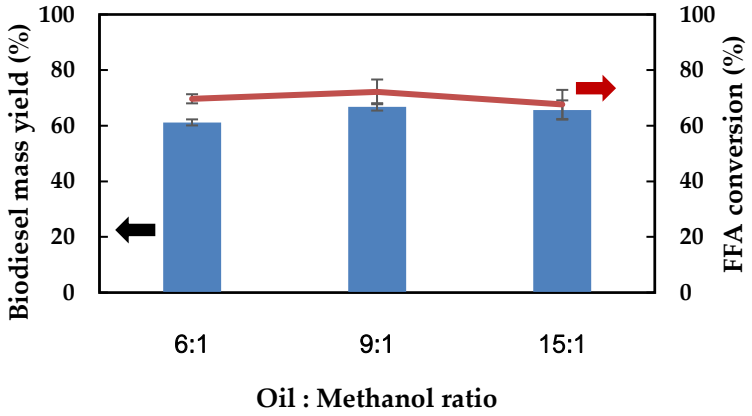


Figure 7. Effect of methanol to oil molar ratio on biodiesel mass yield (%) and FFA conversion (%) using 2 M sulfonated CaO, catalyst loading 5 wt%, temperature 65 °C, reaction time 3 h.

3.2.3 Effect of temperature

The 2 M sulfonated CaO catalyst with 5 wt% catalyst loading, a methanol: oil ratio of 9:1, and a reaction time of 3 hours was selected to perform the effect of esterification temperature, as shown in Figure 8. When the temperature increased from 55 to 70 °C, a mass yield of 68.93% and the highest FFA conversion of 84.93% were observed at a temperature of 65 °C, which is consistent with the work of Jamil and co-workers [37] at the temperature of 65 °C, with the highest biodiesel content being 94.27%. Normally, high temperatures used in the reaction increase the rate of the esterification reaction. The viscosities of methanol and oil decrease with high reaction temperatures, causing more homogeneity [38]. The effect of temperature on the reaction rate can be explained through the kinetic theory of chemical reactions. An increase in temperature results in higher molecular speeds and an increased reaction rate [39]. However, the reaction at temperatures higher than 70 °C was not possible in this work due to the limitations of the apparatus and the reflux temperature of methanol under normal pressure [40]. Thus, the FFA conversion in this work decreased from 84.93 to 37.89% when the temperature increased. The methanol used in the reaction evaporates and cannot be condensed to react with the oil [41].

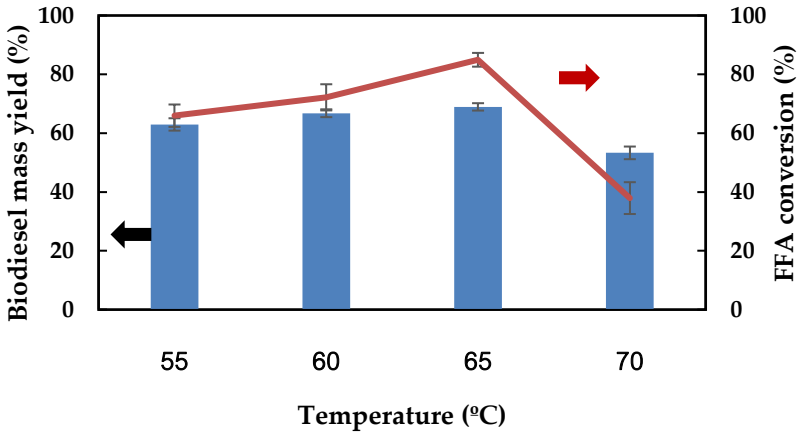


Figure 8. Effect of temperature on FFA conversion using 2 M sulfonated CaO at 5 wt%, methanol to oil molar ratio was 9:1, and reaction time of 3 h.

3.2.4 Effect of reaction time

The effect of reaction time at 3, 6, and 9 hours for esterification of WCO was investigated using the 2 M sulfonated CaO catalyst with 5 wt% catalyst loading, a methanol: oil ratio of 9:1, and a temperature of 65 °C. The result is shown in Figure 9. At 3 hours, the mass yield was 66.96%, and the FFA conversion was 84.93%.

When the reaction time increases by 6 and 9 hours, the FFA conversion decreases to 77.17 and 71.97%, respectively. The decrease in FFA conversion is consistent with the work of [42], with the highest biodiesel amount equaling 94.6% at reaction time 3. h. After 3 hours, FFA conversion gradually decreased to a similar level. At first, the biodiesel reaction may be low due to the reactants' low compatibility. Then, as the duration increases, compatibility increases. However, if the reaction time exceeds 3 hours, the higher product concentration gradually reduces the biodiesel yield, leading to a quick reaction reverse [43]. The best reaction time when using a homogeneous catalyst is generally 30–120 minutes [44], while the best reaction time for heterogeneous catalysts is 180 minutes or 3 hours [45]. The 2 M sulfonated CaO catalyst used in this work was also optimized at 3 hours, and the best condition was that the catalyst amount was 5 wt%, the methanol: oil ratio was 9:1, and the temperature was 65 °C. Table 5 shows that the acid value of the biodiesel product is 0.18 mg KOH/g of the sample, which is lower than the maximum limit of Thailand's standard biodiesel. Furthermore, the viscosity at 40 °C and density at 15 °C of the biodiesel product in this work fall in the standard range. According to Giakoumis and co-workers [46], the viscosity of the produced fuel influences its fluidity and atomization; a higher viscosity could result in poor atomization and less accurate fuel injector operation.

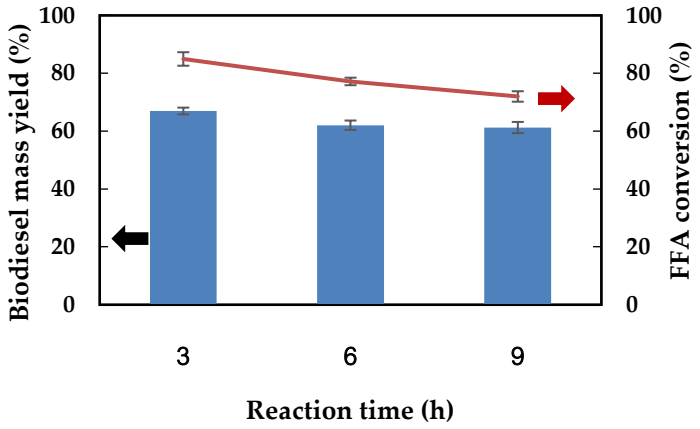


Figure 9. Effect of reaction time on FFA conversion using 2 M sulfonated CaO at 5 wt%, methanol to oil ratio of 9:1, and a temperature of 65 °C.

Table 5. Characteristics and important qualities of biodiesel product using catalyst content of 5 wt%, methanol: oil ratio of 9:1, temperature of 65 ºC, and 3 h reaction times.

Requirements		Thailand standard range	WCO	biodiesel
Density at 15 °C	kg/cm^3	860-900	949.67 ± 3.86	873.43 ± 19.81
Viscosity at 40 °C	cSt	3.5-5.0	14.81 ± 1.34	4.36 ± 0.60
Acid value	mg$_{KOH}$/g	<0.5	1.4 ± 0.24	0.18 ± 0.05
Iodine value	g I_2/100 g	<120	88.22 ± 1.29	27.42 ± 3.44

3.2.5 Reusability of sulfonated CaO catalyst

Ideal catalysts can be reused many times before deactivation takes place. In this work, the catalyst obtained from the optimum condition was washed with n-hexane and methanol and then dried at 70 °C for 12 hours before the next esterification reaction. The reusability data is shown in Figure 10. The percentage of FFA conversion gradually decreased with the reuse of the catalyst in the 3rd round and significantly decreased in the 4th and 5th rounds. The decrease in FFA conversion may be due to the deactivation of the catalyst, causing coke or chemical residues at the active sites with unreacted oil and glycerol [47], which is consistent with the SEM image in Figure 11, indicating a change in the size of the catalyst to larger sizes than a fresh catalyst, which affects the surface area of the catalyst. Thus, the surface area of the catalyst reduces after the catalysis of esterification. In addition, glycerol may remain adsorbed on the surface of the catalyst. This is consistent with the FTIR results as shown in Figure 12, with peaks appearing at wavenumber 2919 and 1467 cm^{-1},

representing the vibrational of the C-H bond stretching for alkane and O-CH_2 groups, respectively, which may be glycerol and mono, di, and triglycerides remaining on the surface of the catalyst. However, an FTIR peak at 1151 cm^{-1} is still observed, which is an asymmetric stretching vibration of the O=S=O of sulfonate groups [12, 14, 15] and 1093 cm^{-1} represents the symmetric stretching of O=S=O in -SO_3^- [12, 15, 18, 20, 22-24]. The ions do not easily escape during biodiesel production due to the strong bond between the calcium group's positive charge and the sulfonate group negative charge [15, 20].

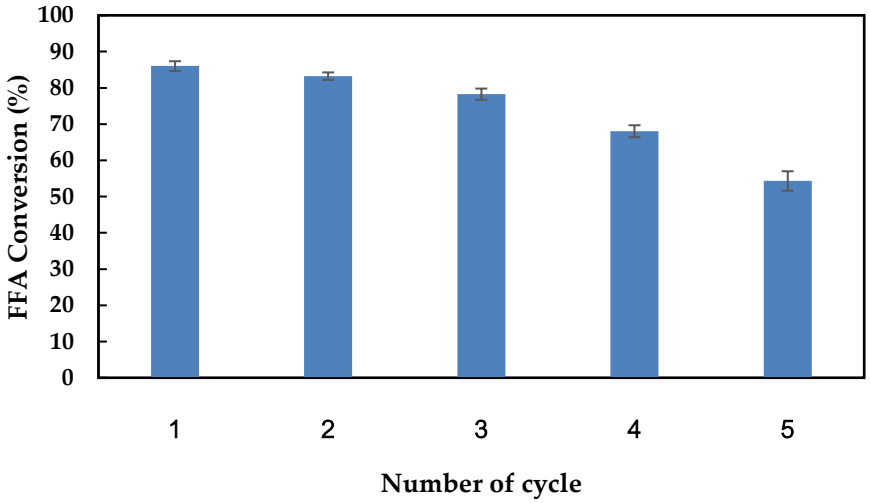


Figure 10. Effect of reuse of a 2 M sulfonated CaO catalyst at 5 wt%, methanol to oil ratio of 9:1, the temperature of 65 °C, and 3 h reaction time.

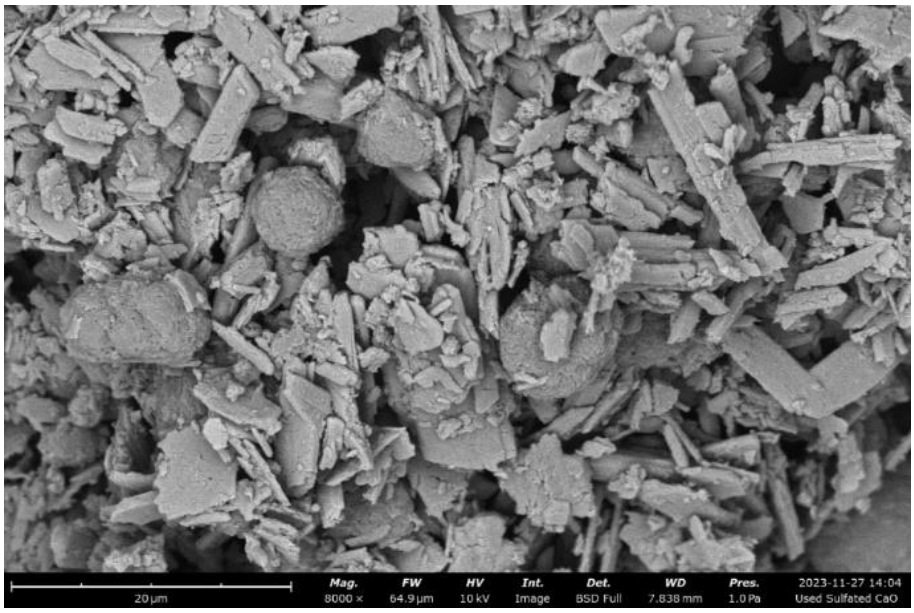


Figure 11. SEM images of reuse 2 M sulfonated CaO.

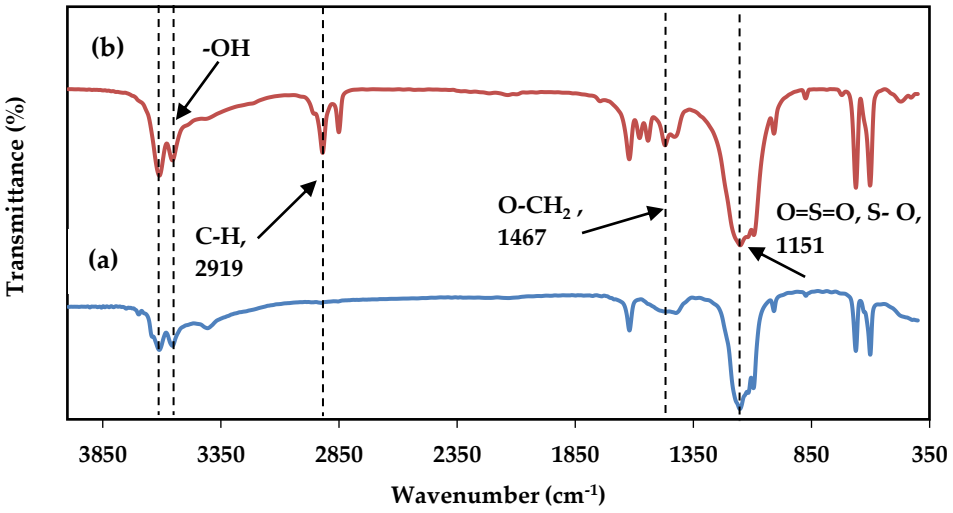


Figure 12. FTIR spectra of (a) fresh 2 M sulfonated CaO and (b) used 2 M sulfonated CaO catalyst.

3.2.6. Proposed mechanism of esterification catalyzed by sulfonated CaO catalyst

The reaction mechanism for the esterification of WCO by the 2 M sulfonated CaO catalyst to produce biodiesel is proposed in Figure 13 based on FTIR and TPD data. When the electrophilic carbonyl group or carboxylic acid group (-COOH) in the FFA molecule reacts with a proton (H^+) at the Brønsted acid sites ($-SO_3H$), a carbocation is formed on the surface of the catalyst. Then, the methanol molecule attacks the carbocation to form an intermediate. A proton shifts from the oxonium ion to the -OH group, forming an activated complex. These intermediates proceed to eliminate a water molecule, resulting in a protonated alkyl ester. The desorption of the alkyl ester from the Brønsted acid site (deprotonation) restores the catalyst [15, 48]. Lewis acid sites (metal ions in low coordination) can also catalyze esterification, as proposed in Figure 14. The presence of Ca active sites in the catalyst can cause strong bonds with the carbonyl oxygen to form intermediate complexes, followed by interactions between the oxygen atoms of methanol and carbonyl carbon. The next step involves the loss and gain of a proton at one oxygen atom to form another intermediate, which in turn loses a water molecule and yields a protonated ester [48]. However, the adsorption of FFA molecules at Lewis acid sites may occur less than at Brønsted acid sites due to the large size of the FFA.

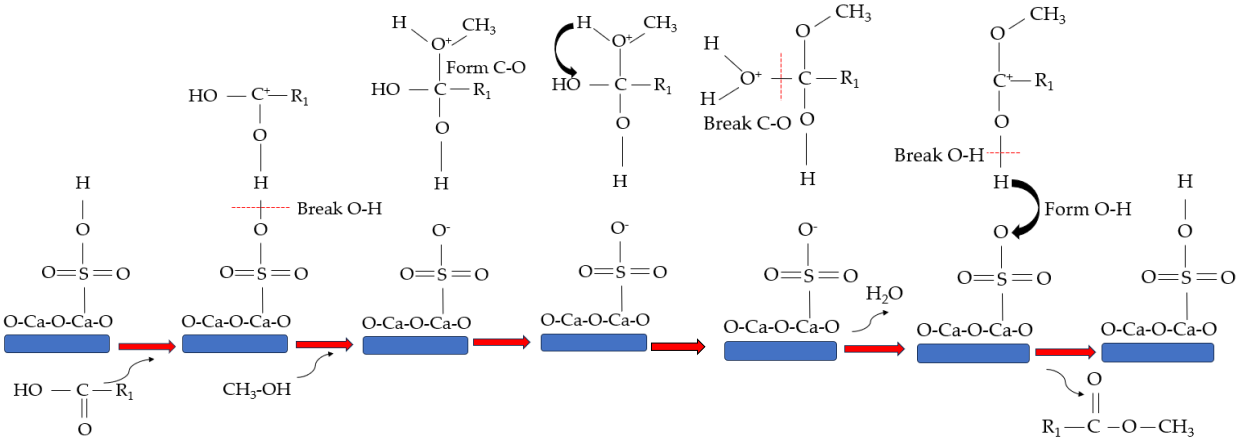


Figure 13. Propose mechanism of esterification using 2 M sulfonated CaO catalyst through Brønsted acid site.

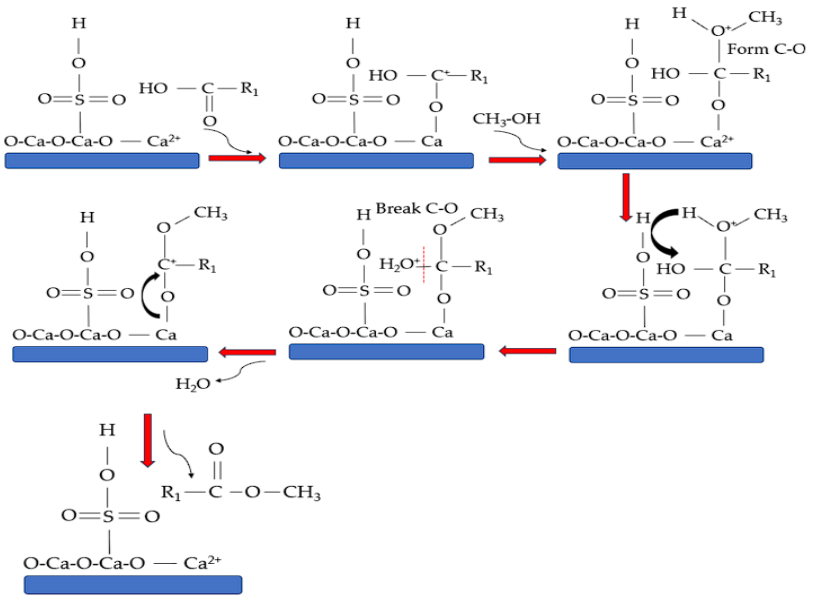


Figure 14. Propose esterification mechanism using 2 M sulfonated CaO catalyst through Lewis acid sites.

4. Conclusions

Sulfonation CaO successfully prepared the low-cost sulfonated CaO catalyst in sulfuric acid at a concentration of 2 M. The surface area increased from 3.98 to 9.20 m^2/g due to this process. The 2 M sulfonated CaO catalyst was found to have an acidity of 7.22 mmol/g and a basicity of 3.86 mmol/g. The optimum conditions for the esterification of WCO to produce biodiesel were determined by utilizing a 2 M sulfonated CaO catalyst, a methanol to oil ratio of 9:1, a reaction time of 3 hours, and a catalyst quantity of 5 wt%. The reaction was conducted at a temperature of 65 ˚C. The efficiency of FFA conversion was 84.9% in the reaction catalyzed by a 2 M sulfonated CaO catalyst. Additionally, the catalyst can be reused at least 2 times by washing it with n-hexane and methanol, provided that optimal conditions are maintained. This cost-effective sulfonated CaO catalyst exhibits promise for further exploration as an industrial catalyst in biodiesel production from edible and non-edible oils with a high free fatty acid, including waste cooking oil.

5. Acknowledgements

Author Contributions: Investigation, writing—original draft preparation: C.D.; conceptualization, methodology: R.J. and P.K.; writing-review and editing: T.C.; supervision, writing-review, and editing: S.C. All authors have read and agreed to the published version of the manuscript.

Funding: This research was financially supported by the Graduate School Dissertation Funding for Thesis, Prince of Songkla University, and Tuition Fee Grants for Graduate Students, Faculty of Science and Technology, Prince of Songkla University.

Conflicts of Interest: The authors declare no conflict of interest.

References

[1] Farabi, M. S. A.; Ibrahim, M. L.; Rashid, U.; Taufiq-Yap, Y. H. Esterification of palm fatty acid distillate using sulfonated carbon-based catalyst derived from palm kernel shell and bamboo. *Energy Conversion and Management* **2019**, *181*(September 2018), 562–570. https://doi.org/10.1016/j.enconman.2018.12.033

[2] Amenaghawon, A. N.; Obahiagbon, K.; Isesele, V.; Usman, F. Optimized biodiesel production from waste cooking oil using a functionalized bio-based heterogeneous catalyst. *Cleaner Engineering and Technology* 2022, *8*(April), 1-11. 100501. https://doi.org/10.1016/j.clet.2022.100501

[3] Baskar, G.; Kalavathy, G.; Aiswarya, R.; Abarnaebenezer Selvakumari, I. Advances in bio-oil extraction from nonedible oil seeds and algal biomass. *In Advances in Eco-Fuels for a Sustainable Environment* **2019**, 187–210. Elsevier. https://doi.org/10.1016/B978-0-08-102728-8.00007-3

[4] Okoduwa, I. G.; Oiwoh, O.; Amenaghawon, A. N.; Okieimen, C. O. A biobased mixed metal oxide catalyst for biodiesel production from waste cooking oil: reaction conditions modeling, optimization and sensitivity analysis study. *Journal of Engineering Research (Kuwait)* **2024**, February. https://doi.org/10.1016/j.jer.2024.03.009

[5] Deeba, F.; Kumar, B.; Arora, N.; Singh, S.; Kumar, A.; Han, S. S.; Negi, Y. S. Novel bio-based solid acid catalyst derived from waste yeast residue for biodiesel production. *Renewable Energy* **2020**, *159*, 127–139. https://doi.org/10.1016/j.renene.2020.05.029

[6] Chanakaewsomboon, I.; Tongurai, C.; Photaworn, S.; Kungsanant, S.; Nikhom, R. Investigation of saponification mechanisms in biodiesel production: Microscopic visualization of the effects of FFA, water and the amount of alkaline catalyst. *Journal of Environmental Chemical Engineering* **2020**, *8*(2), 1-40. https://doi.org/10.1016/j.jece.2019.103538

[7] Etim, A. O.; Musonge, P.; Eloka-Eboka, A. C. An effective green and renewable heterogeneous catalyst derived from the fusion of bi-component biowaste materials for the optimized transesterification of linseed oil methyl ester. *Biofuels, Bioproducts and Biorefining* **2021**, *15*(5), 1461–1472. https://doi.org/10.1002/bbb.2252

[8] Kedir, W. M.; Wondimu, K. T.; Weldegrum, G. S. Optimization and characterization of biodiesel from waste cooking oil using modified CaO catalyst derived from snail shell. *Heliyon* **2023**, *9*(5), e16475. https://doi.org/10.1016/j.heliyon.2023.e16475

[9] Faruque, M. O.; Razzak, S. A.; Hossain, M. M. Application of heterogeneous catalysts for biodiesel production from microalgal oil—a review. *Catalysts* **2020**, *10*(9), 1–25. https://doi.org/10.3390/catal10091025

[10] Al-Saadi, A.; Mathan, B.; He, Y. Biodiesel production via simultaneous transesterification and esterification reactions over SrO–ZnO/Al_2O_3 as a bifunctional catalyst using high acidic waste cooking oil. *Chemical Engineering Research and Design* **2020**, *162*(2018), 238–248. https://doi.org/10.1016/j.cherd.2020.08.018

[11] Chen, G. Y.; Shan, R.; Yan, B. B.; Shi, J. F.; Li, S. Y.; Liu, C. Y. Remarkably enhancing the biodiesel yield from palm oil upon abalone shell-derived CaO catalysts treated by ethanol. *Fuel Processing Technology*, **2016**, *143*, 110–117. https://doi.org/10.1016/j.fuproc.2015.11.017

[12] Istadi, I.; Anggoro, D. D.; Buchori, L.; Rahmawati, D. A.; Intaningrum, D. Active acid catalyst of sulphated zinc oxide for transesterification of soybean oil with methanol to biodiesel. *Procedia Environmental Sciences* **2015**, *23*, 385–393. https://doi.org/10.1016/j.proenv.2015.01.055

[13] Syazwani, O. N.; Rashid, U.; Mastuli, M. S.; Taufiq-Yap, Y. H. Esterification of palm fatty acid distillate (PFAD) to biodiesel using Bi-functional catalyst synthesized from waste angel wing shell (*Cyrtopleura costata*). *Renewable Energy* **2019**, *131*, 187–196. https://doi.org/10.1016/j.renene.2018.07.031

[14] Syazwani, O. N.; Ibrahim, M. L.; Wahyudiono, Kanda, H.; Goto, M.; Taufiq-Yap, Y. H. Esterification of high free fatty acids in supercritical methanol using sulfated angel wing shells as catalyst. *Journal of Supercritical Fluids* **2017**, *124*, 1–9. https://doi.org/10.1016/j.supflu.2017.01.002

[15] Valizadeh, S.; Valizadeh, B.; Khani, Y.; Jae, J.; Hyun Ko, C.; Park, Y. K. Production of biodiesel via esterification of coffee waste-derived bio-oil using sulfonated catalysts. *Bioresource Technology* **2024**, *404*(May), 130908. https://doi.org/10.1016/j.biortech.2024.130908

[16] Kouzu, M.; Kasuno, T.; Tajika, M.; Sugimoto, Y.; Yamanaka, S.; Hidaka, J. Calcium oxide as a solid base catalyst for transesterification of soybean oil and its application to biodiesel production. *Fuel* **2008**, 87(12), 2798–2806. https://doi.org/10.1016/j.fuel.2007.10.019

[17] Kiefer, J.; Strk, A.; Kiefer, A. L.; Glade, H. Infrared spectroscopic analysis of the inorganic deposits from water in domestic and technical heat exchangers. *Energies* **2018**, *11*(4). https://doi.org/10.3390/en11040798

[18] Juan-Alcañiz, J.; Gielisse, R.; Lago, A.B.; Ramos-Fernandez, E.V.; Serra-Crespo, P.; Devic, T.; Guillou, N. Serre, C.; Kapteijna, F.; Gascon; J. Towards acid MOFs-catalytic performance of sulfonic acid functionalized architectures. *Catalysis Science & Technology* **2013**, *3*(9), 2311–2318, https://doi: 10.1039/c3cy00272a

[19] Nayebzadeh, H.; Hojjat, M. Fabrication of SO_4^{2-}/MO–Al_2O_3–ZrO_2 (M = Ca, Mg, Sr, Ba) as solid acid–base nanocatalyst used in trans/esterification reaction. *Waste and Biomass Valorization*, **2020**, *11*(5), 2027–2037. https://doi.org/10.1007/s12649-018-0526-0

[20] Liu, F.; Ma, X.; Li, H.; Wang, Y.; Cui, P.; Guo, M.; Yaxin, H.; Lu, W.; Zhou, S.; Yu, M. Dilute sulfonic acid post functionalized metal organic framework as a heterogeneous acid catalyst for esterification to produce biodiesel. Fuel, **2020**, *266*(January), 117149. https://doi.org/10.1016/j.fuel.2020.117149

[21] Hussein, A. I.; Ab-Ghani, Z.; Mat, A. N. C.; Ghani, N. A. A.; Husein, A.; Rahman, I. A. Synthesis and characterization of spherical calcium carbonate nanoparticles derived from cockle shells. *Applied Sciences (Switzerland)* **2020**, *10*(20), 1–14. https://doi.org/10.3390/app10207170

[22] Farabi, M. S. A.; Ibrahim, M. L.; Rashid, U., Taufiq-Yap, Y. H. Esterification of palm fatty acid distillate using sulfonated carbon-based catalyst derived from palm kernel shell and bamboo. *Energy Conversion and Management* **2019**, *181*(September), 562–570. https://doi.org/10.1016/j.enconman.2018.12.033

[23] Xiong, X.; Yu, I. K. M.; Chen, S. S.; Tsang, D. C. W.; Cao, L.; Song, H.; Kwon, E. E.; Ok, Y. S.; Zhang, S.; Poon, C. S. Sulfonated biochar as acid catalyst for sugar hydrolysis and dehydration. *Catalysis Today* **2018**, *314*(February), 52–61. https://doi.org/10.1016/j.cattod.2018.02.034

[24] Melo H. P.; Cruz, A. J.; Candeias, A.; Mirão, J.; Cardoso, A. M.; Oliveira, M. J.; Valadas, S. Problems of analysis by FTIR of calcium sulphate-based preparatory layers: The case of a group of 16th-century Portuguese paintings. *Archaeometry* **2014**, *56*(3), 513–526. https://doi: 10.1111/arcm.12026

[25] Tangboriboon, N.; Unjan, W.; Sangwan, W.; Sirivat, A. Preparation of anhydrite from eggshell via pyrolysis. *Green Processing and Synthesis* **2018**, *7*(2), 139–146. https://doi.org/10.1515/gps-2016-0159

[26] McQuillan, A. J.; Osawa, M.; Peak, D.; Ren, B.; Tian, Z. Q. Experiments on adsorption at hydrous metal oxide surfaces using attenuated total reflection infrared spectroscopy (ATRIRS) (IUPAC Technical Report). *Pure and Applied Chemistry*, **2019**, *91*(12), 2043–2061. https://doi.org/10.1515/pac-2019-0211

[27] Ali, R. M.; Abd El Latif, M. M; Farag, H. A. Preparation and characterization of $CaSO_4$–SiO_2–CaO/SO_4^{2-} composite for biodiesel production. *American Journal of Applied Chemistry* **2015**, *3*(3-1), 38-45. https://doi: 10.11648/j.ajac.s.2015030301.16.

[28] Zhu, Z.; Liu, Y.; Cong, W.; Zhao, X.; Janaun, J.; Wei, T.; Fang, Z. Soybean biodiesel production using synergistic CaO/Ag nano catalyst: Process optimization, kinetic study, and economic evaluation. *Industrial Crops and Products* **2021**, *166*(666), 113479. https://doi.org/10.1016/j.indcrop.2021.113479

[29] Shi, G.; Yu, F.; Wang, Y.; Pan, D.; Wang, H.; Li, R. A novel one-pot synthesis of tetragonal sulfated zirconia catalyst with high activity for biodiesel production from the transesterification of soybean oil. *Renewable Energy* **2016**, *92*, 22–29. https://doi.org/10.1016/j.renene.2016.01.094

[30] Zhang, G.; Cao, D.; Wang, X.; Guo, S.; Yang, Z.; Cui, P.; Wang, Q.; Dou, Y.; Cheng, S.; Shen, H. α-calcium sulfate hemihydrate with a 3D hierarchical straw-sheaf morphology for use as a remove Pb^{2+} adsorbent. *Chemosphere* **2022**, *287*. https://doi.org/10.1016/j.chemosphere.2021.132025

[31] Marchetti, J. M.; Pedernera, M. N.; Schbib, N. S. Production of biodiesel from acid oil using sulfuric acid as catalyst: Kinetics study. *International Journal of Low-Carbon Technologies* **2011**, *6*(1), 38–43. https://doi.org/10.1093/ijlct/ctq040

[32] Ganesan, S.; Nadarajah, S.; Chee, X. Y.; Khairuddean, M.; Teh, G. B. Esterification of free fatty acids using ammonium ferric sulphate-calcium silicate as a heterogeneous catalyst. *Renewable Energy* **2020**, *153*, 1406–1417. https://doi.org/10.1016/j.renene.2020.02.094

[33] Sunarno, Zahrina, I.; Reni Yenti, S.; Sri Irianty, R.; Setia Utama, P. Catalytic co-pyrolysis of palm oil empty fruit bunch and waste tire using calcium oxide catalysts for upgrading bio-oil. *Materials Today: Proceedings* **2023**, *87*, 321–326. https://doi.org/10.1016/j.matpr.2023.03.290

[34] Lani, N. S.; Ngadi, N.; Yahya, N. Y.; Rahman, R. A. Synthesis, characterization and performance of silica impregnated calcium oxide as heterogeneous catalyst in biodiesel production. *Journal of Cleaner Production* **2017**, *146*, 116–124. https://doi.org/10.1016/j.jclepro.2016.06.058

[35] Farooq, M.; Ramli, A.; Subbarao, D. Biodiesel production from waste cooking oil using bifunctional heterogeneous solid catalysts. *Journal of Cleaner Production* **2013**, *59*, 131–140. https://doi.org/10.1016/j.jclepro.2013.06.015

[36] Safakish, E.; Nayebzadeh, H.; Saghatoleslami, N.; Kazemifard, S. Comprehensive assessment of the preparation conditions of a separable magnetic nanocatalyst for biodiesel production from algae. *Algal Research* **2020**, *49*(May), 101949. https://doi.org/10.1016/j.algal.2020.101949

[37] Jamil, F.; Murphin Kumar, P. S.; Al-Haj, L.; Tay Zar Myint, M.; Al-Muhtaseb, A. H. Heterogeneous carbon-based catalyst modified by alkaline earth metal oxides for biodiesel production: parametric and kinetic study. *Energy Conversion and Management: X* **2021**, *10*(May 2020), 100047. 1-10. https://doi.org/10.1016/j.ecmx.2020.100047

[38] Abdelhady, H. H.; Elazab, H. A.; Ewais, E. M.; Saber, M.; El-Deab, M. S. Efficient catalytic production of biodiesel using nano-sized sugar beet agro-industrial waste. *Fuel* **2020**, *261*(October 2019), 116481. 1-12. https://doi.org/10.1016/j.fuel.2019.116481

[39] Abbah, E. C.; Nwandikom, G. I.; Egwuonwu, C. C.; Nwakuba, N. R. Effect of reaction temperature on the yield of biodiesel from neem seed oil. *American Journal of Energy Science* **2016**, *3*(3), 16–20. http://www.openscienceonline.com/journal/energy

[40] Xie, W.; Wan, F. Basic ionic liquid functionalized magnetically responsive Fe_3O_4@HKUST-1 composites used for biodiesel production. *Fuel* **2018**, *220*(February), 248–256. https://doi.org/10.1016/j.fuel.2018.02.014

[41] Hazmi, B.; Rashid, U.; Ibrahim, M. L.; Nehdi, I. A.; Azam, M.; Al-Resayes, S. I. Synthesis and characterization of bifunctional magnetic nano-catalyst from rice husk for production of biodiesel. *Environmental Technology and Innovation* **2021**, 21, 101296. https://doi.org/10.1016/j.eti.2020.101296

[42] Mokhatr Mohamed, M.; El-Faramawy, H. An innovative nanocatalyst α-Fe_2O_3/AlOOH processed from gibbsite rubbish ore for efficient biodiesel production via utilizing cottonseed waste oil. *Fuel* **2021**, *297*(May 2020), 120741. https://doi.org/10.1016/j.fuel.2021.120741

[43] Xia, S.; Li, J.; Chen, G.; Tao, J.; Li, W.; Zhu, G. Magnetic reusable acid-base bifunctional Co Doped $Fe2O_3$–CaO nanocatalysts for biodiesel production from soybean oil and waste frying oil. *Renewable Energy* **2022**, *189*, 421–434. https://doi.org/10.1016/j.renene.2022.02.122

[44] Verma, P.; Sharma, M. P. Review of process parameters for biodiesel production from different feedstocks. *Renewable and Sustainable Energy Reviews* **2016**, *62*, 1063–1071. https://doi.org/10.1016/j.rser.2016.04.054

[45] Ruhul, A. M.; Kalam, M. A.; Masjuki, H. H.; Fattah, I. M. R.; Reham, S. S.; Rashed, M. M. State of the art of biodiesel production processes: A review of the heterogeneous catalyst. *RSC Advances* **2015**, *5*(122), 101023–101044. https://doi.org/10.1039/c5ra09862a

[46] Giakoumis, E. G. A statistical investigation of biodiesel physical and chemical properties, and their correlation with the degree of unsaturation. *Renewable Energy* **2013**, *50*, 858–878. https://doi.org/10.1016/j.renene.2012.07.040

[47] Abdullah, R. F.; Rashid, U.; Ibrahim, M. L.; Hazmi, B.; Alharthi, F. A.; Nehdi, I. A. Bifunctional nano-catalyst produced from palm kernel shell via hydrothermal-assisted carbonization for biodiesel production from waste cooking oil. *Renewable and Sustainable Energy Reviews* **2021**, *137*(May 2020), 110638. https://doi.org/10.1016/j.rser.2020.110638

[48] Alam, M. A.; Deng, L.; Ngatcha, A. D. P.; Fouegue, A. D. T.; Wu, J.; Zhang, S.; Zhao, A.; Xiong, W.; Xu, J. Biodiesel production from microalgal biomass by Lewis acidic deep eutectic solvent catalysed direct transesterification. *Industrial Crops and Products* **2023**, *206*(May), 117725. https://doi.org/10.1016/j.indcrop.2023.117725

ASEAN
Journal of Scientific and Technological Reports
Online ISSN:2773-8752

Research article

Biological Oxidation of Dissolved Methane in Palm Oil Mill Biogas Effluents Using an Anoxic Methane-Oxidizing Consortium

Chonticha Leamdum[1, 5], Chaisit Niyasom[2], Sukonlarat Chanthong[3, 5], and Nantharat Phruksaphithak[4, 5*]

[1] International College, Thaksin University, Songkhla 90000, Thailand
[2] Department of Biology, Faculty of Science and Digital Innovation, Thaksin University, Phatthalung 93210, Thailand;
[3] Bio4gas (Thailand) Company Limited, Phatthalung 93210, Thailand
[4] Department of Chemistry, Faculty of Science and Digital Innovation, Thaksin University, Phatthalung 93210, Thailand
[5] Center of Excellence for Agricultural Innovation and Bioproducts of Thaksin University, Phatthalung 93210, Thailand
* Correspondence: nantharat@tsu.ac.th; (N. Phruksaphithak)

Citation:
Leamdum, C., Niyasom, C., Chanthong, S., Phruksaphithak, N. Biological oxidation of dissolved methane in palm oil mill biogas effluents using an anoxic methane-oxidizing consortium. *ASEAN J. Sci. Tech. Report.* **2025**, *28*(1), e255940. https://doi.org/10.55164/ajstr.v28i1.255940

Article history:
Received: September 17, 2024
Revised: October 31, 2024
Accepted: November 2, 2024
Available online: December 14, 2024

Publisher's Note:
This article has been published and distributed under the terms of Thaksin University.

Abstract: This study investigated the potential of anoxic methane-oxidizing consortia This study investigated the potential of anoxic methane-oxidizing consortia for mitigating dissolved methane in palm oil mill biogas effluents. Microbial consortia from five soil sources were evaluated under various conditions. The cattle farm effluent-derived consortium demonstrated the highest methane reduction efficiency of 76.89% after a 3-week incubation period, with a methane consumption rate of 49.37 mg-CH_4/m^2/d. The landfill soil consortium showed the second-highest performance with a 75.48% reduction efficiency under shaking conditions. Environmental factors significantly influenced methane oxidation performance. Optimal conditions were identified as 35°C, pH 7.0, 0.5 mg/L dissolved oxygen, 55 mg/L nitrate concentration, and 5 g/L NaCl. Plastic media enhanced methane reduction efficiency for most microbial sources, particularly for the cattle farm effluent consortium (67.07% efficiency). Characterization of the palm oil mill biogas effluent revealed a COD of 13.15 g/L, BOD of 7.11 g/L, and total Kjeldahl nitrogen of 0.73 g/L. Carbon mass balance analysis confirmed biological methane oxidation, with 45% converted to CO_2, 38% incorporated into biomass, and 12% as dissolved organic carbon. The developed system can potentially mitigate up to 23,067 t CO_2e/year for an average palm oil mill, with associated cost savings of approximately 115,335 USD/year through carbon credits, assuming a credit value of 5 USD/t CO_2e. These findings demonstrate the potential of anoxic methane-oxidizing consortia for greenhouse gas mitigation in the palm oil industry. The study provides insights into optimal conditions and microbial sources for efficient methane oxidation, paving the way for developing effective biological treatment systems for palm oil mill effluents.

Keywords: Anoxic methane oxidation; Palm oil mill effluent; Greenhouse gas mitigation; Microbial consortia; Biogas treatment

1. Introduction

The global palm oil industry has experienced rapid growth in recent decades, with production increasing from 15.2 million tonnes in 1995 to 77.28 million tonnes in 2024 [1]. This expansion has led to a significant increase in palm

oil mill effluent (POME), a high-strength wastewater generated during palm oil extraction. POME is characterized by its high organic content, with chemical oxygen demand (COD) typically ranging from 50,000 to 70,000 mg/L [2]. The substantial organic load of POME makes it an ideal feedstock for biogas production through anaerobic digestion. Biogas production from POME offers a promising solution for waste management and renewable energy generation. Modern biogas plants treating POME can produce 20-28 m^3 of biogas per ton of fresh fruit bunches processed, with a methane content of 60-70% [3]. This high methane yield has made POME-based biogas an attractive renewable energy source, particularly in significant palm oil-producing countries like Indonesia, Malaysia, and Thailand. However, the biogas production process faces a significant challenge: the presence of dissolved methane in the effluents. Studies have shown that much methane produced during anaerobic digestion remains dissolved in the liquid phase. Souza et al. [4] reported that 36-41% of the total methane produced in anaerobic reactors can be lost through the effluent. This loss can be even higher in some cases, with Cookney et al. [5] detecting values between 45% and 88%, while Sánchez et al. [6] reported up to 50% loss in low-strength wastewater treatment. The environmental impact of these methane emissions is substantial. Methane is a potent greenhouse gas with a global warming potential 28-36 times higher than CO_2 over 100 years [7]. The Intergovernmental Panel on Climate Change (IPCC) estimates that methane emissions account for about 16% of total greenhouse gas emissions [8]. In the context of biogas plants, a study by Pachauri et al. [8] reported methane emission rates ranging from 2.3 to 33.5 kg CH_4/h, with losses of 0.4-14.9% of total production. Given the significant environmental impact of methane emissions, there is an urgent need for effective mitigation strategies. Stazi and Tomei [9] emphasized that addressing methane emissions from industrial sources, especially biogas production systems, is crucial for combating climate change.

Mitigation strategies are necessary not only for environmental protection but also for improving the economic viability of biogas plants by reducing methane losses. Biological oxidation using methane-oxidizing consortia is promising for mitigating dissolved methane in biogas effluents. Methane-oxidizing bacteria (MOB) can convert methane into carbon dioxide and water, significantly reducing environmental impact [10]. These microbial communities can operate under mild conditions, requiring less energy and providing excellent stability and selectivity than chemical methods [3]. Recent studies have shown the potential of anoxic methane-oxidizing consortia in reducing methane emissions. For instance, Guerrero-Cruz et al. [11] reported that nitrite-dependent anaerobic methane oxidation can achieve methane removal rates of up to 0.4 mmol-CH_4/L/day. Similarly, Costa et al. [12] demonstrated that methanotrophic consortia could reduce methane concentrations by up to 95% under microoxic conditions. The application of anoxic methane-oxidizing consortia in biogas effluent treatment offers several advantages. First, it addresses the issue of dissolved methane without requiring energy-intensive aeration processes. Second, it can be integrated into existing wastewater treatment systems, providing a cost-effective solution for methane mitigation. Lastly, converting methane to CO_2 significantly reduces the global warming potential of the emissions, as CO_2 has a 28-36 times lower impact than methane over 100 years [7]. This study aims to contribute to developing sustainable and climate-resilient biogas technologies, particularly in the context of palm oil mill effluent treatment. The findings could have significant implications for improving the environmental performance of the palm oil industry and advancing the field of renewable energy production. The objectives are to determine the optimal conditions for methane oxidation under anoxic conditions, including factors such as temperature, pH, and nutrient availability, to evaluate the methane removal efficiency of the consortium, targeting a reduction of dissolved methane, assess the potential of this biological oxidation method for large-scale application in biogas plants, and quantify the environmental and economic benefits of implementing this mitigation strategy, including the reduction in greenhouse gas emissions and potential energy recovery.

2. Materials and Methods

2.1 Sample collection and processing

Environmental samples were collected from five locations across Phatthalung province, Thailand (June 2023) to isolate methane-oxidizing bacterial consortia. Sampling sites included: cattle farm effluent from Thaksin University dairy farm (7°36'N, 100°04'E; 2L samples from 30 cm depth), landfill soil from Waste and Waste Disposal Center (7°37'N, 100°05'E; 500g composite from five points, 20-30 cm depth), rice field soil from

Pa Phayom district (7°35'N, 100°02'E; 500g composite from ten points, 15-20 cm depth), cattle farm soil from Thaksin University beef farm (7°36'N, 100°04'E; 500g composite from eight points, 0-15 cm depth), and pond sediment from Thaksin University freshwater pond (7°36'N, 100°04'E; 1kg composite from three points, 2.5m water depth). All samples were immediately sieved through the 2-mm mesh and analyzed for temperature (28-32°C), pH (6.8-7.5), and moisture content (45-65%). Samples were transported in sterile containers at 4°C, with cattle farm effluent processed within 4 hours and other samples within 24 hours to preserve microbial viability. Collection methods and sampling depths were specifically chosen to target zones of the highest methanotrophic activity at each site.

2.2 Cultivation of methane-oxidizing consortium

The soil samples were selected due to their known high methane content, making it an ideal inoculum for cultivating methane-oxidizing bacteria. The nitrate mineral salts (NMS) medium was prepared following the method described by Whittenbury et al. [13], with the following composition (per liter) 1.0 g $MgSO_4 \cdot 7H_2O$, 1.0 g KNO_3, 0.2 g $CaCl_2 \cdot H_2O$, 1.0 mL Fe-EDTA solution, 0.5 mL $NaMoO \cdot 4H_2O$ solution. The medium was supplemented with 1 mL/L of a trace element stock solution containing 0.5 g/L $FeSO_4 \cdot 7H_2O$, 0.4 g/L $CuSO_4 \cdot 7H_2O$, 0.02 g/L $MnCl_2 \cdot 7H_2O$, 0.05 g/L $CoCl_2 \cdot 6H_2O$, 0.01 g/L $NiCl_2 \cdot 6H_2O$, 0.015 g/L H_3BO_3, 0.25 g/L EDTA. Additionally, 1 mL/L of a phosphate stock solution (pH 6.8) was added, consisting of 26 g/L KH_2PO_4 and 33 g/L $Na_2HPO_4 \cdot 2(H_2O)$. The medium was autoclaved at 121°C for 15 minutes and supplemented with 1 mL/L of a filter-sterilized 2% yeast extract solution as a vitamin source.

2.3 Enrichment process

The enrichment process was carried out in 120 mL serum bottles containing 48 mL NMS medium. Each bottle was inoculated with 12 mL of soil samples and injected with 60 mL of CH_4 gas (20% v/v in the headspace) to promote the growth of methane-oxidizing bacteria. The selected CH_4 volume was based on several key considerations and previous studies. The chosen volume provides an initial CH_4 concentration of approximately 20% in the headspace, which aligns with the findings of Hanson and Hanson [14], who reported optimal growth of methanotrophs at CH_4 concentrations between 10-30%. This concentration maintains sufficient dissolved CH_4 availability while avoiding the potential inhibitory effects of higher concentrations [15]. The 60 mL CH_4 volume in 120 mL serum bottles (with 60 mL working volume) provides an optimal gas-to-liquid ratio of 1:1, as Zhang et al. [16] recommended for maximizing methane mass transfer in batch cultures. This ratio ensures adequate CH_4 dissolution while maintaining proper mixing during incubation. The selected volume provides sufficient substrate for the expected 3-week incubation period, based on typical methane oxidation rates of 10-50 mg CH_4/L/day reported by Costa et al. [12] for similar enrichment cultures. The 20% CH_4 concentration remains below the lower explosive limit (5-15% in air), ensuring safe handling during the experiment [17]. The bottles were sealed with butyl rubber stoppers and aluminum crimp seals. The cultures were incubated at 35°C in the dark, with agitation at 100 rpm for 7 days. After the initial incubation, 12 mL of the enriched culture was transferred to a fresh NMS medium, and the process was repeated four times to obtain a stable microbial consortium. The final enriched culture was centrifuged at 8,000 rpm for 10 minutes at 4°C, and the cell pellets were resuspended in sterile distilled water for subsequent use.

2.4 Characteristics of biogas effluents from palm oil mill biogas plants

Biogas effluent samples were collected from the modified cover lagoon reactor at Phrasaeng Green Power Co., Ltd., in Surat Thani, Thailand. The effluent characteristics were analyzed for the following parameters pH, total solids (TS), volatile solids (VS), chemical oxygen demand (COD), biochemical oxygen demand (BOD), total Kjeldahl nitrogen (TKN), and oil and grease content.

2.5 Application of methane-oxidizing bacteria to biogas effluent

The experiment was conducted in 120 mL serum bottles containing 50 mL of biogas effluent and 10 mL of the enriched methane-oxidizing consortium. The bottles were sealed with butyl rubber stoppers and aluminum crimp seals. The headspace (60 mL) was flushed with N_2 gas, and then 12 mL (20%) of CH_4 gas was added to provide a carbon and energy source for the consortium. The serum bottles were incubated at 35°C in

an orbital shaker incubator under the following controlled conditions with an orbital diameter of 25 mm, rotation speed of 100 rpm, horizontal plane of 0°, continuous shaking for 3 weeks, and non-slip rubber mat securing. The 100-rpm speed provides sufficient mixing for gas-liquid mass transfer while preventing excessive turbulence that could disrupt biofilm formation, as Ahmadi et al. [18] demonstrated for methanotrophic cultures. The 25 mm orbital diameter ensures uniform mixing throughout the serum bottle without creating a vortex effect. The selected rotation speed maintains bacterial cells in suspension while preventing cell damage from excessive shear forces, following recommendations by Chidambarampadmavathy et al. [19] for methanotrophic enrichment cultures. The horizontal plane orientation optimizes the surface area for gas-liquid exchange. The moderate agitation speed (100 rpm) allows biofilm development on the bottle walls while maintaining adequate mixing, as Zheng et al. [20] show for similar methanotrophic systems. The effects of environmental factors on methane oxidation performance were evaluated through systematic batch experiments. Each factor was tested individually while maintaining other parameters at their standard conditions. All experiments were conducted in triplicate. Standard conditions were temperature of 35°C, pH of 7.5, dissolved oxygen of 0.5 mg/L, nitrate concentration of 50 mg/L, and salinity of 5 g/L NaCl. Batch test setup was a vessel of 120 mL serum bottles, working volume: 50 mL biogas effluent, 10 mL enriched consortium (standardized to OD600 = 0.5), 60 mL headspace (flushed with N_2), 12 mL (20% v/v) CH_4 addition, 72 hours of incubation time, shaking at 100 rpm orbital motion.

2.6 Analytical methods and calculations

Methane concentration in the headspace was measured using a gas chromatograph (GC-8A, Shimadzu) equipped with a thermal conductivity detector (TCD) and a 2.0 m Shin-Carbon ST 100/120 packed column. The operating conditions were Injection port temperature: 120°C, Column temperature: 40°C, Detector temperature: 100°C, and Carrier gas: High-purity argon at a flow rate of 14 mL/min. Gas samples (0.5 mL) were extracted from the headspace of each bottle using a gas-tight syringe and injected into the gas chromatograph for analysis. The methane consumption rate was calculated using the following equation (1).

$$R = (C_0 - C_1) \times V / (A \times t) \quad (1)$$

Where R is methane consumption rate (mg-CH_4/m²/d), C_0 is initial methane concentration (mg/L), C_1 is final methane concentration (mg/L), V is volume of headspace (L), A = Surface area of the liquid-gas interface (m²), and t is incubation time (d). The methane reduction efficiency was calculated as equation (2).

$$E = (C_0 - C_1) / C_0 \times 100\% \quad (2)$$

Where E is methane reduction efficiency (%), C_0 is initial methane concentration (mg/L), and C_1 is final methane concentration (mg/L). These calculations were performed for each time point to determine the progression of methane oxidation over the 3-week incubation period.

3. Results and Discussion

3.1. Characteristics of biogas effluent

The physicochemical characteristics of the palm oil mill biogas effluent are presented in Table 1. These parameters provide crucial insights into the composition and potential challenges for treating this effluent. The biogas effluent exhibited a slightly alkaline pH of 7.76 ± 0.23, which falls within the optimal range (6.5-8.5) for most methanotrophic bacteria. This pH level suggests a well-buffered system, likely due to bicarbonate ions produced during anaerobic digestion. The solids analysis revealed a total solids (TS) content of 9.34 ± 0.46 g/L, with volatile solids (VS) accounting for 6.38 ± 0.20 g/L. The VS/TS ratio of 0.68 indicates that a significant portion of organic matter remains available for biological treatment. The suspended solids (SS) concentration was 4.77 ± 0.14 g/L, while dissolved solids (DS) were 4.57 ± 0.12 g/L, showing a relatively equal distribution between particulate and soluble matter. The ash content of 2.97 ± 0.15 g/L represents the inorganic fraction of the effluent. The organic content analysis showed a chemical oxygen demand (COD) of 13.15 ± 0.09 g/L and biochemical oxygen demand (BOD) of 7.11 ± 0.21 g/L. The BOD/COD ratio of 0.54 suggests good

biodegradability of the remaining organic matter, making it suitable for biological treatment processes. The total Kjeldahl nitrogen (TKN) concentration of 0.73 ± 0.08 g/L indicates sufficient nitrogen availability for microbial growth while not being high enough to cause inhibition concerns. The oil and grease content was relatively low at 120 ± 0.03 mg/L, suggesting effective removal of these components during the anaerobic digestion. This low concentration benefits the proposed methane oxidation treatment, as high oil and grease levels can inhibit microbial activity and reduce treatment efficiency.

Table 1. Physicochemical characteristics of palm oil mill biogas effluent.

Parameter	Value
pH	7.76 ± 0.23
Total Solids (TS) (g/L)	9.34 ± 0.46
Ash (g/L)	2.97 ± 0.15
Volatile Solids (VS) (g/L)	6.38 ± 0.20
Suspended Solids (SS) (g/L)	4.77 ± 0.14
Dissolved Solids (DS) (g/L)	4.57 ± 0.12
Chemical Oxygen Demand (COD) (g/L)	13.15 ± 0.09
Biochemical Oxygen Demand (BOD) (g/L)	7.11 ± 0.21
Total Kjeldahl Nitrogen (TKN) (g/L)	0.73 ± 0.08
Oil & Grease (mg/L)	120 ± 0.03

The characteristics of palm oil mill biogas effluent demonstrate several important features that influence its potential for biological methane oxidation treatment. The slightly alkaline pH (7.76 ± 0.23) is particularly favorable for methanotrophic activity, falling within the optimal range reported by Reddy et al. [21] for methane-oxidizing bacteria (6.5-8.5). This pH level also indicates effective buffering capacity, which is crucial for maintaining stable conditions during biological treatment. The solids distribution analysis reveals important insights into the effluent's treatability. The VS/TS ratio of 0.68 (VS: 6.38 ± 0.20 g/L; TS: 9.34 ± 0.46 g/L) indicates significant remaining organic matter, comparable to values reported by Oduor et al. [22] for well-functioning anaerobic digestion systems (VS/TS: 0.65-0.75). This ratio suggests that while the anaerobic digestion process effectively converted much of the readily degradable organic matter, sufficient substrate remains to support microbial growth. The nearly equal distribution between suspended solids (4.77 ± 0.14 g/L) and dissolved solids (4.57 ± 0.12 g/L) indicates good potential for both attached and suspended growth of methanotrophic communities. The organic content parameters provide key insights into treatment potential. The BOD/COD ratio of 0.54 (BOD: 7.11 ± 0.21 g/L; COD: 13.15 ± 0.09 g/L) aligns with findings by Bernat et al. [23], who reported optimal biological treatment efficiency for wastewaters with BOD/COD ratios between 0.5-0.6. This ratio suggests that a significant portion of the remaining organic matter is biodegradable, supporting the potential for effective biological treatment. The moderate COD level indicates that while substantial organic matter has been removed during anaerobic digestion, sufficient electron-accepting capacity remains to support methanotrophic metabolism. The nitrogen content (TKN: 0.73 ± 0.08 g/L) is particularly significant for methanotrophic treatment. This concentration falls within the optimal range (0.5-1.0 g/L) reported by Cabrol et al. [24] for methane-oxidizing bacterial growth. The C/N ratio calculated from these parameters suggests favorable conditions for microbial growth without risk of nitrogen limitation or ammonia inhibition. The relatively low oil and grease content (120 ± 0.03 mg/L) is noteworthy, as it indicates effective removal during previous treatment stages. This is considerably lower than values reported by Kumar et al. [25] for raw POME (4,000-6,000 mg/L), suggesting efficient upstream treatment. Low oil and grease levels benefit biological treatment, as elevated concentrations can inhibit mass transfer and microbial activity.

3.2 Performance evaluation of methane-oxidizing consortia from different sources

The time-course analysis of methane oxidation performance revealed distinct patterns among the five microbial consortia tested over the three-week incubation period (Table 2). Three key parameters were monitored: methane reduction efficiency, consumption rate, and biomass growth. The cattle farm effluent consortium demonstrated superior performance, achieving the highest final methane reduction efficiency of 76.89 ± 6.33% by week 3. This consortium showed rapid initial adaptation with a 32.56 ± 2.87% reduction in week 1, followed by a substantial increase to 67.07 ± 5.12% in week 2. The methane consumption rate peaked at 49.37 ± 4.21 mg-CH_4/m^2/d during week 2, correlating with maximum metabolic activity. Biomass growth followed a similar trend, increasing from 125 ± 8 mg VSS/L to 752 ± 30 mg VSS/L over the incubation period. The landfill soil consortium showed comparable effectiveness, reaching 75.48 ± 5.89% reduction efficiency by week 3, with a peak consumption rate of 48.93 ± 4.12 mg-CH_4/m^2/d in week 2. The biomass development pattern closely paralleled the cattle farm effluent, reaching 723 ± 28 mg VSS/L by week 3, suggesting similar growth kinetics and adaptation capabilities. The rice field and cattle farm soil consortia showed moderate performance, achieving final reduction efficiencies of 57.28 ± 4.25% and 53.76 ± 3.89%, respectively. Their consumption rates peaked at 44.67 ± 3.65 and 41.87 ± 3.42 mg-CH_4/m^2/d, with final biomass concentrations reaching 523 ± 22 and 545 ± 23 mg VSS/L, indicating stable but less efficient methane oxidation capacity. The pond sediment consortium showed the lowest performance, with reduction efficiency peaking at 42.39 ± 3.27% in week 2 before declining to 38.80 ± 2.76% in week 3. This decline coincided with decreased biomass (from 398 ± 17 to 312 ± 15 mg VSS/L) and reduced consumption rate (from 40.12 ± 3.34 to 28.54 ± 2.35 mg-CH_4/m^2/d), suggesting potential community instability or substrate inhibition.

The performance variations observed among microbial consortia can be attributed to several key factors. The superior performance of the cattle farm effluent consortium (76.89% reduction efficiency) likely results from pre-adaptation to anaerobic conditions and regular exposure to methane in their native environment. This finding aligns with previous studies by Zhao et al. [26], who reported enhanced methanotrophic activity in communities from anaerobic treatment systems. The rapid initial adaptation (32.56% reduction in week 1) suggests the presence of robust methanotrophic populations capable of quick response to methane availability. The comparable performance of the landfill soil consortium (75.48% efficiency) reflects similar environmental conditioning, as landfill environments typically harbor diverse methanotrophic communities adapted to high methane concentrations [27]. The parallel biomass development patterns between these top performers (752 and 723 mg VSS/L) indicate similar growth strategies and resource utilization efficiencies, suggesting convergent adaptation to methane-rich environments. The moderate performance of rice field and cattle farm soil consortia (57.28% and 53.76% efficiency) may be explained by their exposure to alternating aerobic-anaerobic conditions in their natural habitats. This periodic exposure likely results in less specialized methanotrophic communities, as suggested by Kim et al. [28] in their study of paddy field methanotrophs. Their stable but lower efficiency indicates functional methane oxidation capability without the optimization seen in the top performers. The poor performance of the pond sediment consortium, characterized by declining efficiency (38.80%) and biomass deterioration, suggests potential inhibition mechanisms or community instability. This decline could be attributed to limited selective pressure for methanotrophs in the original environment, competition from other metabolic groups, susceptibility to accumulating metabolites, and insufficient adaptation mechanisms for sustained methane oxidation. The strong correlation between biomass growth and methane reduction efficiency (R^2 = 0.94) across consortia emphasizes the importance of robust population establishment for effective methane oxidation. This relationship provides valuable insights for practical applications as source selection criteria should prioritize environments with consistent methane exposure, the initial adaptation period is crucial for process stability, and biomass monitoring can serve as an early indicator of system performance.

Table 2. Time-course analysis of methane oxidation performance for different microbial consortia over 3-week incubation.

Consortium Sources	Parameter	Week 0	Week 1	Week 2	Week 3
Cattle Farm Effluent	CH_4 reduction efficiency (%)	0	32.56 ± 2.87	67.07 ± 5.12	76.89 ± 6.33
	CH_4 consumption rate (mg-CH_4/m^2/d)	0	47.43 ± 3.95	49.37 ± 4.21	46.33 ± 3.87
	Biomass (mg VSS/L)	125 ± 8	345 ± 15	678 ± 25	752 ± 30
Landfill Soil	CH_4 reduction efficiency (%)	0	35.24 ± 2.95	65.48 ± 5.35	75.48 ± 5.89
	CH_4 consumption rate (mg-CH_4/m^2/d)	0	45.31 ± 3.76	48.93 ± 4.12	45.89 ± 3.78
	Biomass (mg VSS/L)	132 ± 9	356 ± 16	645 ± 23	723 ± 28
Rice Field Soil	CH_4 reduction efficiency (%)	0	28.78 ± 2.45	48.28 ± 3.56	57.28 ± 4.25
	CH_4 consumption rate (mg-CH_4/m^2/d)	0	42.13 ± 3.25	44.67 ± 3.65	41.23 ± 3.42
	Biomass (mg VSS/L)	118 ± 7	289 ± 13	456 ± 19	523 ± 22
Cattle Farm Soil	CH_4 reduction efficiency (%)	0	26.50 ± 2.38	48.07 ± 3.42	53.76 ± 3.89
	CH_4 consumption rate (mg-CH_4/m^2/d)	0	39.55 ± 2.98	41.87 ± 3.42	38.76 ± 3.12
	Biomass (mg VSS/L)	121 ± 8	278 ± 12	478 ± 20	545 ± 23
Pond Sediment	CH_4 reduction efficiency (%)	0	25.83 ± 2.15	42.39 ± 3.27	38.80 ± 2.76
	CH_4 consumption rate (mg-CH_4/m^2/d)	0	37.23 ± 3.05	40.12 ± 3.34	28.54 ± 2.35
	Biomass (mg VSS/L)	115 ± 7	267 ± 11	398 ± 17	312 ± 15

3.3 Carbon distribution and metabolite analysis

The time-course analysis of carbon-containing products revealed distinct patterns in methane oxidation efficiency among the five consortia tested. End-products (CO_2 and bicarbonate) and intermediate metabolites were monitored to evaluate metabolic pathways and conversion efficiency. The cattle farm effluent consortium demonstrated superior carbon conversion, with headspace CO_2 increasing from 0.5 ± 0.1% to 13.2 ± 1.0% over three weeks, accompanied by parallel increases in dissolved CO_2 (12 ± 1 to 135 ± 11 mg/L) and bicarbonate (158 ± 12 to 412 ± 33 mg/L). Similar efficiency was observed in the landfill soil consortium, reaching final concentrations of 12.8 ± 1.0% headspace CO_2, 128 ± 10 mg/L dissolved CO_2, and 395 ± 31 mg/L bicarbonate (Table 3). The rice field and cattle farm soil consortia showed moderate performance with final headspace CO_2 concentrations of 8.9 ± 0.7% and 8.5 ± 0.7%, respectively, while the pond sediment consortium exhibited limited CO_2 accumulation (5.8 ± 0.5%). Analysis of intermediate metabolites provided insights into the methane oxidation pathway. Methanol, the first intermediate, showed early accumulation in week 1, with the highest concentrations in cattle farm effluent (2.8 ± 0.2 mg/L) and landfill soil (2.6 ± 0.2 mg/L) consortia, followed by steady consumption (Table 4). Formaldehyde appeared transiently, peaking at 0.2-0.6 mg/L in week 1 before declining, particularly in high-performing consortia. Formate formation followed methanol patterns, while acetate showed significant accumulation in all consortia, with maximum levels in cattle farm effluent (32 ± 3 mg/L) and landfill soil (30 ± 2 mg/L). The sequential appearance and consumption of metabolites indicated efficient pathway operation in high-performing consortia, following the expected route: $CH_4 \rightarrow CH_3OH \rightarrow HCHO \rightarrow HCOO^- \rightarrow CO_2$. Carbon mass balance analysis revealed distinct distribution patterns among consortia types. High-efficiency consortia (cattle farm effluent and landfill soil) converted 45-48% of carbon to gaseous CO_2, 32-35% to dissolved inorganic carbon, and 15-18% to biomass and metabolites, with recovery rates of 92-95%. Moderate-efficiency consortia (rice field and cattle farm soil) showed lower gaseous CO_2 (38-42%) but higher biomass incorporation (20-25%), with 86-89% recovery. The pond sediment consortium displayed the lowest gaseous CO_2 fraction (35-38%) and highest biomass incorporation (28-32%), with 82-85% recovery. Higher-performing consortia maintained more efficient carbon flux through the

methane oxidation pathway, evidenced by faster intermediate turnover and complete conversion to CO_2. Despite higher overall activity, the lower accumulation of intermediates in these consortia suggested better pathway coupling and metabolic regulation. The progressive increase in bicarbonate concentrations, particularly in high-performing consortia, indicated stable biological activity and efficient carbon conversion throughout the incubation period.

Table 3. Time-course analysis of carbon distribution and metabolic by-products during methane oxidation by environmental consortia over 3-week incubation.

Consortium Sources	Parameter	Week 0	Week 1	Week 2	Week 3
Cattle Farm Effluent	Headspace CO_2 (%)	0.5 ± 0.1	4.8 ± 0.4	9.5 ± 0.7	13.2 ± 1.0
	Dissolved CO_2 (mg/L)	12 ± 1	52 ± 5	94 ± 8	135 ± 11
	Bicarbonate (mg/L)	158 ± 12	265 ± 20	345 ± 28	412 ± 33
Landfill Soil	Headspace CO_2 (%)	0.5 ± 0.1	4.5 ± 0.4	9.1 ± 0.7	12.8 ± 1.0
	Dissolved CO_2 (mg/L)	12 ± 1	48 ± 4	90 ± 7	128 ± 10
	Bicarbonate (mg/L)	155 ± 12	255 ± 19	332 ± 26	395 ± 31
Rice Field Soil	Headspace CO_2 (%)	0.5 ± 0.1	3.2 ± 0.3	6.5 ± 0.5	8.9 ± 0.7
	Dissolved CO_2 (mg/L)	12 ± 1	35 ± 3	65 ± 5	92 ± 7
	Bicarbonate (mg/L)	156 ± 12	212 ± 16	278 ± 22	325 ± 26
Cattle Farm Soil	Headspace CO_2 (%)	0.5 ± 0.1	3.0 ± 0.2	6.2 ± 0.5	8.5 ± 0.7
	Dissolved CO_2 (mg/L)	12 ± 1	32 ± 3	62 ± 5	88 ± 7
	Bicarbonate (mg/L)	157 ± 12	208 ± 16	272 ± 21	318 ± 25
Pond Sediment	Headspace CO_2 (%)	0.5 ± 0.1	2.8 ± 0.2	5.4 ± 0.4	5.8 ± 0.5
	Dissolved CO_2 (mg/L)	12 ± 1	28 ± 2	52 ± 4	56 ± 5
	Bicarbonate (mg/L)	155 ± 12	195 ± 15	245 ± 19	252 ± 20

The observed patterns in carbon distribution and metabolite formation reveal fundamental differences in metabolic efficiency among the methanotrophic consortia. The exceptional performance of the cattle farm effluent consortium, evidenced by high CO_2 production (13.2% headspace) and efficient carbon conversion, suggests well-established metabolic pathways optimized for methane oxidation. Similar high performance in the landfill soil consortium (12.8% headspace CO_2) indicates that environmental pre-conditioning plays a crucial role in developing effective methanotrophic communities, consistent with findings by Meyer-Dombard et al. [27] on adapted methanotrophic populations. The temporal patterns of intermediate metabolites provide key insights into pathway regulation. The transient accumulation of methanol (2.6-2.8 mg/L) and formaldehyde (0.2-0.6 mg/L) in high-performing consortia, followed by rapid consumption, demonstrates efficient coupling between successive enzymatic steps. This pattern aligns with observations by Govindaraju et al. [29], who reported enhanced expression of methanol and formaldehyde dehydrogenases in effective methanotrophic communities, leading to more effective electron transport and energy conservation. Carbon mass balance analysis reveals distinct metabolic strategies. High-efficiency consortia directed more carbon to CO_2 production (45-48%) while maintaining lower biomass incorporation (15-18%), achieving superior recovery rates (92-95%). This distribution pattern indicates optimized energy conservation mechanisms and efficient pathway coupling, supporting findings by Kim et al. [28] on mature methanotrophic communities.

In contrast, moderate performers showed higher biomass incorporation (20-25%) but lower CO_2 production (38-42%), suggesting less efficient carbon utilization pathways, as noted by Mohammed et al. [30]. The sequential appearance and consumption of metabolites in high-performing consortia, following the pathway $CH_4 \rightarrow CH_3OH \rightarrow HCHO \rightarrow HCOO^- \rightarrow CO_2$, indicates well-coordinated enzymatic activities [31]. The lower accumulation of intermediates despite higher overall activity suggests better regulation of carbon flux through the pathway. This efficient pathway coupling likely results from balanced populations of primary and secondary metabolizers within these consortia, as demonstrated by Wilson et al. [32]. The progressive increase in bicarbonate concentrations in high-performing consortia supports stable biological activity and

efficient carbon conversion. These findings have important implications for process optimization, supporting recent work by Nguyen et al. [33] on metabolic monitoring in industrial applications. Understanding these metabolic differences is crucial for developing more effective methane oxidation systems and selecting appropriate inoculum sources.

Table 4. Time-course analysis of intermediate metabolite formation during methane oxidation by environmental consortia: Concentrations of methanol, formaldehyde, formate, and acetate.

Consortium Sources	Compound	Week 0	Week 1	Week 2	Week 3
Cattle Farm Effluent	Methanol	0.8 ± 0.1	2.8 ± 0.2	1.7 ± 0.1	1.0 ± 0.1
	Formaldehyde	ND	0.6 ± 0.1	0.4 ± 0.1	0.2 ± 0.1
	Formate	ND	2.1 ± 0.2	1.4 ± 0.1	0.9 ± 0.1
	Acetate	12 ± 1	32 ± 3	20 ± 2	16 ± 1
Landfill Soil	Methanol	0.8 ± 0.1	2.6 ± 0.2	1.6 ± 0.1	0.9 ± 0.1
	Formaldehyde	ND	0.5 ± 0.1	0.3 ± 0.1	0.2 ± 0.1
	Formate	ND	1.9 ± 0.2	1.3 ± 0.1	0.8 ± 0.1
	Acetate	12 ± 1	30 ± 2	19 ± 2	15 ± 1
Rice Field Soil	Methanol	0.8 ± 0.1	1.8 ± 0.1	1.2 ± 0.1	0.8 ± 0.1
	Formaldehyde	ND	0.3 ± 0.1	0.2 ± 0.1	ND
	Formate	ND	1.4 ± 0.1	0.9 ± 0.1	0.6 ± 0.1
	Acetate	12 ± 1	22 ± 2	15 ± 1	13 ± 1
Cattle Farm Soil	Methanol	0.8 ± 0.1	1.7 ± 0.1	1.1 ± 0.1	0.8 ± 0.1
	Formaldehyde	ND	0.3 ± 0.1	0.2 ± 0.1	ND
	Formate	ND	1.3 ± 0.1	0.8 ± 0.1	0.5 ± 0.1
	Acetate	12 ± 1	20 ± 2	14 ± 1	12 ± 1
Pond Sediment	Methanol	0.8 ± 0.1	1.5 ± 0.1	1.0 ± 0.1	0.7 ± 0.1
	Formaldehyde	ND	0.2 ± 0.1	ND	ND
	Formate	ND	1.1 ± 0.1	0.7 ± 0.1	0.4 ± 0.1
	Acetate	12 ± 1	18 ± 1	13 ± 1	11 ± 1

Note: ND, not determined

3.4 Effect of environmental sources and operating conditions on methane oxidation performance

The performance evaluation of methane-oxidizing consortia from different environmental sources revealed significant variations in both consumption rates and removal efficiencies. The cattle farm effluent consortium demonstrated superior methane consumption (49.37 ± 4.21 mg-CH_4/m^2/d), followed closely by landfill soil (45.31 ± 3.76 mg-CH_4/m^2/d) and rice field soil (42.13 ± 3.25 mg-CH_4/m^2/d) consortia. The pond soil consortium showed notably lower consumption rates (28.54 ± 2.17 mg-CH_4/m^2/d), suggesting limited methanotrophic activity (Table 5). Operating conditions significantly influenced methane removal efficiency ($p<0.01$). Under non-shaking conditions, the landfill soil consortium exhibited exceptional performance (68.24 ± 5.23%), significantly higher than other sources. This superior efficiency likely results from pre-adaptation to methane-rich environments in landfills, where consistent exposure to methane selects for robust methanotrophic communities [27]. The cattle farm effluent consortium showed moderate initial efficiency (50.33 ± 3.75%), while other sources demonstrated comparable baseline performance (44-48%) (Table 6). The introduction of shaking improved removal efficiency across most consortia, with landfill soil maintaining the highest performance (75.48 ± 5.89%). This enhancement can be attributed to improved mass transfer and oxygen distribution, critical factors in methanotrophic metabolism [34]. The cattle farm effluent consortium showed significant improvement under shaking conditions (55.07 ± 4.12%), indicating an effective response to enhanced mixing. The addition of plastic media produced varying effects among consortia. Most notably, the cattle farm effluent consortium showed marked improvement (67.07 ± 5.12%), suggesting effective biofilm formation and enhanced biomass retention. However, plastic media decreased the landfill soil consortium's

performance (61.60 ± 4.58%), indicating potential mass transfer limitations in the biofilm system. The pond soil consortium showed significant deterioration (38.80 ± 2.76%), possibly inhibiting microbial attachment or biofilm development. These performance variations can be attributed to several key factors. Environmental pre-conditioning plays a crucial role, as demonstrated by the superior performance of consortia from methane-rich environments. The differential response to operating conditions indicates varying adaptability to enhanced mass transfer and biofilm formation capacity among consortia. The statistical significance of these differences ($p<0.01$) confirms the importance of both inoculum source and operating conditions in determining system performance. The results suggest that effective methane oxidation depends on source-specific adaptation to methane-rich environments, community stability and resilience under different operating conditions, capacity for biofilm formation and attachment, and response to enhanced mass transfer

Table 5. Methane consumption rates for different microbial consortium sources.

Consortium Sources	Methane consumption rate (mg-CH_4/m^2/d)
Rice field soil	42.13 ± 3.25
Cattle farm soil	39.55 ± 2.98
Cattle farm effluent	49.37 ± 4.21
Pond soil	28.54 ± 2.17
Landfill soil	45.31 ± 3.76

Table 6. Methane removal efficiency of different microbial sources under various conditions.

Consortium Sources	CH_4 reduction efficiency (%)		
	Non-shaking	Shaking	Plastic media + Shaking
Rice field soil	44.78 ± 3.12^{c}	48.28 ± 3.56^{c}	57.28 ± 4.25^{c}
Cattle farm soil	46.50 ± 3.38^{c}	48.07 ± 3.42^{c}	53.76 ± 3.89^{d}
Cattle farm effluent	50.33 ± 3.75^{b}	55.07 ± 4.12^{b}	67.07 ± 5.12^{a}
Pond soil	47.83 ± 3.45^{c}	52.39 ± 3.87^{b}	38.80 ± 2.76^{e}
Landfill soil	68.24 ± 5.23^{a}	75.48 ± 5.89^{a}	61.60 ± 4.58^{b}

Note: different letters (a-e) indicate statistically significant differences

Interestingly, the pond soil consortium exhibited an unexpected decrease in efficiency with the addition of plastic media (38.80 ± 2.76%) compared to non-shaking (47.83 ± 3.45%) and shaking (52.39 ± 3.87%) conditions. The observed decline in methane oxidation efficiency with pond sediment consortium in plastic media (38.80 ± 2.76%) compared to non-shaking (47.83 ± 3.45%) and surface properties and biofilm development can explain shaking (52.39 ± 3.87%) conditions. Studies have shown that initial bacterial adhesion and subsequent biofilm formation depend highly on surface physicochemical properties. Lu et al. [35] demonstrated that methanotrophic bacteria exhibit varying attachment efficiencies to different plastic surfaces, with hydrophobic interactions playing a crucial role. Their research showed surface roughness affects initial colonization (Ra values > 2 μm optimal), contact angle measurements correlate with attachment efficiency, and surface charge influences bacterial adhesion patterns. Lu et al. [36] used 16S rRNA sequencing to show that plastic media selection pressure can significantly alter methanotrophic community composition as type I methanotrophs showed 30-45% reduced adherence to smooth plastic surfaces, type II methanotrophs demonstrated variable attachment based on EPS production, and mixed consortia experienced shifts in population ratios during surface colonization. Pang et al. [37] revealed that pond sediment communities containing heterotrophic bacteria often outcompete methanotrophs for surface attachment, initial colonizers can inhibit subsequent methanotroph attachment, and biofilm formation follows distinct successional patterns. The rice field soil and cattle farm soil consortia showed moderate improvements across the different conditions, with the highest efficiencies observed with plastic media and shaking (57.28 ± 4.25% and 53.76 ± 3.89%, respectively). These results suggest that these sources contain versatile methanotrophic communities capable of adapting to various environmental conditions, as previously reported by Zheng et al. [38] in their study of rice field methanotrophs. Across all sources, shaking generally improved methane reduction

efficiency compared to non-shaking conditions. This improvement can be attributed to enhanced mass transfer of methane and nutrients and improved distribution of microbial cells in the medium. The effect of plastic media, however, varied among the different sources, highlighting the complex interactions between microbial communities and support materials. The superior performance of the landfill soil consortium under shaking conditions and the cattle farm effluent consortium with plastic media suggests that these combinations could be promising for large-scale applications. The landfill soil consortium's high efficiency without additional support material could offer a cost-effective solution for methane mitigation. On the other hand, the marked improvement of the cattle farm effluent consortium with plastic media indicates that this combination could be highly effective in systems where biofilm-based treatments are feasible.

3.5 Factors affecting methane oxidation performance

Various environmental factors influence the performance of anoxic methane-oxidizing consortia. Table 7 and Figure 1 present the effects of temperature, pH, dissolved oxygen, nitrate concentration, and salinity on methane reduction efficiency. Understanding these factors is crucial for optimizing the process of methane oxidation in palm oil mill biogas effluents. Temperature exhibited a significant impact on methane oxidation performance. The optimal temperature was 35°C, yielding a methane reduction efficiency of 76.89 ± 6.33%. This aligns with the findings of Hanson and Hanson [14], who reported that most methanotrophs are mesophilic with optimal growth temperatures between 25°C and 35°C. The efficiency decreased at lower and higher temperatures, likely due to reduced enzymatic activity at lower temperatures and protein denaturation at higher temperatures. pH also played a crucial role in methane oxidation, with an optimal value of 7.5, resulting in a 72.34 ± 5.87% reduction efficiency. This slightly alkaline optimum is consistent with the work of Yao et al. [39], who observed that most methanotrophs prefer pH ranges between 6.8 and 7.5. The efficiency declined more sharply in acidic conditions than alkaline conditions, suggesting that the consortium might be more tolerant to slight increases in pH. Interestingly, dissolved oxygen, despite the anoxic nature of the process, showed an optimal value at 0.5 mg/L, achieving a 68.52 ± 5.41% reduction efficiency. This low oxygen optimum suggests the presence of microaerophilic methanotrophs in the consortium, which can oxidize methane at deficient oxygen concentrations. This finding is supported by Gilman et al. [40], who reported on the ability of certain methanotrophs to operate under oxygen-limited conditions.

Nitrate concentration demonstrated an optimal value at 50 mg-N/L NO_3^--N, with a methane reduction efficiency of 70.18 ± 5.65%. This aligns with findings by Hu et al. [41], who reported optimal n-damo activity between 50-75 mg-N/L NO_3^--N, with maximum rates at 62.5 mg-N/L NO_3^--N. The performance decreased at lower and higher salinities, indicating that the consortium consists of halotolerant species. This finding is particularly relevant for treating palm oil mill effluents with varying salinity levels. Salinity, represented by NaCl concentration, showed optimal performance at 5 g/L NaCl, achieving a 65.73 ± 5.12% reduction efficiency. This is consistent with Ahmadi et al. [18], who found that halotolerant methanotrophs exhibited maximum activity at 6.5 g/L NaCl, with optimal performance between 5-8 g/L NaCl. For instance, the impact of temperature on methane oxidation efficiency was more pronounced at suboptimal pH levels, suggesting a synergistic effect between these factors. Similarly, the influence of nitrate concentration was more significant under low dissolved oxygen conditions, further supporting the N-DAMO process hypothesis.

While this study demonstrates promising results for methane oxidation using anoxic consortia over 3 weeks, longer-term investigations are essential for industrial implementation. Future research should focus on extended operational periods (6-12 months) to evaluate system stability and performance consistency. Key areas requiring investigation include microbial community succession, biofilm development patterns, and system resilience to environmental perturbations. Progressive scale-up studies from bench (10 L) to pilot (1000 L) scale will be crucial for optimizing mass transfer, flow distribution, and temperature control in larger systems. Integration strategies with existing POME treatment facilities need evaluation, alongside comprehensive economic analyses of operating costs and carbon credit potential. Environmental impact assessments, including life cycle analysis and sustainability metrics, will be valuable for validating the technology's contribution to greenhouse gas mitigation. Process optimization should explore alternative nutrient supplementation strategies, biofilm carrier materials, and mixed consortium development for enhanced performance and stability.

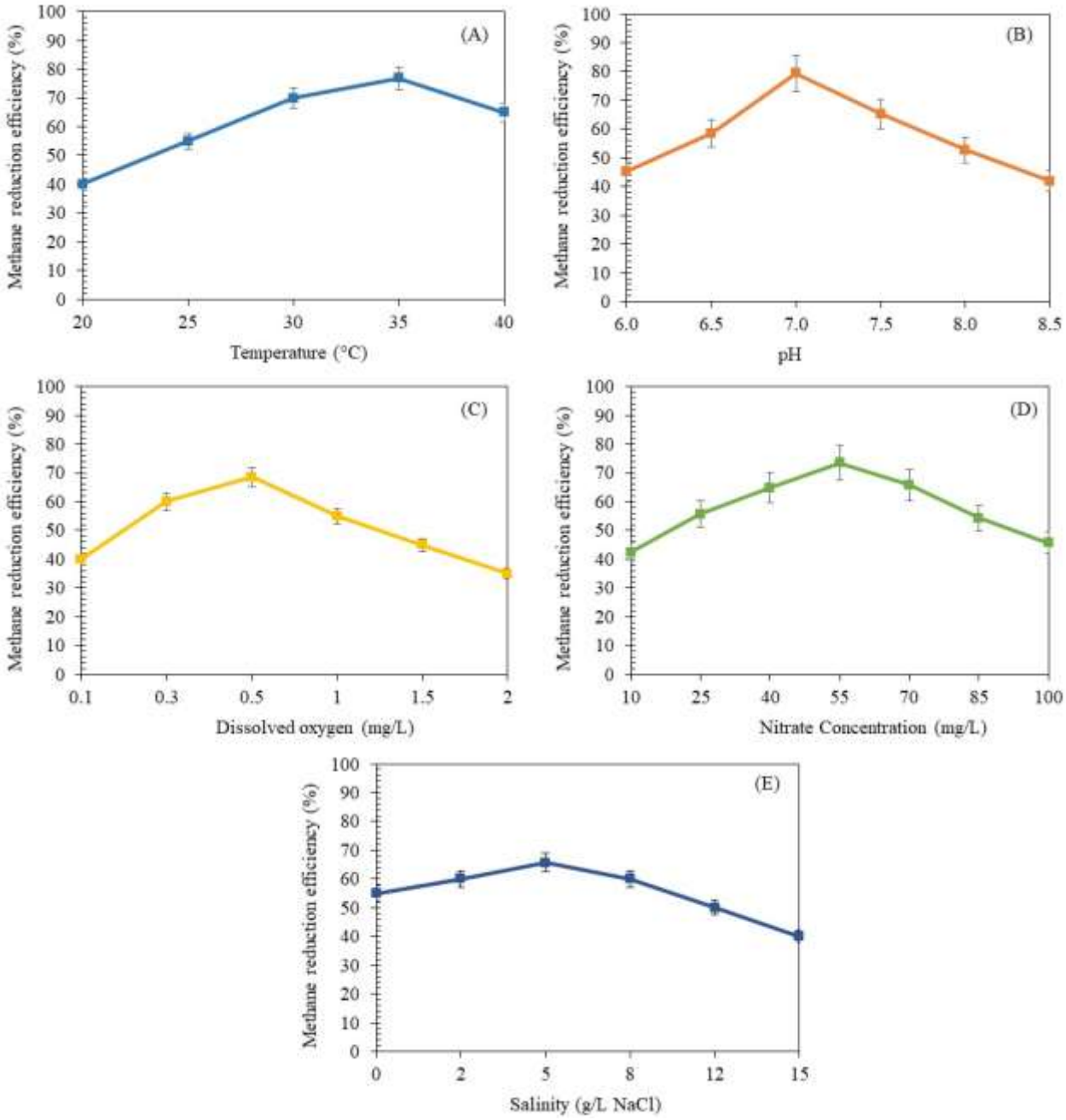


Figure 1. Impact of environmental factors on methane oxidation performance.

Table 7. Effect of environmental factors on methane oxidation performance.

Factors	Range tested	Optimal value	CH_4 reduction efficiency (%)
Temperature (°C)	20 - 40	35 ± 1.05	76.89 ± 6.33
pH	6.0 - 8.5	7.5 ± 0.22	72.34 ± 5.87
Dissolved Oxygen (mg/L)	0.1 - 2.0	0.5 ± 0.01	68.52 ± 5.41
Nitrate Concentration (mg/L)	10 - 100	50 ± 1.5	70.18 ± 5.65
Salinity (g/L NaCl)	0 - 15	5 ± 0.15	65.73 ± 5.12

3.6 Implications for greenhouse gas mitigation in the palm oil industry

The potential for greenhouse gas mitigation by implementing anoxic methane-oxidizing consortia in palm oil mill effluent treatment was evaluated based on industry standards and current carbon market values. Recent studies and market data support the calculations and estimations. The baseline calculations for POME generation were established using standard industry parameters from a typical medium-sized palm oil mill. The 60 tonnes of Fresh Fruit Bunches (FFB) mill capacity per hour represents a common operational scale in Southeast Asia [42][1]. The operating schedule of 20 hours per day accounts for necessary maintenance periods and shift changes, while the 300 operating days per year considers seasonal variations, scheduled maintenance, and holidays. The POME generation rate of 0.7 m^3 per tonne of FFB processed reflects standard extraction efficiency and typical water usage patterns. These parameters yield an annual POME production of 252,000 m^3/year, calculated as: hourly capacity (60 t/h) × daily operation (20 h/d) × annual operation (300 d/y) × POME generation rate (0.7 m^3/t). This calculation provides a realistic baseline for assessing methane emissions and treatment requirements. The methane generation potential from POME was calculated based on its chemical oxygen demand (COD) and established conversion factors. Using an average COD concentration of 51,000 mg/L for untreated POME [43][2] and considering standard anaerobic treatment parameters, the calculations incorporated a methane conversion factor of 0.25 kg CH_4/kg COD removed and typical COD removal efficiency of 85%. Applied to the annual POME production of 252,000 m^3, this yields 2,733.75 tonnes CH_4/year, demonstrating significant potential for methane capture and treatment in palm oil mills. The environmental impact of methane emissions was evaluated using the latest IPCC [44][3] global warming potential (GWP) factor of 28 for a 100-year time horizon. The calculated annual methane generation of 2,733.75 tonnes translates to 76,545 tonnes CO_2e/year. However, industry data from Jupesta et al. [45][4] indicates typical mill emissions range between 28,000-32,000 t CO_2e/year. We adopted 30,000 t CO_2e/year for conservative estimation as our baseline, aligning with industry averages while avoiding potential overestimation. Current carbon market analysis reveals varying credit values, with compliance markets averaging 7.85 USD/t CO_2e and voluntary markets ranging from 3-15 USD/t CO_2e. To maintain conservative economic projections, we selected 5 USD/t CO_2e as our reference value, ensuring a realistic assessment of potential financial benefits while accounting for market fluctuations (Table 8).

The economic feasibility of implementing anoxic methane-oxidizing systems in palm oil mills was assessed through a comprehensive cost-benefit analysis. Initial capital investment ranges from 275,000 to 375,000 USD, encompassing basic infrastructure (150,000-200,000 USD), monitoring equipment (50,000-75,000 USD), and installation costs (75,000-100,000 USD). These estimates are based on current market prices and recent implementation projects in Southeast Asia. Annual operating expenses are calculated as percentages of key financial parameters. Labor costs constitute 20% of carbon credit value, reflecting skilled operator requirements and technical supervision. Maintenance expenses are 10% of capital investment, ensuring proper system upkeep and performance. Monitoring activities require 5% of the carbon credit value, covering regular testing and compliance verification. Consumables, including chemical supplies and replacement parts, account for 15% of carbon credit value. The payback period analysis demonstrates favorable investment returns across different efficiency scenarios. High-efficiency operations (80% methane reduction) achieve the quickest return on investment at 2.8-3.8 years. Medium efficiency scenarios (65% reduction) require 3.5-4.5 years, while low-efficiency operations (50% reduction) need 4.5-5.5 years. These calculations incorporate conservative carbon credit valuations and account for potential market fluctuations.

The relationship between methane reduction efficiency and cost savings is not perfectly linear, as seen in Figure 2. The results demonstrate a substantial potential for reducing methane emissions from POME. In the optimal conditions achieved in this study, with a methane reduction efficiency of 76.89%, we estimate a reduction of 23,067 t CO_2e/year for an average palm oil mill. Assuming a carbon credit value of 5 USD/t CO_2e, the optimal conditions scenario could result in cost savings of 115,335 USD/year. This level of mitigation falls between the medium and high-efficiency scenarios, indicating that the developed system performs well within practical expectations. This is due to the diminishing returns as efficiency increases, a common phenomenon in biological treatment systems noted by Mohammad et al. [46][5] in their review of POME treatment technologies. These findings have broader implications for the palm oil industry's sustainability efforts. As

Esiri et al. [47] noted, the industry faces increasing pressure to reduce its environmental footprint. Implementing effective methane treatment systems like the one developed in this study could significantly contribute to meeting sustainability goals and improving the industry's public image. Moreover, the potential for integrating this treatment system into existing biogas capture facilities at palm oil mills presents an opportunity for synergistic benefits. It would reduce methane emissions and enhance the quality of biogas for energy generation, as suggested by Nasution et al. [48] in their study on integrated POME treatment systems. However, it's crucial to consider the practical challenges of implementing such systems at an industrial scale. Factors such as initial investment costs, operational complexities, and the need for skilled personnel to manage biological treatment systems must be carefully evaluated. Future studies should focus on pilot-scale implementations to assess these practical aspects and refine the technology for industrial use. In conclusion, the anoxic methane-oxidizing consortium developed in this study shows significant potential for greenhouse gas mitigation in the palm oil industry. With substantial environmental benefits and promising economic incentives, this technology could play a crucial role in enhancing the sustainability of palm oil production. However, further research is needed to optimize the industrial-scale application system and fully understand its long-term impacts and benefits.

Table 8. Estimated greenhouse gas mitigation potential and economic benefits for a typical palm oil mill

Treatment Scenario	CH_4 Reduction (%)[6]	Annual CO_2e Reduction (t/y)[7]	Carbon Credit Value (USD/y)[8]	Operating Cost (USD/y)[9]	Net Benefit (USD/y)
Baseline	0	0	0	0	0
Low efficiency	50 ± 2.5	15,000 ± 750	75,000 ± 3,750	15,000 ± 750	60,000 ± 3,000
Medium efficiency	65 ± 3.3	19,500 ± 975	97,500 ± 4,875	19,500 ± 975	78,000 ± 3,900
High efficiency	80 ± 4.0	24,000 ± 1,200	120,000 ± 6,000	24,000 ± 1,200	96,000 ± 4,800

Notes: [42] [1]Based on standard mill operations (60 t FFB/h capacity), [43] [2]Calculated using validated conversion factors, [44] [3]Using IPCC AR6 GWP values, [45] [4]Industry average from MPOB database, [46] [5]Conservative market estimate, [6]Measured in laboratory studies, [7]Calculated from baseline emissions, [8]Based on 5 USD/t CO_2e, [9]Including maintenance, monitoring, and operation.

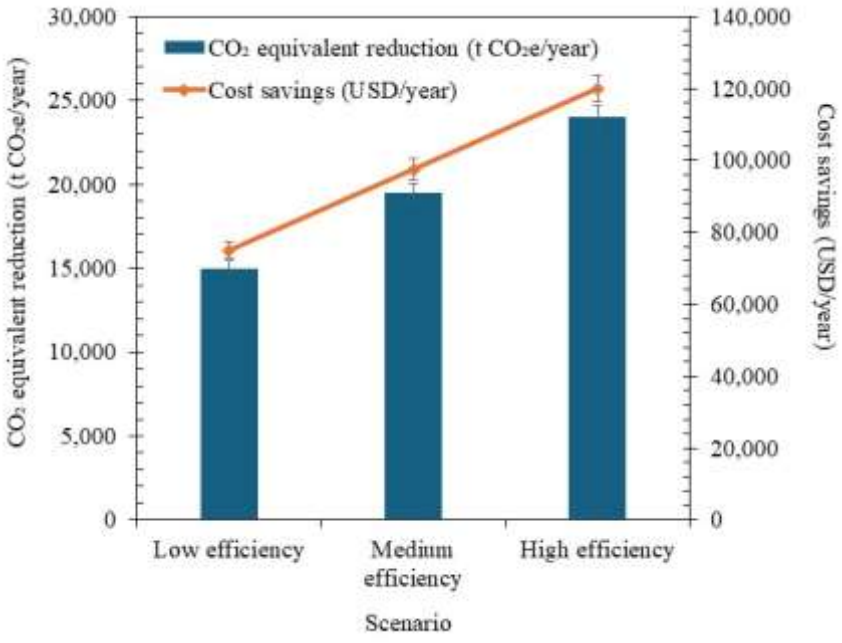


Figure 2. Comparison of greenhouse gas mitigation potential and cost savings for different treatment scenarios.

Several significant challenges must be considered when scaling this laboratory-scale methane oxidation system to industrial applications. Process engineering challenges include mass transfer limitations, as the efficient gas-liquid contact achieved in 120 mL serum bottles will be difficult to replicate in large reactors. Temperature control becomes more complex due to heat generation in large volumes and the formation of temperature gradients. Biological stability presents another major concern, where maintaining consistent microbial community composition becomes challenging under variable industrial conditions and competition from indigenous microorganisms. Operational constraints include managing continuous flow systems instead of batch operations, with variable POME discharge rates affecting process stability. Real-time monitoring and control systems become essential but complex to implement effectively. The reactor design must address these challenges while considering space limitations and cost-effectiveness. Installation requires significant capital investment (275,000-375,000 USD) for infrastructure, monitoring equipment, and specialized gas collection and biomass retention systems. Long-term process stability and performance verification need extensive pilot-scale testing before full implementation. Economic viability depends on optimizing operating costs, particularly for energy consumption, chemical requirements, and maintenance. These challenges necessitate careful engineering solutions and comprehensive pilot studies to validate the technology's industrial applicability.

4. Conclusions

This study investigated the potential of anoxic methane-oxidizing consortia for mitigating dissolved methane in palm oil mill biogas effluents. The key findings are the anoxic methane-oxidizing consortium derived from cattle farm effluent demonstrated the highest methane reduction efficiency of 76.89% after a 3-week incubation period, and methane consumption rates varied significantly among different microbial sources, with cattle farm effluent (49.37 mg-CH_4/m^2/d) and landfill soil (45.31 mg-CH_4/m^2/d) showing the highest rates. Environmental factors significantly influenced methane oxidation performance, with optimal conditions identified as Temperature: 35°C, pH: 7.5, Dissolved oxygen: 0.5 mg/L, Nitrate concentration: 50 mg/L, Salinity: 5 g/L NaCl. Plastic media enhanced methane reduction efficiency for most microbial sources, particularly for the cattle farm effluent consortium (67.07% efficiency). The developed system can mitigate up to 23,067 t CO_2e/year for an average palm oil mill, with associated cost savings of approximately 115,335 USD/year through carbon credits. The anoxic methane-oxidizing system can be incorporated into current biogas plants to enhance methane capture and reduce effluent emissions. This technology can be implemented as a standalone solution for mills without biogas facilities to mitigate methane emissions from POME. Adopting this technology can significantly reduce the greenhouse gas footprint of palm oil production, improving the industry's sustainability profile. The substantial reduction in methane emissions can be translated into carbon credits, providing an additional revenue stream for palm oil mills.

5. Acknowledgements

The financial support for this research was generously provided by the National Science and Research Fund (NSRF) and the Program Management Unit for Human Resources & Institutional Development, Research and Innovation (PMU-B) (grant number B13F660062).

Author Contributions: Conceptualization, experimental design, C.L., N.P., C.N., carrying out experiment and data acquisition, C.L, S.C., writing and editing, C.L., N.P., C.N.,

Funding: This research was funded by the National Science and Research Fund (NSRF) and the Program Management Unit for Human Resources & Institutional Development, Research and Innovation (PMU-B) (grant number B13F660062).

Conflicts of Interest: The authors declare no conflict of interest.

References

[1] USDA, United States Department of Agriculture. Foreign Agricultural Service: Production – Palm oil. **2024**. Available at: https://fas.usda.gov/data/production/commodity/4243000 (accessed on 29 October 2024).

[2] Chaikitkaew, S.; In-Chan, S.; Singkhala, A.; Tukanghan, W.; Mamimin, C.; Reungsang, A.; Birkeland N.K.; O-Thong, S. *Clostridium thailandense* sp. nov., a novel CO_2-reducing acetogenic bacterium isolated from

peatland soil. *International Journal of Systematic and Evolutionary Microbiology* **2022**, *72*(2). https://doi.org/10.1099/ijsem.0.005254.
[3] O-Thong, S.; Mamimin, C.; Kongjan, P.; Reungsang, A. Two-stage fermentation process for bioenergy and biochemicals production from industrial and agricultural wastewater. *Advances in Bioenergy* **2020**, *5*, 249-308. https://doi.org/10.1016/bs.aibe.2020.04.007.
[4] Souza, C.L.; Chernicharo, C.A.L.; Aquino, S.F. Quantification of dissolved methane in UASB reactors treating domestic wastewater under different operating conditions. *Water Science & Technology* **2011**, *64*(11), 2259-2264. https://doi.org/10.2166/wst.2011.695.
[5] Cookney, J.; Mcleod, A.; Mathioudakis, V.; Ncube, P.; Soares, A.; Jefferson, B.; McAdam, E. Dissolved methane recovery from anaerobic effluents using hollow fibre membrane contactors. *Journal of Membrane Science* **2016**, *502*, 141-150. https://doi.org/10.1016/j.memsci.2015.12.037
[6] Sánchez, A.; Rodríguez-Hernández, L.; Buntner, D.; Esteban-García, A. L.; Tejero, I.; Garrido, J. M. Denitrification coupled with methane oxidation in a membrane bioreactor after methanogenic pre-treatment of wastewater. *Journal of Chemical Technology & Biotechnology* **2016**, *91*(12), 2950-2958. https://doi.org/10.1002/jctb.4913
[7] U.S. EPA, United States Environmental Protection Agency, 2020. EPA's: Air Quality-Cities and Counties. Available online:https://www.epa.gov/air-trends/air-quality-cities-and-counties. (accessed on 27 August 2024).
[8] Pachauri, R.K.; Allen, M.R.; Barros, V.R.; Broome, J.; Cramer, W.; Christ, R.; Church, J.A.; Clarke, L.; Dahe, Q.; Dasgupta, P.; et al. (Eds.), Climate Change 2014: Synthesis Report. Contribution of Working Groups I, II and III to the Fifth Assessment Report of the Intergovernmental Panel on Climate Change. IPCC, Geneva, Switzerland.
[9] Stazi, V.; Tomei, M.C. Dissolved methane in anaerobic effluents: A review on sustainable strategies for optimization of energy recovery or internal process reuse. *Journal of Cleaner Production* **2021**, *317*, 128359. https://doi.org/10.1016/j.jclepro.2021.128359.
[10] Samanta, D.; Sani, R.K. Methane Oxidation via Chemical and Biological Methods: Challenges and Solutions. *Methane* **2023**, *2*, 279-303. https://doi.org/10.3390/methane2030019
[11] Guerrero-Cruz, S.; Stultiens, K.; Versantvoort, W. M.; Jetten, M. S.; Kartal, B. Key physiology of a nitrite-dependent methane-oxidizing enrichment culture. *Applied and Environmental Microbiology* **2019**, *85*(8). https://doi.org/10.1128/AEM.00124-19.
[12] Costa, R.; Okada, D.; Delforno, T.; Foresti, E. Methane-oxidizing archaea, aerobic methanotrophs and nitrifiers coexist with methane as the sole carbon source. *International Biodeterioration & Biodegradation* **2019**, *138*, 57-62. https://doi.org/10.1016/j.ibiod.2019.01.005.
[13] Whittenbury, R.; Phillips, K.C.; Wilkinson, J.F. Enrichment, isolation and some properties of methane-utilizing bacteria. *Journal of General Microbiology* **1970**, *61*(2), 205-218. https://doi.org/10.1099/00221287-61-2-205.
[14] Hanson, R.S.; Hanson, T.E. Methanotrophic bacteria. *Microbiological Reviews* **1996**, *60*(2), 439-471. https://doi.org/10.1128/mr.60.2.439-471.1996.
[15] Hernandez, M.E.; Beck, D.A.C.; Lidstrom, M.E.; Chistoserdova, L. Oxygen availability is a major factor in determining the composition of microbial communities involved in methane oxidation. *PeerJ* **2015**, *3*, e801. https://doi.org/10.7717/peerj.801.
[16] Zhang, W.; Zhao, Y.; Wang, J.; Gao, Y.; Zhou, L.; Sun, S.; Tang, M.; Peng, Y.; Guo, W.; Wang, H. Effect of nitrate concentration on anaerobic methane oxidation coupled to denitrification in membrane biofilm reactor after prolonged storage. *Water, Air, & Soil Pollution* **2024**, *235*, 246. https://doi.org/10.1007/s11270-024-07040-5.
[17] Kalyuzhnaya, M.G.; Gomez, O.A.; Murrell, J.C. The methane-oxidizing bacteria (Methanotrophs). In: McGenity, T. (eds) Taxonomy, Genomics and Ecophysiology of Hydrocarbon-Degrading Microbes. Handbook of Hydrocarbon and Lipid Microbiology. **2019**. Springer, Cham. https://doi.org/10.1007/978-3-030-14796-9_10.
[18] Ahmadi, F.; Bodraya, T.; Lackner, M. Methane biofiltration processes: A summary of biotic and abiotic factors. *Methane* **2024**, 3(1), 122-148. https://doi.org/10.3390/methane3010008.
[19] Chidambarampadmavathy, K.; Karthikeyan, O.; Huerlimann, R.; Maes, G.; Heimann, K. Response of mixed methanotrophic consortia to different methane to oxygen ratios. *Waste Management* **2017**, *61*, 220-228. https://doi.org/10.1016/j.wasman.2016.11.007.
[20] Zheng, X.; Li, H.; Wang, Z.; Sun, Z.; Zhao, L. Intermediates production in methane oxidation coupled with denitrification: Current status, challenges, and future opportunities. *Fermentation* **2023**, *9*(7), 645. https://doi.org/10.3390/fermentation9070645.

[21] Reddy, K.R.; Rai, R.; Green, S.; Jyoti, K.C. Effect of pH on methane oxidation and community composition in landfill cover soil. *Journal of Environmental Engineering* **2020**, *146*. 04020037. https://doi.org/10.1061/(ASCE)EE.1943-7870.0001712.

[22] Oduor, W.W.; Wandera, S.M.; Murunga, S.I.; Raude, J.M. Enhancement of anaerobic digestion by co-digesting food waste and water hyacinth in improving treatment of organic waste and bio-methane recovery. *Heliyon* **2022,** 8(9), e10580. https://doi.org/10.1016/j.heliyon.2022.e10580.

[23] Bernat, K.; Zaborowska, M.; Zielińska, M.; Wojnowska-Baryła, I.; Ignalewski, W. Biological treatment of leachate from stabilization of biodegradable municipal solid waste in a sequencing batch biofilm reactor. *International Journal of Environmental Science and Technology* **2021**, *18*, 1047–1060. https://doi.org/10.1007/s13762-020-02915-6.

[24] Cabrol, L.; Thalasso, F.; Gandois, L.; Sepulveda-Jauregui, A.; Martinez-Cruz, K.; Teisserenc, R.; Tananaev, N.; Tveit, A.; Svenning, M.M.; Barret, M. Anaerobic oxidation of methane and associated microbiome in anoxic water of Northwestern Siberian lakes. *Science of The Total Environment* **2020**, *736*, 139588. https://doi.org/10.1016/j.scitotenv.2020.139588.

[25] Kumar, D.J.P.; Mishra, R. K.; Chinnam, S.; Binnal, P.; Dwivedi, N.A comprehensive study on anaerobic digestion of organic solid waste: A review on configurations, operating parameters, techno-economic analysis and current trends. *Biotechnology Notes* **2024**, 5, 33-49. https://doi.org/10.1016/j.biotno.2024.02.001.

[26] Zhao, Y.; Liu, Y.; Cao, S.; Hao, Q.; Liu, C.; Li, Y. Anaerobic oxidation of methane driven by different electron acceptors: *A review. Science of The Total Environment* **2024**, *946*, 174287. https://doi.org/10.1016/j.scitotenv.2024.174287.

[27] Meyer-Dombard, D.R.; Bogner, J.E.; Malas, J. A review of landfill microbiology and ecology: a call for modernization with 'next generation' technology. *Frontiers in Microbiology* **2020,** *11*, 1127. https://doi.org/10.3389/fmicb.2020.01127. PMID: 32582086.

[28] Kim, C.; Walitang, D.I.; Roy Choudhury, A.; Lee, Y.; Lee, S.; Chun, H.; Heo, T.; Park, K.; Sa, T. Changes in soil chemical properties due to long-term compost fertilization regulate methane turnover related gene abundances in rice paddy. *Applied Sciences* **2022**, 12(5), 2652. https://doi.org/10.3390/app12052652.

[29] Govindaraju, A.; Good, N.M.; Zytnick, A.M.; Martinez-Gomez, N.C. Employing methylotrophs for a green economy: One-carbon to fuel them all and through metabolism redesign them. *Current Opinion in Microbiology* **2022**, *67*, 102145. https://doi.org/10.1016/j.mib.2022.102145.

[30] Mohammed, S.; Eljack, F.; Al-Sobhi, S.; Kazi, M. A systematic review: The role of emerging carbon capture and conversion technologies for energy transition to clean hydrogen. *Journal of Cleaner Production* **2024**, 447, 141506. https://doi.org/10.1016/j.jclepro.2024.141506.

[31] Sahoo, K.K.; Goswami, G.; Das, D. Biotransformation of methane and carbon dioxide into high-value products by methanotrophs: current state of art and future prospects. *Frontiers in Microbiology* **2021**, *12*, 636486. https://doi.org/10.3389/fmicb.2021.636486.

[32] Wilson, R.M.; Tfaily, M.M.; Rich, V.I.; Keller, J.K.; Bridgham, S.D.; Zalman, C.M.; Meredith, L.; Hanson, P.J.; Hines, M.; Pfeifer-Meister, L.; Saleska, S.R.; Crill, P.; Cooper, W.T.; Chanton, J.P.; Kostka, J.E. Hydrogenation of organic matter as a terminal electron sink sustains high CO_2:CH_4 production ratios during anaerobic decomposition. *Organic Geochemistry* **2017**, *112*, 22-32. https://doi.org/10.1016/j.orggeochem.2017.06.011.

[33] Nguyen, A.D; Chau, T.H.T.; Lee, E.Y. Methanotrophic microbial cell factory platform for simultaneous conversion of methane and xylose to value-added chemicals. *Chemical Engineering Journal* **2021**, *420*, 127632. https://doi.org/10.1016/j.cej.2020.127632.

[34] Patel, S.K.; Singh, D.; Pant, D.; Gupta, R.K.; Busi, S.; Singh, R.V.; Lee, J. Polyhydroxyalkanoate production by methanotrophs: recent updates and perspectives. *Polymers* **2023**, *16*(18), 2570. https://doi.org/10.3390/polym16182570.

[35] Lu, J.; Yan, W.; Shang, W.; Sun, F.; Li, A.; Sun, J.; Li, X.; Mu, J. Simultaneous enhancement of nitrate removal flux and methane utilization efficiency in MBfR for aerobic methane oxidation coupled to denitrification by using an innovative scalable double-layer membrane. *Water Research* **2021**, *194*, 116936. https://doi.org/10.1016/j.watres.2021.116936.

[36] Lu, J.; Shen, Q.; Li, X.; Sun, F.; Yi, J.; Dong, W.; Yan, W.; Du, H.; Mu, J. Surface-manipulated membranes to accelerate biofilm formation and to resist bacterial detachment in MBfR for aerobic methane oxidation coupled to denitrification. *Chemical Engineering Journal* **2022**, *430*, 132629. https://doi.org/10.1016/j.cej.2021.132629.

[37] Pang, S.; Zhang, S.; Lv, X.; Han, B.; Liu, K.; Qiu, C.; Wang, C.; Wang, P.; Toland, H.; He, Z. Characterization of bacterial community in biofilm and sediments of wetlands dominated by aquatic macrophytes. *Ecological Engineering* **2016**, *97*, 242-250. https://doi.org/10.1016/j.ecoleng.2016.10.011.
[38] Zheng, Y.; Huang, R.; Wang, B.Z.; Bodelier, P.L.E.; Jia, Z.J. Competitive interactions between methane- and ammonia-oxidizing bacteria modulate carbon and nitrogen cycling in paddy soil. *Biogeosciences* **2014**, *11*(12), 3353-3368. https://doi.org/10.5194/bg-11-3353-2014.
[39] Yao, X.; Wang, J.; Hu, B. How methanotrophs respond to pH: A review of ecophysiology. *Frontiers in Microbiology* **2022**, *13*. https://doi.org/10.3389/fmicb.2022.1034164.
[40] Gilman, A.; Fu, Y.; Hendershott, M.; Chu, F.; Puri, A. W.; Smith, A. L.; Pesesky, M.; Lieberman, R.; Beck, A. C.; Lidstrom, M. E. Oxygen-limited metabolism in the methanotroph *Methylomicrobium buryatense* 5GB1C. *PeerJ* **2017**, *5*. https://doi.org/10.7717/peerj.3945.
[41] Hu, Z.; Ru, D.; Wang, Y.; Zhang, J.; Jiang, L.; Xu, X.; Nie, L. Optimization of a nitrite-dependent anaerobic methane oxidation (n-damo) process by enhancing methane availability. *Bioresource Technology* **2019**, *275*, 101-108. https://doi.org/10.1016/j.biortech.2018.12.035.
[42] Agustiar; Roma; Romanos; Aulia, M.R.; Ramayana. Mass balance of palm waste energy potential in palm oil processing in South West Aceh, Indonesia. IOP Conference Series: Earth and Environmental Science **2024**, *129*, 012076. https://doi.org/10.1088/1755-1315/1297/1/012076.
[43] Ng, D.K.; Wong, S.L.; Andiappan, V.; Ng, L.Y. Mathematical optimisation for sustainable bio-methane (Bio-CH_4) production from palm oil mill effluent (POME). *Energy* **2023**, *265*, 126211. https://doi.org/10.1016/j.energy.2022.126211.
[44] IPCC, Climate Change 2023: Summary for Policymakers. In: Climate Change 2023: Synthesis Report. Contribution of Working Groups I, II and III to the Sixth Assessment Report of the Intergovernmental Panel on Climate Change [Core Writing Team, H. Lee and J. Romero (eds.)]. IPCC, Geneva, Switzerland, **2023**. pp. 1-34, https://doi.org/10.59327/IPCC/AR6-9789291691647.001.
[45] Jupesta, J.; Akimoto, K.; Boer, R. 2022. Is it possible to achieve carbon neutrality in palm oil production? In: He, BJ., Prasad, D., Pignatta, G., Jupesta, J. (eds) Climate Change and Environmental Sustainability. Advances in Science, Technology & Innovation. Springer, Cham. https://doi.org/10.1007/978-3-031-12015-2_8.
[46] Mohammad, S.; Baidurah, S.; Kobayashi, T.; Ismail, N.; Leh, C.P. Palm oil mill effluent treatment processes—A review. *Processes* **2021**, *9*(5), 739. https://doi.org/10.3390/pr9050739.
[47] Esiri, A.E.; Babayeju, O.A.; Ekemezie, I.O. Implementing sustainable practices in oil and gas operations to minimize environmental footprint. *GSC Advanced Research and Reviews* **2024**, *19*(03), 112–121. https://doi.org/10.30574/gscarr.2024.19.3.0207.
[48] Nasution, M.A.; Wulandari, A.; Ahamed, T.; Noguchi, R. Alternative POME treatment technology in the implementation of roundtable on sustainable palm oil, Indonesian Sustainable Palm Oil (ISPO), and Malaysian Sustainable Palm Oil (MSPO) Standards Using LCA and AHP Methods. *Sustainability* **2019**, *12*(10), 4101. https://doi.org/10.3390/su12104101.

ASEAN
Journal of Scientific and Technological Reports
Online ISSN:2773-8752

Research article

Identifying Niche Factors for Planting Vetiver Grass in Thailand

Yaowaret Jantakat[1*], Pongpun Juntakut[2] and Chomphak Jantakat[3]

[1] Faculty of Sciences and Liberal Arts, Rajamangala University of Technology Isan, Khonkaen, 40000, Thailand
[2] Department of Civil Engineering, Chulachomklao Royal Military Academy, Nakhonnayok, 26000, Thailand
[3] Faculty of Business Administration, Vongchavalitkul University, Nakhonratchasima, 30000, Thailand
* Correspondence: yaowaret.ja@rmuti.ac.th

Citation:
Jantakat, Y.; Juntakut, P.; Jantakat, C. Indentifying niche factors for planting vietiver grass in Thailand. *ASEAN J. Sci. Tech. Report.* **2025**, *28*(1), e254975. https://doi.org/10.55164/ajstr.v28i1.254975

Article history:
Received: July 10, 2024
Revised: November 17, 2024
Accepted: November 20, 2024
Available online: February 16, 2025

Publisher's Note:
This article has been published and distributed under the terms of Thaksin University.

Abstract: This study aims to identify niche factors to use in mapping potential areas of vetiver grass planting in Thailand. Pak Chong district of Nakhon Ratchasima province is selected as a case study. There were 4 used datasets: existing planted vetiver data, 3 topographical data (DEM, slope, and aspect), bioclimatic data, and the modified soil data. These datasets were transformed into GIS data with WGS 1984 and Zone 48N and were processed by ecological niche factor analysis (ENFA) in BIOMAPPER. ENFA produced the habitat suitability (HS) index for planting vetiver grass and provided understanding of spatial dispersion ability and tolerance of vetiver grass ecology to the current environment. The analyzed results showed that HS-based ENM2 has the highest possibility for planting vetiver grass, with AVI 0.93 and CVI 0.07. The ENM2 included 97% marginality (the ability for spatial distribution in the study area) and 3% specialization (durability in the study area). Moreover, this ENM2 explicitly indicates the existing vetiver grasses have more highly spatial distribution than durability in the study area with niche factors such as BIO1: the mean annual temperature (25-31°C), BIO5: mean monthly maximum temperature (30-38°C), BIO6: mean monthly minimum temperature (17-27°C) and elevation (600-1,300 m), respectively. The obtained niche factor (e.g., BIO1, BIO5, BIO6, and elevation) will be implemented to map potential areas of vetiver grass in the Center for Promoting the Utilization of Vetiver Grass under the Royal Initiative Project (CPUVGRIP) of Forest Royal Department (FRD) in Nakhon Ratchasima, Thailand further.

Keywords: Vetiver grass; Habitat suitability; Ecological niche modeling; Spatial distribution

1. Introduction

King Rama IX gave the first royal initiative since 1991 to encourage the utilization of vetiver in Thailand for soil and water conservation after receiving information from the World Bank [1]. From the past to the present (about 28 years), many Thai agencies (both government and private sectors) have promoted vetiver grass use in Thailand as a suitable way for Thai society to address these problems with a simple technology that was easy to implement and cost-effective compared to other methods [2,3,4]. The government developed "The Committee to Master Plan the Development and Campaigning for the Use of Vetiver." It made the Land Development Department (LDD) a central unit responsible for breeding, propagating, and distributing vetiver

varieties. The Office of the Royal Development Projects Board was responsible for distributing vetiver varieties to prevent discrepancies and usage of wrong species that may damage agricultural areas. The species Vetiveria Zizanioides was identified by the World Bank as the most effective at preventing soil erosion [2]. Thus, it was promoted for use in Thailand. These results were then expanded to Thai government agencies such as the Royal Forest Department (FRD) and the Department of Highways (DOH).

I reviewed many papers relevant to ecological modeling and assessment in this work. Ecological Niche Modeling (ENM) remains important for exploiting habitat suitability, as shown in the articles by Chen and colleagues [5] and Mathur and colleagues [6]. In ecology, the dimensions of an environmental niche vary from one species to another. The relative importance of specific environmental variables for one species may vary according to the geographic and biotic contexts [7]. A species' niche encompasses physical and environmental conditions that interact with other existing species, such as predation or competition [8,9]. The niche of a species is ancillary to environmental factors, which affect the ability of a species to survive and endure [10]. The study of ENM is worked on by software such as Maxent [11], Biomapper [12], ModEco [13], OpenModeller [14], and R [15]. This paper used ENM in the Biomapper program because Ecological Niche Factor Analysis (ENFA) proved to be a suitable method for modeling environmental species distributions, regardless of the presence-only dataset size [16]. Moreover, Biomapper is a kit of GIS and statistical tools designed to build Habitat Suitability (HS) models and maps for any animal or plant-centered on ENFA that allows computing HS models without the need for the absence of data [17].

Therefore, the objective of this study proposes the identification of niche factors for HS of vetiver grass planting to support soil and water conservation for Thai concerned agencies such as the Center for Promoting the Utilization of Vetiver Grass under the Royal Initiative Project (CPUVGRIP) in Nakhon Ratchasima province. The obtained niche factor will use to generate a map for potential vetiver grass planting areas further.

1.1 Ecology and environment of vetiver grass

Vetiver grass has grown over various sites and in various environmental conditions. However, Grimshaw [18] and Truong [19] explicitly the ecological characteristics of vetiver grass are based on three main environmental factors: climate, topography, and soil, and more details as follows:

1. Climate factor: vetiver grass can tolerate temperatures up to 40°C [18].
2. Topographic factor: vetiver grass can be planted and survive from 200 to 2000 m. [19].
3. Soil factor: there are many experiments such as vetiver tolerates high levels of salinity and shows a 50% dry matter yield reduction [20]; the tolerance of vetiver to a range of soil pH has been carried out and demonstrates the tolerance of vetiver to pH levels as low as 3.3 with soil Al toxicity levels of 68% - indications are that vetiver may be one of the most tolerant crops and pasture species to Al toxicity [21].

1.2 Study area

The study area is the Pak Chong district of Nakhon Ratchasima province, northeastern Thailand. The study area has 1,825.20 km2 and is situated approximately between latitudes from 14° to 15° N and longitudes from 100° to 102°E, as shown in Figure 1. For common physical data of the study area, topography includes a series of complex mountains that range in elevation from 200 m to 1,300 m above mean sea level (MSL); climatic data is dominantly affected by the monsoon that is measured and monitored by meteorological stations of the Thailand Meteorological Department (TMD); soil data is mainly classified as slope complex by Land Development Department (LDD) of Thailand.

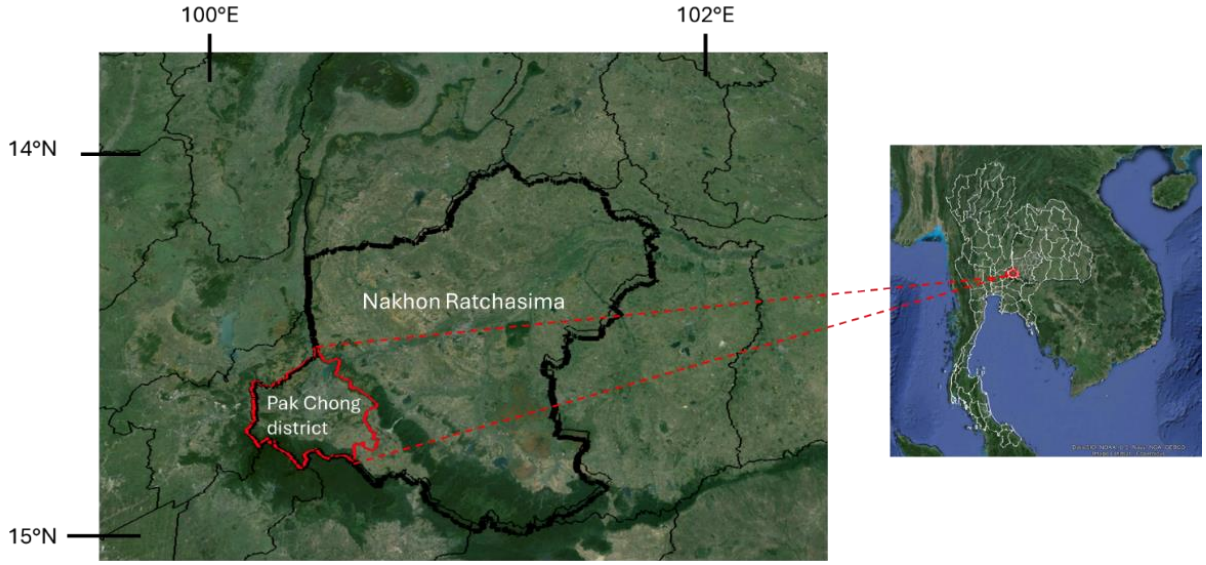
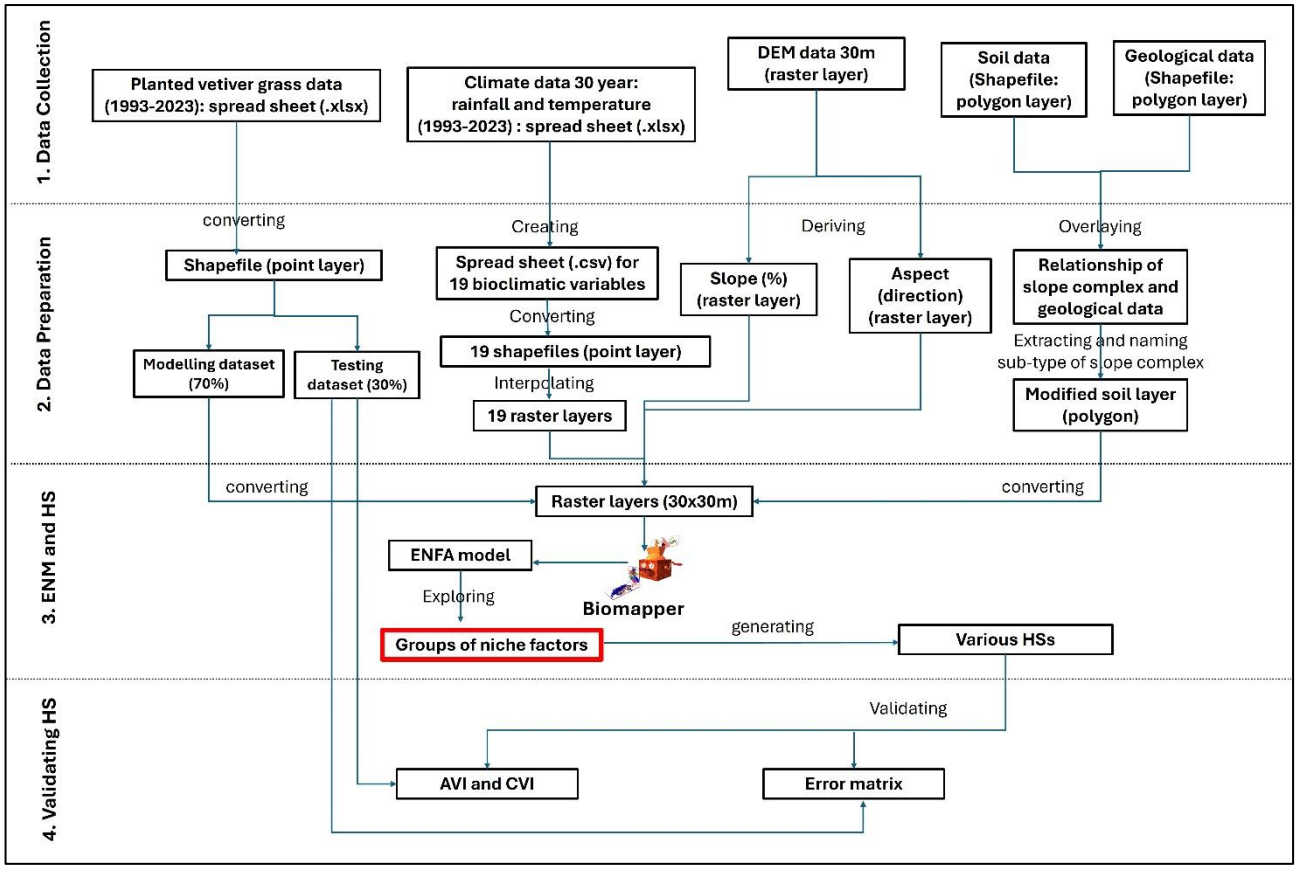


Figure 1. Location of study area.

2. Materials and Methods

This study requires the identification of niche factors for planting vetiver grass in Thailand. Pak Chong district of Nakhon Ratchasima province is the case study. A group of niche factors were identified by ENFA modeling in Biomapper and then generated HS for planting vetiver grass. Therefore, the framework of methodological steps in this study can be presented in Figure 2, and more details of each step are below.



Remark: The red shows the purpose of this study

Figure 2. The framework of the study's methodological steps

2.1 Data collection

This study collected datasets: 1) the planted vetiver grass data (1991-2023), 2) rainfall and temperature data (1991-2023), 3) Digital Elevation Model (DEM) 30 m, 4) soil data and 5) geological data, were summarized as Table 1. This study used the vetiver data between 1991 and 2023 (the latest data) because it was begun by the first royal initiative in 1991 to study the utilization of vetiver in Thailand for soil and water conservation until the present. Therefore, other data would be collected during the same time as well.

Table 1. Data collection for this study

Environmental data	Characteristics of available data	Sources
1. Vetiver and soil	- Vetiver Data was in spreadsheet data (.xlsx) and digital reports. - Soil data was in the form of vector-based GIS (polygon layer) and digital reports	Land Development Department (LDD)
2. Rainfall and temperature	Data was in monthly mean rainfall, and temperature was in spreadsheet data (.xlsx) and digital reports.	Thailand MeteorologicalDepartment (TMD)
3. DEM 30 m	Data was in raster-based GIS with a 30 x 30 m cell size and digital reports.	Department of National Parks, Wildlife and Plant Conservation (DNP)
4. Geology	Data was in vector-based GIS (polygon layer) and digital reports.	Department of Mineral Resources (DMR)

2.2 Data preparation

In this step, the collected data were checked the attribute data and then were prepared in the form of GIS, all the same as the geographical system of WGS 1984 and Zone 48N in QGIS program version 3.28.1 as follows:

2.2.1 The vetiver dataset

The vetiver data were collected from LDD 1991-2023. They focused on the 100 currently implemented points, which were then converted into shapefile (point layer). These vetiver points were divided into 2 datasets: one for creating ENM and HS (70 vetiver points or 70 percent) and another for validation (30 vetiver points or 30 percent). The 70/30 percent (modeling/testing) was chosen because it emphasizes the lowest accuracy assessment that the model can accept as the research paper of Gholamy et al. [22] and Tuan et al. [23]. Moreover, this study did not only regard the mentioned concept of ratio above but also considered the existing land use type of the vetiver grass locations for dividing modeled and validated datasets, as in Table 2 and Figure 3.

Table 2. The existing land use types of the vetiver grass points for dividing modelled and validated sets

Land use types	Modelling points	Validating points	Total
1. Agricultural area	35	15	50
2. Forest area	12	5	17
3. Roadside a steep slope	9	4	13
4. The edge of the water sources	14	6	20
Total	70	30	100

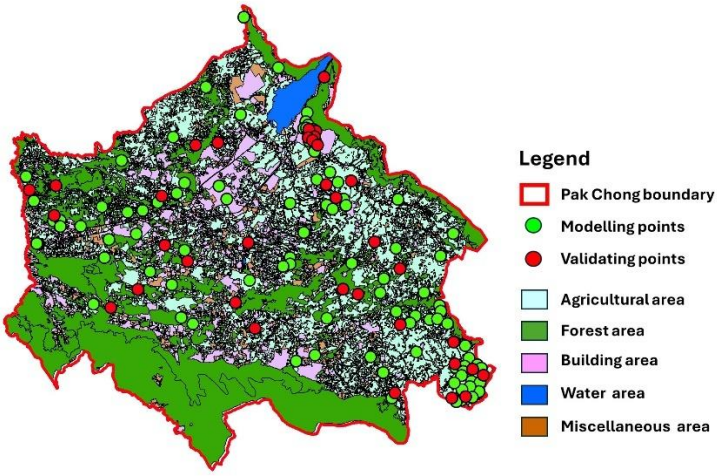


Figure 3. The existing land use types of the vetiver grass points for dividing modelled and validated sets

2.2.2 The rainfall and temperature dataset

These climatic data were characterized by using the monthly mean rainfall and temperature data from 33 climatological stations of TMD 1991-2023 that cover the study area (e.g., Nakhonsawan, Takfa Agromet., Chainat Agromet., Ayuttaya, Pathumthani, Suphanburi, Lopburi, Buachum, Pilot station, Samutprakarn, Suvarnabhumi Airport, Bangkok metropolis, Bangkok port (Klong Toei), Bang Na Agromet., Don Muang airport, Chachoengsao, Prachinburi, Aranyaprathet, Sakaew, Chonburi, Kosichang, Laemchabang, Mahasarakham, Chiyaphum, Nakhonratchasima, Pakchong agromet., Chok chai, Surin, Surin agromet., Burirum, Nang rong, Wichian buri). Then these two climatic data were used for calculating 19 bioclimate variables (as Figure 4) based on paper of O'Donnell et al. [24] (e.g., BIO1: Annual Mean Temperature; BIO2: Annual Mean Diurnal Range; BIO3: Isothermality; BIO4: Temperature Seasonality (Standard Deviation); BIO5: Max Temperature of Warmest Month; BIO6: Min Temperature of Coldest Month; BIO7: Annual Temperature Range; BIO8: Mean Temperature of Wettest Quarter; BIO9: Mean Temperature of Driest Quarter; BIO10: Mean Temperature of Warmest Quarter; BIO11: Mean Temperature of Coldest Quarter; BIO12: Annual Precipitation; BIO13: Precipitation of Wettest Month; BIO14: Precipitation of Driest Month; BIO15: Precipitation Seasonality (CV); BIO16: Precipitation of Wettest Quarter; BIO17: Precipitation of Driest Quarter; BIO18: Precipitation of Warmest Quarter; BIO19: Precipitation of Coldest Quarter).

This study used bioclimate data because it better represents the types of seasonal trends pertinent to the physiological constraints of different species based on evidence from PRISM Climate Data from Oregon State University [25]. The output of the calculated bioclimate was stored in an Excel program and then saved as .csv to convert into a shapefile (point layer) and interpolated as a raster layer.

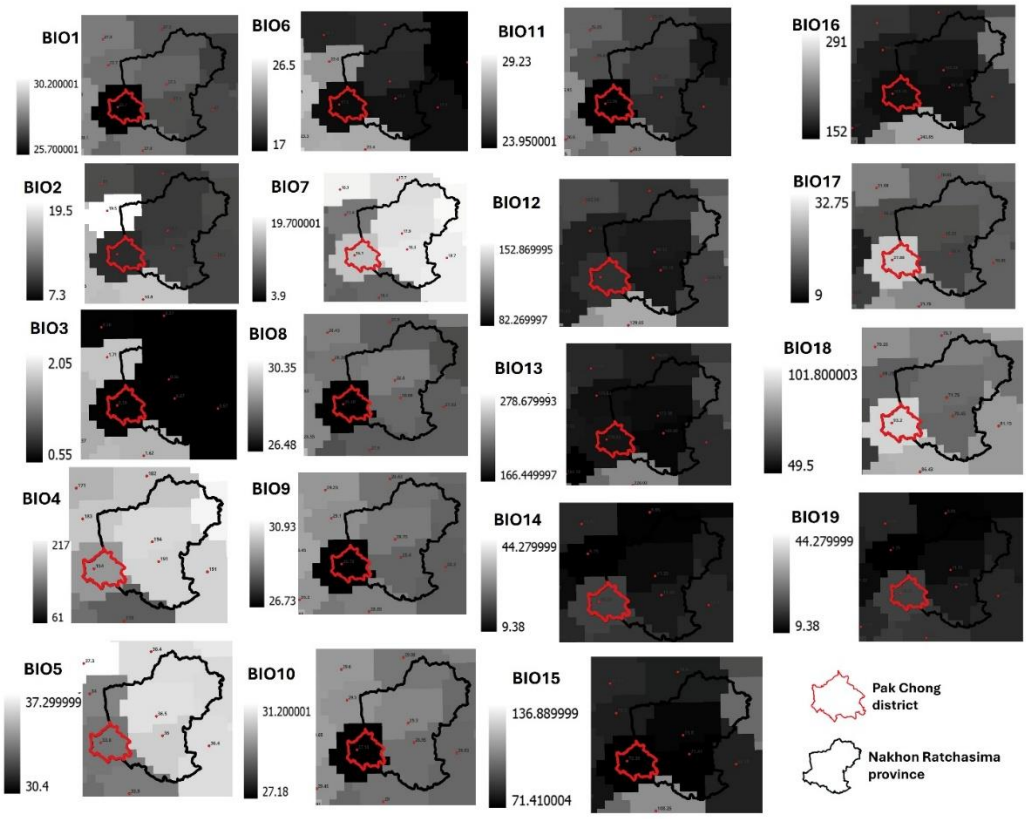


Figure 4. 19 bioclimatic layers for this study

2.2.3 The topographical dataset

The courtesy of DNP gained DEM with a cell size of 30 x 30 m. Elevation data (m) was directly extracted from DEM, while slope (degree) and aspect (direction) were also derived from DEM, as shown in Figure 5.

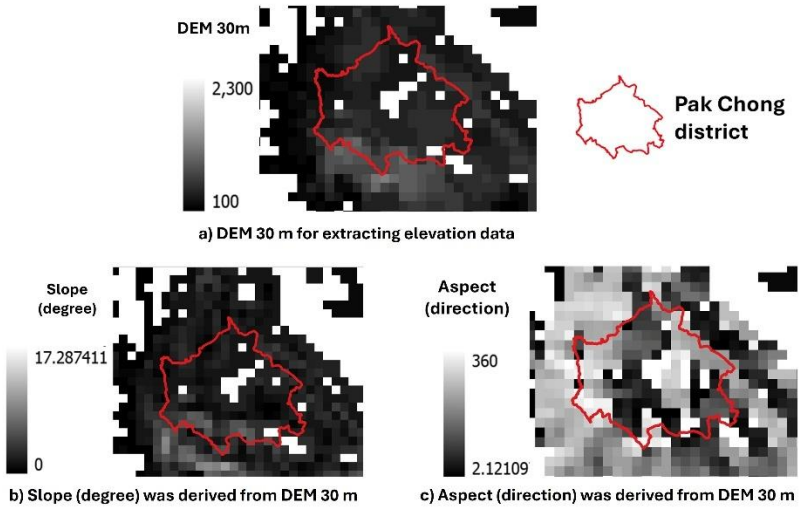


Figure 5. Three topographical layers (DEM 30m, slope, and aspect) for this study

2.2.4 The modified soil data

Some areas where soil data were classified as slope complex in the study area. Therefore, the modified soil data in this study was produced by overlaying between a layer of soil data from LDD and a layer of geological data from DMR. Here, soil data were analyzed using the characteristics of geological formation to classify subtypes of modified soil data, as shown in Figure 6.

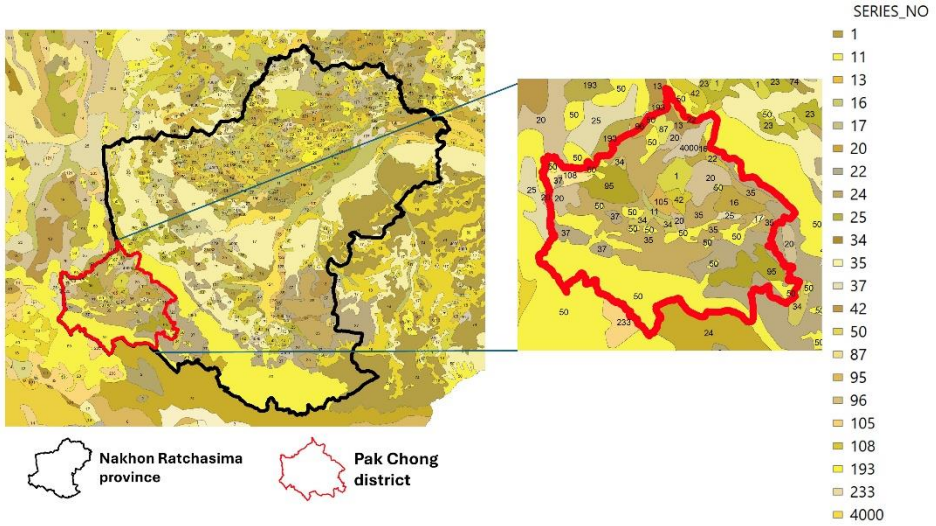


Figure 6. The modified soil data for this study

2.3 ENM and HS

In this step, we produced many ENMs-based ENFA to identify a group of niche factors for potential areas of vetiver grass planting, which were then generated as various HSs. These processes were operated in Biomapper 4.0, developed by Hirzel and colleagues [11].

In this study, all prepared data in 3.2 were converted into raster data. For ENM, raster data input ENM included 70 vetiver points' layers, 19 bioclimatic (variables) layers, 3 topographic layers (DEM, slope, and aspect), and the modified soil data. In the process, ENFA was used to produce the HS index, providing an understanding of spatial dispersion ability and tolerance of vetiver grass ecology to the current environment. ENM and validation included steps as follows:

1. Checking discrepancies: The datasets were transformed into raster format with 30 x 30 m. resolution and checked for discrepancies (they were simultaneously overlaid to verify discrepancies (same area, same spatial unit, and cell value).

2. Producing ENM: The raster-based GIS of 4-dataset was computed (in each cell) by marginality coefficient (it measured how vetiver grasses disperse with the mean environmental conditions of the study area) and specialization coefficient (it measured how vetiver grasses tolerate environmental variations of the study area). The equation of ENM production from Hirzel and colleagues [11] can be modified for this study as follows:

Marginality coefficient (m_i):

$$m_i = \frac{|m_{G\mp}m_s|}{1.96\sigma_G} \quad (1)$$

Where m_G is mean of overview spatial dispersion ability in the study area
m_s is mean of vetiver grass distribution
σ_G is a variation of overview spatial dispersion ability in the study area

Specialization coefficient (s_i):

$$s_i = \frac{\sigma_G}{\sigma_S} \quad (2)$$

Where σ_G is the standard deviation of overview spatial dispersion ability in the study area
σ_S is the standard deviation of the focal vetiver grass distribution

3. Computing HS: The median algorithm was used to compare the distribution of physical factors based on total marginality and specialization with a distribution of vetiver grass in the study area. The niche value varies between 0 and 100 or 0 and 1, from unsuitable to optimal niche. The equation of HS computation from Hirzel and colleagues [11] can be modified for this study as follows:

$$H(c) = \frac{1}{\sum w_i} \sum_{f=1}^{N_f} W_f \, Hm(f,c) \quad (3)$$

Where $H(c)$ is the total niche index for vetiver grass distribution in the study area
$Hm(f,c)$ is a partial niche for each factor (f)
W_f is automatically weighted for each factor (f)

2.4 Validating HSs

The testing dataset (30 vetiver points or 30 percent) was used for HS validation. Two evaluators in Biomapper were the Absolute Validation Index (AVI) and the Contrast Validation Index (CVI). The AVI checked the accuracy between the assessed and actual values, which was determined by varying from 0 to 1. The CVI is the AVI minus wrongly assessed value. If AVI and CVI values are preferred by 1, HS will be a better HS.

3. Results and Discussion

3.1 Identifying niche factors for the potential area of vetiver grass planting-based analysis of ENM and HS

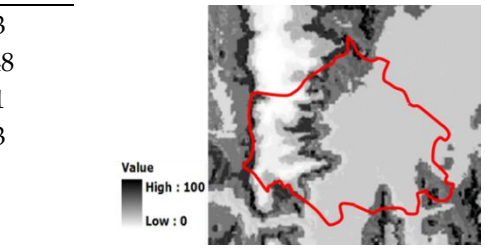
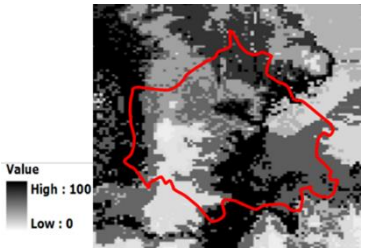
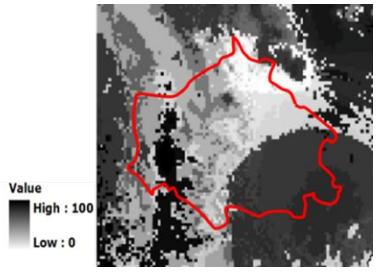
In niche factors' identification for planting vetiver grass, HS indices were produced by ENM in Biomapper, then analyzed to determine relationships between the studied environmental variables and find combinations of niche factors to produce the best HS index of vetiver grass. In this study, ENM in Biomapper, also called, 'ENFA' was explained by marginality and specialization coefficients of the studied environmental variables for vetiver grass, was computed and combined to generate a global HS-based median algorithm with the HS index varied from 0 to 100 as shown in Table 3.

The first niche model (ENM1) included 4 niche factors: BIO14, BIO15, BIO2 and BIO7. The proportion of explainable information preferred 92% of marginality, indicating that the distribution of HS for vetiver grass in the study area was greater than the species variation. Moreover, BIO14 and BIO15 were more statistically significant than BIO2 and BIO7 in ENM because they had a high coefficient of marginality.

The second niche model (ENM2) included 4 niche factors: BIO1, BIO5, BIO6 and elevation. The proportion of explainable information preferred 97% of marginality, indicating that the distribution of HS for vetiver grass in the study area was greater than the species variation. Moreover, BIO1 and BIO5 were more statistically significant than BIO6 and elevation in ENM because they had a high coefficient of marginality.

The third niche model (ENM3) included 3 niche factors: BIO4, BIO12 and BIO13. The proportion of explainable information preferred 79% of marginality, indicating that the distribution of HS for vetiver grass in the study area was more significant than the species variation. Moreover, BIO4 was more statistically significant than BIO12 and BIO13 in ENM because BIO4 had a high coefficient of marginality.

Table 3. Identifying niche factors and HS for planting vetiver grass

ENMs	Niche factors	Marg.	Spec.			HS for planting vetiver grass
			1	2	3	
1. ENM1	BIO14 (mm)	0.718	0.244	-0.379	0.643	
	BIO15 (SD)	0.620	-0.362	0.708	-0.748	
	BIO2 (°C)	0.243	0.690	-0.582	0.111	
	BIO7 (°C)	-0.204	0.577	0.124	0.123	
	Overall	0.085	6.475	0	0	
	percent of explanation	92	6	1	1	
HS1 (ENM1) = [1/(0.725+0.268+0.007+0.001)] x [0.725H(marg.,c) + 0.268H(spec.1,c) + 0.007H(spec.2,c) + 0.001H(spec.3,c)						
2. ENM2	BIO1 (°C)	-0.667	0.378	0	0	
	BIO5 (°C)	0.561	0.639	0	0	
	BIO6 (°C)	0.327	-0.617		0	
	Elevation (m)	0.364	0.263		0	
	Overall	0.187	13.277	0	0	
	percent of explanation	97	3	0	0	
HS2 (ENM2) = [1/(1.968+0.027)] x [1.968H(marg.,c) + 0.027H(spec.1,c)						
3. ENM3	BIO4	1.000	-0.050	-0.080	0	
	BIO12	0.000	-0.830	-0.460	0	
	BIO13	0.090	0.560	0.890	0	
	Overall	0.132	3.437	0	0	
	percent of explanation	79	17	4	0	
HS3 (ENM3) = [1/(1.787+0.169+0.444)] x [1.787H(marg.,c) + 0.169H(spec.1,c) + 0.444H(spec.2,c)						

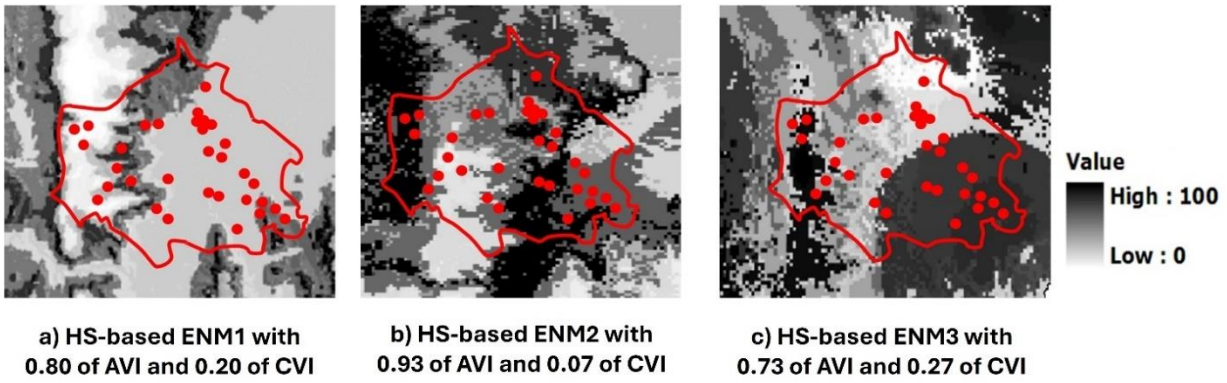
Remark: - BIO1: mean annually temperature (°C); BIO2: mean monthly temperature range (°C); BIO4: mean annually temperature seasonality (SD); BIO5: mean monthly maximum temperature (°C); BIO6: mean monthly minimum temperature (°C); BIO7: mean annually temperature range (°C); BIO12: mean annually precipitation (mm); BIO13: mean monthly maximum precipitation (mm); BIO14: mean monthly minimum precipitation (mm); BIO15: mean annually precipitation seasonality (SD); Elevation (m);

- Marg. = Marginality and Spec. = specialization
- Positive and negative signs of marginality and specialization coefficient indicate each ecological model prefers higher or lower than the global distribution in each variable of the environment.
- SD is the standard deviation

3.2 Validating HS

This study used AVI and CVI in Biomapper to validate the HS of vetiver grass-based ENM. AVI provided an overall assessment of HS, and CVI defined the difference between AVI and CVI. Thus, all derived HS-index-based ENM was validated by AVI and CVI based on the prepared testing dataset of vetiver grass locations (30 points), as shown in Figure 7. The distribution of the testing dataset evaluated the 3-obtained HS of vetiver grass, which were here computed by AVI and CVI (if the testing dataset was randomly fallen in

value of HS index equal to or higher than 70, was recommended as the suitable HS for planting vetiver grass) and then were validated to identify the best HS for the potential area of vetiver grass planting.



Remark: if the testing dataset randomly fell in value of HS index equal to or higher than 70, it was recommended as the suitable HS for planting vetiver grass.

Figure 7. HS Validation-based AVI and CVI

Figure 7 shows that HS-based ENM2 has the highest possibility for the best HS for planting vetiver grass in this study, with AVI 0.93 and CVI 0.07. The ENM2 included 97% marginality (the ability for spatial distribution in the study area) and 3% specialization (durability in the study area). Moreover, this ENM2 explicitly indicates the existing vetiver grasses have more highly spatial distribution than durability in the study area with niche factors such as BIO1: the mean annual temperature (25-31°C), BIO5: mean monthly maximum temperature (30-38°C), BIO6: mean monthly minimum temperature (17-27°C) and elevation (600-1,300 m), respectively. These niche factors are related to the research of Grimshaw and Faiz [26] and Truong and colleagues [27], who mentioned that the ecology of vetiver grass can tolerate drought or high temperatures.

4. Conclusions

This study identified niche factors for planting vetiver grass to implement in soil and water conservation areas in Pak Chong district, Thailand. Therefore, the HS-based ENM2 has the highest possibility of being the best HS for planting vetiver grass in the study area. This HS was derived by using 4 niche factors: BIO1 (25-31°C), BIO5 (30-38°C), BIO6 (17-27°C) and elevation (600-1,300 m). In the best HS of vetiver grass, the proportion of explainable information preferred marginality coefficients that revealed the distribution of HS for vetiver grass in the study area was more significant than the species variation. Moreover, BIO1 and BIO5 were more statistically significant than BIO6 and elevation in ENM because they had a high coefficient of marginality. The obtained niche factor (e.g., BIO1, BIO5, BIO6, and elevation) will be implemented to map potential areas of vetiver grass in the Center for Promoting the Utilization of Vetiver Grass under the Royal Initiative Project (CPUVGRIP) of Forest Royal Department (FRD) in Nakhon Ratchasima, Thailand further.

5. Acknowledgements

Thank you for vetiver grass and soil data from the Land Development Department (LDD) of Thailand, climatic data from the Thailand Meteorological Department (TMD), DEM from OpenTopography, Biomapper from Dr. Alexandre HIRZEL at the University of Lausanne, Switzerland. Thank you to the Faculty of Sciences and Liberal Arts, Rajamangala University of Technology Isan (www.rmuti.ac.th), which has supported time and facilities.

Author Contributions: Conceptualization, Y.J.; methodology, Y.J., and P.J.; data acquisitions, C.J.; software, Y.J.; ecological niche modeling, Y.J., and P.J.; validation, Y.J., and P.J.; writing—review and editing, Y.J., P.J. and C.J. All authors have read and agreed to the published version of the manuscript."

Funding: This research received no external funding.

Conflicts of Interest: The authors declare no conflict of interest.

References

[1] The Office of the Royal Development Projects Board (ORDPB). "The Seventh International Vetiver Conference (ICV7) May 29-June 1 2023". Available from: https://www.vetiver.org/network-services/conference-proceedings/ [Accessed 4 November 2024].

[2] The Committee on Master Plan for Development and Campaign for the use of vetiver, "The Master Plan of the Royal Project to Develop and Promote the Development and Use of Vetiver No.6 (2017-2021)". Available from: http://agkb.lib.ku.ac.th/faek/search_detail/result/215032. [Accessed 9 April 2024].

[3] The Committee on Master Plan for Development and Campaign for the use of vetiver, "The Master Plan of the Royal Project to Develop and Promote the Development and Use of Vetiver No.4 (2007-2011)". Available from: http://thvn.rdpb.go.th/Files/Plan/1-ilovepdf-compressed%20(1).pdf. [Accessed 9 April 2024].

[4] Leknoi, U.; Likitlersuang, S. Good practice and lesson learned in promoting vetiver as solution for slope stabilization and erosion control in Thailand. *Land Use Policy*. **2020**, *99*, 105008. https://doi.org/10.1016/j.landusepol.2020.105008

[5] Chen, S.; Xiao, Y.; Xiao, Z.; Ma, D.; Li, J.; Herrera-Ulloa, A. Prediction of suitable habitat shifts and assessment of ecological niche overlaps for three Tridentiger species with intertidal and subtidal characteristics under future climate changes. *Marine Pollution Bulletin*. **2024**, *198*, 115827. https://doi.org/10.1016/j.marpolbul.2023.115827

[6] Mathur, M.; Mathur, P.; Purohit, H. Ecological niche modelling of a critically endangered species Commiphora wightii (Arn.) Bhandari using bioclimatic and non-bioclimatic variables. *Ecological Process*. **2024**, *12*(8). https://doi.org/10.1186/s13717-023-00423-2

[7] Peterson, A. T.; Soberon, J.; Pearson, R. G.; Anderson, R. P.; Martinez-Meyer, E.; Nakamura, M.; Araujo, M. B. *Ecological Niches and Geographic Distributions*. Oxfordshire, the United Kingdom: *Princeton University Press* **2011**, 23-48. https://doi.org/10.23943/princeton/9780691136868.003.0003

[8] Sillero, N.; Arenas-Castro, S.; Enriquez-Urzelai, U.; Vale, C. G.; Sousa-Guedes, D.; Martinez-Freiria, F.; Real, R.; Barbosa, A. M. Want to model a species niche? A step-by-step guideline on correlative ecological niche modelling. *Ecological Modelling*, **2021**, *456*, 109671. https://doi.org/10.1016/j.ecolmodel.2021.109671

[9] National Geographic, "Niche". Available from: https://www.nationalgeographic.org/encyclopedia/niche/. [Accessed 12 April 2024].

[10] Dotson, J. D. "Ecological Niche: Definition, Types, Importance & Examples". Available from: https://sciencing.com/ecological-niche-definition-types-importance-examples-13719219.html. [Accessed 12 April 2024].

[11] Phillips, S.J.; Anderson, R.P.; Dudík, M.; Schapire, R.E.; Blair, M.E. Opening the black box: an opensource release of maxent. *Ecography*. 2017, 40, 887–893. https://doi.org/10.1111/ecog.03049

[12] Hirzel, A. H.; Hausser, J.; Perrin, N. Biomapper 1.0-4.0. Available from: https://www2.unil.ch/biomapper/products.html. [Accessed 13 April 2024].

[13] Guo, Q.; Liu, Y. ModEco: an integrated software package for ecological niche modeling. *Ecography*. **2010**, *33*(4), 637-642. https://doi.org/10.1111/j.1600-0587.2010.06416.x

[14] Enrique, M.; Mu˜noz, D. S.; Giovanni, R.; De, Siqueira, M. F.; De, Sutton, T.; Brewer, P. Open Modeller: a generic approach to species' potential distribution modelling. *Geoinformatics*. **2009**, *15*, 111–135. https://doi.org/10.1007/s10707-009-0090-7

[15] R Core Team, "R: A Language and Environment for Statistical Computing. Vienna, Austria". Available from: https://www.R-project.org/ [Accessed 13 April 2024].

[16] Costa, H.; Medeiros, V.; Azevedo, E. B.; Silva, L. Evaluating ecological-niche factor analysis as a modelling tool for environmental weed management in island systems. *Weed Research*. **2013**, *53*(3), 221-230. https://doi.org/10.1111/wre.12017

[17] Université de Lausanne. "Biomapper". Available from: https://www2.unil.ch/biomapper/what_is_biomapper.html. [Accessed 13 April 2024].

[18] Grimshaw, R. G. "Vetiver System: A Green Investment for Sustainable Development". Available from: https://www.vetiver.org/ICV4pdfs/P02.pdf [Accessed 4 November 2024].

[19] Truong, P.; Van, T. T.; Pinners, E. "Vetiver System Applications: Technical Reference Manual". Available from: https://www.vetiver.org/BB-v1r.pdf [Accessed 5 November 2024].

[20] National Research Council. ''Vetiver Grass: A thin green line against erosion". Available from: https://pdf.usaid.gov/pdf_docs/Pnabp484.pdf [Accessed 4 November 2024].
[21] Yoon, P.K. "A Look See at Vetiver Grass in Malaysia by". Available from: https://www.vetiver.org/MAL_PK.Yoon%20Look%20see/START.HTM [Accessed 4 November 2024].
[22] Gholamy, A.; Kreinovich, V.; Kosheleva, O. "Why 70/30 or 80/20 Relation Between Training and Testing Sets: A Pedagogical Explanation". Available from https://scholarworks.utep.edu/cgi/viewcontent.cgi?article=2202&context=cs_techrep [Accessed 6 November 2024].
[23] Tuan, T. A.; Hong, P. V.; Tam, T. T.; Nguyet, N. T. A.; Dung, N. V.; Trong, T. P.; Huy, P. T.; Phong, T. V. Land susceptibility in Phuoc Son, Quang Nam: A deep learning approach. *Vietnam Journal of Earth Sciences*. **2024**, *47*(1), 44-62. https://doi.org/10.15625/2615-9783/21658
[24] O'Donnell, M.S.; Ignizio, D.A., Bioclimatic predictors for supporting ecological applications in the conterminous United States. *U.S. Geological Survey Data Series* **2012**, *691*, 10. https://doi.org/10.3133/ds691
[25] The USDA Risk Management Agency. "PRISM Climate Data". Available from: https://prism.oregonstate.edu/ [Accessed 6 November 2024].
[26] Grimshaw, R. G.; Faiz, A. "Vetiver Grass: Application for Stabilization of Structures". Available from: https://onlinepubs.trb.org/Onlinepubs/conf/1995/cp6/v1/cp6v1-010.pdf [Accessed 13 April 2024].
[27] Trong, P.; Nanakorn, W.; Tan Van, T.; Pinners, E. *Vetiver System Applications – Technical Reference Manual*. Bangkok, BKK: Office of the Royal Development Projects Board **2013**, 1-14.

ASEAN
Journal of Scientific and Technological Reports
Online ISSN:2773-8752

Research article

Risk Assessment and Geospatial Mapping of Ammonia Transportation Hazards: A Case Study of Thungsong, Thailand

Pisit Kolsaman[1], Supabhorn Yimthiang[2], Preeda Sansakorn[3], Junjira Mahaboon[4*]

[1] School of Public Health, Walailak University, Thaiburi, Thasala, Nakhon Si Thammarat, 80160, Thailand
[2] School of Public Health, Walailak University, Thaiburi, Thasala, Nakhon Si Thammarat, 80160, Thailand
[3] School of Public Health, Walailak University, Thaiburi, Thasala, Nakhon Si Thammarat, 80160, Thailand
[4] School of Public Health, Walailak University, Thaiburi, Thasala, Nakhon Si Thammarat, 80160, Thailand
* Correspondence: hjunjira@wu.ac.th

Citation:
Kolsaman, P.; Yimthinang, S.; Sansakorn, P.; Mahaboon, J. Risk assessment and geospatial mapping of ammonia transportation hazards: A case study of Thungsong, Thailand *ASEAN J. Sci. Tech. Report.* **2025**, *28*(1), e254894. https://doi.org/10.55164/ajstr.v28i1.254894

Article history:
Received: July 16, 2024
Revised: November 13, 2024
Accepted: November 20, 2024
Available online: February 16, 2025

Publisher's Note:
This article has been published and distributed under the terms of Thaksin University.

Abstract: The transportation of ammonia—a widely used industrial chemical—presents significant risks, including leaks, fires, and explosions. This study aimed to assess the risks of transporting ammonia in the southern part of Thailand and to create a detailed risk evaluation using geospatial methods. We used the Areal Locations of Hazardous Atmospheres (ALOHA) to comprehensively simulate five ammonia accident scenarios: toxic vapor cloud, flammable areas (flash fire and jet fire), boiling liquid expanding vapor explosion (BLEVE), and vapor cloud explosion while risk, severity, and evacuation routes were mapped using ArcGIS software. The simulation results reveal that variations in wind direction influence ammonia spread across different seasons. In summer and winter, the wind direction is northeast, and in the rainy season, it shifts to southwest. In scenario 1, the red zone extends 2,400 meters from the source, with ammonia levels reaching up to 505,000 ppm, while in scenario 2, the red zone spans 368 meters. Explosive hazards (BLEVE and VCE) have ranges of 207 and 310 meters, respectively. While our study provides detailed mapping of ammonia hazard zones, future studies are needed to incorporate socio-economic factors into geospatial analyses to improve evacuation strategies and risk mitigation. Consequently, the maps produced can be utilized as essential decision-making tools in emergency response planning and management, which may reduce the death toll during a disaster in the future.

Keywords: Ammonia transportation accidents; Risk assessment; Risk mapping; ALOHA; Evacuation route map

1. Introduction

The rapid growth of industrial development has escalated the demand for raw materials [1], leading to a substantial increase in the production, distribution, and transportation of hazardous chemicals. In Thailand, approximately 120 million tons of dangerous goods are transported, with trucks being the primary mode of transportation. Some studies in China have shown that approximately 95% of hazardous materials (HAZMAT) are transported from producers to customers by trucks [2, 3]. Around 55% of hazardous materials were transported via roadways [1, 4]. According to previous studies [2, 5], 90% of hazardous materials transportation occurs on highways, intersections,

and along rural and urban roads. The significant risks posed by truck crashes identify them as critical issues in road transportation [1, 6]. Several studies pointed out that the high risk due to transportation activities is comparable to or even more critical than the risk due to fixed installations [7]. The risk associated with various road transportation cases is representative of hazardous materials transported by land in many countries [8]. The same kind of accidental scenarios in terms of frequency and severity may occur in fixed plants and transportation systems. Nevertheless, whether it's an accident or a toxic gas release incident, it can cause heavy casualties and severe economic losses. Additionally, transport accidents may occur close to, and sometimes within, densely populated areas [7, 9]. Transportation activities can provoke major fires, explosions, and toxic release events [10]. Previous studies have predominantly focused on ammonia transportation accidents, primarily emphasizing dispersion, fire, and explosion scenarios. For example, Inanloo and Tansel conducted a study investigating the accidental release of ammonia, predicting the consequences of ammonia transportation [5]. The failure of a 22-ton ammonia storage tank truck in Dakar [11].

Ammonia is in a gas or liquid state under pressure. If under normal pressure conditions, it will be a colorless gas with a strong pungent odor [5, 12-14]. Although ammonia becomes a liquid at -33.4°C under pressure and low temperatures, it is stable at normal temperatures and lighter than air [2, 14, 15]. Due to these properties, accidents can be frequent annually. This is mainly caused by trucks' transportation of hazardous materials, which serves as the primary source of these incidents. Health effects are due to the inhalation of ammonia released into the atmosphere, which is the main route of exposure [2, 15, 16]. The health risk assessment involves toxicology in evaluating ammonia exposure, including routes/pathway concentration of ammonia entering the body dose, frequency of exposure, duration of exposure, and characteristics of the exposed population. Ammonia toxicity occurs when sensitive individuals are exposed to external ammonia sources through ingestion, inhalation, or direct contact with the skin or eyes. Ammonia toxicity has both acute and chronic adverse effects on patients. For example, exposure to levels exceeding 30 ppm results in immediate irritation of the nose and throat [17, 18]. Effects on various systems in the body effects on the respiratory: ammonia is an irritant to the human upper respiratory tract. Other effects of ammonia can range from severe irritation to the eyes, nose, and throat and difficulty breathing, pulmonary edema, pink frothy sputum, skin burns blisters, and severe burns on the skin and in the mouth, throat, lungs, and eyes, leading to death [12, 15, 19-24]. The effects of ammonia exposure and decreased lung function have also been evaluated [25]. High ammonia concentrations can acutely affect the cardiovascular system in humans, causing increased pulse, elevated blood pressure, bradycardia, and even cardiac arrest [17, 26, 27]. Some studies indicate that exposure to ammonia concentrations above 2,500 ppm for approximately 30 seconds can be fatal [12].

Although assessing the risk of road transport crashes involves considering the probability of occurrence and the severity of their consequences, ammonia transport truck crashes remain unpredictable. Studies have investigated potential events like collisions, overturning, tank ruptures, and the leakage or ignition of substances inside, which can cause fires or explosions. The consequences of toxic release and blast overpressure were modeled for various worst-case scenarios of the critical units. Both structural damage and human mortality/injury were converted into economic terms using suitable probability functions, frequency, and cost parameters related to property damage and compensation for fatalities [28]. The ALOHA software is widely used in simulating the spread of chemicals leaking into the air according to the climate, and the chemical characteristics of ALOHA allow for the simulation of various toxic gas emissions situations, calculating the velocity of chemicals coming out of ammonia tanks. Previous studies showed research has been performed using ALOHA software to assess incidents in road transportation [1, 5, 29, 30]. ALOHA has been used in this study to analyze the risk and identify the population under threat. Several studies have been done for ammonia or other chemical risk assessments based on the dispersion model [31, 32]. ALOHA can simulate situations of leakage from storage tanks in cases where there is no ignition, such as toxicity (toxic vapor clouds), flammability, thermal radiation, explosions like boiling liquid into vapor, BLEVEs (Boiling Liquid Expanding Vapor Explosions), fires with flame jets (Jet fires), explosions of vapor cloud explosions and pool fires [33-36].

The variables considered in the simulation are the amount of cloud cover, air temperature, relative humidity, wind speed, and wind direction [23, 37-39]. During the cold season, temperature fluctuations cause

freeze-thaw cycles in bioretention systems, affecting soil structure, permeability, and microbial activity, reducing stormwater and pollutant filtration effectiveness. This accident on the highway can lead to ammonia release, posing a risk to ecosystems by potentially causing eutrophication in nearby waters. Effective management strategies are needed to minimize ammonia leaching and maintain pollutant removal efficiency in regions with freeze-thaw cycles [40, 41]. For ammonia transport, any integration with or impact by bioretention systems designed to manage stormwater and reduce pollutants is unlikely to face freeze-thaw-related challenges in Thailand. Instead, considerations would focus on factors like high rainfall, heat, and runoff management, ensuring that ammonia handling does not lead to contamination risks within these systems. Researchers used ALOHA to spot intended to create an ammonia distribution model [31].

A GIS-based method has been proposed for vulnerable point mapping and application. Maps of the impact toxic threat zone, radiation threat zone, and impact area zone of accident outcome are prepared using ArcGIS. Many studies have presented the integrated applications of ALOHA and GIS as powerful tools for risk assessment and population vulnerability assessment [31, 38, 42, 43]. ALOHA and ArcGIS are integrated in this study. Addressing the knowledge gap of no previous studies on road ammonia transport in this area, our research employs a systematic and evidence-based approach to evaluate the risks and develop comprehensive risk mapping using geospatial tools. The objectives of this study were to evaluate the risks associated with ammonia transportation and develop a comprehensive mapping for risk evaluation using geospatial tools. Therefore, this study focuses on conducting a thorough risk assessment for the transportation of ammonia along national highways. These highways, being vital routes for ammonia transportation and have statistics of accidents many times, might pose potential risks to the vicinity general populations. The novelty of this paper is the integration of the assessment of ammonia transportation accidents and the implementation of risk and evacuation mapping.

2. Materials and Methods

The methodology employed in this study to define the nature and calculate the extent of a possible release of ammonia transportation on the population of Thungsong district, Nakhon Si Thammarat, Thailand, and surrounding a five-step approach applied to five scenarios was illustrated in Figure 1.

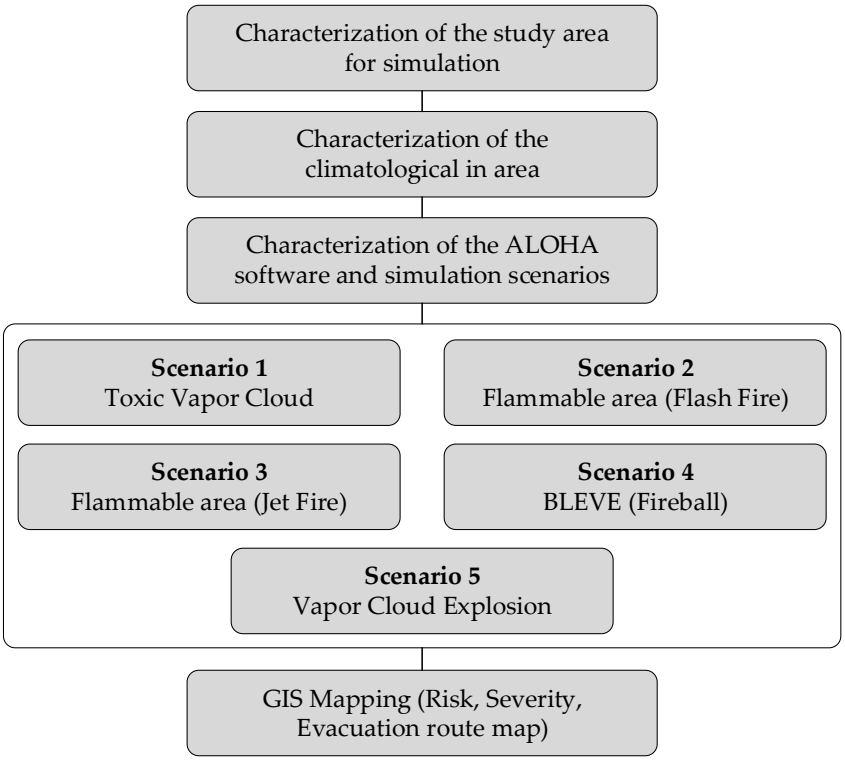


Figure 1. Conceptual framework of research.

2.1 Characterization of the study area for simulation

Ammonia transportation routes pass through Highway No. 41 in Nakhon Si Thammarat province. The Thungsong district was selected in the present study because of the daily ammonia transportation, variety of fuels/hazardous chemicals, and enormous quantities on this highway. The number of ammonia trucks on Nakhon Si Thammarat highways varies based on demand, industrial activity, transport schedules, and regulations. Transportation authorities or logistics companies typically monitor this data. No such study has been conducted on this highway area. Figure 2 and Table 2 show the characteristics of the ammonia emission source and its location in Thungsong, inhabited by 116,757 people and a vulnerability group of 37,720 people.

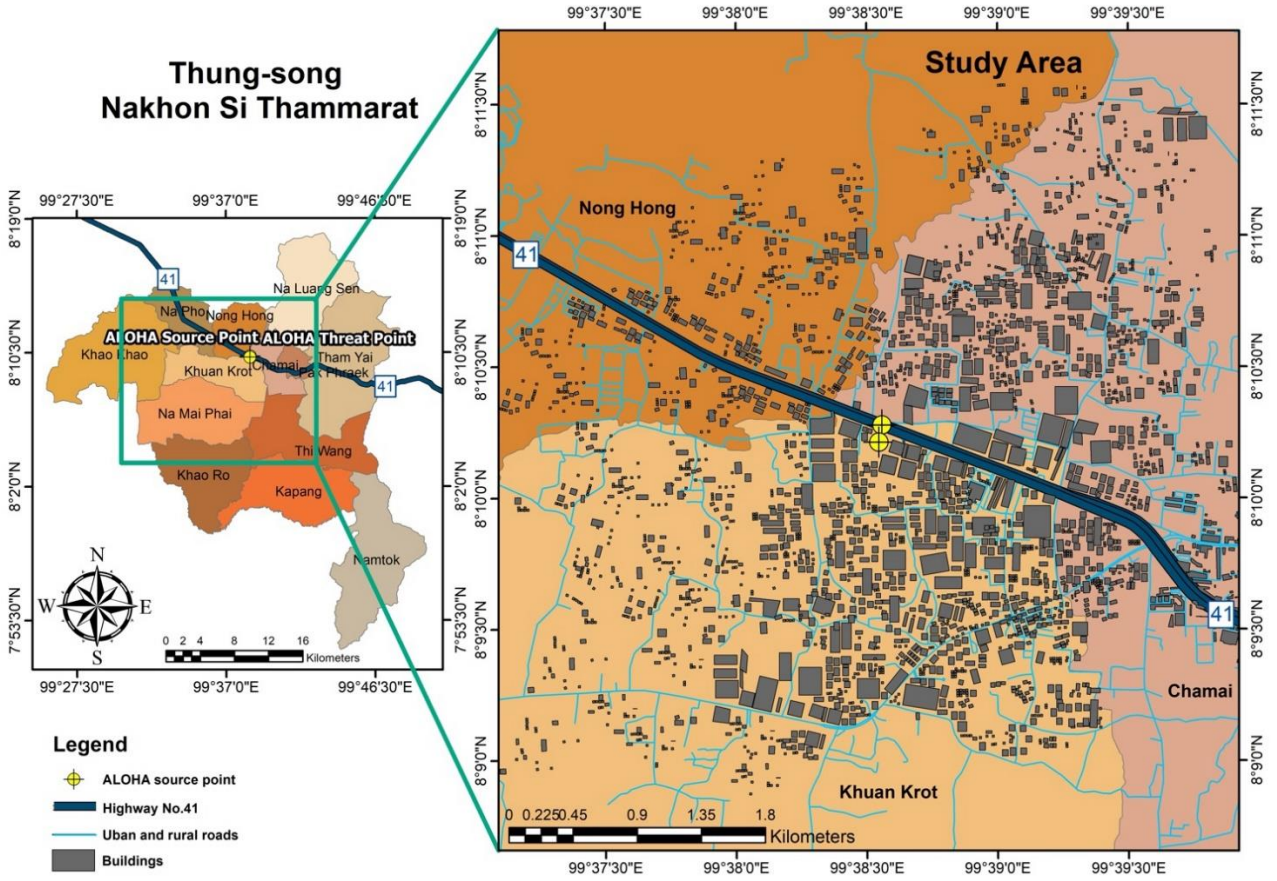


Figure 2 The study area of ammonia transportation routes passes through Highway No. 41 in Nakhon Si Thammarat province.

2.2 Data collection

A survey for data collection on the selected ammonia transport tank was carried out regarding the type of ammonia tanker and and the toxicity of ammonia, considering packaging conditions, diameter, and capacity of the storage tanker. To estimate the risk and effect on the population and surrounding environment, the population data was collected from the population registration statistics (monthly), the Registration Administration Office, the Department of Provincial Administration (2022), and secondary data obtained from the Ministry of Public Health database. The human research project certification document from the Human Research Ethics Committee, Walailak University. For injured analysis, the data regarding a number of populations was collected for the forecast risk and preparedness evacuation plan. For network analysis, the data regarding traffic routing was collected to prepare an evacuation plan.

The weather parameters and meteorological data for the studied area spanning 2020-2024 were collected. The data are provided by the Thai Meteorological Department of Nakhon Si Thammarat province station. For the analysis, meteorological data variables taken into account for this study are air temperature,

wind direction and speed, relative humidity, and cloudiness. For the current and worst situations, several studies estimated the impacts of source release variables (i.e., tank length and diameter) and climatic circumstances (i.e., wind speed, cloud cover, air temperature, and relative humidity) [44]. Nakhon Si Thammarat experiences two monsoon seasons: the southwest monsoon (mid-May to mid-October) with rain from the Indian Ocean and the northeast monsoon (mid-October to mid-February) with cooler winds and occasional rain from China. Thailand's weather is generally divided into summer (mid-February to mid-May), rainy (mid-May to mid-October), and winter (mid-October to February).

2.3 ALOHA software and Consequence analysis

ALOHA was developed by the National Oceanic and Atmospheric Administration (NOAA) and The Environmental Protection Agency (EPA). ALOHA software forecasts the impact or severity of an ammonia release incident. The ALOHA software is a program that has been widely accepted and has suitable features to be used in simulating the spread of chemicals leaking into the air according to the climate and the chemical characteristics of ALOHA allow simulation of various toxic gas emissions situations, calculating the velocity of chemicals coming out of ammonia tanks. Previous studies showed that it has been performed using ALOHA software to assess incidents in road transportation [1, 5, 29, 30] and examine the impact area of the jet fire computed with the ALOHA program [44]. ALOHA has been used in this study to analyze the risk and identify the population under threat. Research has been done on ammonia and other chemical risk assessments using dispersion models [31, 32]. Some studies have simulated dispersion and evaluated the impact on populations and structures [45]. ALOHA can simulate situations of leakage from storage tanks in cases where there is no ignition (toxic vapor clouds), explosions like boiling liquid into vapor, BLEVEs (Boiling Liquid Expanding Vapor Explosions), fires with flame jets (Jet fires), explosions of vapor cloud explosions and pool fires [33] is predicted. The level of concern (LOC) is the reference concentration for assessing the impact during release. The software uses models to describe the dispersion and movement of ammonia and its effects as a spread of ammonia gas, fire, and explosion. Table 3 summarizes the source from the tank and scenarios that ALOHA models. It provided results on threat zones plot, and footprints is a map indicating areas at risk (toxicity, flammability, thermal radiation, or blast force overpressure). In case LOC exceeds in area, people and property are calculated threats. Threat at the point is a graph illustrating the variation of the concentration and time at a point of interest. Text summaries are scenario information, including the physical properties of ammonia, and describe the threat zone and distance. [46] assessment of the consequences of the toxic gas release in major hazards of specified human toxic response for acute exposure to ammonia, etc., expressing susceptibility of population exposure to stressing agents is that of probit analysis.

The scenarios to be studied are selected from the probability that might occur when ammonia is released in the accident storage tanks. Table 1 Consequence scenarios modeling refers to calculating or estimating numerical values. Scenarios involving toxic dispersion, flammable area, boiling liquid expanding vapor explosion (BLEVE), and vapor cloud explosion (VCE) have potential effects and impacts on people in the area inevitably, which often cause a large number of casualties and property losses, environmental health, and safety [47].

Table 1. Expected frequencies (per year) of loss of containment events [48].

Incident cases	Frequency per year
Instantaneous tank car release	3.1E-09
Continuous release of large connection	3.1E-09
Full bore hose	2.2E-06
Leak hose	2.2E-05
Full bore arm	1.7E-08
Leak arm	1.7E-07
Instantaneous storage tank failure	5.0E-07

Table 2. Source and characteristic of assessment point.

Location	Distance from the source (m)	Location name	Characterization
Source	0	Ammonia tank car accident	Ammonia tank car, Stainless or carbon steel, capacity of 9,600 gallons Estimated Weight: 20,360 lbs, Gauges: Level gauges set at 85%, Operating pressure: 100-500 psi, Maximum pressure: 500 psi
Point 1	100	Chamai 1	Possible affected community, LPG gas station: 1, hotel: 1 Temple, community, restaurants, company, village. Maximum 95 inhabitants.
Point 2	350	Chamai 2	Possible affected community, PTT LPG gas station, village, community, restaurants 1,035 inhabitants.
Point 3	500	Chamai 3	Possible affected community, village, community, restaurants 1,848 inhabitants.
Point 4	1,000	Chamai 4	Possible affected community, temple, village, community, restaurants 3,334 inhabitants.
Point 5	1,500	Chamai 5, Khuankrot 1	Possible affected community, village, community, temple, hotel, gasoline station, college, restaurants 3,973 inhabitants.
Point 6	2,100	Chamai 6, Khuankrot 2	Possible affected community, 4,733 inhabitants. Hospital: 1, Medical clinic: 1, School: 2, Market, village, community, restaurants

Table 3. Modeling scenarios of ALOHA software [23, 49].

Source	Toxic scenarios	Fire scenarios	Explosion scenarios
Tank			
Not Burning	Toxic Vapor cloud	Flammable Area (Flash fire)	Vapor Cloud Explosion (VCE)
Burning		Flammable Area (Jet fire)	
Boiling Liquid Expanding Vapor Explosion (BLEVE)		Fireball	

2.4 GIS Mapping

In the case of ammonia transport accidents, mapping involves overlaying relevant data on maps. People's vulnerability maps and risk maps are created using ArcGIS. Overlay with all vulnerable point mapping is performed by overlaying physically and socially vulnerable points in GIS [43]. These maps effectively categorize the studied area into distinct threat zones, disseminate spatial data for assessing risks in each area through mapping, show the distribution of the population who could be exposed to ammonia, and provide a comprehensive visual representation of the risks associated with ammonia transport. Severity, risk, and evacuation route maps are important emergency preparedness and response planning tools. Severity maps display a hazard's potential impact and intensity in a specific area. These maps help emergency management officials and the public understand the level of risk associated with different hazards, such as disasters like chemical spills or industrial accidents. The severity map typically uses color coding or other visual indicators to show areas at high, medium, or low risk of being affected by a hazard. By analyzing severity maps, emergency planners can prioritize resources, make informed decisions, and develop response strategies to mitigate the impact of the hazard. Risk maps provide a comprehensive overview of the likelihood of a hazard occurring in a given area and the potential consequences of that hazard. These maps combine information on the probability of an event with the population's vulnerability and infrastructure in the affected area.

Risk maps are essential for identifying high-risk zones, vulnerable populations, critical infrastructure, and other factors that could influence emergency response and recovery efforts. By analyzing risk maps, decision-makers can allocate resources effectively, implement preventive measures, and enhance community

resilience to disasters. Evacuation route maps are designed to guide individuals and communities in safely evacuating an area in an emergency or disaster. These maps highlight designated evacuation routes, assembly points, shelters, and other important information people need to know to evacuate efficiently and safely. Evacuation route maps ensure orderly and timely evacuations, especially in high-risk areas prone to hurricanes, wildfires, or tsunamis. By familiarizing themselves with evacuation route maps, residents can take proactive measures to protect themselves and their families during emergencies and reduce the risk of injuries or fatalities.

2.5 Population health risk assessment

Health risk assessment involves the general population and vulnerability group considering acute effects such as irritation, respiratory problems, systemic toxicity, and long-term health effects from chronic exposure. Concern number of injured persons are affected by ammonia release. The probability of damage to an exposed population and an individual results in consequences for the population. Proximity to the accident site includes residents within a defined radius of the transportation route and individuals in institutions such as schools, hospitals, temples, and nursing homes near the accident site. These criteria ensure a comprehensive identification of individuals at increased risk during an ammonia transportation accident, enabling targeted protective measures and efficient resource allocation during emergency response planning.

3. Results and Discussion

3.1 Meteorological data in the study area

A variety of factors, both physical and geographical, influence meteorological data. These factors can impact weather patterns, climatic conditions, and atmospheric phenomena, shaping the data collected by meteorological instruments and sensors. Several factors influence the spread of ammonia clouds, including wind speed, temperature, relative humidity, and the extent of cloud cover [4, 23, 37]. The risk of release was assessed by selecting the average values of wind direction, wind speed, and temperature across four seasons [50]. Data on weather and meteorological parameters in the study area during 2020-2024 were collected from the Meteorological Department of Nakhon Si Thammarat province station. The weather variables were averaged.

3.1.1 Air temperature

The annual average air temperature is 29.74°C during the period. This study categorized the seasonal summer (February-May) and rainy season (June-September). The highest air temperature is in April (37°C). The maximum air temperature in the winter (October-January) is 35°C, while the lowest monthly average occurs in December and January at 23.8°C and 23.25°C, respectively. December and January are the coldest months when the minimum temperatures of 22°C and 23°C are recorded. Atmospheric stability class E represents slightly stable atmospheric stability conditions.

3.1.2 Wind direction and wind speed

The wind direction in summer and winter is southwest, with speeds of 4.1 miles per hour and 3.76 miles per hour, respectively (as measured at the height of 10 meters by a fixed meteorological tower at the site). In the rainy season, the wind will be in the northeast direction and wind speed of 3.8 mph. Therefore, the worst-case scenario study chose low wind speeds. Low wind speeds can cause the spread of ammonia in the air to last longer and have a high concentration compared to high and variable wind speeds. Ammonia dispersion vapor cloud will move in a downwind direction and spread in a crosswind. Dispersion calculations provide an estimate of the area affected. The modeling of ammonia dispersion involves predicting the movement and spread of ammonia when it leaks into the atmosphere. Typically, the dispersion occurs in the downwind direction or follows the same path as the wind, and the increase in wind speed reduces the diffusion height of the ammonia gas cloud in the downwind direction [20].

3.1.3 Relative humidity

The relative humidity maximum value is 100% in November. The annual average relative humidity maximum is 89.44%. Normally, the southern region of Thailand has a hot and humid climate, and there is a lot of rain even in the hot weather. On the other hand, in this study, the minimum relative humidity was chosen because low humidity will prevent the diffusion of ammonia while maintaining a high concentration

in the atmosphere and does not dilute ammonia. Therefore, the study obtained the values of the more severe variables in the simulation. The summer (February-May) and rainy season (June-September) are 39%RH and 52%RH, respectively. But in winter (October-January), it is 62%RH.

3.1.4 Cloud cover

The sky is over half covered by clouds during June-September, with 7-tenths in the rainy season. In summer and winter, cloud cover averages 5-tenths, while the sky in January-April does not have cloud cover.

Table 4. Variable meteorological data and model of simulation ALOHA software.

Variable	Summer (Feb-May)	Rainy (Jun-Sep)	Winter (Oct-Jan)
Temperature; °C	37	37	35
Relative Humidity; %RH	39	52	62
Wind speed: mph	4.10	3.80	3.76
Wind direction; degree	NE	SW	NE
Cloud cover; %	50%	70%	50%
Model of release	Tank release	Tank release	Tank release
End Time	60 minutes	60 minutes	60 minutes

3.2 Condition for the ALOHA software

The study used parameters suitable to simulate the worst-case scenario, considering meteorological variations between seasons. For the meteorology variables, average values were used as the data for input to software over the five years considered (2020-2024), which was low. The following meteorology parameters allow estimating the dispersion, heat radiation, and overpressure (blast force) of the ammonia: air temperature, wind direction and wind speed, relative humidity, and cloud cover use the average values (maximum values for air temperature and minimum values for wind speed and humidity).

- The researcher selects the dispersion, fire, and explosion models based on the released ammonia and the condition under which the probability leak occurs.
- The leak is from a hole in a horizontal cylindrical tank.
- Tank Diameter: 6 feet.
- Tank length: 45.4 feet.
- Tank Volume: 9,600 gallons
- A tank contains liquid and an internal temperature of 35°C
- Chemical Mass in Tank: 19.9 tons; the tank is 85% full.
- Circular Opening Diameter: 4 inches.
- An opening is 10 inches from the tank bottom.
- Max Average Sustained Release Rate: 10,900 kilograms/minute (averaged over a minute or more).
- Total amount Released: 16,970 kilograms.
- AEGL-1 (60 min): 30 ppm
- AEGL-2 (60 min): 160 ppm
- AEGL-3 (60 min): 1,100 ppm
- Lower Explosive Limit (LEL): 60% 90,000 ppm (Flame Pockets).
- Lower Explosive Limit (LEL): 10% 15,000 ppm.
- Thermal radiation 10.0 kW/(m^2): potentially lethal within 60 seconds.
- Thermal radiation 5.0 kW/(m^2): 2nd degree burns within 60 seconds.
- Thermal radiation 2.0 kW/(m^2): pain within 60 seconds
- Overpressure (blast force): 8.0 psi = destruction of buildings
- Overpressure (blast force): 3.5 psi = serious injury likely
- Overpressure (blast force): 1.0 psi = shatters glass
- Note: The chemical escaped as a mixture of gas and aerosol (two-phase flow).

3.3 Analysis of ammonia release for five scenarios

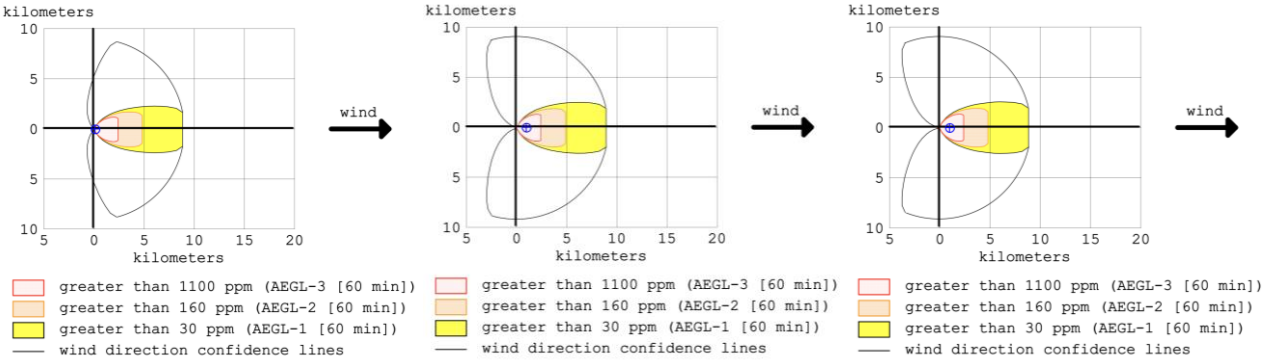
3.3.1 Scenario 1: toxic vapor cloud modeling of ammonia

This scenario aims to determine concentration estimates at the point downwind, distances of the toxic threat zone, and the direction of the toxic ammonia cloud that affected people's vicinity. Figure 3 illustrates the plot of the toxic ammonia cloud's toxic threat zones in case of a transportation accident release. The X-axis indicates the distance from the source to the affected point, and the Y-axis is the width of the toxic cloud. Category three plotted areas (indicated by different colors: red, orange, and yellow zone) represent ammonia exceeding the LOC values and wind direction confidence lines. The red zone shows the expected concentrations equal to 1,100 ppm or above, which corresponds to Acute Exposure Guideline Levels (AEGL-3) (the airborne concentration, expressed as parts per million (ppm) or milligrams per cubic meter (mg/m^3), of a substance above which it is predicted that the general population, including susceptible individuals, could experience life-threatening health effects or death). In the orange zone, the area of ammonia concentration exceeds 160 ppm, which corresponds with AEGL-2 (the airborne concentration (expressed as ppm or mg/m^3) of a substance above which it is predicted that the general population, including susceptible individuals, could experience irreversible or other serious, long-lasting adverse health effects or an impaired ability to escape). In the yellow zone, the ammonia concentration is 30 ppm, which is the AEGL-1, the airborne concentration (expressed as ppm or mg/m^3) of a substance above which it is predicted that the general population, including susceptible individuals, could experience notable discomfort, irritation, or certain asymptomatic nonsensory effects. However, the effects are not disabling and are transient and reversible upon cessation of exposure.

All three tiers (AEGL-1, AEGL-2, and AEGL-3) used for exposure periods of 60 minutes are selected by the software automatically. ALOHA will provide the AEGL values with a 60-minute exposure duration as the default toxic LOCs. Even though AEGLs are available for five exposure durations, only the 60-minute AEGLs are provided in ALOHA (because it models the release for 60 minutes from the start time). Acute Exposure Level Guidelines (AEGLs) are used by emergency planners and responders all over the world to help them deal with uncommon, generally accidental, chemical releases into the atmosphere. AEGLS are specified concentrations of airborne pollutants that have the potential to cause health consequences and are intended to protect older adults, children, and other people who may be vulnerable. Notably, during the summer season, the determination of hazard distances based on ERPG-2 [51] revealed the longest distance for ammonia reaching 5,400 meters. The software could contingency plan and analyze the affected population, and it can forecast concentration exposure levels in the affected area.

Table 5. Summary distances of ammonia release in all scenarios.

Scenario	Distance from the source (m)								
	Summer			Rainy			Winter		
	Red	Orange	Yellow	Red	Orange	Yellow	Red	Orange	Yellow
Scenario 1: Toxic Vapor cloud	2,400	4,800	8,900	2,500	4,500	8,900	2,400	4,900	8,900
Scenario 2: Flammable Area (Flash fire)	368	-	893	358	-	889	359	-	888
Scenario 3: Flammable Area (Jet fire)	36	64	110	35	63	108	34	62	107
Scenario 4: BLEVE (Fireball)	207	301	476	204	297	469	204	296	468
Scenario 5: Vapor Cloud Explosion (VCE)	310	364	639	304	359	630	304	360	628



(a) (b) (c)

Figure 3. Footprint ammonia toxic threat zone scenario 1 (a) summer (b) rainy (c) winter.

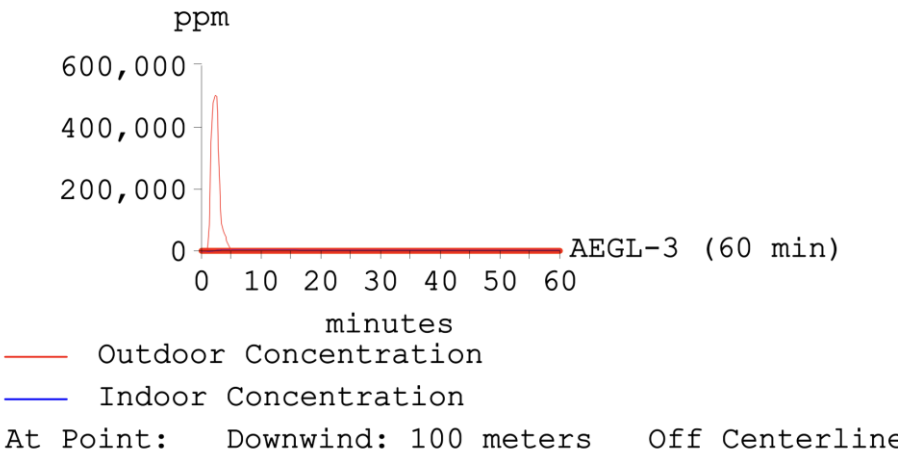


Figure 4a. Concentration at point 100 m. from source.

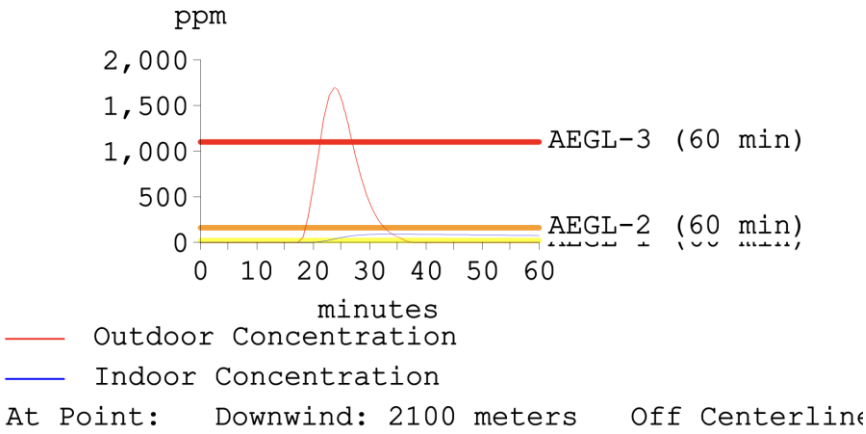


Figure 4b. Concentration at point 2,100 m. from source.

Figures 4a and 4b have concentration at a point in the red zone in the summer season. Figure 4a corresponds to point 1, located 100 meters from the accident source. After 5 minutes, the accident caused an indoor concentration exceeding the AEGL-3 at 6,270 ppm. During the first 5 minutes of the accident, a maximum outdoor concentration exceeding 505,000 ppm is likely to be exposure that can cause immediate lethal. Location point 6 is located at a distance from downwind 2,100 meters from the accident source, as shown in Figure 4b. This area is in part of the red zone, with indoor concentration exceeding AEGL-1 at 94.6 ppm and maximum outdoor concentration exceeding AEGL-3 level at 1,680 ppm are predicted 25 minutes after the incident, which it is predicted that the general population, including vulnerable individuals, could

face life-threatening health consequences or death. The released concentration is higher than the exposure limit of Immediately Dangerous to Life and Health (IDLH) 300 ppm. In summary, results show that the most dangerous occurs during the first 25 minutes after ammonia release. This analysis was performed for each season of the year and distances. Furthermore, Table 5 summarizes the results indicating the maximum distance of the three zones and all seasons.

3.3.2 Scenario 2: Flammable Area (Flash fire)

The objective of this scenario is to determine concentration estimates at the point downwind, distances of the flammability threat zone, and direction of the flammable area of the vapor cloud during an accident. The flammable area footprint of ammonia cloud zones at risk of fire is shown in Figure 5. The two zones are depicted with two colors: the red zone represents ammonia concentrations over 90,000 ppm—matching LOC-3 level (i.e., 60% of the LEL) with flame pockets—while the yellow zone signifies concentrations exceeding 15,000 ppm, corresponding to LOC-1 level (i.e., 10% LEL of ammonia). Figure 5 and Table 5 also show that the risk is limited to a distance of 368 meters from the source in the red zone and yellow zone, a distance of 893 meters, and the red zone has a high risk of fire and threat at blue point have concentration estimates at the point downwind 100 meters. It has a maximum concentration outdoors, as shown by the red line in Figure 5. The forecasted flammable vapors are 505,000 ppm, exceeding 60% LEL during the first 5 minutes after the ammonia release, and the blue line forecasted concentration indoors does not reach the LOC-1 level with 6,280 ppm; however, concentration in the blue line does not exceed LOC-1 level, but high concentration effected to people a wide area shows in Figure 5.

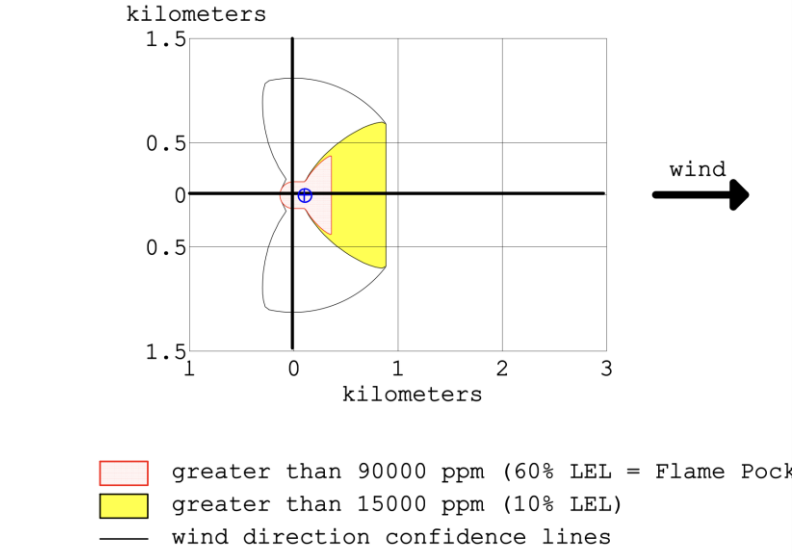


Figure 5. Distances of ammonia flammable threat zone (flash fire).

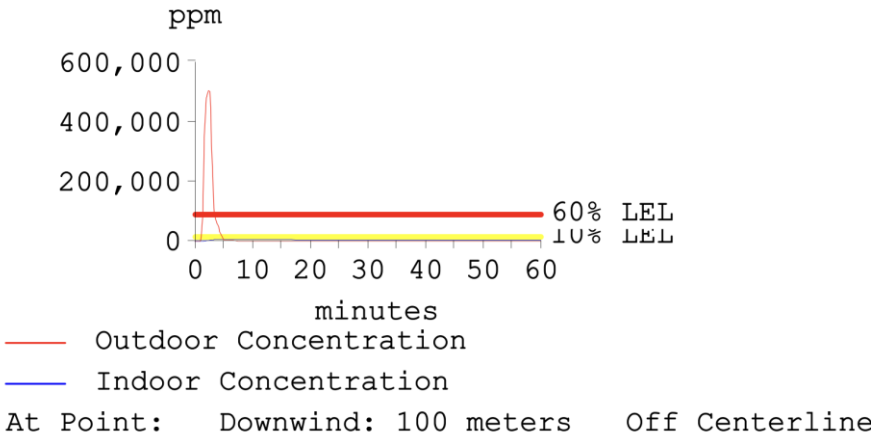


Figure 6. Concentration at point flammable area (flash fire).

3.3.3 Scenario 3: Flammable Area (Jet fire)

This scenario determines the thermal radiation of the jet fire. The jet fire modeling involved calculating thermal radiation measured in kW/m² using a specialized jet fire model. In this context, thermal radiation represents the heat energy emitted by the jet fire source. The thermal radiation at 110 meters from the most distant jet fire source within the yellow zone was determined to be 2.0 kW/m². This value suggests that the thermal radiation at that distance can induce pain within 60 seconds due to its intensity. Thermal radiation estimates that the blue point at the orange zone was determined to be 5.0 kW/m². Thermal radiation at 64 meters might cause 2-degree burns within 60 seconds. The red zone is 10.0 kW/m², so it can potentially be lethal within 60 seconds, and given the high population density, an accident could result in a catastrophic event leading to a significant loss of life. Within 2 min after ammonia release, jet fire has thermal radiation to second-degree burn and pain, and the maximum thermal radiation is 7.02 kW/m², as shown in Figure 7, 8. It is noteworthy that ammonia, in this scenario, exhibits a thermal radiation distance of 110 meters. The farthest distance from the source of the jet fire, as illustrated in Figure 7, is established to be 110 meters during the summer. This information is crucial for assessing the potential heat impact on surrounding areas and structures, aiding in developing safety measures and emergency response plans to mitigate the consequences of an ammonia jet fire incident.

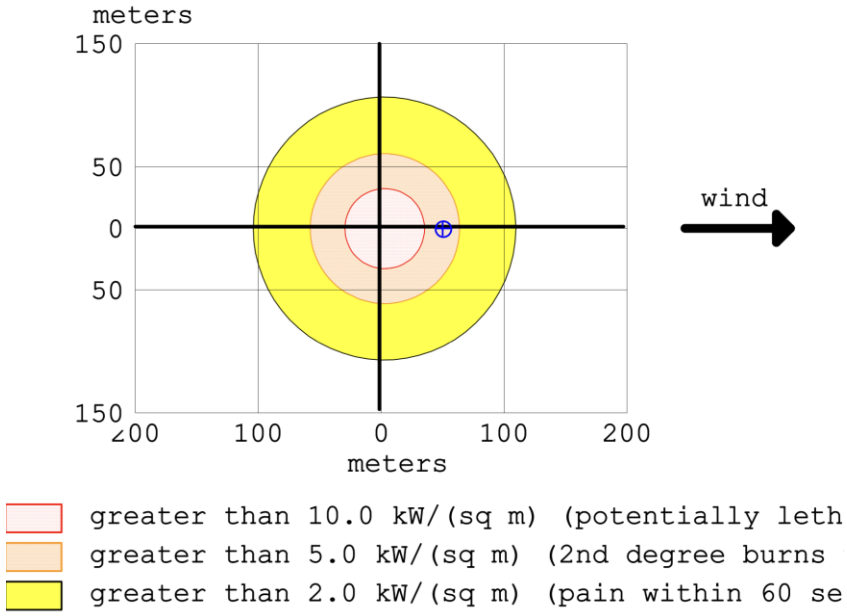


Figure 7. Distances of thermal radiation threat zone jet fire.

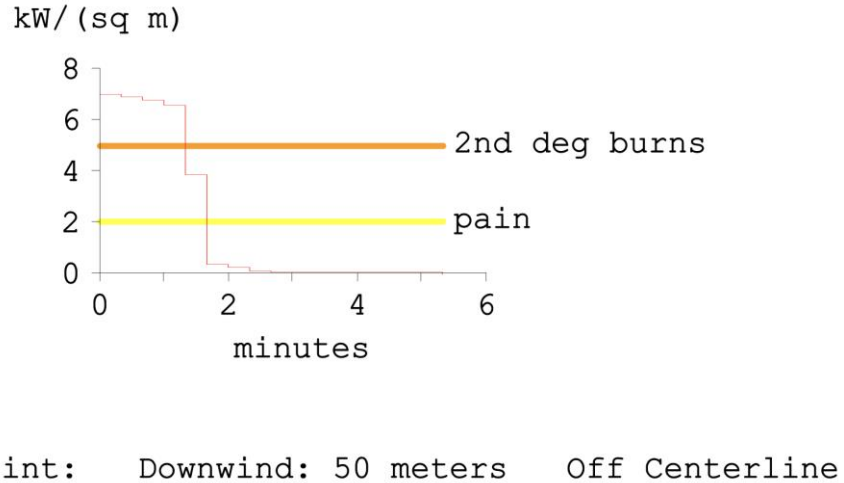


Figure 8. Thermal radiation at point jet fire.

3.3.4 Scenario 4: BLEVE (Fireball)

This scenario determines the thermal radiation from the fireball. Results from the ammonia BLEVE modeling were calculated using the fireball model. The fireball model calculates the dynamics of the fireball, including its size and shape, based on factors such as ammonia release rate, initial conditions, and environmental variables. Additionally, the model helps estimate the range of thermal radiation the fireball produces, which is critical for assessing potential damage to structures and the risk to individuals in the vicinity. The calculated thermal radiation at a specific distance, precisely 207 meters from the closest BLEVE source in the red zone, was determined to be 10.0 kW/m^2. This value indicates the intensity of the thermal radiation at that distance can be potentially lethal within 60 seconds. The orange zone, which is 301 meters, might cause 2-degree burns within 60 seconds. The yellow zone thermal radiation at a specific distance, precisely 476 meters from the farthest jet fire source, was determined to be 2.0 kW/m^2. This value indicates the intensity of the thermal radiation at that distance can cause pain within 60 seconds. As shown in Figure 9, the estimated thermal radiation reaches a maximum of 28.8 kW/m^2 at that point, featuring a fireball 152 meters in diameter and lasting 10 seconds.

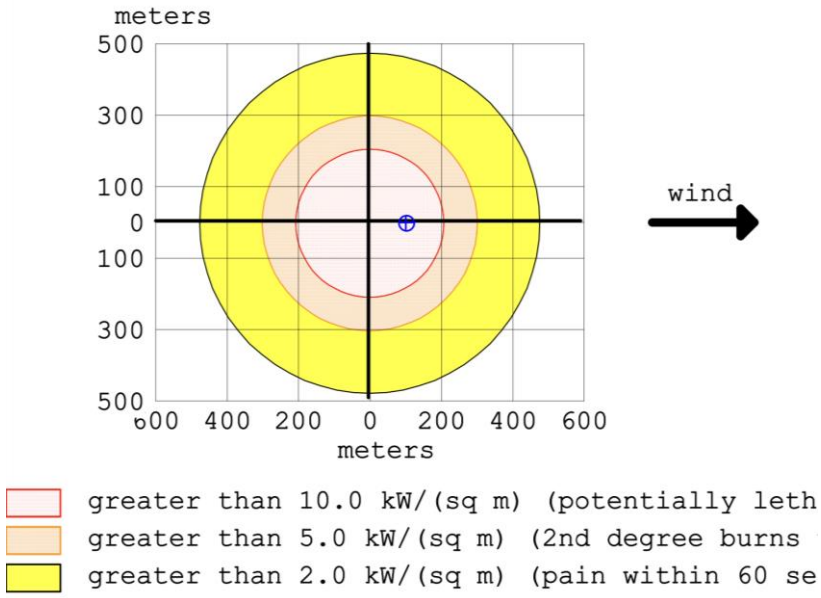


Figure 9. Distances of thermal radiation threat zone BLEVE (fireball).

3.3.5 Scenario 5: Vapor Cloud Explosion (VCE)

This scenario determines the ammonia cloud's overpressure (blast force) threat zone, which is estimated using the ammonia VCE model as an empirical model. The blast forces from the vapor cloud explosion in the yellow zone were 639 meters from the farthest VCE source at LOC-1 with 1.0 psi can a shattered glass, and the orange zone simulated pressure was 3.5 psi is serious injury likely with distances of 364 meters. The red zone was determined to have an overpressure blast force of 8.0 psi, which destroyed buildings at distances of 310 meters. This scenario has a release duration of 5 minutes and a maximum average sustained release rate of 11,200 kilograms/min (averaged over a minute or more). The total amount released is 16,970 kilograms. Threat at point downwind 100 meters has an overpressure estimate at the point with an overpressure of 293 psi, exceeding LOC-3 8.0 psi. The explosion was violent enough to destroy buildings. Blast forces of ammonia, highest at distances more than 630 m in the rainy season, are presented in Figure 10. Table 5 shows data distances from accident point sources in all five scenarios and seasons.

According to the main results of scenario 1 in summer, red, orange, and yellow threat distances were found to be 2.4 km, 4.8 km, and 8.9 km downwind, respectively. Compared with other seasons, such as rainy, red, orange, and yellow, threat distances were 2.5 km, 4.5 km, and 8.9 km, respectively. The winter in the red, orange, and yellow threat distances were found to be 2.4 km, 4.9 km, and 8.9 km downwind, respectively ,

finding that the distance in the yellow zone in the three seasons was no different. In Scenario 2, the ammonia-induced fire poses the highest risk at 368 meters from the accident source's red zone (60% LEL) during summer. During the rainy and winter seasons, the limited fire risk is approximately the same at 358 meters and 359 meters, respectively, and in other scenarios, the distances do not differ significantly. This indicates that ammonia transportation accidents under strong meteorological conditions can enable poisonous gas to travel long distances quickly, negatively affecting social life and the economy. Evaluate the risks associated with ammonia transportation and the possible undesirable consequences of any truck accident leak or rupture. As examples from the previous studies, the consequences of possible accidents were determined using the ALOHA program.

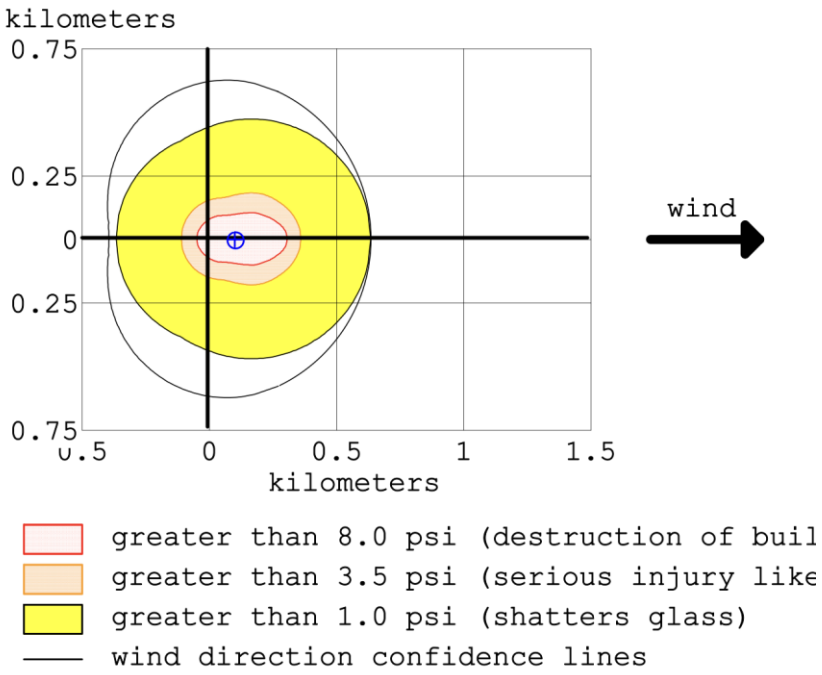


Figure 10. Distances of overpressure (blast force) threat zone.

Table 6 summarizes the most dangerous circumstances in the accident of ammonia transportation for the six study points. The most dangerous moment of ammonia concentration outdoors in scenario 1 is 505,000 ppm during the first 5 minutes after the release. Point 2 350 meters concentration 97,500 ppm during the first 10 minutes after the release. The data indicate that outdoor concentrations in scenarios 1 and 2 exceed the EPA's highest toxicity level (AEGL-3). An indoor LOC-3 (AEGL-3) concentration is observed at point 2, while concentrations at points 3 to 6 surpass AEGL-1. The maximum outdoor concentrations in scenarios 1 and 2 are consistent across all seasons due to identical data inputs and simulated results. Previous studies also indicated that the toxic vapor cloud scenario resulted in the most hazardous situation [23, 31].

The consequences modeling of various accident outcomes, a dispersion of toxic vapor cloud will move in a downwind direction and spread in a crosswind. In the case of ammonia, the intensity of heat radiation in scenario 3 flammable area (jet fire) is the least, not exceeding LOC-2 (5 kW/m^2) point 1 maximum intensity with 2.39 kW/m^2. This may be not only due to low heat of combustion and vaporization values but also to intensity greater than 2.0 kW/m^2, which can cause pain within 60 seconds. Figure 7 shows the toxic threat zone, thermal threat zone, and overpressure (blast force) threat zone of ammonia created by toxic vapor cloud, BLEVE, and VCE that is superimposed and visualized in the Google Earth map [43, 50]. The effect on the residents in the vicinity led to a domino effect.

Table 6. Summary of the most impact distances and maximum concentration of ammonia release on all scenarios.

Season	Distance from the emission source (m)	Max concentration outdoor					Max concentration indoor		Most dangerous moment
		Scenario 1: Toxic Vapor Cloud (ppm) (AEGL -3)	Scenario 2: Flammable area (Flash Fire) (ppm) (60% LEL)	Scenario 3: Flammable area (Jet Fire) (kW/m²)	Scenario 4: BLEVE (Fireball) (kW/m²)	Scenario 5: Vapor Cloud Explosion (psi)	Scenario 1: Toxic Vapor Cloud (ppm) (AEGL-1)	Scenario 2: Flammable area (Flash Fire) (ppm) (10% LEL)	
Summer	Point 1 100	505,000	505,000	2.390	28.800	293	6,270	6,280	First 5 min. after the release
	Point 2 350	97,500	97,500	0.187	3.720	4.040	1,620	1,620	The first 10 min. after the
	Point 3 500	51,600	51,600	0.088	1.810	1.560	1,060	1,060	The first 10 min. after the
	Point 4 1,000	11,600	11,600	0.020	0.428	0.498	379	380	First 20 min. after the release
	Point 5 1,500	4,180	4,180	0.009	0.182	0.283	183	183	First 25 min. after the release
	Point 6 2,100	1,680	1,680	0.004	0.089	0.182	94	95	First 35 min. after the release
Rainy	Point 1 100	497,000	497,000	2.320	28.100	293	6,170	6,180	First 5 min. after the release
	Point 2 350	93,200	93,200	0.182	3.610	3.820	1,610	1,610	The first 10 min. after the
	Point 3 500	49,600	49,600	0.085	1.760	1.530	1,060	1,060	The first 10 min. after the
	Point 4 1,000	11,600	11,600	0.020	0.414	0.490	398	399	First 20 min. after the release
	Point 5 1,500	4,270	4,280	0.008	0.176	0.279	197	197	First 25 min. after the release
	Point 6 2,100	1,740	1,740	0.004	0.086	0.180	103	104	First 35 min. after the release
Winter	Point 1 100	508,000	508,000	2.250	28	293	6,120	6,130	First 5 min. after the release
	Point 2 350	93,800	93,800	0.176	3.590	3.870	1,560	1,560	The first 10 min. after the
	Point 3 500	49,600	49,600	0.083	1.740	1.540	1,030	1,030	The first 10 min. after the
	Point 4 1,000	11,600	11,600	0.019	0.411	0.472	385	386	First 20 min. after the release
	Point 5 1,500	4,240	4,240	0.008	0.175	0.269	190	191	The first 30 min. after the
	Point 6 2,100	1,720	1,730	0.004	0.085	0.174	99	100	First 35 min. After the release

Considering the location and distance of the threat zone, the areas most affected by the accidental release are Chamai and Khonkrot; therefore, these areas were selected for the vulnerability study. Vulnerable groups, such as children under 5 and elderly individuals over 65, exhibit varying sensitivity to ammonia, affecting their ability to escape the threat zone promptly [16]. People with heart illness, physical limitations, and respiratory system problems. This is consistent with the findings of [25] study on impaired lung function. This impairs the person's ability to respond in areas such as vision, hearing, and perception. Intellectual disabilities may limit comprehension of the issue, or a disabled person may be unable to seek assistance from a career in an emergency. Being more sensitive to ammonia, vulnerable populations face higher risks than the general public when accidents occur along ammonia transport routes. Exposure to ammonia is more severe than in people with perfect health. In addition to the aligned study [32], results reflect that the residents residing in highly populated areas near the accidental site tend to be more vulnerable. In the event of an ammonia transportation accident in Thungsong, a risk map is utilized to protect and prevent impact on the local population. According to simulated results, meteorological variations demonstrate that wind directions are northeast in summer and winter and shift to southwest during the rainy season. These wind directions directly impact the neighborhoods located nearby. Accidental ammonia releases on roads will significantly affect a high percentage of the surrounding population, causing adverse effects on human health, the environment, and properties close to the accident site.

3.4 GIS mapping

3.4.1 Severity, risk, and evacuation route maps

The severity of accidental ammonia transportation mapping within the threat zone is assessed using ArcGIS. It provides necessary information about the population vicinity of the threat zone. When the source point of an accident has a population density exceeding 12,000 inhabitants, the threat zone identified to the area may directly affect and severely impact the population and cover economic and vulnerable areas with a population density of more than 30,000 inhabitants, as shown in Figure 11. Risk map Figure 12 shows the radius of the spread of overpressure corresponding to 10 kW/m^2, the largest for ammonia in summer and lowest in rainy and winter. It shows a distance of toxicity dispersion and flammable threat zone of radiation footprint. Superimposing layers prepare vulnerability and severity maps, consistent with this study by Rajeev et al. [43]. Study area, risk, and vulnerability maps were prepared using ArcGIS software. The risk measures the exposure probability of the population, vulnerable groups, and sensitive target places, such as hospitals, schools, residential areas, villages, temples, etc., to ammonia release.

ArcGIS can evaluate the spatial reach of different scenarios that may spread or disperse to nearby source points. The population in the surrounding area is also factored in, with higher population densities leading to increased severity. The severity map of the study area is shown in Figure 11. The sensitive targets placed within the study area are identified, and their relative is assessed by overlay analysis. Then, population density, emergency services, and hospitals are identified and quantified. Population density serves as a measure of societal vulnerability, making densely populated areas in need of immediate attention during accidents. Residential regions with high population densities should be given priority in emergency preparedness strategies [32, 52, 53]. Risk mapping, also created by GIS in this study, overlaid the toxic threat zone, radiation threat zone, and overpressure threat zone map into a risk map that identified high-risk areas. The risk map can be used as a decision-making tool to prepare emergency plans and land use planning, which might decrease the impact of the ammonia transportation accident in the future. Chau et al. created a risk map for the entire facility, with traffic light colors serving as danger indications [54]. Developed a methodology for risk management and emergency decision-making of offshore oil spill accidents, which is implemented with Bayesian by Li et al. [55]. Hence, evacuation mapping uses decision-making to prepare evacuation routes or response plans that identify safety points and areas that can be used as assembly points and emergency services if the accident risk is significant. The network analysis technique of GIS is used to design buffer zones for such accidents. Buffer areas identified are 3 schools, 4 hospitals, 2 temples, and five villages located in unacceptable risk areas, as shown in Figure 13.

In conclusion, severity, risk, and evacuation route maps are vital components of emergency preparedness and response, delivering critical information to decision-makers, emergency personnel, and the

public, such as in a small spill, initially isolating individuals within 30 meters of the affected area. Maintain a distance of 100 meters during daylight hours and 200 meters at night. Initially, individuals within 150 meters of the area should be isolated for a large spill. Maintain an 800-meter distance during the day and 2,300 meters at night. Utilizing these maps effectively enables communities to strengthen their resilience, decrease the impact of disasters, and save lives during urgent situations. ArcGIS plays a fundamental role in producing comprehensive risk maps for emergency management by combining spatial data, conducting hazard assessments, evaluating vulnerabilities, analyzing risks, and aiding decision-making processes. With ArcGIS technology, emergency planners can enhance risk assessments, optimize response strategies, and implement resilience-building measures, thereby improving community safety and minimizing disaster repercussions.

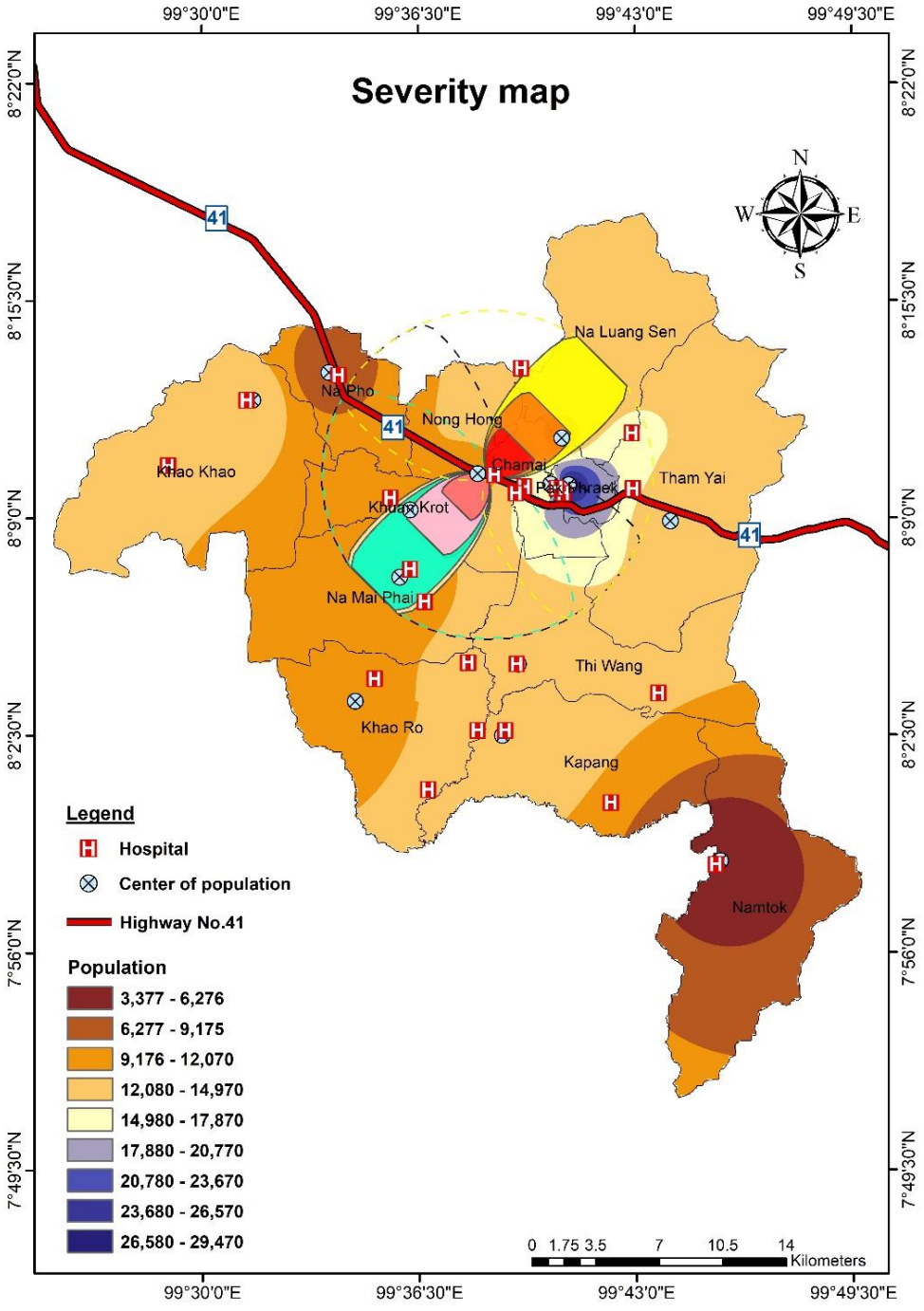


Figure 11. Severity map.

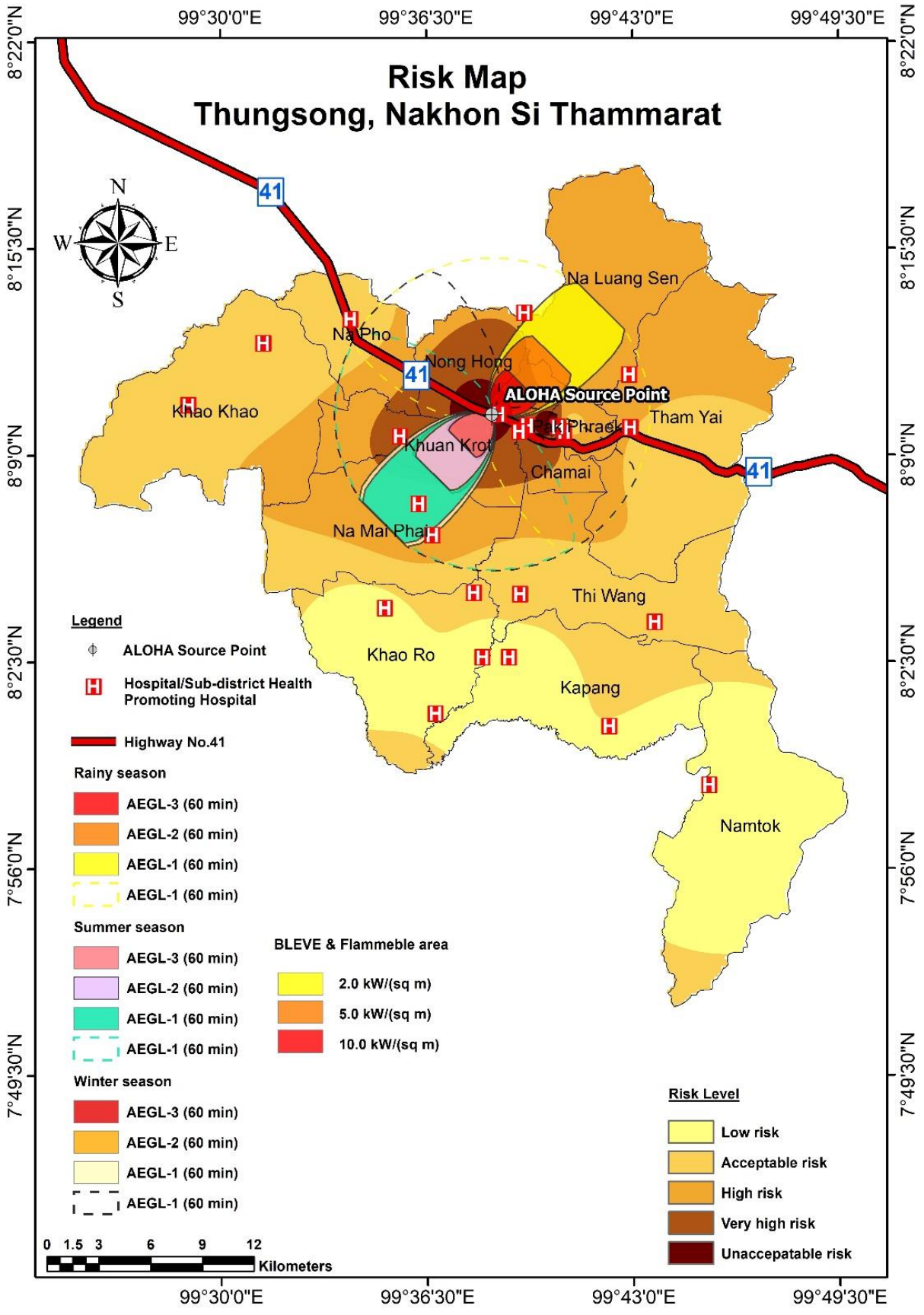


Figure 12. Risk map of the studied area.

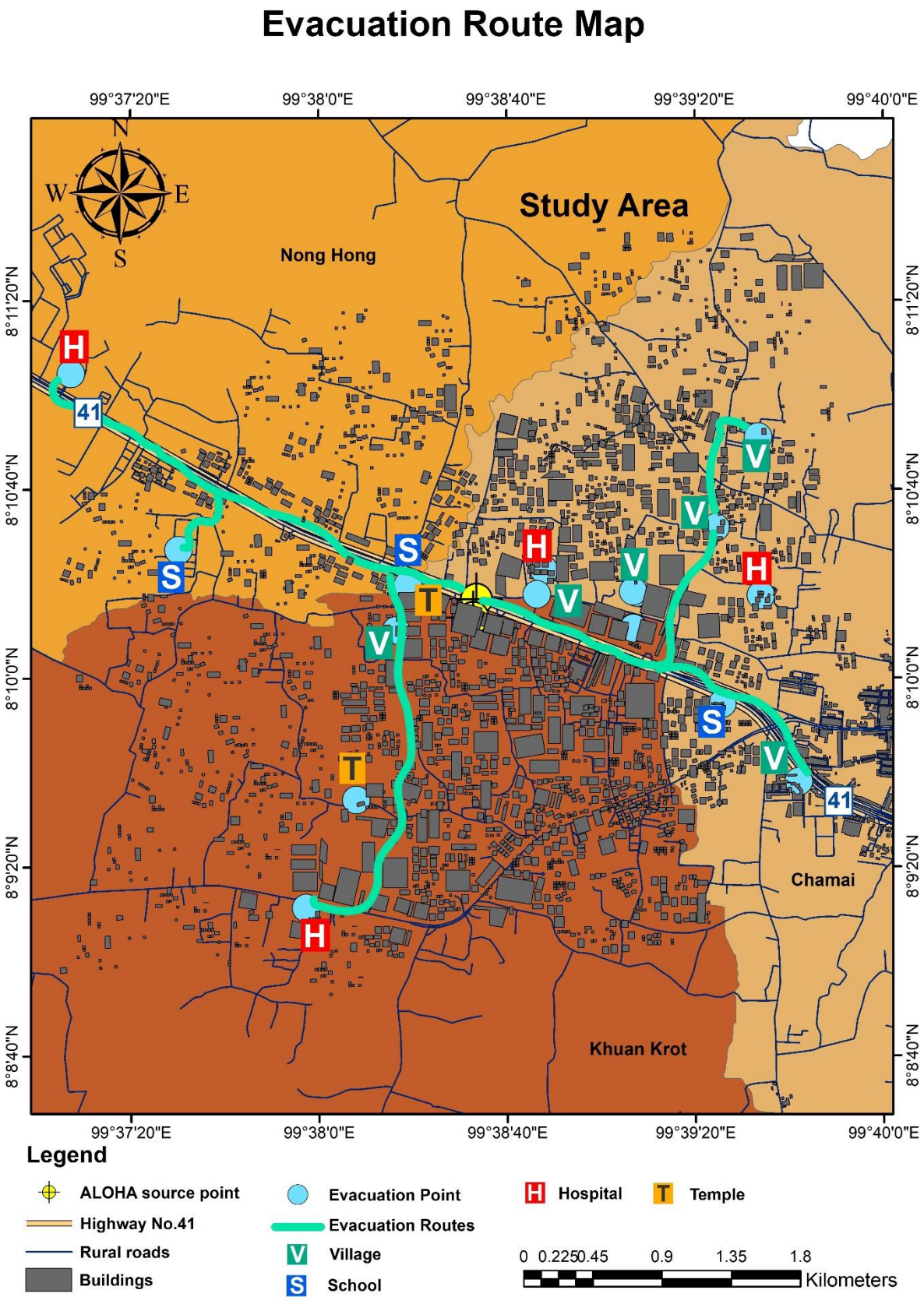


Figure 13. Evacuation map of the studied area.

4. Conclusions

This study assessed ammonia emission risks in a densely populated area by overlaying ALOHA results onto ArcGIS to create threat zone maps. In scenario 1, the red danger zone extends 2,400 meters from the source, with ammonia levels reaching up to 505,000 ppm, while in scenario 2, the red zone spans 368 meters. Explosive hazards (BLEVE and VCE) have ranges of 207 and 310 meters, respectively. In Thungsong, areas including 3 schools, 4 hospitals, 2 temples, and 5 villages are in unacceptable risk zones, exposing residents to ammonia levels exceeding 1,100 ppm, posing severe health risks. The study highlights the need for safety measures, evacuation plans, and continuous training to protect vulnerable populations and critical infrastructure. Future work should include real-time meteorological data to improve ammonia dispersion accuracy and adapt risk assessments for climate change impacts. The maps created are essential tools for emergency response planning and decision-making. Developing detailed evacuation maps and risk assessment tools is essential for effective emergency response within emergency plans. Moreover, implementing ongoing training programs and emergency drills for local authorities and communities can increase readiness and expedite response times. A limitation of this research is its reliance on static risk maps that do not account for real-time changes in environmental conditions, population movements, or ammonia dispersion patterns, which can vary with weather and other dynamic factors. This limits the ability to provide timely, adaptable responses during an actual ammonia release incident, highlighting the need for dynamic, real-time risk mapping in future studies.

5. Acknowledgements

The authors thank the School of Public Health, Walailak University (Grant No. 01/2564 & 01/2565) for the financial support.

Authorship contributions: Conceptualization: P.K.; methodology: P.K., S.Y., P.S., and J.M.; software: P.K.; validation: P.K.; formal analysis: P.K.; investigation: P.K.; data curation: P.K.; writing-original draft preparation: P.K.; writing - review and editing: S.Y., P.S., and J.M.; visualization: P.K.; supervision: J.M.; project administration: J.M. All authors have read and agreed to the published version of the manuscript.

Funding: This research was supported by the School of Public Health, Walailak University (Grant No. 01/2564 & 01/2565)

Conflicts of Interest: The authors declare no conflict of interest.

References

[1] Jabbari, M.; Atabi, F.; Ghorbani, R., Key airborne concentrations of chemicals for emergency response planning in HAZMAT road transportation- margin of safety or survival. *Journal of Loss Prevention in The Process Industries* **2020,** *65*, 104139.

[2] Bondžić, J.; Sremački, M.; Popov, S.; Mihajlović, I.; Vujić, B.; Petrović, M., Exposure to hazmat road accidents - Toxic release simulation and GIS-based assessment method. *J Environ Manage* **2021,** *293*, 112941.

[3] Fan, T.; Chiang, W.-C.; Russell, R., Modeling urban hazmat transportation with road closure consideration. *Transportation Research Part D: Transport and Environment* **2015,** *35*, 104-115.

[4] Brzozowska, L., Computer simulation of impacts of a chlorine tanker truck accident. *Transportation research part D: transport and environment* **2016,** *43*, 107-122.

[5] Inanloo, B.; Tansel, B., Explosion impacts during transport of hazardous cargo: GIS-based characterization of overpressure impacts and delineation of flammable zones for ammonia. *Journal of Environmental Management* **2015,** *156*, 1-9.

[6] Ghaleh, S.; Omidvari, M.; Nassiri, P.; Momeni, M.; Lavasani, S., Pattern of safety risk assessment in road fleet transportation of hazardous materials (oil materials). *Safety Science* **2019,** *116*, 1-12.

[7] Vianello, C.; Maschio, G., Quantitative risk assessment of the Italian gas distribution network. *Journal of Loss Prevention in the Process Industries* **2014,** *32*, 5-17.

[8] Bubbico, R.; Maschio, G.; Mazzarotta, B.; Milazzo, M. F.; Parisi, E., Risk management of road and rail transport of hazardous materials in Sicily. *Journal of Loss Prevention in the Process Industries* **2006,** *19*(1), 32-38.
[9] Fabiano, B.; Currò, F.; Palazzi, E.; Pastorino, R., A framework for risk assessment and decision-making strategies in dangerous good transportation. *Journal of Hazardous Materials* **2002,** *93*(1), 1-15.
[10] Egidi, D.; Foraboschi, F. P.; Spadoni, G.; Amendola, A., The ARIPAR project: analysis of the major accident risks connected with industrial and transportation activities in the Ravenna area. *Reliability Engineering & System Safety* **1995,** *49*(1), 75-89.
[11] Bouet, R.; Duplantier, S.; Salvi, O., Ammonia large scale atmospheric dispersion experiments in industrial configurations. *Journal of Loss Prevention in the Process Industries* **2005,** *18*(4), 512-519.
[12] Junior, M. M.; e Santos, M. S.; Vidal, M. C. R.; de Carvalho, P. V. R., Overcoming the blame game to learn from major accidents: A systemic analysis of an Anhydrous Ammonia leakage accident. *Journal of loss prevention in the process industries* **2012,** *25*(1), 33-39.
[13] Tan, W.; Du, H.; Liu, L.; Su, T.; Liu, X., Experimental and numerical study of ammonia leakage and dispersion in a food factory. *Journal of Loss Prevention in the Process Industries* **2017,** *47*, 129-139.
[14] Yarandi, M. S.; Mahdinia, M.; Barazandeh, J.; Soltanzadeh, A., Evaluation of the toxic effects of ammonia dispersion: consequence analysis of ammonia leakage in an industrial slaughterhouse. *Medical gas research* **2021,** *11*(1), 24.
[15] Gangopadhyay, R.; Das, S., Ammonia leakage from refrigeration plant and the management practice. *Process Safety Progress* **2008,** *27*(1), 15-20.
[16] Sanchez, E. Y.; Represa, S.; Mellado, D.; Balbi, K. B.; Acquesta, A. D.; Colman Lerner, J. E.; Porta, A. A., Risk analysis of technological hazards: Simulation of scenarios and application of a local vulnerability index. *Journal of Hazardous Materials* **2018,** *352*, 101-110.
[17] Roney, N.; Llados, F., Toxicological profile for ammonia. **2004**.
[18] Sekizawa, S.-i.; Tsubone, H., Nasal receptors responding to noxious chemical irritants. *Respiration physiology* **1994,** *96*(1), 37-48.
[19] Bai, Z.; Dong, Y.; Wang, Z.; Zhu, T., Emission of ammonia from indoor concrete wall and assessment of human exposure. *Environment international* **2006,** *32*(3), 303-311.
[20] Cheng, J.; Shen, J.; Jia, L.; Hu, K. In *Simulation analysis of the influence of leakage location and flow rate on the leakage of liquid ammonia tank*, International Conference on Computational Modeling, Simulation, and Data Analysis (CMSDA 2021), SPIE: **2022**, 232-236.
[21] Inanloo, B.; Tansel, B.; Jin, X.; Bernardo-Bricker, A., Cargo-specific accidental release impact zones for hazardous materials: risk and consequence comparison for ammonia and hydrogen fluoride. *Environment Systems and Decisions* **2016,** *36*(1), 20-33.
[22] NIOSH, Ammonia: Exposure Routes and Symptoms. **2019**.
[23] Orozco, J. L.; Caneghem, J. V.; Hens, L.; González, L.; Lugo, R.; Díaz, S.; Pedroso, I., Assessment of an ammonia incident in the industrial area of Matanzas. *Journal of Cleaner Production* **2019,** *222*, 934-941.
[24] Tan, W.; Lv, D.; Guo, X.; Du, H.; Liu, L.; Wang, Y., Accident consequence calculation of ammonia dispersion in factory area. *Journal of Loss Prevention in the Process Industries* **2020,** *67*, 104271.
[25] Tepper, A.; Comstock, G. W.; Levine, M., A longitudinal study of pulmonary function in fire fighters. *American journal of industrial medicine* **1991,** *20*(3), 307-316.
[26] George, A.; Bang, R. L.; Lari, A.-R.; Gang, R. K.; Kanjoor, J. R., Liquid ammonia injury. *Burns* **2000,** *26*(4), 409-413.
[27] Montague, T. J.; Macneil, A. R., Mass ammonia inhalation. *Chest* **1980,** *77*(4), 496-498.
[28] Rahman, N.; Ansary, M. A.; Islam, I., GIS based mapping of vulnerability to earthquake and fire hazard in Dhaka city, Bangladesh. *International Journal of Disaster Risk Reduction* **2015,** *13*, 291-300.
[29] Bariha, N.; Mishra, I. M.; Srivastava, V. C., Fire and explosion hazard analysis during surface transport of liquefied petroleum gas (LPG): a case study of LPG truck tanker accident in Kannur, Kerala, India. *Journal of loss prevention in the process industries* **2016,** *40*, 449-460.

[30] Chakrabarti, U. K.; Parikh, J. K., Route risk evaluation on class-2 hazmat transportation. *Process Safety and Environmental Protection* **2011,** *89*(4), 248-260.
[31] Anjana, N.; Amarnath, A.; Nair, M. H., Toxic hazards of ammonia release and population vulnerability assessment using geographical information system. *Journal of environmental management* **2018,** *210*, 201-209.
[32] Li, F.; Bi, J.; Huang, L.; Qu, C.; Yang, J.; Bu, Q., Mapping human vulnerability to chemical accidents in the vicinity of chemical industry parks. *Journal of Hazardous Materials* **2010,** *179*(1), 500-506.
[33] NOAA, E., ALOHA: USER'S MANUAL **2007**.
[34] Han, Z. Y.; Weng, W. G., Comparison study on qualitative and quantitative risk assessment methods for urban natural gas pipeline network. *Journal of Hazardous Materials* **2011,** *189*(1), 509-518.
[35] Patal, P.; Sohani, N., Hazard evaluation using ALOHA tool in storage area of an oil refinery. *International Journal of Research in Engineering and Technology* **2015,** *4*(12), 204-209.
[36] Khan, F. I.; Abbasi, S. A., An assessment of the likelihood of occurrence, and the damage potential of domino effect (chain of accidents) in a typical cluster of industries. *Journal of Loss Prevention in the Process Industries* **2001,** *14*(4), 283-306.
[37] AlRukaibi, F.; Alrukaibi, D.; Alkheder, S.; Alojaiman, S.; Sayed, T., Optimal route risk-based algorithm for hazardous material transport in Kuwait. *Journal of Loss Prevention in the Process Industries* **2018,** *52*, 40-53.
[38] Anjana, N.; Amarnath, A.; Chithra, S.; Harindranathan Nair, M.; Jose, S. K., Population vulnerability assessment around a LPG storage and distribution facility near Cochin using ALOHA and GIS. *International Journal of Engineering Science Invention* **2015,** *4*(6), 23-31.
[39] Meysami, H.; Ebadi, T.; Zohdirad, H.; Minepur, M., Worst-case identification of gas dispersion for gas detector mapping using dispersion modeling. *Journal of Loss Prevention in the Process Industries* **2013,** *26*(6), 1407-1414.
[40] Hu, T.; Xiong, J.; Zhou, J.; Xia, Q., Nitrogen removal performance of bioretention cells under freeze-thaw cycles: Effects of filler structure and microbial community. *Journal of Environmental Management* **2024,** *369*, 122380.
[41] Zhou, J.; Xiong, J.; Zhu, J.; Xie, X.; Ni, J.; Liu, Y.; Wang, X., Effects of freeze-thaw cycles on nutrient removal from bioretention cells. *Journal of Environmental Management* **2023,** *325*, 116556.
[42] Khanmohamadi, M.; Bagheri, M.; Khademi, N.; Ghannadpour, S. F., A security vulnerability analysis model for dangerous goods transportation by rail – Case study: Chlorine transportation in Texas-Illinois. *Safety Science* **2018,** *110*, 230-241.
[43] Rajeev, K.; Soman, S.; Renjith, V. R.; George, P., Human vulnerability mapping of chemical accidents in major industrial units in Kerala, India for better disaster mitigation. *International journal of disaster risk reduction* **2019,** *39*, 101247.
[44] Besiktas, R.; Baltaci, H.; Akkoyunlu, B. O., Simulation of the Jet Fire Using Atmospheric Dispersion Modeling (ALOHA): A Case Study of Natural Gas Pipeline in Istanbul, Türkiye. *Atmosphere* **2024,** *15*(4), 456.
[45] Jirsa, P., An Analysis of the Cumulative Uncertainty Associated with a Quantitative Consequence Assessment of a Major Accident. *Process Safety and Environmental Protection* **2007,** *85* (3), 256-259.
[46] Griffiths, R. F., The use of probit expressions in the assessment of acute population impact of toxic releases. *Journal of Loss Prevention in the Process Industries* **1991,** *4*(1), 49-57.
[47] Zhou, Y.; Hu, G.; Li, J.; Diao, C., Risk assessment along the gas pipelines and its application in urban planning. *Land Use Policy* **2014,** *38*, 233-238.
[48] Duijm, N. J.; Markert, F.; Paulsen, J. L., *Safety assessment of ammonia as a transport fuel*. Risø National Laboratory: 2005.
[49] Gyenes, Z.; Wood, M. H.; Struckl, M., *Handbook of scenarios for assessing major chemical accident risks*. Publications Office of the European Union: 2017.
[50] Zhang, D.; Mao, Z.; Gong, M.; Ren, J.; Zuo, S.; Chen, X., Study on optimization of shelter locations and evacuation routes of gas leakage accidents in chemical industrial park. *Process Safety and Environmental Protection* **2023,** *177*, 556-567.

[51] Lee, H. E.; Sohn, J.-R.; Byeon, S.-H.; Yoon, S. J.; Moon, K. W., Alternative risk assessment for dangerous chemicals in South Korea regulation: Comparing three modeling programs. *International journal of environmental research and public health* **2018,** *15*(8), 1600.

[52] Tahmid, M.; Dey, S.; Syeda, S. R., Mapping human vulnerability and risk due to chemical accidents. *Journal of Loss Prevention in the Process Industries* **2020,** *68*, 104289.

[53] Sengupta, A.; Bandyopadhyay, D.; Roy, S.; van Westen, C. J.; van der Veen, A., Challenges for introducing risk assessment into land use planning decisions in an Indian context. *Journal of Loss Prevention in the Process Industries* **2016,** *42*, 14-26.

[54] Chau, K.; Djire, A.; Vaddiraju, S.; Khan, F., Process Risk Index (PRI) – A methodology to analyze the design and operational hazards in the processing facility. *Process Safety and Environmental Protection* **2022,** *165*, 623-632.

[55] Li, X.; Zhu, Y.; Abbassi, R.; Chen, G., A probabilistic framework for risk management and emergency decision-making of marine oil spill accidents. *Process Safety and Environmental Protection* **2022,** *162*, 932-943.

ASEAN
Journal of Scientific and Technological Reports
Online ISSN:2773-8752

Research article

Ultrasonic-Assisted Production and Shelf-Life Assessment of Functional Beverage from Purple Rice (*Oryza sativa* L.)

Pornsawan Sombatnan[1, 6], Yardfon Tanongkankit[2*], Nukrob Narkprasom[3], Chanawat Nitatwichit[4], and Sureewan Rajchasom[5]

[1] Faculty of Engineering and Agro-Industry, Maejo University, Chiang Mai, 50290, Thailand
[2] Faculty of Engineering and Agro-Industry, Maejo University, Chiang Mai, 50290, Thailand
[3] Faculty of Engineering and Agro-Industry, Maejo University, Chiang Mai, 50290, Thailand
[4] Faculty of Engineering and Agro-Industry, Maejo University, Chiang Mai, 50290, Thailand
[5] Faculty of Engineering and Agro-Industry, Maejo University, Chiang Mai, 50290, Thailand
[6] College of Integrated Science and Technology, Rajamangala University of Technology Lanna, Chiang Mai, 50220, Thailand
* Correspondence: yardfon@mju.ac.th

Citation:
Sombatnan, P.; Tanongkankit, Y.; Narkprasom, N., Nitatwichit, C., Rajchasom, S. Ultrasonic-assisted production and shelf-life assessment of functional beverage from purple rice (*Oryza sativa* L.) . *ASEAN J. Sci. Tech. Report.* **2025**, *28*(1), e255396. https://doi.org/10.55164/ajstr.v28i1.255396

Article history:
Received: August 8, 2024
Revised: November 13, 2024
Accepted: November 20, 2024
Available online: February 16, 2025

Publisher's Note:
This article is published and distributed under the terms of the Thaksin University.

Abstract: Finding a new antioxidant-enriched source and understanding a non-thermal technique for functional beverage production is required to expand the range of new functional beverages and enhance their quality. The effects of various parameters of ultrasonic-assisted production (UAP) from purple rice, including the solid-liquid ratio (1:1, 1:2, 1:3, and 1:4.), treatment temperature (30, 40, 50, 60, 70, and 80°C) and treatment time (10, 20, 30, 40, 50 and 60 min) on total anthocyanin content were determined. A comparison between the yield of total anthocyanin obtained by the traditional and ultrasonication methods was performed. Kinetic reaction and coefficient temperature (Q_{10}) were also employed to predict the shelf life of purple rice beverages. Based on our findings, using UAP with the solid-liquid ratio of 1:2 at 60°C for 30 min was the most favorable condition for achieving the highest yield of total anthocyanin with the shortest treatment time. The yield of total anthocyanin in purple rice beverages produced using ultrasonication was 4 times higher than that of traditional methods. The second-order reaction was the best model to describe anthocyanin degradation during storage at temperatures 35-55°C. The predicted half-life of anthocyanin at 5, 15, and 25°C were 397.68, 44.35, and 5.73 days, respectively. The predicted shelf-life calculated using the average Q_{10} value of 1.415 were 12, 9, and 6 days at 5, 15, and 25°C, respectively.

Keywords: Anthocyanin; Half-life time; Kinetic; Ultrasonication; Q_{10}

1. Introduction

The functional beverage market is one of the fastest-growing industries among the functional food market segments. According to the previous report of Gupta et al. [1], the functional beverage market is forecasted to grow at a Compound Annual Growth Rate (CAGR) of 7.5% from 2022–2027, reaching $208.13 billion. The search for new natural sources of functional beverages and better production techniques to enhance their quality are required for the industry to expand the range of new functional beverages.

Purple rice (*Oryza sativa* L.) is commonly cultivated in North and Northeast Thailand. Its color, from deep purple to black, is exhibited by anthocyanin pigment. Anthocyanin compound is mostly found in the outer grain layers, comprising the pericarp and aleurone layers, accounting for 85% of

the whole grain content [2]. The compound has been reported to be beneficial for human health and protect against free radicals, leading to exceptional properties such as antioxidant and anticancer activity [3]. Purple rice is an interesting option for developing into a functional beverage product because of its benefits. A traditional production process of beverages from purple rice normally begins with rice milling, then boiling it with water for 30 minutes and filtration to obtain clear purple drinks [4]. This traditional method involves thermal treatment that can cause a loss of bioactive compounds, leading to low-quality products. Thus, quality improvement of rice beverages would be concerned with increasing the product's sales and being competitive in national and international markets.

Various non-thermal processing methods, such as pulse electric field, ultrasonication, and high hydrostatic pressure, have been applied in beverage production to intensify bioactive compounds [5, 6]. Among these methods, ultrasonication is an efficient and convenient method. It also requires a relatively low power consumption than other methods. Ultrasonication is performed using ultrasound with a frequency of 20–100 kHz. When ultrasonic waves oscillate through the medium, acoustic cavitation occurs, which is the phenomenon of forming, expanding, and eventual implosive collapse of microbubbles. Consequently, a large amount of energy and shear forces are generated to break cell-wall matrices, thus facilitating the diffusion of target compounds into the solvent [7]. The effect of cavitation on the yield of bioactive compounds in beverages is associated with several factors, such as temperature, frequency, solid and solvent ratio, and ultrasonication duration. As a food product produced by new processing is developed, the shelf life of the food product is investigated to ensure its quality and stability during storage and sales. The indicator of unsatisfactoriness or exceeding the accepted food quality standards can be expressed by microbial spoilage and loss in nutrient content. A kinetic model of nutrient changes and temperature coefficient (Q_{10}) at different temperatures can be evaluated for shelf-life prediction. Therefore, this research aimed to study the effects of ultrasonic-assisted production parameters, including temperature, solid-liquid ratio, and duration of ultrasonication throughout the shelf-life evaluation using kinetic reaction and Q_{10} of this new product.

2. Materials and Methods

2.1 Samples

Purple rice (*Oryza sativa* L.) was provided from the local grinding mill in Doi-Saket, Chiang Mai, Thailand (moisture content was 12% wet basis). Before each experiment, the purple rice was packed in a vacuum plastic bag and stored at room temperature.

2.2 Chemical reagents

Potassium chloride, sodium acetate, and distilled water were purchased from Northern Chemical Co., Ltd. and Union Science Co., Ltd. All chemicals were analytical grade.

2.3 Ultrasonic-assisted processing

Single-factor experiments were conducted in this study. The effects of solid-liquid ratio, temperature, and treatment time on total anthocyanin content were determined by varying the level of one parameter and keeping two parameters constant [8, 9, 10].

2.3.1. effect of solid-liquid ratio on total anthocyanin content

The purple rice (20 g) was added into a 250 mL beaker with 20, 40, 60, and 80 g of distilled water resulting in solid-liquid ratio of 1:1, 1:2, 1:3, and 1:4. The beakers were then placed in ultrasonic bath (Model GT Sonic-D6, Guangzhou, China) with controlled temperature, treatment time, frequency and power of 50°C, 30 min, 40 kHz and 150 W, respectively. After the treatment, the solid was removed, and a transparent purple liquid was kept in an amber glass bottle to determine the total anthocyanin content.

2.3.2. effect of temperature on total anthocyanin content

The beakers containing purple rice and water with a 1:3 ratio were placed in an ultrasonic bath (Model GT Sonic-D6, Guangzhou, China) at 30, 40, 50, 60, 70, and 80°C for 30 min. The constant frequency and power were applied at 40 kHz and 150 W. After the treatment, the solid was removed, and a transparent purple liquid was kept in an amber glass bottle to determine the total anthocyanin content.

2.3.3. effect of treatment time on total anthocyanin content

The beakers containing purple rice and water with a 1:3 ratio were placed in an ultrasonic bath (Model GT Sonic-D6, Guangzhou, China) at 50 °C for 10, 20, 30, 40, 50, and 60 min. The frequency and power were controlled at 40 kHz and 150 W. After the treatment, the solid was removed, and a transparent purple liquid was kept in an amber glass bottle to determine the total anthocyanin content.

2.4 Traditional processing

The purple rice was boiled for 30 min with a 1:3 ratio between purple rice and water, followed by filtration with a cheesecloth. The solid was removed, and a transparent purple liquid was kept in an amber glass bottle for further analysis.

2.5 Total anthocyanin content

The total anthocyanin content of the purple rice extract was determined by the pH differential method [11]. The purple rice extract was diluted tenfold with distilled water and centrifuged at 3,000 rpm for 15 min (Hettich zentrifugen, EBA 20, Baden Württemberg, Germany). Afterward, 200 μL of the supernatant was collected and added with 2 mL of potassium chloride buffer (pH 1.0) and 2 mL of sodium acetate buffer solution (pH 4.5). The mixture solution was incubated in the dark at ambient temperature for 30 min. The absorbance (A) was measured by UV-Vis spectrophotometer (Spectrum Instruments, SP-UV 200 spectrophotometer, Grosshansdorf, Germany). The incubated mixture solution was measured at 510 and 700 nm, respectively. Distilled water was served as a blank. Then, the absorbance of the solution was used to calculate the total anthocyanin content using the following equation (1).

$$\text{Total anthocyanin content (mg/g)} = \frac{A_{\text{diff}} \times Mw \times df \times 1{,}000}{\varepsilon} \quad (1)$$

where A_{diff} is $(A_{510nm} - A_{700nm})_{pH\ 1.0} - (A_{510nm} - A_{700nm})_{pH4.5}$, M_w is the molecular weight of cyanidin-3-glucoside (449.2 g/mol), ε is the molar absorptivity (26,900 $M^{-1}cm^{-1}$), and *df* is the dilution factor.

2.6 Shelf-life evaluation

The purple rice beverages produced using ultrasonication with the suggested condition were pasteurized by heating at 60°C for 15 min and contained in an amber glass bottle. The samples were then stored in an incubator (Binder, BD 115, Herrenberg, Germany) with accelerated temperatures at 35, 45 and 55°C temperatures and subjected to total anthocyanin content and pH analysis on days 0, 1, 3, and 7.

2.6.1 Kinetic reaction

The changes in total anthocyanin content during storage could be expressed in zero-, first- and second-order as shown in equations (2), (3), and (4), respectively. The order of the kinetic reaction was investigated by performing regression with the ideal coefficient of determination (R^2) [12].

$$\text{Zero order;} \quad C_A - C_{A0} = -kt \quad (2)$$

$$\text{First order;} \quad -\ln (C_A/C_{A0}) = kt \quad (3)$$

$$\text{Second order;} \quad 1/C_A - 1/C_{A0} = kt \quad (4)$$

where k = the rate constant, C_A = total anthocyanin content (mg/g) at the storage time, C_{A0} = initial value of total anthocyanin content (mg/g), and t is storage time (days)

After the reaction order was determined, the dependence of the degradation rate constant on temperature was determined by applying the Arrhenius equation as shown in equation (5). The activation energy was obtained by plotting a ln$k$ against the reciprocal of the absolute temperature (1/T), and the slope of the linear graph was equivalent to $-Ea/RT$ [13, 14]. The half-life indicating the time needed for 50% degradation of anthocyanins during storage was also calculated.

$$\ln k = \ln k_0 - \frac{E_a}{RT} \quad (5)$$

where k = rate constant, k_0 = Arrhenius constant, R = gas constant (8.314 J/mol.K), T = temperature (K), and Ea = activation energy (J/mol).

2.6.2 Temperature coefficient (Q_{10})

Shef-life evaluation can be determined to estimate the temperature's effect on the reaction rate increase by 10°C, which is called the Q_{10} value. The Q_{10} value and the predicted shelf life were calculated following equation (6) [15]. The shelf-life endpoint of the beverage was defined when the pH value was below 4.5, which was the critical point of pH in beverage products [16].

$$Q^{\Delta T} = \frac{Q_{s(T)}}{Q_{s(T+\Delta T)}} \quad (6)$$

where $Q_{s(T)}$ = shelf life at T°C and $Q_{s(T+\Delta T)}$ = shelf life at T+ΔT°C.

2.7 Statistical analysis

The data were subjected to an analysis of variance (ANOVA) and presented as mean values with standard deviations. Differences between mean values were analyzed using Duncan's multiple-range tests. Values were considered at a confidence level of 95%. All statistical analyses were performed using SPSS® software (version 29) (SPSS Inc., Chicago, IL). All experiments were performed in triplicate. The constant values from the curve-fitting model and the highest coefficients of determination (R^2 values) were determined using Microsoft Excel.

3. Results and Discussion

3.1 Effect of solid-liquid ratio on total anthocyanin content during ultrasonic-assisted processing

Figure 1 shows the total anthocyanin content at different solid-liquid ratios during ultrasonic-assisted processing. It was found that an increase in the ratio of purple rice and water from 1:1 to 1:2 and 1:3 resulted in a slight increase in the total anthocyanin content. However, when the purple rice and water ratio reached 1:4, the total anthocyanin content significantly decreased ($p<0.05$). This might be because, at the very low solid-liquid ratio, the viscosity of the solution was high, leading to difficulty in the cavitation effect. With the higher amount of water, the solution's viscosity was reduced, resulting in a more significant cavitation effect and enhancement of the diffusivity and dissolution of the solute into the solvent. On the other hand, at a very high solid-liquid ratio, the decrease in anthocyanin yield can be caused by the extreme formation of the cavitation effect, which leads to the degradation of the compound itself [17]. This result was agreed with Rittisak et al. [18], who reported that an increase in the yield of anthocyanin extracted from broken riceberry rice occurred as changing solid-liquid ratio from 1:2.5 to 1:5. The further increase in the solid-liquid ratio to 1:7.5 resulted in a significant decrease in the yield of anthocyanin.

3.2 Effect of temperature on total anthocyanin content during ultrasonic-assisted processing

As shown in Figure 2, the results revealed that rising treatment temperature initially increased total anthocyanin content. Then, as the temperature approached 60°C, the total anthocyanin content had no significant difference ($p<0.05$). However, a slight decrease in total anthocyanin content was noted when the temperature exceeded 70°C. This could be because cavitation bubbles formed abundantly at high temperatures. Upon their subsequent collapse, many shear forces were generated to improve the cell wall fragmentation, leading to a higher anthocyanin yield. The further increase in temperature promoted many cavitation bubbles, causing thermal degradation and degradation of the desirable compound. Additionally, a decrease in surface tension of solvent at higher temperatures resulted in the lower intensity of collapse of the cavitation bubble, hence reducing the mass transfer of the component to be extracted [17]. A similar pattern of the changes in the total anthocyanin content at different temperatures was reported by Thuy et al. [19]. Their results showed that the total anthocyanin content of the butterfly pea flower extract using ultrasonication increased when the temperature increased from 60°C to 70°C and tended to decrease when the temperature reached 80°C.

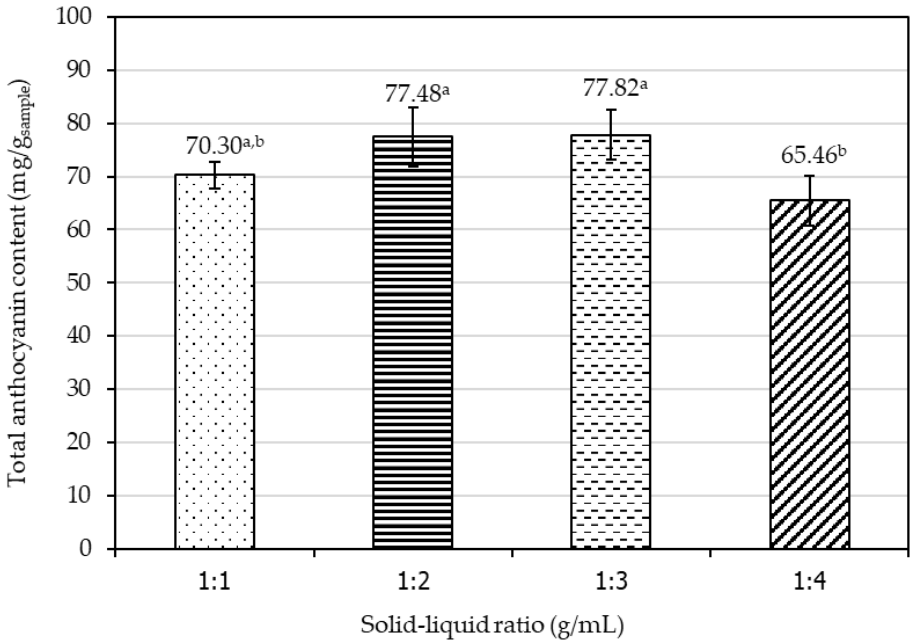


Figure 1. Total anthocyanin content at different solid-liquid ratios. Data are mean values with error bars indicating ± SD. Different lowercase letters indicate a significant difference ($p<0.05$).

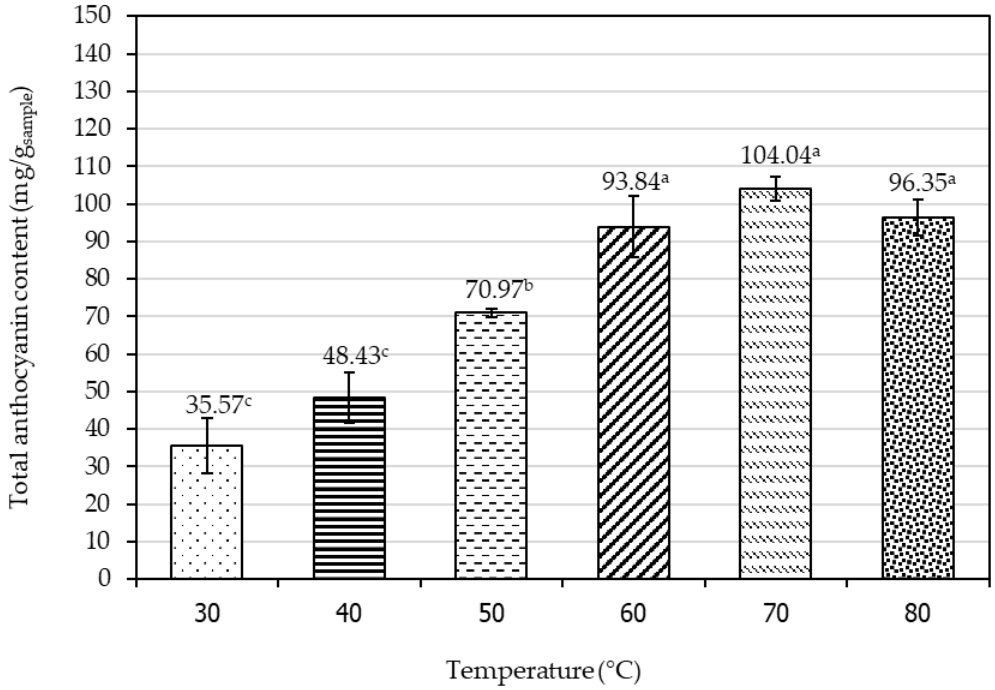


Figure 2. Total anthocyanin content at different treatment temperatures. Data are mean values with error bars indicating ± SD. Different lowercase letters indicate a significant difference ($p<0.05$).

3.3 Effect of treatment time on total anthocyanin content during ultrasonic-assisted processing

Figure 3 illustrates the effect of treatment time on the yield of total anthocyanin. It was observed that the pattern of change in total anthocyanin content is similar to the effect of temperature. An increase in treatment time initially resulted in a higher yield of total anthocyanin, and thereafter, the yield slightly decreased on prolonged treatment time. The initial increase in treatment time could explain this. The cavitation effect of the ultrasound enhanced the swelling, hydration, fragmentation, and pore formation of the plant

tissue matrix, facilitating the diffusion of target compounds into the solvent. Nevertheless, the extended exposure time caused structural damage to the solute, and the yield of total anthocyanin declined. Similarly, Lui et al. [20] reported that the yield of anthocyanins markedly increased with longer extraction time using ultrasonication and reached the peak value at 40 min. However, a decrease in the anthocyanin content was observed when the extraction time was prolonged over 40 min.

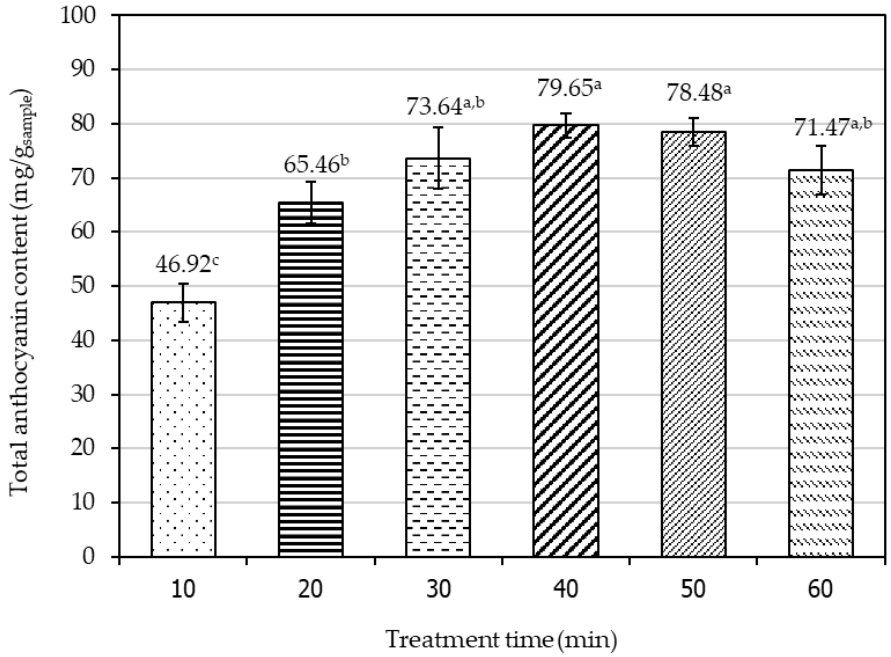


Figure 3. Total anthocyanin content at different treatment times. Data are mean values with error bars indicating ± SD. Different lowercase letters indicate a significant difference ($p<0.05$).

In summary, the significant factors affecting the total anthocyanin content during ultrasonic-assisted processing were the solid-liquid ratio, treatment temperature, and time. To achieve the maximum total anthocyanin content alongside the lowest operating costs, ultrasonication with a solid-liquid ratio of 1:2 at 60°C for 30 min was suggested to be the most favorable condition. Moreover, a comparison of the total anthocyanin content using ultrasonic-assisted processing with the suggested condition and traditional processing was investigated, as seen in Figure 4. It was observed that ultrasonication provided higher total anthocyanin content than traditional processing. This might be because the thermal degradation of the anthocyanin compound occurred during traditional processing [21]. Hence, ultrasonication with a solid-liquid ratio of 1:2 at 60°C for 30 min was selected for further shelf-life evaluation.

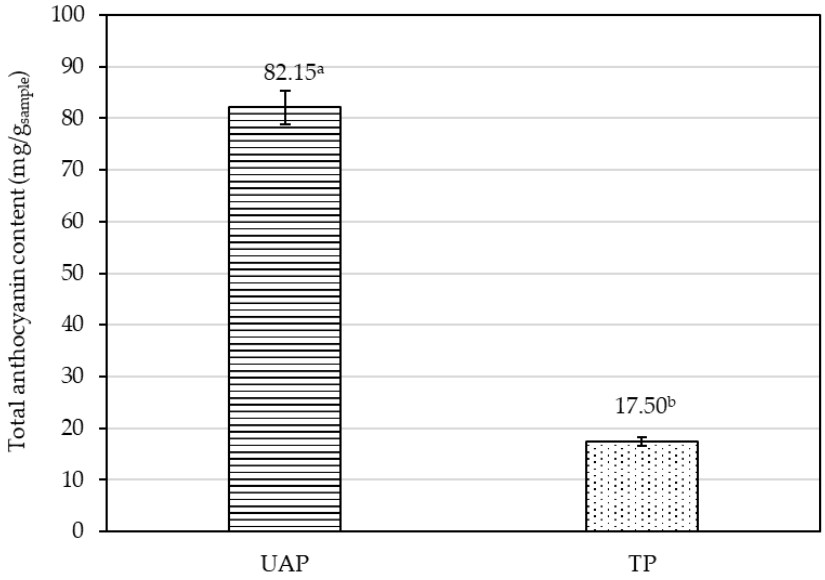


Figure 4. Total anthocyanin content undergoing ultrasonic assisted processing (UAP) and traditional processing (TP). Data are mean values with error bars indicating ± SD. Different lowercase letters indicate a significant difference ($p<0.05$).

3.4 Shelf-life evaluation

3.4.1 Kinetic reaction

Figure 5 illustrates variations in total anthocyanin content during the storage of purple rice beverages at different temperatures. It was found that the overall trend was a decrease in total anthocyanin content with the extension of storage time. The results also revealed that higher storage temperatures lowered total anthocyanin content as expected. Interestingly, a sharp decrease in total anthocyanin content by 40% and 76% was exhibited at 45 and 55°C, respectively, after 1 day of storage. The results are consistent with those of Muche et al. [22], who found that total anthocyanin content in grape juice decreased considerably with longer storage time. More than 70% loss of total anthocyanin content in the grape juice was also noted at storage temperatures of 25°C and 35°C.

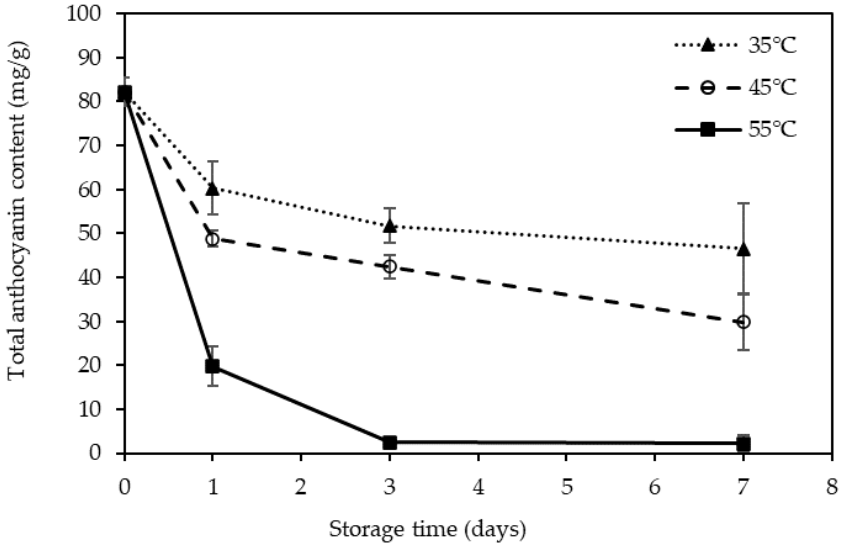


Figure 5. Changes in total anthocyanin content in purple rice beverages during storage at different temperatures.

The kinetic parameters of zero-, first- and second reaction and coefficient determination (R^2) at different storage temperatures were summarized in Table 1. It was clear that higher storage temperatures resulted in greater *k* values, indicating faster anthocyanin degradation. The reaction order was determined based on the highest determination coefficient representing a better-fitting modeling result. It was found that anthocyanin degradation during storage followed the second-order reaction with the highest R^2 value in the range of 0.992-0.999. The results were similar to a previous study by Ng and Cheok [23], who reported that the order reaction model represented the degradation of total anthocyanins extracted from *Garcinia Mangostana* L. rind with the highest value of coefficient determination in comparison to zero- and first- order.

Table 1. Kinetic parameters and coefficient determination (R^2)

Order	Temperature (°C)	*k*	R^2
Zero-order	35	4.201	0.685
	45	6.044	0.703
	55	8.702	0.506
First order	35	0.073	0.811
	45	0.074	0.996
	55	0.036	0.580
Second order	35	0.023	0.999
	45	0.038	0.987
	55	0.772	0.992

The second-order kinetic data were then used for determining Arrhenius parameters, including activation energy (E*a*) and k_0 value representing the dependence of the degradation rate constant on temperature. Figure 6 shows the Arrhenius plot of the ln *k* value with 1/*T*. It was found that the activation energy and the k_0 value were 1.46×10^5 J/mol and 9.074×10^{22} d^{-1}. The predicted half-life time of anthocyanins during storage at ambient (25°C) and refrigerated temperatures (5 and 15°C) were subsequently determined. As seen in Table 2, the results indicated that anthocyanins could be preserved for more than a month under storage at refrigerated temperature.

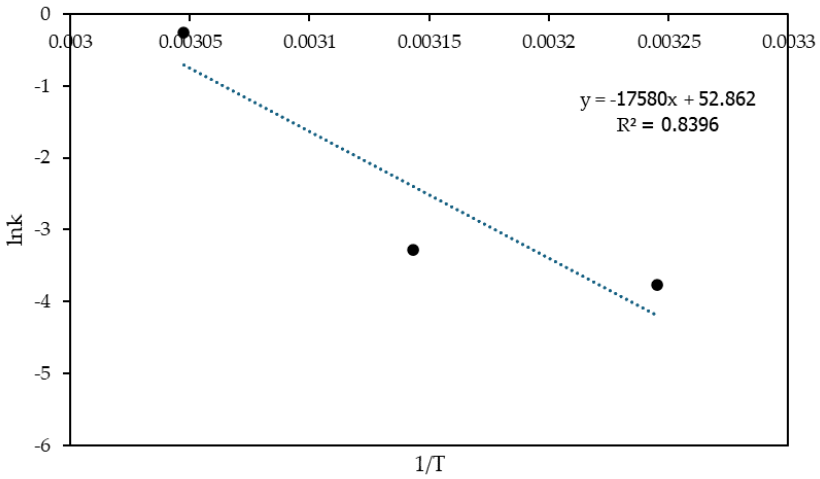


Figure 6. Relationship between the value of 1/T to ln k.

Table 2. The predicted half-life time of anthocyanins

Temperature (°C)	*K* (day^{-1})	Half-life time (days)
5	3.226×10^{-5}	397.68
15	2.892×10^{-4}	44.35
25	2.238×10^{-3}	5.73

3.4.2 Temperature coefficient (Q_{10})

Changing the pH value of beverages can be used as an index for microorganism spoilage [24]. The unacceptable point for low-acidicity beverages was defined as their pH values were below 4.5 [16, 24]. Figure 7 presents the pH values of purple rice beverages during storage at different temperatures. It can be seen that the pH values of samples were lower than 4.5 on days 4, 3, and 2 of storage at 35, 45, and 55°C, respectively. Hence, the Q_{10} value would be 1.50 and 1.33 when determined at temperatures from 35 to 45°C and 45 to 55°C, respectively. The average Q_{10} value of 1.415 and the storage temperature of 45°C were used to evaluate the predicted shelf life at different temperatures, as shown in Table 3.

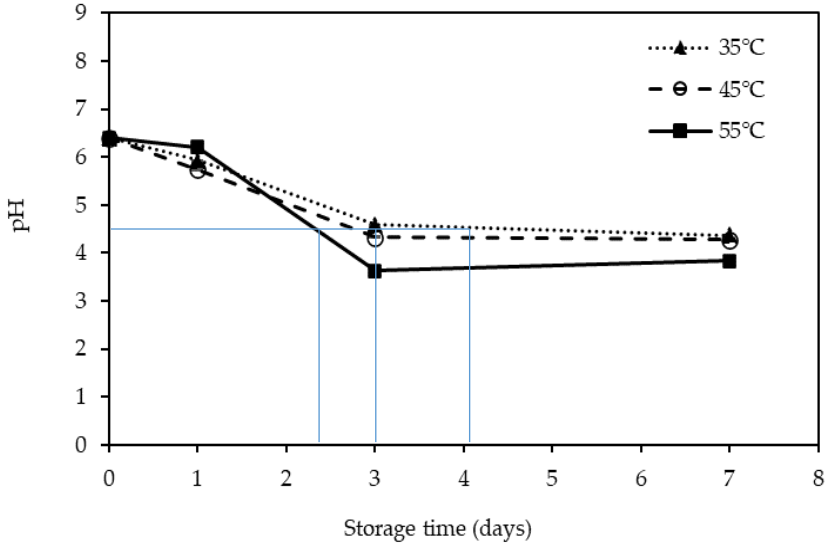


Figure 7. Changes in pH values of purple rice beverages during storage at different temperatures.

Table 3. The predicted shelf-life determined at different temperatures

Temperature (°C)	Predicted shelf life (days)
5	12
15	9
25	6

Overall, the shelf life of the purple rice beverages could be evaluated using the kinetic reaction of anthocyanin degradation and Q_{10}. Notably, the half-life times obtained from the kinetic reaction exhibited a more extended period when compared to the predicted shelf life calculated from Q_{10}. To achieve food security, the shelf life of the purple rice beverages was thus considered based on the Q_{10} since the pH value indicated spoilage of the beverages.

4. Conclusions

The effects of ultrasonic-assisted production parameters, including solid-liquid ratio, treatment temperature and time, were investigated to enhance the quality of purple rice beverages. A comparison of total anthocyanin content in purple rice beverages produced by ultrasonication and traditional methods was also determined. Furthermore, the predicted shelf life using the kinetic reaction of anthocyanin degradation and Q_{10} was evaluated under accelerated temperature. Our finding indicated that higher total anthocyanin content occurred when the solid-liquid ratio increased from 1:1 to 1:2 and reached a constant value at the solid-liquid ratio of 1:3. Once the solid-liquid ratio was 1:4, the total anthocyanin content significantly decreased. The treatment temperature had a significant effect on the total anthocyanin content. Increasing treatment temperatures resulted in higher total anthocyanin content and then gradually dropped when the temperature exceeded 70°C. Similarly, an extended treatment time led to a higher total anthocyanin content before the slight decrease in the total anthocyanin content exhibited at 60 min of treatment time. Based on the findings,

it could be concluded that using ultrasonic-assisted production with the solid-liquid ratio of 1:2 at 60°C for 30 min was suggested. In addition, a higher total anthocyanin content was obtained when employing the ultrasonication method under the suggested condition than when employing a traditional method. For the shelf-life evaluation, the degradation kinetics of total anthocyanin during storage at 35, 45, and 55°C followed the second-order reaction. The predicted half-life values at 5, 15 and 25°C were 397.68, 44.35 and 5.73 days, respectively. The predicted shelf life was also determined using the average Q_{10} value of 1.415. It was found that the shelf life of the purple rice beverages at 5, 15, and 25°C were 12, 9, and 6 days, respectively. Sensory and microbial analysis is recommended for future work to assess shelf life more accurately.

Author Contributions: Conceptualization, P.S. and Y.T.; methodology, P.S., Y.T., N.N. and C.N.; formal analysis, P.S.; investigation, P.S.; resources, S.R..; data curation, P.S.; writing—original draft preparation, P.S. and Y.T.; writing—review and editing, P.S. and Y.T.; visualization, Y.T.; supervision, Y.T.; project administration, Y.T.; funding acquisition, S.R.

Funding: This research was funded by Thailand Science Research and Innovation (TSRI) in 2022.

Conflicts of Interest: The authors declare no conflict of interest.

References

[1] Gupta, A.; Sanwal, N.; Bareen, M.A.; Barua, S.; Sharma, N.; Olatunji, O.J.; Nirmal, N.P.; Sahu, J.K. Trends in functional beverages: Functional ingredients, processing technologies, stability, health benefits, and consumer perspective. *Food Res. Int.* **2023**, *170*, 113046.

[2] Yamuangmorn, S.; Prom-u-Thai, C.; The potential of high-anthocyanin purple rice as a functional ingredient in human health. *Antioxidants* 2**021**, *10*, 833.

[3] Cui, L.; Zhang, Z.; Li, H.; Li, X.; Chen, T. Optimization of ultrasound assisted extraction of phenolic compounds and anthocyanins from perilla leaves using response surface methodology. *Food Sci. Technol. Res.* **2017**, *23(4*), 535-543.

[4] Niyomvong, N.; Namnood, T.; Foithongsuk, G.; Boondaeng, A.; Apiwatanapiwat, W.; Chanchai, P.; Vaithanomsat, P. Adding value to corn and purple rice through production of a homemade soft drink. *J Sci Technol MSU.* **2021**, *40*(6), 387-393.

[5] Jadhav, H.B.; Annapure, U.S.; Deshmukh, R.R. Non-thermal technologies for food processing. *Front. Nutr.* **2021**, *8*, 657090.

[6] Rios-Corripioa, G.; Pena, M.M.; Chanes, W.-C.; Guerrero-Beltran, J. Pulsed electric field processing of a pomegranate (*Punica granatum* L.) fermented beverage. *Innov. Food Sci. Emerg. Technol.* **2022**, *79*, 103045.

[7] Majid, I.; Nayik, G.A.; Nanda, V. Ultrasonication and food technology: A review. *Food Sci. Technol.* **2015**, *1*, 1071022.

[8] Hao, J.; Wang, Z.; Jia, Y.; Sun, L.; Fu, Z.; Zhao, M.; Li, Y.; Yuan, N.; Cong, B.; Zhao, M.; Ge, G. Optimization of ultrasonic-assisted extraction of flavonoids from *Lactuca indica* L. cv. Mengzao and their antioxidant properties. *Front. Nutr.* **2023**, *10*, 1065662.

[9] Cui, L.; Zhang, Z.; Li, H.; Li, N.; Li, N.; Chen, T. Optimization of ultrasound assisted extraction of phenolic compounds and anthocyanins from perilla leaves using response surface methodology. *Food Sci. Technol. Res.* **2017**, *23(4)*, 535-543.

[10] Jing, C.-L.; Dong, X.-F.; Tong, J.-M. Optimization of ultrasonic-assisted extraction of flavonoid compounds and antioxidants from alfalfa using response surface method. *Molecules*. **2015**, *20*, 15550-15571.

[11] Tonutare, T.; Moor, U.; Szajdak, L. Strawberry anthocyanin determination by pH differential spectroscopic method-how to get true results?. *Acta Sci. Pol-Hortoru.* **2014**, *13(3)*, 35-47.

[12] Bilbie, C.; Ghizdareanu, A. Comparative analysis of estimated shelf life, approaching accelerated aging methods. *Sci. Bull. Series F. Biotechnologies* **2021**, 104-111.

[13] Singh, R.R.B.; Ruhil, A.P.; Jain, D.K.; Patel, A.A.; Patil, G.R. prediction of sensory quality of UHT milk - A comparison of kinetic and neural network approaches. *J. Food Eng.* **2009**, *92*, 146–151.

[14] Jha, A.; Patel, A.A. Kinetics of HMF formation during storage of instant Kheer mix powder and development of a shelf-life prediction model. *J. Food Process Pres.* **2012**, *38*(1), 125–135.

[15] Fu, B.; Labuza, T.P. Shelf-life testing: procedures and prediction methods. In *Quality in frozen food*, Erickson, M.C., Hung, Y.-C.; Springer: Boston, MA. **1997**, 377-415.

[16] Shaik, M.I.; Hamdi, I.H.; Sarbon, N.M. A comprehensive review on traditional herbal drinks: Physicochemical, phytochemicals and pharmacology properties. *Food Chem. Adv.* **2023**, *3*, 100460.

[17] Kumar, K.; Srivastav, S.; Sharanagat V.S. Ultrasound assisted extraction (UAE) of bioactive compounds from fruit and vegetable processing by-products: A review. *Ultrason. Sonochem.* **2021**, *70*, 105325.

[18] Rittisak, S.; Detchewa, P.; Savedboworn, W.; Phungamngoen, C. Application of the Plackett-Burman design for screening and optimisation of factors affecting the aqueous extract for total anthocyanin content of broken riceberry rice. *Int. Food Res. J.* **2023**, *30*(3), 649-655.

[19] Thuy, N.M.; Ben, T.C.; Minh V.Q.; Tai, N.V. Effect of extraction techniques on anthocyanin from butterfly pea flowers (*Clitoria ternatea* L.) cultivated in Vietnam. *J. App. Biol. Biotech.* **2021**, *9*(6), 173-180.

[20] Liu, Y.; Zhao, Y.; Zhuo, Y.; Li, Y.; Meng, J.; Wang, Y.; Li, H. Ultrasound-assisted extraction of anthocyanins from malus 'royalty' fruits: Optimization, separation, and antitumor activity. *Molecules* **2022**, *27*, 4299.

[21] Das, A.B.; Goud, V.V.; Das, C. Extraction of phenolic compounds and anthocyanin from black and purple rice bran (*Oryza sativa* L.) using ultrasound: A comparative analysis and phytochemical profiling. *Ind. Crops and Prod.* **2017**, *95*, 332-341.

[22] Muche, B.M.; Speers, R.A.; Rupasinghe H.P.V. Storage temperature impacts on anthocyanins degradation, color changes and haze development in juice of "Merlot" and "Ruby" grapes (*Vitis vinifera*). *Front. Nutr.* **2018**, *5*, 100.

[23] Ng, K.L.; Cheok, C.Y. Evaluation of thermal degradation kinetic order of anthocyanins extracted from *Garcinia Mangostana* L. rind. *Prog. Energy Environ*. **2020**, *13*, 16-25.

[24] Kregiel, D. Health Safety of soft drinks: contents, containers, and microorganisms. Biomed Res. Int. **2015**, 128697.

ASEAN
Journal of Scientific and Technological Reports
Online ISSN:2773-8752

Research article

The Effect of KOH and Fe_2O_3 on Natural Rubber Latex Film for Excretion Bag

Sonchai Intachai[1], Kantrakorn Suwanraksa[2], Tantika Charoenlap[3], Nureeya Bintuan[4], Weerawut Naebpetch[5], and Panita Sumanatrakul[6*]

[1] Innovative Materials Chemistry for Environment Center, Faculty of Science and Digital Innovation, Thaksin University, Phatthalung, 93210, Thailand
[2] Faculty of Science and Digital Innovation, Thaksin University, Phatthalung, 93210, Thailand
[3] Faculty of Science and Digital Innovation, Thaksin University, Phatthalung, 93210, Thailand
[4] Faculty of Science and Digital Innovation, Thaksin University, Phatthalung, 93210, Thailand
[5] Faculty of Engineering, Thaksin University, Phatthalung, 93210, Thailand
[6] Faculty of Engineering, Thaksin University, Phatthalung, 93210, Thailand
* Correspondence: spanita@tsu.ac.th

Citation:
Intachai, S.; Suwanraksa, K.; Charoenlap, T.; Bintuan, N.; Naebpetch, W.; Sumanatrakul, P. The effect of KOH and Fe_2O_3 on natural rubber latex film for excretion bag. *ASEAN J. Sci. Tech. Report.* **2025**, *28*(1), e255538. https://doi.org/10.55164/ajstr.vx28i1.255538

Article history:
Received: August 17, 2024
Revised: November 16, 2024
Accepted: November 20, 2025
Available online: February 16, 2025

Publisher's Note:
This article has been published and distributed under the terms of Thaksin University.

Abstract: The excretion bag is an interesting innovation for elderly society, though a cost-effective, easy-to-use, and environmentally-friendly product remains challenging. To optimize mechanical features, the film bag was developed using Para rubber, a natural polymer as main composition by varying KOH stabilizer and Fe_2O_3 pigment. The formation of latex films was carried out using a $CaCl_2$ coagulant dipping process. Microscopy, SEM, and FT-IR were used to investigate the products obtained and their biodegradation. The biodegradation of the bag products spontaneously proceeded after 90-day soil burial. Adding KOH tailored the tensile strength, elongation at break, and tear strength for the mechanical properties of the as-formed films. Meanwhile, mixing Fe_2O_3 increased tensile strength but decreased elongation at break and tear strength. The obtained Para rubber bag may provide an optional innovation for facilitating the beloved elder on the excretion and other corresponding activities.

Keywords: Excretion bag; Natural rubber; Latex film; KOH; Fe_2O_3

1. Introduction

The population aged 65 and over is predicted to increase to 23 % by 2030, where one of the corresponding issues for elderly individuals is the high risk of falls due to aging-based physiological changes. Approximately 60-67 % of older adult falls occur inside the home or its immediate surroundings, often due to environmental hazards [1-2]. Toileting is a significant risk factor, with 34% of falls, especially at night, and nearly half at the bedside. Falls are hazardous for older people, with 28-35 % of those aged 65 and over at risk, rising to 32-42 % for those aged 70 and over, especially going to the bathroom. Additionally, at least 50 % of people aged over 65 face a fall each year, leading to increased hospitalization and medical costs [3-4].

Home environmental hazards, particularly standing and walking, result in high fall-induced injuries, where bathrooms and bedrooms are the most common places for these falls. Many studies have shown that the proximity between the bedroom and the bathroom and the installation of grab bars enhance safety. A bedside excretion device could reduce fall risks, supporting healthy aging [5-6]. Home hazard removal interventions have demonstrated a 38-39% reduction in fall rates among at-risk older individuals. The varied home

bathroom layouts require providers to tailor safety solutions for each case [7-9]. Almost all NR applications require high tear and wear resistance due to their strength and compressibility. Therefore, NR is used in many household products such as gloves, condoms, mattresses, pillows, laptop or phone casings, and so on [10-12]. Moreover, the benefits of NR-based innovation are renewability, biodegradability, and lower cost than synthetic rubber. Additionally, the rising price of crude oil and concerns about global warming are key factors driving the interest in NR's renewable material [13-14].

One effective solution for home health aides is a bedside excretion bag to mitigate the risk of nighttime falls. However, no current invention is made from 100% natural rubber. Natural rubber latex (NRL) or Para rubber is an excellent material for excretion bags due to its flexibility, high strength, tear resistance, and biodegradability [15-16]. Many natural rubber goods, including household and medical products, are molded using a simple dipping process. [17-19]. The structure of NRL, primarily composed of isoprene (C_5H_8) units, allows certain bacteria to degrade, making it environmentally friendly. Microbial degradation of rubber is advantageous as it does not produce harmful by-products and is energy-efficient [20-22].

Additive agents like KOH and pigments enhance the mechanical properties of NRL films. Besides, the optimal amount of dispersing agent can improve tensile strength and tear resistance [23-24]. In addition, various researchers have reported that iron oxide (Fe_2O_3) can act as an effective reinforcing filler by increasing the cross-linking density [25-26]. Therefore, this research created the excretion bag using natural rubber latex, focusing on suitable formulas and production methods by dipping. Furthermore, mechanical properties such as tensile strength, elongation at break and tear resistance, and biodegradability were also investigated. This work may provide a valuable procedure for developing innovation for facilitating an elder on excretion.

2. Materials and Methods

High ammonia-concentrated natural rubber latex (HA-NRL) was purchased from Geefin Rubbertech Co., LTD in Songkhla province, Thailand, where its dry rubber content was 60.0%. All of the used substances were obtained from Phatthana Chemical Co., LTD at Songkhla province, Thailand, which comprised of potassium hydroxide (KOH), sulfur (S_8), zinc diethyldithiocarbamate (ZDEC), zinc-2-mercaptobenzothiazole (ZMBT), zinc oxide (ZnO), Wingstay L, red iron oxide pigment (Fe_2O_3) and calcium chloride ($CaCl_2$). Before compounding, each chemical dispersion was prepared by grinding in a ball mill for 72 h, except for KOH and $CaCl_2$ aqueous solution.

2.1 Preparation of rubber compound

The NRL film was prepared by compounding the ingredients, as shown in Table 1, in an EMS-51®Sharp electric mixer. High ammonia-concentrated NRL was slowly stirred at 1st speed for 4 min, and KOH solution was firstly added by varying in 0 and 2 phr. Then, the appropriated amounts of S_8, ZDEC, ZMBT, Wing stay L, and ZnO dispersions were added to the latex matrix under stirring for 9 min. Next, Fe_2O_3 pigment dispersion was added by varying in 0 and 0.2 phr, where the total mixing time did not exceed 15 min. These film compounds were poured into 10×10×0.3 cm^3 of mirror mold and left to set at ambient temperature for 5 min before vulcanization at 80°C for 1 h and 30 min in a hot air oven. The vulcanized film was washed with water several times to remove non-reacted chemicals and then dried in the oven at 50°C for 12 h. The obtained rubber film sheet was collected in a desiccator overnight.

2.2 Preparation of excretion bag

Formula and process for excreta bags from Para rubber, including mold design, were claimed protection in the petty patent of invention. Thailand followed the request number of 2403000835. To prepare the latex compound, it was started by stirring concentrated latex to remove ammonia using the lowest paddle speed (level 1) for 4 min. Then KOH, S_8, ZDEC, ZMBT, and Wingstay L were mixed, respectively, under continually spinning until 9 min. Next, ZnO and Fe_2O_3 were added and then continuously incubated in a 10-liter tank at level 1 paddle speed. The latex compound possessed a shelf life of approximately 24 hours. For the rubber waste collection bag production using the dipping method, the procedures were started by preparing a 10 % w/v $CaCl_2$ solution to act as a coagulant for the latex compound. Even a layer of $CaCl_2$ solution was applied to coat the mold with a thickness not exceeding 2 mm. The dried mold was dipped into the prepared latex compound, rotating slowly in alternating directions for about 2 min to ensure fine coating.

The latex compound was partially set on the mold, and the coated mold was cured in the hot air oven with a fan at 100°C for 1 h.

The cooled product was coated with talcum powder to remove the rubber waste collection bag from the mold. Finally, the rubber waste collection bag was placed on a three-legged commode, as shown in Figure 1.

Table 1. Various ingredients for para latex compounding formulation.

Ingredients	[1]TSC (%)	[2]phr	Roles
HA-NRL	60	100	Matrix
S_8	50	1.0	Vulcanizing agent
ZDEC	50	1.0	Accelerator
ZMBT	50	1.0	Accelerator
ZnO	50	5.0	Activator
Wingstay L	50	0.2	Antioxidant
KOH	10	0, 2.0	Stabilizer
Fe_2O_3	3	0, 0.2	Pigment

[1]TSC is total solid content; [2]phr is part per hundred rubber.

2.3 Characterizations

2.3.1. Morphologies

The surface morphologies of the NRL compounds were examined using an optical microscope (OM), specifically a stereo microscope with a digital camera instrument with an optical objective of 15X, model SZ2-ILST. SEM analysis was conducted using a Scanning Electron Microscope machine (FEI: Quanta 450 FEG), where the acceleration voltage was set at 10 KV. Before analysis, NRL film samples were mounted on aluminum specimen stubs and coated with a gold-palladium layer.

2.3.2 Fourier transform infrared (FT-IR) analysis

Fourier-transformed infrared (FT-IR) spectroscopy using a Perkin Elmer Spectrum One FT-IR spectrophotometer was applied to explore the functional group of the samples in the wavenumber range of 4000 - 600 cm^{-1}.

2.3.3 Tensile properties

The tensile test was carried out with an Instron Universal Testing Machine using a C-type dumbbell specimen according to ASTM D412. The crosshead speed for the Instron tensile machine was set at 500 mm/min. The tensile strength of NRL films and elongation at break were taken five times, and the average results were calculated.

2.3.4 Tear resistance

The tear strength test was carried out according to ASTM D624 by using an Instron Universal Testing Machine with a C-type specimen, and the thickness of the sample was measured before the tear test with a micrometer. The crosshead speed was set at 500 mm/min. The obtained results were based on the average of five samples.

2.3.5 Thermal aging

The hot-air aging test was carried out in a circulating oven at 70°C for 3 days before the dumbbell-shaped rubber sheets' mechanical properties were tested on a tensile tester with a 500 mm/min strain rate according to ASTM D412. Aging coefficient (k) was calculated using the following equation (1):

$$\text{Aging coefficient} = \frac{(TS_a \times EB_a)}{(TS_u \times EB_u)} \times 100\% \quad (1)$$

TS_a and TS_u are the tensile strengths of the aged and un-aged samples. EB_a and EB_u are the elongation at break of the aged and un-aged samples, respectively.

2.3.6 Soil burial testing

The soil was collected from 0–10 cm depth, and the samples were buried at a depth of 8–9 cm from the soil surface for 90 days under, allowing air diffusion. Each sample was buried in a separate compost soil with pH around 7. The temperature of decomposition environment was controlled around 30°C with relative humidity of 80 %. The soil moisture was maintained at 80 % by water control.

3. Results and Discussion

3.1 Physical feature morphologies before and after soil burial testing

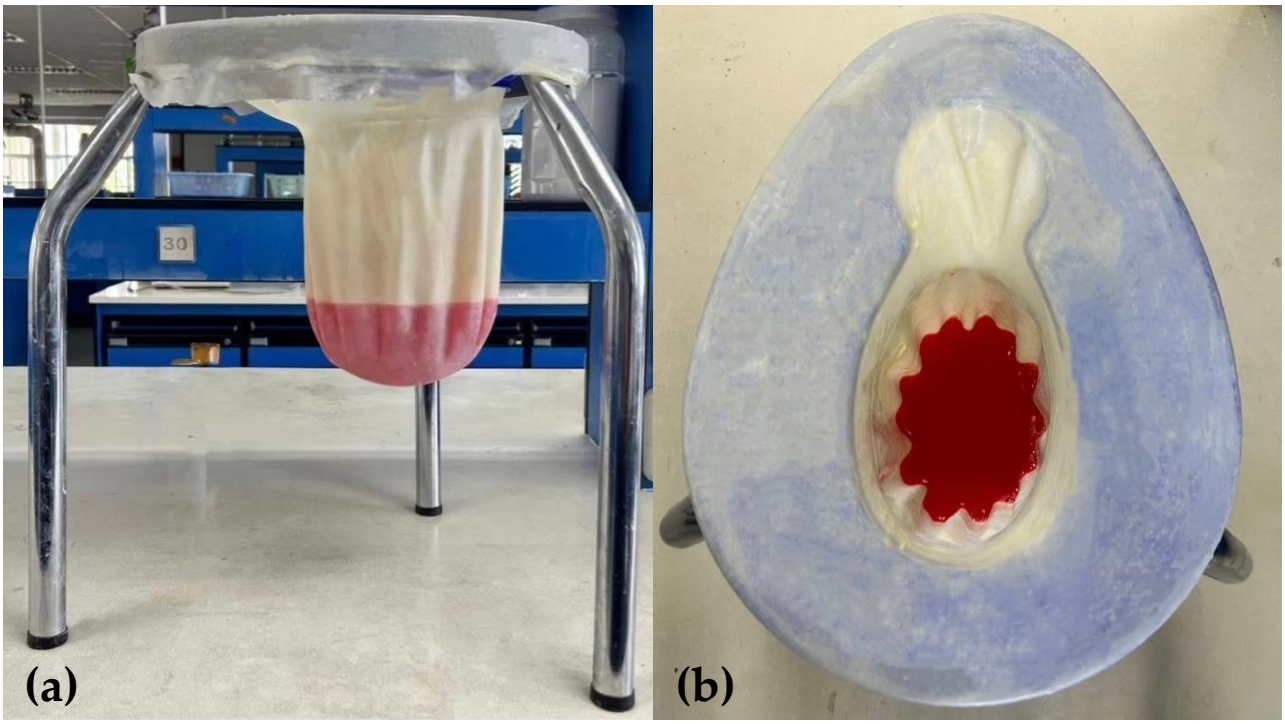


Figure 1. Excretion bag product at (a) side view and (b) top view.

Figure 1 shows the excretion bag product made from NRL compound mixed with KOH and Fe_2O_3. It was noted that the utilization of this product was effortless, especially in facilitating the excretion of elders. Interestingly, it was a cost-effective product, just 3 $ per piece relative to the others on the market, such as adult diapers (5 $ per piece). Additionally, this excretion bag accommodated large amounts of water around 3 L. After use, the as-prepared bag could be easily washed with water and continually reused until the 4th cycle, keeping relatively high performance. It was thought that NRL material is resistant to chemicals, water, fatigue, wear, tear, and abrasion due to high tensile strength that can adhere easily to other materials [10-12].

To verify the morphology of products and their surface change after the biodegradation, the microscopic images were investigated, as displayed in Figure 2. Before testing, the surface of the waste collection bag mixed with KOH (Figure 2a) and Fe_2O_3 pigment (Figure 2b) was mainly smooth without any apparent change. As seen in the microscopic image in Figure 2b, the light red surface was observed, attributing to the presence of Fe_2O_3 pigment. For 45 days of soil burial, both of the films (Figures 2(c) and 2(d)) crumbled, and the surfaces became rougher and exhibited fractures, cracks, and holes, attributing to the biodegradation by soil microorganisms [27]. The degree of degradation was independent due to the uncontrolled biotic and abiotic factors. However, the thickness and form of materials played a crucial role in the biodegradation process under soil burial and composting conditions [28-30]. The microbial activities proposed the mechanism of biodegradation in light, heat, water, and air, as shown in Figure 3. Meanwhile, the biodegradation of the product containing Fe_2O_3 was further run through the reduction-oxidation process by Fe_2O_3 catalyst followed by Karimi-Avargani et al. (2024) [31]. As a result, the prepared films could be a preferable choice owing to biodegradability based on zero waste and environmentally friendly.

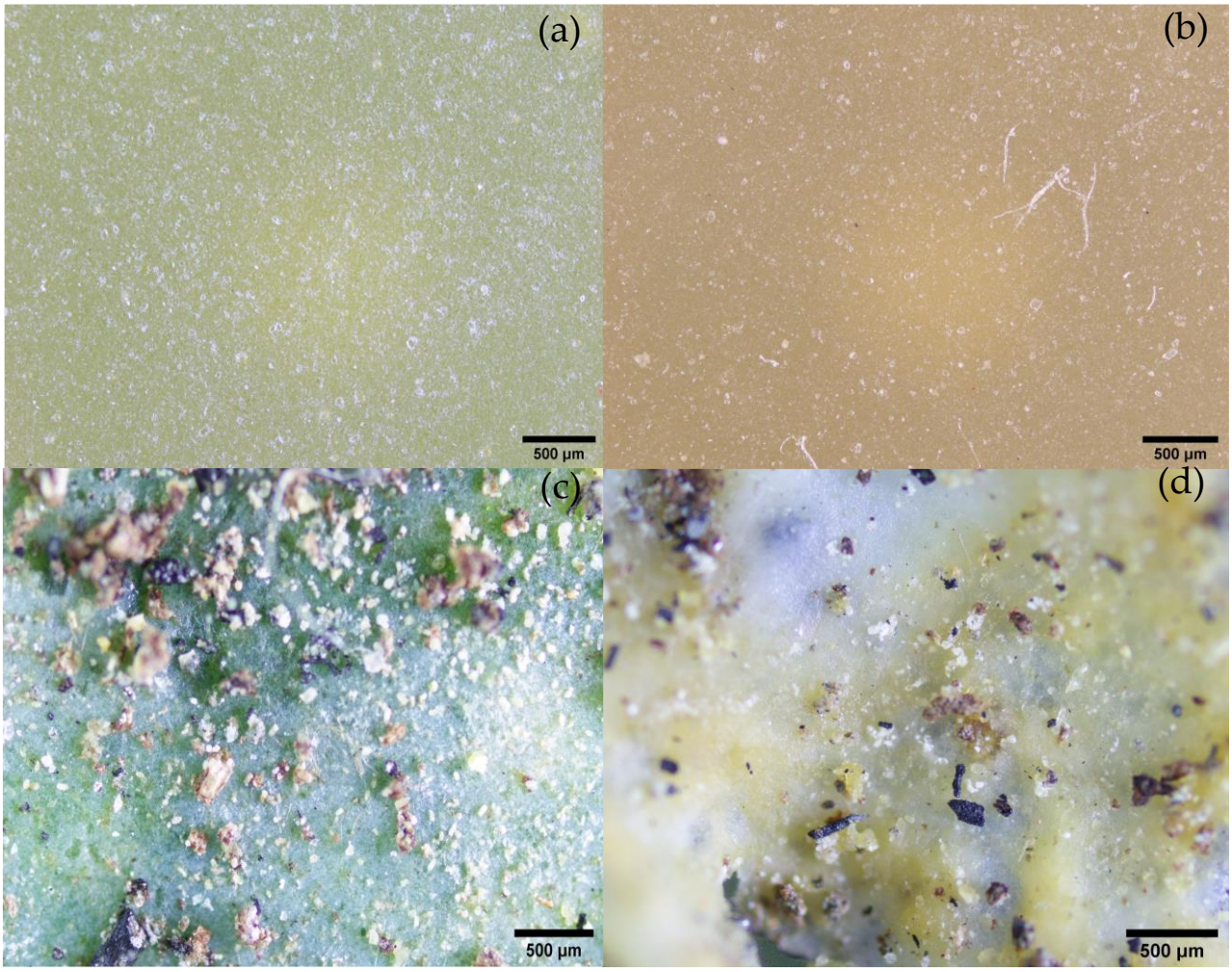


Figure 2. Microscopic images of the bag mixed with KOH (a, c) and Fe_2O_3 (b, d) before (a-b) and after (c-d) soil burial 45 days.

Various techniques were applied to confirm the biodegradation, and the bags' SEM images after being deposited for different long periods were investigated, as depicted in Figure 4. As seen in Figure 4a, the SEM image of the bag exhibited densely packed sheets corresponding to NRL's crosslink-framework structure [32-33]. By varying the biodegradation period, microbial colonies were observed after 12 weeks (Figure 4b). As the period elapsed, the microbial colonies and the hollow region on latex films' surface began to spread (Figures 4c and 4d). These gram-positive characteristics of microorganisms (mycelium type) consumed the polyisoprene chain (NRL film) as a sole energy source to generate an enzyme with further hydrolyzing glucosidic linkages in rubber compound [34-35]. The results could confirm the biodegradation mechanism through the soil system containing rich microorganisms [36].

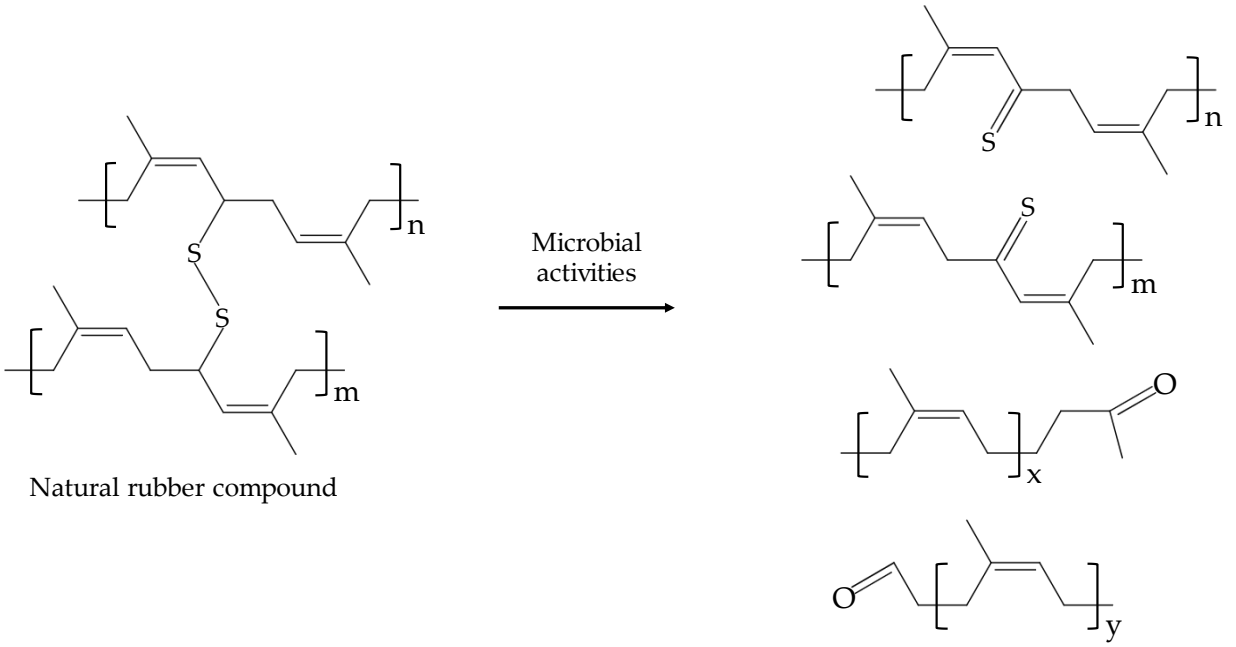


Figure 3. Proposed mechanism of natural rubber compound biodegradation.

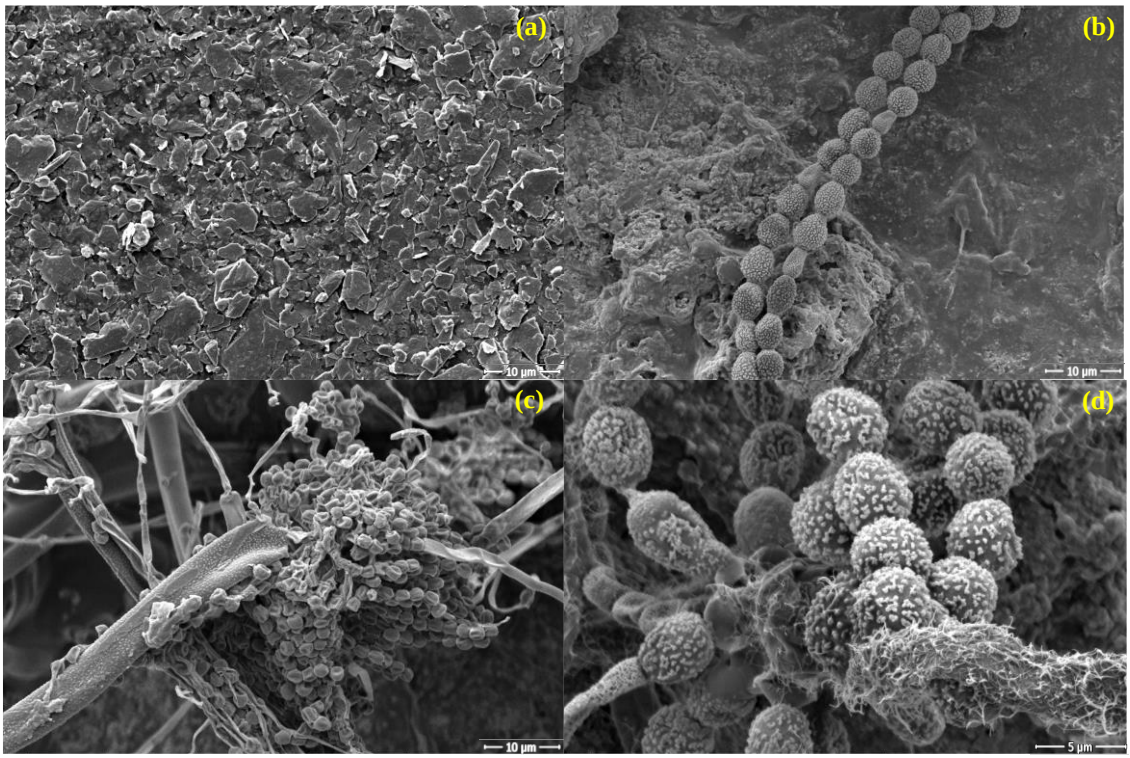


Figure 4. Morphologies of the bag (a) before and after soil burial for (b) 45 days, (c) 90 days at 5000x, and (d) 90 days at 12000x.

3.2 Functional groups from FTIR analysis

Besides, the characteristics of chemical species in the product mixed with KOH and Fe_2O_3 were investigated by using the FT-IR spectra based on functional groups, as shown in Figure 5. For the FT-IR spectrum of NRL film (before soil burial) showed the different infrared bands in the wavelength range 4000 – 650 cm^{-1}, where those located at 3676 cm^{-1} (hydroxyl groups at the mineral surface), 3286 – 3315 cm^{-1} (–OH),

2918 – 2960 and 1437 – 1449 cm^{-1} ($–CH_3$), 2851 – 2853 and 1375 – 1378 cm^{-1} ($–CH_2$), 1637 cm^{-1} (C–C) and 834 – 839 cm^{-1} (C–CH). The findings correspond to the FT-IR characteristics of cis-1,4-polyisoprene, that is, rubber monomer [37-38]. Relative to the infrared spectrum of fresh NRL film, most FT-IR bands for the NRL films after soil burial for 45 days and 90 days were similarly observed, indicating the presence of the same functional groups (cis-1,4-polyisoprene) [39-40]. However, the infrared intensities were lower, suggesting lower monomer units because of the shortening of the polymer chains by microbial [41-42]. Besides, the change in two FT-IR bands was observed. The band appeared at 1628 cm^{-1} because the C–O bond of aryl ketone was stronger, whereas that appeared at 3676 cm^{-1} was weaker and disappeared for the sample deposited for 90 days, and the N-H bond of the amide group at 1542 cm^{-1} also appeared [43]. These reasonable observations were consistent with polyisoprene chain scission's oxidation and hydrolysis processes [44-45].

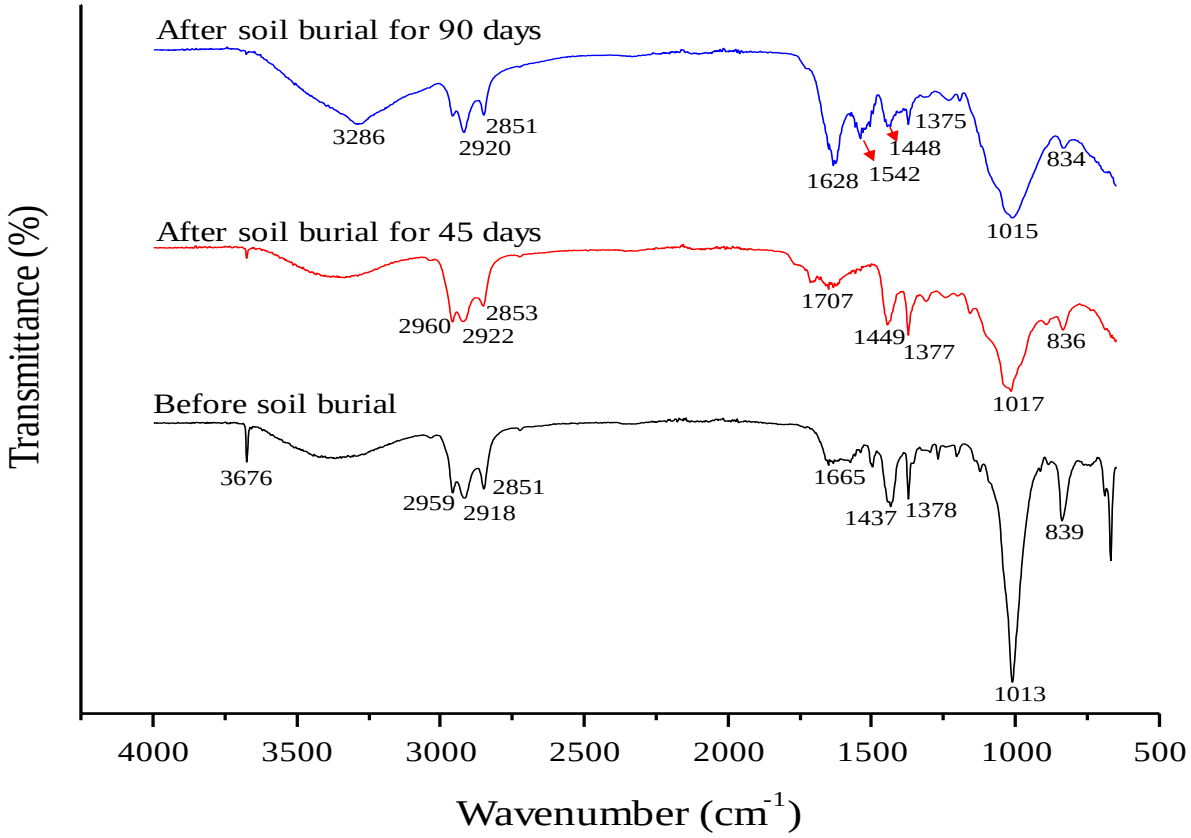


Figure 5. FT-IR spectra for the as-prepared film and after soil burial for 45 and 90 days.

3.3 Mechanical properties

The mechanical properties of NRL products and those prepared by mixing KOH and/or Fe_2O_3 before and after aging were demonstrated by such features as tensile strength (Figure 6), elongation at break (Figure 7), and tear resistance (Figure 8), where all of the data are summarized in Table 2. Before aging, in Figure 6, the addition of KOH and/or Fe_2O_3 increasingly affected the tensile strength of rubber films. Relative to without the addition of KOH (16.75 ± 0.53 MPa), KOH could promote the highest strength of the rubber film (28.05 ± 0.55 MPa), suggesting an excellent stabilizer [38-39].

Table 2. Tensile strength, elongation at break, and tear resistance with different parameters for Para excretion bag.

Parameters	Tensile strength (MPa)	Elongation at break (%)	Tear resistance (N/mm)
KOH	28.05±0.55	1134.60±17.09	46.53±0.05
KOH after aging	27.73±0.59	1038.82±17.32	38.37±0.26
without KOH	16.75±0.53	1066.73±16.97	35.71±0.01
without KOH after aging	9.59±0.27	925.62±9.08	30.82±0.31
KOH and Fe_2O_3	27.30±0.37	1105.57±17.39	41.84±0.40
KOH and Fe_2O_3 after aging	24.40±0.78	888.23±6.44	36.63±0.52
Fe_2O_3	25.76±0.34	1056.20±18.70	24.59±0.32
Fe_2O_3 after aging	22.92±0.12	821.13±6.29	21.33±0.43

Meanwhile, Fe_2O_3 could also tailor the tensile strength (25.76±0.34 MPa), which could be a good second stabilizer to reinforce the films. These phenomena arose from the perfect vulcanization process because KOH and Fe2O3 could drive the complete vulcanization reaction between polyisoprene with S8 [44-45], supporting the good distribution on the rubber film surface (Figure 4a). Interestingly, after aging, the tensile strength of all modified products was significantly higher than that of the film without adding KOH after aging. In addition, the strength of the modified films with KOH and/or Fe_2O_3 after aging was slightly reduced compared to those before aging. These results indicated that KOH and Fe_2O_3 could protect the heat treatment of the rubber film.

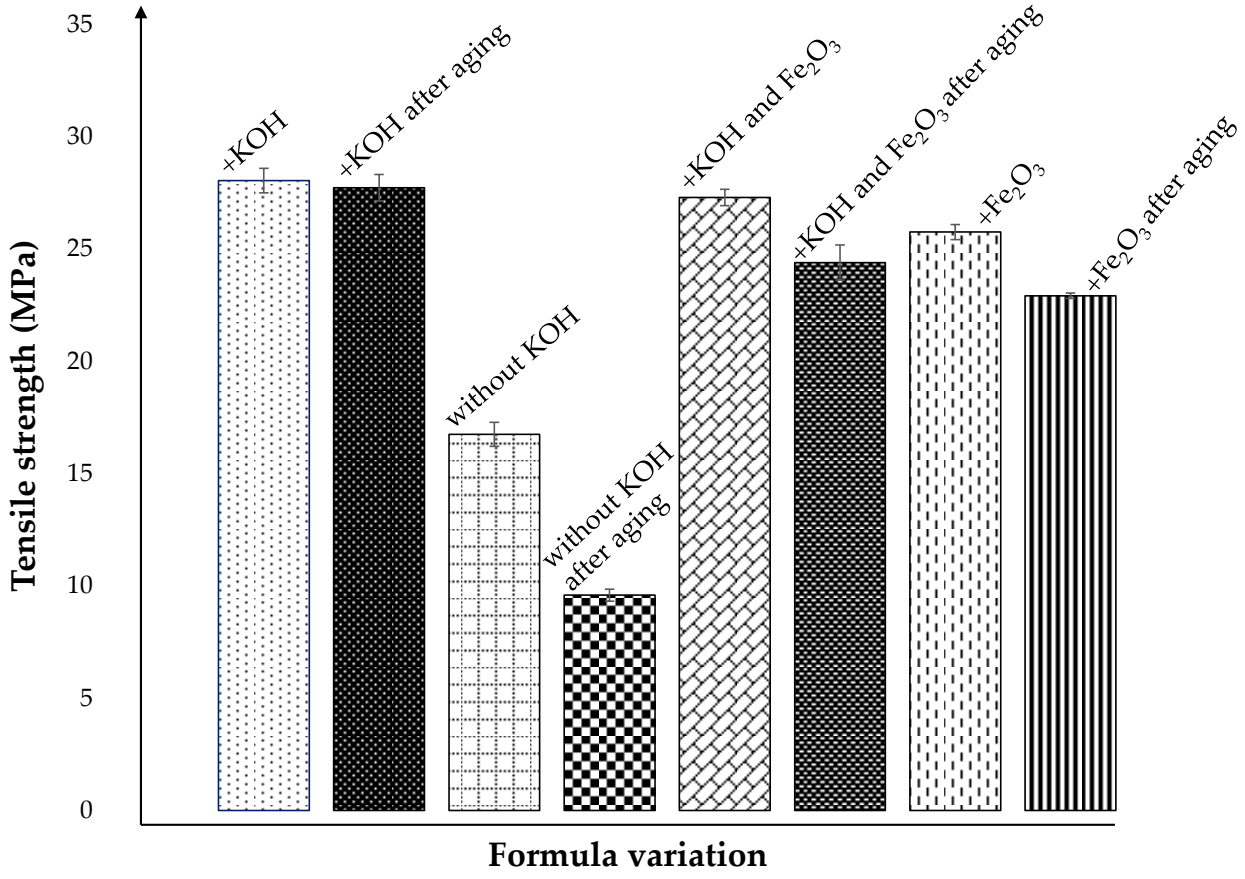


Figure 6. Tensile strength of NRL compounds with the effect of KOH and/or Fe_2O_3.

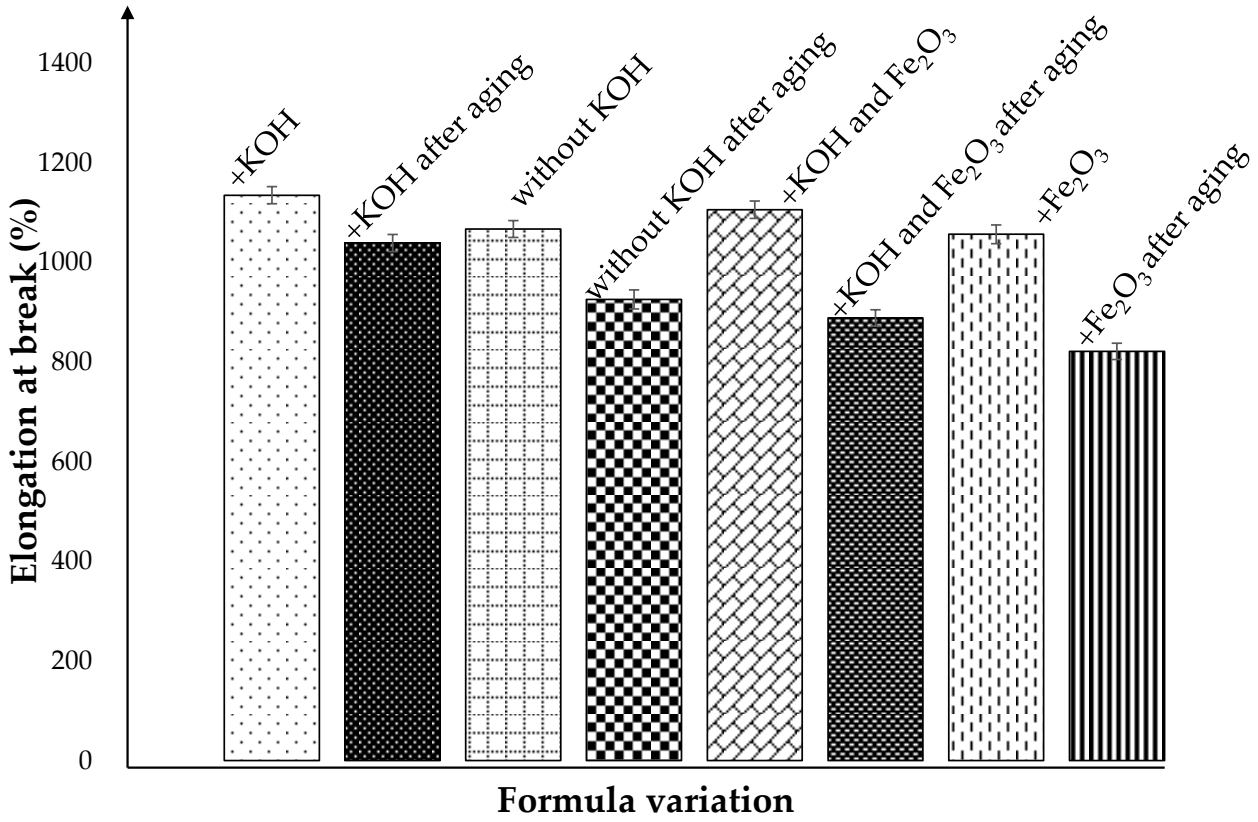


Figure 7. Elongation at break of NRL compounds with the effect of KOH and/or Fe_2O_3.

The effect of KOH and/or Fe_2O_3 was further investigated, demonstrated by elongation at NRL compound break, as shown in Figure 7. Without the addition of KOH (1066.73±16.97 %), the presence of KOH in the film could tailor the elongation at break (1134.60±17.09 %) because the vulcanization process reached the optimal condition of 2.0 phr KOH. On the other hand, the elongation at the break of the films was slightly increased by adding KOH and Fe_2O_3 (1105.57±17.39 %) due to the reduction in the rigidity of the films [25-26]. The value was slightly reduced by adding Fe2O3 (1056.20±18.70 %), which might slightly lengthen the rubber compound's hard segment. To compare the film after aging, the elongation at break for the product mixed with KOH showed a higher value than that without KOH, indicating high thermal stability. However, the presence of both KOH and Fe_2O_3 and only Fe_2O_3 in the films made the elongation at break slightly lower, indicative of the stricter component produced by adding excess Fe_2O_3 amounts.

3.4 Tear resistance

As seen in Figure 8, the tear resistance of NRL samples (before and after aging) was enhanced when KOH (46.53±0.05 and 38.37±0.26 N/mm) and both KOH and Fe_2O_3 (41.84±0.40 and 36.63±0.52 N/mm) were mixed, which could be indicated that the use of KOH and Fe_2O_3 caused the rubber films more tear resistant relative to without the addition of KOH (35.71±0.01 and 30.82±0.31 N/mm). It has arisen from the effect of stabilizers and inorganic components [44-45]. Whereas both values (before and after aging) were decreased for adding only Fe_2O_3 (24.59±0.32 and 21.33±0.43 N/mm), supporting the more rigid rubber compound with the enhanced stiffness.

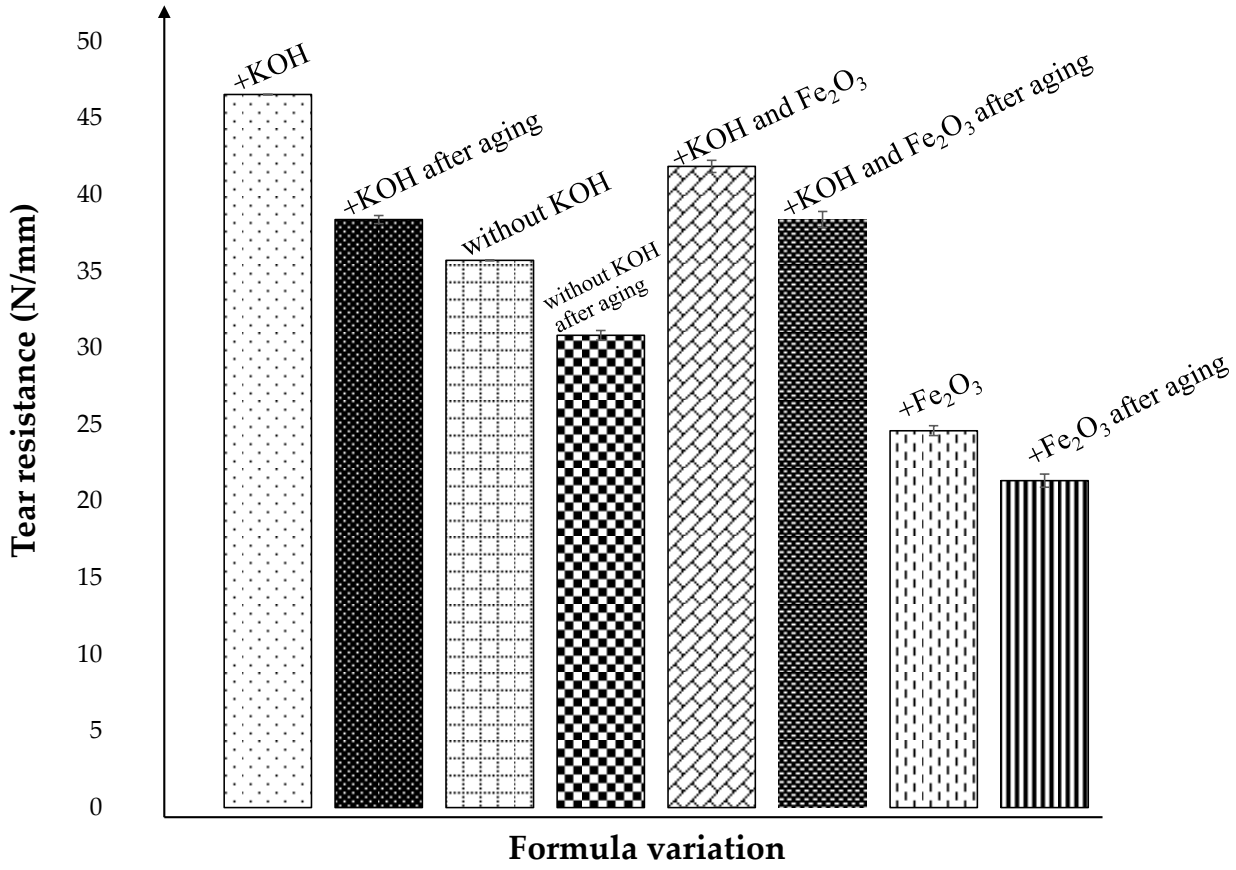


Figure 8. Tear resistance of NRL compounds with the effect of KOH and/or Fe_2O_3.

3.5 Thermal aging

Table 3. Aging coefficient with different parameters for Para excretion bag.

Parameters	Aging coefficient (%)
KOH	90.51
without KOH	49.63
KOH and Fe_2O_3	71.81
Fe_2O_3	69.17

From Table 3, The aging coefficients were calculated based on the deformation energy before and after aging, which were analyzed to assess the effect of stabilizer and pigment on the stability of the compounds. These thermo-oxidative aging coefficients of compounds containing KOH (90.51 %), both KOH and Fe_2O_3 (71.81 %), and Fe_2O_3 (69.17 %) were higher than that without the addition of KOH (49.63 %), confirming that the presence of stabilizer and pigment increased the aging resistance. Therefore, the stabilizer proved to be the most effective anti-aging substance. Additionally, the addition of pigment also significantly improved the stability of the compound [46].

4. Conclusions

This study was achieved by fabricating an excretion bag made from Para rubber compound with the addition of KOH and/or Fe_2O_3. The physical characteristics of the products were satisfactory, showing high reusable performance due to the chemical and mechanical features of natural rubber latex and biodegradation after the burial for 90 days through bio-activities by microorganisms. The effect of KOH could increase the tensile strength (11.30 MPa), elongation at break (67.87 %), and tear strength (10.82 N/mm), and these values were slightly lower after aging, indicating an efficient stabilizer. Additionally, the blending of Fe_2O_3 tailored

the tensile strength (9.01 MPa) as the role of the second stabilizer. As the optimal conditions, the presence of both KOH and Fe_2O_3 could enhance all three mechanical characteristics, attributed to the stabilizers' synergistic effect. This study may provide a valuable process and optional innovation to produce a Para rubber bag for older adults to use at the bedside or other corresponding activities to protect them from falling risk.

5. Acknowledgements

We sincerely acknowledge the Center of Rubber Technology for Community, Faculty of Engineering, Department of Physical Science, Faculty of Science and Digital Innovation, Thaksin University for supporting the equipment and instruments.

Author Contributions: Conceptualization, supervision and funding acquisition, P.S.; methodology, S.I., P.S., K.S., T.C.; Investigation, S.I., P.S., N.B., W.N.; writing—original draft preparation, S.I., P.S.; writing—review and editing, P.S. All authors have read and agreed to the published version of the manuscript.

Funding: This research was supported by the National Science and Innovation Fund (NSRF), Thaksin University (Research project grant: 66A105000017), Fiscal Year 2023.

Conflicts of Interest: The authors declare no conflict of interest.

References

[1] Beaudoin, M.; Atoyebi, O.A.; Mortenson, W.B.; Auger, C.; Demers, L.; Wister, A.; Plante M.; Routhier, F. Interviews with family caregivers of older adults: Their experiences of care and the integration of assistive technology in care. *Technology and Disability* **2020**, *32*, 199–209.

[2] Gell, N.M.; Brown, H.; Karlsson, L.; Peters D.M.; Mroz, T.M. Bathroom Modifications, Clutter, and Tripping Hazards: Prevalence and Changes after Incident Falls in Community-Dwelling Older Adults. *Journal of Aging and Health* **2020**, *32*, 1636-1644.

[3] Rose, G.; Decalf, V.; Everaert K.; Bower, W.F. Toileting-related falls at night in hospitalised patients: The role of nocturia. *Australas J Ageing* 2020, *39*, e70-e76.

[4] Roggeman, S.; Weiss, J.P.; Van Laecke, E.; Vande Walle, J.; Everaert K.; Bower, W.F. The role of lower urinary tract symptoms in fall risk assessment tools in hospitals: a review. *F1000Res* **2020**. https://doi.org/10.12688/f1000research.21581.1

[5] Zhao, Y.L.; Alderden, J.; Lind B.; Stibrany, J. Risk factors for falls in homebound community-dwelling older adults. *Public Health Nurs* **2019**, *36*, 772-778.

[6] Joshi, R.; Joseph, A.; Mihandoust, S.; Hoskins, L.; O'Hara, S.; Dye C.J.; Madathil, K.C. Understanding Key Home and Community Environment Challenges Encountered by Older Adults Undergoing Total Knee or Hip Arthroplasty. *Gerontologist* **2021**, *61*, 1071-1084.

[7] Keglovits, M.; Clemson, L.; Hu, Y.L.; Nguyen, A.; Neff, A.J.; Mandelbaum, C.; Hudson, M.; Williams, R.; Silianoff, T.; Stark, S. A scoping review of fall hazards in the homes of older adults and development of a framework for assessment and intervention. *Aust Occup Ther J* **2020**, *67*, 470-478.

[8] King, E.C.; Boscart, V.M.; Weiss, B.M.; Dutta, T.; Callaghan, J.P.; Fernie, G.R. Assisting Frail Seniors with Toileting in a Home Bathroom: Approaches Used by Home Care Providers. *Journal of Applied Gerontology* **2017**, 1–34. https://doi.org/10.1177/0733464817702477.

[9] Zhuang, M.; Li, J.; Chen, H.; Yang, Y.; Song, X.; Li, P.; Shi, L. Research Progress on Risk Factors and Prevention Strategies of Falls in Elderly Inpatients. *International Journal of Clinical and Experimental Medicine Research* **2021**, *5*, 101-105.

[10] Boonmahitthisud, A.; Boonkerd, K. Sustainable development of natural rubber and its environmentally friendly composites. *Current Opinion in Green and Sustainable Chemistry* **2021**, *28*, https://doi.org/10.1016/j.cogsc.2021.100446.

[11] Jayalakshmy, M.S. Applications of Rubber Based Biocomposites and Bionanocomposites. *Advanced Structured Materials* **2017**, *56*, 167–176.

[12] Chittella, H.; Yoon, L.W.; Ramarad S.; Lai, Z-W. Rubber waste management: A review on methods, mechanism, and prospects. *Polymer Degradation and Stability* **2021**, *194*. https://doi.org/10.1016/j.polymdegradstab.2021.109761.

[13] Thomas, S.K.; Parameswaranpillai, J.; Krishnasamy, S.; Begum, P.M.S.; Nandi, D.; Siengchin, S.; George, J.J.; Hameed, N.; Salim N.V.; Sienkiewicz, N. A comprehensive review on cellulose, chitin, and starch as fillers in natural rubber biocomposites. *Carbohydrate Polymer Technologies and Applications* **2021**, https://doi.org/10.1016/j.carpta.2021.100095.

[14] Blanchard, R.; Ogunsona, E.O.; Hojabr, S.; Berry, R.; Mekonnen, T.H. Synergistic Cross-linking and Reinforcing Enhancement of Rubber Latex with Cellulose Nanocrystals for Glove Applications. *ACS Appl. Polym. Mater* **2020**, *2*, 887−898.

[15] Boonying, P.; Boonpavanitchakul, K.; Kangwansupamonkon, W. Green Bio-composite Coating Film from Lignin/Pre-vulcanized Natural Rubber Latex for Controlled-release Urea Fertilizer. *Journal of Polymers and the Environment* **2023**, *31*, 1642–1655.

[16] Nair, K.P. Rubber (Hevea brasiliensis). In Tree Crops (Harvesting Cash from the World's Important Cash Crops), Springer, Cham. **2021**, 287-332.

[17] Chen, S.F.; Wong, W.C. Vulcanization composition for reducing allergenic potential and elastomeric articles formed therewith. US Patent 10,759,913 B2, **2020**.

[18] Lucas, D.M.; Amarasekera, S.; Narasimhan, D.; Kung, A.A.L. Dip-formed synthetic polyisoprene latex articles with improved intraparticle and interparticle cross-links. US Patent 10,538,609 B2, **2020**.

[19] Chen, S.F.; Wang, S.; Wong, W.C.; Chong, C.S. Glove coating and manufacturing process. US Patent 10,517,338 B2, **2019**.

[20] Soares, F.A.; Steinbüchel, A. Natural rubber degradation products: Fine chemicals and reuse of rubber waste. *European Polymer Journal* **2022**, https://doi.org/10.1016/j.eurpolymj.2022.111001.

[21] Rose, K.; Steinbüchel, A. Biodegradation of Natural Rubber and Related Compounds: Recent Insights into a Hardly Understood Catabolic Capability of Microorganisms. *Applied and Environmental Microbiology* **2005**, *71*, 2803–2812.

[22] Ibrahim, S.; Daik, R.; Abdullah, I. Functionalization of Liquid Natural Rubber via Oxidative Degradation of Natural Rubber. *Polymers* **2014**, *6*, 2928-2941.

[23] Matos, C.F.; Galembeck, F.; Zarbin, A.J.G. Multifunctional materials based on iron/iron oxide-filled carbon nanotubes/natural rubber composites. *Carbon* **2012**, *50*, 4685-4695.

[24] Smejda-Krzewicka, A.; Olejnik, A.; Strzelec, K. The role of iron(III) oxide in chloroprene and butadiene rubber blends' cross-linking, structure, thermal and mechanical characteristics. *Iranian Polymer Journal* **2019**, *28*, 313–323.

[25] Maznah, K.S.; Baharin, A.; Hanafi, I.; Azhar M.E.; Hakim, M.H.M.R. Effect of soaking in potassium hydroxide solution on the curing, tensile properties and extractable protein content of natural rubber latex films. *Polymer Testing* **2008**, *27*, 1013–1016.

[26] Sutanto, T.D.; Setiaji, B.; Wijaya K.; Suharto, T.E. Effect of KOH as Stabilizer on Mechanical and Chemical Properties of Liquid Rubber Compound. *Asian Journal of Chemistry* **2014**, *26*, 8371-8374.

[27] Amir-Hashim, M.Y.; Roslim, R.; Rosni, M.W. Physical Properties and Surface Morphology of Natural Rubber Latex Films Intended for Seedling Bag Application. *J. Rubb. Res* **2012**, *15*, 243–254.

[28] Akabane, T. Production method & market trend of rubber gloves. *International Polymer Science and Technology* **2016**, *43*, 45–50.

[29] Sasidharan, K.K.; Joseph, R.; Rajammal, G.; Pillai P.V.; Gopalakrishnan, K.S. Studies on the Dipping Characteristics of RVNRL and NR Latex Compounds. *Journal of Applied Polymer Science* **2001**, *81*, 3141–3148.

[30] Rojruthai, P.; Payungwong N.; Sakdapipanich, J.T. A model study on the impact of metal ions on pre-vulcanization of concentrated natural rubber latex and dipped-products. *Progress in Rubber Plastics and Recycling Technology* **2022**, *38*, 125–138.

[31] Karimi-Avargani, M.; Biria, D.; Dehghanifar, Sh.; Bazooyar, F.; Skrifvars, M. Accelerating degradation of natural rubber latex gloves by a consortium of microorganisms in an agricultural soil sample. *International Journal of Environmental Science and Technology* **2024**, https://doi.org/10.1007/s13762-024-06005-9.

[32] Cartabia, M.; Girometta, C.E.; Milanese, C.; Baiguera, R.M.; Buratti., S.; Branciforti, D.S.; Vadivel, D.; Girella, A.; Babbini, S.; Savino, E.; Dondi, D. Collection and Characterization of Wood Decay Fungal Strains for Developing Pure Mycelium. *Mats. J. Fungi* **2021**, https://doi.org/ 10.3390/jof7121008.

[33] Misman, M.A.; Azura, A.R. Overview on the potential of Biodegradable Natural Rubber Latex Gloves for commercialization. *Advanced Materials Research* **2014**, *844*, 486-489.

[34] Bode, H.B.; Kerkhoff K.; Jendrossek, D. Bacterial Degradation of Natural and Synthetic Rubber. *Biomacromolecules* **2001**, *2*, 295-303.

[35] Afiq, M.M.; Azura, A.R. Effect of sago starch loadings on soil decomposition of Natural Rubber Latex (NRL) composite films mechanical properties. *International Biodeterioration & Biodegradation* **2013**, *85*, 139–149.

[36] Sarkar, B.; Mandal, S. Microbial Degradation of Natural and Synthetic Rubbers. In: MP Shah (Ed.). Microbial Bioremediation & Biodegradation. Springer Nature Singapore Pte Ltd., **2020**, 527–550.

[37] Ramakanth, D.; Akhila, K.; Gaikwad K.K.; Maji, P.K. UV-activated oxygen scavenging system based on natural rubber latex from Hevea brasiliensis for active packaging applications. *Industrial Crops & Products* **2022**, https://doi.org/10.1016/j.indcrop.2022.114658

[38] Yahya, S.R.; Rashid, A.A.; Azahari, B. Soil Burial studies for Biodegradation of Natural Rubber Latex Films. *Advanced Materials Research* **2014**, *844*, 406–409.

[39] Shakun, A.; Sarlin E.; Vuorinen, J. Energy dissipation in natural rubber latex films: The effect of stabilizers, leaching and acetone-treatment. *J Appl Polym Sci* **2021**, https://doi.org/10.1002/app.49609.

[40] Walpalage, S.; Ganga, I.; Silva, K.M.D. Development of Correlation Between Potassium Hydroxide Number and Conductivity of Concentrated Natural Rubber Latex. *J Appl Polym Sci* **2008**, *107*, 1066–1070.
[41] Palaty, S.; Devi, P.V.; Honey, J. Effect of Storage on the Colloidal Properties of Room-temperature Prevulcanised Natural Rubber Latex. *Progress in Rubber, Plastics and Recycling Technology* **2011**, *27*, 201-213.
[42] Ling, Y.T.Q; Heng, Y.X.; Chan, H.H.; Yap, Y.J.; Lee, S.Y.; Koh, R.Y.; Liew, Y.K.; Manaf, S.N.Q.; Ang, D.T.C.; Mok, K.L. Evaluation of biocompatible palm-based polymeric surfactants for potential natural rubber latex stabilisation applications. *Journal of Rubber Research* **2021**, *24*, 369–380.
[43] Rojruthai, P.; Sakdapipanich, J.; Wiriyanantawong, J.; Ho, C.-C.; Chaiear, N. Effect of Latex Purification and Accelerator Types on Rubber Allergens Prevalent in Sulphur Prevulcanized Natural Rubber Latex: Potential Application for Allergy-Free Natural Rubber Gloves. *Polymers* **2022**, *14*, 4679. https://doi.org/10.3390/polym14214679.
[44] Sasidharan, K.K.; Joseph, R.; Palaty, S.; Gopalakrishnan, K.S.; Rajammal G.; Pillai, P.V. Effect of the Vulcanization Time and Storage on the Stability and Physical Properties of Sulfur-Prevulcanized Natural Rubber Latex. *J Appl Polym Sci* **2005**, *97*, 1804–1811.
[45] Andrade, K.L.; Ramlow, H.; Floriano, J.F.; Acosta, E.D.; Faita, F.L.; Machado, R.A.F. Latex and natural rubber: processing techniques for biomedical applications. *Braz. J. Chem. Eng* **2023**, *40*, 913–927.
[46] Masek, A.; Zaborski, M.; Piotrowska, M. Controlled degradation of biocomposites ENR/PCL containing natural antioxidants. *C. R. Chimie* **2014**, *17*, 1128–1135.

ASEAN
Journal of Scientific and Technological Reports
Online ISSN:2773-8752

Research article

Influence of Molding Condition and Moisture Content of Arecanut Leaf Sheath on Quality of Food Plates

Ladda Prasan[1], Chaiwat Jumpholkul [2, 5], Ruamporn Nikhom[3], and Weerawut Naebpetch[4*]

[1] Faculty of Humanities and Social Sciences, Thaksin University, Songkhla, 90000, Thailand
[2] Faculty of Engineering, Thaksin University, Phatthalung, 93210, Thailand
[3] Faculty of Engineering, Thaksin University, Phatthalung, 93210, Thailand
[4] Faculty of Engineering, Thaksin University, Phatthalung, 93210, Thailand
[5] Center of Excellence for Agricultural Innovation and Bioproducts of Thaksin University, Phatthalung 93210, Thailand
* Correspondence: weerawut.n@tsu.ac.th

Citation:
Prasan, L.; Jumpholkul, C.; Nikhom, R.; Naebpetch, W. Influence of molding condition and moisture content of arecanut leaf sheath on quality of food plates *ASEAN J. Sci. Tech. Report.* **2025**, *28*(1), e254700. https://doi.org/10.55164/ajstr.v28i1.254700

Article history:
Received: June 25, 2024
Revised: November 14, 2024
Accepted: December 14, 2024
Available online: February 16, 2025

Publisher's Note:
This article has been published and distributed under the terms of Thaksin University.

Abstract: This research focuses on the molding conditions for producing areca nut leaf sheath-based food plates. Food plate samples from the Arecanut leaf sheath were prepared using compression molding. The molding temperature varied at 150, 160, and 170 °C, and the molding time was 1, 2, and 3 min. The quality of the obtained plates was assessed based on their physical appearance. Increasing the molding temperature and molding time obtained smoother and more beautiful surfaces. However, the most suitable molding condition was a temperature of 170 °C for 2 min. The moisture content of areca nuts before molding should be in the range of 20–60 wt.%. The research findings will assist those looking to produce food packaging from the arecanut leaf sheath by providing insights into their components and optimal molding conditions. This will streamline the process, reducing the time spent studying molding conditions and minimizing production waste.

Keywords: Arecanut leaf sheath; Food packaging; Molding condition; Optimal moisture content range and Minimizing production waste

1. Introduction

The packaging industry has often emphasized the importance of production costs and product quality rather than considering the disposal of used packaging. As a result, the amount of waste generated has increased, especially food and beverage packaging that degrades slowly or is non-biodegradable. Also, around 95–99% of plastic materials are synthetic plastics produced by petrochemical industries from non-renewable sources [1]. Synthetic plastic products find extensive applications in medical appliances, packaging, and building materials. In India, the packaging sector alone consumes 43% of the synthetic polymers produced annually. Improper disposal methods, such as burning, produce toxic pollution that impacts human health and the environment. Visible environmental problems arise from discarded packaging littering streets, directly affecting communities and the environment. This is particularly true of food and beverage containers made from plastics and foams, contributing to marine litter. Additionally, this type of packaging can release pollutants into the air. Certain production processes involve harmful substances like chlorofluorocarbons that deplete the ozone layer, contributing to global warming and the consequent heatwaves, droughts, and flooding. When packaging-related waste becomes significant, it leads to various environmental

problems that may cause irreversible damage. This, in turn, generates diverse impacts such as the depletion of natural resources, air pollution, water pollution, waste proliferation, rising global temperatures, ozone layer depletion, and shifts in biodiversity.

The food and processed products industry uses more packaging than other businesses. Four types of materials are used to produce food packaging: glass, metal, plastic, and paper-based materials. Each type of packaging material has advantages and disadvantages, and there is a growing trend towards using environmentally friendly packaging materials. This trend has become a global phenomenon due to the increasing awareness of environmental conservation. Consequently, packaging made from readily biodegradable and environmentally friendly paper or paper-based materials has gained popularity. This shift towards eco-friendly practices has prompted interest in recycling processes that enable materials to be reused.

Developed nations have actively advocated adopting recycling technologies and using biodegradable packaging made from natural materials [2]. Concurrently, public authorities in developing nations are increasingly addressing concerns surrounding plastic packaging. Notably, several African countries, including Benin and Rwanda, have recently imposed bans on the use of non-biodegradable packaging [3]. Before plastic food packaging was embraced in these developing countries, people traditionally sourced packaging materials from their immediate environment. Indeed, numerous African, Asian, and Latin American countries traditionally used leaves as a natural wrap for food [4-6]. Given the abundance of large leaves in the surrounding vegetation, they have been extensively tested and proven for long-term use. They are recognized as being non-toxic and free of dyes or irritants [5, 6]. The primary consideration in selecting suitable leaves for food packaging is their availability [6, 7]. Additional criteria encompass their flexibility post-treatment, width, impact on organoleptic properties of food, and ease of treatment, preservation, and transportation [6-8].

This study focuses on the molding conditions suitable for producing food packaging from the arecanut leaf sheath with the compression molding technique. The molding condition was investigated at 150, 160, and 170 °C temperatures for 1, 2, and 3 min, using areca nut leaf sheath with moisture levels ranging from 10% to 80%. This research will unravel the composition of the arecanut leaf sheath and the shaping conditions, offering a more straightforward path forward. Sharpening this understanding trims down the time needed to explore molding techniques and cuts back on waste during production, making the process more efficient and refined.

2. Materials and Methods

2.1 Materials

Areca nut leaf sheath was obtained from the areca palm (Areca catechu), which grows in much of the tropical Pacific (Melanesia and Micronesia), South Asia, Southeast Asia, and parts of East Africa. The areca nut leaf sheath used in this research was obtained from areca palms in Phatthalung Province, Thailand. The arecanut leaf sheath used in the experiment should be thoroughly washed with water, scrubbed on both sides with a sponge until clean, and then baked to reach the desired moisture content. The moisture content of the arecanut leaf sheath is measured using a drying method, where the proportion of moisture is calculated by comparing the weight lost during drying to the initial weight.

2.2 Equipments

The compression molding machine used in this research (model VC200, Hong Yaw Thai Company Limited, Thailand) and metal food plate mold are shown in Figure 1.



Figure 1. Mold for forming food plates.

2.3 Methods

The food plate samples were made by compression molding the arecanut leaf sheath at 150, 160, and 170 °C for 1, 2, and 3 min. The quality of the obtained plates was assessed based on their physical appearance and tensile testing. The perfection of the physical appearance of the sample will mainly be seen from the surface. The surface must be smooth, complex, and free from cracks or tears from the molding process. For the tensile strength, the dumb-bell test specimen (i.e., five samples per formulation) was die cut from the press-cured sheets, and tests were carried out at room temperature with a tensile tester Model UT-2060 (U-Can Dynatex Inc., Taiwan) at a crosshead speed of 50 mm/min according to ASTM D412. A schematic diagram of the molding process is shown in Figure 2

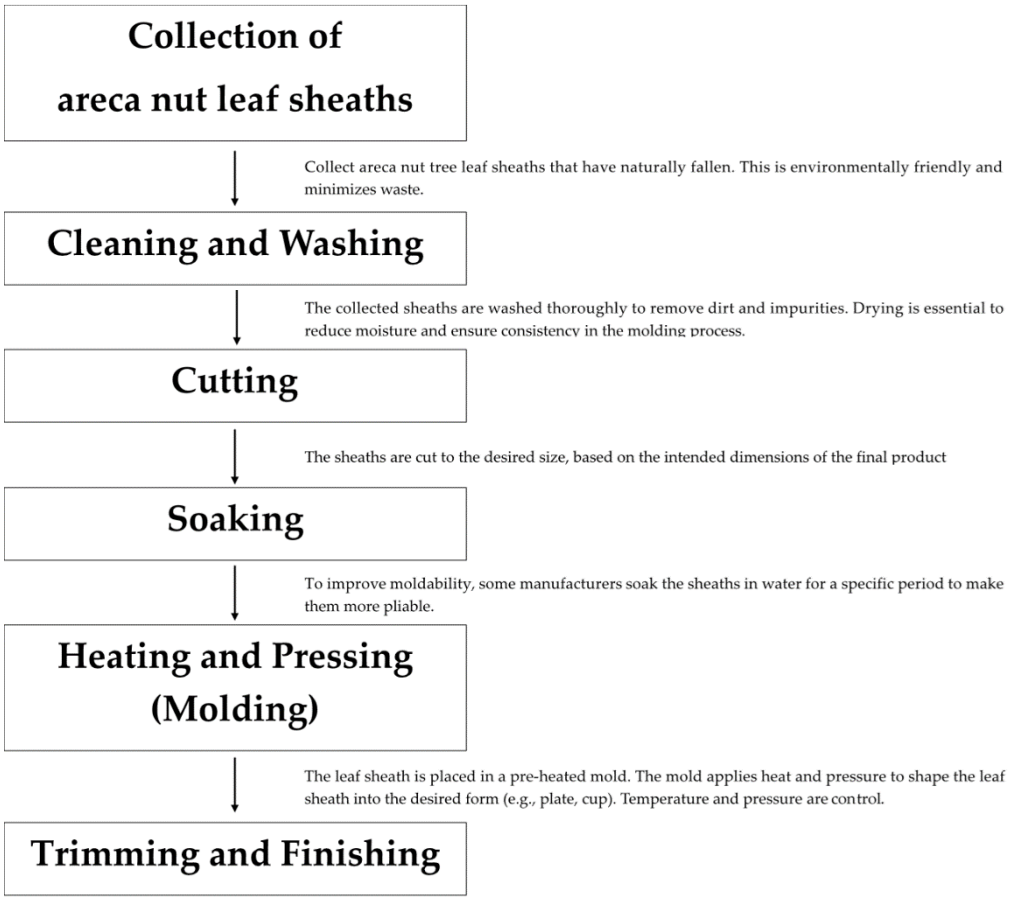


Figure 2. A schematic diagram of the molding process.

3. Results and Discussion

3.1 Results

3.1.1 Influence of temperature and time on plate formation

In this study, we investigated the optimal condition for molding food plates from areca nut leaf sheath. The primary objective was to identify the lowest molding temperature and shortest duration that produced robust, aesthetically pleasing containers that maintained their shape over an extended period of use. The experimental conditions were applied to the arecanut leaf sheath with a moisture content of 20%. The results are illustrated in Figures 3 and 4.

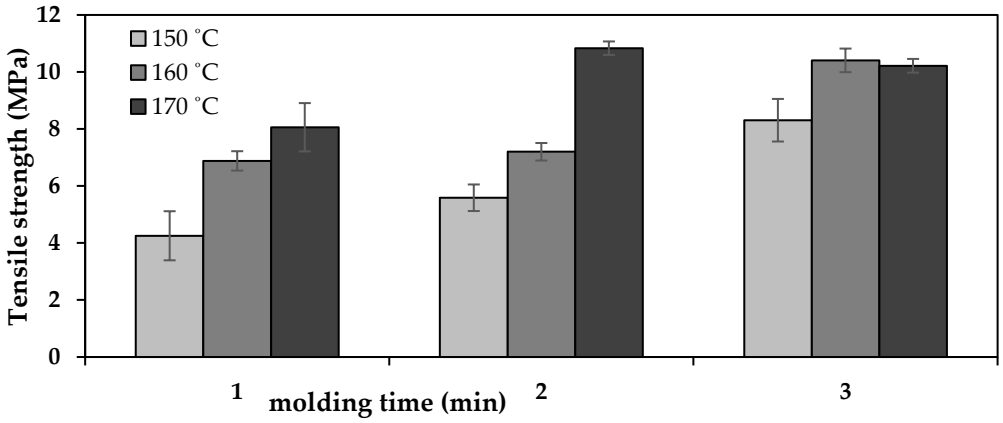


Figure 3. Tensile strength of food plates made from Arecanut leaf sheath molded under different conditions.

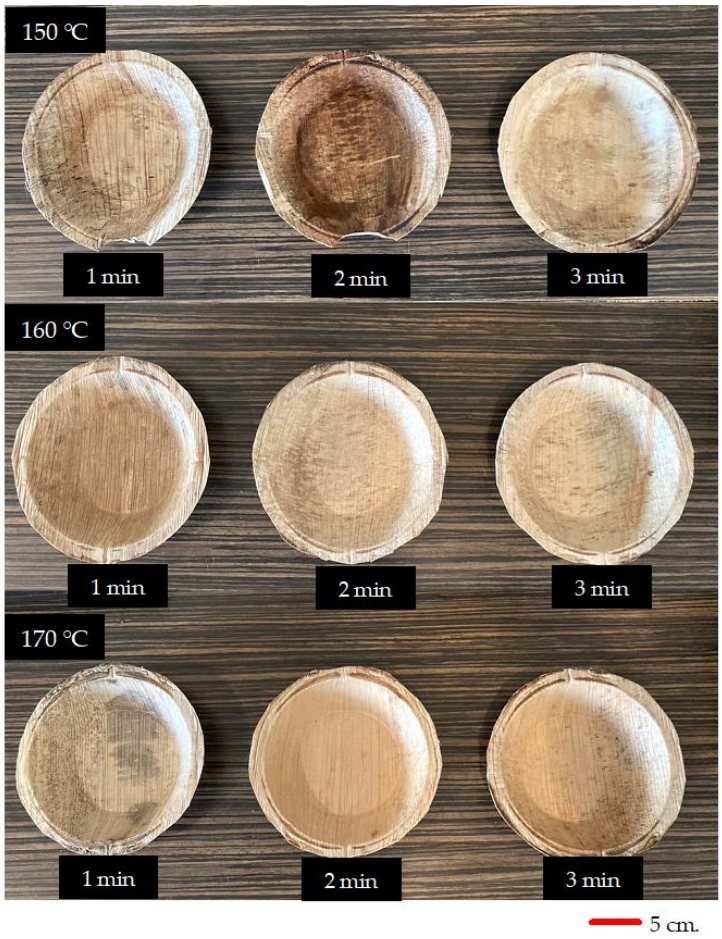


Figure 4. The physical appearance of food plates made from Arecanut leaf sheath molded under different conditions.

Figure 3 illustrates the tensile strength of areca sheaths pressed at temperatures of 150, 160, and 170 °C for 1, 2, and 3 minutes. The experiment revealed that increasing the forming time also increases the strength of the arecanut leaf sheath plates. This is due to the extended time allowing lignin in the areca nut leaf sheath to melt and act as a binder, enhancing fiber adhesion and thus improving plate strength. Additionally, higher forming temperatures were found to enhance plate strength, likely because as the temperature rises, more lignin melts and binds the fibers more effectively, resulting in stronger arecanut leaf sheath plates.

The molding of arecanut leaf sheath plates at a temperature of 150 °C required 3 min to produce a smooth surface (Fig. 5A). When the molding duration was less than 3 min, the surface of the plate was uneven (Fig. 5(B)). Molding at 150 °C for all durations produced plates with cracks in the base of the plate (Fig. 5(C)) that were attributed to the reduced flexibility of the leaf sheath when molded at this temperature. The leaf sheath did not conform to the mold in this condition.

The molding of arecanut leaf sheath plates at a temperature of 160 °C for 2 and 3 min produced plates with relatively smooth surfaces (Fig. 6A) similar to plates molded at 150 °C for 3 min. However, approximately 30% of the plates exhibited cracks in the base (Fig. 6(B)). Therefore, the actual production of molded products at 160 °C would pose the risk of a 30% defect rate, which is considered high in manufacturing processes.

The molding of arecanut leaf sheath plates at 170 °C for 2 and 3 min (Fig. 7(A)) produced relatively smooth surfaces, similar to plates molded at 160 °C. Moreover, no cracks were in the base of any plates molded at 170 °C (Fig. 7(B)). This result indicated that, at 170 °C, the fibers of the areca nut leaf sheath could soften sufficiently to conform to the mold without experiencing the stress that would produce cracks and defects in the material of the final product.



Figure 5. Food plates made from areca nut leaf sheath molded at 150 ˚C.



Figure 6. Food plates made from areca nut leaf sheath molded at 160 ˚C.



Figure 7. Food plates made from areca nut leaf sheath molded at 170 ˚C.

The most suitable molding condition was a temperature of 170 °C for 2 min. This finding is consistent with a previous study investigating the mechanical and thermal properties of arecanut leaf sheath fibers reinforced with polypropylene. The fibers' chemical composition and tensile strength analysis showed that the arecanut leaf sheath comprised cellulose at 66%, hemicellulose at 7%, and lignin at 20%. Notably, lignin is a crucial component in areca nut leaf sheath, significantly influencing its molding characteristics. Therefore, the optimal molding condition identified in this study aligns with the chemical composition and emphasizes the importance of lignin in molding areca nut leaf sheath [9].

Lignin is a complex compound of carbon, hydrogen, and oxygen. It exists in various subunits, making it a high-molecular-weight, complex polymer. Lignin is the second most abundant natural polymer globally, after cellulose. It is characterized by a molecular mass exceeding 10,000 atomic mass units and is known as a hydrophobic aromatic polymer [10]. Lignin is predominantly found in the secondary cell wall and the middle lamella between fiber layers. In addition to bonding the molecules of hemicellulose and cellulose together to enhance strength, lignin also aids in reducing water permeability between the cellulose matrix and cell walls, providing plant tissues protection against microbial degradation [11, 12].

Lignin exhibits a glass transition temperature (Tg) of around 90 °C and a melting temperature (Tm) of approximately 170 °C [13]. These properties are crucial in understanding why arecanut leaf sheath can be effectively molded at 170 °C. At 170 °C, the lignin in the arecanut leaf sheath starts to melt, facilitating the transformation of the material to conform to the mold. Upon removal from the mold, lignin transitions from a molten polymer to a glass-like solid, resulting in a lasting change in shape.

3.1.2 Influence of arecanut leaf sheath moisture content on plate forming



Figure 8. Effect of moisture content on the appearance of food plates made from areca nut leaf sheath.

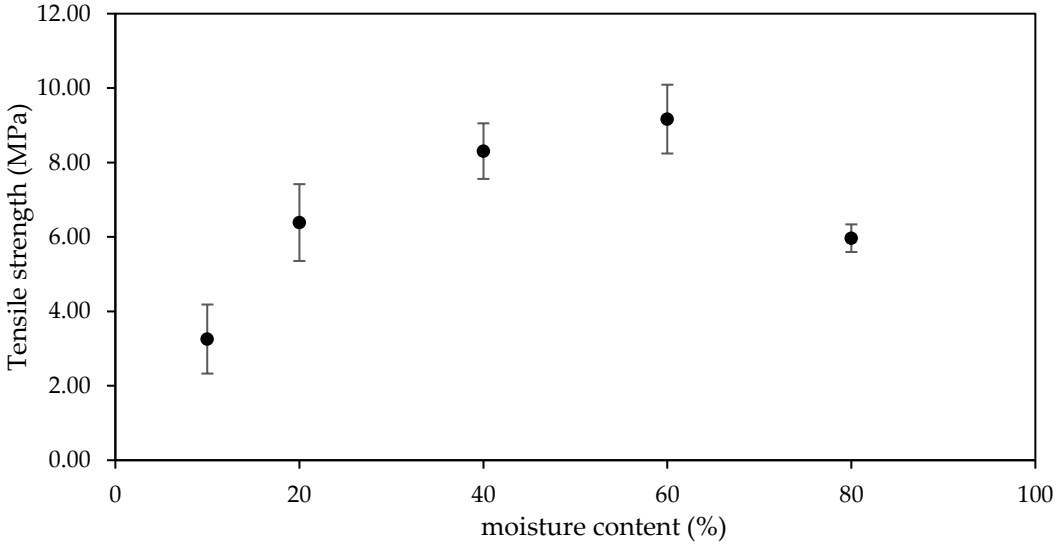


Figure 9. Effect of moisture content on the appearance of food plates made from areca nut leaf sheath.

After determining the optimal temperature and duration for molding food plates from the arecanut leaf sheath, the suitable moisture content of the leaf sheath was investigated. Areca nut leaf sheath, when dried, becomes rigid and brittle. Moisture content is, therefore, a crucial determinant of the flexibility of the leaf sheath fibers during molding. This flexibility is essential for the plate to conform well to the mold without cracking. However, excessive moisture can potentially impact the quality of the molded products. Therefore, the moisture content varied at 10, 20, 40, 60, and 80%, as measured by weight. The molding condition was maintained at 170 °C for 2 min. Areca nut leaf sheath with a moisture content of 10% by weight before molding could not be successfully shaped without cracking due to the excessive rigidity and brittleness of the leaf sheath (Fig. 8). When the moisture content was 80% by weight, the molded pieces exhibited warping. This defect was attributed to a phase change from moisture to gas during molding that caused the workpieces to swell. Areca nut leaf sheath with a moisture content ranging from 20% to 60% by weight was suitable for molding, resulting in well-shaped, smooth pieces that did not crack during processing. The results of the physical characteristics of arecanut leaf sheath plates formed at varying moisture levels align closely with the strength test results shown in Figure 9. It was observed that as the moisture content of the areca nut leaf sheaths increased from 10% to 60%, the strength of the plates also improved. However, when the moisture content exceeded 60%, the strength of the plates decreased. Based on the physical and mechanical properties, soaking the areca nut leaf sheaths to achieve a moisture content of approximately 20-60% by weight produced plates with relatively high strength and minimal waste. Therefore, the optimal moisture content range for forming these workpieces is between 20% and 60% by weight. Based on these findings, areca nut leaf sheath was used to produce the products shown in Figure 10.

3.2 Discussion

Areca nut leaf sheath plates provide a high food safety standard due to their natural, chemical-free composition, heat tolerance, and natural antimicrobial properties. They are generally safe for hot and cold foods and avoid many contaminants associated with conventional disposable food ware. With proper manufacturing and adherence to hygiene standards, these plates offer a food-safe, eco-friendly option that aligns well with health-conscious and environmentally aware consumers.

Areca nut leaf sheaths hold significant promise as an eco-friendly material for sustainable food packaging, mainly due to their biodegradability and suitability for single-use applications. Naturally compostable, areca leaf sheaths break down within months without releasing harmful chemicals, making them a compelling alternative to single-use plastics, contributing heavily to persistent waste issues. Sourced from agricultural by-products, these leaf sheaths offer a low-impact alternative to petrochemical-based plastics, supporting circular economy principles and reducing overall packaging carbon footprints. Beyond their environmental benefits, areca leaf sheaths have a unique, rustic appearance that appeals to eco-conscious

consumers and brands focused on sustainability. Their visual appeal can strengthen brand identity, aligning with values of reduced plastic use and environmental responsibility while allowing companies to highlight their commitment to sustainable practices in marketing efforts that resonate with environmentally aware audiences. With abundant by-product availability in areca nut-producing regions like India and Southeast Asia, using areca leaf sheaths could stimulate local economies by providing additional income for farmers and creating rural employment. While initial production costs may be higher than traditional plastics, scaling up manufacturing and reducing waste management expenses could lead to greater cost efficiency. Incentives or subsidies for biodegradable packaging materials could also make these products more economically viable.

However, challenges remain in ensuring a stable supply of high-quality leaf sheaths to meet increasing demand. Factors such as climate, processing methods, and regional differences can impact material quality, and processing requires water, which can be an issue in drought-prone areas. Innovations in water conservation or recycling during production could further enhance the environmental profile of areca nut leaf sheaths, supporting their potential as a sustainable solution in the food packaging industry. Scaling the compression process of arecanut leaf sheath plates for industrial production is feasible but requires investment in automation, quality control, and sustainable practices. Addressing material consistency, labor, and energy usage challenges will be critical for success. With these systems in place, areca leaf plates could reach a level of production that meets global demand, offering an eco-friendly alternative in a scalable, economically viable way. Though production costs for areca nut leaf packaging might initially be higher than plastic, scaling up production and reducing the need for waste management could eventually make it more economical. Additionally, subsidies or incentives for using biodegradable materials could offset some of these costs. However, Increased demand for this material can support local economies, provide additional income streams for farmers, and create jobs in rural areas.



Figure 10. Food containers made from areca nut leaf sheath.

4. Conclusions

A study of the influence of temperature and time on the molding of food containers from areca nut leaf sheath indicated that the best conditions for forming food containers from areca nut leaf sheath were a molding temperature of 170 ˚C for 2 min and an arecanut leaf sheath moisture content before molding in the range of 20-60 wt.%. The current arecanut leaf sheath plate molding process primarily has consistency, efficiency, and scalability limitations. Addressing these with more automated, environmentally controlled, and energy-efficient solutions can support large-scale production. Through these improvements, the process could achieve better quality control, higher throughput, and reduced costs, positioning areca nut leaf plates as a more competitive alternative to conventional disposable tableware. The experiment results indicate that food containers made from areca sheaths can be successfully produced and are viable for practical use. However, calculations of production costs and selling prices reveal that these containers are much more expensive than plastic alternatives, which may reduce their appeal despite their environmental benefits. Future research will focus on reducing production costs to make the prices of areca sheath containers more competitive.

5. Acknowledgements

The authors thank the Program Management Unit on Area Based Development (PMU A) for support for research funding. Center of Rubber Technology for Community (CRTC), Faculty of Engineering, Thaksin University is also acknowledged for the space and machinery to do research.

References

[1] Mangaraj, S.; Yadav, A.; Bal, L. M.; Dash, S. K.; Mahanti, N. K. Application of biodegradable polymers in food packaging industry: A comprehensive review. *Journal of Packaging Technology and Research* **2019**, *3*, 77-96.

[2] Han, J. W.; Ruiz-Garcia, L.; Qian, J. P.; Yang, X. T. Food packaging: A comprehensive review and future trends. *Comprehensive Reviews in Food Science and Food Safety* **2018**, *17*, 860-877.

[3] Nielsen, T. D.; Holmberg, K.; Stripple, J. Need a bag? A review of public policies on plastic carrier bags–Where, how and to what effect?. *Waste management* **2019**, *87*, 428-440.

[4] Lascurain, M.; López-Binnqüist, C.; Avendaño, S.; Covarrubias, M. The plants leaves used to wrap tamales in the Mexican state of Veracruz. *Economic Botany* **2017**, *71*, 374-379.

[5] Mensah, J. K.; Adei, E.; Adei, D.; Ashie, M. D. Perceptions of the use of indigenous leaves as packaging materials in the ready-to-eat cornmeals. *International Journal of Biological and Chemical Sciences* **2012**, *6*, 1051-1068.

[6] Ng, C. Plant leaves in food preparation and packaging. *UTAR Agriculture Science Journal (UASJ)* **2015**, *1*, 34-39.

[7] Onzo, F. C.; Azokpota, P.; Akissoe, N.; Agbani, O. P. Biodiversité des emballages-feuilles végétales utilisées dans l'artisanat agroalimentaire au Sud du Bénin. *Journal of Applied Biosciences* **2013**, *72*, 5810-5821.

[8] Mustafa, M.; Nagalingam, S.; Tye, J.; Shafii, A. H.; Dolah, J. Looking back to the past: revival of traditional food packaging. *In 2nd Regional Conference on Local Knowledge (KEARIFAN TEMPATAN)* **2012**, *1*, 1-17.

[9] Poddar, P.; Islam, M. S.; Sultana, S.; Nur, H. P.; Chowdhury, A. M. S. Mechanical and thermal properties of short arecanut leaf sheath fiber reinforced polypropyline composites: TGA, DSC and SEM analysis. *J Material Sci Eng* **2018**, *5*, 2169-0022.

[10] Yinghuai, Z.; Yuanting, K. T.; Hosmane, N. S. Applications of ionic liquids in lignin chemistry. *Ionic Liquids—New Aspects for the Future*; IntechOpen: London, UK, **2013**, 315-346.

[11] Kirk, T. K.; Farrell, R. L. Enzymatic" combustion": the microbial degradation of lignin. *Annual Reviews in Microbiology* **1987**, *41*, 465-501.

[12] Cathala, B.; Saake, B.; Faix, O.; Monties, B. Evaluation of the reproducibility of the synthesis of dehydrogenation polymer models of lignin. *Polymer degradation and stability* **1998**, *59*, 65-69.

[13] Patel, J. P.; Parsania, P. H. Characterization, testing, and reinforcing materials of biodegradable composites. *Biodegradable and Biocompatible Polymer Composites: Processing, Properties and Applications*; Woodhead Publishing is an imprint of Elsevier: Duxford, UK, **2017**, 55-78.

ASEAN
Journal of Scientific and Technological Reports
Online ISSN:2773-8752

Research article

Image Based Papaya (*Carica Papaya* Linn.) seed germination evaluation by ResNet50

Chomtip Pornpanomchai[1]*

[1] Faculty of Information and Communication Technology, Mahidol University, Nakhon Phathom, 13170, Thailand
* Correspondence: e-mail address: chomtip.por@mahidol.ac.th

Citation:
Pornpanomchai, C. Image based Papaya (*Carica Papaya* Linn.) seed germination evaluation by ResNet50. *ASEAN J. Sci. Tech. Report.* **2025**, *28*(1), e254804. https://doi.org/10.55164/ajstr.v28i1.254804

Article history:
Received: July 1, 2024
Revised: December 3, 2024
Accepted: December 6, 2024
Available online: February 17, 2025

Publisher's Note:
This article has been published and distributed under the terms of Thaksin University.

Abstract: The researchers developed a papaya seed germination evaluation system (PSGES) using ResNet50, a convolutional neural network, to evaluate papaya seed germination potential from single seed images. Using a comprehensive dataset of 12,600 papaya seed images, they allocated 11,600 images for training (with an 80/20 training-testing split) and 1,000 images for validation. The system achieved impressive performance metrics, with an overall accuracy of 99.58% and an average processing time of 1.4705 seconds per image. The training dataset demonstrated exceptional performance with 0.9958 accuracy, 0.9980 precision, 0.9972 recall, and 0.9976 F1-score. When compared to existing seed evaluation methods in the literature, PSGES showed superior precision at 99.59%, significantly outperforming Rice (ANN) at 92.80%, Beet (NIR) at 89.00%, and Chili (ANN) at 71.71%. The study revealed a papaya seed germination rate of 84.92%, calculated from (10,000 + 20 + 677 + 3) ÷ 12,600 × 100. Notably, ResNet50 demonstrated superior performance compared to six other CNN architectures tested, including AlexNet, GoogLeNet, Inceptionv3, ResNet18, ResNet101, and VGG16, in both training and validation performance metrics.

Keywords: Convolutional neural network; Papaya; Pattern recognition; ResNet50; Seed germination evaluation.

1. Introduction

Papaya (*Carica papaya* Linn) is one of the most popular fruits cultivated in tropical areas worldwide. It was initially from Central America [1]. Papaya fruit has various nutrients and many unique properties. Papayas contain carbohydrates, proteins, lipids, dietary fiber, beta-carotene, sodium, potassium, iron, calcium, zinc, phosphorus, copper, manganese, and magnesium [2]. Additionally, papayas have antioxidant, anti-cancer, anti-dengue, anti-malarial, anti-infertility, anti-diabetes, insecticidal, and anti-AIDS activities [3]. People consume papaya in both the mature and unripe stages. They eat mature papaya as a fresh fruit and unripe papaya in vegetable salads. Som Tum is one of the most famous Thai foods, and it is made from unripe papaya [4]. Papaya, like other fruits, is propagated from its seeds. All fruit seeds should be collected from mature, healthy, pest-free, and disease-free fruits [5]. Typically, papaya seeds take more than ten days to germinate, with germination rates of less than 80% [5].

Researchers applied various techniques to produce several seed germination measurements, as shown in Table 1. Lanjhiyana and Sahu [5] showed that the germination rates of rangpur lime (*Citrus limonia*) seeds and

papaya (*Caricvera papaya* Linn) seeds are 93.33% and 66.17%, respectively. Marchi and Cicero (2017) employed Seed Vigor Imaging System (SVIS) software to evaluate carrot (*Daucus carota* L. Brasilia) seed vigor with germination rates of 87.00% [6]. Yang et al. [7] used hyperspectral image processing technology to realize the germination prediction of sugar beets (*Beta vulgaris*) seeds with carrot germination rates of 33.33% and a system precision of 95.50%. Pang et al. [8] employed a convolutional neural network (CNN) to identify and predict corn (*Zea mays* L.) seed germination with a system precision rate of 99.96% and a seed germination rate of 62.00%. Severiano et al. [9] used X-ray and Seed Vigor Image System (SVIS) software to analyze Formosa papaya seed germination and found germination rates of 74.5%. Zhou et al. [10] made beet seed germination predictions using near-infrared hyperspectral images of 3072 seeds. The experiments showed germination rates of 50.00% with precision rates of 89.00%. Genze et al. [11] employed convolutional neural networks (CNN) for germination prediction of three species of seeds, maize (*Zea mays*), rye (*Secale cereal*), and pearl millet (*Pennisetum glaucum*), with precision rates of 97.90%, 94.20%, and 94.30%, respectively. Using image processing, Lurstwut and Pornpanomchai [12] evaluated rice (Oryza sativa L.) seed germination. The experiments showed a precision of 73.49% and rice seed germination rates of 74.59%, with an average access time of 8.31 seconds per image. Pornpanomchai et al. [13] evaluated chili (*Capsicum frutescence*) seed germination using Euclidean distance and neural network techniques with precision rates of 59.71% and 71.71%, respectively. The experiments had chili seed germination rates of 75.40% with an average access time of 0.74 seconds per image.

Table 1. Comparison of seed types and germination rates from previous research.

Researchers	Seed type	Germination Rates (%)
Lanjhiyana *et al*. [5]	rangpur lime (*Citrus limonia*)	93.33
	papaya (*Caricvera papaya* Linn)	66.17
Marchi and Cicero [6]	carrot (*Daucus carota* L. Brasilia)	87.00
Yang *et al.* [7]	sugar beet (*Beta vulgaris*)	33.33
Pang *et al.* [8]	corn *(Zea mays* L.)	62.00
Severiano *et al.* [9]	papaya (*Carica papaya* L. var. Formosa)	74.50
Zhou *et al*. [10]	beet (*Beta maritima*)	50.00
Lurstwut and Pornpanomchai [12]	rice (*Oryza sativa* L.)	74.59
Pornpanomchai *et al.* [13]	chili (*Capsicum frutescence*)	75.40

2. Materials and Methods

2.1 System hardware and software specifications

The PSGES (Papaya Seed Germination Evaluation System) was developed using computer hardware and software. The central processing unit used an AMD Ryzen Pro 7 5850U with Radeon graphics at 1.90 GHz with 16 GB of RAM. The operating system was Windows 11. MATLAB R2020b (license number 40598465) was used for software development. A Xiaomi Redmi Note 8 mobile phone was used for papaya imagery. To avoid copyright issues, the researchers created their papaya seed dataset called the "Papaya dataset." The system design used in this research is as follows.

2.2 Papaya seed sampling

All papayas in this research were purchased from a local market in Bangkok, Thailand, from September to December 2023. Figures 1 (a) and (b) show the Holland papaya and papaya seeds. A papaya seed image before germination is shown in Figure 1 (c), and after germination in Figure 1 (d).

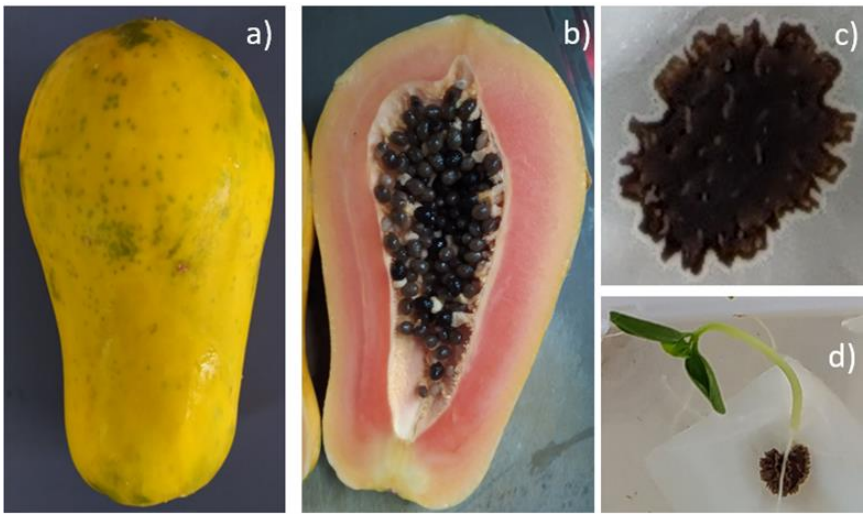


Figure 1. Sample of papaya imagery in this research (a) a whole papaya fruit, (b) bisection of papaya with a group of seeds, (c) a papaya seed before germination, and (d) a papaya seed after germination for 20 days.

2.3 Convolutional neural network

This research employed ResNet50 to evaluate papaya seed images. ResNet50 is a convolutional neural network (CNN) in the MATLAB toolbox. CNNs are some of the most potent recognition methods to identify unknown images in a dataset [14]. ResNet50 has three main components: feature extraction, classification, and output classification functions, as depicted in Figure 2. The operation of ResNet50 is done as follows. First, an input image is acquired. Then, feature extraction is repeatedly done in the convolution and pooling layer until it extracts all input image features. Next, the full connection component uses all neural network input layer features and classifies an input image to show to an output layer. Finally, the output classification component displays the most similar image between the input and dataset images [15].

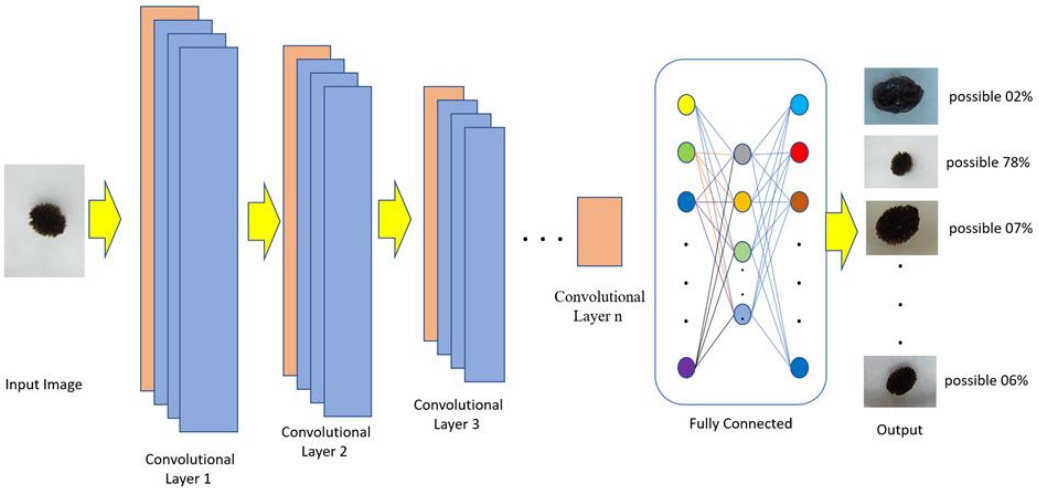


Figure 2. Convolutional neural network architecture

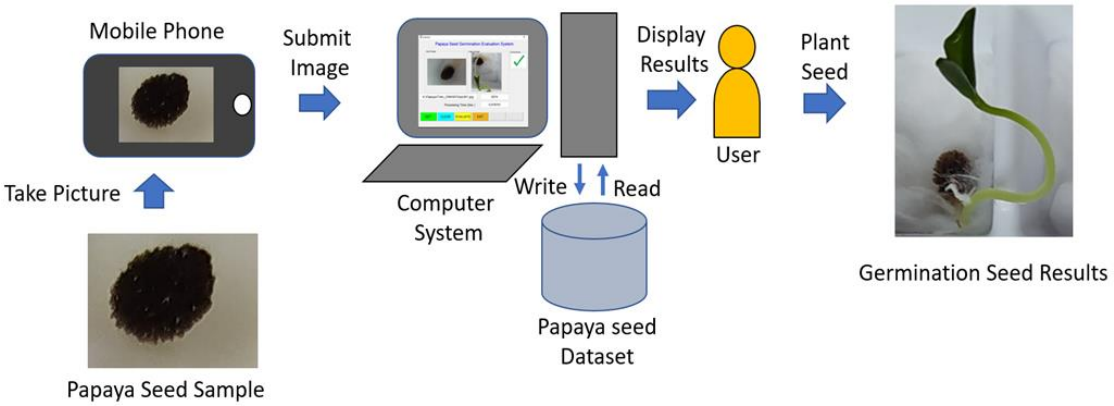


Figure 3. PSGES conceptual diagram

2.4 PSGES conceptual diagram

The PSGES conceptual diagram has three steps, as shown in Figure 3. The first step is to capture a papaya seed image using a mobile phone camera. Then, the seed image is transferred to the computer system to evaluate the seed's germination potential. Finally, based on the image, the system shows the results to the user.

2.5 PSGES flowchart

The PSGES flowchart depicts three main processes: image-making, training, and evaluation (as shown in Figure 4). The imagery process has two main routines and one decision sub-process, which are 1) the papaya image collecting process, 2) the papaya imaging process, and 3) the training process or evaluation sub-process. The training process consists of two routines and one sub-process, which are 1) training the ResNet50 routine, 2) planting and validating the germination seeds process, and 3) making decisions to train the sub-process further. Finally, the evaluation process has a main routine and two sub-processes, which are 1) image recognition by ResNet50, 2) display of evaluation results sub-process, and 3) decision to evaluate more papaya images sub-process. Each process has the following details.

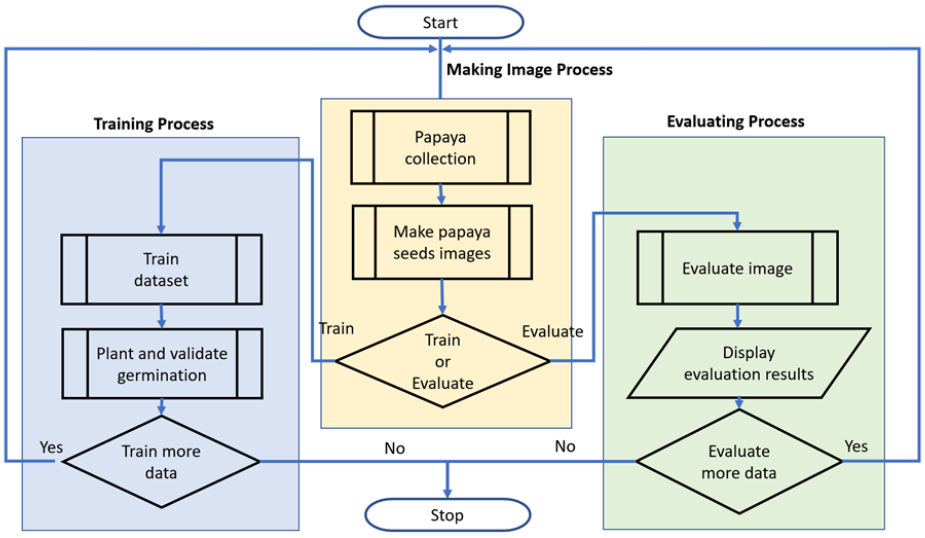


Figure 4. PSGES flowchart

2.5.1 image making process

The image-making process consists of two main routines: the papaya collection routine and the make papaya seeds images routine. Details of these processes are as follows.

2.5.1.1 Papaya collection routine

This research used seven papaya fruits after their bisection. Researchers needed to remove the sarcotesta from the seeds for good germination results. The papaya sarcotesta is an outer and usually soft fleshy jelly covering around the seeds. This research employed 1,260 papaya seeds, which have sizes of 0.5-0.6 cm x 0.3-0.4 cm (length x width), as shown in Figure 1 (c).

2.5.1.2 Make papaya seed images routine

This research planted papaya seeds in a clear 35 cm x 22 cm x 2.5 cm (width x length x height) plastic box with a cover, as shown in Figure 5 (a). The plastic box is separated into 40 small 4.0 cm x 4.0 cm x 2.5 cm (width x length x height) compartments, and each compartment contains a papaya seed on a piece of cotton, as shown in Figure 5 (b). This research used a simple mobile phone camera to make papaya seed JPG format images in each compartment that were 3,000 pixels x 4,000 pixels with a resolution of 72 dpi. Finally, we cropped each papaya seed image into a JPG file format of 300 pixels x 300 pixels x 3 planes with a resolution of 72 dpi, as shown in Figure 5 (c). Each cropped papaya seed image is assigned a unique ID number for referencing.

2.5.1.3 Make decisions in training or evaluate processes

After making papaya seed images, the next step is to decide to do a training or evaluation process according to the following details.

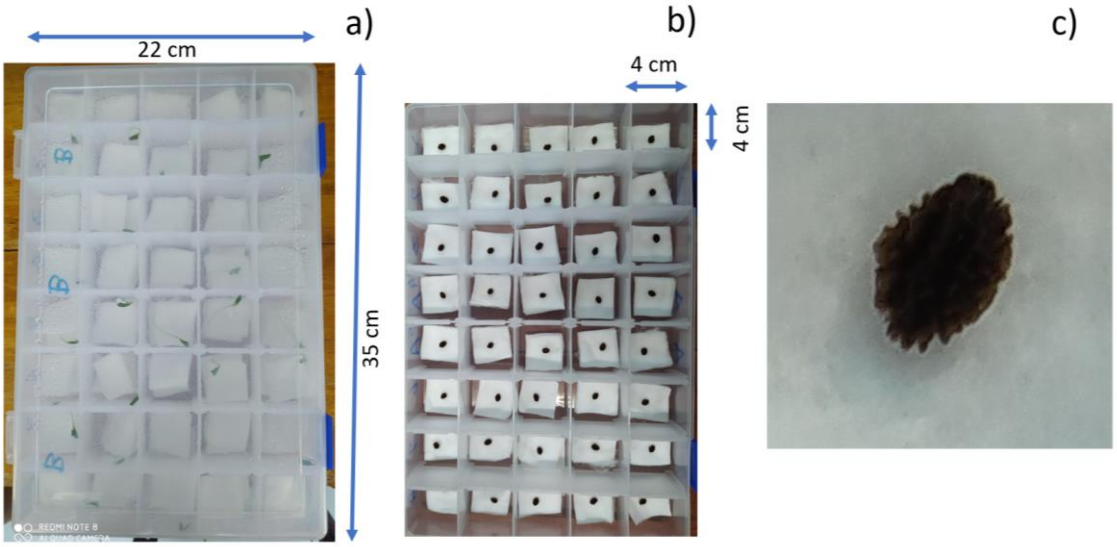


Figure 5. (a) plastic box for planting papaya seeds, (b) papaya seeds on pieces of cotton in compartments, and (c) cropped image of a papaya seed.

2.5.2 Training process

The training process consists of two main routines and one sub-process. They are 1) train dataset routine, 2) plant and validate germination routine, and 3) decision to further train. Each routine has the following details.

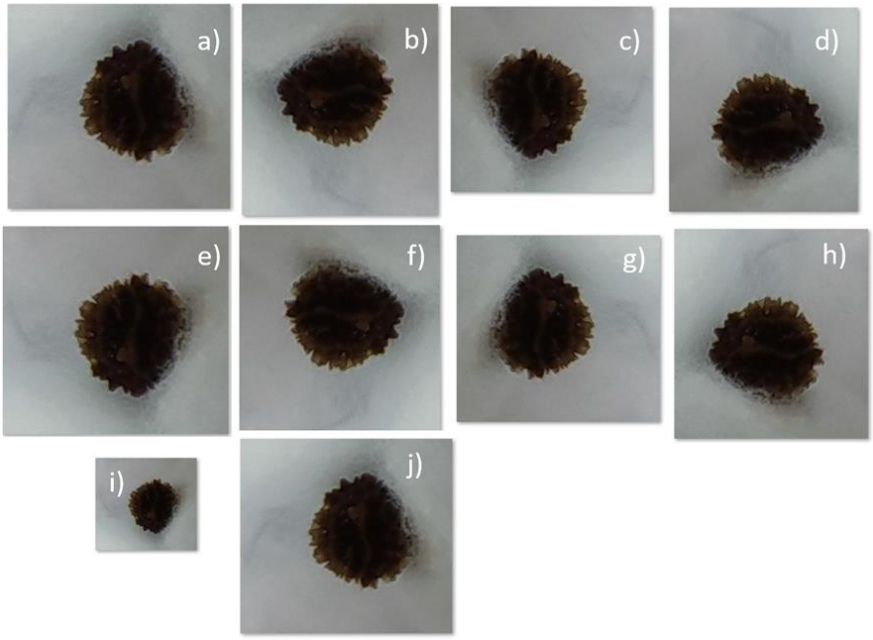


Figure 6. PSGES augmented images (a) original image, (b) original image rotated 90◎, (c) original image rotated 180◎, (d) original image rotated 270◎, (e) original image flipped, (f) flipped image rotated 90◎, (g) flipped image rotated 180◎, (h) flipped image rotated 270◎, (i) resized original image with ratio 1:0.5, and (j) resized original image with ratio 1:2.5

2.5.2.1 Train dataset routine

PSGES employed a powerful CNN called "ResNet50", available in the MATLAB toolbox, to train the system on the papaya dataset. ResNet50 resized all papaya seed images to 224 pixels x 224 pixels x 3 planes before including them in the system training dataset. PSGES employed 11,600 papaya seed images in the training dataset, from which 80% of the images were randomly selected for the training dataset, and 20% were for the testing dataset. The system used 1,000 papaya images to validate its performance. This research also employed a data augmentation technique to increase the number of papaya seed images in the dataset. The augmentation method rotated the original papaya images (as shown in Figure 6 (a)) into 90◎, 180◎ , and 270◎ images, as shown in Figures 6 (b), 6 (c) and 6 (d), respectively. After that, the augmentation method flipped the original papaya images (Figure 6 (e)). Then, it rotated the flipped image into 90◎, 180◎ , and 270◎ images, as shown in Figures 6 (f), 6 (g) and 6 (h), respectively. Finally, the augmentation method resized an original image with the ratio of 1:0.5 and 1:2.5, as shown in Figures 6 (i) and 6 (j), respectively. The papaya dataset contained 12,600 images (1,260 x 10) for training.

2.5.2.2 Plant and validate germination routine

PSGES used images of 1,260 planted papaya seeds to validate every seed for germination. The system directly mapped all papaya seed images before germination with all papaya seed images after germination, as shown in Figures 7 (a) and (b).

2.5.2.3 Decide to train further using more data

The last step of the dataset training process is to further train using more data from the system dataset or stop the PSGES program.

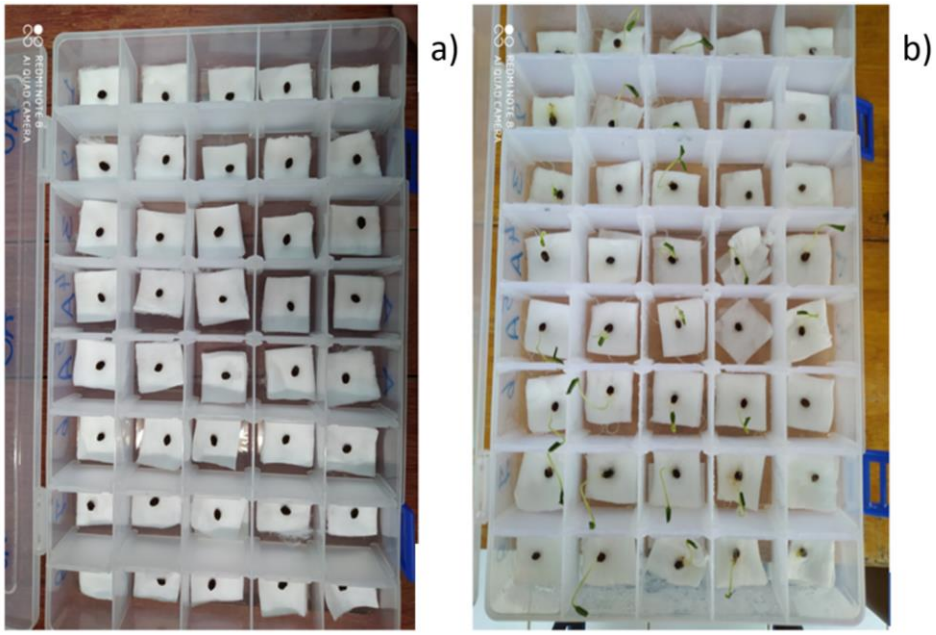


Figure 7 Papaya seeds image (a) before germination and (b) after germination

2.5.3 Evaluation process

The evaluation process consists of a main routine and two sub-processes. These are 1) the image evaluation routine, 2) the display evaluation results sub-process, and 3) the decision to evaluate more papaya images sub-process. Each routine and sub-process are detailed as follows.

2.5.3.1 Evaluate image routine

PSGES employed ResNet50 to train a papaya seed dataset and to evaluate papaya seeds by matching input papaya seed images with all images in the training dataset. Finally, the PSGES illustrated the best image matching to the PSGES graphical user interface (GUI).

2.5.3.2 Results illustration sub-process

PSGES shows papaya seed germination evaluation results via a graphical user interface. The GUI has three components: a graphics window, text boxes, and push buttons, as shown in Figure 8. Each component is described as follows.

The four graphical windows are 1) a graphics window showing the papaya seed input image, 2) a graphics window showing an actual papaya seed germination, 3) a graphics window showing an evaluation of papaya seed germination, and 4) a graphics-window check-box showing an evaluation result, respectively labeled 1 to 4 in Figure 8. A check-box ☑ symbol) represents a correct papaya seed evaluation, while an x-box ☒ represents an incorrect evaluation.

Three text boxes are 1) the input path and filename, 2) the matching folder name, and 3) the average processing time. These are, respectively, labeled 5 to 7 in Figure 8.
The five push-buttons are 1) the get image button to retrieve the input papaya seed image, 2) the clear button for deleting all GUI values, 3) the evaluate button to match a papaya seed image with all papaya images in the dataset, 4) actual papaya seed germination or failure to germinate, and 5) an exit button to stop the PSGES. These are shown as labels 8 to 12 in Figure 8, respectively.

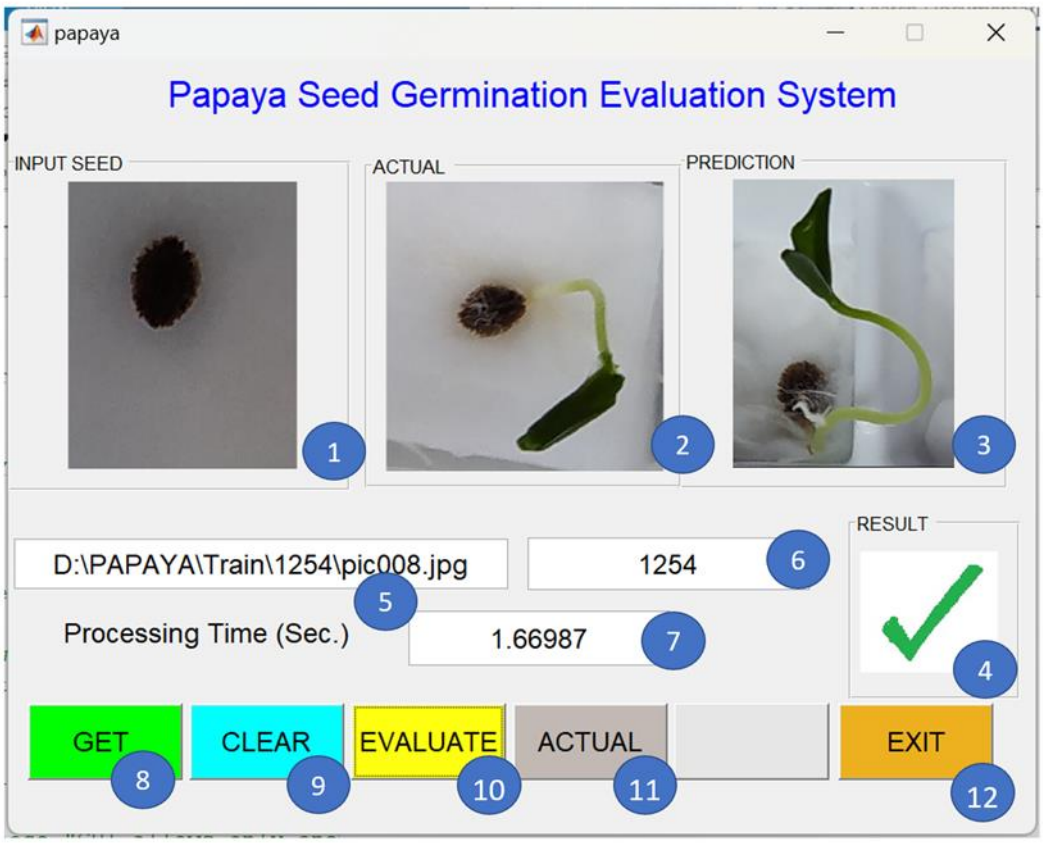


Figure 8. PSGES graphic user interface

2.5.3.3 Decide to evaluate more seed images

The last sub-process of evaluation is to decide between evaluating more papaya seed images or stopping the PSGES program.

2.6 Statistical values

Accuracy, precision, recall, and F1-scores were used to compare the performance of seven CNN structures: AlexNet, GoogLeNet, Inceptionv3, ResNet18, ResNet50, ResNet101, and VGG16. The accuracy, precision, recall, and F1-score equations are as follows.

2.6.1 Accuracy statistical value

The accuracy value, defined in Equation (1), is the ratio of images matching the correct value and the total number of images.

$$Accuracy = \frac{TP+TN}{TP+FP+TN+FN} \quad (1)$$

2.6.2 Precision statistical value

The precision value is the number of true positives divided by the number of true positives plus the number of false positives, as shown in Equation (2).

$$Precision = \frac{TP}{TP+FP} \quad (2)$$

2.6.3 Recall statistical value

A recall value is the capability of the system to associate an image with other relevant images within a dataset. The recall value is the number of true positives divided by the number of true positives plus the number of false negatives, as shown in Equation (3).

$$Recall = \frac{TP}{TP+FN} \quad (3)$$

2.6.4 F1-score statistical value

The F-score is a harmonic mean of precision and recall. It can be interpreted as a weighted average of precision and recall. This parameter is shown in Equation (4).

$$F1 - Score = \frac{2\ X\ Precision\ X\ Recall}{Precision+Recall} \quad (4)$$

3. Results

This research was conducted using seven different convolutional neural networks: 1) Alex Net, 2) GoogLeNet, 3) Inceptionv3, 4) ResNet18, 5) ResNet50, 6) ResNet101, and 7) VGG16, all using the same PSGES dataset. The MATLAB 2020b version supports these seven different convolutional neural network types. Comparisons of accuracy, precision, recall, and F1 score follow Equations 1– 4.

The PSGES employed 12,600 papaya images in these experiments, separated into 11,600 images (1,160 seeds x 10 images) to train the dataset and 1,000 images (100 seeds x 10 images) to validate the system. The system randomly selected 80% of 11,600 images to train the system dataset and 20% to test the system dataset. The germination rate of papaya seeds for the training dataset is 86.37% (10,020 ◎ 11,600 x 100), and the germination rate of papaya seeds for validating the dataset is 68.00% (680 ◎ 1,000 x 100). The confusion matrix comparison of the different CNN models for the training and validation datasets are shown in Tables 2 and 3, respectively.

Table 2. Comparison of the different CNN models for the training dataset

	CNN Model	True Positive	False Positive	False Negative	True Negative
1.	AlexNet	9,187	833	852	728
2.	GoogLeNet	9,973	47	52	1,528
3.	Inceptionv3	9,998	22	29	1,551
4.	ResNet18	9,991	29	26	1,554
5.	ResNet50	10,000	20	28	1,552
6.	ResNet101	9,925	95	1,275	305
7.	VGG16	9,997	23	35	1,545

Table 3. Comparison of the different CNN models for the validation dataset

CNN Model	True Positive	False Positive	False Negative	True Negative
1. AlexNet	598	82	296	24
2. GoogLeNet	614	66	295	25
3. Inceptionv3	597	83	274	46
4. ResNet18	582	98	283	37
5. ResNet50	677	3	317	3
6. ResNet101	609	71	288	32
7. VGG16	615	65	297	23

Moreover, the PSGES employed four statistical values for checking the system performance: 1) accuracy, 2) precision, 3) recall, and 4) F1-score, as shown in Equations (1)– (4). All statistical values were calculated from the confusion matrix to determine 1) true positive (TP), 2) false positive (FP), 3) true negative (TN), and 4) false negative (FN) values.

The PSGES also employed these four statistical values to evaluate the seven CNN model training dataset performance levels, as shown in Table 4. Inceptionv3 has the shortest training dataset time for the training dataset, while GoogLeNet has the longest training dataset time, 761.20 and 1,678.90 seconds, respectively. ResNet50 has the highest accuracy, performance, and F1-score, 0.9958, 0.9980, and 0.9976, respectively. AlexNet has the lowest performance, precision, recall, and F1-score, 0.8637, 0.9168, 0.9151, and 0.9159, respectively.

ResNet50 generates the highest performance, precision, recall, and F1-score for the validation dataset, 0.6800, 0.9956, 0.6811, and 0.8080, respectively. ResNet18 gives the lowest accuracy, performance, and F1-score, 0.6190, 0.8559, and 0.7524, respectively.

Based on the experimental results, ResNet50 was chosen for the PSGES to train and evaluate papaya seed germination owing to its highest accuracy in training and validating datasets, 0.9958 for the training dataset and 0.6800 for validating the system. A comparison of the accuracy, precision, recall, and F1 scores of different CNN models for training and validation is shown in Tables 4 and 5, respectively. The germination rates of papaya seeds in this research are 84.92% ((10,000 + 20 + 677 +3) ÷ 12,600 x 100).

Table 4. Performance comparison among the different CNN models for the training dataset

CNN Model	Accuracy	Precision	Recall	F1-score	Training Time (sec)
1. AlexNet	0.8637	0.9168	0.9151	0.9159	1,643.50
2. GoogLeNet	0.9915	0.9953	0.9948	0.9951	1,678.90
3.Inceptionv3	0.9956	0.9978	0.9971	0.9974	761.20
4. ResNet18	0.9952	0.9971	0.9974	0.9972	1,080.10
5. ResNet50	0.9958	0.9980	0.9972	0.9976	785.02
6. ResNet101	0.8818	0.9905	0.8861	0.9354	1,259.30
7. VGG16	0.9950	0.9977	0.9965	0.9971	1,145.40

Table 5 Comparison performance among the different CNN models for the validation dataset

CNN Model	Accuracy	Precision	Recall	F1-score	Training Time (sec)
1. AlexNet	0.6220	0.8794	0.6689	0.7598	220.34
2. GoogLeNet	0.6390	0.9029	0.6755	0.7728	1,643.50
3. Inceptionv3	0.6430	0.8779	0.6854	0.7698	685.58
4. ResNet18	0.6190	0.8559	0.6728	0.7534	1,080.10
5. ResNet50	0.6800	0.9956	0.6811	0.8080	721.38
6. ResNet101	0.6410	0.8956	0.6789	0.7724	1,259.30
7. VGG16	0.6380	0.9044	0.6743	0.7726	1,145.40

Accuracy and loss graphs for training ResNet50 are shown in Figures 9 (a) and 9 (b), respectively. Setting parameters for training ResNet50 have one epoch per iteration, a 0.01 learning rate, and a maximum of 16 epochs.

Papaya seed germination sample evaluations are shown in Figure 10. Figure 10 (a) shows an accurate positive evaluation in which the evaluated and planted seeds germinated. Figure 10 (b) shows a false positive evaluation, in which the evaluated seed germinated, but the planted seed was un-germinated. In Figure 10 (c), a false negative evaluation is presented, where the evaluated seed was un-germinated, but the planted seed germinated. Finally, Figure 10 (d) shows a true negative evaluation, where both the evaluated and planted seeds were ungerminated.

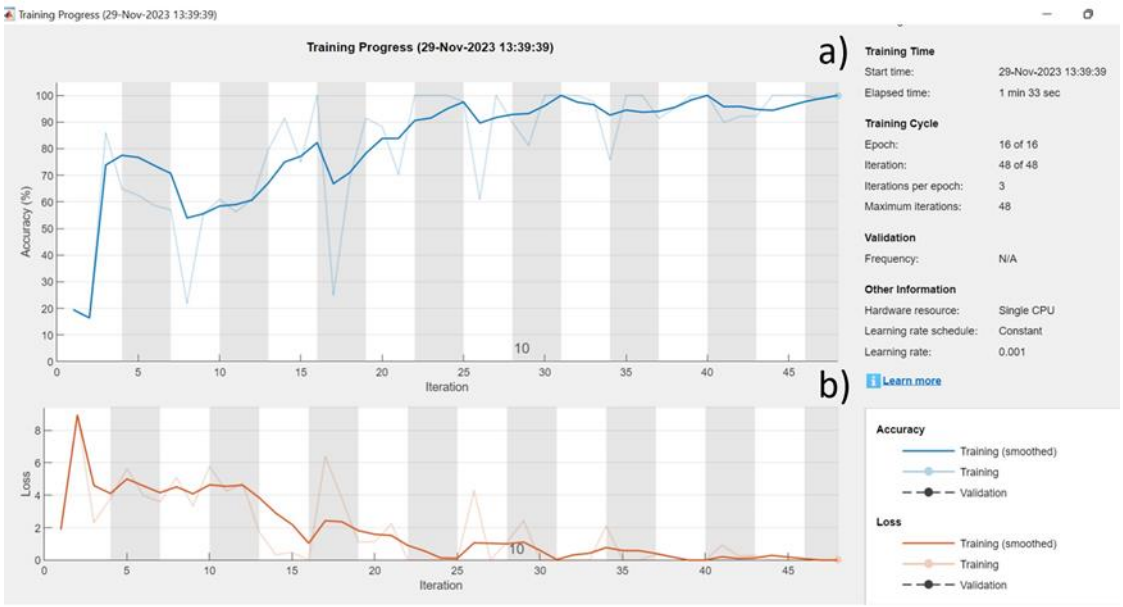


Figure 9. Accuracy and loss curves for training ResNet50 in the PSGES

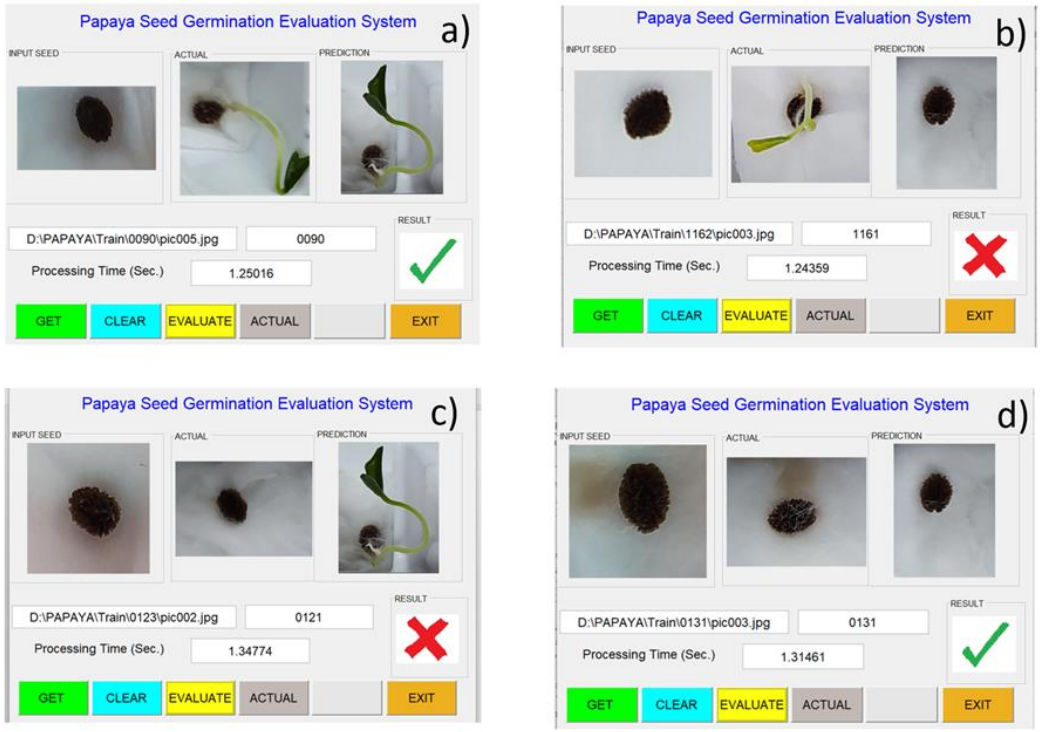


Figure 10. PSGES GUI sample screens, (a) true positive, and (b) true negative, (c) false negative, and (d) false positive

4. Discussion

Evaluating plant seed germination is a very challenging task for many researchers. Previously, researchers evaluated seed germination by physiological, biochemical, and stress tolerance tests [6], all destructive methods. Currently, researchers are attempting to apply non-destructive methods, using X-rays [9], infrared radiation [10], and image processing [12, 13]. There is no consensus about which method is best. Both X-ray and infrared methods require sophisticated equipment to evaluate seed germination. However, image processing is not only non-destructive but also uses simple equipment. Farmers can use a mobile phone camera and computer to evaluate seed germination. A comparison among various kinds of plant seeds is shown in Table 6. Lurstwut and Pornpanomchai (2017) employed an artificial neural network (ANN) to evaluate the germination of 34,835 rice seeds using their color, shape, and texture attributes. They used only a single rice seed image to evaluate seed germination with a precision rate of 92.80%. Marchi and Cicero (2017) used a seed vigor imaging system (SVIS) to evaluate carrot seed germination. Zhou et al. (2020) evaluated the germination of 3,072 beet seeds using near-infrared hyperspectral images with an 89.00% accuracy. Pornpanomchai et al. (2020) used chili seed attributes, shape, color, and texture to evaluate their germination. The experiments were conducted using an ANN with a precision rate of 71.71%. The current research used ResNet50, a convolutional neural network (CNN) available in the MATLAB toolbox. The PSGES employed only a single papaya seed image to evaluate its germination with a precision rate of 99.59%.

Table 6 Comparison of various kinds of seeds for germination evaluation

Researcher (Year)	Seed Type	Dataset Size	Technique	Precision (%)
Lurstwut (2017) [12]	rice	34,835	ANN	92.80
Marchi and Cicero (2017) [6]	carrot	350	SVIS	n/a
Zhou (2020) [10]	beet	3,072	NIR	89.00
Pornpanomchai *et al*. (2020) [13]	chili	2,820	ANN	71.71
This Research (2024)	papaya	12,600	CNN	99.59

5. Conclusions

The PSGES fulfills the objective of this research, which is to develop a computer system for evaluating papaya seed germination using only a single image. Its dataset consists of 12,600 papaya seed images, 11,600 images for a training dataset, and the remaining 1,000 images for a validation dataset. The average precision rates of the system are 0.9980 for training the dataset and 0.9959 for the system validation. The average access time of the system is 1.4705 sec/image. The PSGES is also compared for its performance against that of various kinds of CNNs. Experimental results show a state-of-the-art image-based papaya seed germination evaluation. Papaya is a fruit planted from seeds, and its seeds have a very low germination rate. Therefore, this research can help farmers reduce costs and time spent planting papaya because they can select seeds that will be more likely to germinate. Researchers can apply techniques in this research to evaluate the germination of other kinds of fruit seeds, such as oranges, longan, mango, and durian. A mobile phone application based on this research can be developed.

The limitations of this research are the low germination rates and the long time required to plant papaya seeds in order to conduct the experiments. The researchers need a large number of papaya seeds for a training dataset and more time to build a larger dataset. Normally, large datasets have higher precision than smaller ones. Moreover, farmers will have more confidence in a larger papaya seed dataset.

6. Acknowledgments

This research was supported by the Faculty of Information and Communication Technology (ICT) at Mahidol University. The authors are very thankful for their support.

Author: Contributions: Conceptualization, experimental design, carrying out experiment, data acquisition, writing and editing, C.P.

Funding: This research received no funding.

Conflicts of Interest: The authors declare no conflict of interest.

References

[1] Burns, p.; Saengmanee, P.; Utkhao, W.; Terdwongworakul, A.; Thaipong, K.; Doung-Ngern, U.; Siripanich, J. Comparison of fruit texture and aquaporin gene expression in papaya "Khak Nual" cultivated under varying conditions. *Journal of Horticultural Science and Biotechnology* **2023**, *98*(6), 758-771. https://doi.org/10.1080/14620316.2023.2206396

[2] Dotto, J.M. & Siri, A.A. Nutraceutical value of Carica papaya: A review. *Scientific African* **2021**, *13*, 1-16. https://doi.org/10.1016/j.sciaf.2021.e00933

[3] Jiao, M.; Liu, C.; Prieto, M.A.; Lu, X.; Wu, W.; Sun, J.; Oliveira, P.G.; Tang, X.; Xiao, J.; Gandara, J.S.; Hu, D.; Li, N. Biological Functions and Utilization of Different Part of the Papaya: A Review. *Food Reviews International* **2023**, *39*(9), 6781–6804. https://doi.org/10.1080/87559129.2022.2124415

[4] Nugroho, D.; Surya, R.; Janshongsawang, J.; Janshongsawang, A.; Benchawattananon, R. Som tum, the famous ethnic food of Thailand: its benefit and innovations. *Journal of Ethnic Foods* **2023**, *10*, 1-11. https://doi.org/10.1186/s42779-023-00204-4

[5] Lanjhiyana, R. & Sahu, G.D. A review on influence of seed pretreatment on germination parameters of papaya (Carica papaya L.). *The Pharma Innovation Journal* **2023**, *12*(9), 1895-1899. https://www.thepharmajournal.com

[6] Marchi, J.L. & Cicero, S.M. Use of the software Seed Vigor Imaging System (SVIS®) for assessing vigor of carrot seeds. *Scientia Agricola* **2017**, *74*(6), 469-473. https://doi.org/10.1590/1678-992X-2016-0220

[7] Yang, J.; Sun, L.; Xing, W.; Feng, G.; Bai, H.; Wang, J. Hyperspectral prediction of sugarbeet seed germination based on gauss kernel SVM. *Spectrochimica Acta Part A: Molecular and Biomolecular Spectroscopy* **2021**, *253*, 1-9. https://doi.org/10.1016/j.saa.2021.119585

[8] Pang, L.; Men, S.; Yan, L. Rapid vitality estimation and prediction of corn seeds based on spectra and images using deep learning and hyperspectral imaging techniques. *IEEE Access* **2020**, *8*, 123026-123036. http:// doi.org/10.1109/ACCESS.2020.3006495

[9] Severiano, R.L.; Pinheiro, P.R.; Gomes, F.G.J. Demartelaere ACF, Pereira MD. Image analysis of papaya seeds submitted to sarcotesta removal methods. *Pesquisa Agropecuária Tropical*. **2018**, *48*(4), 461-467. http://doi: 10.1590/1983-40632018v4853699

[10] Zhou, S.; Sun, L.; Xing, W.; Feng, G.; Ji, Y.; Yang, J.; Liu, S. Hyperspectral imaging of beet seed germination prediction. *Infrared Physics and Technology*. **2020**, *108*, 1-7. https://doi.org/10.1016/j.infrared.2020.103363

[11] Genze, N.; Bhati, R.; Grieb, M.; Schultheiss, S.J.; Grimm, D.G. Accurate machine learning-based germination detection, prediction and quality assessment of three grain crops. *Plant methods*. **2020**, *16*, 1-11. https://doi.org/10.1186/s13007-020-00699-x

[12] Lurstwut, B. & Pornpanomchai, C. Image analysis based on color, shape and texture for rice seed (Oryza sativa L.) germination evaluation. *Agriculture and Natural Resources*. **2017**, *51*, 381-389. https://doi.org /10.1016/j.anres.2017.12.002

[13] Pornpanomchai, C.; Jongsriwattanaporn, S.; Pattanakul, T.; Suriyun, W. Image analysis on color and texture for chili (Capsicum frutescence) seed germination. *Science Engineering and Health Studies*. **2020**, *14*(3), 169-183. https://doi.org/10.14456/sehs.2020.16

[14] Erdem, D.; Beke, A.; Kumbasar, T. A deep learning-based pipeline for teaching control theory: transforming feedback control systems on whiteboard into MATLAB. *IEEE Access*. **2022**, *8*, 84631- 84641. http://doi:10.1109/ACCESS.2020.2992614

ASEAN
Journal of Scientific and Technological Reports
Online ISSN:2773-8752

Research article

Clove Position on the Induction of Single-Clove Garlic, Yield, and Bioactive Compounds

Tanapon Tumsuk[1], Kamon Thippachote[2], Suriya Tateing[3], Siwaporn Thumdee[4], and Jutamas Kumchai[5]*

[1] Department of Plant and Soil Sciences, Faculty of Agriculture, Chiang Mai University, Chiang Mai, 50200, Thailand
[2] Department of Plant and Soil Sciences, Faculty of Agriculture, Chiang Mai University, Chiang Mai, 50200, Thailand
[3] Department of Plant and Soil Sciences, Faculty of Agriculture, Chiang Mai University, Chiang Mai, 50200, Thailand
[4] Department of Plant and Soil Sciences, Faculty of Agriculture, Chiang Mai University, Chiang Mai, 50200, Thailand
[5] Department of Plant and Soil Sciences, Faculty of Agriculture, Chiang Mai University, Chiang Mai, 50200, Thailand
* Correspondence: jutamas.k@cmu.ac.th

Citation:
Tumsuk, T.; Thippachote, K.; Tateing, S; Thumdee, S.; Kumchai, J. Clove position on the induction of single-clove garlic, yield, and bioactive compounds. *ASEAN J. Sci. Tech. Report.* **2025**, *28*(1), e256297. https://doi.org/10.55164/ajstr.v28i1.256297

Article history:
Received: October 13, 2024
Revised: November 25, 2024
Accepted: November 27, 2024
Available online: February 17, 2025

Publisher's Note:
This article has been published and distributed under the Thaksin University.

Abstract: Garlic is a valuable crop renowned for its medicinal properties and nutritional value, widely consumed in raw and processed. In Thailand's garlic production system, common garlic predominates, while single-clove garlic represents a smaller portion but commands higher prices due to its elevated levels of bioactive compounds and associated health benefits, leading to increased market demand. Research indicates that planting smaller cloves may enhance single-clove garlic production. Garlic cultivation in Thailand is primarily concentrated in the northern and northeastern regions, with only 1-2% of the production area dedicated to single-clove garlic. This study aimed to increase single-clove garlic yields by comparing different clove positions to optimize production and bioactive compound content, providing practical guidance for farmers. The experiment involved two treatments: inner cloves (0.5-0.8 g) and outer cloves (0.8-1.1 g). Yield components and bioactive compounds were analyzed. Results showed that outer cloves produced 100% common garlic bulbs, while inner cloves yielded 98.4% common bulbs and 1.6% single-clove garlic. Despite higher fresh yields of common bulbs from outer cloves, inner cloves produced 40.56 kg/ha of single-clove garlic. Weight loss after 30 days was 41–42% for common bulbs and 54.73% for single-clove garlic. Single-clove garlic showed more significant reductions in bulb and neck diameter. Notably, single-clove garlic contained the highest allicin content (35.79 mg/g FW) and DPPH inhibition (30.51%), indicating superior antioxidant properties. These findings suggest that planting inner cloves effectively promotes single-clove garlic production with enhanced bioactive properties, offering valuable insights for farmers.

Keywords: Single-clove garlic; Clove position; Allicin; Antioxidant; Bulb

1. Introduction

Garlic (*Allium sativum* L.) is an economically important vegetable, widely consumed in Thailand and globally. It is a herbaceous plant with nutrient-rich cloves that form an underground bulb. Garlic cloves contain major bioactive compounds, primarily organosulfur compounds such as allicin, alliin, and S-allyl-cysteine [1-2]. Allicin is a compound derived from the conversion of alliin. The synthesis of allicin in garlic plants is highly complex. The primary pathway begins with the roots absorbing sulfur compounds from the growing medium in the form of sulfate, which is then transported to the chloroplasts in

the leaves for the synthesis of glutathione. This process ultimately leads to the production of alliin. The alliin is then transported to the cytoplasm of organelles responsible for food storage, where it is converted into allicin by the enzyme alliinase, stored in vacuoles [3-4].

Allicin, a key compound in garlic, is formed when garlic is crushed, leading to various biological activities that contribute to its therapeutic potential. It exhibits significant antioxidant properties linked to its ability to modulate reactive oxygen species (ROS), which are implicated in various diseases. Allicin has been shown to lower blood glucose levels and enhance insulin sensitivity, making it beneficial for managing diabetes. Moreover, consumption of garlic, rich in allicin, may confer protective effects against conditions such as cardiovascular diseases and cancer [5-7].

In Thailand, garlic consumption includes domestically produced garlic, with small, pungent cloves used in households and processed products, and imported garlic, featuring larger cloves typically used in restaurants and industrial settings. The main garlic production areas are in the northern and northeastern regions, where farmers prefer growing native garlic varieties with small cloves due to their strong, pungent aroma and their ability to thrive in Thailand's environmental conditions. The physical characteristics of garlic are closely related to the environmental and geographical factors of its growing regions [8]. Studies using DNA fingerprinting techniques, such as RAPD and microsatellite analysis, on garlic from cultivation areas in Thailand have revealed distinct patterns of genetic variation based on regional farming practices. In northern Thailand, farmers often practice rotational planting, introducing seed cloves from different sources. This has led to genetic diversity and the naming of varieties based on their place of cultivation, such as Chiang Mai, Pai, and Nam Pat varieties. In contrast, farmers in the northeastern region, such as in Sisaket, tend to manage and reuse seed cloves within their own farms, without introducing new genetic material from external sources. This practice results in high genetic similarity within the local garlic population [9-10].

In production, research suggests that inner cloves can promote the formation of single-clove (solo) garlic [11], which comprises only 1-2% of total production This variety is particularly prized for its higher antioxidant properties and commands a premium price. It is often used for pickling, as its strong odor is attributed to higher sulfide content [7-8,12-14]. Additionally, garlic is now commonly processed into black garlic, a method aimed at enhancing the concentration of key bioactive compounds, thereby increasing its value and positioning it as a health-oriented product [15].

Garlic cloves naturally sprout into new plants under favourable conditions. Farmers use these cloves for planting, with new cloves forming around the central flower stalk (scape) and developing in layers. Outer cloves are formed earlier, and typically larger than inner cloves [16]. Garlic bulbs are mainly composed of water and carbohydrates, with fructans as the primary carbohydrate. Garlic also contains proteins, pectin, minerals, and polyamines. The growth phase before bulb formation is crucial for determining bulb yield and size, as leaves play a significant role in accumulating carbohydrates via photosynthesis [17]. Factors influencing bulb size include varietal characteristics and optimal harvest timing, as clove formation is affected by environmental conditions such as temperature and day length. These factors impact phytohormone levels and other components of bulb growth [17-19]. Desta *et al*. [20] found that larger cloves increase yields, bulb size, and clove number, while smaller cloves, which accumulate fewer nutrients, may lead to single-clove garlic formation.

Thus, this research aims to identify the appropriate garlic clove position that induce the production of single-clove garlic, increasing its yield and bioactive compounds. The study will provide guidelines for farmers to optimize single-clove garlic cultivation.

2. Materials and Methods

2.1 The effect of clove position in garlic seed bulbs on single-clove garlic formation

The experiment utilized Thai garlic from Chiang Mai variety, characterized by thin outer skins, purple-red or light pink hues, and a strong aroma. Garlic bulb were divided into two treatments: outer cloves (0.8-1.1 g) and inner cloves (0.5-0.8 g), with the latter located near the central scape (Figure 1). Clove sizes within each group were uniform. A randomized complete block design (RCBD) with six replications, each containing 60 plants planted in loam soil, was implemented (Figure 3). The drip irrigation system was used with a planting distance of 20 × 20 cm along the drip lines. To control weed growth, appropriate pest

management practices were employed. Water was provided based on the growth stages of the garlic and adjusted accordingly: 3-5 days per irrigation cycle during the early growth stage, 5-7 days per cycle after 30 days of planting, and 7-10 days per cycle during the bulbing stage. Watering was ceased 10 days before harvest. Fertilizer was delivered through the irrigation system. At 30 and 45 days after planting, a 15-15-15 NPK fertilizer was applied at a rate of 300 kg/ha. During the bulbing stage at around 60 days, a 13-13-21 NPK fertilizer was applied at a rate of 300 kg/ha every 14 days for two applications, along with foliar fertilizer sprayed. Harvesting occurred when leaf tips dried, brown leaves outnumbered green ones, and 110-120 days had elapsed [14]. The data collected included the ratio, fresh weight, and dry weight of garlic bulb types. Dry weight measurements were taken 30 days post-harvest to assess weight loss and calculate the weight loss percentage of the garlic plants [21]. Statistical differences were analyzed by using IBM SPSS Statistics. Means were compared at a 95% confidence level. The experiment was conducted at the Agricultural Innovation Research, Integration, Demonstration, and Training Center, Faculty of Agriculture, Chiang Mai University, Thailand, during the winter season from November 2022 to March 2023. The average temperature recorded during the experiment ranged from 20°C to 25°C (Figure 2).

$$\text{Weight loss}(\%) = \frac{(\text{fresh weight} - \text{weight after curing})}{\text{fresh weight}} \times 100$$



Figure 1. Characteristics of garlic bulb and clove: A normal garlic bulb consists of multiple cloves. The outer cloves refer to the cloves encircling the outermost layer of the bulb, while the inner cloves are located closer to the scape in the axial position (a). In contrast, a single-clove bulb (or solo bulb) lacks lateral cloves, containing only a single, unified clove (b).

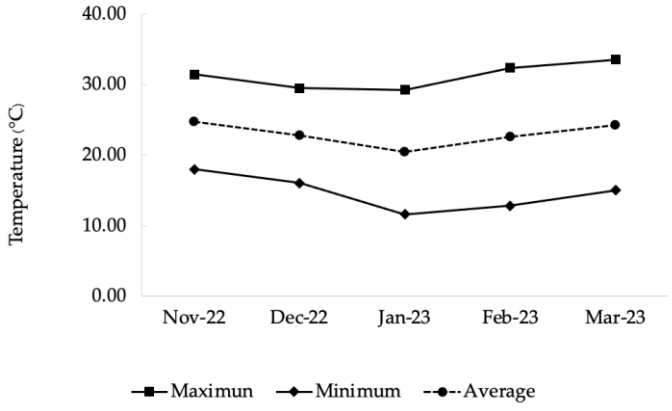


Figure 2. Temperature recorded during the experiment from November 2022 to March 2023.

2.2 Analysis of the active compound content and antioxidant activity in garlic

The active compounds were analyzed from dry garlic cloves (Figure 3). Allicin content was determined following a modified protocol from Zhu *et al*. [22], with HPLC analysis (Agilent 1260 Infinity II)

performed according to modified methods from Bocchini *et al*. [23] and DPPH scavenging activity was analyzed following modified methods from Wongsa *et al*. [24]

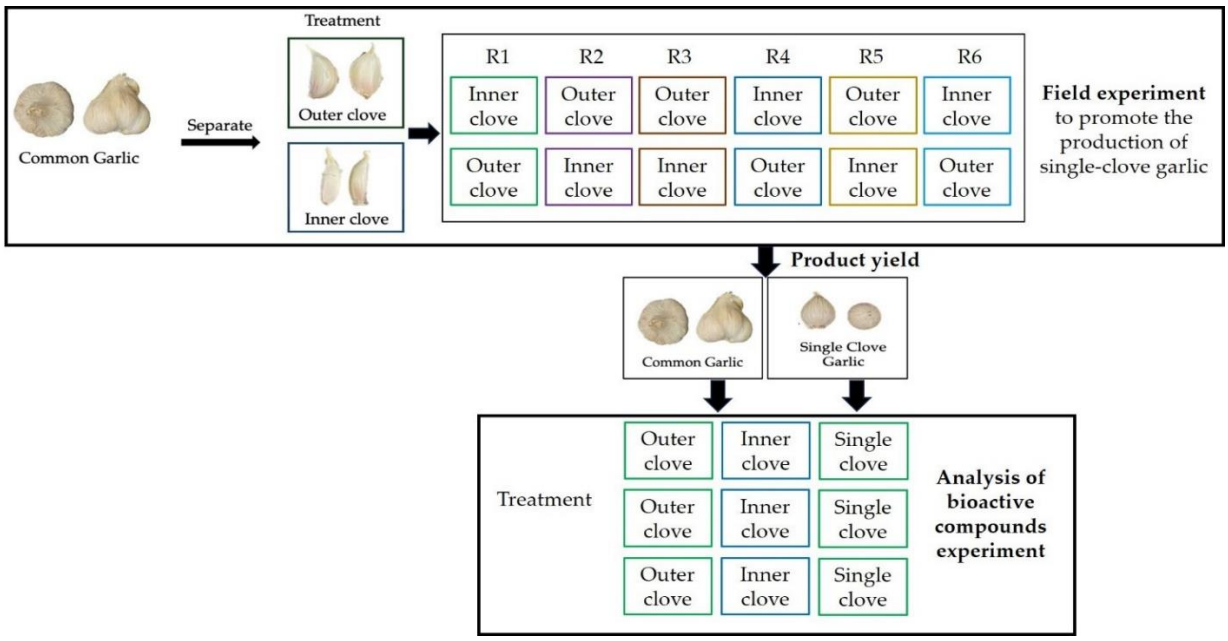


Figure 3. Schematic diagram of the experimental design.

3. Results

3.1 Mother clove position in garlic seed bulbs on single-clove garlic formation

Harvest yield analysis based on planted clove proportion. The harvest yield analysis revealed that garlic grown from outer cloves achieved a total bulb count of 85.00%, all of which were classified as normal bulbs (100.00%). In contrast, garlic grown from inner cloves produced a total bulb count of 84.17%, with 98.40% developing into normal bulbs. A significant difference was observed in the proportion of normal bulbs between these two groups ($P \leq 0.05$). Notably, garlic grown from outer cloves did not produce any single-clove bulbs, whereas inner cloves yielded 1.6% single-clove bulbs (Table 1, Figure 4). The fresh weight yield of normal garlic bulbs from outer cloves were 14,653.25 kg/hectare and 12,970.25 kg/hectare form inner cloves, with no statistically significant difference. However, inner cloves produced significantly more single-clove bulbs (40.56 kg/hectare) compared to outer cloves (0 kg/hectare). The total yields, including both normal and single-clove bulbs, were 14,653.25 kg/hectare for outer cloves and 13,011.81 kg/hectare for inner cloves, with no statistically significant difference ($P \leq 0.05$) (Table 1).

Table 1. The average percentage of total bulbs, normal bulbs, single-clove bulbs, total fresh yield weight, and total marketable weight with harvesting day.

Mother clove Position of normal bulb	Total bulb (%)	The ratio of normal bulb (%)	The ratio of single clove (%)	Fresh yield weight of normal bulb (kg/ha)	Fresh yield weight of single clove (kg/ha)	Total marketable weight (kg/ha)
Outer clove	85.00	100.00 a	0.00 b	14,653.25 a	0.00 b	14,653.25
Inner clove	84.17	098.40 b	1.60 a	12,970.25 b	40.56 a	13,010.81
T-test	ns	*	*	*	*	ns
CV (%)	10.46	1.01	10.93	23.09	26.36	23.14

Mean within the same column followed by different letters significantly differed between treatments at $P \leq 0.05$.
ns = no statistically significant difference
* = statistically significant difference ($P \leq 0.05$)

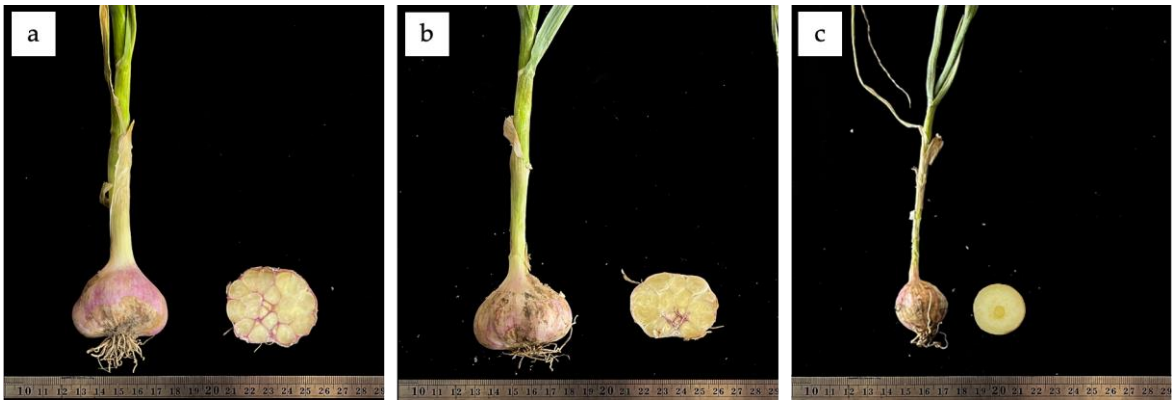


Figure 4. Characteristics of garlic bulbs obtained from planting: normal bulb from the outer clove (a); normal bulb from the inner clove (b); and single-clove bulb from the inner clove (c).

The weight of normal bulbs obtained from mother plants with outer and inner cloves showed no statistically significant difference after harvesting and air-drying. The initial weight of normal bulbs from mother plants with outer and inner cloves was 32.98 g and 29.69 g, respectively. The weight decreased from harvest to week 4 (30 days after harvest), reaching 19.31 g and 17.23 g, respectively. This represents a weight loss of 41.47% and 42.40%, respectively (Table 2). Single-clove garlic from inner cloves weighed 19.79 g after harvesting and 17.46 g after drying, with a weight loss of 53.73% (Table 3 and Figure 5). However, the dry weight yield of single-clove garlic decreased by more than 50% compared to multi-clove (normal) garlic.

Table 2. Bulb weight of normal garlic after harvest (-ing), weight after drying, and weight loss percentage.

Bulb type	Bulb weight after harvest (g/bulb)	Bulb weight after 30 days drying (g/bulb)	Bulb weight loss (%)
Normal bulb of outer clove	32.98	19.31	41.47
Normal bulb of inner clove	29.69	17.23	42.40
T-test	ns	ns	ns
CV (%)	23.09	25.18	5.83

Mean within the same column followed by different letters significantly differed between treatments at P≤0.05.
ns = no statistically significant difference

Table 3. Bulb weight of single-clove garlic after harvest (-ing), weight after drying, and weight loss percentage.

Bulb type	Bulb weight at harvest (g/bulb)	After drying at 30 days (g/bulb)	Bulb weight loss (%)
Single clove of outer clove*	—	—	—
Single clove of inner clove	05.63	02.53	53.73

* The data did not detect single-clove garlic from outer clove.
This table presents the average data for single-clove garlic without any statistical analysis.

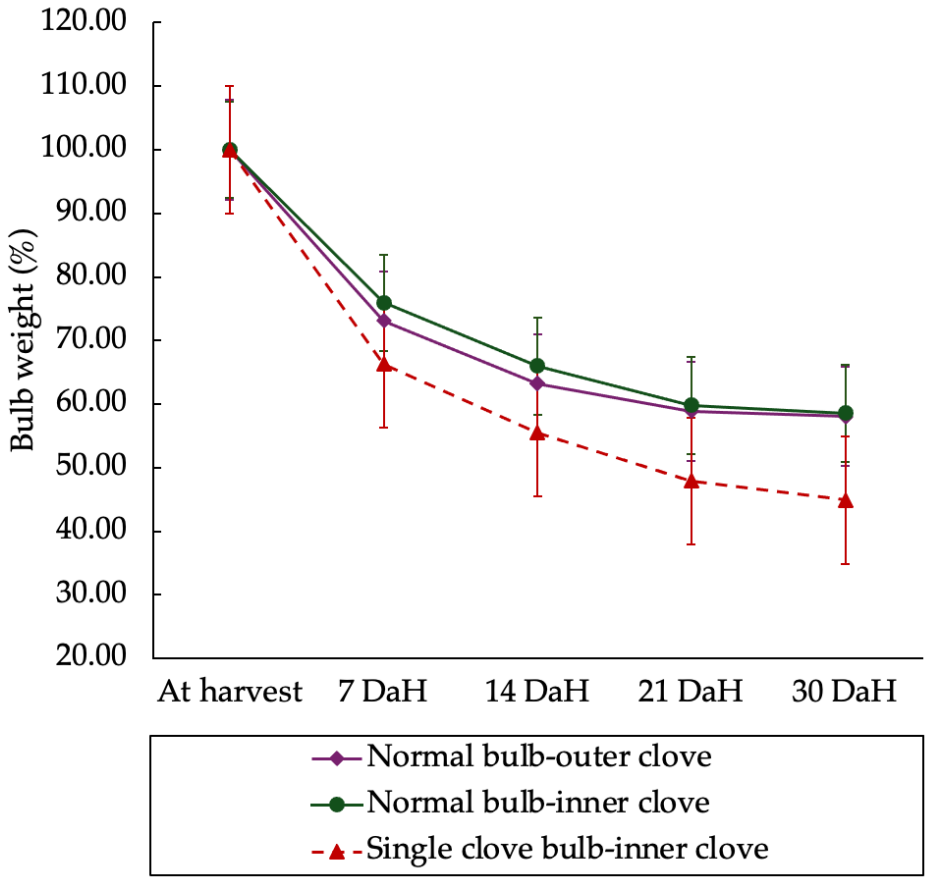


Figure 5. The percentage of bulb weight loss after harvesting and drying *(Day after harvest (DaH))

The fresh produce obtained had bulb diameters ranging from 41.51 to 19.79 mm. Normal bulbs from outer and inner cloves measured 41.51 mm and 38.61 mm in diameter, respectively, with no statistically significant difference. After air-drying for 30 days, normal bulbs from outer and inner cloves measured 39.55 mm and 36.53 mm in diameter, respectively, representing weight loss percentages of 4.70% and 5.36%, with no statistically significant difference (Table 4). Meanwhile, bulbs from inner cloves had a diameter of 19.79 mm at harvest. After drying, single-clove garlic from these bulbs decreased to 17.46 mm in diameter, representing a size reduction of 11.08% (Table 5).

Table 4. Bulb diameters of normal bulb garlic after harvest (-ing) and after 30 days of drying, along with the percentage decrease in bulb diameter during the drying period.

Bulb type	**Fresh bulb diameter (mm)**	**Bulb diameter after 30 days drying (mm)**	**Percentage decrease in bulb diameters (%)**
Normal bulb of outer clove	41.51	39.55	04.70
Normal bulb of inner clove	38.61	36.53	05.36
T-test	ns	ns	ns
CV (%)	28.56	30.15	47.01

Mean within the same column followed by different letters significantly differed between treatments at P≤0.05. ns = no statistically significant difference

Table 5. Bulb diameters of single-clove garlic after harvest (-ing) and after 30 days of drying, along with the percentage decrease in bulb diameter during the drying period.

Bulb type	Fresh bulb diameter (mm)	Bulb diameter after 30 days drying (mm)	Percentage decrease in bulb diameters (%)
Single clove of outer clove*	—	—	—
Single clove of inner clove	19.79	17.46	11.08

* The data did not detect single-clove garlic from outer clove.
This table presents the average data for single-clove garlic without any statistical analysis.

The neck width of bulbs from mother plants with outer and inner cloves was measured. The neck diameter of fresh bulbs ranged from 7.71 to 4.37 mm. The necks of normal bulbs from outer and inner cloves measured 7.71 mm and 7.33 mm in diameter, respectively, with no statistically significant difference. The bulbs had a neck diameter of 4.37 mm. After air-drying for 30 days, the necks showed shrinkage. The necks of normal bulbs from outer and inner cloves measured 6.90 mm and 6.58 mm, respectively, representing size reductions of 10.62% and 10.53%, with no statistically significant difference (Table 6). Meanwhile, the neck of dried bulbs from inner cloves decreased to 2.45 mm in diameter, representing a size reduction of 42.45% (Table 7).

Table 6. Size of the garlic neck of normal bulbs at harvest (-ing), after curing, and the reduction in neck size.

Bulb type	Neck diameter (mm)		Percentage decrease in neck diameters (%)
	Measured at harvest	After drying for 30 days	
Normal bulb of outer clove	7.71	6.90	10.62
Normal bulb of inner clove	7.33	6.58	10.53
T-test	ns	ns	ns
CV (%)	11.24	13.44	35.80

Mean within the same column followed by different letters significantly differed between treatments at P≤0.05.
ns = no statistically significant difference

Table 7. Size of the garlic neck of single clove at harvest (-ing), after curing, and the reduction in neck size.

Bulb type	Neck diameter (mm)		Percentage decrease in neck diameters (%)
	Measured at harvest	After drying for 30 days	
Single clove of outer clove	—	—	—
Single clove of inner clove	4.37	2.45	42.45

* The data did not detect single-clove garlic.
This table presents the average data for single-clove garlic without any statistical analysis.

The average number of cloves per bulb from normal bulbs obtained from mother plants with outer and inner cloves was 14.77 and 13.01, respectively. The average weight of cloves per bulb was 1.08 g and 1.06 g per clove, respectively, with no statistically significant difference between these values (Table 8).

Table 8. The number of cloves and the weight of cloves per bulb, 30 days after drying.

Bulb type	Number of cloves	Clove weight (g)
Normal bulb of outer clove	14.77	1.09
Normal bulb of inner clove	13.00	1.08
T-test	ns	ns
CV (%)	17.24	16.15

Mean within the same column followed by different letters significantly differed between treatments at P≤0.05. ns = no statistically significant difference

Comparing the use of outer and inner cloves for cultivation, it was found that bulb size had a strong positive correlation with neck size, yield weight, number of cloves, and clove weight, with correlation coefficients of 0.811, 0.922, 0.799, and 0.644, respectively. Neck size also showed a strong positive correlation with yield weight and number of cloves, with coefficients of 0.794 and 0.848, respectively. Yield weight had a strong positive correlation with the number of cloves and clove weight, with coefficients of 0.829 and 0.707, respectively (Table 9).

Table 9. Correlation between bulb size, neck size, yield weight, number of cloves, and clove weight of garlic grown using different clove positions for planting.

	Bulb size	Neck size	Bulb weight	Clove number	Clove weight
Bulb size	1				
Neck size	.811**	1			
Bulb weight	.922**	.794**	1		
Clove number	.799**	.848**	.829**	1	
Clove weight	.644*	.293	.707*	.256	1

* Correlation is significant at the 0.05 level (2-tailed).
** Correlation is significant at the 0.01 level (2-tailed).

3.2 Allicin and antioxidant activity

When considering the types of garlic cloves for bioactive compounds, it was found that single-clove garlic had the highest average amounts of allicin and DPPH inhibition, with 35.79 mg g^{-1} FW and 30.51%, respectively. These values were significantly different from those of normal bulbs obtained from both outer and inner cloves (Table 10).

Table 10. Bioactive compounds, including allicin and DPPH inhibition, in various types of garlic.

Bulb type	Allicin (mg g^{-1} FW)	DPPH inhibition (%)
Single clove	35.79 a	30.51 a
Normal bulb of outer clove	15.71 b	24.30 c
Normal bulb of inner clove	20.60 b	27.86 b
F-test	*	*
CV (%)	38.35	9.97

Mean within the same column followed by different letters significantly differed between treatments at P≤0.05. * = statistically significant difference (P≤0.05)

4. Discussion

4.1 Mother clove position in garlic seed bulbs on single-clove garlic formation

The results indicated that inner cloves induced single-clove garlic, which is smaller in size and differs in shape from the outer cloves. Qin *et al*. [25] reported that using single-clove garlic as seed is an effective method to achieve higher yields in garlic production, while small cloves can be repurposed to generate single-clove bulbs for future use. Single-clove garlic has only one clove that serves as the storage organ, typically

round and smaller than regular garlic. It forms due to incomplete development during the 60-90 days post-planting, influenced by seed quality, environmental conditions, and genetic factors, unlike regular garlic, which forms multiple cloves per bulb [12, 14, 16, 26]. Rungcharoen *et al*. [26] reported that the average fresh weight of normal garlic bulbs was 12,500 kg/ha at 110-120 days for Thai garlic across all production areas in Thailand. The formation of single-clove garlic also reduced yield due to its smaller size and weight compared to normal garlic bulbs [19]. Seed size plays a crucial role in garlic growth and yield, with single-clove seeds providing more nutrients to seedlings. Both garlic plants from single-clove seeds and multi-clove (common) seeds exhibited normal growth and development [25].

Garlic weight loss is attributed to moisture loss, which has been reported to reach 45-50% during the first month post-harvest due to leaf and outer sheath desiccation, and pest damage. Another factor is nutrient availability during cultivation; improper use of chemical fertilizers can lead to reduced garlic weight and faster desiccation during growth and storage, resulting in post-harvest weight and size loss [26-28]. In this experiment, both fertilizer formulas were applied at the same rate, but the application periods differed according to the age of the garlic. However, when calculated, the total nitrogen amount ranged from 40-47 kg/ha, which resulted in a weight loss rate of garlic ranging from 41.47% to 53.73%. Innoi *et al*. [28] reported that applying nitrogen fertilizer at rates of 62.50-193.75 kg/ha in the farmer demonstration area increased leaf number, bulb size, and fresh yield compared to no nitrogen application. However, after one month of drying, the 125.00 kg/ha nitrogen treatment showed a 51.01% weight loss, with 4.73-5.40% clove damage after five months. These findings suggest that the reduction in bulb size during storage correlates with weight loss, which can be used to calculate storage requirements for future sales or planting. Single-clove garlic seeds produced plants with significantly higher fresh and dry mass, larger bulbs, and greater leaf area compared to multi-clove seeds [25].

The trend analysis of garlic bulb weight over time reveals a significant negative linear correlation between the number of days after harvest (DaH) and bulb weight percentage. The trendline equation ($y = -1.4374x + 89.241$), where Y represents the bulb weight percentage and X represents days after harvest, demonstrates a consistent decline in weight. With a coefficient of determination ($R^2 = 0.7372$), the analysis indicates a strong statistical relationship between storage duration and weight loss. The downward slope of the trendline illustrates a substantial and progressive reduction in bulb weight over time, highlighting the critical impact of storage duration on garlic quality and preservation (Figure 6).

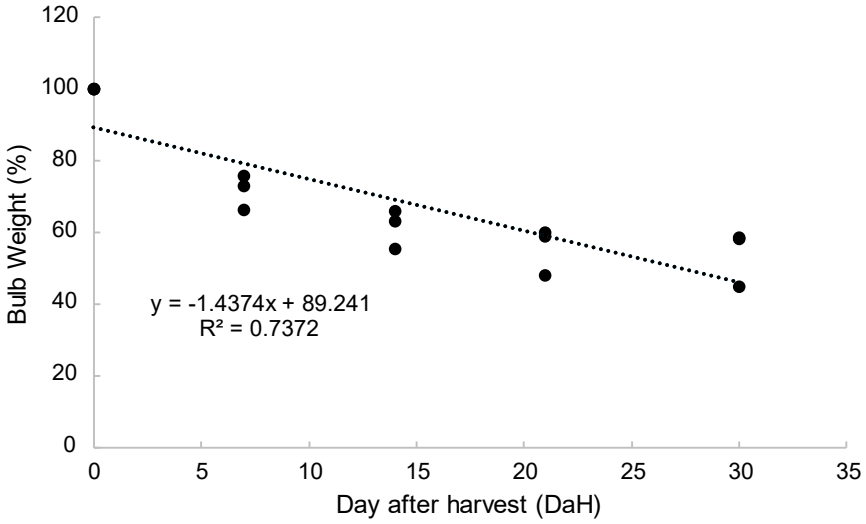


Figure 6. The correlation between storage duration and percentage of bulb weight reveals a consistent weight reduction pattern.

Optimal garlic storage requires careful post-harvest handling to preserve crop quality and longevity. After harvesting, plants should be dried in a shaded, well-ventilated area, maintaining their structural

integrity and minimizing disturbance. To prevent disease transmission, avoid washing or cutting the stems and leaves. Once the stems and leaves are thoroughly dried, meticulously sort the garlic by bulb size, removing any shriveled or diseased specimens. Cluster the sorted bulbs and suspend them in a well-ventilated space, protected from direct sunlight, to maximize storage life [14, 16].

Typically, clove size (clove position) ranging from 5.51 to 3.5 grams affects the yield components of garlic bulbs. Larger clove seeds result in higher shoot dry mass, larger neck and bulb diameters, more cloves per bulb, and greater average clove weight [20]. Research by Calimpang *et al*. [29] reveals the nuanced impact of garlic clove size on plant growth, categorizing cloves into four distinct weight ranges: small (1.0-1.49g), medium (1.50-1.99g), large (2.0-2.50g), and extra-large (2.51-3.0g). While larger cloves consistently produce more vigorous plants with higher fresh and dry bulb weights, empirical studies demonstrate no significant variations in yield per plant or hectare across different clove sizes. This counterintuitive finding suggests that although larger cloves enhance specific growth parameters, they do not guarantee proportional yield increases. Complementing these findings, Malashri *et al*. [30] observed that larger cloves generate more extensive leaf development and increased leaf area, thereby improving photosynthetic efficiency and overall plant growth. Their study, conducted using Thai garlic with smaller clove sizes, further underscores the complex relationship between clove size and agricultural performance.

The outer cloves (larger size) and inner cloves (smaller size) did not show significant differences in yield components. This is likely due to cultivation management practices (fertilizer and water supply) and environmental factors. Optimal water and fertilizer management is crucial for improving crop productivity and maintaining the ecological environment, especially under fluctuating climate conditions [31].

Bulb and clove form during the transition of vegetative growth to bulb formation at 60-90 days after planting. Key factors affecting bulb quality and weight during this period include an optimal environment, such as high daytime temperatures and longer daylight hours, the genetic traits, and the variability of garlic [16-17, 32-35].

Another important aspect of bulb growth is the role of leaves in carbohydrate accumulation through photosynthesis, which is crucial for yield and bulb size [17]. The data suggest that early, well-adapted growth leads to prolonged carbohydrate accumulation, resulting in larger bulb size, greater weight, and increased number of cloves.

4.2 Allicin and antioxidant activity

The experimental results indicated that the number of key compounds found in single-clove garlic was higher than in regular garlic. Kunasakdakul *et al*. [36] found that single-clove garlic contains higher levels of key compounds like allicin and alliin compared to regular garlic. The factors influencing garlic composition specifically sulfur-containing volatile compounds, which are responsible for the pungent smell and taste of garlic [37] include geographic, environmental, and climatic differences, variety, storage duration, and dormancy period [6].

Allicin and sulfur compound content in garlic are influenced by physiological processes, variety, and environmental conditions during growth. The nitrogen-sulfur ratio in the growing medium affects the accumulation of sulfur compounds such as alliin, the precursor of allicin, which is related to garlic's flavor and aroma [24, 38-40]. Alliin levels vary within the garlic plant, being lowest in the roots and highest in the buds, indicating that plant physiology and specific functions play roles in alliin accumulation, stored in vacuoles. Leaf damage converts alliin to allicin, reducing alliin levels [3-4]. Alliin levels are the highest in buds and decrease in older leaves after injury, with younger tissues tending to have a higher concentration of alliin.

The formation of cloves in garlic bulbs is influenced by lateral buds in the leaf axils, typically occurring in younger leaves. As the first leaves swell from accumulating food and energy, subsequent leaves form and become the primary storage parts, surrounded by the first leaves [16]. It is possible that inner cloves are younger and, therefore, tend to have higher allicin levels than outer cloves.

4.3 Economic analysis of common garlic and single-clove garlic

The comparative economic analysis of common garlic and single-clove garlic reveals complex market dynamics and production challenges. Common garlic, a staple crop widely cultivated globally, maintains

robust market demand but typically yields a lower price per kilogram compared to its specialized counterpart [41, 42]. In contrast, single-clove garlic emerges as a premium product, distinguished by its distinctive characteristics smaller bulbs, nuanced aromatic profile, and exceptional versatility in value-added product development, such as black garlic and artisanal pickled preparations. These unique attributes propel single-clove garlic to command a significantly higher market price, often surpassing common garlic by several multiples, despite demonstrating lower per-unit area yield [43]. However, this economic potential is tempered by substantial production challenges. The cultivation of single-clove garlic involves higher production costs, primarily stemming from the intricate and labor-intensive clove separation process. Furthermore, the limited proportion of plants successfully producing single-clove garlic introduces considerable uncertainty, potentially compromising the economic viability of large-scale commercial production.

The economic landscape surrounding single-clove garlic demands comprehensive research and strategic innovation. Future studies must focus on optimizing production methodologies, reducing operational costs, and enhancing overall efficiency. By systematically addressing these challenges, researchers and agricultural professionals can develop sustainable strategies that maximize the economic potential of single-clove garlic, ultimately creating more attractive opportunities for farmers seeking to diversify their crop portfolios.

5. Conclusions

This study concludes that to increase the proportion of single-clove garlic, inner cloves should be used as the mother plant due to their higher single-clove bulb formation rate than outer cloves. Moreover, the findings from this study suggest that for Thai farmers focused on producing normal garlic bulbs, it is recommended to use outer cloves as the mother plant. This is due to their higher proportion of normal bulb formation and potential for better bulb weight. Alternatively, planting both types together is suggested for easier separation during harvest. Overall, Thai single-clove garlic has higher bioactive compounds and antioxidant capacity compared to normal garlic, supporting the recommendation to consume Thai single-clove garlic to benefit local farmers. Further research and development are needed to enhance the proportion of single-clove garlic to improve production efficiency.

6. Acknowledgements

This work was supported by Faculty of Agriculture, Chiang Mai University and Graduate School, Chiang Mai University.

Author Contributions: Conceptualization, J.K., T.T. and S.T.; methodology, J.K., T.T., K.T., S.T. and S.T.; software, T.T.; validation, J.K. and T.T.; formal analysis, J.K. and T.T.; investigation, J.K., K.M. and S.T.; resources, J.K., K.T., S.T. and T.T.; data curation, J.K. and T.T.; writing original draft preparation, J.K. and T.T.; writing review and editing, J.K., S.T. and T.T.; visualization, J.K.; supervision, J.K., S.T. and S.T.; project administration, J.K.; funding acquisition, J.K. and S.T. All authors have read and agreed to the published version of the manuscript.

Funding: This research was partially supported by the Teaching Assistants and Research Assistants Scholarship, with research funding provided by the Multidisciplinary and Inter disciplinary School (MIdS) of Chiang Mai University, Chiang Mai, Thailand.

Conflicts of Interest: The authors declare no conflict of interest.

References

[1] Diretto, G.; Rubio-Moraga, A.; Argandona, J.; Castillo, P.; Gomez-Gomez, L.; Ahrazem, O. Tissue-specific accumulation of sulfur compounds and saponins in different parts of garlic cloves from purple and white ecotypes. *Molecules*. **2017**, *22*, 1359.

[2] Szychowski, K.A.; Rybczynska-Tkaczyk, K.; Gawel-Beben, K.; Swieca, M.; Karas, M.; Jakubczyk, A.; Matysiak, M.; Binduga, U.E.; Gminski, J. Characterization of active compounds of different garlic (*Allium sativum* L.) cultivars. *Polish Journal of Food and Nutrition Sciences*. **2018**, *68*, 73-81.

[3] Jones, M.G.; Collin, H.A.; Tregova, A.; Trueman; Trueman, L.; Brown, L.; Cosstick, R.; Hughes, J.; Milne, J.; Wilkinson, M.C.; Tomsett A.B.; Thomas, B. The biochemical and physiological genesis of alliin in garlic. *Medicinal and Aromatic Plant Science and Biotechnolology.* **2007**, *1*, 21-24.
[4] Yang, X.; Su, Y.; Wu, J.; Wan, W.; Chen, H.; Cao, X.; Wang, J.; Zhang, Z.; Wang, Y.; Ma, D.; Loake, G.J.; Jiang, J. Parallel analysis of global garlic gene expression and alliin content following leaf wounding. *BMC Plant Biology.* **2021**, *21*, 1-10.
[5] Batiha, E.G.; Beshbishy, A.M.; Wasef, L.G.; Elewa, Y.H.A.; Al–Sagan, A.A.; Abd-Elhack, M.E.; Taha, A.E.; Abd–Elhakim, Y.M.; Devkota, H.P. Chemical constituents and pharmacological activities of garlic (Allium sativum L.): A Review. *Nutrients*. **2020**, *12*, 1-21.
[6] Pakakaew, P.; Taesuwan, S.; Phimolsiripol, Y.; Utama-ang N. Comparison between the physicochemical properties, bioactive compounds and antioxidant activities of Thai and Chinese garlics. *Current Applied Science and Technology*. **2021**, *22*, 1-11.
[7] Susanti, Y.; Adriani, M.; Adi, A.C. Effect of single clove garlic extract (*Allium Sativum* Linn) on blood sugar levels, malondialdehyde, insulin levels and insulin resistance (experiments in rats (Rattus novergicus) induced by streptozotocin. *STRADA: Jurnal Ilmiah Kesehatan*. **2020**, *9*, 954-963.
[8] Horticultural Research Institute. Current garlic production situation. Available online: https://www.doa.go.th/hort/?p=19232 (accessed 26 April 2023). (In Thai)
[9] Austin, J.; Rattanakosol, P.; Chokpachuen, J.; Siriyan, R.; Sakuanrungsirikul, S.; Ketsakul, S.; Rukkaphan, A. and Nimkingrat, T. Verification the identity of garlic from different growing area. *Thai Agricultural Research Journal.* **2016,** *34*, 253-269. (In Thai)
[10] Innoi, A. Optimum rate of nitrogen fertilizer for garlic production in northern Thailand. Master thesis. Chiang Mai University, Chiang Mai, Thailand. **2018**. (In Thai)
[11] Thailand Agricultural Research Repository. Single-clove garlic, adding value through processing. Available online: https://blog.arda.or.th/1559/vegetables/กระเทียมโทน/ (accessed 16 August 2024). (In Thai)
[12] Arifah, S.N.; Atho'illah, M.F.; Lukiati, B.; Lestari, S.R. Herbal medicine from single clove garlic oil extract ameliorates hepatic steatosis and oxidative status in high fat diet mice. *The Malaysian Journal of Medical Sciences*. **2020**, *27*, 46-56.
[13] Gofur, A.; Wulandari, I.; Arifah, S.N.; Athoillah, M.F.; Witjoro, A.; Lestari, S.R. Single clove garlic (Allium sativum) essential oil as an inhibitor of Staphylococcus aureus bacteria. Biosaintifika: *Journal of Biology and Biology Education*. **2019**, *11*, 77-83.
[14] Samritluan, K. Garlic; Nanmeebooks: Bangkok, Thailand, 52 p. (In Thai)
[15] Kaewpiboon, C.; Boonnak, N. Evaluation of the antioxidant activities of black single bulb form of elephant garlic (*Allium ampeloprasum* var. *ampeloprasum*). *Thai Science and Technology Journal*. **2020**, *29*, 111-118. (In Thai)
[16] Meredith, T.J. The complete book of garlic: a guide for gardeners, growers, and serious cook; Timber Press: Oregon, US., **2008**, 330.
[17] Atif, M.J.; Amin, B.; Ghani, M.I.; Ali, M.; Cheng, Z. Variation in morphological and quality parameters in garlic (*Allium sativum* L.) bulb influenced by different photoperiod, temperature, sowing and harvesting time. *Plants*. **2020**, *155*, 1-15.
[18] Atif, M.J.; Amin, B.; Ghani, M.I.; Ali, M.; Liu, X.; Zhang, Y.; Cheng, Z. *Allium sativum* L. (Garlic) bulb enlargement as influenced by differential combinations of photoperiod and temperature. *Food Chemistry*. **2021**, *338*, 1-9.
[19] Wu, C.; Wang, M.; Dong, Y.; Cheng, Z.; Meng, H. Growth, bolting and yield of garlic (*Allium sativum* L.) in response to clove chilling treatment. *Scientia Horticulturae*. **2015**, *194*, 43-52.
[20] Desta, B.; Tena, N.; Amare, G. Growth and Bulb Yield of Garlic as Influenced by clove size. *The Scientific World Journal*. **2021**, *2021,* 1-7.
[21] Anikoh, P. O.; Ozivave, Z. O.; Ogbaje, H.; Metiboba, C. T.; Egbunu, M. M. Effect of bulb size, Dept of bulb storage and bulb orientation on storage loss of onion (*Allium cepa* L.). *FUDMA Journal of Agriculture and Agricultural Technology*. **2023,** *9,* 41-49.
[22] Zhu, Q.; Kakino, K.; Nogami, C.; Ohnuki, K.; Shimizu, K. An LC-MS/MS-SRM method for simultaneous quantification of four representative organosulfur compounds in garlic products. *Food Analytical Methods*. **2016**, *9*, 3378-3384.

[23] Bocchini, P., C. Andalò, R. Pozzi, G.C. Galletti and A. Antonelli. Determination of diallyl thiosulfinate (allicin) in garlic (*Allium sativum* L.) by high-performance liquid chromatography with a post-column photochemical reactor. *Analytica Chimica Acta*. **2001**, *441*(1), 37-43.
[24] Wongsa, P.; Spreer, W.; Sruamsiri, P.; Müller, J. Allicin and total phenolic content and antioxidant activity in conventional and organic garlic. *Acta Horticulturae*. **2016**, *1125*, 129-136.
[25] Qin, F.F.; Xu, H.L.; Xu, Q.C.; Li, F.; Fujimiya, S. The single-clove garlic used as seed for high yield. In Proceedings of the 233rd Crop Science Society of Japan, Kanto, Japan, 27 March 2012; 286.
[26] Rungcharoen, J.; Mitharn, S.; Suriyawong, N. Selection of garlic cultivars and technology of garlic cultivation in highland areas. Available online: https://research.hrdi.or.th/research/detail/359/. (accessed 26 April 2023). (In Thai)
[27] Shiferaw, D.; Nigussie-Dechassa, R.; Woldetsadik, K.; Shama, J.; Getachew, T. Bulb quality of garlic (*Allium sativum* L.) as influenced by the application of inorganic fertilizers. *African Journal of Agricultural Research*. **2014**, *9*, 784-796.
[28] Innoi, A.; Kunasakdakul, K.; Santasup, C. Optimum rate of nitrogen fertilizer for garlic production in Khun Yuam district, Mae Hong Son province. *Journal of Agriculture*. **2019**, *35*, 215-226. (In Thai)
[29] Calimpang, I.; Bane-Eng, M.; Sagun, A. Classification of clove sizes as planting material to the bulb yield of garlic var. Ilocos white. *Journal of Biodiversity and Environmental Sciences*. **2023,** *22,* 62-69.
[30] Malashri; Shashidhar, Tr. Impact of planting methods and clove size on growth, yield and economics of garlic (*Allium sativum* L.). *International Journal of Chemical Studies*. **2020,** *6,* 1853-1856.
[31] Feng, J.; Hussain, H.A.; Hussain, S.; Shi, C.; Cholidah, L.; Men, S.; Ke, J.; Wang, L. Optimum water and fertilizer management for better growth and resource use efficiency of rapeseed in rainy and drought seasons. *Sustainability*. **2020,** *12*, 703. https://doi.org/10.3390/su12020703
[32] Ammarellou, A. Bulb production of 38 Iranian garlic (*Allium sativum* L.) cultivars in greenhouse conditions. *Journal of Medicinal plants and By-product*. **2017**, *6*, 105-110.
[33] Lopez-Bellido, F.J.; Lopez-Bellido, R.J.; Muñoz-Romero, V.; Fernandez-Garcia, P.; Lopez-Bellido, L. New phenological growth stages of garlic (*Allium sativum*). *Annals of Applied Biology*. **2016**, *169*, 423-439.
[34] Mathew, D.; Forerb, Y.; Rabinowitchc, H.D.; Kamenetsky, R. Effect of long photoperiod on the reproductive and bulbing processes in garlic (*Allium sativum* L.) genotypes. *Environmental and Experimental Botany*. **2011**, *71*, 166-173.
[35] Westerfield, R.; Adams, D.; Eaker, T. Homegarden series: garlic production for the gardener. Full review. Available online: https://secure.caes.uga.edu/extension/publications/files/pdf/C%20854_8.PDF. (accessed 14 Jun 2023).
[36] Kunasakdakul, K.; Panyakorn, W.; Panya, K.; Chaichana, I.; Buranapanichpan, S.; Santasup, C.; Yaiprasarn, K., Chantaracha, A.; Rattanaplome, N.; Samana, M., Tajumpa, E.; Kongmee, W.; Prayoonsaengrasamee, S.; Panse, W.; Suwan-apa, W.; Angkaen; Inthraprasit, T.; Wongpanya, S. Promoting farmers' potential for producing garlic and shallots using organic farming systems. Available online: https://digital.library.tu.ac.th/tu_dc/frontend/Info/item/dc:172148. (accessed 26 April 2023). (In Thai)
[37] Tresina, P.S.; Santhiya Selvam, M.; Doss, A.; Mohan. V.R. Chapter 3 - Antidiabetic bioactive natural products from medicinal plants studies. In Natural Products Chemistry; Editor Rahman, A.; Elsevier: California, US. **2022**, *75*, pp. 75-118.
[38] Arzanlou, M.; Bohlooli, S. Introducing of green garlic plant as a new source of allicin. *Food Chemistry*. **2010**, *120*, 179-183.
[39] Bloem, E.; Haneklaus, S.; Schnug, E. Influence of fertilizer practices on S-containing metabolites in garlic (*Allium sativum* L.) under field conditions. *Journal of Agricultural and Food Chemistry*. **2010**, *58*, 10690-10696.
[40] Nasim S.A.; Dhir, B.; Samar, F.; Rashmi, K.; Mahmooduzzafar; Mujib, A. Sulphur treatment alters the therapeutic potency of alliin obtained from garlic leaf extract. *Food and Chemical Toxicology*. **2009**, *47*, 888-892.
[41] Office of Agricultural Economics. Agricultural production index. Available online: https://translate.google.com/?sl=th&tl=en&text=ดัชนีผลผลิตสินค้าเกษตร&op=translate (accessed 26 October 2024). (In Thai)
[42] Ministry of Commerce. Garlic price (2023-2024). Available online: https://regional.moc.go.th/th/file/get/file/20240227555fe7b149358dfbad39d3e2cc2a3d19091016.pdf (accessed 26 October 2024). (In Thai)
[43] Thai News Agency MCOT Pcl. Pricing of Nam Pad single clove garlic. Available online: https://tna.mcot.net/agriculture-905044#google_vignette (accessed 26 October 2024). (In Thai)

ASEAN
Journal of Scientific and Technological Reports
Online ISSN:2773-8752

Research article

Estimating the Ratios of Masonry Wall and Wall Finishing Work to the Building Area, Considering Only the Area within the Building's Boundaries: A Case Study of a Two-story Reinforced Concrete House

Watcharapong Deewong[1*]

[1] Faculty of Technology, Udon Thani Rajabhat University, Udon Thani, 41000, Thailand
* Correspondence: dwatchr@udru.ac.th

Citation:
Deewong, W. Estimating the ratio of masonry wall and wall finishing work to the building area, considering only the area within the building's boundaries: a case study of a two-story reinforced concrete house. *ASEAN J. Sci. Tech. Report.* **2025**, *28*(1), e255748. https://doi.org/10.55164/ajstr.v28i1.255748

Article history:
Received: September 3, 2024
Revised: December 6, 2024
Accepted: December 9, 2024
Available online: February 17, 2025

Publisher's Note:
This article has been published and distributed under the terms of Thaksin University.

Abstract: This research aims to study the ratios of the quantity of masonry wall and wall finishing per unit of a major factor that can be easily calculated: the building area, considering only the area that falls within the building's boundaries. A two-story reinforced concrete residential house is used as a case study. Building area calculation and detailed quantity takeoff of masonry wall and wall finishing are implemented for the house designs of 56 samples. Pearson's correlation coefficient determines the relationship between the major factor and the quantity of work studied to identify a major factor's practicality. The ratios of the quantities of work studied to the major factor are examined using mean statistics and the distribution range according to the Empirical Rule with a 95% coverage probability. The results indicate that the size of the floor area within the building's boundaries is suitable as a major factor for a rough estimation of masonry wall and wall finishing, as it shows a very high correlation with the quantities of work studied. When testing the results against three house designs, it was found that the ratios calculated from the detailed takeoffs of the three houses fell within the range of the study's results and that the differences from the average study results were within the acceptable accuracy range of the rough estimation method, which could vary by 20-30%.

Keywords: Ratio; Rough estimation; Masonry wall; Wall finishing work

1. Introduction

Masonry walls are widely used in construction due to their strength, durability, and aesthetic appeal. Additionally, they bond well with the structural systems of buildings, often made of reinforced concrete, as cement is a key component in both [1]. Calculating the quantity of masonry walls is the most critical task in the architectural category, as it serves as a reference for estimating the quantity of wall finishing work, which includes plastering and painting, as well as various wall cladding materials such as wall tiles [2].

Estimating the quantity of masonry walls in a building project is a complex and time-consuming process [3]. At the same time, quantifying the finishing work on walls is equally challenging. To conduct a detailed quantity takeoff for both types of work, information from various construction drawings is required, including floor plans, elevations, sections, and details for doors, windows, as well as bathrooms and stairs, which are necessary because there may be bathroom or storage walls located underneath the stairs. Consequently,

there is a significant chance of errors, whether from inaccurate measurements or counts, incorrect calculation formulas, or simply forgetting items. One common approach to verify the accuracy or identify discrepancies in detailed quantity takeoffs is to compare the calculations with rough estimates [4].

Rough or preliminary estimation is used when speed is essential, but high accuracy is not yet required. It is based on the idea that various constructions have a single major factor that determines the price, and this variable is directly proportional to the construction cost. This estimation method yields approximately accurate results within a range of 20-30% [4]. Examples of the aforementioned key factors include building area or volume and usage quantity, such as the number of hotel rooms and the number of hospital beds. This approach serves for direct price estimation and is applied to roughly estimate the quantities of various significant tasks in construction work.

The rough estimation of work quantities using a single major factor has been widely used for a long time in the structural category, particularly in reinforced concrete structures. Reference ratio figures are from various sources, including textbooks and research studies [5-8]. In the architectural category, there are only masonry wall works, often presented as linear regression equations with the building area as the major factor [3, 9-10]. However, no information could be found in any sources, including books, manuals, or research studies for wall finishing work.

Wall finishing work involves plastering, painting, or applying decorative materials on the surface of masonry walls [4]. Generally, the total area of wall finishing work is equal to twice the area of the masonry wall [2], depending on whether both sides of the wall are finished. Nevertheless, this relationship is sufficient to demonstrate that the total quantity of wall finishing is related to the area of the masonry. Therefore, if the building area can be defined as a major factor for estimating the masonry area, it is reasonable to estimate the total wall finishing work area.

The Valuers Association of Thailand [11] has provided guidelines for calculating the area of a building, stating that only the area within the structural boundaries of the building should be considered. Roof areas are not included. Areas that extend from the building, such as washing areas, balconies, and parking spaces, will only be included if they are under the roof of the building or have a structure that is integral to the building's structure. Examples of areas that should be included are washing areas or parking spaces under the building's roof and upper-level balconies structurally connected to the building. Some areas that should not be included are external washing areas and parking lots that are not under the building's roof. However, the area calculation based on this concept aims to use the obtained area size to estimate the preliminary construction costs. Therefore, it includes the overhanging areas of the building that are not within the boundary of the wall construction work, such as upper balconies, which may not be necessary for a rough estimate of the masonry wall and wall finishing quantities. This has led the researcher to wonder whether removing the overhanging areas and using only the area within the building's boundaries would be reasonable as a major factor for a rough estimate of the masonry wall and wall finishing work quantities. If this can be done, it would make the work process easier and more efficient.

According to the above argumentations, this study examines the ratios of masonry wall and wall finishing to a unit of the major factor, which can be easily calculated, i.e., building area, considering only the area within the building's boundaries. This refers to the area of the building that lies within the confines of its structure or the building itself. The overhanging area is included only when there are surrounding walls. The study focuses specifically on the case of two-story reinforced concrete residential houses and has the following specific objectives:

1) To study the relationship between the significant factor, i.e., building area, considering only the area within the building's boundaries, and the quantity of masonry wall and wall finishing, to identify the practicality of using it as a significant factor for rough quantity estimation of masonry wall and wall finishing.

2) To study the average and range of distribution of the ratios of masonry wall and wall finishing to the building area, considering only the area within the building's boundaries.

2. Materials and Methods

The study method consists of three main steps: (1) sample selection, (2) quantity measurement, and (3) data analysis.

2.1 Sample Selection

The two-story house designs studied consist of 56 samples, selected using purposive sampling from the free house designs, the Ban Yim, for the public project, phase 3, by the Bangkok Metropolitan Administration. This number is sufficient as it aligns with the Central Limit Theorem, which states that if there are more than 30 samples, the sample group will exhibit a normal distribution [12]. In addition, it is a number greater than 28 samples, which is the minimum required sample size for testing the significance of the correlation between two variables, with a large expected effect size (r=0.5), a significance level (α) of 0.05, and a power of the test equal to 0.8 [13]. The criteria for selecting samples of two-story houses are as follows:

1) It must be a two-story residential house with complete architectural and structural engineering work details.

2) All house walls, exterior and interior, must be made of one type of masonry material, such as brick, lightweight block, concrete block, etc.

3) All masonry panels must have the characteristics of standard masonry panels, meaning they should be laid in a straight line without any curved lines, and the panels must be positioned vertically without tilting.

2.2 Quantity Measurement

2.2.1 Building area

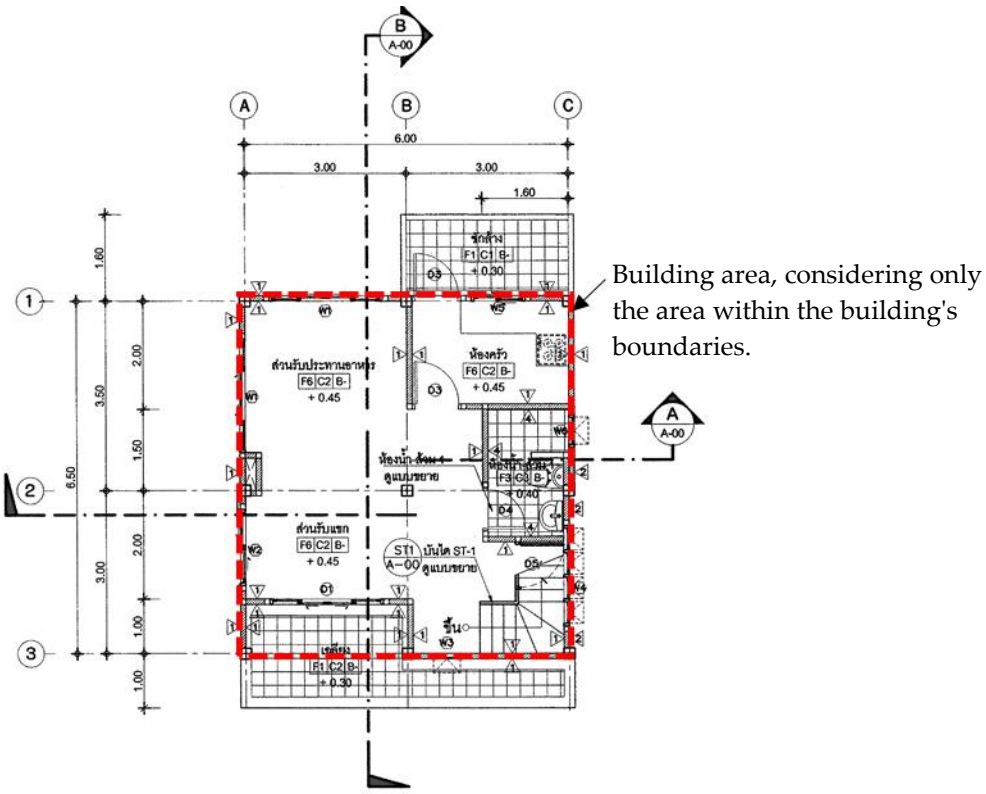


Figure 1. Guidelines for measuring the area of a building, considering only the area within the building's boundaries.

Considering only the area that falls within the building's boundaries, the building area is proposed to be a significant factor for rough quantity estimation of masonry wall and wall finishing. This refers to the area of the building that lies within the confines of its structure or the building itself. The overhanging area is included only when there are surrounding walls. The size of the area is calculated in square meters, and the measurements of the various sides will be taken from the outer edge to the outer edge of the columns or beams, as shown in Figure 1; it is adapted from the free house design, ID33, of the Ban Yim for the public project, phase 3, by the Bangkok Metropolitan Administration [14].

2.2.2 Quantity of masonry wall

The quantity of masonry walls will be calculated from the square-meter net wall area. This can be determined by summing the whole area of each wall panel and subtracting the total area of all openings or door and window frames without deducting the area of columns and lintels. Smaller than 0.1 square meter openings won't be considered [15] since it has a minimal effect on the overall quantity of masonry wall. The length of the wall panels will be measured without deducting the size of the columns, as this is more convenient and yields a calculation result that does not differ significantly from deducting the size of the columns [2] (p. 56), especially for buildings with columns not exceeding 0.25 meters in size [16]. For the height of the walls, consider the underside of the beams or floors as applicable [16]. As for measuring the size of openings or doors and windows, consider the outer edges of the frames [2] (pp. 63-64).

In buildings, the masonry wall can be either single-layer or double-layer. Therefore, the quantity takeoff must be calculated separately for each part. However, to simplify the overall study, the quantity of double-layer masonry walls is converted into single-layer masonry walls by multiplying by two [17]. Next, merge it with the quantity of single-layer masonry wall, known as equivalent single-layer masonry wall. Therefore, the quantity of masonry wall work in this study is divided into three parts: 1) single-layer masonry wall, 2) double-layer masonry wall, and 3) equivalent single-layer masonry wall. The details of the calculation formula are as shown in equations (1) – (3).

$$\text{SB} = \text{Total area of single-layer masonry wall panel} - \text{Total area of openings on single-layer masonry} \quad (1)$$

$$\text{DB} = \text{Total area of double-layer masonry wall panel} - \text{Total area of openings on double-layer masonry} \quad (2)$$

$$\text{eqSB} = \text{SB} + 2 \cdot \text{DB} \quad (3)$$

When: SB = The quantity of single-layer masonry wall, m^2
DB = The quantity of double-layer brick wall work, m^2
eqSB = The quantity of equivalent single-layer masonry wall, m^2

2.2.3 Quantity of wall finishing work

The quantity of wall finishing will be calculated in square meters. The types of finishing can be divided into two categories: 1) finishing with cement or plaster to prepare for painting or coating, and 2) finishing with wall cladding materials, such as tiles [2]. The finishing area not only includes the surface of the wall panels but also extends to the surfaces of the structure and other materials that need to be finished with the same type of material to create a continuous surface. Calculating the quantity of wall finishing is divided into two parts: 1) external wall finishing and 2) internal wall finishing, for convenience in using the information for verification and reference when calculating the area of wall surface finishing according to various sub-items [2].

The total quantity of external wall finishing is estimated from the sum of the surface area of the outer side of the exterior walls and the outer surface of the reinforced concrete structure. Since the length of the walls has already included the size of the columns, the surface of the reinforced concrete structure is only calculated for the beam sections. The total quantity of internal wall finishing is estimated from the sum of the inner surface area of the exterior walls and both sides of the interior walls. The details of the calculation formula are as shown in equations (4) – (5)

$$\text{FNex} = \text{Outer surface area of exterior masonry wall} + \text{Outer surface area of reinforced concrete beam} \quad (4)$$

$$\text{FNin} = \text{Inter-surface area of exterior masonry wall} + \text{Surface area of both sides of inner masonry wall} \quad (5)$$

When: FNex = The quantity of exterior wall finishing work, m^2
FNin = The quantity of interior wall finishing work, m^2

2.3 Data Analysis

Data analysis is divided into four main parts, namely:

1) The analysis of general characteristics of data using descriptive statistics includes frequency (N), percentage (%), mean ($\overline{X}$), and standard deviation (SD).

2) The relationship between the significant factor, i.e., building area, considering only the area within the building's boundaries, and the quantity of masonry wall and wall finishing, is analyzed using Pearson's Correlation Coefficient. Among the relationships examined are:

2.1) The relationship between the major factor and equivalent single-layer masonry wall quantity.

2.2) The relationship between the major factor and exterior wall finishing work quantity.

2.3) The relationship between the major factor and the interior wall finishing work quantity.

In this regard, the consideration of the correlation coefficient (r) for interpreting the level of correlation uses the following criteria [18]:

r equals 0 means no correlation.

r is between 0.01 – 0.09, which means it is deficient.

r is between 0.10 – 0.29, which means it is low.

r is between 0.30 – 0.49, which means moderate.

r is between 0.50 – 0.69, which means it is high.

r is between 0.70 – 0.89, which means it is very high.

r is between 0.90 – 1.00, which means it is almost perfect.

3) The analysis to find the mean and the distribution range of the ratios of the quantities of work studied to the significant factor consists of 1) calculating the mean ($\overline{X}$) and the standard deviation (SD), and 2) determining the range of distribution of the ratios according to the Empirical Rule with a 95% coverage probability, which states that if the data is usually distributed, approximately 95% of the data will be in the range of $\overline{X} \pm 2SD$ [19]. Among the ratios studied include:

3.1) The ratio of equivalent single-layer masonry wall quantity to the building area, considering only the area within the building's boundaries.

3.2) The ratio of the quantity of exterior wall finishing work to the building area, considering only the area within the building's boundaries.

3.3) The ratio of the quantity of interior wall finishing work to the building, considering only the area within the building's boundaries.

4) Testing the mean and range of the ratios obtained from the study by comparing them with those calculated from 3 other two-story houses that are not part of the sample group.

3. Results and Discussion

The results of this research study are divided into four main topics: 1) general characteristics of the data, 2) the relationship between the main factor and the quantities of work studied, 3) the mean and range of the distribution of the ratios of the quantities of work studied to the major factor, and 4) testing of the mean and range of the distribution of the ratios obtained from the study.

3.1 General Characteristics of the Data

The preliminary data analysis of the selected two-story house designs, totaling 56 samples (details as shown in Table 1), reveals that:

1) The area of the building, considering only the part within the building's boundaries, ranges from 62.32 to 317.04 square meters; the mean ($\overline{X}$) is equal to 162.39 square square meters (SD = 44.50).

2) The quantity of single-layer masonry walls has an area ranging from 101.74 to 416.54 square meters; the mean ($\overline{X}$) is equal to 234.23 square square meters (SD = 60.81).

3) The quantity of double-layer masonry wall has an area ranging from 0.00 to 243.78 square meters; the mean ($\bar{X}$) is equal to 53.54 square square meters (SD = 55.90).

4) The quantity of masonry wall, when converted to equivalent single-layer masonry walls, has an area ranging from 200.58 to 700.82 square meters; the mean ($\bar{X}$) is equal to 341.31 square square meters (SD = 106.24).

5) The quantity of work for exterior wall finishing has an area ranging from 153.08 to 352.58 square meters; the mean ($\bar{X}$) is equal to 239.62 square square meters (SD = 49.82).

6) The quantity of work for interior wall finishing ranges from 187.11 to 627.37 square meters. the mean ($\bar{X}$) is equal to 352.09 square square meters (SD = 89.61).

Table 1. The building area and the quantities of work studied for 56 sample house designs.

Descriptions	Min. (m^2)	Max. (m^2)	$\bar{X}$ (m^2)	SD (m^2)
Building area, only the area within the building's boundaries (Abb), m^2	62.32	317.04	162.39	44.50
The quantity of single-layer masonry wall (SB), m^2	101.74	416.54	234.23	60.81
The quantity of double-layer masonry wall (DB), m^2	0.00	243.78	53.54	55.90
The quantity of equivalent single-layer masonry wall (eqSB), m^2	200.58	700.82	341.31	106.24
The quantity of exterior wall finishing work (FNex), m^2	153.08	352.58	239.62	49.82
The quantity of interior wall finishing work (FNin), m^2	187.11	627.37	352.09	89.61

3.2 Relationship between the Main factor and the Quantities of Work Studied

The analysis of the relationship between the major factor, which is the area of the building specific to the boundaries of the structure, and the quantities of work studied (details as shown in Table 2) reveals that the major factor has a very high positive correlation with all three quantities of work studied, with statistical significance at the 0.01 level. The quantity of interior wall finishing work has the highest correlation coefficient with the major factor (r = 0.840), followed by the quantity of equivalent single-layer masonry wall and the quantity of exterior wall finishing work, respectively (r = 0.773 and r = 0.725). Therefore, it is practical to use the area of the building specific to the boundaries of the structure as the major factor for a rough estimation of the quantity of equivalent single-layer masonry wall, exterior wall finishing work, and interior wall finishing work.

Table 2. Relationship between the main factor and the quantities of work studied.

Pairs of Relationships	r	Correlation Interpretation
Building area, only the area within the building's boundaries (Abb) and The quantity of equivalent single-layer masonry wall (eqSB)	0.773**	Very high positive
Building area, only the area within the building's boundaries (Abb) and The quantity of exterior wall finishing work (FNex)	0.725**	Very high positive
Building area, only the area within the building's boundaries (Abb) and The quantity of interior wall finishing work (FNin)	0.840**	Very high positive

** Correlation is a significant level at the 0.01 (2-tailed).

3.3 Mean and Range of the Distribution of the Ratios of the Quantities of Work Studied to the Major Factor

The analysis of the ratios of the quantities of work studied to the major factor, which is the size of the building area, specifically within the boundaries of the building (details as shown in Table 3), reveals that:

1) The ratio of the quantity of equivalent single-layer masonry wall to the building area, considering only the area within the building's boundaries (eqSB/Abb), has a mean ($\bar{X}$) of 2.07 (SD = 0.43) and a distribution range that covers 95% of the data according to empirical rules, between 1.21 and 2.93.

2) The ratio of the quantity of exterior wall finishing work to the building area, considering only the area within the building's boundaries (FNex/Abb), has a mean ($\bar{X}$) of 1.49 (SD = 0.27), and the range of distribution covers 95% of the data, according to empirical rules, is between 0.95 and 2.03.

3) The ratio of the quantity of interior wall finishing work/area of the building area, considering only the area within the building's boundaries (FNin/Abb), has a mean ($\bar{X}$) of 2.14 (SD = 0.36) and a distribution range that covers 95% of the data according to empirical rules, which is 1.42 – 2.86.

Table 3. Mean and range of the distribution of the ratios of the quantities of work studied to the major factor.

Ratios	N	$\bar{X}$ (m²)	SD (m²)	Distribution range with a 95% coverage probability	
				$\bar{X}$ - 2SD (m²)	$\bar{X}$ + 2SD (m²)
The quantity of equivalent single-layer masonry wall (eqSB)/ Building area, only the area within the building's boundaries (Abb)	56	2.07	0.43	1.21	2.93
The quantity of exterior wall finishing work (FNex)/ Building area, only the area within the building's boundaries (Abb)	56	1.49	0.27	0.95	2.03
The quantity of interior wall finishing work (FNin)/ Building area, only the area within the building's boundaries (Abb)	56	2.14	0.36	1.42	2.86

3.4 Testing of the Mean and Range of the Distribution of the Ratios Obtained from the Study

Three additional two-story reinforced concrete residential houses that are not part of the sample group are selected to test the results obtained from the study. The area of the building is measured precisely for the parts within the building's boundaries, and a detailed quantity takeoff is conducted for the masonry and wall finishing work. The details of the quantity takeoff are shown in Table 4. Subsequently, essential ratios were calculated: 1) the quantity of single-layer masonry work per the area of the building within the building's boundaries, 2) the quantity of exterior wall finishing work per the area of the building within the building's boundaries, and 3) the quantity of interior wall finishing work per the area of the building within the building's boundaries. These calculated values are then compared with the mean and range of ratios obtained from the study results. Overall, the comparison reveals that the ratios calculated from the three houses fell within the range of the study results, with the most significant difference from the average study result being 27.52%, which is within the acceptable margin of error for rough estimation methods that may vary by 20-30% [4]. The details of the comparison are in Table 5.

Table 4. The building area and the quantities of work were studied for three additional house designs.

House no.	Building area, only the area within the building's boundaries (Abb), m²	The quantity of single-layer masonry wall (SB), m²	The quantity of double-layer masonry wall (DB), m²	The quantity of equivalent single-layer masonry wall (eqSB), m²	The quantity of exterior wall finishing work (FNex), m²	The quantity of interior wall finishing work (FNin), m²
1	128.32	279.76	18.31	316.38	243.95	333.42
2	169.70	278.73	26.41	331.54	236.72	379.81
3	220.96	277.49	54.34	386.18	245.69	426.58

Table 5. Comparing the ratios of the selected houses with the mean and range of the ratios from the study.

House no.	eqSB/Abb			FNex/Abb			FNin/Abb		
	Ratio of selected house	Diff. from Derived Mean $\bar{X}$ = 2.07	Compare with Derived Range [1.21, 2.93]	Ratio of selected house	Diff. from Derived Mean $\bar{X}$ = 1.49	Compare with Derived Range [0.95, 2.03]	Ratio of selected house	Diff. from Derived Mean $\bar{X}$ = 2.14	Compare with Derived Range [1.42, 2.86]
1	2.47	19.32%	within the range	1.90	27.52%	within the range	2.60	21.50%	within the range
2	1.95	– 5.80%	within the range	1.39	– 6.71%	within the range	2.24	4.67%	within the range
3	1.75	– 15.46%	within the range	1.11	– 25.50%	within the range	1.93	– 9.81%	within the range

4. Conclusions

The detailed quantity of masonry wall and wall finishing work is complex and challenging, with a significant chance of errors. This research study investigates the ratios, both in average and distribution range, of the quantities of masonry and wall finishing work per unit of a major factor that can be easily calculated, i.e., the building area, considering only the area that falls within the building's boundaries. This is intended for use in rough estimates of the quantities of masonry and wall finishing work in the case of a two-story concrete residential house. Estimators or stakeholders can utilize the ratio values from this study to compare or verify any discrepancies in the detailed quantity takeoff of building projects comparable to the sample under study. However, this study's methodology applies to other construction projects. The findings of the study can be summarized as follows:

1) The area of the building, considering only the area within the building's boundaries, is suitable to be a primary variable for a rough estimate of the quantity of single-layer brickwork, external wall finishes, and internal wall finishes, as it has a very high correlation with all three tasks (with r values ranging from 0.7 to 0.89).

2) The ratio of the quantity of equivalent single-layer brick walls to the area of the building, considering only the area within the building's boundaries, has an average value of 2.07, with a distribution range that covers 95% of the data between 1.21 and 2.93.

3) The ratio of the quantity of work for exterior wall finishing to the area of the building, considering only the area within the building's boundaries, has an average value of 1.49, with a distribution range that covers 95% of the data between 0.95 and 2.03.

4) The ratio of the quantity of interior wall finishing work to the area of the building, considering only the area within the building's boundaries, has an average value of 2.14, with a distribution range that covers 95% of the data between 1.42 and 2.86.

5) The testing of the average and range of the ratios obtained from the study, compared to the ratios calculated from the detailed measurements of three two-story houses, found that the ratios from all three houses fell within the range of the study results and differed from the average study result by no more than 30%, which is within the accuracy limits of the preliminary estimation method.

However, when considering the usage of double-layer masonry walls in the sample house designs, it is found that the minimum value is 0 square meters. There is no usage, while the maximum value is 243.78 square meters. This shows that the sample house designs utilize double-layer masonry walls in varying quantities, which may affect the ratio of equivalent single-layer masonry work relative to the building area. Therefore, in future studies, guidelines should address this issue, such as standardizing the sample house designs to have similar proportions of double-layer masonry work.

Author Contributions: Conceptualization, methodology, formal analysis, validation, and writing—original draft preparation, W.D.

Funding: This research received no external funding.

Conflicts of Interest: The authors declare no conflict of interest.

References

[1] Deewong, W. *Control and Inspection in Construction* [Online]; Udon Thani Rajabhat University: Udonthai, Thailand, **2021**, 100. https:// technology.udru.ac.th/ book. (accessed on 10 May 2024).
[2] Supasri, P. *Bidding and Cost Mastering*; S. Asia Press: Bangkok, Thailand, **2004**.
[3] Monkaew, S.; Choosakul, C. Develop an Estimating Factor to Help Estimating Masonry Wall Area of Two Stories Houses. *ASEAN J. Sci. Tech. Report*. **2021**, *24*(2), 115-124.
[4] Chovichien, V. *Construction Cost Estimation*, 8th ed.; P.S. Commercial: Bangkok, Thailand, **2010**.
[5] Intulak, P. *Construction Materials, Cost Estimation, and Bidding Tips*, 4th ed.; Odeonstore: Bangkok, Thailand, **1990**, 239-241.
[6] Sunthornsamai, P. *Estimating the Quantity of Construction Materials for a Building (Shortcut Method)*, 6th ed.; TPA Publishing: Bangkok, Thailand, **2005**.
[7] Dangprasert, S.; Bal-yen, M.; Chaivijarn, C. *Unit Quantity Estimate for 5-9 Story Residential Buildings*. In Civil Engineering and Local Development, Proceedings of the 15th National Convention on Civil Engineering (NCCE15), Ubon Ratchathani, Thailand, May 12-14, 2010, Ubon Ratchathani University: Ubon Ratchathani, **2010**, CEM007.
[8] Chaiwijarn, C.; Jarusbumrungroj, P; Woracharoensin, T; Sirisonthi, A.; Wongsopit, K. The Comparison Study of Unit Quantities Estimation for 5-8 and 3-5 Storeys Residential Buildings. *Kasem Bundit Engineering Journal*. **2017**, *7*(2), 94-107.
[9] Prapaporn, W.; Chetchotisak, P. *The Material Quantity Relationship of Reinforce Concrete Building Analysis by Using the Multiple Regressions Model*. In Civil Engineering Beyond the Limit Development, Proceedings of the 22nd National Convention on Civil Engineering (NCCE22), Nakhon Ratchasima, Thailand, July 18-20, 2017; Rajamangala University of Technology Isan and Suranaree University of Technology: Nakhon Ratchasima, **2017**, CEM-111.
[10] Prapaporn, W.; Boonrat, P.; Tapanthong, P.; Kawmungkun, K. The Limitation of Reinforcement Quality Reservation for Reinforced Concrete Structure Using Building Information Modeling: BIM. *Kasem Bundit Engineering Journal*. **2019**, *9*(3), 62-83.
[11] The Valuers Association of Thailand, *Standard Price List for Construction Costs of Houses and Buildings 2023-2024* [Online]. https://vat.or.th. (accessed on 10 May 2024).
[12] Field, A. *Discovering Statistics Using IBM SPSS Statistics*, 4th ed.; Sage: London, UK, **2013**, 871.
[13] Cohen, J. A Power Primer. *Psychological Bulletin*, **1992**, *112*(1), 155–159.
[14] Bangkok Metropolitan Administration, *Ban Yim for the Public Project* [Online]. https://sites.google.com/view/yota-bma-smilehouse-phase3/home. (accessed on 10 May 2024).
[15] The Engineering Institute of Thailand under H.M.The King's Patronage (EIT), *Guidelines for Measuring the Quantity of Building Construction*, 7th ed.; EIT: Bangkok, Thailand, **2016**, *25*.
[16] Suwansukroad, N. *Construction Estimation*, 5th ed.; Khon Kaen University: Khon Kaen, Thailand, **2006**.
[17] Kawee Wangniwetkul, *Construction Cost Estimating*; SE-ED: Bangkok, Thailand, **2009**, *144*.
[18] De Vaus, D. A. *Surveys in Social Research*, 5th ed.; Allen & Unwin: NSW, Australia, **2002**, *259*.
[19] Johnson, A. R.; Bhattacharyya, G. K. *Statistics: Principal and Method*, 6th ed.; John Wiley & Sons: Hoboken, NJ, **2010**, *53*.

ASEAN
Journal of Scientific and Technological Reports
Online ISSN:2773-8752

Research article

Enhancing Voltage Stability of a Microgrid in the Presence of PV Plants Using Storage System

Nirdesh Singh[1*], and D. K. Jain[2]

[1] Deenbandhu Chhotu Ram University of Science and Technology Sonepat, 131039, India
[2] Deenbandhu Chhotu Ram University of Science and Technology Sonepat, 131039, India
* Correspondence: singh.niru28@gmail.com

Citation:
Singh, N.; Jain, D.K.; Enhancing voltage stability of a microgrid in the presence of PV plants using storage system. *ASEAN J. Sci. Tech. Report.* **2025**, *28*(1), e254201. https://doi.org/10.55164/ajstr.v28i1.254201

Article history:
Received: May 22, 2024
Revised: October 16, 2024
Accepted: November 9, 2024
Available online: February 16, 2025

Publisher's Note:
This article has been published and distributed under the terms of Thaksin University.

Abstract: Due to the nearly inertia-free nature of the voltage source converter (VSC) based microgrid (MG), any fluctuations in the generation profile have an extremely detrimental effect on the voltage profile. A load imbalance at the point of common coupling (PCC) exacerbates the issue even further. Energy storage systems are critical components that ensure stability and dependability in microgrids with a significant proportion of renewable energy sources (RES). Coordination control between the PV (photo voltaic) and the BESS is necessary for power balance. This article describes a corrective voltage control (CVC) scheme for microgrid voltage regulation. An active and reactive power control strategy is suggested to reduce voltage fluctuations and thus mitigate the adverse effects of an unbalanced load. Incorporated battery energy storage devices will undergo dynamic charging during off-peak hours to minimize voltage dropouts and discharge during peak hours to prevent voltage spikes while regulating the PV inverter output's rapid fluctuations to a predetermined value. The outcomes validate the viability of the control schemes and Ess's integration into the microgrid.

Keywords: Corrective voltage control; Renewable energy source; Photo voltaic; Battery energy storage system

1. Introduction

The necessity to decarbonize to mitigate the effects of climate change and the difficulties associated with meeting the rising demand for electrical energy has brought to the forefront the significance of microgrids in facilitating the efficient integration of renewable energy sources. Despite the considerable research on microgrids over the past few years, numerous unresolved obstacles require attention. The ongoing risk of voltage collapse continues to make voltage stability analysis and development a significant concern for operators of power systems.

A microgrid is an integrated collection of distributed energy resources (DERs), storage systems, and connected loads that can communicate with the primary grid via a single point of common coupling (PCC) [1]. The utility's point of common coupling (PCC) is the only connection point for disconnecting or reconnecting. A microgrid must meet the interface and interoperability standards set up at the PCC, such as the one for connecting inverters in IEEE Standard 1547 [2]. So, MGs can be utilized to deliver electricity to remote places, making it easier to produce, distribute, and control the flow of electricity to consumers in the area. Microgrids are similar to conventional power grids in

many respects. Like standard grids, they make power, send it to where it's needed, control it with voltage regulation, and switch gears. Microgrids provide closer intimacy between electricity generation and consumption than conventional electrical networks. It leads to greater efficiency and reduced transmission loss. MGs are one of the key concepts that will promote the deployment of high renewable energy source (RES) penetrations in our electricity systems[3]. Table 1 shows the difference between a microgrid's autonomous and grid-connected modes.

Table 1. Differences between grid-connected and autonomous microgrids

Specifications	Independent	Grid Connected
Operating mode	Isolated	Incorporated with grid
Primary driving factors	Sustainability of remote and rural locations and efficiency as well	Cost, efficiency, and Power quality reliability enhancement,
Use of demand response strategies	Required	Desirable
Use of Storage	To be independent	For reacting to signs of price

By participating in ancillary services, microgrids can support the primary grid. They can aid in voltage regulation, frequency control, and power quality enhancement, thereby enhancing the stability and dependability of the grid. In certain circumstances, extra power generated by microgrids can be transferred back to the central infrastructure, strengthening the system's overall resiliency and adaptability. Microgrids play an essential role in today's electrical infrastructure by increasing reliability, incorporating renewable energy, boosting energy efficiency, facilitating demand response, assisting the grid, and strengthening local communities. Microgrids will likely be more significant in attaining a resilient and sustainable energy future as the energy landscape changes.

There has been a notable surge in the need for cleaner energy resources in recent decades. As a result, decision-makers in every nation have devised long-term strategies to secure energy from renewable sources. Therefore, these strategies diminish reliance on conventional energy sources and implement alternative energy technologies in their place. Consequently, there is an emerging international trend among nations to transition towards sustainable energy sources and diminish reliance on conventional fossil fuels for energy provision. Among various renewable energy sources, solar and wind energy are considered the most reliable sources. In the last decade, solar Photovoltaic (PV) capacity has increased rapidly globally [4]. Integrating photovoltaic (PV) plants into microgrids is gaining popularity and has substantial advantages to energy systems. The projected installed capacity was anticipated to peak at 714 gigawatts (GWp) by 2020 [5]. Moreover, with an incremental annual power generation of 127 GWp in the same year, solar photovoltaic (PV) emerged as the swiftest-growing renewable energy technology. Given ongoing cost reductions, this trajectory is expected to endure, leading to a global tripling of installed solar PV capacity by the decade's end [6]. Integrating photovoltaic (PV) systems into microgrids reflects the expanding recognition of the advantages of green energy, distributed generation, and energy resilience. As PV technology keeps getting better and costs go down, PV plants are likely to play an even more significant part in the future growth of microgrids, helping the move towards cleaner, more sustainable, and decentralized energy systems.

1.1 The Concept of Voltage Stability and its Significance in Power Systems

Voltage Stability is integral to Power Systems. This is the ability of a network to keep voltage levels steady and acceptable at all places within the system. It ensures that the magnitudes of voltage and phase angles stay within acceptable limits so that electrical equipment can work well and the power grid stays stable overall.

A microgrid-integrated system exhibits voltage instability when at least one bus/feeder demonstrates a negative V-Q sensitivity. The phenomenon of microgrid voltage stability is classified broadly according to system disturbances. However, it can be further categorized according to several other factors. This includes distinguishing whether the microgrid operates in isolation or is connected to the primary grid. Additionally, the focus of the study can be delineated by examining the stability of the DC-link voltage, analyzing the system's response to minor or significant disturbances, and comprehensively addressing various

variables affecting microgrid voltage stability. These variables encompass the sensitivity of the Q-V droop, load behavior, inverter dynamics, and the dynamics of other components such as tap changers in under load transformers. Figure 1 visually represents specific classifications and their corresponding influencing factors.

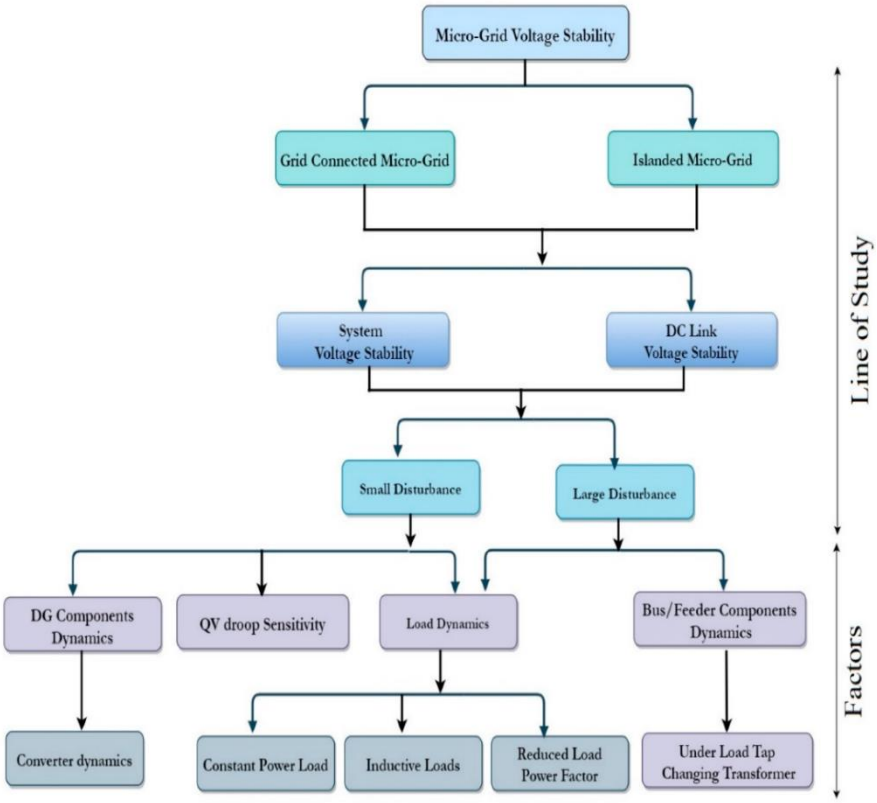


Figure 1. Study line in microgrids for voltage stability.

1.2 Importance and Objective of the Research

In recent years, there has been a discernible shift in focus from conventional power sources to renewable energy alternatives for electricity generation due to concerns related to air pollution and raw material shortages. This transition aims to ensure the production of high-quality electric power to meet the demands of consumers. In tandem with this shift, microgrid systems have been developed to integrate renewable-based power generation with traditional sources, effectively addressing load demand fluctuations. Integrating renewable energy sources, conventional power systems, and energy storage systems in a microgrid configuration offers a comprehensive solution for stabilizing frequency and voltage at PCC during emergency load situations. This approach mitigates the shortcomings associated with conventional power systems and obviates the need for a secondary controller, a notable advancement in power system design. This paper aims to make a microgrid with solar (PV) plants more stable in terms of voltage. A corrective voltage control (CVC) method is used to make this happen. This paper aims to suggest and study how well the CVC plan works to control and keep voltage levels in the microgrid system within acceptable boundaries.

2. Literature review

The increasing power of RES will affect how the current energy system works. The biggest problem with RES is that it's hard to know how much power will be available in different weather situations. Research findings demonstrate that alterations in power, referred to as "ramp rates," can lead to a substantial power escalation or reduction, amounting to as much as 90% of the estimated capacity per minute [8] and up to 66% within a 10-second timeframe. According to the International Electrotechnical Commission (IEC) standard 61000-2-2 [9], swift voltage fluctuations exceeding 3% of the nominal value are deemed unacceptable for low-voltage (LV) distribution systems. Voltage consistency is essential for the correct operation and durability of

electrical equipment. Most equipment is designed to function effectively within a particular voltage range. Voltage levels that are too high or too low can cause equipment malfunctions, decreased performance, and even equipment damage [10].

Unstable or fluctuating voltages can cause variations in frequency, flickering lighting, overheating equipment, and distorted waveforms [11]. By offering stable voltage levels, the quality of power is improved, providing consumers with a reliable and efficient source of electricity. Maintaining consistent voltage demands careful attention to managing several moving parts, including generators, transformers, capacitors, and control devices. Maintaining system dependability, optimizing power transfer, and easing the integration of new technologies and renewable energy sources are all possible by conducting a voltage stability study and implementing suitable voltage control measures. PV facilities can have positive and adverse impacts on power system voltage stability. Understanding these effects is essential for effectively managing voltage fluctuations and reactive power imbalances. Consequently, a remedy for balancing the power outputs of photovoltaic and wind energy is required. Furthermore, voltage fluctuations are the most detrimental at the distribution grid level, threatening the regional electricity grid and its devices. In contrast, governments and regulatory bodies have demanded a higher power quality standard due to increased irregular loads, power utilization, and the proliferation of distributed generation (DG) systems [12].

Instability of the voltage is primarily a local phenomenon that begins with a reactive power imbalance. Significantly contributing to voltage instability is a sudden change in demand. In addition, transient clouds rapidly affect the power output of the PV systems. Some power quality problems, like voltage swings in the LV grid, are usually solved by grid reinforcement to strengthen the LV grid [13, 14]. Voltage fluctuations are diminished when the grid is reinforced due to the LV grid cables' increased capacity and decreased resistance. Nonetheless, this method of voltage regulation is prohibitively expensive and requires the replacement of a large number of LV cables; as a result, it is considered undesirable [15]. Another method to regulate voltage is power curtailments [16]. Curtailment serves as a method for managing the power output of a photovoltaic (PV) system by manipulating the working voltage and current within the system's inverter [17]. This involves restraining the power output of the PV system, particularly in response to sudden increases in power output or uniformly in anticipation of an impending degradation. Alternative approaches to regulate the voltage profile encompass reactive power control and the deployment of tap changers [18, 19]. However, the efficacy of reactive power control is constrained in low-voltage (LV) grids, particularly within urban LV grids, owing to the relatively short cable lengths [13], [20]. Tap changers are considered insufficient in addressing voltage fluctuations, as their capability is limited to regulating voltage near the transformer substation [21]. In contrast, the challenges posed by voltage fluctuations induced by photovoltaic (PV) power generation are particularly pronounced at the remote end of the cable [22].

In low-voltage distribution networks, particularly in distribution lines where line parameters exhibit significant disparities, solutions derived from transmission line applications prove only partially effective. In this context, reactive power compensation demonstrates diminished adequacy compared to the combined benefits of active and reactive power compensation. This phenomenon is notably pronounced in lines where substantial series resistance dominates the overall impedance of the line. The confluence of heightened load demand levels and intermittent fluctuations in solar photovoltaic (PV) power output precipitates gradual and abrupt voltage oscillations within the corresponding low-voltage (LV) distribution feeder. For economic reasons, electricity systems work closer to their operating limitations, increasing the likelihood of blackouts. Many recent extensive blackouts, such as those in Southern California [23] and South Australia [24] in 2016, were caused by voltage breakdowns. The incidents were ascribed to the absence of dynamic voltage support (DVS) capabilities in the presence of voltage drops and the inability to endure multiple faults. Substantial research has been conducted on the impact of Photovoltaic Power Plants (PVPs) on system stability, particularly with a focus on voltage stability [25]. In a noteworthy study, the authors of [26] utilized the Nordic test system to investigate the influence of Large-Scale Photovoltaic Plants (LSPVPs) on Low-Tension (LT) voltage stability, taking into account voltage regulation at the plant level.

The investigators in [27] employed a meticulous methodology to analyze the impact of Photovoltaic (PV) systems on Low-Tension (LT) voltage stability. As posited by [28], enhanced controllers for Large-Scale

Photovoltaic Plants (LS-PVPs) have the potential to deliver superior dynamic reactive power responses, thereby bolstering LT voltage stability. Synthesizing the insights from these three antecedent studies, it is deduced that implementing plant-level voltage regulation for LS-PVPs contributes to augmenting LT voltage stability. Nevertheless, adopting a judicious approach to forestall voltage collapse is imperative. As a result, an advanced voltage management technique is required to avoid LT voltage instability.

Static compensators, or STATCOMs, serve as voltage regulation solutions by injecting reactive power at the load connection point [29]. This approach proves advantageous when deployed in transmission or distribution systems characterized by predominantly inductive line impedance. When applied specifically to distribution lines, these devices are called DSTATCOMs [30]. However, the efficacy of voltage regulation with DSTATCOM becomes compromised in low-voltage grids, primarily due to the substantial reactive power demands necessary to compensate for the elevated R/X line grid ratio prevalent in weak grids [31]. This component introduces two noteworthy challenges. Firstly, it requires a converter with an exceptionally high nominal power to ensure effective regulation. Secondly, it induces an excessive reactive power flow in the distribution transformer, potentially damaging equipment. In response to these challenges, [32] suggests a Minimum PowerPoint Tracking (MPPT) scheme. This approach enables the supply voltage to oscillate around the nominal voltage while adhering to local regulatory standards, effectively addressing the identified issues. Furthermore, [33] delves into a voltage-based storage control strategy for managing distributed solar Photovoltaic (PV) power in conjunction with battery systems. However, the paper acknowledges the need to confront practical challenges, including but not limited to limited Battery Energy Storage System (BESS) capacity and unexpected variations in PV generation, as highlighted in [34]. The study explores active and reactive power control measures to mitigate overvoltage limit violations by forecasting the curtailment threshold based on the past 15 seconds of PV output. Notably, the proposed control approach must exhibit more effectiveness when confronted with substantial changes in PV output. Reference [35] delves into peak shaving using Battery Energy Storage Systems (BESS), focusing on load data. On the other hand, [36] explores a load-shifting mechanism that leverages BESS to transition energy consumption from peak to off-peak hours. However, all approaches in [35,36] could be enhanced further by requiring a minimum voltage level on the distribution feeder to initiate peak shaving/load shifting. Some research has been done on the effect of PVPs on stability, precisely voltage stability [37-39]. Nonetheless, a method for mitigating the harmful impacts of PVPs on LT voltage stability has yet to be developed in these experiments. Historically, power quality issues, such as voltage swings in the LV grid, have occurred. Similarly, in [40], the authors propose a decentralized emergency control solution addressing Low-Tension (LT) voltage instability. Considering the on-load tap-altering capability, this controller monitors the generator's reactive powers and gearbox voltages. In response to the imperative of averting voltage collapse, the study devises a solution grounded in under-voltage load shedding. While Energy Storage Systems (ESS) stand out as versatile resources widely adopted in contemporary power systems globally, their optimal integration into transmission networks necessitates nuanced considerations. Challenges include determining the optimal position and capacity, alongside grappling with the associated investment expenses for maximizing the ESS's efficacy within the network.

3. Research gap from the literature review

The foremost objective of the studies in the literature review section was to reduce the voltage at PCC by voltage regulators, droop control, and on-load tap changers (OLTC) by renewable curtailment in power systems during unexpected load-changing situations. Some researchers also include STATCOM, some decentralized emergency control solutions, and several algorithm-based controllers for voltage control. Nonetheless, these voltage regulation methods are relatively inexpensive and require the replacement of a large number of LV cables; as a result, it is considered undesirable [15]. Also, no algorithm-based controller provides a better-controlled response. Therefore, a suitable controller with superior optimization is required to better control power systems during sudden load demand conditions or any variation in solar or distributed power generation. The CVC technique is easily implemented to solve voltage variation problems by controlling active and reactive powers.

4. Changes in voltage caused by changes in solar output

The variation in voltage produced by the sharp changes in the PV inverter output is investigated using a PV system that is connected to a distribution system, as in Fig. 2. It is assumed in this section that the ESS still needs to be incorporated with the solar system.

The relationship between the quantity of change in the magnitude and angle of voltage in a distribution system caused by a change in active power (P) and reactive power (Q) is as follows:

$$\begin{bmatrix}\sigma_{P\delta} & \sigma_{P|V|}\\ \sigma_{Q\delta} & \sigma_{Q|V|}\end{bmatrix}\begin{bmatrix}\Delta\delta\\ \Delta[V]\end{bmatrix}=\begin{bmatrix}\Delta P\\ \Delta Q\end{bmatrix} \quad (1)$$

Here, $\boldsymbol{\sigma_{P\delta}}$, $\boldsymbol{\sigma_{P|V|}}$, $\boldsymbol{\sigma_{Q\delta}}$, $\boldsymbol{\sigma_{Q|V|}}$ are the active and reactive power sensitivity matrices correspondingly concerning the magnitude and angle of voltage. The vector Δδ represents variations in voltage angles, while the vector Δ[V] signifies alterations in voltage magnitudes [ΔV]. The vectors ΔP and ΔQ denote net active and reactive power changes, respectively. Equation (1) may be interpreted as a system of linear equations akin to the form expressed in equation (2).

$$A * X = B \quad (2)$$

Here,

$$\text{A} = \begin{bmatrix}\sigma_{P\delta} & \sigma_{P|V|}\\ \sigma_{Q\delta} & \sigma_{Q|V|}\end{bmatrix} \quad (3)$$

$$\text{X} = \begin{bmatrix}\Delta\delta\\ \Delta[V]\end{bmatrix} \quad (4)$$

$$\text{B} = \begin{bmatrix}\Delta P\\ \Delta Q\end{bmatrix} \quad (5)$$

Using equation (2), the change in the magnitude of voltage at the point of interconnection (PoI) of a PV system can be determined by using Cramer's rule as given in (6).

$$\Delta[V_i] = \frac{Det\begin{bmatrix}\sigma_{P\delta} & \Delta P\\ \sigma_{Q\delta} & \Delta Q\end{bmatrix}}{Det\begin{bmatrix}\sigma_{P\delta} & \sigma_{P|V|}\\ \sigma_{Q\delta} & \sigma_{Q|V|}\end{bmatrix}} \quad (6)$$

Where $\Delta[V_i]$ is the change of voltage at any i_{th} bus. In this case, that i_{th} bus is the point of common coupling, and Det means determinant. The variation in load demand and the output of the PV inverter will determine how much the active and reactive power changes.

5. Proposed Method

The microgrid being examined comprises a battery, photovoltaic (PV) panel, and constant and variable demands. The proposed corrective voltage control (CVC) scheme aims to reduce fluctuations induced by mismatches between solar PV output and load. The corrective Voltage Control (CVC) approach is employed to control and keep voltage levels within acceptable limits in a power system, especially in the presence of fluctuations in voltage or instability. The CVC scheme modifies the system's reactive power injection or absorption to fix voltage problems and restore stability. Fig. 1 displays the theoretical block diagram of a typical battery storage coupled to a photovoltaic system that will be examined in this work. The battery storage will be charged and discharged to reduce the erratic solar PV production at the PCC.

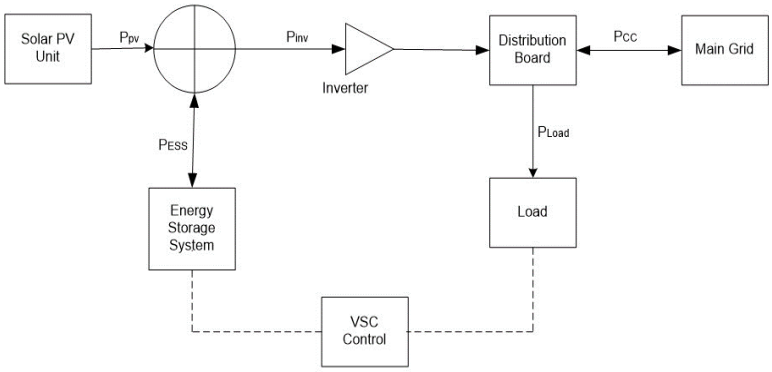


Figure 2. Schematic representation of the solar system connected with the battery

According to Fig. 2, an inverter connects the solar PV unit and the battery storage to the grid and the household load. As indicated by Eq. (1) below, the BESS output (P_{Bess}) and the load (P_{Load}), must be equal to the power output of the PV panel (P_{pv}) and the power absorption/injection from and to the grid.

$$P_{Grid} + P_{pv} = P_{Bess} + P_{Load} \tag{7}$$

Power absorption and injection from and to the grid P_{Grid} must be regulated by modifying the P_{Bess} to maintain the voltage characteristics of the linked power distribution feeder within the usual operating limits.

5.1 Principle of Operation and Control

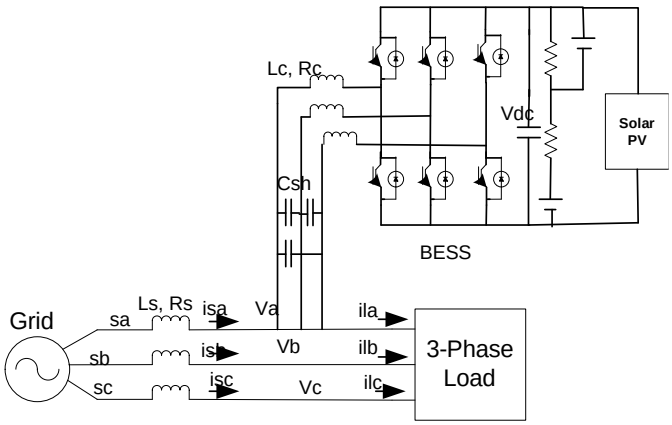


Figure 3. System configuration

The system configuration is illustrated in Fig. 3, and Fig. 4 illustrates the algorithm for the control scheme. The proposed microgrid system, comprising conventional power sources, renewable energy generation, and energy storage, represents a holistic approach to power system design. By seamlessly blending these components, the system ensures a stable and reliable power supply and minimizes environmental impact and resource dependency. This innovative solution marks a significant step forward in the quest for sustainable and resilient power systems capable of meeting the evolving needs of consumers, especially during critical load scenarios. In this scheme, the three-phase reference source currents comprise two key components: an in-phase component and a quadrature component relative to the phase voltages. The in-phase component of the reference source current ($I^*_{sad}, I^*_{sbd}, I^*_{scd}$) charges the BESS battery and supplies active power to the load. This active power component can be regulated to maintain a constant power output at the point of common coupling (PCC), ensuring stable power generation. The amplitude I^*_{smd} is multiplied by the in-

phase unit vectors (U_a , U_b , U_c), which are calculated by dividing the AC voltages (V_a, V_b, V_c) by their amplitude (V_m), resulting in the in-phase components of the reference currents ($I^*_{sad}, I^*_{sbd}, I^*_{scd}$). The quadrature components of the reference source currents ($I^*_{saq}, I^*_{sbq}, I^*_{scq}$) are required to regulate the AC voltage at the point of common coupling (PCC). These quadrature unit vectors are derived from the in-phase unit vectors. The AC voltage (V_m), at the PCC, is measured and compared with a reference voltage, with the resulting voltage error processed by a proportional-integral (PI) controller. The PI controller's output I^*_{smq} establishes the amplitude of the reactive current required by the system, which the BESS supplies. By multiplying the quadrature unit vectors W_a , W_b , W_c $with$ I^*_{smq} quadrature components of the reference source currents ($I^*_{saq}, I^*_{sbq}, I^*_{scq}$) are generated. The total reference source currents ($I^*_{sa}, I^*_{sb}, I^*_{sc}$) are obtained by summing the in-phase and quadrature components. A PWM-based current controller then ensures that the BESS currents accurately follow the reference source currents.

5.2 Control Scheme

The various components of the proposed system are modeled and integrated to form a comprehensive system model. The control scheme, illustrated in Fig. 4, is primarily employed to derive the reference source currents, which are then utilized in the PWM current controller of the BESS's voltage source inverter (VSI).

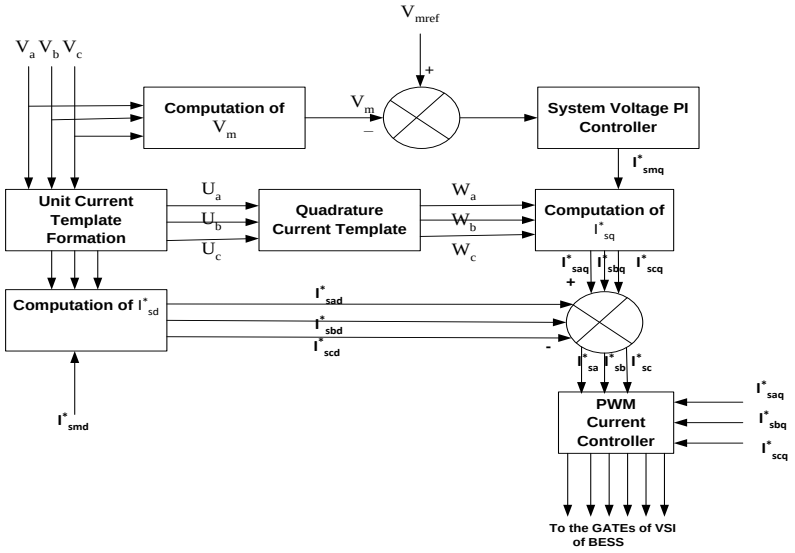


Figure 4. Algorithm of controller

These reference source currents consist of an in-phase and quadrature components, which are determined sequentially, as outlined in the following section.

The unit vectors in phase with Va, Vb, and Vc are derived as in equation 10:

$$U_a = \frac{V_a}{V_m}; \qquad U_b = \frac{V_b}{V_m}; \qquad U_c = \frac{V_c}{V_m} \tag{10}$$

Where V_m is the amplitude of the AC terminal voltage at the PCC and can be calculated as;

$$V_m = \frac{2}{3}\sqrt{({V_a}^2 + {V_b}^2 + {V_c}^2)} \tag{11}$$

Where V_a, V_b, and V_c are the instantaneous voltages at PCC and can be derived as:

$$V_a = V_{san} - R_s i_{sa} - L_s P i_{sa},\ V_b = V_{sbn} - R_s i_{sb} - L_s P i_{sb},\ V_c = V_{scn} - R_s i_{sc} - L_s P i_{sc} \tag{12}$$

Where P represents the time differential operator (d/dt) and L_s and R_s are per phase source inductance and resistance, respectively. V_{san}, V_{sbn} *and* V_{scn} are the three-phase instantaneous input supply voltages at PCC and are expressed as:

$$V_{san} = V_m \sin(\omega t); \quad V_{sbn} = V_m \sin(\omega t - 2\pi/3); \quad V_{scn} = V_m \sin(\omega t + 2\pi/3) \tag{13}$$

The peak value, denoted as *Vm*, and the angular frequency (ω=2πf) of the power supply are established parameters in this context. The derivation of unit vectors orthogonal to *Va*, *Vb*, and *Vc* involves implementing a quadrature transformation on the in-phase unit vectors *Ua*, *Ub*, and *Uc* as,

$$W_a = -U_b / \sqrt{3} + U_c / \sqrt{3} \tag{14}$$

$$W_b = \sqrt{3}\, U_a /2 + (U_b - U_c)/(2\sqrt{3}) \tag{15}$$

$$W_c = -\sqrt{3}\, U_a /2 + (U_b - U_c)/(2\sqrt{3}) \tag{16}$$

The quadrature component of the reference source currents is computed as:
The voltage error V_{er} at PCC at the nth sampling instant is as:

$$V_{er(n)} = V_{ref(n)} - V_{m(n)} \tag{17}$$

The output of the PI controller at the nth sampling instant is expressed as;

$$I^*_{smq(n)} = I^*_{smq(n-1)} + K_P\{V_{er(n)} - V_{er(n-1)}\} + K_i V_{er(n)} \tag{18}$$

Where K_P and K_i are the proportional and integral constants of the PI controller, respectively, and the subscript (*) represents the reference quantity.

The quadrature components of the reference source currents are estimated as,

$$I^*_{saq} = I^*_{smq} W_a \quad I^*_{sbq} = I^*_{smq} W_b \quad I^*_{scq} = I^*_{smq} W_c \tag{19}$$

In-phase components of the reference source currents are estimated as

$$I^*_{sad} = I^*_{smd} U_a \quad I^*_{sbd} = I^*_{smd} U_b \quad I^*_{scd} = I^*_{smd} U_c \tag{20}$$

Where I^*_{smd} is considered as the fixed value corresponding to the constant source current.
The total reference source currents are the sum of the in phase components and quadrature components of the reference source currents and are given as:

$$I^*_{sa} = I^*_{saq} + I^*_{sad} \quad I^*_{sb} = I^*_{sbq} + I^*_{sbd} \quad I^*_{sc} = I^*_{scq} + I^*_{scd} \tag{21}$$

The in-phase component of the reference source current ($I^*_{sad}, I^*_{sbd}, I^*_{scd}$) charges the BESS battery and supplies active power to the load.

6. Results and Discussion

The design of a Simulink model for Peak PowerPoint Tracking involves the utilization of 100 KW at 1000 W/m² PVAs. Each of the 66 parallel strings (5 modules SunPower SPR-305E-WHT-U connected in series) comprises the system's 100.735 KW (66 × 305.226 × 5). The temperature and solar irradiance evaluation units

are degrees Celsius and W/m², respectively. The PV array block is equipped with two inputs, which accommodate fluctuations in the sun's temperature and irradiance. The PV array's output is linked to DC-to-DC boost converters with input frequencies of 5 KHz. The outputs are connected to the DC bus of the 3-phase, three-level Pulse Width Modulation Voltage Source Converter. The tracking system generates the intended voltage by manipulating the duty cycle. At the same time, peak power is measured from the PVA terminals using the incremental conductance (IC) method, also called the maximum power point tracking strategy. The VSC has both internal and external control capabilities. The internal portion of the PWM-VSC regulates the quadrature current components (I_d, I_q), which represent the active and reactive components, respectively. The external portion of the PWM-VSC regulates the DC link voltage. It is worth noting that the PWM-VSC is maintained at a 20% higher level than the solar farm's rating. The voltage output of the PVA is increased from 272 VDC to 640 VDC via the boost converter. The PWM-VSC utilizes modulating reference voltage signals (V_{abcref}) that have been converted from the current controller's output voltage (V_d) and (V_q), which are typically 540 V_{dc} to 600 Vac at the common point. A filter circuitry has been coupled to the network to remove any distortion produced by the PWM-VSC. The design network in MATLAB/SIMULINK is simulated.

This session presents the findings of an investigation conducted to ascertain the impact of load fluctuations on the performance of a rated solar farm, with the power of the PVAs maintained at their rated capacity. There is an unacceptable voltage at the point of common coupling because it exceeds 10 percent of its rated value. This investigation examined three distinct scenarios involving variable load. In this study, the load varies gradually, and, in the case where the solar generation is more than the demand of load, a reverse current starts flowing. It is evident from the results (Fig. 5 and Fig. 6) that solar power generation remains constant under constant temperature and irradiance conditions. However, the fluctuations in PCC voltage and DC-link voltage are caused by this variation. A corrective voltage control (CVC) scheme is proposed to put these values in a permissible range.

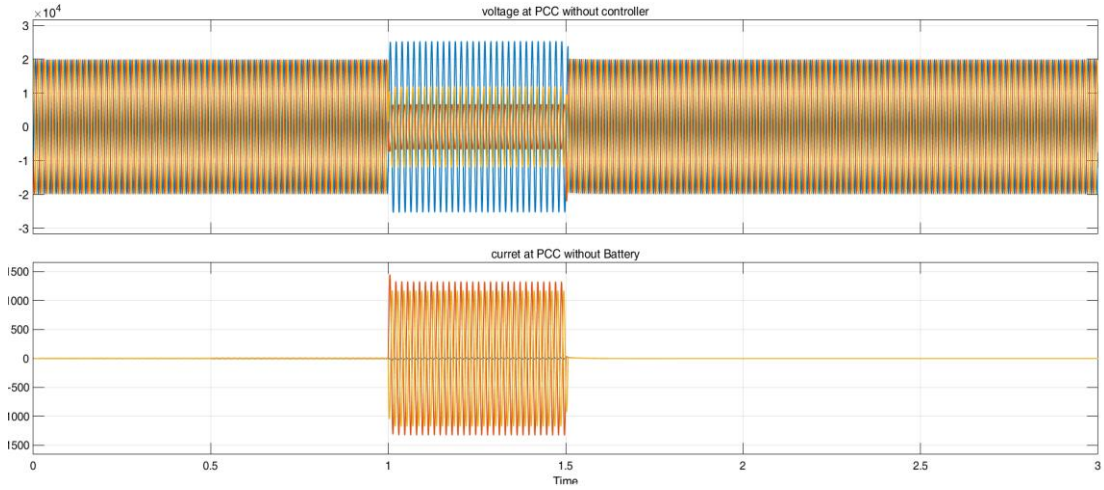


Figure 5. Variation of voltage at PCC without controller

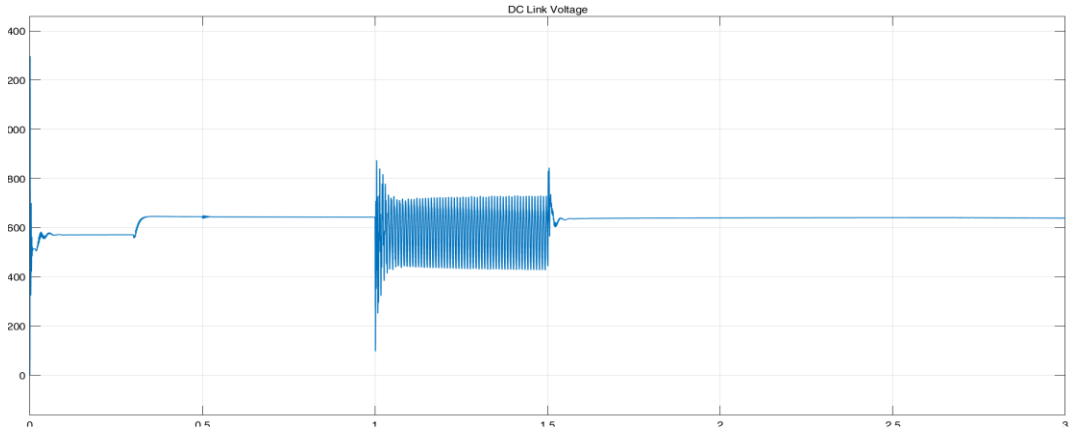


Figure 6. Variation of DC link voltage without controller

Specifications for battery and solar PV are shown in Fig 7 and 8, respectively. Fig. 9, Fig. 10, and Fig. 11 show the voltage at PCC, DC link voltage, and the power-sharing of solar, grid, and load.

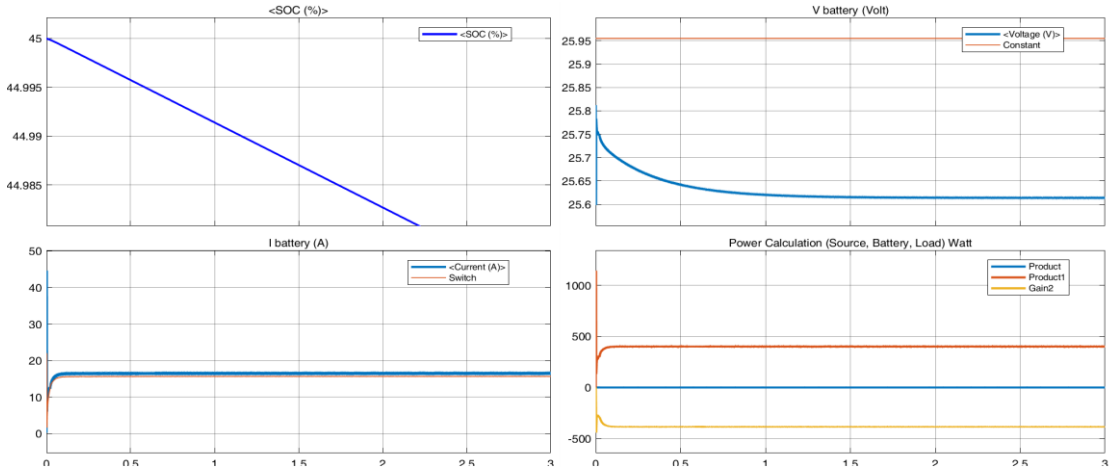


Figure 7. Specifications of battery

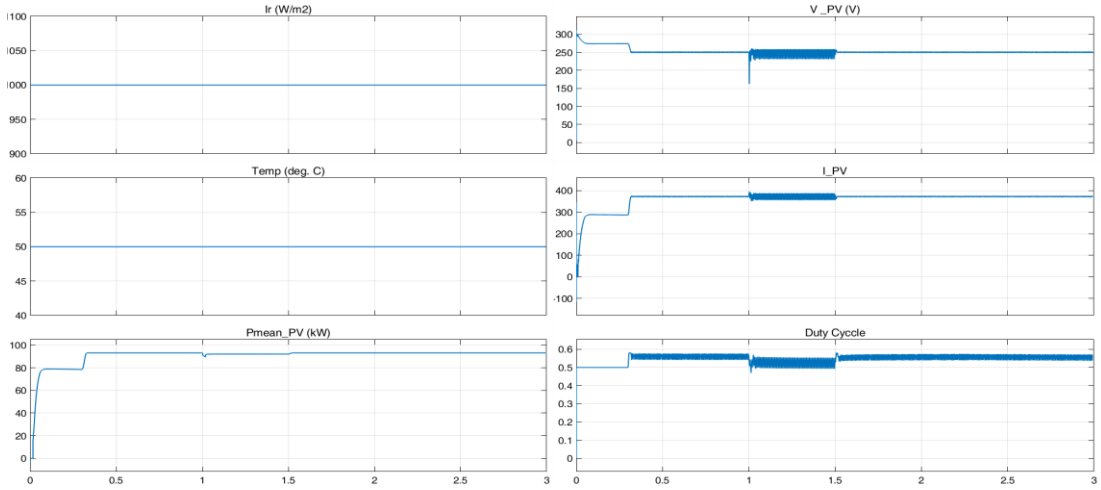


Figure 8. Specifications of solar

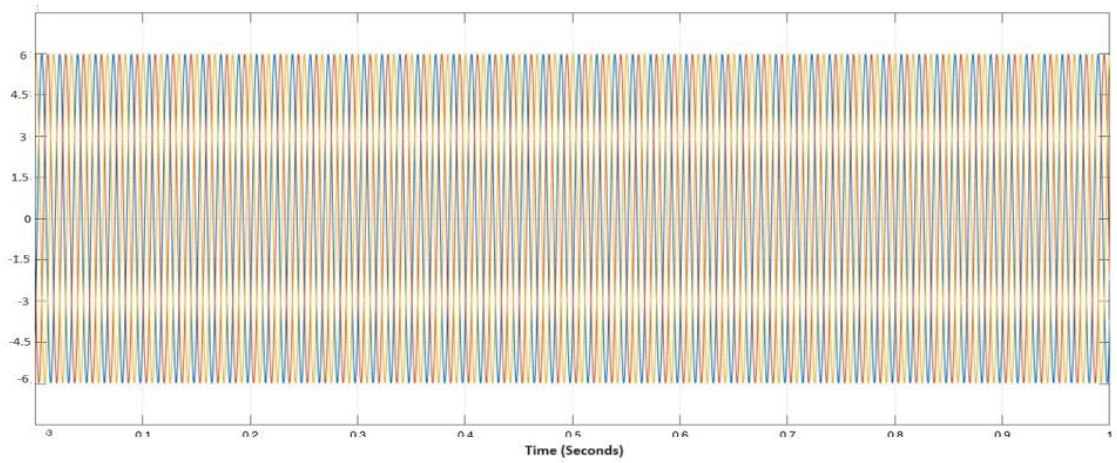


Figure 9. Voltage at PCC with controller

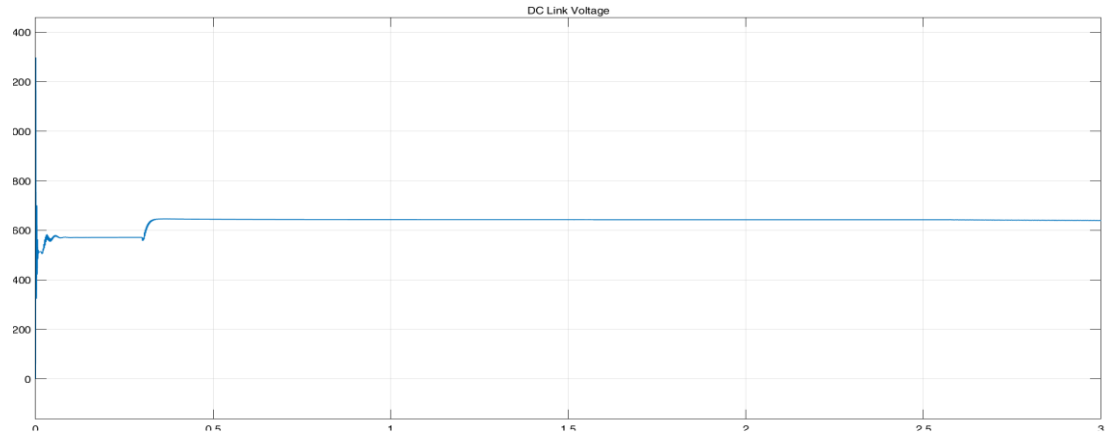


Figure 10. DC link voltage with a controller

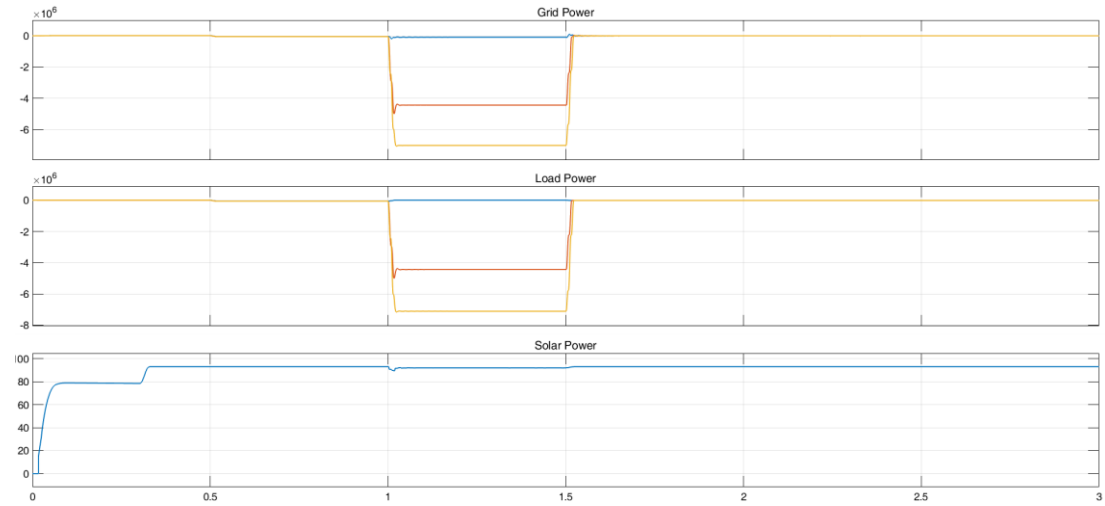


Figure 11. power sharing of the solar grid and load

7. Conclusion

The stability improvement of microgrid systems is a crucial aspect of their successful operation. Voltage has been one of the leading causes of voltage collapse and blackouts, so it's essential to have a system that is safe from a voltage stability point of view and less likely to collapse. This research article examines the

voltage stability for a varying load system. It proposes an optimal improvement strategy by utilizing a control scheme to optimize controlling a BESS's real and reactive power output. A system with a PV generator, a grid, a storage system, and a load built into a microgrid is being studied. This paper describes a novel corrective voltage control (CVC) method that checks the terminal voltage to keep it from dropping and rising. Both grid-on and islanding modes operate the CVC and converter control. We can exchange electricity with the grid because of the DC-AC bi-directional converter. The interlinking converter in grid-connected mode operates in converter/inverter mode based on the load need. The energy storage system helps regulate the microgrid's voltage level and provides a constant power supply. PV power and stored energy meet the load requirement when the system is in grid-off mode. The suggested scheme allows us to regularly exchange electricity between all sources and loads. Simulations are used to examine the primary goals of the recommended strategy, which include preserving the PCC voltage and quickly restoring the DC bus voltage in the event of a disruption. The CVC scheme effectively maintains the desired control over the DC bus and PCC voltage, whether in the islanded or grid-on modes.

8. Future Directions

Finally, further research from this study could look into several ways to improve the use of energy storage systems in MGs with DERs. First, including more complicated MG configurations and large-scale models would help us learn how to improve things and scale them up in different situations. Adding advanced machine learning methods or artificial intelligence algorithms could also improve the controllers' adaptation. Lastly, looking into regulatory and economic frameworks that encourage advanced control strategies in MGs could make it easier for them to be widely used and have a bigger effect on grid resilience and the integration of green energy.

Author Contributions: The authors confirm their contribution to the paper as follows: study conception and design: Singh, N., Jain, D. K.; analysis and interpretation of results: Singh, N., Jain, D. K.; manuscript preparation: Singh, N. Both the authors reviewed the results and approved the final version of the manuscript.

Funding: This research article did not receive any funding.

Conflicts of Interest: Authors declare no conflict of interest.

References

[1] Rajesh, K.S.; Dash, S.S.; Rajagopal, R.; Sridhar, R. A review on control of AC microgrid. *Renew. Sustain. Energy Rev.* **2017**, *71*, 814–819.

[2] Mahmoud, M.S. Microgrid Control Problems and Related Issues. In Book *Microgrid: Advanced Control Methods and Renewable Energy System Integration,* Elsevier: Amsterdam, The Netherlands, **2017**, 1–42.

[3] Mohammed, A.; Refaat, S.S.; Bayhan, S.; Abu-Rub, H. AC microgrid control and management strategies: Evaluation and review. *IEEE Power Electron. Mag*. **2019**, *6*, 8–31.

[4] Photovoltaics Report: Tech. report, Fraunhofer Institute for Solar Energy Systems. **2021**. Available online*:* https://www.ise.fraunhofer.de/content/dam/ise/de/documents/publications/studies/Photovoltaics-eport.pdf.

[5] Renewable capacity statistics 2020: Tech. rep. International Renewable Energy Agency, Abu Dhabi. **2021**. Available online: https://www.irena.org/publications/2021/March/Renewable-Capacity-Statistics.

[6] World energy outlook 2020: Tech. rep. IEA, Paris. Available online: https://www.iea.org/reports/world-energy-outlook-2020.

[7] Owe, J. The planet's future: Climate change will cause civilization to collapse. available online: *https://www.independent.co.uk/environment/climate-change/1742759.*

[8] Kreuwel, F.P.; Knap W.H.; Visser L.R.; Van Sark W.G. Analysis of high frequency photovoltaic solar energy fluctuations. *Sol Energy*, **2020**, *206*, 381–389.

[9] Electromagnetic Compatibility (EMC)—Part 2-2: Environment-Compatibility Levels for Low-Frequency Conducted Disturbances and Signalling in Public Low-Voltage Power Supply Systems, Standard 61000- 2-2, Mar. 2002.

[10] Voltage Fluctuations in the Electric Supply System. Available online: http:// www.elec.uow.edu.au/ apqrc/content/technotes/technote7.pdf (November 2024)
[11] IEEE Application Guide for IEEE Std 1547, IEEE Standard for Interconnecting Distributed Resources with Electric Power Systems, Standard 1547.2-2008, **2009**, 1–207.
[12] Yu, X.; Cecati, C.; Dillon, T.; Simoes, M. The new frontier of smart grids. *IEEE Ind. Electron. Mag.* **2011**, *5*. 49–63.
[13] Van Oirsouw, P.; Cobben, J. Grids for distribution of electricity publication phase to phase 2020.
[14] Von Appen, J.; Stetz, T.; Braun, M.; Schmiegel, A. Local voltage control strategies for PV storage systems in distribution grids *IEEE Trans Smart Grid*, **2014**, *5*, 1002–1009.
[15] Von Appen, J.; Braun, M.; Stetz, T.; Diwold, K.; Geibel, D. Time in the sun: the challenge of high PV penetration in the German electric grid *IEEE Power Energy Mag*, **2013**, *11*, 55–64.
[16] Chaudhary, P.; Rizwan, M. Voltage regulation mitigation techniques in distribution system with high PV penetration *A review Renew Sustain Energy Rev*, **2018**, *82*, 279–328.
[17] Howlader, A.M.; Sadoyama, S.; Roose, L.R.; Chen, Y. Active power control to mitigate voltage and frequency deviations for the smart grid using smart PV inverters *Appl Energy*, **2020**, *258*.
[18] Liu, X.; Cramer, A.M.; Liao, Y. Reactive power control methods for photovoltaic inverters to mitigate short-term voltage magnitude fluctuations *Electr Power Syst Res*, **2015**, *127*, 213–220.
[19] Yan, R.; Marais, B.; Saha, T.K. Impacts of residential photovoltaic power fluctuation on on-load tap changer operation and a solution using DSTATCOM *Electr Power Syst Res,* **2014**, *111,* 185–193.
[20] Das, C.K.; Bass, O.; Kothapalli, G.; Mahmoud, T.S.; Habibi, D. Overview of energy storage systems in distribution networks: Placement, sizing, operation, and power quality *Renew Sustain Energy Rev*, **2018**, *91*, 1205–1230.
[21] Babacan, O.; Torre, W.; Kleissl, J. Siting and sizing of distributed energy storage to mitigate voltage impact by solar PV in distribution systems *Sol Energy*, **2017**, *146*, 199–208.
[22] Brinkel, N.; Gerritsma, M.; AlSkaif, T.; Lampropoulos, I.; Van-Voorden, A.; Fidder, H. Impact of rapid PV fluctuations on power quality in the low-voltage grid and mitigation strategies using electric vehicles *Int J Electr Power Energy Syst*, **2020**, *118*, Article 105741.
[23] 1200 MW Fault Induced Solar Photovoltaic Resource Interruption Disturbance Report. Tech. Rep.; NERC; 2017.
[24] Australian Energy Market Operator. Black System South Australia 28 September 2016. Tech. Rep.; AEMO; 2017.
[25] Adewuyi, O.B.; Lotfy, M.E.; Akinloye, B.O.; Rashid Howlader, H.O.; Senjyu, T.; Narayanan, K. Security-constrained optimal utility-scale solar pv investment planning for weak grids: Short reviews and techno-economic analysis *Appl Energy* **2019**, *245*, 16–30.
[26] Ospina, L.D.P.; Correa, A.F.; Valov, M.; Lammert, G.; Premm, D. Impact of plant level voltage control of large-scale inverter based generators on long-term voltage stability. In: *2018 Power Systems Computation Conference (PSCC)*, **2018**, 1–7.
[27] Munkhchuluun, E.; Meegahapola, L.; Impact of the solar photovoltaic (pv) generation on long-term voltage stability of a power network. In: *2017 IEEE Innovative Smart Grid Technologies - Asia (ISGT-Asia)*, **2017**, 1–6.
[28] Munkhchuluun, E.; Meegahapola, L.; Vahidnia, A. Long-term voltage stability with large-scale solar-photovoltaic (pv) generation. *Int J Electrical Power Energy Syst* **2020**, *117*, Article 105663.
[29] Singh, B.; Saha, R.; Chandra, A.; Al-Haddad, K. Static synchronous compensators (STATCOM): a review, *IET Power Electron.* **2009**, *2*, 297–324.
[30] Hock, R. T.; De Novaes, Y.R.; Batschauer, A.L. A voltage regulator for power quality improvement in low-voltage distribution grids, *IEEE Trans. Power Electron.* **2018**, 2050–2060.
[31] Kabir, M.N.; Mishra, Y.; Ledwich, G.; Dong, Z.Y.; Wong, K.P. Coordinated control of grid-connected photovoltaic reactive power and battery energy storage systems to improve the voltage profile of a residential distribution feeder *IEEE Trans. Ind. Inform.* **2014**, *10*, 967–977.

[32] Hock, R.T.; De Novaes, Y.R.; Batschauer, A.L. A voltage regulator for power quality improvement in low-voltage distribution grids *IEEE Trans. Power Electron.* **2018**, 2050–2060.
[33] Kennedy, J.; Ciufo, P.P.; Agalgaonkar, A. Voltage-based storage control for distributed photovoltaic generation with battery systems *J. Energy Storage* **2016**, *8*, 274–285.
[34] Ghosh, S.; Rahman, S.; Pipattanasomporn, M. Distribution voltage regulation through active power curtailment with PV inverters and solar generation forecasts *IEEE Trans. Sustain. Energy* **2017**, *8*, 13–22.
[35] Ananda-Rao, K.; Ali, R.; Taniselass, S.; Baharudin, N. Microcontroller based battery controller for peak shaving integrated with solar photovoltaic *4th IET Clean Energy and Technology Conference (CEAT)*, **2016**, 1–6.
[36] Beniwal, N.; Hussain, I.; Singh, B. Control and operation of a solar PVbatterygrid-tied system in fixed and variable power mode *IET Gener. Transm. Distrib* **2018**, *12,* 2633–2641.
[37] Shah, R.; Mithulananthan, N.; Bansal, R.; Ramachandaramurthy, V. A review of key power system stability challenges for large-scale PV integration *Renew Sustain Energy Rev* **2015**, *41*, 1423–36.
[38] Eftekharnejad, S.; Vittal, V.; Heydt, G.; Keel, B.; Loehr, J. Impact of increased penetration of photovoltaic generation on power systems *IEEE Trans Power Syst* **2013**, *28,* 893–901.
[39] Adewuyi, O.B.; Lotfy, M.E.; Akinloye, B.O.; Rashid Howlader, H.O.; Senjyu, T.; Narayanan, K. Security-constrained optimal utility-scale solar pv investment planning for weak grids: Short reviews and techno-economic analysis *Appl Energy*, **2019**, *245*, 16–30.
[40] Islam, S.R.; Sutanto, D.; Muttaqi, K.M.; Coordinated Decentralized Emergency Voltage and Reactive Power Control to Prevent Long-Term Voltage Instability in a Power System *IEEE Trans Power Syst* **2015** *30,* 2591–603.

ASEAN
Journal of Scientific and Technological Reports
Online ISSN:2773-8752

Research article

Detection of COVID-19, Pneumonia, and Tuberculosis Using Convolutional Neural Networks and Ensemble of Deep Learning Architectures

Rituraj Jain[1*], Simon Kasahun Bekele[2], Damodharan Palaniappan[3], Kumar Parmar[4], Ramesh Babu P[5], and Anandkumar M. Trivedi[6]

[1] Department of Information Technology, Marwadi University, Rajkot, Gujarat, India
[2] Engineer, Cooperative Bank of Oromia, Addis Ababa, Ethiopia
[3] Department of Information Technology, Marwadi University, Rajkot, Gujarat, India
[4] Department of Information Technology, Marwadi University, Rajkot, Gujarat, India
[5] Department of CSE, KL Education Foundation, Bowrampet, Hyderabad, Telangana, India
[6] Learning & Development Department, Mantra Softech India Pvt. Ltd, Ahmedabad, Gujarat, India
* Correspondence: jainrituraj@yahoo.com;

Citation:
Jain, R.; Bekele, K.S.; Palaniappan, D.; Parmar, K.; P B.R.; Trivedi M.A. Detection of COVID-19, pneumonia, and tuberculosis using convolutional neural networks and ensembleof deep learning architectures. *ASEAN J. Sci. Tech. Report.* **2025**, *28*(1), e253662. https://doi.org/10.55164/ajstr.v28i1.253662

Article history:
Received: May 22, 2024
Revised: October 16, 2024
Accepted: November 9, 2024
Available online: February 16, 2025

Publisher's Note:
This article has been published and distributed under the terms of Thaksin University.

Abstract: Testing, diagnosis, and treatment must be done quickly in the current scenario, where the COVID-19 pandemic continues to affect the world's health. Pneumonia and Tuberculosis (TB) are always very concerning chest diseases, and COVID-19 has also been added to this list. Chest X-rays (CXR) and CT scans are major sources for diagnosing respiratory disorders. As CT scans are a little bit costlier and take more time, as well as expose patients to mild radiation, the use of CXR is increasing for the diagnosis of chest diseases. This study uses CXR images to accurately identify diseases using the developed MobileNetV2, ResNet50, VGG19, and DenResCov-19 Convolutional Neural Network (CNN). The models were analyzed and tested using the publicly available 13805, 5840, and 4200 chest x-ray images for COVID-19, pneumonia, and TB cases. The in-house mobile app employs a variety of deep-learning models to identify diseases from chest X-rays. With 99.79% accuracy and 96.89% F1-score, ResNet50 is the best model architecture for COVID-19 classification. The ResNet50 pneumonia classification model was 99.17% accurate and had an F1-score of 94.52%. With 99.88% TB detection accuracy and 99.64% F1-score, MobileNetV2 and ResNet50 were equivalent. Comparing model efficacy on the dataset was fascinating.

Keywords: CNN, COVID-19, Pneumonia, Radiography, Tuberculosis

1. Introduction

The lungs play a vital role in the human physiological system as they undergo expansion and contraction processes to facilitate oxygen intake and carbon dioxide expulsion. Lung disorders encompass a range of respiratory ailments that impact respiration's physiological structures and functions, leading to conditions affecting the airways, lung tissues, and pulmonary circulation. Certain respiratory infections, such as the common cold and influenza, may result in minimal discomfort and annoyance. However, there are other respiratory infections, such as pneumonia, TB, and lung cancer, that pose a significant threat to life and lead to the development of severe acute respiratory

complications. The early detection of the illnesses above during the initial stages of infection can significantly enhance the likelihood of survival and mitigate human fatalities. Chest radiography and Computed Tomography (CT) imaging are commonly employed diagnostic procedures for identifying and assessing these conditions [1,2].

In recent decades, medical practitioners have encountered challenges in accurately diagnosing diseases, leading to needless interferences in healthcare and malpractice litigation for stakeholders. Many studies conducted through interdisciplinary collaboration between medical and engineering researchers have extensively investigated the effectiveness of computer-aided diagnosis within the medical domain. Some automated diagnosis systems utilized in medicine can also be classified as expert systems due to their aim of emulating the diagnostic reasoning of medical experts. Furthermore, it is worth noting that computer-aided detection systems utilized in medicine can effectively analyze intricate and substantial volumes of clinical data [3]. Computer-aided detection systems have the potential to assist doctors in gaining novel perspectives on data and utilizing acquired knowledge to enhance diagnostic precision. Because of this, the systems are considered intelligent because they use feedback methods to improve their efficiency over time.

The most recent advancements in analysis and classification tools rely on Machine Learning (ML) applications and DL techniques, demonstrating their effectiveness as computer-based tools. Recent advancements and investigations in ML and DL have demonstrated that automated tools have yielded remarkable outcomes surpassing those achieved by human identification in several application domains. Figure 1 illustrates the sequential stages of identifying features and subsequent categorization using image processing techniques on datasets, including CXR or CT images. ML and DL systems can effectively incorporate and analyze vast datasets to facilitate system learning and provide accurate predictions. The main goals of DL models are to discover and classify image properties within extensive datasets accurately. Most contemporary thriving industries, such as healthcare, have attained very impactful discoveries through DL-based systems [4]. DL may also be employed to develop systems capable of adequately predicting and diagnosing diseases based on visual data. Previous studies have shown evidence of the efficacy of this approach in the detection of TB [5-9], pneumonia [10-18], and COVID-19 [11, 15, 18-25] without the need for human interaction. The subsequent sections of the manuscript are organized in the following manner: The second half of the material delves into the principles and theories around convolutional neural networks. Section 3 analyzes and examines relevant scholarly contributions within the existing body of literature. Section 4 provides an overview of the approach employed in the proposed system, while Section 5 presents a concise summary of the findings obtained from the system.

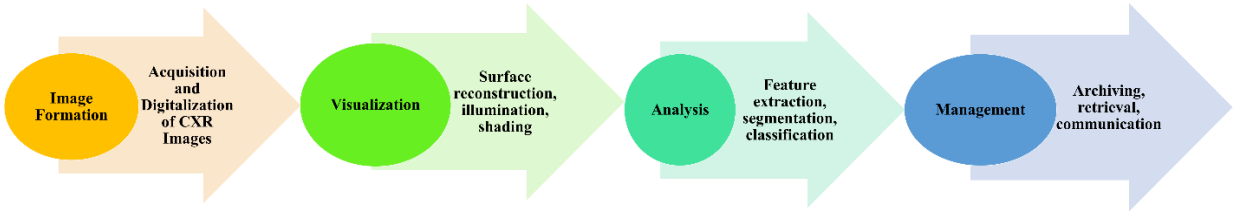


Figure 1. Representation of classification model based on image processing

2. Convolutional Neural Networks (CNNs) Architecture

CNNs are highly successful in recognizing and classifying features within image datasets. The architecture consists of three distinct layers, namely convolutional, pooling, and fully-connected layers. The convolutional approach employed by the convolutional layer facilitates the identification and extraction of the primary features inherent in the collection of images. Convolution kernels and learnable filters facilitate the extraction of internal image characteristics and deep vital data. To validate the output of the neurons, the dot product between the weight of the kernel and the local region will be utilized. Equation 1 illustrates the convolution process.

$$z = w_i^l * y^{(j)} \tag{1}$$

where * represents a cross product of weight and local regions of the kernel, W_i^l is the weights of the 1st layer ith filter kernel for CNN, and $y^{(j)}$ is the 1st layer's jth local region of CNN.

To use neural networks to solve complex problems, it is necessary to use a convolution operation, followed by the utilization of an activation function, such as sigmoid, Rectified Linear Units (ReLU), and so on. The function above generates the activation map, which encompasses the filter responses. ReLU outperforms classic activation functions such as sigmoid and tanh due to its ability to accelerate the training of neural networks by a factor of four, leading to reduced computational expenses. The ReLU function is defined by (2) [26], where *y* is the input.

$$g(y) = \begin{cases} 0 \ for \ y < 0 \\ y \ for \ y \geq 0 \end{cases} \tag{2}$$

Similarly, the incorporation of the last layer involves the utilization of the SoftMax activation function, which serves to enhance the efficacy of the neural network. The SoftMax function is given in (3) [26].

$$\sigma(c)_j = \frac{e^{z_i}}{\sum_{j=1}^{K} e^{z_j}} \tag{3}$$

where z_i is the raw output (logit) of class *I*, *K* is the total number of classes, and e is the base of the natural logarithm (approximately equal to 2.71828).

In addition to including convolution layers, CNNs have pooling layers responsible for processing the output generated by the convolution layers. The fundamental aim of the pooling layer is to decrease the dimensions of the feature map, resulting in compression while preserving relevant information. This will lead to decreased computation times and less overfitting. CNN attains a heightened degree of awareness through many iterations of convolution and pooling layers, ultimately leading to the integration of fully connected (FC) layers. The weights and biases implemented in these layers facilitate connectivity between neurons of different layers. The fully connected layer's final layer consists of as many output neurons as there are classes to be recognized. The categorization procedure makes use of this layer.

ResNet50 is one of the family of Residual Networks members, which overcame the problem of vanishing gradients in deep networks and was completed using skip connections. It became possible to train such a network efficiently, even with 50 layers. This design incorporates several residual blocks, whereby every block is built from convolutional layers followed by batch normalization and ReLU activation to ensure smooth propagation of the gradients. ResNet50 is typically utilized for applications where high accuracy is needed. It can take input images of size 224x224 pixels. VGG19 was one of the early influential CNN architectures with a deep and simple structure. It contains 16 stacked small 3x3 filter convolutional layers followed by three fully connected layers at the tail end. Although the network is deep, applying max pooling after stacks of convolutional layers is pretty straightforward. This architecture also accepts 224x224 pixel images and has become a benchmark model for various image classification tasks due to reliable performance.

MobileNetV2 is designed with efficiency in mind, especially in mobile and edge device settings where one does not have too much computational power. This architecture uses depthwise separable convolutions that split the operation of convolutions into two parts: depthwise and pointwise. They result in an extremely low number of parameters and computational cost. Further, MobileNetV2 uses linear bottlenecks and residual connections important for fast information flow. Its design is applied when simultaneous high accuracy and high-speed performance are desired without heavyweight hardware. Another crucial CNN architecture based on dense connections within the layers is DenseNet, particularly in its use as DenResCov-19 for detecting COVID-19. In DenseNet, every layer is given input from all layers that have been processed previously to boost feature propagation and reduce the number of parameters needed while enhancing gradient flow. Generally, DenseNet is composed of a series of dense blocks, the transitions of which are followed by a

reduction in the dimensionality of the feature maps. Because of its strong feature extraction capabilities, this architecture has proven useful in medical imaging tasks, such as detecting COVID-19 diseases.

There have been several attempts to determine whether or not DL models help predict COVID-19, pneumonia, and TB. Due to its ability to assist in the automatic identification of viruses in medical imaging modalities like CT scans and X-rays, DL has seen widespread use in the field of diagnostics. Patterns and characteristics linked to COVID-19, pneumonia, and TB have been successfully identified with the help of CNN. One proposed approach for successful DL-based COVID-19 screening is a voting-based technique pioneered by Silva and Luz. It has achieved higher accuracy than existing state-of-the-art approaches [19]. Using multi-modality data and clinical specialists' views is crucial for ensuring accurate and efficient diagnosis of COVID-19 since treating each CT imaging slice independently might lead to potentially misleading outcomes [19,20]. AI-based approaches have been commonly employed for COVID-19 screening, diagnosis, and prediction. However, there are issues with their ability to generalize due to the training and testing process using images from the same dataset [19,21]. DL methods, specifically CNN, Recurrent Neural Networks (RNN), and Long Short-Term Memory (LSTM), have been utilized to identify, diagnose, and classify COVID-19. These approaches have demonstrated encouraging outcomes, even with limited data availability [20,21]. In addition to DL methods, many other ML techniques, such as Support Vector Machines (SVM), logistic regression, random forests, and decision trees, have been effectively employed to identify and predict the severity of COVID-19 [21,22]. The methodologies above have been employed to simulate patient outcomes and forecast the degree of severity, likelihood of ICU admission, and fatality rates. These predictions are derived from an analysis of clinical factors, blood tests, and quantitative CT parameters [22].

In general, using artificial intelligence (AI) and ML in medical imaging has improved the accuracy of diagnosing COVID-19 by analyzing CXR and CT images. Furthermore, integrating several modalities in AI models can enhance the intelligence of medical systems in diagnosing and predicting COVID-19 [20]. However, it is worth noting that DL has exhibited impressive results in the context of COVID-19 applications. This is exemplified by the Truncated Inception Net, a CNN model based on DL techniques. The model above has achieved a remarkable accuracy of 99.96% in identifying COVID-19-positive cases, distinguishing them from patients with pneumonia and those in good condition [23]. Similarly, the AI system CAD4COVID-XRay identified CXR images explicitly as COVID-19 pneumonia with an AUC of 81%, making it effective in low-resource situations where diagnostic equipment is not accessible [23]. However, establishing trust in DL models' accuracy is crucial before investing resources in developing drugs to attack protein targets identified by the models [24]. The paper extensively examines existing literature concerning the present state and prospective advancements in utilizing DL techniques for detecting COVID-19 [23,25].

The identification of TB using automated means has garnered considerable interest in recent years, resulting in several scholarly articles that showcase cutting-edge DL methodologies. A thorough examination of the existing literature has been carried out to explore the use of DL methods in identifying TB. This review aims to support researchers in creating a Computer-Aided Diagnosis (CAD) system that can effectively diagnose TB by employing DL classifiers. The review emphasizes the need to assess the precision of CAD systems by employing distinct datasets for evaluation, apart from those used for training. Additionally, it underscores the need to acknowledge the constraints present in current studies regarding methodologies and stated accuracy to inform the development of CAD systems in subsequent research endeavors. This study primarily centers on using DL classifiers to diagnose TB through the analysis of CXR. Numerous DL approaches have been employed for TB screening, prediction, and diagnosis. It isn't easy to compare the approaches due to several aspects, such as the types of datasets used, the number of image samples, the assessment metrics employed, and the tuning of model parameters [27]. In the current era of new technologies, ML and DL techniques are prevalent in diagnosing TB using indicators from a dataset of chest radiographs, sputum smears, and biomarkers sources [28]. The progression of CAD adheres to a conventional structure comprising four distinct stages: pre-processing, segmentation, feature extraction, and classification. Pre-trained CNNs have been employed to train extensive datasets such as the RSNA, Pediatric pneumonia, and Indiana datasets. This utilization has enhanced accuracy in TB diagnosis utilizing modality-specific DL

models. The feature extraction process entails identifying discriminative characteristics utilized for further investigation [27]. Furthermore, prior methodologies for TB detection have utilized pre-trained CNN models. Additionally, TB diagnosis has been carried out using techniques such as handcrafting, ML, and DL, as mentioned in reference [28]. The study's primary objective was to examine the CAD system, utilizing one or more DL approaches as the classifier for TB detection [27].

In [29], the authors highlighted the significant capacity of DL to transform the diagnosis and treatment of respiratory illnesses. DL systems demonstrate a high skill level in accurately diagnosing different lung illnesses by analyzing complex patterns in large datasets. This advancement not only improves the process of making medical decisions but also has the potential to influence the treatment of respiratory diseases significantly. Moreover, using extreme learning machine approaches offers an additional approach to identifying respiratory disorders, particularly the urgent issue of COVID-19 [30]. By utilizing the efficient structure of Convolutional Neural Networks (CNNs), these algorithms are highly effective in extracting essential characteristics from medical images, enabling precise illness identification. The partnership between CNN architecture and extreme learning machines highlights a viable strategy for enhancing healthcare results, specifically in respiratory health[30]. Authors of [31] have significantly contributed to this subject by creating a Chest Infection Diagnostic Model. Using transfer learning and a multistage multiclass architecture, this model improves accuracy in diagnosing a wide range of chest diseases, including common colds and severe pneumonia. These developments give healthcare personnel more accurate diagnostic abilities, potentially improving patient care and outcomes.

Incorporating artificial intelligence (AI) and knowledge distillation techniques in CAD systems represents a notable advancement in diagnosing pneumonia, TB, and COVID-19 [32]. By condensing information from intricate AI models into more efficient systems, these CAD platforms demonstrate remarkable precision comparable to human specialists in analyzing chest radiographs. The combination of AI-driven innovation and medical imaging holds great promise for the future of precision medicine and the accuracy of diagnostics [32]. DL plays a crucial role in CT imaging for accurately categorizing respiratory illnesses such as pneumonia, TB, and COVID-19. By analyzing large CT datasets, DL algorithms may detect tiny patterns that suggest certain illnesses. This enables the early and accurate detection of diseases. This innovative method has great promise for enhancing medical diagnostics and patient outcomes in chest illnesses [33].

The emergence of Vision Transformers signifies state-of-the-art progress in identifying pneumonia using chest X-ray images. By harnessing sophisticated ML algorithms, Vision Transformers efficiently process images to detect distinctive indicators of pneumonia, facilitating prompt interventions and ultimately preserving lives. The integration of technology and healthcare highlights the profound capacity of artificial intelligence to revolutionize illness detection and patient treatment [34].

A deep transfer learning convolutional neural network approach was proposed by Sai et al. (35), which can distinguish between viral pneumonia, bacterial pneumonia, and COVID-19. The training dataset consisted of 5856 chest radiographs, which were used to train a pre-trained ResNet-50V2 model for 100 epochs. The training method resulted in an accuracy rate and test score of 94%. The attainment of a high level of precision was aided by increasing the number of epochs and incorporating a dropout layer following the dense layer. The CNN (Convolutional Neural Network) architecture is commonly employed for binary and multiclass classification tasks. The training dataset consisted of 3877 CT and X-ray images, with 1917 of them being of patients diagnosed with COVID-19. The performance of the binary classifier was evaluated, yielding an accuracy of 99.64%.

Additionally, the classifier demonstrated a recall rate of 99.58%, precision of 99.56%, F1 score of 99.59%, and a perfect receiver operating characteristic (ROC) score of 100%. A total of 6077 images were utilized for training the model. The number of individuals diagnosed with COVID-19 was 1917, whereas 1960 individuals were deemed healthy. Additionally, there were 2200 reported occurrences of pneumonia. The authors reported accuracy, sensitivity, precision, F1-score, and ROC values of 98.28%, 98.25%, 98.22%, 98.23%, and 99.87% correspondingly for the multiclass classification [36].

To speed up the COVID-19 diagnostic process, Oguz et al. [37] employed a dataset of 1345 CT scan images acquired from a research hospital. The images are subjected to various DL algorithms, such as ResNet-50, ResNet-101, AlexNet, and GoogleNet, as well as additional categorization techniques like SVM, Random Forest, Decision Trees, and others. During the pre-processing phase, the dimensions of the CT images were decreased by implementing maximum pooling. In addition, the Rectified Linear Unit (ReLU) activation function was included in each convolutional layer. The experimental findings indicated that ResNet-50 and SVM outperformed the other models, achieving an accuracy rate of 96.3% and an F1-score of 95.87%. Nevertheless, the effectiveness of this methodology is constrained by the amount of data used and may not demonstrate robust applicability to unfamiliar data. As the quantity of utilized classes increases, there is a corresponding drop in the model's accuracy. Hussain et al. [38] presented their findings, showcasing the development of a deep Convolutional Neural Network model named 'CoroDet,' consisting of 22 layers. The dataset utilized in this study comprised a total of 7390 images, with 2843 images representing COVID-19 patients, 3108 images representing normal cases, and 1439 images representing instances of pneumonia caused by both viral and bacterial infections. The deep Convolutional Neural Network model was utilized for three distinct class classifications: COVID-19, Pneumonia-Bacteria, and Normal. A four-class classification, including COVID-19, Pneumonia-Bacteria, Normal, and Pneumonia-Viral, was also performed. Notably, no preprocessing of the data was conducted before these classifications. The methodology devised by the researchers resulted in an accuracy rate of 99.1% for classifiers with two classes, 94.2% for classifiers with three classes, and 91.2% for classifiers with four classes. Nevertheless, these conclusions may be enhanced by the augmentation of data, equalizing class instances, and implementing data pre-processing techniques to mitigate noise.

3. Materials and Methods

This research aims to construct a DL framework that can accurately categorize COVID-19, Pneumonia, and TB into normal and pathological categories. The suggested system employs a DL convolutional neural network. Its main use is image categorization and analysis, where each network layer applies a distinct set of filters. The outcomes of each layer are obtained by the fusion of a range of 100 to 1000 filters. The results are ultimately transmitted to the subsequent neural network layer. Figure 2 illustrates the suggested methodology for the detection model, which aims to distinguish normal and infected cases for each illness. The training process utilizes the Keras and Tensorflow software libraries. The proposed model would incorporate many stages, including dataset acquisition, partitioning, preprocessing, training, and testing/evaluation.

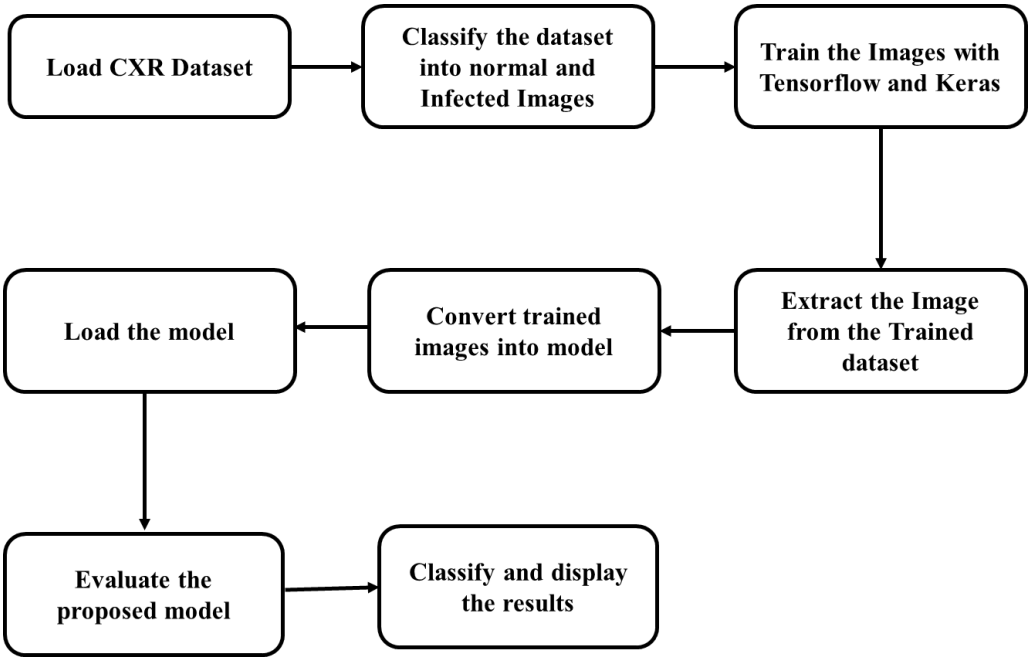


Figure 2. Proposed system's framework

Figure 3 shows the block diagram of the proposed system. The proposed model takes as input X-ray samples of images associated with each detected disease. The first convolutional layer receives image input, which is processed using a specified activation function. The pooling layer is introduced successively after the activation function layer. The utilization of a max pooling layer serves the purpose of diminishing the spatial dimensions of the representation. The suggested model includes a secondary convolutional layer that follows the same layer sequence as the first layer, including an activation layer, a pooling layer, and a max-pooling layer.

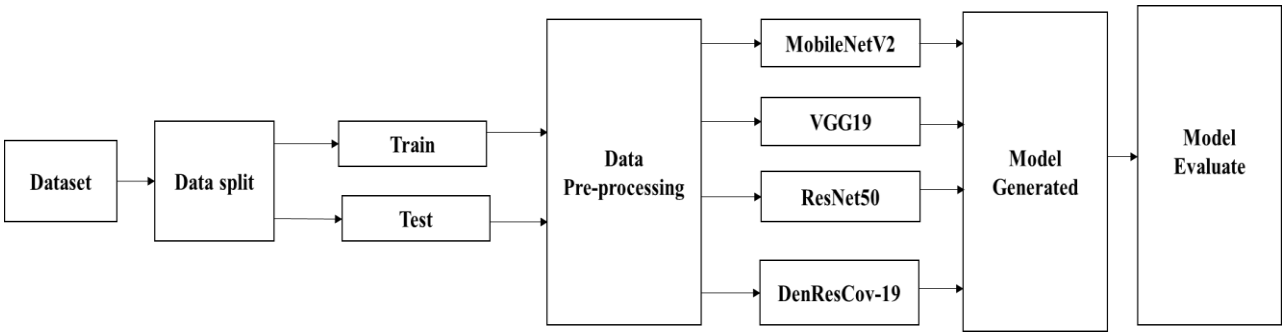


Figure 3. Block diagram of the proposed system

In the initial stage, the input images are subjected to a random partitioning method, whereby the data image is divided into 80% for training purposes and 20% for validation. Pre-processing techniques such as normalization and scaling are also applied to the images using relevant functions. Then, in the second and third stages, DL algorithms are deployed. The second step involves the process of feature extraction, which is achieved by employing ResNet50, VGG19, MobilenetV2, DenResCov-19, and CNN algorithms. Employing a fully linked network is utilized at the image categorization stage.

The architecture of the CNN, as outlined in section 2 and depicted in figure 4, comprises an input layer, an output layer, and hidden layers that are formed of convolutional layers with Rectified Linear Units (ReLU), pooling layers, and fully connected layers. The input datasets for this network consist of X-ray images representing both normal and sick occurrences for each illness, along with three RGB channels. The dimensions of the chosen input data set are 224 x 224. The provided dataset is inputted into the first layer, known as the convolutional layer, which utilizes the Rectified Linear Unit (ReLU) activation function. The initial layer employs a kernel with the size of 224 x 224 and produces 32 output channels to diminish the feature map. Additionally, it generates 32 output channels to further lower the feature map to a size of 112. The maximum values for each window will be documented when filtered using the stride. The procedure above will be executed for every individual dataset of filtered images. The third layer of the network consists of a convolutional layer with a kernel size of 112 x 112, followed by a pooling layer with a kernel size of 7 x 7, which precedes the fully connected layer. Furthermore, the network incorporates a flattened layer that is fully linked. The SoftMax function incorporates a fully linked layer into the model architecture. The ultimate layer will be employed to make predictions regarding the classification of an image, namely whether it is normal or contaminated with a disease.

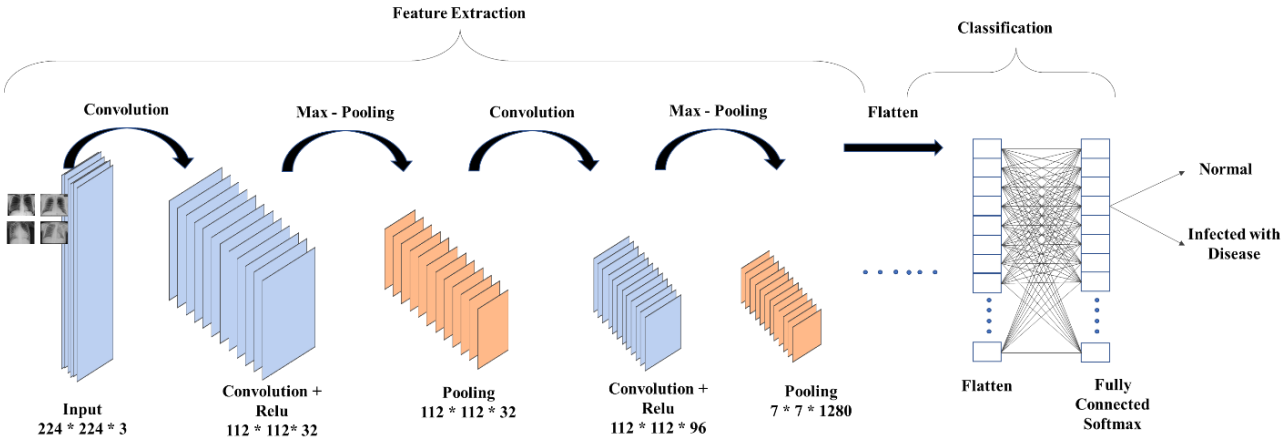
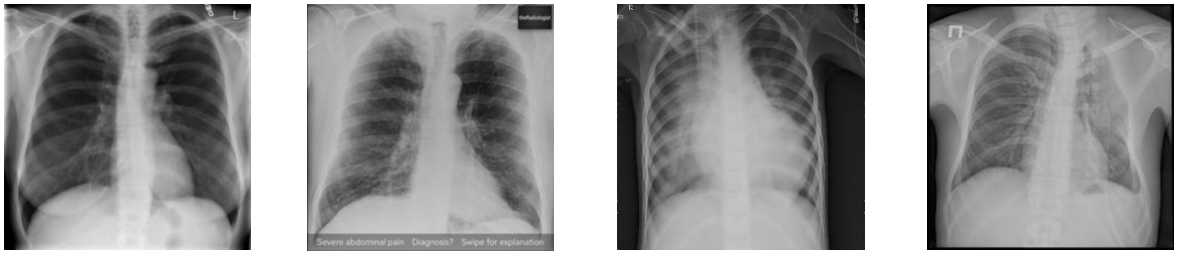


Figure 4. CNN model architecture used for the proposed system

3.1 Dataset

In addition to healthy examples, X-ray images of COVID-19, pneumonia, and TB were accessible and collected from dependable sources [38-40]. Figure 5 presents X-ray image samples utilized in this work, showcasing (A) a normal case, (B) a case of COVID-19, (C) a case of pneumonia, and (D) a case of TB. The COVID-19 dataset comprises 13,805 images, encompassing both normal and diseased cases. These images are further separated into 11,044 for training and 2,761 for testing purposes. The dataset consists of a total of 5840 images, encompassing both normal and infected instances of pneumonia. These images are further separated into 4672 images for training and 1168 images for testing purposes. The dataset used in this study consists of a total of 4200 images, encompassing both normal and infected instances of pneumonia. These images have been separated into two subsets: 3360 images for training purposes and 840 images for testing purposes. Table 1 presents the specific information of the dataset stated before.



(a) (b) (c) (d)

Figure 5. X-ray image samples (a) normal (b) COVID-19 (c) pneumonia (d) tuberculosis

3.2 Preprocessing and Data Augmentation

The datasets comprise X-ray images with varying resolutions. In contrast, the CNN models require the image dataset to adhere to specific size requirements. Consequently, the X-ray images within the dataset were uniformly scaled to dimensions of 224 * 224. Decreasing the dimensions of the input image has the effect of expediting the image processing procedure, hence hastening the model's performance for the specific associated job. The primary concern associated with image datasets is overfitting. Data augmentation is a widely employed strategy in ML, wherein small alterations are introduced to an image during each training epoch. This approach is favored due to its ability to substantially augment the volume of training data and effectively mitigate the issue of overfitting. Several augmentation techniques were employed in this study, encompassing image rotation, range shearing, range zooming, and horizontal flips.

Using a random splitting method, the dataset was divided into two subsets, namely the validation subset and the training subset. The validation subset accounted for 20% of the data, while the training subset

accounted for 80%. This division was implemented to ensure that the variability included in the X-ray images adhered to the required parameters for training the proposed model. The CNN model's ability to leverage additional data beyond the original dataset is essential for attaining high levels of accuracy.

Table 1. Details of Dataset of COVID-19, pneumonia, and tuberculosis used for this research study

Dataset of Diseases	Types of Images	Training Images	Testing Images	Total Images
COVID 19 [38]	Normal	8152	2038	10,190
	COVID 19 Infected	2892	723	3,615
	Total	11044	2761	13805
Pneumonia [39]	Normal	1260	315	1,575
	Pneumonia Infected	3412	853	4,265
	Total	4672	1168	5840
Tuberculosis [40]	Normal	2800	700	3500
	Tuberculosis Infected	560	140	700
	Total	3360	840	4200

3.3 System Realization

The present study employs an Android application developed internally utilizing the Arduino integrated development environment (IDE). The DL model was deployed on the web using Tensorflow.js, while the same model was deployed on an Android-based application using the Tensorflow-Lite API. The system underwent testing using datasets to verify its ability to recognize both normal and disease-infected instances and assess the performance of the developed model software program, which operated as anticipated. Figure 6 (a), (b), and (c) illustrate the Android applications that were built for this study.

4. Results and Discussion

The present study aimed to evaluate the performance of four different CNN models, MobileNetv2, VGG19, ResNet50, and DenResCov-19, in identifying COVID-19, Pneumonia, and TB. The models underwent training, during which their precision and losses were evaluated. Subsequently, the test efficacy was measured and compared to findings from other studies. In all experimental trials, the parameter values employed for the number of epochs, batch size, and dropout were 50, 32, and 0.5, respectively. The dataset was partitioned into 80% training and 20% testing sets. The experimental hardware consisted of an Intel i7-10750H processor. The GPU is Nvidia GTX 1660Ti, and RAM is 16GB.

The dataset images were classified into two groups, normal and afflicted with illness, using our suggested system that underwent training for 20 epochs. The accuracy, loss curves, and confusion matrix of the COVID-19 detection model using MobileNetv2, VGG19, ResNet50, and DenResCov-19 are depicted in Figures 7(a), (b), (c), and (d) accordingly. These figures illustrate the models' performance throughout the training and validation phases, spanning a total of 20 epochs. Likewise, the outcomes for Pneumonia and TB are demonstrated by 8(a), (b), (c), (d) and 9(a), (b), (c), (d).

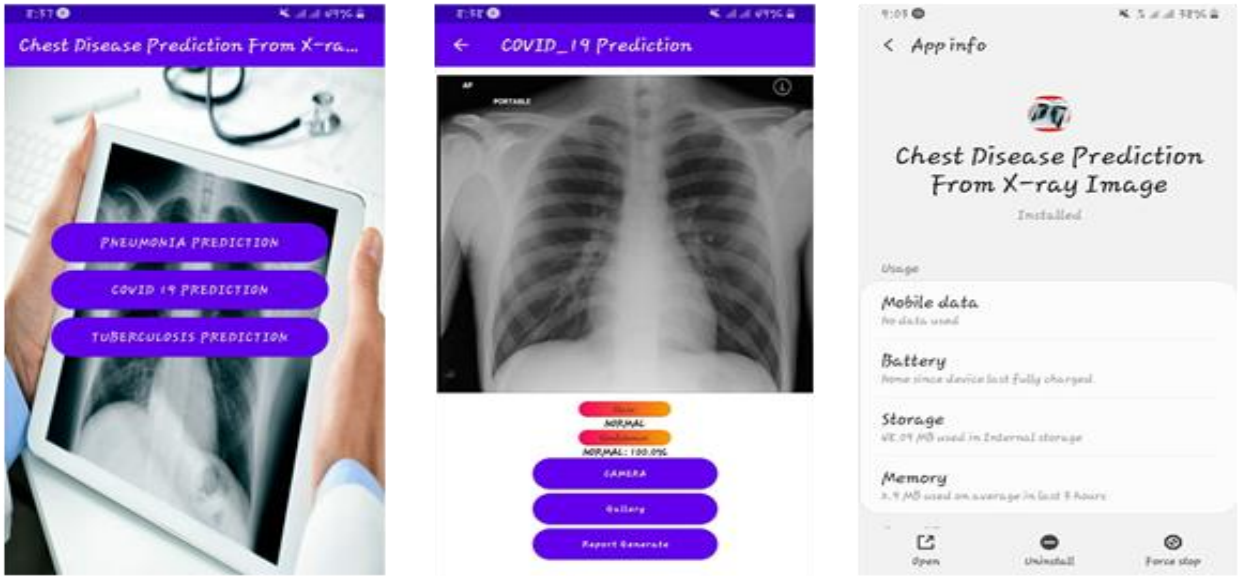


Figure 6. Android App developed for the realization of the proposed system

Table 2 presents comprehensive data about the accuracy and loss metrics for training and validation phases over 20 epochs for each model of COVID-19, Pneumonia, and TB.

Table 2. Accuracy % and loss in training and validation over 50 epochs of detection model using MobileNetV2, VGG19, ResNet50, DenResCov-19

Disease Name	Model Name	Accuracy %		Loss	
		with the training dataset	with the validation set	with the training dataset	with the validation set
COVID-19	MobileNetV2	99.36	97.39	0.0219	0.0729
	VGG19	97.96	94.97	0.0619	0.0128
	Resnet50	99.79	98.37	0.0094	0.0556
	DenResCov-19	99.24	97.72	0.029	0.068
Pneumonia	MobileNetV2	99.12	96.92	0.0309	0.1004
	VGG 19	98.39	96.58	0.0512	0.1023
	Resnet50	99.17	97.09	0.0271	0.0852
	DenResCov-19	98.42	96.23	0.0473	0.0934
Tuberculosis	MobileNetV2	99.89	99.4	0.0011	0.0154
	VGG 19	99.82	99.4	0.0075	0.0207
	Resnet50	99.88	99.4	0.0012	0.0181
	DenResCov-19	99.77	99.29	0.0023	0.0195

The loss curves in Figures 7, 8, and 9 demonstrate a minimal discrepancy between the training and validation loss curves, suggesting that the models have achieved satisfactory convergence. Furthermore, no indications of overfitting were seen throughout the training and validation processes. The confusion matrix is employed to represent the system's performance metrics. Additional assessment metrics can be developed using the available data to emphasize the system's performance being discussed. The confusion matrix yields a True Positive outcome when the system accurately classifies an infected case as the correct disease. A False Positive outcome occurs when the system incorrectly identifies a normal case as one of the disease cases. True

Negative is achieved when the system correctly classifies a normal case as normal, indicating the absence of disease. Lastly, a False Negative outcome arises when the system misclassifies an infected case as normal.

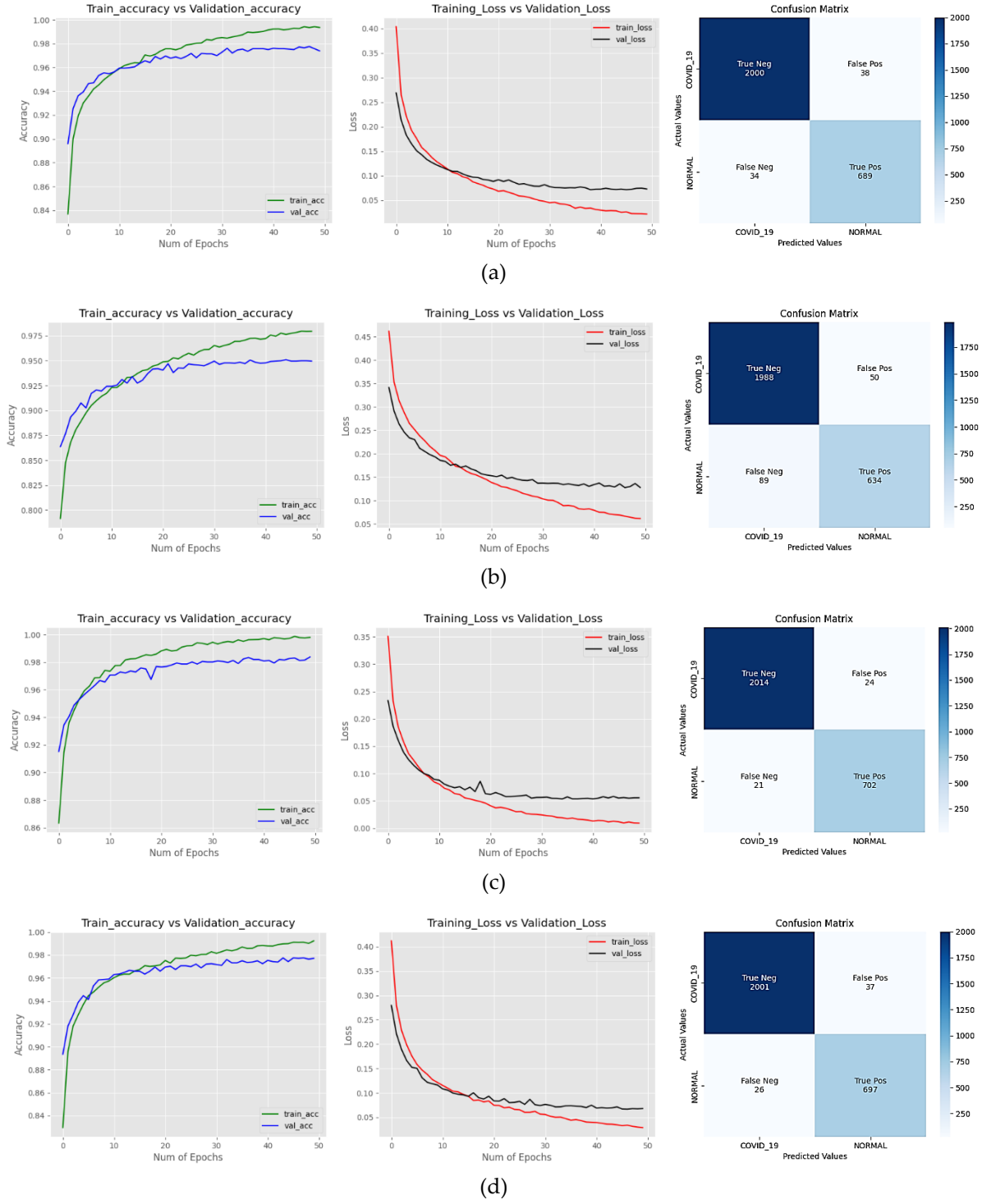


Figure 7. Accuracy curve, loss curves, confusion matrix of COVID-19 detection model using (a)MobileNetv2 (b)VGG19 (c)ResNet50 (d)DenResCov-19

An evaluation was undertaken to assess the performance of the classification model constructed in this study. This evaluation involved the consideration of several derived parameters: True Positive Rate (TPR), True Negative Rate (TNR), False Negative Rate (FNR), and False Positive Rate (FPR) as specified in (4-7) [41].

Additionally, performance metrics such as precision, accuracy, and F1 score, reported as in (8-10) [42], were also considered. The additional metrics, recall and specificity, are equivalent to the TPR described in (4) and the TNR outlined in (6).

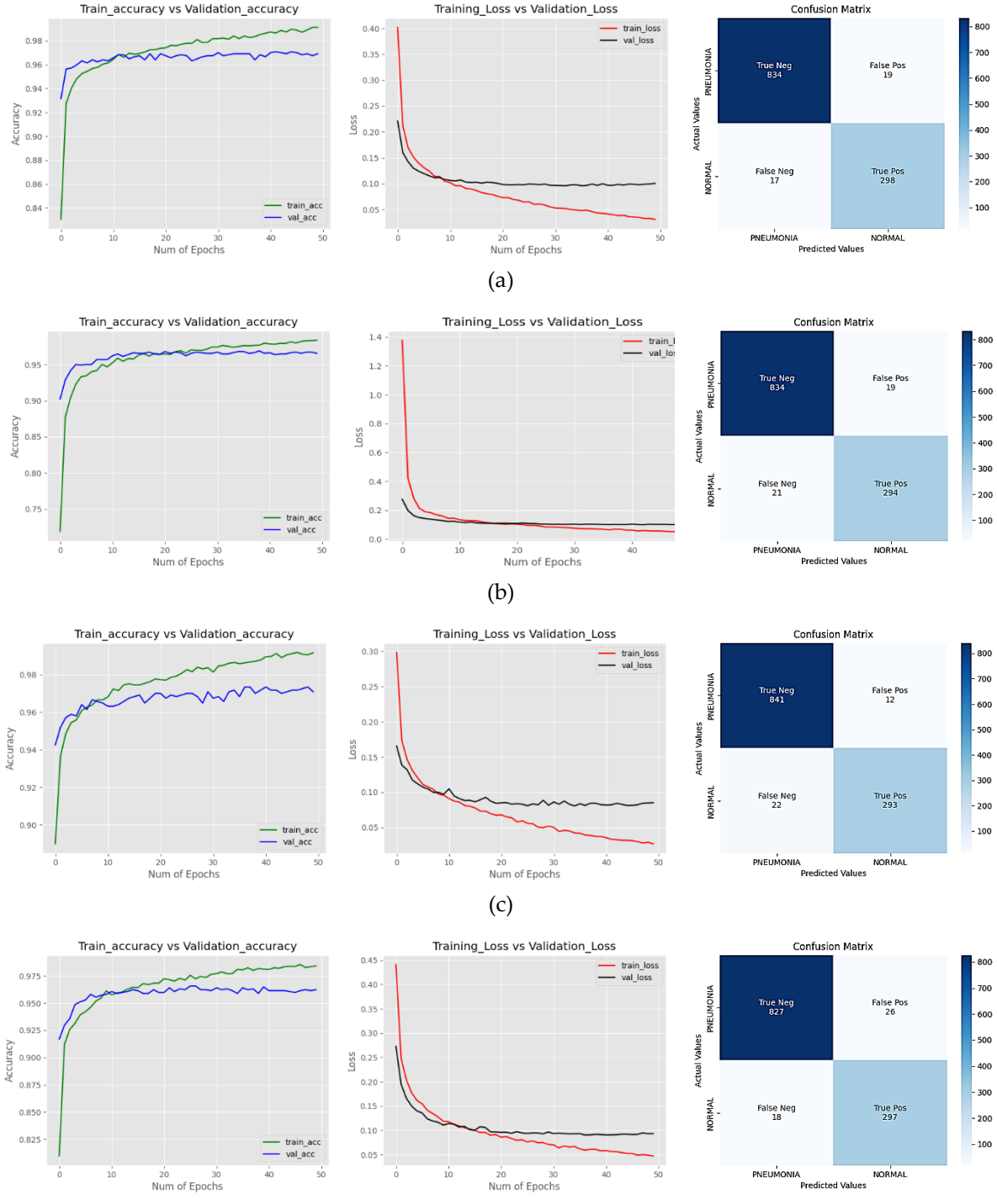
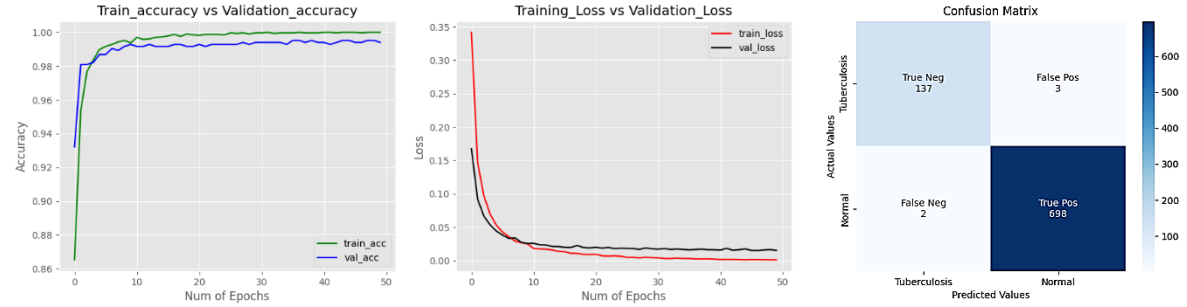
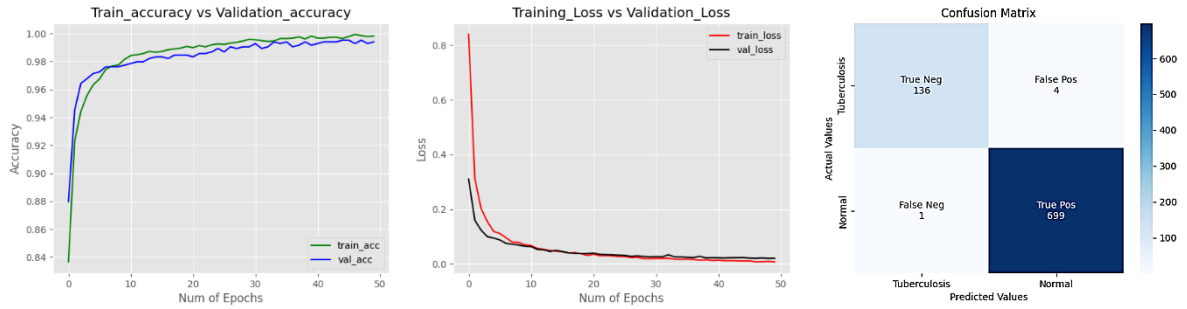


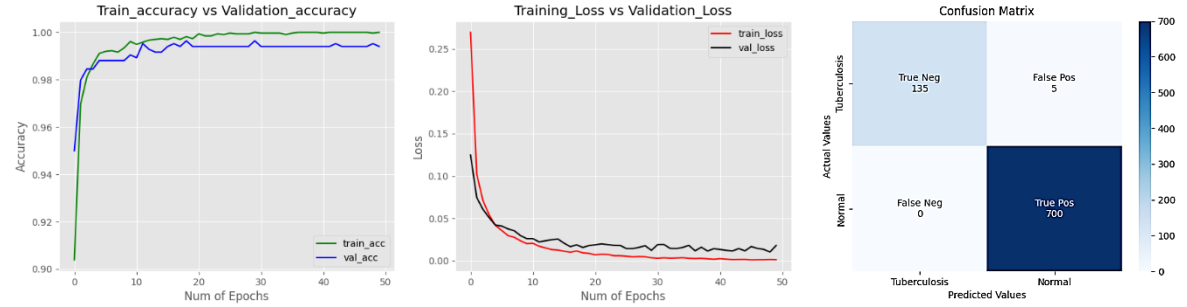
Figure 8. Accuracy curve, loss curves, confusion matrix of Pneumonia detection model using (a)MobileNetv2 (b)VGG19 (c)ResNet50 (d)DenResCov-19



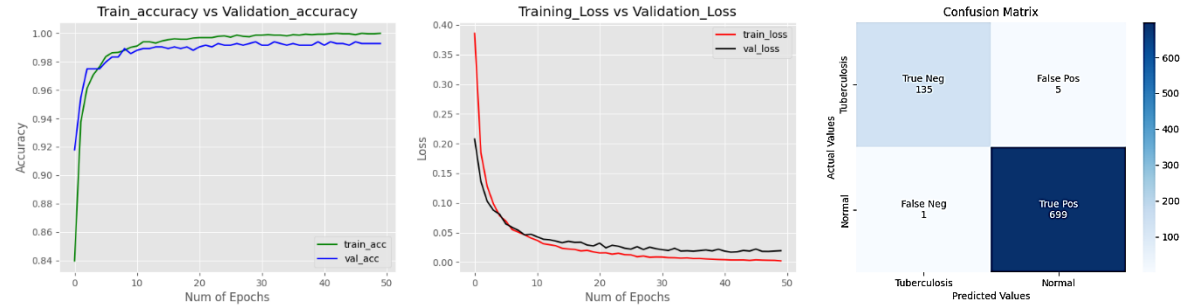
(a)



(b)



(c)



(d)

Figure 9. Accuracy curve, loss curves, confusion matrix of TB detection model using (a) MobileNetv2 (b) VGG19 (c) ResNet50 (d) DenResCov-19

$$TPR = \frac{Tpos}{Tpos + Fneg} \tag{4}$$

$$FNR = \frac{Fneg}{Tpos + Fneg} \tag{5}$$

$$TNR = \frac{Tneg}{Tneg + Fpos} \tag{6}$$

$$FPR = \frac{Fpos}{Tneg + Fpos} \tag{7}$$

$$\Pr ecision = \frac{Tpos}{Tpos + Fpos} \tag{8}$$

$$Accuracy = \frac{Tpos + Tneg}{Tpos + Tneg + Fpos + Fneg} \tag{9}$$

$$F1\ Score = \frac{2 * \Pr ecision * \mathrm{Re} call}{\Pr ecision + \mathrm{Re} call} \tag{10}$$

The assessment of precision functions as a method to measure the efficacy and feasibility of the proposed system. The precision metric is utilized to determine the true proportion of positive predictions. The recall measure, or the sensitivity measure, evaluates the proportion of correct predictions generated by the suggested model. The F1-score is commonly defined in academic literature as the inverse mean of the recall and accuracy metrics, which are widely employed for assessing the performance of a model. The equations above can provide a deeper understanding of the suggested system. The classification report of the suggested system is presented in Table 3.

According to the data shown in Table 3, it is evident that the ResNet50 model architecture outperforms the other models utilized in terms of performance. The ResNet50 model achieves an accuracy of 99.79% and an F1 score of 96.89% for COVID-19, while for pneumonia classification, it attains an accuracy of 99.17% and an F1 score of 94.52%. The performance of TB diagnosis using the MobileNetV2 and ResNet50 models exhibited nearly identical levels of accuracy, achieving a rate of 99.88%. The F1 score, which measures the balance between precision and recall, also reached 99.64%. One notable discovery in our research is the comparison of the efficacy of different models using the provided dataset.

Table 3. Performance evaluation of different measures for the proposed system

Disease Name	Model Name	Measures							
		TPR	FNR	TNR	FPR	Precision	Recall the same as TPR	Specificity same as TNR	F1-Score
COVID-19	MobileNetV2	0.9530	0.0470	0.9814	0.0186	0.9477	0.9530	0.9814	0.9503
	VGG19	0.8769	0.1231	0.9755	0.0245	0.9269	0.8769	0.9755	0.9012
	Resnet50	0.9710	0.0290	0.9882	0.0118	0.9669	0.9710	0.9882	0.9689
	DenResCov-19	0.9640	0.0360	0.9818	0.0182	0.9496	0.9640	0.9818	0.9568
Pneumonia	MobileNetV2	0.9460	0.0540	0.9777	0.0223	0.9401	0.9460	0.9777	0.9430
	VGG 19	0.9333	0.0667	0.9777	0.0223	0.9393	0.9333	0.9777	0.9363
	Resnet50	0.9302	0.0698	0.9859	0.0141	0.9607	0.9302	0.9859	0.9452
	DenResCov-19	0.9429	0.0571	0.9695	0.0305	0.9195	0.9429	0.9695	0.9310
Tuberculosis	MobileNetV2	0.9971	0.0029	0.9786	0.0214	0.9957	0.9971	0.9786	0.9964
	VGG 19	0.9986	0.0014	0.9714	0.0286	0.9943	0.9986	0.9714	0.9964
	Resnet50	1.0000	0.0000	0.9643	0.0357	0.9929	1.0000	0.9643	0.9964
	DenResCov-19	0.9986	0.0014	0.9643	0.0357	0.9929	0.9986	0.9643	0.9957

5. Discussion on Clinical Applicability

The proposed models, particularly ResNet50 and MobileNetV2, are now ready for application in clinical workflows to aid radiologists in determining these diseases quickly and efficiently: COVID-19, pneumonia, and tuberculosis. They have high accuracies at 99.79% for COVID-19 and 99.88% for tuberculosis, and these models might become a trustworthy tool for early detection, thus allowing for earlier management of patients and their treatments. With incredibly high accuracy rates obtained by the proposed models, they can be valuable tools supporting a radiologist's decision to make faster and more accurate diagnoses. This could become valuable where expertise by radiologists is fewer and farther between. The models used in this study- the MobileNetV2 especially- are highly computationally efficient and may be deployed even within resource-constrained environments. Where medical and CT scan professionals or units are difficult to access, the system may be a cost-effective and practical solution for disease detection and diagnosis by using only X-ray machines in a less densely populated or deprived area. The interface of proposed models into a mobile app will afford many telemedicine opportunities in which service providers can assess the X-rays taken by patients remotely. This could be particularly useful in the COVID-19 pandemic, where telemedicine diagnosis reduces contact exposure to healthcare workers and patients. Although these models demonstrate high performance on the datasets used here, the clinical environment may present a challenge, including noisiness, poor quality, or incompleteness of the X-ray images. Testing and validating the system in the clinical environment will be necessary to ascertain that the system can handle the variability associated with such situations.

6. Conclusions

Besides the ongoing COVID-19 pandemic, timely detection of diseases such as pneumonia and TB positively impacts patient mortality rates. To enhance the quality of healthcare services while minimizing expenses and reaction time, creating a mobile application that incorporates Convolutional Neural Networks and an Ensemble of DL Architectures is imperative. This application would be utilized inside energy-efficient medical devices to facilitate the automated identification of illnesses. An in-house mobile application of convolutional neural networks was developed using four different DL architecture models (MobileNetV2, ResNet50, VGG19, and DenResCov-19). These models were trained on COVID-19, pneumonia, and TB images from an open-access dataset. The models were utilized to classify the CXR image and discern the presence of COVID-19, pneumonia, TB, and healthy individuals. When evaluating several models for the detection of COVID-19, it was shown that the ResNet50 model architecture had superior performance, achieving an accuracy of 99.79%, an F1 score of 96.89%, and a precision of 96.69%. The ResNet50 model architecture demonstrates superior performance compared to previous models utilized in the detection of pneumonia, achieving an accuracy of 99.17%, an F1 score of 94.52%, and a precision of 96.07%. The performance of TB detection using the MobileNetV2 and ResNet50 models exhibited similar results, achieving an accuracy of 99.88% and 99.64% F1 score. Additionally, the precision rates for the MobileNetV2 and ResNet50 models were 99.57% and 99.29%, respectively. One of the noteworthy outcomes of our study is the comparison of the effectiveness of several models on the provided dataset. The entire data confirmed the proposed technique's efficacy and efficiency. In the foreseeable future, there will be a comprehensive collection of CT scan data, including data on diverse lung illnesses, to train the model and enhance the healthcare industry. All data sets were subsamples of specific sources, such as publicly available repositories like Kaggle, which would introduce geographic and institutional biases, potentially limiting the broader generalisability of the models to diverse populations or healthcare settings. For instance, the data can reflect particular demographic groups or medical institutions and thus may not represent more general populations in other parts of the world. Furthermore, validation in real-world clinical settings remains necessary since the proposed models were stringently tested on these datasets. Models might face noisy, low-quality, or ambiguous X-ray images in practical applications not found in this study's clean and preprocessing datasets. Testing in actual clinical environments would thus better give insight into the robustness and applicability of models to real-world challenges and variability in image quality.

Author Contributions: Conceptualization, methodology, testing, and writing—original draft preparation, R.J., S.B., D.P., K.P., R.P., and A.T.

Funding: This research received no external funding

Conflicts of Interest: The authors declare no conflict of interest.

References

[1] Shen, D.; Wu, G.; Suk, H.-I. Deep Learning in Medical Image Analysis. *Annual Review of Biomedical Engineering* **2017**, *19*(1), 221–248. https://doi.org/10.1146/annurev-bioeng-071516-044442

[2] Yanase, J.; Triantaphyllou, E. A systematic survey of computer-aided diagnosis in medicine: Past and present developments. *Expert Systems With Applications* **2019**, *138*, 112821. https://doi.org/10.1016/j.eswa.2019.112821

[3] Khan, M. A.; Quasim, M. T.; Alghamdi, N. S.; Khan, M. Y. A Secure Framework for Authentication and Encryption Using Improved ECC for IoT-Based Medical Sensor Data. *IEEE Access* **2020**, *8*, 52018–52027. https://doi.org/10.1109/access.2020.2980739

[4] Sathitratanacheewin, S.; Sunanta, P.; Pongpirul, K. Deep learning for automated classification of tuberculosis-related chest X-Ray: dataset distribution shift limits diagnostic performance generalizability. *Heliyon* **2020**, *6*(8), e04614. https://doi.org/10.1016/j.heliyon.2020.e04614

[5] Gao, X. W.; James-Reynolds, C.; Currie, E. Analysis of tuberculosis severity levels from CT pulmonary images based on enhanced residual deep learning architecture. *Neurocomputing* **2019**, *392*, 233–244. https://doi.org/10.1016/j.neucom.2018.12.086

[6] Hooda, R.; Mittal, A.; Sofat, S. Automated TB classification using ensemble of deep architectures. *Multimedia Tools and Applications* **2019**, *78*(22), 31515–31532. https://doi.org/10.1007/s11042-019-07984-5

[7] Chandra, T. B.; Verma, K.; Singh, B. K.; Jain, D.; Netam, S. S. Automatic detection of tuberculosis related abnormalities in Chest X-ray images using hierarchical feature extraction scheme. *Expert Systems With Applications* **2020**, *158*, 113514. https://doi.org/10.1016/j.eswa.2020.113514

[8] Lopes, U. K.; Valiati, J. F. Pre-trained convolutional neural networks as feature extractors for tuberculosis detection. *Computers in Biology and Medicine* **2017**, *89*, 135–143. https://doi.org/10.1016/j.compbiomed.2017.08.001

[9] Kumar, J. S.; Balamurugan, S. A. A.; Sasikala, S. Analysis of Deep Learning Techniques for Tuberculosis Disease. *SN Computer Science* **2021**, *2*(4). https://doi.org/10.1007/s42979-021-00680-y

[10] Rahimzadeh, M.; Attar, A. A modified deep convolutional neural network for detecting COVID-19 and pneumonia from chest X-ray images based on the concatenation of Xception and ResNet50V2. *Informatics in Medicine Unlocked* **2020**, *19*, 100360. https://doi.org/10.1016/j.imu.2020.100360

[11] Luján-García, J. E.; Yáñez-Márquez, C.; Villuendas-Rey, Y.; Camacho-Nieto, O. A Transfer Learning Method for Pneumonia Classification and Visualization. *Applied Sciences* **2020**, *10*(8), 2908. https://doi.org/10.3390/app10082908

[12] Stephen, O.; Sain, M.; Maduh, U. J.; Jeong, D.-U. An Efficient Deep Learning Approach to Pneumonia Classification in Healthcare. *Journal of Healthcare Engineering* **2019**, 2019, 1–7. https://doi.org/10.1155/2019/4180949

[13] Lascu, M.-R. Deep Learning in Classification of Covid-19 Coronavirus, Pneumonia and Healthy Lungs on CXR and CT Images. *Journal of Medical and Biological Engineering* **2021**, *41*(4), 514–522. https://doi.org/10.1007/s40846-021-00630-2

[14] Sirazitdinov, I.; Kholiavchenko, M.; Mustafaev, T.; Yixuan, Y.; Kuleev, R.; Ibragimov, B. Deep neural network ensemble for pneumonia localization from a large-scale chest x-ray database. *Computers & Electrical Engineering* **2019**, *78*, 388–399. https://doi.org/10.1016/j.compeleceng.2019.08.004

[15] Asnaoui, K. E. Design ensemble deep learning model for pneumonia disease classification. *International Journal of Multimedia Information Retrieval* **2021**, *10*(1), 55–68. https://doi.org/10.1007/s13735-021-00204-7

[16] Sirazitdinov, I.; Kholiavchenko, M.; Mustafaev, T.; Yixuan, Y.; Kuleev, R.; Ibragimov, B. Deep neural network ensemble for pneumonia localization from a large-scale chest x-ray database. *Computers & Electrical Engineering* **2019**, *78*, 388–399. https://doi.org/10.1016/j.compeleceng.2019.08.004

[17] Goyal, S.; Singh, R. Detection and classification of lung diseases for pneumonia and Covid-19 using machine and deep learning techniques. *Journal of Ambient Intelligence and Humanized Computing* **2021**, *14*(4), 3239–3259. https://doi.org/10.1007/s12652-021-03464-7

[18] Rahmani, A. M.; Azhir, E.; Naserbakht, M.; Mohammadi, M.; Aldalwie, A. H. M.; Majeed, M. K.; Karim, S. H. T.; Hosseinzadeh, M. Automatic COVID-19 detection mechanisms and approaches from medical images: a systematic review. *Multimedia Tools and Applications* **2022**, *81*(20), 28779–28798. https://doi.org/10.1007/s11042-022-12952-7

[19] Soomro, T. A.; Zheng, L.; Afifi, A. J.; Ali, A.; Yin, M.; Gao, J. Artificial intelligence (AI) for medical imaging to combat coronavirus disease (COVID-19): a detailed review with direction for future research. *Artificial Intelligence Review* **2021**, *55*(2), 1409–1439. https://doi.org/10.1007/s10462-021-09985-z

[20] Heidari, A.; Navimipour, N. J.; Unal, M.; Toumaj, S. The COVID-19 epidemic analysis and diagnosis using deep learning: A systematic literature review and future directions. *Computers in Biology and Medicine* **2021**, *141*, 105141. https://doi.org/10.1016/j.compbiomed.2021.105141

[21] Gomes, R.; Kamrowski, C.; Langlois, J.; Rozario, P.; Dircks, I.; Grottodden, K.; Martinez, M.; Tee, W. Z.; Sargeant, K.; LaFleur, C.; Haley, M. A Comprehensive Review of Machine Learning Used to Combat COVID-19. *Diagnostics* **2022**, *12*(8), 1853. https://doi.org/10.3390/diagnostics12081853

[22] Alafif, T.; Tehame, A. M.; Bajaba, S.; Barnawi, A.; Zia, S. Machine and Deep Learning towards COVID-19 Diagnosis and Treatment: Survey, Challenges, and Future Directions. *International Journal of Environmental Research and Public Health* **2021**, *18*(3), 1117. https://doi.org/10.3390/ijerph18031117

[23] Shorten, C.; Khoshgoftaar, T. M.; Furht, B. Deep Learning applications for COVID-19. *Journal of Big Data* **2021**, *8*(1). https://doi.org/10.1186/s40537-020-00392-9

[24] Rehman, A.; Iqbal, M. A.; Xing, H.; Ahmed, I. COVID-19 Detection Empowered with Machine Learning and Deep Learning Techniques: A Systematic Review. *Applied Sciences* **2021**, *11*(8), 3414. https://doi.org/10.3390/app11083414

[25] Bekele, S. K.; Gutema, M. G.; Tujuba, E. D.; Jain, R.; Bekuma, Y. IoT-Deep Learning Based Face Mask Detection System for Entrance and Exit Door. *International Journal of Electrical and Electronics Research* **2022**, *10*(3), 751–759. https://doi.org/10.37391/ijeer.100356

[26] Munadi, K.; Muchtar, K.; Maulina, N.; Pradhan, B. Image Enhancement for Tuberculosis Detection Using Deep Learning. *IEEE Access* **2020**, *8*, 217897–217907. https://doi.org/10.1109/access.2020.3041867

[27] Balakrishnan, V.; Kherabi, Y.; Ramanathan, G.; Paul, S. A.; Tiong, C. K. Machine learning approaches in diagnosing tuberculosis through biomarkers - A systematic review. *Progress in Biophysics and Molecular Biology* **2023**, *179*, 16–25. https://doi.org/10.1016/j.pbiomolbio.2023.03.001

[28] Jaiswal, A. K.; Tiwari, P.; Kumar, S.; Gupta, D.; Khanna, A.; Rodrigues, J. J. P. C. Identifying pneumonia in chest X-rays: A deep learning approach. Measurement **2019**, *145*, 511–518. https://doi.org/10.1016/j.measurement.2019.05.076

[29] Ahmed, M. S.; Rahman, A.; AlGhamdi, F.; AlDakheel, S.; Hakami, H.; AlJumah, A.; AlIbrahim, Z.; Youldash, M.; Khan, M. A. A.; Ahmed, M. I. B. Joint Diagnosis of Pneumonia, COVID-19, and Tuberculosis from Chest X-ray Images: A Deep Learning Approach. *Diagnostics* **2023**, *13*(15), 2562. https://doi.org/10.3390/diagnostics13152562

[30] Nahiduzzaman, Md.; Goni, M. O. F.; Islam, Md. R.; Sayeed, A.; Anower, Md. S.; Ahsan, M.; Haider, J.; Kowalski, M. Detection of various lung diseases including COVID-19 using extreme learning machine algorithm based on the features extracted from a lightweight CNN architecture. *Journal of Applied Biomedicine* **2023**, *43* (3), 528–550. https://doi.org/10.1016/j.bbe.2023.06.003

[31] Ali, M. U.; Kallu, K. D.; Masood, H.; Tahir, U.; Gopi, C. V. V. M.; Zafar, A.; Lee, S. W. A CNN-Based Chest Infection Diagnostic Model: A Multistage Multiclass Isolated and Developed Transfer Learning Framework. *International Journal of Intelligent Systems* **2023**, 2023, 1–12. https://doi.org/10.1155/2023/6850772

[32] Kabir, M. M.; Mridha, M. F.; Rahman, A.; Hamid, Md. A.; Monowar, M. M. Detection of COVID-19, pneumonia, and tuberculosis from radiographs using AI-driven knowledge distillation. *Heliyon* **2024**, *10*(5), e26801. https://doi.org/10.1016/j.heliyon.2024.e26801

[33] Kaewlek, T.; Tanyong, K.; Chakkaeo, J.; Kladpree, S.; Chusin, T.; Yabsantia, S.; Udee, N. Classification of Pneumonia, Tuberculosis, and COVID-19 on Computed Tomography Images using Deep Learning. *Trends in Sciences* **2023**, *20*(11), 6974. https://doi.org/10.48048/tis.2023.6974

[34] Singh, S.; Kumar, M.; Kumar, A.; Verma, B. K.; Abhishek, K.; Selvarajan, S. Efficient pneumonia detection using Vision Transformers on chest X-rays. *Scientific Reports* **2024**, *14*(1). https://doi.org/10.1038/s41598-024-52703-2

[35] Monowar, K. F.; Hasan, Md. A. M.; Shin, J. Lung Opacity Classification With Convolutional Neural Networks Using Chest X-rays; 11th International Conference on Electrical and Computer Engineering (ICECE), *IEEE*, **2020**. https://doi.org/10.1109/icece51571.2020.9393135

[36] Oğuz, Ç.; Yağanoğlu, M. Detection of COVID-19 using deep learning techniques and classification methods. *Information Processing & Management* **2022**, *59*(5), 103025. https://doi.org/10.1016/j.ipm.2022.103025

[37] Hussain, E.; Hasan, M.; Rahman, M. A.; Lee, I.; Tamanna, T.; Parvez, M. Z. CoroDet: A deep learning based classification for COVID-19 detection using chest X-ray images. *Chaos Solitons & Fractals* **2020**, *142*, 110495. https://doi.org/10.1016/j.chaos.2020.110495

[38] COVID-19 Radiography Database. Kaggle. https://www.kaggle.com/datasets/tawsifurrahman/covid19-radiography-database (accessed 2024-02-19).

[39] Chest X-Ray Images (Pneumonia). Kaggle. https://www.kaggle.com/datasets/paultimothymooney/chest-xray-pneumonia/code?resource=download (accessed 2024-02-17).

[40] Tuberculosis (TB) Chest X-ray Database. Kaggle. https://www.kaggle.com/datasets/tawsifurrahman/tuberculosis-tb-chest-xray-dataset (accessed 2024-02-10)

[41] Rahman, M. M.; Manik, Md. M. H.; Islam, Md. M.; Mahmud, S.; Kim, J.-H. An Automated System to Limit COVID-19 Using Facial Mask Detection in Smart City Network. *2020 IEEE International IOT, Electronics and Mechatronics Conference (IEMTRONICS)* **2020**. https://doi.org/10.1109/iemtronics51293.2020.9216386

[42] Loey, M.; Manogaran, G.; Taha, M. H. N.; Khalifa, N. E. M. A hybrid deep transfer learning model with machine learning methods for face mask detection in the era of the COVID-19 pandemic. *Measurement* **2020**, *167*, 108288. https://doi.org/10.1016/j.measurement.2020.108288



ASEAN
Journal of Scientific and Technological Reports
Online ISSN:2773-8752

ASEAN
Journal of Scientific and Technological Reports
Online ISSN: 2773-8752

Article type

Type of the Paper (Article, Review, Communication, etc.) *about 8,000 words maximum*

Title (Palatino Linotype 18 pt, bold)

Firstname Lastname[1], Firstname Lastname[2] and Firstname Lastname[2*]

[1] Affiliation 1; e-mail@e-mail.com
[2] Affiliation 2; e-mail@e-mail.com
* Correspondence: e-mail@e-mail.com; (one corresponding authors, add author initials)

Citation:
Lastname, F.; Lastname, F.; Lastname, F. Title. *ASEAN J. Sci. Tech. Report.* **2023**, *26*(X), xx-xx. https://doi.org/10.55164/ajstr.vxxix.xxxxxx

Article history:
Received: date
Revised: date
Accepted: date
Available online: date

Publisher's Note:
This article is published and distributed under the terms of the Thaksin University.

Abstract: A single paragraph of about 400 words maximum. Self-contained and concisely describe the reason for the work, methodology, results, and conclusions. Uncommon abbreviations should be spelled out at first use. We strongly encourage authors to use the following style of structured abstracts, but without headings: (1) Background: Place the question addressed in a broad context and highlight the purpose of the study; (2) Methods: briefly describe the main methods or treatments applied; (3) Results: summarize the article's main findings; (4) Conclusions: indicate the main conclusions or interpretations.

Keywords: keyword 1; keyword 2; keyword 3 (List three to ten pertinent keywords specific to the article yet reasonably common within the subject discipline.)

1. Introduction

The introduction should briefly place the study in a broad context and highlight why it is crucial. It should define the purpose of the work and its significance. The current state of the research field should be carefully reviewed and critical publications cited. Please highlight controversial and diverging hypotheses when necessary. Finally, briefly mention the main aim of the work. References should be numbered in order of appearance and indicated by a numeral or numerals in square brackets—e.g., [1] or [2, 3], or [4–6]. See the end of the document for further details on references.

2. Materials and Methods

The materials and methods should be described with sufficient details to allow others to replicate and build on the published results. Please note that your manuscript's publication implicates that you must make all materials, data, computer code, and protocols associated with the publication available to readers. Please disclose at the submission stage any restrictions on the availability of materials or information. New methods and protocols should be described in detail, while well-established methods can be briefly described and appropriately cited.

Interventional studies involving animals or humans, and other studies that require ethical approval, must list the authority that provided approval and the corresponding ethical approval code.

2.1 Subsection

2.1.1. Subsubsection

3. Results and Discussion

This section may be divided by subheadings. It should provide a concise and precise description of the experimental results, their interpretation, as well as the experimental conclusions that can be drawn.Authors should discuss the results and how they can be interpreted from previous studies and the working hypotheses. The findings and their implications should be discussed in the broadest context possible. Future research directions may also be highlighted.

3.1. Subsection

3.1.1. Subsubsection

3.2. Figures, Tables, and Schemes

All figures and tables should be cited in the main text as Figure 1, Table 1, etc.



Figure 1. This is a figure. Schemes follow the same formatting.

Table 1. This is a table. Tables should be placed in the main text near the first time they are cited.

Title 1	Title 2	Title 3
entry 1	data	data
entry 2	data	data [1]

[1] Table may have a footer.

3.3. Formatting of Mathematical Components

This is example 1 of an equation:

$$a = 1, \tag{1}$$

The text following an equation need not be a new paragraph. Please punctuate equations as regular text. This is example 2 of an equation:

$$a = b + c + d + e + f + g + h + i + j + k + l + m + n + o + p + q + r + s + t + u \tag{2}$$

The text following an equation need not be a new paragraph. Please punctuate equations as regular text. The text continues here.

4. Conclusions

Concisely restate the hypothesis and most important findings. Summarize the significant findings, contributions to existing knowledge, and limitations. What are the future directions? Conclusions MUST be well stated, linked to original research question & limited to supporting results.

5. Acknowledgements

Should not be used to acknowledge funders – funding will be entered as a separate. As a matter of courtesy, we suggest you inform anyone whom you acknowledge.

Author Contributions: For research articles with several authors, a short paragraph specifying their individual contributions must be provided. The following statements should be used "Conceptualization, X.X. and Y.Y.; methodology, X.X.; software, X.X.; validation, X.X., Y.Y. and Z.Z.; formal analysis, X.X.; investigation, X.X.; resources, X.X.; data curation, X.X.; writing—original draft preparation, X.X.; writing—review and editing, X.X.; visualization, X.X.; supervision, X.X.; project administration, X.X.; funding acquisition, Y.Y. All authors have read and agreed to the published version of the manuscript." Please turn to the CRediT taxonomy for the term explanation. Authorship must be limited to those who have contributed substantially to the work reported.

Funding: Please add: "This research received no external funding" or "This research was funded by NAME OF FUNDER, grant number XXX" and "The APC was funded by XXX". Check carefully that the details given are accurate and use the standard spelling of funding agency names at https://search.crossref.org/funding. Any errors may affect your future funding.

Conflicts of Interest: Declare conflicts of interest or state "The authors declare no conflict of interest." Authors must identify and declare any personal circumstances or interest that may be perceived as inappropriately influencing the representation or interpretation of reported research results. Any role of the funders in the design of the study; in the collection, analyses or interpretation of data; in the writing of the manuscript, or in the decision to publish the results must be declared in this section. If there is no role, please state "The funders had no role in the design of the study; in the collection, analyses, or interpretation of data; in the writing of the manuscript, or in the decision to publish the results".

References

References must be numbered in order of appearance in the text (including citations in tables and legends) and listed individually at the end of the manuscript. We recommend preparing the references with a bibliography software package, such as EndNote, ReferenceManager to avoid typing mistakes and duplicated references. Include the digital object identifier (DOI) for all references where available.

Citations and references in the Supplementary Materials are permitted provided that they also appear in the reference list here.

In the text, reference numbers should be placed in square brackets [ ] and placed before the punctuation; for example [1], [1–3] or [1, 3]. For embedded citations in the text with pagination, use both parentheses and brackets to indicate the reference number and page numbers; for example [5] (p. 100), or [6] (pp. 101–105).

Using the American Chemical Society (ACS) referencing style

[1] Author 1, A.B.; Author 2, C.D. Title of the article. *Abbreviated Journal Name* Year, *Volume*, page range.

[2] Author 1, A.; Author 2, B. Title of the chapter. In *Book Title*, 2nd ed.; Editor 1, A., Editor 2, B., Eds.; Publisher: Publisher Location, Country. **2007**, Volume *3*, pp. 154–196.

[3] Author 1, A.; Author 2, B. *Book Title*, 3rd ed.; Publisher: Publisher Location, Country, **2008**, pp. 154–196.
[4] Author 1, A.B.; Author 2, C. Title of Unpublished Work. *Abbreviated Journal Name* stage of publication (under review; accepted; in press).
[5] Author 1, A.B. (University, City, State, Country); Author 2, C. (Institute, City, State, Country). Personal communication, 2012.
[6] Author 1, A.B.; Author 2, C.D.; Author 3, E.F. Title of Presentation. In Title of the Collected Work (if available), Proceedings of the Name of the Conference, Location of Conference, Country, Date of Conference; Editor 1, Editor 2, Eds. (if available); Publisher: City, Country, Year (if available); Abstract Number (optional), Pagination (optional).
[7] Author 1, A.B. Title of Thesis. Level of Thesis, Degree-Granting University, Location of University, Date of Completion.
[8] Title of Site. Available online: URL (accessed on Day Month Year).

Reviewers sugestion

1. Name, Address, e-mail
2. Name, Address, e-mail
3. Name, Address, e-mail
4. Name, Address, e-mail

URL link:

Notes for Authors >>
https://drive.google.com/file/d/1r0zegnIVeQqe4iLQyT1xDEIinNggINPD/view?usp=sharing
https://drive.google.com/file/d/1r0zegnIVeQqe4iLQyT1xDEIinNggINPD/view?usp=sharing

Online Submissions >> https://ph02.tci-thaijo.org/index.php/tsujournal/user/register

Current Issue >> https://ph02.tci-thaijo.org/index.php/tsujournal/issue/view/16516

AJSTR Publication Ethics and Malpractice >> https://ph02.tci-thaijo.org/index.php/tsujournal/ethics

Journal Title Abbreviations >> http://library.caltech.edu/reference/abbreviations



ASEAN
Journal of Scientific and Technological Reports
Online ISSN:2773-8752



ASEAN
Journal of Scientific and Technological Reports
Online ISSN:2773-8752

ASEAN Journal of Scientific and Technological Reports (AJSTR)
Institute of Research and Innovation, Thaksin University, Phatthalung Campus
222 Moo. 2, Baan Prao Sub-District, Papayom District, Phatthalung, 93210, Thailand
Tel. +668 1540 7304

